frontiers | Research Topics

Atrial fibrillation: Technologies for investigation, monitoring and treatment, volume II

Edited by
Omer Berenfeld, Axel Loewe, Juan Pablo Martínez, Jose F. Rodriguez Matas and Valentina Corino

Published in
Frontiers in Physiology
Frontiers in Cardiovascular Medicine
Frontiers in Medicine

ISSN 1664-8714
ISBN 978-2-8325-2466-4
DOI 10.3389/978-2-8325-2466-4

About Frontiers

Frontiers is more than just an open access publisher of scholarly articles: it is a pioneering approach to the world of academia, radically improving the way scholarly research is managed. The grand vision of Frontiers is a world where all people have an equal opportunity to seek, share and generate knowledge. Frontiers provides immediate and permanent online open access to all its publications, but this alone is not enough to realize our grand goals.

Frontiers journal series

The Frontiers journal series is a multi-tier and interdisciplinary set of open-access, online journals, promising a paradigm shift from the current review, selection and dissemination processes in academic publishing. All Frontiers journals are driven by researchers for researchers; therefore, they constitute a service to the scholarly community. At the same time, the *Frontiers journal series* operates on a revolutionary invention, the tiered publishing system, initially addressing specific communities of scholars, and gradually climbing up to broader public understanding, thus serving the interests of the lay society, too.

Dedication to quality

Each Frontiers article is a landmark of the highest quality, thanks to genuinely collaborative interactions between authors and review editors, who include some of the world's best academicians. Research must be certified by peers before entering a stream of knowledge that may eventually reach the public - and shape society; therefore, Frontiers only applies the most rigorous and unbiased reviews. Frontiers revolutionizes research publishing by freely delivering the most outstanding research, evaluated with no bias from both the academic and social point of view. By applying the most advanced information technologies, Frontiers is catapulting scholarly publishing into a new generation.

What are Frontiers Research Topics?

Frontiers Research Topics are very popular trademarks of the *Frontiers journals series*: they are collections of at least ten articles, all centered on a particular subject. With their unique mix of varied contributions from Original Research to Review Articles, Frontiers Research Topics unify the most influential researchers, the latest key findings and historical advances in a hot research area.

Find out more on how to host your own Frontiers Research Topic or contribute to one as an author by contacting the Frontiers editorial office: frontiersin.org/about/contact

Atrial fibrillation: Technologies for investigation, monitoring and treatment, volume II

Topic editors

Omer Berenfeld — University of Michigan, United States
Axel Loewe — Karlsruhe Institute of Technology (KIT), Germany
Juan Pablo Martínez — University of Zaragoza, Spain
Jose F. Rodriguez Matas — Polytechnic University of Milan, Italy
Valentina Corino — Polytechnic University of Milan, Italy

Citation

Berenfeld, O., Loewe, A., Martínez, J. P., Rodriguez Matas, J. F., Corino, V., eds. (2023). *Atrial fibrillation: Technologies for investigation, monitoring and treatment, volume II*. Lausanne: Frontiers Media SA. doi: 10.3389/978-2-8325-2466-4

Table of contents

frontiers | Frontiers in Physiology

TYPE Editorial
PUBLISHED 04 May 2023
DOI 10.3389/fphys.2023.1209458

OPEN ACCESS

EDITED AND REVIEWED BY
Ruben Coronel,
University of Amsterdam, Netherlands

*CORRESPONDENCE
Omer Berenfeld,
oberen@med.umich.edu
Jose F. Rodriguez Matas,
josefelix.rodriguezmatas@polimi.it

RECEIVED 20 April 2023
ACCEPTED 25 April 2023
PUBLISHED 04 May 2023

CITATION
Berenfeld O, Corino V, Loewe A, Martínez JP and Rodriguez Matas JF (2023), Editorial: Atrial Fibrillation: Technologies for Investigation, Monitoring and Treatment, Volume II. *Front. Physiol.* 14:1209458. doi: 10.3389/fphys.2023.1209458

Editorial: Atrial Fibrillation: Technologies for Investigation, Monitoring and Treatment, Volume II

Omer Berenfeld[1]*, Valentina Corino[2,3], Axel Loewe[4], Juan Pablo Martínez[5,6] and Jose F. Rodriguez Matas[7]*

[1]Center for Arrhythmia Research, University of Michigan, Ann Arbor, MI, United States, [2]Biosignals, Bioimaging and Bioinformatics Laboratory (B3Lab), Department of Electronics, Information and Bioengineering (DEIB), Politecnico di Milano, Milano, Italy, [3]Cardio Tech-Lab, Centro Cardiologico Monzino IRCCS, Milan, Italy, [4]Institute of Biomedical Engineering, Karlsruhe Institute of Technology (KIT), Karlsruhe, Germany, [5]Biomedical Signal Interpretation and Computational Simulation Group, Aragón Institute of Engineering Research, IIS Aragón, Universidad de Zaragoza, Zaragoza, Spain, [6]Centro de Investigación Biomédica en Red en Bioingeniería, Zaragoza, Spain, [7]LaBS, Department of Chemistry, Material and Chemical Engineering "Giulio Natta", Politecnico di Milano, Milano, Italy

KEYWORDS

atrial fibrillation, mapping, detection, ablation, rate control, prediction, machine learning

Editorial on the Research Topic
Atrial Fibrillation: Technologies for Investigation, Monitoring and Treatment, Volume II

Introduction

Following the great interest in the first edition of the Frontiers Research Topic devoted to technology related to the understanding, management, and therapy of atrial fibrillation (AF), we are glad to present a second collection of additional articles on the Research Topic. AF remains the most common sustained clinical arrhythmia (Chugh et al., 2014; Zoni-Berisso et al., 2014), the leading cause of embolic stroke, and an increased risk for heart failure and mortality (Benjamin et al., 2017; Roth et al., 2017). AF is a major societal and financial burden (Kowalski et al., 2022) likely due to its heterogenous, multifactorial, and progressive nature as well as its suboptimal therapy (Heijman et al., 2018). It has been recently demonstrated that early AF rhythm-control therapies of ablation or antiarrhythmic drugs within the first year of AF diagnosis are beneficial (Eckardt et al., 2022; Dickow et al., 2023) but come at a heavy financial cost (Gottschalk et al., 2023) that is calling for further research and developments. This second volume of the Research Topic continues to aim at the challenge of the burden of AF. It consists of 15 original papers that focus, as with the first edition, on technological advances for the improved understanding of AF and better diagnosis, management, and therapy of arrhythmia. A total of 95 students and faculty of diverse scientific backgrounds have contributed to the papers and highlighted the importance of multidisciplinary research for advancing the understanding and therapy of AF. We are grateful to all the contributors to the first and present Research Topic articles

for their time and efforts. The articles in this second volume of the Research Topic can be grouped and are briefly summarized as follows.

Mapping, characterizing, and predicting atrial fibrillation

It has been proposed that high dominant frequency and rotor regions play a significant role in perpetuating AF. Ehnesh et al. analyzed non-contact recordings from inside the left atrium of 10 persistent AF patients and found that spatial correlation between these two features at any given time is poor but they colocalize in certain regions over time, mainly in the septum. In patients in whom high-dominant frequency ablation terminated the AF, there was some overlapping with longer-lasting rotor sites, but the relationship was complex overall. The study by Jenkins et al. focused on the accuracy of quantifying the lifetime of phase singularity points representing AF re-entrant patterns. The paper argues that the duration of the observation can affect the likelihood of detecting long vs. short lifetimes and suggests that to minimize the dependency on the observation duration, the individual lifetimes, rather than averages of probability distributions, should be considered.

Regions characterized by low voltage activity in atrial mapping are considered to be arrhythmogenic and a target for ablation. Van Schie et al. used a specialized multiple-electrode system to perform intraoperative simultaneous unipolar and omnipolar voltage mapping in opposing endocardial and epicardial right atrial surfaces during sinus rhythm. The study found that the low voltage regions frequently appeared exclusively on either one of the surfaces and suggests that the addition of the omnipolar mapping, where far field and directionality effects are minimized, to the unipolar mapping adds fidelity to the localization of low voltage regions.

The non-invasive electrocardiographic imaging (ECGi) approach is proposed for an effective mapping of AF and ablation guidance but is still a challenging technology. Fambuena-Santos et al. used ECGi and a new rotor detection algorithm to map AF in patients that underwent pulmonary vein isolation. They found that the total rotor number was higher in patients with follow-up arrhythmia recurrence than in those that remained in sinus rhythm and in whom the phase singularity point concentration was higher in the pulmonary vein region. The consistency between the findings on re-entrant pattern distribution and the expected mechanisms suggested the technology could offer useful information.

Efforts to optimize the inverse problem solution at the center of the ECGi approach by various time-frequency decomposition techniques are presented in the article by Yadan et al. the authors applied different mode decomposition algorithms on five simulated and two AF patients datasets to rank the accuracy and efficiency of their performance to hopefully improve the solution of the inverse problem in the clinic.

Approximately 30% of patients undergoing cardiac surgery develop AF post-operatively and predicting who will develop arrhythmia on an individual basis could guide therapeutic management. Kang He et al. developed a machine learning method for the single-lead monitoring of patients after cardiac surgery and concluded that their method could improve the detection of postoperative AF in those patients. Ah Ran Oh et al. also used a machine learning method in post-operative patients, however with non-cardiac surgery, and found that including the top five variables of age, lung operation, operation duration, history of coronary artery disease, and hypertension results in the area under the receiver operating characteristic curve for postoperative AF of 0. 80 that indicates the ability of prediction.

Body surface potential maps were processed by McCann et al. to predict catheter ablation outcomes in persistent AF patients. The investigators developed new indices based in part on a principal component analysis to quantify the reconstruction of the full set of the body surface signals with a subset of the signals, as well as a non-dipolar component index. They then associated the levels of those indices with restoring sinus rhythm or recurrence of arrhythmia following single-procedure catheter ablation.

Atrial fibrillation ablation and drug effects

Radiofrequency (RF) catheter ablation to terminate AF is challenging in some, particularly persistent, AF patients, and efforts are ongoing to increase its success rate. Successful catheter-based RF ablation depends on adequate lesion formation. Alken et al. analyzed contact force and local impedance in 730 RF applications of a novel open-irrigated single-tip catheter in 20 repeat AF ablation patients. A drop of more than 20 Ω in local impedance following the ablation was considered as an adequate lesion formation and was found to be better predictable by the combined rather than a separated force and baseline impedance quantification.

Machine learning methods have been proposed to improve the guidance of ablation. Ogbomo-Harmitt et al. studied the feature attribution of AF data subjected to deep learning algorithms to interpret the results of the algorithms and enhance confidence in the proposed ablation strategy. They used simplified computer models based on patients' MRI data to suggest that the regions with the most informative features colocalized with pro-arrhythmogenic regions.

In silico studies are also used to interpret and guide pharmacological intervention to terminate AF. Dasi et al. performed simulations on a population of human structurally normal atrial computer models that suggest that AF depends on the formation of discordant alternans. Cardioversion using 10 antiarrhythmic drugs applied to those models was found to be optimal when refractoriness was maximized and was predictable with 70% accuracy from either ionic or ECG properties. Machine learning methods are also used in computer simulation studies to better understand the relationships between pharmacological treatments and the characteristics of the underlying atrial tissue. Sanchez de la Nava et al. used artificial intelligence in a computational proof-of-concept study with the ability to predict susceptibility for conduction blocks in fibrotic atrial tissue and antiarrhythmic drug regime. Simulations on a population of simplified 2D atrial models suggest that fibrosis can alter the expected behavior of several commonly used drugs and that the model profile leading to the different effects might be predicted by data analysis using artificial intelligence.

In most patients, in addition to efforts to terminate AF, concomitant pharmacological efforts are also made to decrease the ventricular rate (Heijman et al., 2021) and would benefit from a better understanding. Karlsson et al. studied the influence of several β-blockers and calcium channel blockers on the atrio-ventricular node conduction in a cohort of permanent AF patients and found differential delays that could be important in treatment selection. On a related topic, Plappert et al. demonstrated that the incorporation of the effects of the autonomic nervous system on conduction in a mathematical model of the atrio-ventricular node is necessary to replicate ventricular rate changes in clinical tilt test data. Abdollahpur et al. investigated respiratory modulation as a surrogate for the autonomic nervous system modulation of the atrial activity during AF by analysis of the f-wave frequency. Their proposed orthogonal subspace projection approach (Varon et al., 2019) showed robustness in detecting respiratory-induced changes on simulated data but results on clinical data were heterogeneous without significant differences between baseline and deep breathing.

Conclusion

We are excited to present a second Research Topic collection of technology-inclined articles describing recent experimental, computational, and clinical studies on AF. The articles ultimately apply to ablation and pharmacological therapies to restore sinus rhythm or control of the ventricular rate and highlight the need for improved comprehensive management of AF and its associated symptoms (Kirchhof, 2017). We hope that scientists, engineers, and clinicians, as well as patients, interested in the topic, will find this overview of basic and translational research trends to be inspiring and promoting a better understanding of the diagnosis and therapies of AF.

Author contributions

All authors listed have made a substantial, direct, and intellectual contribution to the work and approved it for publication.

Funding

OB acknowledges the support from the National Institutes of Health National Heart, Lung, and Blood Institute grants R01-HL118304, R21-HL15369, and R21-EB032661, as well as research grants from Abbott, Medtronic Inc., and CoreMap Inc. JPM acknowledges support by Spain Ministerio de Ciencia e Innovación grant PID 2019-104881RB-I00 and reference group T39-20R (Aragón Government cofounded by FEDER 2014-2020 "Building Europe from Aragon"). VC, AL, JM, and JR acknowledge the support of the European Union's Horizon 2020 Research and Innovation Program under the Marie Skłodowska-Curie Grant Agreement No. 766082. AL acknowledges support from the German Research Foundation (LO 2093/9-1), the European Union's Horizon 2020 research and innovation program under the Marie Skłodowska-Curie grant agreement No. 860974 and from the European High-Performance Computing Joint Undertaking EuroHPC (JU) under grant agreement No 955495. The JU receives support from the European Union's Horizon 2020 research and innovation program from France, Italy, Germany, Austria, Norway, and Switzerland. JFRM acknowledges support from the Italian Ministry of Education, University and Research, Grant number 1613 FISR 2019_03221, CECOMES.

Conflict of interest

The authors declare that the research was conducted in the absence of any commercial or financial relationships that could be construed as a potential conflict of interest.

Publisher's note

References

Benjamin, E. J., Blaha, M. J., Chiuve, S. E., Cushman, M., Das, S. R., Deo, R., et al. (2017). Heart disease and stroke statistics-2017 update: A report from the American heart association. *Circulation* 135 (10), e146–e603. doi:10.1161/cir.0000000000000485

Chugh, S. S., Havmoeller, R., Narayanan, K., Singh, D., Rienstra, M., Benjamin, E. J., et al. (2014). Worldwide epidemiology of atrial fibrillation: A global burden of disease 2010 study. *Circulation* 129 (8), 837–847. doi:10.1161/CIRCULATIONAHA.113.005119

Dickow, J., Kany, S., Roth Cardoso, V., Ellinor, P. T., Gkoutos, G. V., Van Houten, H. K., et al. (2023). Outcomes of early rhythm control therapy in patients with atrial fibrillation and a high comorbidity burden in large real-world cohorts. *Circulation Arrhythmia Electrophysiol.*, e011585. doi:10.1161/CIRCEP.122.011585

Eckardt, L., Sehner, S., Suling, A., Borof, K., Breithardt, G., Crijns, H., et al. (2022). Attaining sinus rhythm mediates improved outcome with early rhythm control therapy of atrial fibrillation: The EAST-AFNET 4 trial. *Eur. heart J.* 43 (40), 4127–4144. doi:10.1093/eurheartj/ehac471

Gottschalk, S., Kany, S., Konig, H. H., Crijns, H. J., Vardas, P., Camm, A. J., et al. (2023). Cost-effectiveness of early rhythm control vs. usual care in atrial fibrillation care: An analysis based on data from the EAST-AFNET 4 trial. *Europace*, euad051. doi:10.1093/europace/euad051

Heijman, J., Guichard, J. B., Dobrev, D., and Nattel, S. (2018). Translational challenges in atrial fibrillation. *Circulation Res.* 122 (5), 752–773. doi:10.1161/CIRCRESAHA.117.311081

Heijman, J., Hohnloser, S. H., and Camm, A. J. (2021). Antiarrhythmic drugs for atrial fibrillation: Lessons from the past and opportunities for the future. *Europace* 23 (2), ii14–ii22. doi:10.1093/europace/euaa426

Kirchhof, P. (2017). The future of atrial fibrillation management: Integrated care and stratified therapy. *Lancet* 390 (10105), 1873–1887. doi:10.1016/S0140-6736(17)31072-3

Kowalski, M., Shah, R., Akhrass, P., and Parikh, V. (2022). Economics and laboratory efficiency of atrial fibrillation ablation. *Curr. Opin. Cardiol.* 37 (1), 22–29. doi:10.1097/HCO.0000000000000932

Roth, G. A., Johnson, C., Abajobir, A., Abd-Allah, F., Abera, S. F., Abyu, G., et al. (2017). Global, regional, and national burden of cardiovascular diseases for 10 causes, 1990 to 2015. *J. Am. Coll. Cardiol.* 70 (1), 1–25. doi:10.1016/j.jacc.2017.04.052

Varon, C., Lazaro, J., Bolea, J., Hernando, A., Aguilo, J., Gil, E., et al. (2019). Unconstrained estimation of HRV indices after removing respiratory influences from heart rate. *IEEE J. Biomed. Health Inf.* 23 (6), 2386–2397. doi:10.1109/JBHI.2018.2884644

Zoni-Berisso, M., Lercari, F., Carazza, T., and Domenicucci, S. (2014). Epidemiology of atrial fibrillation: European perspective. *Clin. Epidemiol.* 6, 6213–6220. doi:10.2147/CLEP.S47385

frontiers | Frontiers in Physiology

TYPE Original Research
PUBLISHED 05 August 2022
DOI 10.3389/fphys.2022.946718

OPEN ACCESS

EDITED BY
Juan Pablo Martínez,
University of Zaragoza, Spain

REVIEWED BY
Vijay S. Chauhan,
Peter Munk Cardiac Centre, Canada
Carlos Sanchez,
University of Zaragoza, Spain

*CORRESPONDENCE
Mahmoud Ehnesh,
me196@leicester.ac.uk

SPECIALTY SECTION
This article was submitted to Cardiac Electrophysiology, a section of the journal Frontiers in Physiology

RECEIVED 17 May 2022
ACCEPTED 14 July 2022
PUBLISHED 05 August 2022

CITATION
Ehnesh M, Li X, Almeida TP, Chu GS, Dastagir N, Stafford PJ, Ng GA and Schlindwein FS (2022), Evaluating spatial disparities of rotor sites and high dominant frequency regions during catheter ablation for PersAF patients targeting high dominant frequency sites using non-contacting mapping. *Front. Physiol.* 13:946718. doi: 10.3389/fphys.2022.946718

Evaluating spatial disparities of rotor sites and high dominant frequency regions during catheter ablation for PersAF patients targeting high dominant frequency sites using non-contacting mapping

Mahmoud Ehnesh[1]*, Xin Li[1,2], Tiago P. Almeida[1,2], Gavin S. Chu[2,3], Nawshin Dastagir[4], Peter J. Stafford[2,3], G. André Ng[2,3] and Fernando S. Schlindwein[1,3]

[1]School of Engineering, University of Leicester, Leicester, United Kingdom, [2]Department of Cardiovascular Sciences, Glenfield Hospital, Leicester, United Kingdom, [3]National Institute for Health Research Leicester Cardiovascular Biomedical Research Centre, Leicester, United Kingdom, [4]Department of International Foundation, Massey University, Auckland, New Zealand

Purpose: Several studies have emphasised the significance of high dominant frequency (HDF) and rotors in the perpetuation of AF. However, the co-localisation relationship between both attributes is not completely understood yet. In this study, we aim to evaluate the spatial distributions of HDF regions and rotor sites within the left atrium (LA) pre and post HDF-guided ablation in PersAF.

Methods: This study involved 10 PersAF patients undergoing catheter ablation targeting HDF regions in the LA. 2048-channels of atrial electrograms (AEG) were collected pre- and post-ablation using a non-contact array (EnSite, Abbott). The dominant frequency (DF, 4–10 Hz) areas with DF within 0.25 Hz of the maximum out of the 2048 points were defined as "high" DF (HDF). Rotors were defined as PSs that last more than 100 ms and at a similar location through subsequent phase frames over time.

Results: The results indicated an extremely poor spatial correlation between the HDF regions and sites of the rotors in pre-versus post-ablation cases for the non-terminated (pre: CORR; 0.05 ± 0.17. vs. post: CORR; −0.030 ± 0.19, and with terminated patients (pre: CORR; −0.016 ± 0.03. post: CORR; −0.022 ± 0.04). Rotors associated with AF terminations had a long-lasting life-span post-ablation (non-terminated vs. terminated 120.7 ± 6.5 ms vs. 139.9 ± 39.8 ms), high core velocity (1.35 ± 1.3 mm/ms vs. 1.32 ± 0.9 mm/ms), and were less meandering (3.4 ± 3.04 mm vs. 1.5 ± 1.2 mm). Although the results suggest a poor spatial overlapping between rotors' sites and sites of AFCL changes in terminated and non-terminated patients, a higher correlation was determined

in terminated patients (spatial overlapping percentage pre: 25 ± 4.2% vs. 17 ± 3.8% vs. post: 8 ± 4.2% vs. 3.7 ± 1.7% $p < 0.05$, respectively).

Conclusion: Using non-contact AEG, it was noted that the correlation is poor between the spatial distribution of HDF regions and sites of rotors. Rotors were longer-lasting, faster and more stationary in patients with AF termination post-ablation. Rotors sites demonstrated poor spatial overlapping with sites of AFCL changes that lead to AF termination.

KEYWORDS

atrial fibrillation, cycle length, high dominant frequency, non-contact mapping, rotors

Introduction

Atrial fibrillation (AF) is the most common arrhythmia, with a fivefold increased risk of stroke (Nattel, 2002) and affecting more than 10% of people aged 65 and over (Freedman et al., 2021).

Catheter ablation proved to be effective for Paroxysmal AF (PAF) (Fichtner et al., 2015), however, as persistent AF (PersAF) is a more complex arrhythmia, it is more difficult to treat (Jalife et al., 2002; Nattel, 2002).

Studies have shown electrically remodelled tissue can potentially host rapid ectopic activity, and single and multiple circuit re-entry, perpetuating AF (Jalife et al., 2002; Nattel, 2002). Atrial electrograms (AEG) characterised by short cycle length (CL) and high-frequency activation (Mansour et al., 2001; Ashihara et al., 2012) have been proposed to identify local abnormal activations during AF (Mansour et al., 2001). Studies suggested that AEG with high-dominant frequencies (HDF) represent atrial regions with rapid ectopic activity (Sanders et al., 2005; Jarman et al., 2012) and these regions have been proposed as potential targets for AF ablation (Atienza et al., 2009). Their ablation resulted in CL prolongation and AF termination (Sanders et al., 2005). However, others argue that it remains unclear whether these sites are spatiotemporally stable (Habel et al., 2010; Jarman et al., 2012; Atienza et al., 2014).

Narayan et al., 2012; Spitzer et al., 2017 proposed targeting re-entry circuits and focal impulse for treating AF, other researchers reported contradictory findings (Balouch et al., 2017; Steinberg et al., 2017) due to rotors being spatiotemporally unstable, suggesting that these rotors may not be associated with AF perpetuation (Yamabe et al., 2016).

The co-localisation relationship study between DF and phase singularity points (PSs) in AEG has revealed that most PSs are located near DF areas, suggesting that wave breaks occur close to those boundaries (Samie et al., 2001; Salinet et al., 2017). Whereas with respect to non-contact AEG (NC-AEG), Salinet et al. (2017), reported that clusters of paired PSs spatially correlate with DF regions. Therefore, identifying ablation targets on NC-AEG using spectral analysis or phase mapping has not been fully understood yet.

AF cycle length (AFCL) has been shown to reflect local atrial refractoriness in animals and humans and has been suggested as a parameter to assess the effectiveness of AF ablation (O'Neill et al., 2009; Rostock et al., 2011). Thus, the study of the co-localisation relationship between HDF regions and rotors (re-entrant activity) and its role in perpetuating AF is important. No study to date has evaluated the spatial correlation between rotor sites and sites of short AFCL that lead to AF termination in NC-AEG.

The present study aims to evaluate 1) the spatial distributions of HDF regions and rotor sites within LA pre-/post- HDF-guided ablation in PersAF, 2) the response of the rotors to HDF-guided ablation, 3) the spatial correlation between rotor sites and sites of AFCL changes that lead to AF termination.

Materials and methods

Electrophysiology study

Ethical approval was secured for the present study from the local ethical committee at the University Hospitals of Leicester, National Health Service (NHS) Trust. Their guidelines were ascribed to and followed accordingly. Ten patients undergoing catheter ablation of PersAF for the first time, with no previous heart disease, were recruited (Bonow et al., 2006). All individuals were in AF at the time the procedure commenced. All antiarrhythmic medications aside from amiodarone were discontinued 5 days prior to the procedure. Routine blood sampling and a twelve-lead of electrocardiogram (ECG) were collected from all participating patients.

Non-contacting mapping

Under local anaesthetic, an ablation catheter was introduced *via* the femoral vein into the right atrium (RA). Then, with fluoroscopic guidance, an inflatable decapolar catheter and a quadripolar catheter were positioned in the

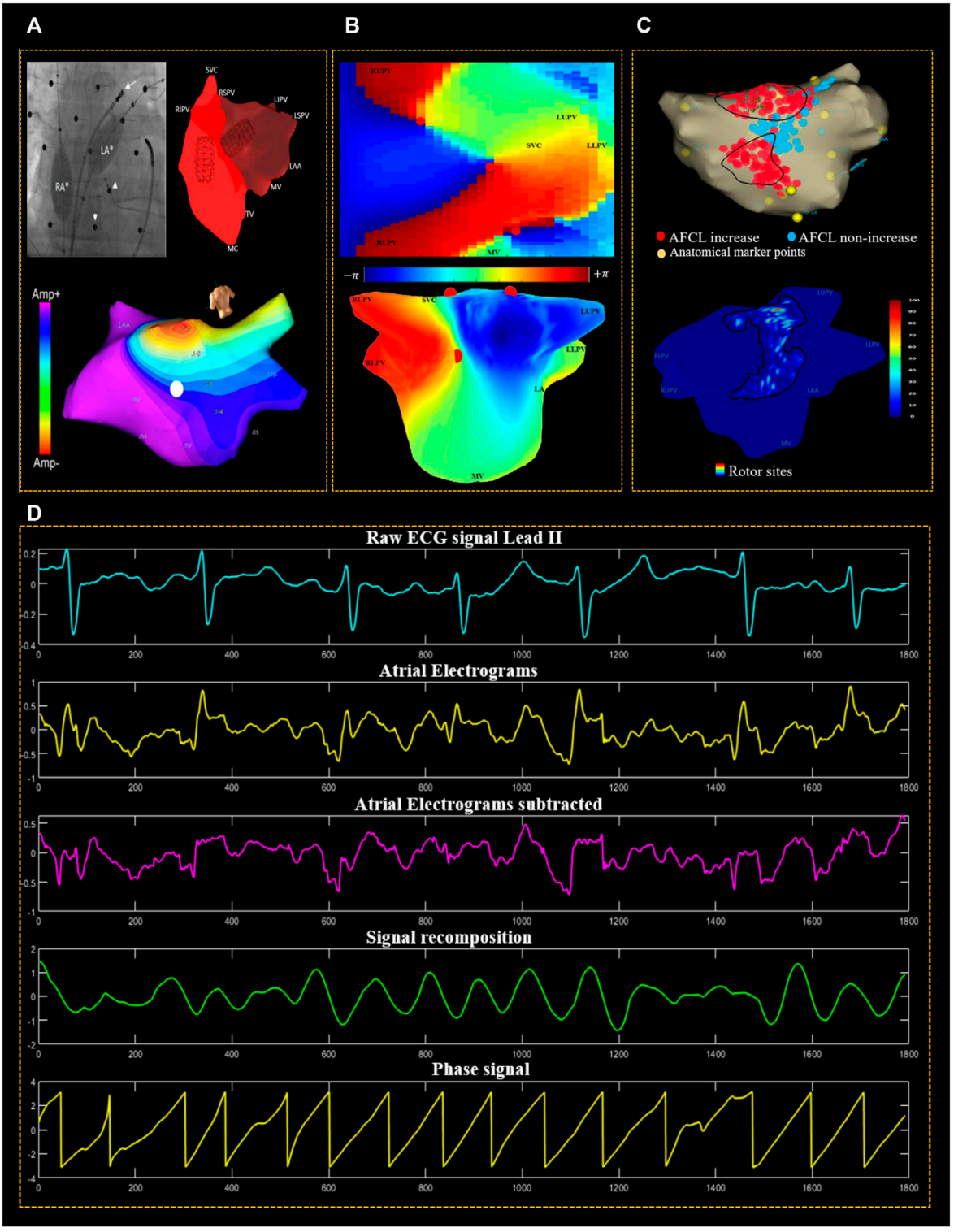

FIGURE 1
The methodological procedure used for data acquisition and signal processing. **(A)** Fluoroscopic image of the non-contact balloon catheters deployed in both the left atrium (LA) and right atrium (RA) (white asterisks). The small white arrows heads point at the active electrodes of the body surface mapping (BSM), and the white arrow points at the ablation catheter. The screenshot of the EnSite velocity mapping system illustrates the LA geometry isopotential/voltage map. **(B)** Reconstructed 2D & 3D of left atrial geometry with a colour-coded phase map; the colour bar indicates that the phase varies from $-\pi$ to $+\pi$ and the colour coding represents this 2π phase range from blue to red. PSs are represented by red circles. **(C)** LA

(*Continued*)

FIGURE 1
Geometry exported from EnSite non-contact mapping system, showing regions in the LA where ablations resulted in AFCL increase (red), AFCL non-increase (blue). Anatomical marker points are indicated by (yellow) dots; and 3D geometry of LA was constructed using in-house software USURP-AF (Understanding the electrophysiological SUbstRate of Persistent Atrial Fibrillation). The colour of the LA 3D geometry indicates a histogram of regions that host rotors, with a colour gradient of red to blue representing the percentage of the most visited to the less often visited region. **(D)** Phase mapping used reconstructed non-contact atrial electrograms (AEG). The aqua signal is the surface ECG (lead II) used as a reference for QRST subtraction of atrial electrograms. The second (yellow) signal is the unipolar AEG. Third, (magenta signal) is the QRST subtracted AEG, fourth (green signal) is the recomposed signal using sinusoidal wavelet reconstruction and fifth, the phase signal (yellow) is found using Hilbert transform.

coronary sinus (CS) and his position, respectively. For all cases, a single transeptal puncture technique was employed to provide access into the patients' left atrium (LA). This was realised by using a non-steerable transeptal sheath channel (Channel sheath, Bard Electrophysiology, United States). Heparin anticoagulation was administered to maintain an activated clotting time >300 s. Using a non-contact mapping (NCM) system (EnSite, Abbott Laboratories, United States) with multiple electrode array (MEA), high-resolution 3D geometries were reconstructed for the LA and RA, using the EnSite Velocity electro-anatomical mapping system (Abbott laboratories; Figure 1A). Using the non-contact MEA, 5-min intervals of intracardiac AEG were simultaneously recorded in AF for 2048 points.

Radiofrequency ablation

Identification of the HDF regions was undertaken for ablation as described in (Salinet et al., 2014). During the ablation, certain criteria were followed to evaluate the ablation response; after ablating each region of HDF, the ablation catheter was used to measure AFCL change in the left atrium appendage (LAA) over 10 cycles. A change in AFCL by 10 ms or more was considered significant (Bezerra et al., 2020). These steps were repeated until one of the pre-determined endpoints was met:

- Conversion of AF to sinus rhythm (SR);
- Conversion of AF to a more organised LA rhythm, or;
- The operator decided to stop the ablation due to a lack of target coverage or for patient safety concerns.

Further AEG recordings were collected post-procedure for another 5 minutes. After the MEA was extracted, a standard Pulmonary Veins isolation (PVI) was performed targeting the Ostia of the Pulmonary Veins (PVs), irrespective of the atrial rhythm. Multipolar Pulmonary Vein Ablation Catheter (PVAC) (Medtronic, Fridley, MN, United States) was used for this ablation in all patients. Four out of the 10 patients had AF termination: One converted to SR and three progressed to atrial Flutter (AFL). There were no adverse events in any of the enrolled patients.

Data collection of atrial electrograms and atrial fibrillation cycle length measurement

A non-contact MEA balloon was used for all patients (EnSite Velocity, Abbott Laboratories, United States). This device collected 2048 points of AF AEG from the endocardial surface of the LA over a period of 5 minutes. These were collected with a sampling frequency of 2034.5 Hz and subsequently exported using a 1–150 Hz band-pass filter set by the Ensite system. The Surface ECG was band-pass filtered (0.5–50 Hz). The collected data were analysed off-line using a MATLAB (MathWorks, United States) in-house developed program. Next, the AEG were resampled at 512 Hz using a cubic spline interpolation technique to reduce the processing time. This is noteworthy because the AEG were primarily sampled at 2034.5 Hz. Down-sampling the electrograms to 512 Hz does not result in loss of information in the AEG (Stevenson and Soejima, 2005). QRST subtraction was performed on the AEG to remove the far-field ventricular influence using the technique previously described in (Salinet et al., 2013). The bipolar signal at the LAA is clearly defined, allowing for an unambiguous manual assessment of AFCL, which has been used as a surrogate for AF organisation in several clinical studies (Haïssaguerre et al., 2004; Rostock et al., 2011; Honarbakhsh et al., 2018a). In this study, the AFCL in LAA was manually measured pre-and post- HDF-guided ablation using the ablation catheter over ten cycles to evaluate ablation response at the ablated site with a ±10 ms change considered significant (Figures 1B, C) (Bezerra et al., 2020).

Frequency domain analysis of the atrial electrograms

The NC-AEG of 60 s-long recordings were then separated into 4 s windows, with an overlap of 2 s. Accordingly, the spectral resolution was 0.25 Hz. Fivefold zero-padding was used and applied to improve the identification of spectral peaks with a frequency step of 0.05 Hz. DF for each of the 2048 points was defined as the highest power between 4–10 Hz. To measure the regularity and variability of AEG

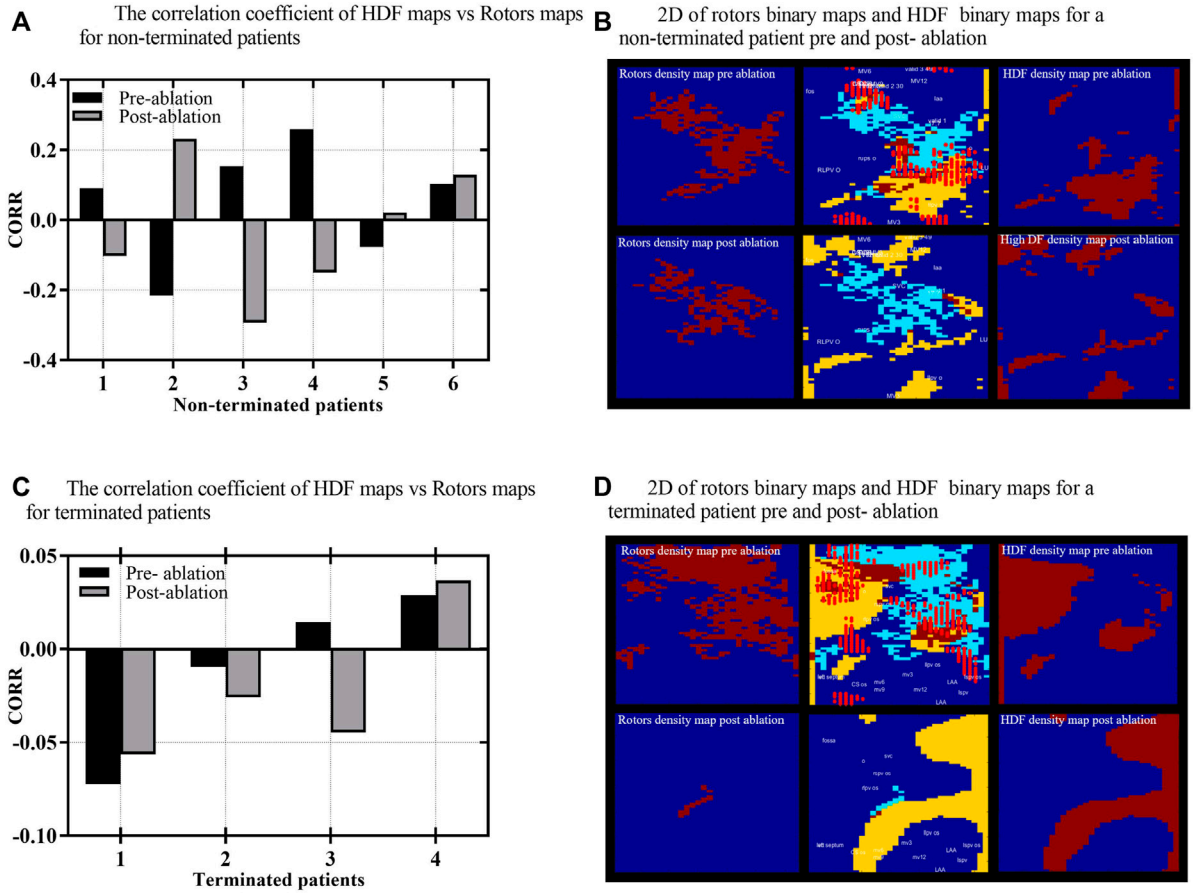

FIGURE 2
(A) The correlation coefficient (CORR) of HDF binary maps versus rotors binary maps for non-terminated. **(B)** 2D rotors binary maps on the right and HDF-binary maps on the left for non-terminated patient pre-and post-ablation. In the middle is a combined map of rotor binary map and HDF-binary map. **(C)** The CORR of HDF binary maps versus rotors binary maps for terminated patients pre-and post-ablation, respectively. **(D)** 2D rotors binary maps on the right and HDF-binary maps on the left for terminated patient pre- and post-ablation; in the middle is a combined map of rotor binary map and HDF-binary map. The yellow colour in combined maps indicates the HDF region, light blue indicates rotors, with the brown colour indicating the overlapping area, and the bright red dots represent ablation lesions marked by the mapping system during the procedure. The other maps are binary with brown indicating either HDF or rotors and blue representing areas that do not host either.

in the spectrum, the regularity index (RI) and organisation index (OI) of each DF were calculated. The RI is calculated by dividing the area under the DF peak and its harmonics by the entire spectra. The OI was calculated as the ratio of the area under the curve of the DF peak to the total power of the spectrum (Tuan et al., 2010). For more information regarding the pre-processing steps of NC-AEG see Section 2.4.

Identification of the high dominant frequency regions

For the 3D geometry of the LA, the area of HDF regions (the 10% top decile of DFs over the 2048 points of the LA) were identified and a colour-scale HDF map was constructed for the LA. The creation of HDF density maps was produced by counting those HDF occurrences for every LA node. Therefore, all atrial areas with HDF were accordingly delineated for all frames regarding each of the 2048 AEG. A recording was made of the number of occasions that the HDF clouds superimposed on another. To achieve this a representation of the 3D LA geometry was used. Such HDF regions are thought of as representative of those locations whereby PersAF arrhythmia is maintained. Accordingly, an HDF "cloud" is formed by the HDF area that is presumed to represent the region's AF activity. An automated algorithm was used to reconstruct the 2D (Figures 2B,D) and 3D HDF maps for (Figures 5C,D,G,H).

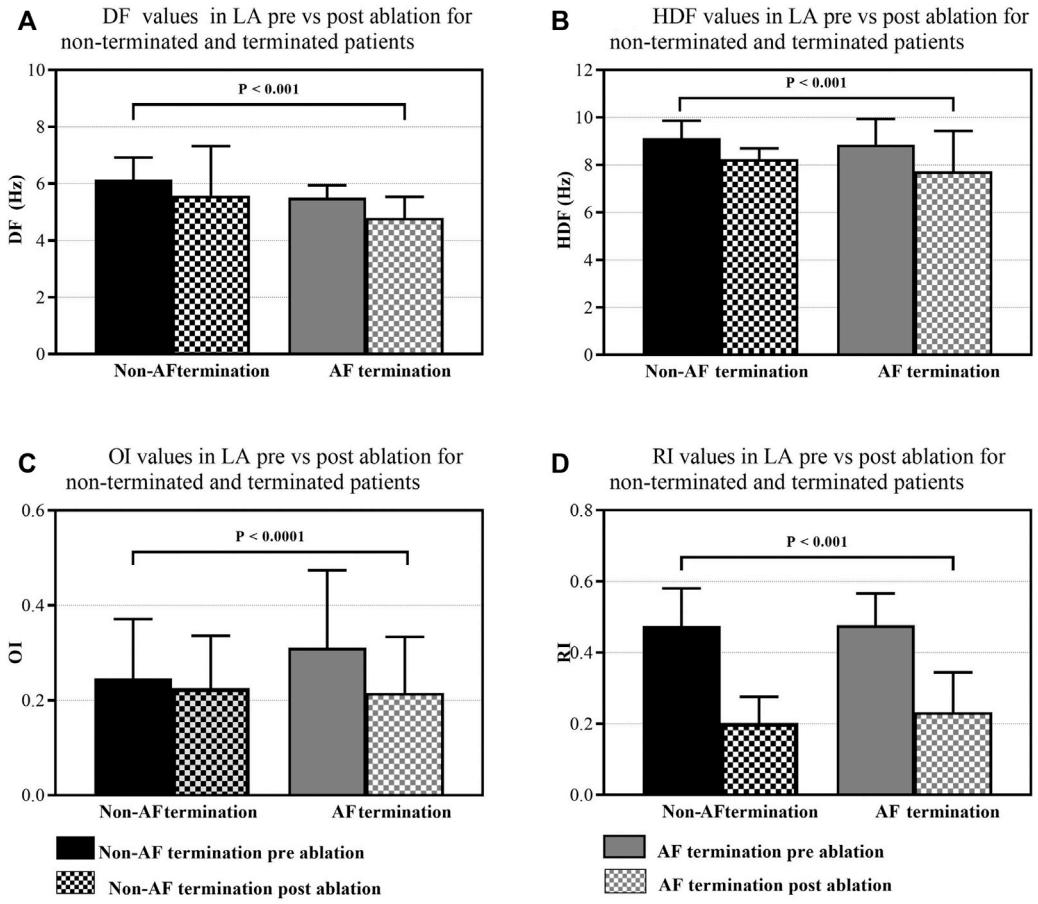

FIGURE 3
Monitoring the effect of HDF-guided ablation in PersAF patients. Bars represent the mean ± SD for each group. **(A)** DF across LA, pre-versus post-ablation for non-terminated and terminated patients. **(B)** HDF values change across LA, pre-versus post-ablation for non-terminated and terminated patients. **(C)** OI values change across LA, pre-versus post-ablation for non-terminated and terminated patients. **(D)** RI values change across LA, pre-versus post-ablation for non-terminated and terminated patients.

Phase mapping of atrial electrograms

Phase analysis is a tool employed to track the progression of the electrical activation of a region of the myocardium (Umapathy et al., 2010). During the AF phase mapping, when analysing spatiotemporal phase maps, there is particular interest regarding points at which the phase goes through an entire cycle (from−π to +π). These are referred to as "phase singularities" PSs. The activation front thereby rotates around the PSs. Several methodological stages are involved in this phase analysis when converting the AEG into a phase map. The sinusoidal decomposition approach was used for the current study, using the following steps (Kuklik et al., 2016).

1). In the "sinusoidal decomposition method" used to recompose the atrial AEG, the representation of the signal is given as the total sum of the sinusoidal wavelets using a frequency that equals the DF and by employing an amplitude that corresponds (is proportional to) the atrial AEG negative gradient. 2) As part of this pre-processing process, a sinusoidal signal is generated that is suited to phase mapping utilising the Hilbert Transform. 3). Phase maps are created by calculating the instantaneous phase of each of the 2048 AEG channels Figure 1D. The phase of all the AEG can be assessed at every point in time over the entire surface of the recordings, thus enabling the construction of the "movie" of the evolution of the phase map. During organised activity, distinct phase patterns will be identified, such as PSs, which are automatically identified using an algorithm based on the topological charge method by (Bray et al., 2001) at the points where the phase progresses through a full cycle (from—π to + π). We tracked the recurrence of PSs with consecutive phase frames with a spatial distance of five nodes or less between consecutive frames. A rotor was defined as a series of PSs lasting over 100 ms and detected at a similar location (5 nodes or less) through subsequent time

frames. As described in (Li et al., 2020), rotor velocity was calculated as the cumulative 3D geometry surface distance divided by the time, whilst rotor displacement was calculated as the surface distance between locations of the rotor appearing and disappearing.

Assessing the spatial correlation between the density maps of rotors' sites and high dominant frequency regions

In order to investigate the spatial correlation between the HDF regions and the sites of rotors density maps, we initially projected both HDF regions and rotors sites on 64 × 32 2D rectangles. The density information was removed to help assess the overlapping between the 2D maps. Figure 2B and D illustrate the 2D binary maps of the HDF regions and rotors' sites, where the AEG of 2048 virtual electrodes were mapped onto a 64 × 32 2D rectangular grid, as described in (Li et al., 2020), HDF regions and rotors' sites were marked as "ones" in a 64 × 32 matrix when they appear and marked as "zeros" where there were no HDF values or rotors at that specific "pixel." The similarity of each 2D HDF binary maps and rotors' binary maps were therefore measured using a 2D Pearson's correlation coefficient (CORR) (Pearson, 1897), similarity index (Eq. 1) where A, B represent the 2D matrices; $\bar{A}$, $\bar{B}$ represent their respective average values, and i and j are the rows and columns of the 2D matrices.

$$CORR = \frac{\sum\left(A_{ij} - \bar{A}\right)\left(B_{ij} - \bar{B}\right)}{\sqrt{\sum\left(A_{ij} - \bar{A}\right)^2\left(B_{ij} - \bar{B}\right)^2}} \quad (1)$$

Secondly, to generate high-density maps of 3D LA geometry; the 64 electrodes on the non-contact MEA catheter are used to estimate AEG in 64 locations on the endocardium, which are further interpolated to provide a total of 2048 AEG, each AEG represented with a node on 3D LA geometry as described in (Li et al., 2020). Next, a colour-scaled LA 3D geometry was constructed, with HDF regions and rotors' sites distributed across the LA. Each node out of the 2048 nodes that construct the 3D LA geometry was evaluated to determine whether or not it contains a value for either HDF regions or rotor sites or not at each time. The colour gradient of the LA geometries indicates the most visited region as red, the less often visited as yellow and the regions not visited at all as blue. IN these maps the ablated areas are marked with light red circles. Finally, up to 12 anatomical regions of the LA were manually marked on the LA geometries (where visible) by expert clinicians using the EnSite Velocity mapping system. Each anatomical region was marked with multiple surface points to create a closed representation of boundary points. The point number and its coordinates were saved and exported for off-line reconstruction showing the following: Roof; Septum (SEPT); MV isthmus (MVI); LAA; Anterior (ANT); and Posterior (POS); Floor; Right lower PVs (RLPV); Right upper PVs (RUPV); Left lower PVs (LLPV); Left upper PVs (LUPV); and Mitral Valve (MV).

This methodology enables the calculation of the spatial correlation between the rotors' sites and HDF regions across the entire LA in both 2D and 3D scales. HDF and rotors' density maps produced from individual 60 s of AEG recordings may highlight persistently dense regions and assist in identifying the individual drivers, which sustain PersAF. Therefore, to understand the co-localisation of rotors sites and the HDF region, we produced a combined map of cumulative rotors within the HDF region Figures 2B,D. This technique enabled the quantitative analysis of the overlap between the HDF regions and the rotors sites (or their non co-localisation) in a combined map. Furthermore, we projected the atrial areas that were ablated (red dots) on the same 2D combined map and 3D LA geometry to evaluate the effects of ablation of the HDF region in the non-termination patients and the termination group. A direct comparison of the pre- and post-ablation maps of HDF regions with rotor maps was carried out in both 2D and 3D maps to assess the effect of the ablation of HDF regions and the spatial distribution of rotors sites for both terminated and non-terminated patients. The spatial correlation between the sites of the rotors and the sites where the AFCL changed and led to AF termination was assessed by high-density maps in both 2D and 3D. Because all nodes associated with AFCL changes and rotors can be projected on 2D and 3D maps, the percentage of spatial overlapping was calculated using an algorithm that automatically reported the percentage of total rotors that coincide with AFCL change sites with respect to the total size of sites where there was AFCL change.

Statistical analysis

All continuous variables with normal distribution were presented as (mean ± standard deviation). Wilcoxon matched-pairs signed-rank tests were performed to analyse non-parametric paired multiple data. Non-parametric unpaired data were analysed by means of the Mann—Whitney test. The pre- and post-ablation of the regional distribution of the sites of the rotors and HDF regions across the LA were compared using ordinary one-way ANOVA. A value of $p < 0.05$ was considered statistically significant.

Results

Baseline characteristics

This study achieved a 40% level of AF termination. A total number of lesion nodes (1,500, $N = 4$) in termination patients

were ablated and (1970, $N = 6$) in non-termination patients. A total of 40,960 AEG and 80 sequential density maps of HDF regions and rotors' sites were analysed to assess the effect of catheter ablation on their spatial stability. The results exhibited a very poor spatial correlation between the HDF regions and rotors sites in pre-versus post-ablation for both the non-terminated (pre: CORR; 0.0525 ± 0.17. vs. post: CORR; −0.0302 ± 0.19, Figure 2A, and with terminated patients (pre: CORR; −0.016 ± 0.03. post: CORR; −0.022 ± 0.04, Figure 2C). Figures 2B,D reveal a very low similarity between the HDF and rotors' maps in non-terminated and terminated patients pre-and post-ablation cases.

Monitoring the effect of left atrium high dominant frequency regions guided ablation in patients with PersAF

HDF-guided ablation prior to PVI has contributed to a slower atrial arrhythmia by decreasing the DF across LA for both groups, non-terminated and terminated patients (pre: 6.14 ± 0.7 Hz, vs. 5.50 ± 0.4 Hz, $p < 0.001$. vs. post: 5.57 ± 1.7 Hz, vs. 4.78 ± 0.7 Hz, $p < 0.001$, Figure 3A). The DF reduction was followed by a slight decrease in global HDF values (Figure 6A), for non-terminated and terminated patients (pre: 9.13 ± 0.7 Hz, vs. 8.85 ± 1.0 Hz, $p < 0.001$. vs. post: 8.25 ± 1.0 Hz, vs. 7.73 ± 0.7 Hz, Figure 3B). Additionally, the frequency organisation and regularity of the AEG of HDF regions as measured with OI and RI demonstrated that OI was significantly higher in terminated patients compared to non-terminated patients (pre: 0.31 ± 0.16 vs. 0.24 ± 0.12, $p < 0.001$, vs. post: 0.21 ± 0.11 vs. 0.22 ± 0.11, $p < 0.0001$ Figure 3C). Also there was statistical significance difference in RI values between non-terminated and terminated patients (pre: 0.47 ± 0.10 vs. 0.47 ± 0.11, vs. post 0.20 ± 0.07 vs. 0.23 ± 0.11, $p < 0.001$, Figure 3D).

The effect of left atrium high dominant frequency-Guided ablation on rotor characteristics

The average number of detected rotors in non-terminated patients was higher than the terminated patients (pre: 39.50 ± 16.2 vs. 19 ± 15.6, vs. post: 11.7 ± 8.1 vs. 4.2 ± 2.4, Figure 4A). Thus, HDF guided ablation significantly affects the number of identified rotors in terminated patients, with a significant reduction (non-terminated patients vs. terminated patients: 29.7 ± 5.2%. vs. 36.1 ± 5.5%, Figure 6B). In contrast, the life-span of the tracked rotors was higher in the terminated group compared to the non-terminated patients prior to ablation (pre: 151.3 ± 69.51 ms vs. 136.4 ± 38.2 ms vs. post: 120.7 ± 6.5 ms vs. 139.9 ± 39.8 ms, Figure 4B). Likewise, rotor core velocity was higher in terminated patients than non-terminated group (pre: 2.8 ± 1.9 mm/ms vs. 0.7 ± 0.9 mm/ms vs. post: 1.35 ± 1.3 mm/ms vs. 1.32 ± 0.9 mm/ms, Figure 4C). However, rotor core displacement was higher in non-terminated compared to terminated patients (pre: 5.6 ± 7.4 mm vs. 3.34 ± 2.7 mm vs. post: 3.4 ± 3.04 mm vs. 1.5 ± 1.2 mm, Figure 4D). Figure 4E denotes the percentage of rotors not ablated (non-terminated patients vs. terminated patients: 70.2% ± 6.5 *Vs.* 63.1% ± 5.4). Figures 5C,D,G,H show that detected stable rotors of AEG lack spatial stability over pre-and post-ablation.

Spatial distribution of high dominant frequency regions and rotors' sites through the left atrium

Despite the fact of AF termination, Figures 5A,B,E,F showed that HDF regions and rotors' sites appear to have a relationship with the most visited anatomical regions of LA for pre and post-ablation. Interestingly the septum is the most visited region—non-terminated patients vs. terminated patients (mean ± SD pre: 41 ± 12.4%. vs. post: 34 ± 9.07%), followed by floor (33 ± 2.30%. vs. post: 30 ± 1.4%), anterior site (29 ± 1.31%. vs. post: 16 ± 2.3%), posterior site (25% ± 1.5. vs. post: 11 ± 0.5%) and roof (18 ± 0.23%. vs. post: 9 ± 0.13%) respectively. Therefore, in 60 s segments of PersAF recordings, the preferential areas visited by the HDF and Rotors were the septum and the floor of the LA, with the highest incidence of PSs compared with the remaining LA areas. RUPV and the anterior wall of the LA presented almost half the incidences of PSs. Figures 5C,D,G,H illustrate the results of the projected HDF regions and rotors' sites on 3D geometries of LA's surface for non-terminated and terminated patients. Relying on a visual inspection, it is clear that rotor sites are localised predominantly around or at the vicinity of HDF regions in both groups. In non-terminated patients, although the dense HDF region locations were targeted, both rotors focal sites and HDF regions were widely dispersed all over the surface of the LA post-ablation. Conversely, with a terminated patient where there was some spatial overlapping between rotors' sites and the targeted HDF region prior to ablation, rotors seemed to have responded to ablation. Moreover, post-ablation density maps appeared free of rotors in this particular patient who converted to SR.

Change in AF cycle length during ablation

For ten patients a total of 3,206 nodes were ablated: AFCL increase (≥10 ms, 947 nodes, 30%), AFCL non-increase (<10 ms, 2,259 nodes, 70%). Figure 6C shows the results of the AFCL measured at all ablation sites pre-ablation for non-terminated and terminated patients (Mean ± SD 170.9 ± 33.7 ms vs. 197.1 ± 15.5 ms, $p < 0.001$, respectively), where the mean of AFCL per patient for non-terminated and terminated pre ablation is (Mean ± SD 99.7 ± 35.4 ms vs. 78.8 ± 12.7 ms), However, the

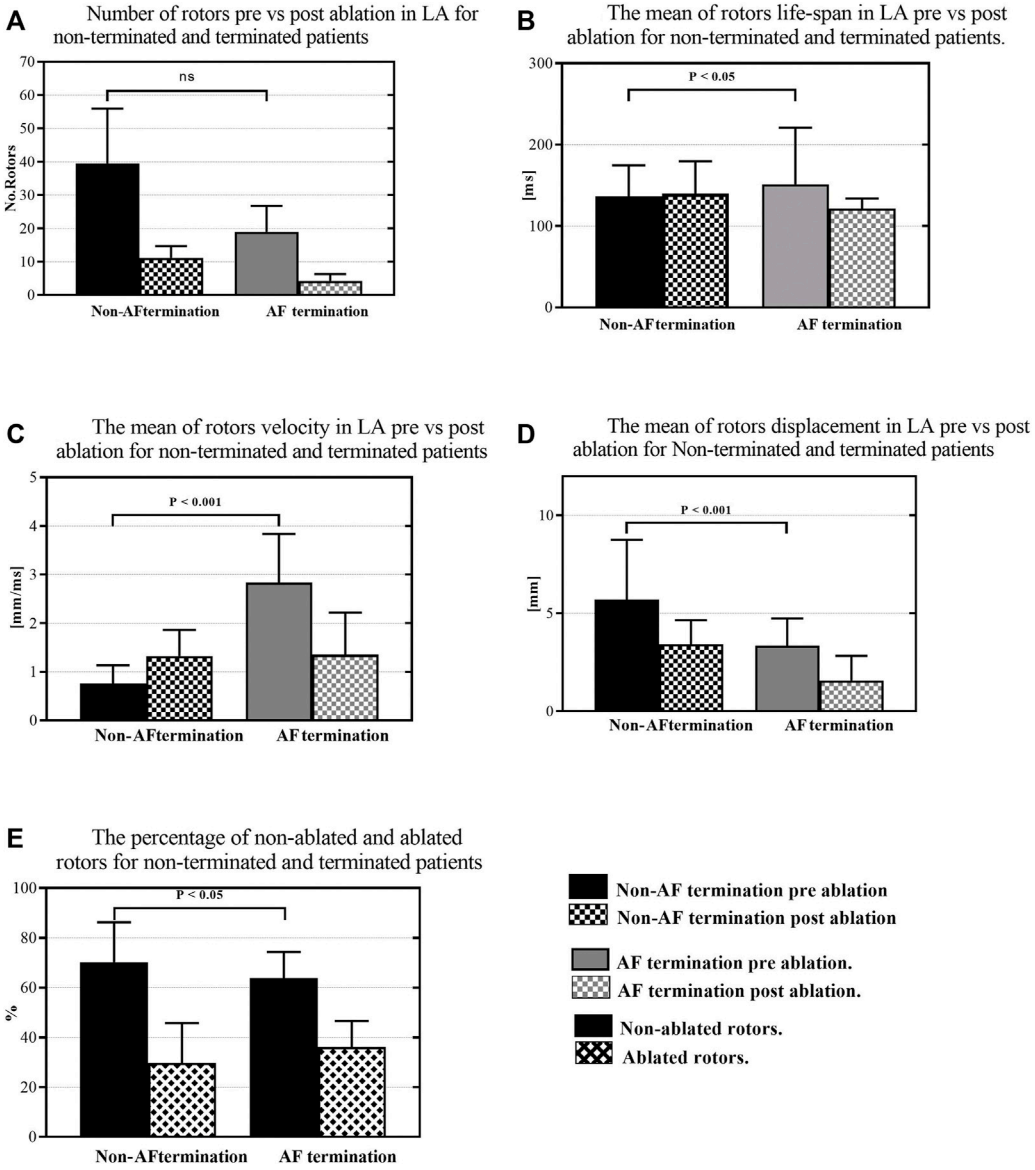

FIGURE 4
The response of the rotors to HDF ablation; **(A)** The number of rotors in pre-versus post-ablation for non-terminated and terminated patients. **(B)** The mean of the rotors life-span in pre-versus post-ablation for non-terminated and terminated patients. **(C)** The mean of the rotors' velocity in pre-versus post-ablation for non-terminated and terminated patients. **(D)** The mean of the rotor displacement in pre-versus post-ablation for non-terminated and terminated patients. **(E)** The percentage of overall non-ablated and ablated rotors in non-terminated and terminated patients.

response of the ablation of the prolongation in AFCL during the procedure was not significant between the two patients groups; post-ablation: AF non-terminated patients vs. AF terminated Figure 6D (Mean ± SD 3 ± 14 ms, vs. 5.5 ± 17.8 ms). Although the results suggest a poor spatial correlation between rotors' sites and sites of the AFCL changes in terminated and non-terminated patients, a higher correlation was found in terminated patients (spatial overlapping percentage pre: 25 ± 4.2% vs. 17 ± 3.8% vs. post: 8 ± 4.2% vs. 3.7 ± 1.7% $p < 0.05$, respectively, Figure 6E).

Discussion

This study provides further insight into the influence of HDF ablation on the spatial stability of HDF regions and rotors' sites. For all patients, the NC-AEG shows that rotors' sites are poorly spatially correlated with HDF regions. High-density maps, HDF and rotors sites appear to have a relationship with LA's most visited anatomical regions for both pre-and post-ablation, interestingly with the septum being the most visited region.

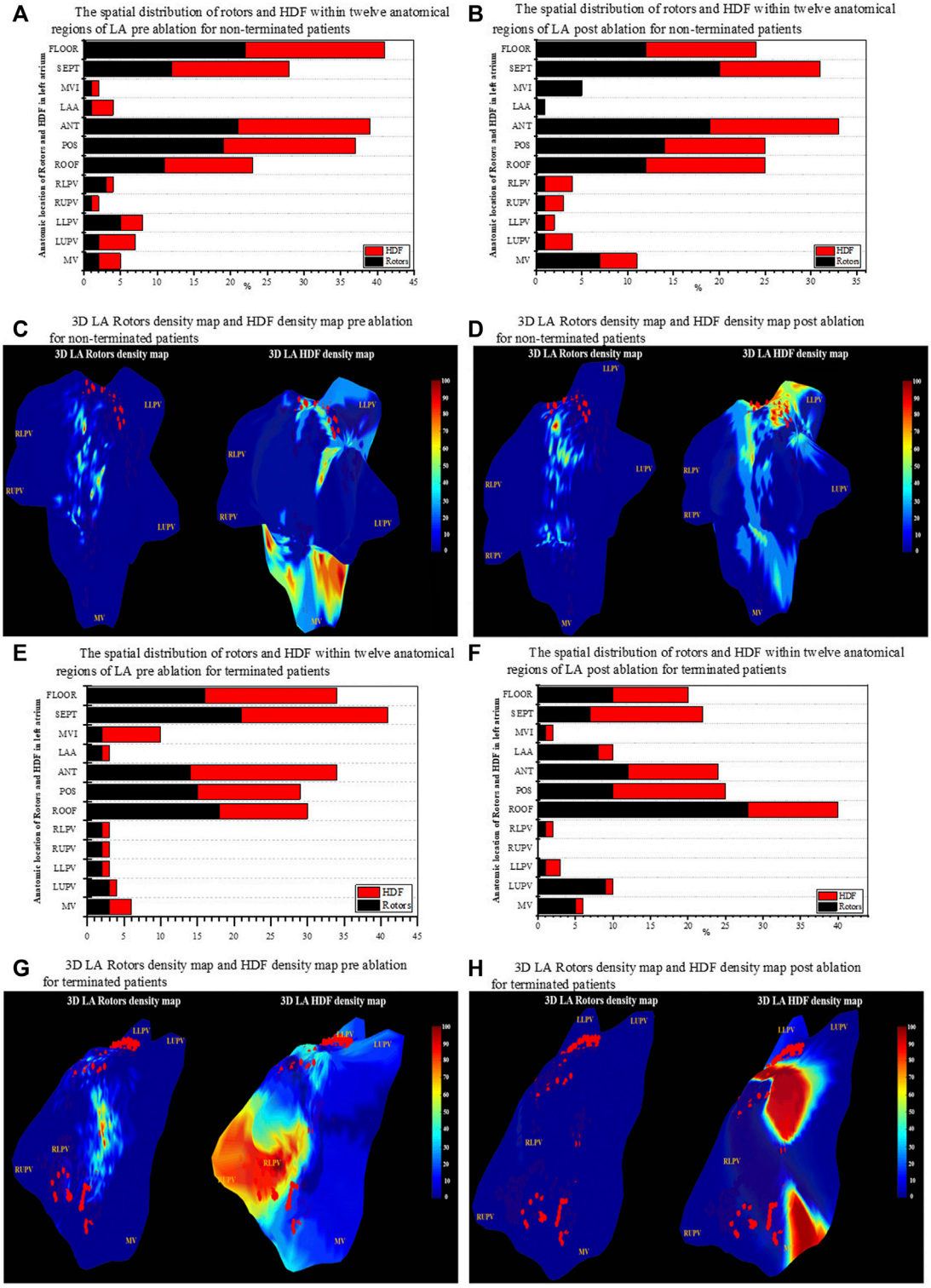

FIGURE 5
Regional distribution of rotors and HDF across the LA region. **(A)** Spatial distribution of HDF and rotors for 12 anatomical regions in LA for non-terminated patient pre-ablation. **(B)** Spatial distribution of HDF and rotors for 12 anatomical regions in LA for non-terminated patients post-ablation. **(C)** 3D LA geometry of rotors density and map HDF density map for non-terminated patient pre ablation. **(D)** 3D LA geometry of rotors density map and HDF density map for non-terminated patients post-ablation. **(E)** Spatial distribution of HDF and rotors for 12 anatomical regions in the LA for terminated patients pre ablation. **(F)** Spatial distribution of HDF and rotors for 12 anatomical regions in the LA for terminated patients post-ablation. **(G)** 3D LA geometry of rotors density map and HDF density map for terminated patients pre-ablation. **(H)** 3D LA geometry of rotors and density map HDF density map for terminated patients post-ablation. The colour bars in **(C,D,G,H)** represent the percentage of rotors sites and HDF regions on the 3D LA geometry. The red dots on the surface of the geometry represent the ablation lesions marked by the mapping system during the procedure.

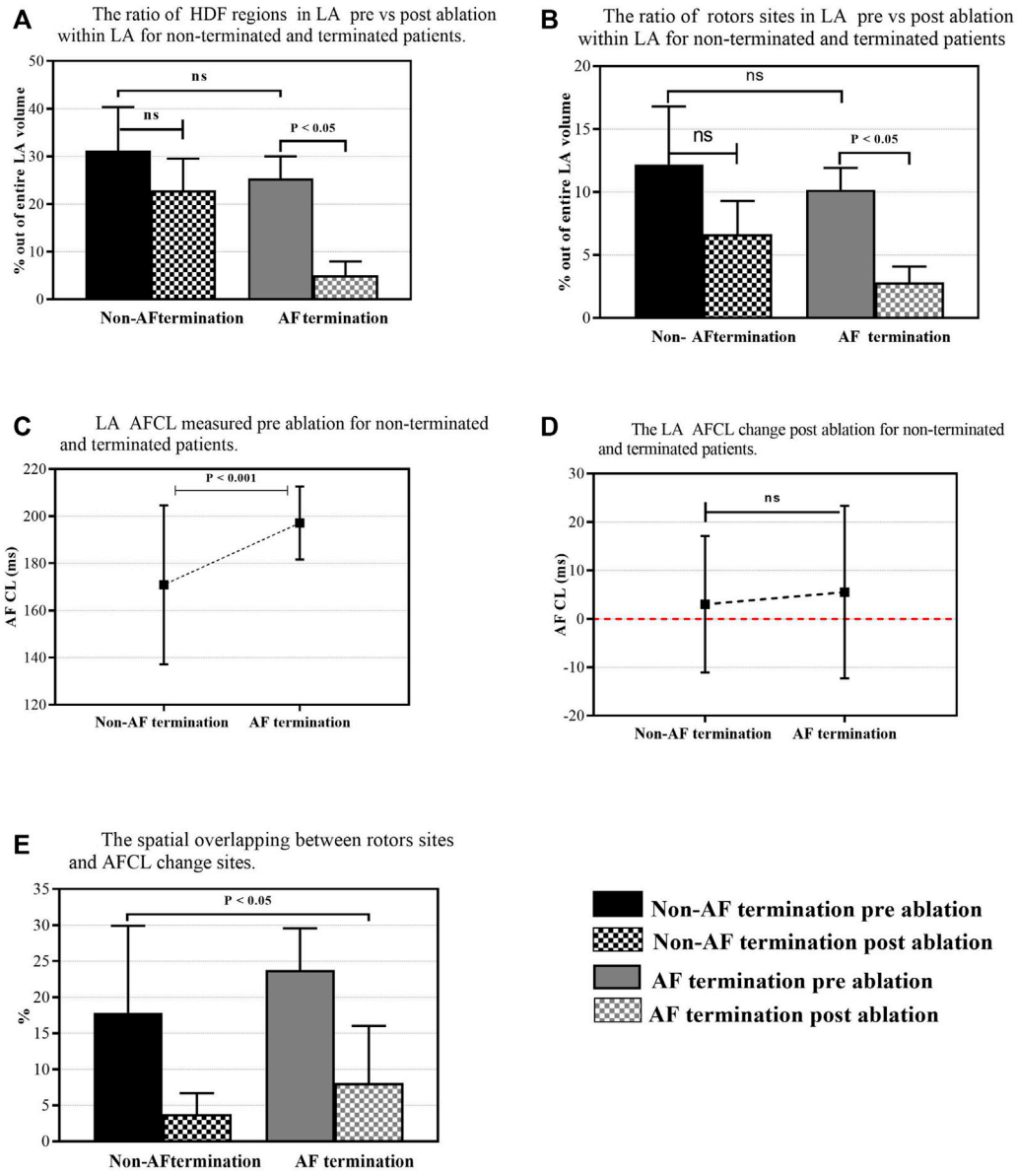

FIGURE 6
The overall percentage of rotors' sites and HDF regions out of the entire LA area. **(A)** The ratio of the rotors' sites through the LA pre-versus post-ablation for non-terminated and terminated patients. **(B)** The ratio of the HDF regions through the LA pre-versus post-ablation for non-terminated and terminated patients. **(C)** LA AFCL measured pre-ablation for non-terminated and terminated patients. **(D)** LA AFCL change was measured post-ablation for non-terminated and terminated patients. **(E)** The spatial overlapping between rotors' sites and AFCL change sites.

HDF guided ablation significantly affects the number of tracked rotors, particularly with a significant reduction in those where AF was terminated. Rotor sites detected in terminated patients had specific characteristics. They had a long-lasting life-span and high core velocity, and they were less meandering than sites detected in non-terminated patients. The rotors' sites demonstrated poor simultaneous spatial overlapping of the location of the rotors and the sites of AFCL changes that lead to AF termination.

Analysing spatial disparities of high dominant frequency regions and rotors' sites across the left atrium

Multiple studies have reported contradictory results regarding the spatial distribution of HDF regions in PersAF patients across LA. Elvan et al. (2009) found that HDF sites are predominantly located in the posterior wall between the pulmonary veins and at the roof across the LA. Sanders et al.

(2005), reported the HDF regions are localised on other non-PV regions of the LA and Suenari et al. (2011), reported that the highest DF were primarily located inside the PVs ostia. Conversely, our results showed that HDF dense regions seemed to have the highest incidence at the septum followed by the floor, anterior wall, and posterior wall of the LA and floor, respectively.

On the other hand, using non-contact mapping during human AF, Yamabe et al. (2016), reported that the rotor activation sites tend to be observed around the roof, septum and left superior PVs. Using a basket catheter, Swarup et al., reported that stable rotors and focal sources lay in multiple locations across LA remote from the PV. The posterior wall was the most visited region followed by the roof, anterior wall, near left PVs, along with the near right side of the PVs. Our results show that rotors were observed with the highest incidence within the septum, followed by the floor, anterior wall, and the posterior wall of the LA, respectively.

Using 3D human AF models, Hwang et al. (2016), reported that the HDF regions were well-correlated with the rotor sites and ablating such HDF sites resulted in slow atrial tachycardia. Our results also suggest a hidden interaction between the rotors and HDF regions. We observed that the HDF regions and the sites of the rotors appear to have a relationship with the LA's most visited anatomical regions for both pre and post-ablation of HDF regions, with the septum being the most visited region, followed by the floor anterior site, posterior site and roof. This interesting correlation could suggest a relationship between both tracked phenomena. The key questions remain: are these active drivers of fibrillation or just simply a passive phenomenon? And is this phenomenon a consequence of the other? Therefore, which is more likely to be the main driver of the overall arrhythmia? The answers remain ambiguous and require further investigation.

Ablation response of targeting high dominant frequency regions

In the present study, ablating the HDF regions prior to PVI coincided with the termination of AF in 4 out of the 10 patients with one patient converting to SR and three patients converting to atrial flutter. In the other six AF patients, the arrhythmia did not terminate even after PVI. Interestingly, for the terminated AF patients, the ablation resulted in a reduction in DF gradient throughout LA. This result is consistent with the findings that suggest targeting the HDF reduces the DF of AF electrograms (Lemola et al., 2006; Takahashi et al., 2006; Tuan et al., 2011) and is associated with an improvement in the ablation outcome (Yoshida et al., 2010). The reduction in DF could be explained as a result of decrease in overall atrial activation rates (Yoshida et al., 2010).

Interestingly, our study also found that OIs were significantly higher when compared between terminated vs. non-terminated AF patients. This finding agrees with previous studies that reported that an increase in OI prior to ablation can predict sites of AF termination (Tuan et al., 2010).

The difference in RI values were also statistically significant among the patient groups prior to ablation. Kalifa et al. (2006) reported that the highest RI regions coincide with the region of HDF region and vice versa. Lin et al. (2016) implied that higher RI values means that the propagation of the waves rotates around the rotor. For all patients, our results showed that the average RI values were higher than 0.4 prior to ablation, and significantly reduced to 0.2 post-ablation. This reduction could be due to the shape of the impinging wavefront at the boundaries of the HDF regions. Our finding agrees with studies stating that DF sites selected by an RI threshold higher than 0.2 are potential candidates for ablation (Traykov et al., 2012).

Rotors response during catheter ablation for PersAF targeting high dominant frequency regions

Literature reveals contradictory results regarding identifying rotor sites during AF mapping using a non-contacting cardiac mapping system. Yamabe et al. (2016), rotor sites were present in only one patient out of the 15 PersAF patients enrolled. According to them, rotors may not be the primary source of perpetuating AF. Lee et al., 2015 have failed to detect rotors or any sustained focal sources in 15 PersAF patients. Contrastingly, in this study using NC-AEG, rotors were observed in all of the 10 recruited patients. Thus, our results are consistent with the findings of (Kanemaru et al., 2016; Kaneko et al., 2019). Many studies have demonstrated the importance of rotor parameters, for instance, rotor life-span, rotor conduction velocity and rotor core displacement (or "rotor meandering") to reflect the spatiotemporal stability of rotors during AF mapping (Hwang et al., 2016; Lim et al., 2017). Lim et al. (2017) reported that in Virtual ablation, using a homogeneous monolayer computer model targeting a high DF area, the successful rate of AF terminations was depended on rotors parameters, where AF easily terminated spontaneously with a lower number of rotors prior to ablation and rotors with a shorter rotors life-span and a certain conduction velocity of ≥0.5 m/s. Nonetheless, our results confirm that rotor sites detected in terminated patients had specific characteristics. It was observed that they have a long-lasting life-span and high core velocity, and they were less meandering compared to sites detected in non-terminated patients. Thereby, rotor sites play an important role in driving or maintaining the AF with PersAF patients. The change in rotor parameters could be explained as a result of the fibrillation complexity in PersAF patients that is related to an increase of spontaneous cell activation in cardiac tissue and atrial

heterogeneity. This might be a consequence of multiple factors, such as ion channel expressions and higher degrees of fibrosis in cardiac tissues (Ashihara et al., 2012; Pandit and Jalife, 2013; Climent et al., 2015). These phenomena affect the rotor formation characteristics of the rotors' parameters. Thus, further studies are necessary to understand the effect of different phenomena, such as ionic basis and fibrosis, on rotors' dynamics behaviour.

Relationship between the rotors' sites and the AF cycle prolongation sites

To improve the outcomes of catheter ablation and increase the predictability of the long-term freedom of PersAF, many studies have investigated the correlation between AF drivers' sites and the site where the AFCL prolongation has occurred at which the AF terminate (Haïssaguerre et al., 2004; Kochhäuser et al., 2017). Honarbakhsh et al. (2018b), used a CARTO Finder mapping system with basket catheter targeting rotational or focal activity drivers for PersAF patients and reported a strong correlation between rotational or focal drivers and fastest AFCL. However, our study has shown that when using NC-AEG during HDF-guided ablation for ten PersAF patients, the rotors' sites demonstrated poor simultaneous spatial overlapping of the location of the rotors and the sites of AFCL changes that lead to AF termination. This discrepancy could be explained because the spatial distribution of the PersAF drivers across the LA may vary according to individual characteristics and arrhythmia durations.

Limitations of the study

This study was conducted with a relatively small sample size (N = 10). As our main aim was to investigate the spatial distributions of the HDF regions and rotor sites using high-density NC-AEG in PersAF, all NC-AEG analysis was restricted to the LA, and the right atrium was not studied here. Also, all analyses were performed retrospectively.

Despite the obvious advantage of providing AEG for the entire chamber via non-contact mapping, there are some limits. Virtual unipolar electrograms created using non-contact electrical mapping were reported to be vulnerable to inaccuracies during the AF recordings. These might be the result of: 1) potential errors in the inverse problem solution (Nakagawa et al., 2019); 2) inaccurate reconstruction of endocardial geometry of LA (Earley et al., 2006); 3) the assumption of electrical isotropic properties of the blood in the cardiac chambers (Meng et al., 2022); and 4) aliasing due to the limited spatial sampling (Zhao et al., 2013). These constraints may also have an influence on defining NC-AEG properties, such as DF and PSs, when compared to contact AEG during AF recordings.

Conclusion

The complex dynamics of high-frequency regions characterised by HDF were poorly spatially correlated with rotors' sites. However, the HDF regions and rotors do visit the same anatomical regions of LA, with the septum being the most visited region followed by the floor, anterior site, posterior site and roof, respectively. Thus, this finding supports the theory that the AF is initiated and maintained by multiple mechanisms across LA. Our results have demonstrated the consistency of using NC-AEG to investigate the re-entrant activity across the LA for PersAF patients. Nevertheless, we discovered that HDF-guided ablation does affect the characteristics of the rotors' sites in those patients where AF was terminated. Remarkably, rotors associated with AF terminations were distinct with particular parameters; they had a long-lasting life-span, high core velocity, and were less meandering across LA compared to sites detected in non-terminated patients. Thus not all rotors' sites are promising targets for PersAF ablation. Using NC-AEG, the sites of the rotors demonstrated poor (simultaneous) spatial overlapping with the sites of AFCL changes that lead to AF termination. This suggests that if there is an interaction between these two PersAF attributes, the dynamics of such interaction is more complex than a simple simultaneous spatial correlation.

Data availability statement

The original contributions presented in the study are included in the article/supplementary material, further inquiries can be directed to the corresponding author.

Ethics statement

The studies involving human participants were reviewed and approved by The studies involving human participants were reviewed and approved by the local ethics committee at the University Hospitals of Leicester NHS Trust and local NHS research ethics committee. The patients/participants provided their written informed consent to participate in this study. The patients/participants provided their written informed consent to participate in this study.

Author contributions

ME and XL: concept/design study, data analysis/interpretation of results, drafting manuscript, critical revision

of the manuscript, statistics, and "off-line" data collection. TA: data analysis/interpretation of results, drafting manuscript, critical revision of the manuscript, and statistics. ND and GC: data analysis/interpretation of results, critical revision of manuscript, and statistics. PS: EP study, data collection, interpretation of results, and critical revision of the manuscript. FS: concept/design study, data analysis/interpretation of results, and critical revision of the manuscript. GN: EP studies and ablation procedures, concept/design study, interpretation of results, and critical revision of the manuscript. All authors contributed to the article and approved the submitted version.

Funding

This work was supported by the NIHR Leicester Biomedical Research Centre, UK. XL received funding from the Medical Research Council UK (MR/S037306/1). TA received funding from the British Heart Foundation (BHF Project Grant no. PG/18/33/33780, Grant AA/18/3/34220). ME received a PhD scholarship from the Libyan Ministry of Higher Education and Scientific Research.

Conflict of interest

GN has received research fellowship from St. Jude Medical and speaker fees and honoraria from Biosense Webster.

The remaining author declares that the research was conducted in the absence of any commercial or financial relationships that could be construed as a potential conflict of interest.

Publisher's note

References

Ashihara, T., Haraguchi, R., Nakazawa, K., Namba, T., Ikeda, T., Nakazawa, Y., et al. (2012). The role of fibroblasts in complex fractionated electrograms during persistent/permanent atrial fibrillation: implications for electrogram-based catheter ablation. *Circ. Res.* 110 (2), 275–284. doi:10.1161/CIRCRESAHA.111.255026

Atienza, F., Almendral, J., Jalife, J., Zlochiver, S., Ploutz-Snyder, R., Torrecilla, E. G., et al. (2009). Real-time dominant frequency mapping and ablation of dominant frequency sites in atrial fibrillation with left-to-right frequency gradients predicts long-term maintenance of sinus rhythm. *Heart Rhythm.* 6 (1), 33–40. doi:10.1016/j.hrthm.2008.10.024

Atienza, F., Almendral, J., Ormaetxe, J. M., Moya, A., Martínez-Alday, J. D., Hernández-Madrid, A., et al. (2014). Comparison of radiofrequency catheter ablation of drivers and circumferential pulmonary vein isolation in atrial fibrillation: a noninferiority randomized multicenter RADAR-AF trial. *J. Am. Coll. Cardiol.* 64 (23), 2455–2467. doi:10.1016/j.jacc.2014.09.053

Balouch, M., Gucuk Ipek, E., Chrispin, J., Bajwa, R. J., Zghaib, T., Berger, R. D., et al. (2017). Impact of rotor temperospatial stability on acute and one-year atrial fibrillation ablation outcomes. *Clin. Cardiol.* 40 (6), 383–389. doi:10.1002/clc.22674

Bezerra, A. S., Yoneyama, T., Soriano, D. C., Luongo, G., Li, X., Ravelli, F., et al. (2020). "Optimizing atrial electrogram classification based on local ablation outcome in human atrial fibrillation," in CinC2020–Computing in Cardiology 2020, Rimini, Italy, September, 13-16 2020. Available at: https://www.cinc2020.org/

Bonow, R. O., Carabello, B. A., Chatterjee, K., De Leon, A. C., Faxon, D. P., Freed, M. D., et al. (2006). ACC/AHA 2006 guidelines for the management of patients with valvular heart disease: a report of the American college of cardiology/American heart association task force on practice guidelines (writing committee to revise the 1998 guidelines for the management of patients with valvular heart disease) developed in collaboration with the society of cardiovascular anesthesiologists endorsed by the society for cardiovascular angiography and interventions and the society of thoracic surgeons. *J. Am. Coll. Cardiol.* 48 (3), e1–e148. doi:10.1016/j.jacc.2006.05.021

Bray, M. A., Lin, S. F., Aliev, R. R., Roth, B. J., and Wikswo, J. P., Jr (2001). Experimental and theoretical analysis of phase singularity dynamics in cardiac tissue. *J. Cardiovasc. Electrophysiol.* 12 (6), 716–722. doi:10.1046/j.1540-8167.2001.00716.x

Climent, A. M., Guillem, M. S., Fuentes, L., Lee, P., Bollensdorff, C., Fernández-Santos, M. E., et al. (2015). Role of atrial tissue remodeling on rotor dynamics: an *in vitro* study. *Am. J. Physiol. Heart Circ. Physiol.* 309, H1964–H1973. doi:10.1152/ajpheart.00055.2015

Earley, M. J., Abrams, D. J., Sporton, S. C., and Schilling, R. J. (2006). Validation of the noncontact mapping system in the left atrium during permanent atrial fibrillation and sinus rhythm. *J. Am. Coll. Cardiol.* 48 (3), 485–491. doi:10.1016/j.jacc.2006.04.069

Elvan, A., Linnenbank, A. C., van Bemmel, M. W., Ramdat Misier, A. R., Delnoy, P. P. H., Beukema, W. P., et al. (2009). Dominant frequency of atrial fibrillation correlates poorly with atrial fibrillation cycle length. *Circ. Arrhythm. Electrophysiol.* 2 (6), 634–644. doi:10.1161/CIRCEP.108.843284

Fichtner, S., Sparn, K., Reents, T., Ammar, S., Semmler, V., Dillier, R., et al. (2015). Recurrence of paroxysmal atrial fibrillation after pulmonary vein isolation: is repeat pulmonary vein isolation enough? A prospective, randomized trial. *Europace* 17 (9), 1371–1375. doi:10.1093/europace/euu389

Freedman, B., Hindricks, G., Banerjee, A., Baranchuk, A., Ching, C. K., Du, X., et al. (2021). World Heart Federation roadmap on atrial fibrillation–a 2020 update. *Glob. Heart* 16 (1), 41. doi:10.5334/gh.1023

Habel, N., Znojkiewicz, P., Thompson, N., Müller, J. G., Mason, B., Calame, J., et al. (2010). The temporal variability of dominant frequency and complex fractionated atrial electrograms constrains the validity of sequential mapping in human atrial fibrillation. *Heart R* 7 (5), 586–593. doi:10.1016/j.hrthm.2010.01.010

Haïssaguerre, M., Sanders, P., Hocini, M., Hsu, L.-F., Shah, D. C., Scavée, C., et al. (2004). Changes in atrial fibrillation cycle length and inducibility during catheter ablation and their relation to outcome. *Circulation* 109 (24), 3007–3013. doi:10.1161/01.CIR.0000130645.95357.97

Honarbakhsh, S., Schilling, R. J., Dhillon, G., Ullah, W., Keating, E., Providencia, R., et al. (2018a). A novel mapping system for panoramic mapping of the left atrium: application to detect and characterize localized sources maintaining atrial fibrillation. *JACC. Clin. Electrophysiol.* 4 (1), 124–134. doi:10.1016/j.jacep.2017.09.177

Honarbakhsh, S., Schilling, R. J., Providencia, R., Keating, E., Chow, A., Sporton, S., et al. (2018b). Characterization of drivers maintaining atrial fibrillation: correlation with markers of rapidity and organization on spectral analysis. *Heart Rhythm.* 15 (9), 1296–1303. doi:10.1016/j.hrthm.2018.04.020

Hwang, M., Song, J.-S., Lee, Y.-S., Li, C., Shim, E. B., Pak, H.-N., et al. (2016). Electrophysiological rotor ablation in *in-silico* modeling of atrial fibrillation: comparisons with dominant frequency, shannon entropy, and phase singularity. *PloS one* 11 (2), e0149695. doi:10.1371/journal.pone.0149695

Jalife, J., Berenfeld, O., and Mansour, M. (2002). Mother rotors and fibrillatory conduction: a mechanism of atrial fibrillation. *Cardiovasc. Res.* 54 (2), 204–216. doi:10.1016/s0008-6363(02)00223-7

Jarman, J. W., Wong, T., Kojodjojo, P., Spohr, H., Davies, J. E., Roughton, M., et al. (2012). Spatiotemporal behavior of high dominant frequency during paroxysmal and persistent atrial fibrillation in the human left atrium. *Circ. Arrhythm. Electrophysiol.* 5 (4), 650–658. doi:10.1161/CIRCEP.111.967992

Kalifa, J., Tanaka, K., Zaitsev, A. V., Warren, M., Vaidyanathan, R., Auerbach, D., et al. (2006). Mechanisms of wave fractionation at boundaries of high-frequency excitation in the posterior left atrium of the isolated sheep heart during atrial fibrillation. *Circulation* 113 (5), 626–633. doi:10.1161/CIRCULATIONAHA.105.575340

Kaneko, S., Yamabe, H., Hoshiyama, T., Kanazawa, H., Ito, M., Kanemaru, Y., et al. (2019). Analysis of the preferable site and stability of rotational reentry: its role for the maintenance of atrial fibrillation. *Heart Vessels* 34 (6), 1014–1023. doi:10.1007/s00380-018-01331-8

Kanemaru, Y., Yamabe, H., Yamabe, H., Kanazawa, H., Ito, M., Kaneko, S., et al. (2016). Role of rotor activation for the maintenance of atrial fibrillation: Relation to the complex fractionated electrogram region. *Circulation* 134, A17292. doi:10.1161/circ.134.suppl_1.13527

Kochhäuser, S., Jiang, C.-Y., Betts, T. R., Chen, J., Deisenhofer, I., Mantovan, R., et al. (2017). Impact of acute atrial fibrillation termination and prolongation of atrial fibrillation cycle length on the outcome of ablation of persistent atrial fibrillation: a substudy of the STAR AF II trial. *Heart R* 14 (4), 476–483. doi:10.1016/j.hrthm.2016.12.033

Kuklik, P., Zeemering, S., van Hunnik, A., Maesen, B., Pison, L., Lau, D. H., et al. (2016). Identification of rotors during human atrial fibrillation using contact mapping and phase singularity detection: technical considerations. *IEEE Trans. Biomed. Eng.* 64 (2), 310–318. doi:10.1109/TBME.2016.2554660

Lee, S., Sahadevan, J., Khrestian, C. M., Cakulev, I., Markowitz, A., and Waldo, D. L. (2015). Simultaneous biatrial high-density (510-512 electrodes) epicardial mapping of persistent and long-standing persistent atrial fibrillation in patients: New insights into the mechanism of Its maintenance. *Circulation* 132 (22), 2108–2117. doi:10.1161/circulationaha.115.017007

Lemola, K., Ting, M., Gupta, P., Anker, J. N., Chugh, A., Good, E., et al. (2006). Effects of two different catheter ablation techniques on spectral characteristics of atrial fibrillation. *J. Am. Coll. Cardiol.* 48 (2), 340–348. doi:10.1016/j.jacc.2006.04.053

Li, X., Almeida, T. P., Dastagir, N., Guillem, M. S., Salinet, J., Chu, G. S., et al. (2020). Standardizing single-frame phase singularity identification algorithms and parameters in phase mapping during human atrial fibrillation. *Front. Physiol.* 11, 869. doi:10.3389/fphys.2020.00869

Lim, B., Hwang, M., Song, J.-S., Ryu, A.-J., Joung, B., Shim, E. B., et al. (2017). Effectiveness of atrial fibrillation rotor ablation is dependent on conduction velocity: an *in-silico* 3-dimensional modeling study. *PLoS one* 12 (12), e0190398. doi:10.1371/journal.pone.0190398

Lin, Y.-J., Lo, M.-T., Chang, S.-L., Lo, L.-W., Hu, Y.-F., Chao, T.-F., et al. (2016). Benefits of atrial substrate modification guided by electrogram similarity and phase mapping techniques to eliminate rotors and focal sources versus conventional defragmentation in persistent atrial fibrillation. *JACC. Clin. Electrophysiol.* 2 (6), 667–678. doi:10.1016/j.jacep.2016.08.005

Mansour, M., Mandapati, R., Berenfeld, O., Chen, J., Samie, F. H., Jalife, J., et al. (2001). Left-to-right gradient of atrial frequencies during acute atrial fibrillation in the isolated sheep heart. *Circulation* 103 (21), 2631–2636. doi:10.1161/01.cir.103.21.2631

Meng, S., Sunderland, N., Chamorro-Servent, J., Bear, L. R., Lever, N. A., Sands, G. B., et al. (2022). Intracardiac inverse potential mapping using the method of fundamental solutions. *Front. Physiol.* 13, 873049. doi:10.3389/fphys.2022.873049

Nakagawa, H., Lockwood, D., Sakamoto, Y., Ikeda, A., and Jackman, W. M. (2019). "7 - catheter 3-dimensional mapping systems," in *Catheter ablation of cardiac arrhythmias*. Editors S. K. S. Huang and J. M. Miller. Fourth Edition (Philadelphia: Elsevier), 101–116.e3.

Narayan, S. M., Krummen, D. E., Shivkumar, K., Clopton, P., Rappel, W. J., and Miller, J. M. (2012). Treatment of atrial fibrillation by the ablation of localized sources: Confirm (conventional ablation for atrial fibrillation with or without focal impulse and rotor modulation) trial. *Journal of the American College of Cardiology* 60 (7), 628–636. doi:10.1016/j.jacc.2012.05.022

Nattel, S. (2002). New ideas about atrial fibrillation 50 years on. *Nature* 415 (6868), 219–226. doi:10.1038/415219a

O'Neill, M. D., Wright, M., Knecht, S., Jaïs, P., Hocini, M., Takahashi, Y., et al. (2009). Long-term follow-up of persistent atrial fibrillation ablation using termination as a procedural endpoint. *Eur. Heart J.* 30 (9), 1105–1112. doi:10.1093/eurheartj/ehp063

Pandit, S. V., and Jalife, J. (2013). Rotors and the dynamics of cardiac fibrillation. *Circ. Res.* 112 (5), 849–862. doi:10.1161/CIRCRESAHA.111.300158

Pearson, K. (1897). Mathematical contributions to the theory of evolution.—on a form of spurious correlation which may arise when indices are used in the measurement of organs. *Proc. R. Soc. Lond.* 60 (359-367), 489–498.

Rostock, T., Salukhe, T. V., Steven, D., Drewitz, I., Hoffmann, B. A., Bock, K., et al. (2011). Long-term single-and multiple-procedure outcome and predictors of success after catheter ablation for persistent atrial fibrillation. *Heart Rhythm.* 8 (9), 1391–1397. doi:10.1016/j.hrthm.2011.04.012

Salinet, J. L., Jr, Madeiro, J. P., Cortez, P. C., Stafford, P. J., Ng, G. A., and Schlindwein, F. S. (2013). Analysis of QRS-T subtraction in unipolar atrial fibrillation electrograms. *Med. Biol. Eng. Comput.* 51 (12), 1381–1391. doi:10.1007/s11517-013-1071-4

Salinet, J. L., Tuan, J. H., Sandilands, A. J., Stafford, P. J., Schlindwein, F. S., Ng, G. A., et al. (2014). Distinctive patterns of dominant frequency trajectory behavior in drug-refractory persistent atrial fibrillation: preliminary characterization of spatiotemporal instability. *J. Cardiovasc. Electrophysiol.* 25 (4), 371–379. doi:10.1111/jce.12331

Salinet, J., Schlindwein, F. S., Stafford, P., Almeida, T. P., Li, X., Vanheusden, F. J., et al. (2017). Propagation of meandering rotors surrounded by areas of high dominant frequency in persistent atrial fibrillation. *Heart R* 14 (9), 1269–1278. doi:10.1016/j.hrthm.2017.04.031

Samie, F. H., Berenfeld, O., Anumonwo, J., Mironov, S. F., Udassi, S., Beaumont, J., et al. (2001). Rectification of the background potassium current: a determinant of rotor dynamics in ventricular fibrillation. *Circ. Res.* 89 (12), 1216–1223. doi:10.1161/hh2401.100818

Sanders, P., Berenfeld, O., Hocini, M., Jaïs, P., Vaidyanathan, R., Hsu, L.-F., et al. (2005). Spectral analysis identifies sites of high-frequency activity maintaining atrial fibrillation in humans. *Circulation* 112 (6), 789–797. doi:10.1161/CIRCULATIONAHA.104.517011

Spitzer, S. G., Károlyi, L., Rämmler, C., Scharfe, F., Weinmann, T., Zieschank, M., et al. (2017). Treatment of recurrent nonparoxysmal atrial fibrillation using focal impulse and rotor mapping (FIRM)-guided rotor ablation: Early recurrence and long-term outcomes. *Journal of Cardiovascular Electrophysiology* 28 (1), 31–38. doi:10.1111/jce.13110

Steinberg, J. S., Shah, Y., Bhatt, A., Sichrovsky, T., Arshad, A., Hansinger, E., et al. (2017). Focal impulse and rotor modulation: acute procedural observations and extended clinical follow-up. *Heart R* 14 (2), 192–197. doi:10.1016/j.hrthm.2016.11.008

Stevenson, W. G., and Soejima, K. (2005). Recording techniques for clinical electrophysiology. *J. Cardiovasc. Electrophysiol.* 16 (9), 1017–1022. doi:10.1111/j.1540-8167.2005.50155.x

Suenari, K., Lin, Y. J., Chang, S. L., Lo, L. W., Hu, Y. F., Tuan, T. C., et al. (2011). Relationship between arrhythmogenic pulmonary veins and the surrounding atrial substrate in patients with paroxysmal atrial fibrillation. *J. Cardiovasc. Electrophysiol.* 22 (4), 405–410. doi:10.1111/j.1540-8167.2010.01932.x

Takahashi, Y., Sanders, P., Jais, P., Hocini, M., Dubois, R., Rotter, M., et al. (2006). Organization of frequency spectra of atrial fibrillation: relevance to radiofrequency catheter ablation. *J. Cardiovasc. Electrophysiol.* 17 (4), 382–388. doi:10.1111/j.1540-8167.2005.00414.x

Traykov, V. B., Pap, R., and Sághy, L. (2012). Frequency domain mapping of atrial fibrillation-methodology, experimental data and clinical implications. *Curr. Cardiol. Rev.* 8 (3), 231–238. doi:10.2174/157340312803217229

Tuan, J., Osman, F., Jeilan, M., Kundu, S., Mantravadi, R., Stafford, P. J., et al. (2010). Increase in organization index predicts atrial fibrillation termination with flecainide post-ablation: spectral analysis of intracardiac electrograms. *Europace* 12 (4), 488–493. doi:10.1093/europace/eup405

Tuan, J., Jeilan, M., Kundu, S., Nicolson, W., Chung, I., Stafford, P. J., et al. (2011). Regional fractionation and dominant frequency in persistent atrial fibrillation: effects of left atrial ablation and evidence of spatial relationship. *Europace* 13 (11), 1550–1556. doi:10.1093/europace/eur174

Umapathy, K., Nair, K., Masse, S., Krishnan, S., Rogers, J., Nash, M. P., et al. (2010). Phase mapping of cardiac fibrillation. *Circ. Arrhythm. Electrophysiol.* 3 (1), 105–114. doi:10.1161/CIRCEP.110.853804

Yamabe, H., Kanazawa, H., Ito, M., Kaneko, S., and Ogawa, H. (2016). Prevalence and mechanism of rotor activation identified during atrial fibrillation by noncontact mapping: lack of evidence for a role in the maintenance of atrial fibrillation. *Heart Rhythm.* 13 (12), 2323–2330. doi:10.1016/j.hrthm.2016.07.030

Yoshida, K., Chugh, A., Good, E., Crawford, T., Myles, J., Veerareddy, S., et al. (2010). A critical decrease in dominant frequency and clinical outcome after catheter ablation of persistent atrial fibrillation. *Heart R* 7 (3), 295–302. doi:10.1016/j.hrthm.2009.11.024

Zhao, J., Yao, Y., Huang, W., Shi, R., Zhang, S., LeGrice, I. J., et al. (2013). Novel methods for characterization of paroxysmal atrial fibrillation in human left atria. *open Biomed. Eng. J.* 7, 29–40. doi:10.2174/1874120701307010029

frontiers | Frontiers in Physiology

TYPE Original Research
PUBLISHED 06 September 2022
DOI 10.3389/fphys.2022.920788

OPEN ACCESS

EDITED BY
Axel Loewe,
Karlsruhe Institute of Technology (KIT), Germany

REVIEWED BY
Nele Vandersickel,
Ghent University, Belgium
Xin Li,
University of Leicester, United Kingdom

*CORRESPONDENCE
Anand N. Ganesan,
anand.ganesan@flinders.edu.au

SPECIALTY SECTION
This article was submitted to Cardiac Electrophysiology, a section of the journal Frontiers in Physiology

RECEIVED 15 April 2022
ACCEPTED 10 August 2022
PUBLISHED 06 September 2022

CITATION
Jenkins EV, Dharmaprani D, Schopp M, Quah JX, Tiver K, Mitchell L, Xiong F, Aguilar M, Pope K, Akar FG, Roney CH, Niederer SA, Nattel S, Nash MP, Clayton RH and Ganesan AN (2022), The inspection paradox: An important consideration in the evaluation of rotor lifetimes in cardiac fibrillation. *Front. Physiol.* 13:920788. doi: 10.3389/fphys.2022.920788

The inspection paradox: An important consideration in the evaluation of rotor lifetimes in cardiac fibrillation

Evan V. Jenkins[1], Dhani Dharmaprani[1,2], Madeline Schopp[2], Jing Xian Quah[1,3], Kathryn Tiver[3], Lewis Mitchell[4], Feng Xiong[5], Martin Aguilar[5], Kenneth Pope[2], Fadi G. Akar[6], Caroline H. Roney[7], Steven A. Niederer[8], Stanley Nattel[5], Martyn P. Nash[9], Richard H. Clayton[10] and Anand N. Ganesan[1,3]*

[1]College of Medicine and Public Health, Flinders University, Adelaide, SA, Australia, [2]College of Science and Engineering, Flinders University, Adelaide, SA, Australia, [3]Department of Cardiovascular Medicine, Flinders Medical Centre, Adelaide, SA, Australia, [4]School of Mathematical Sciences, University of Adelaide, Adelaide, SA, Australia, [5]Montréal Heart Institute and Université de Montréal, Montréal, QC, Canada, [6]School of Medicine, Yale University, New Haven, CT, United States, [7]School of Engineering and Materials Science, Queen Mary University of London, London, United Kingdom, [8]School of Biomedical Engineering and Imaging Sciences, Kings College London, London, United Kingdom, [9]Auckland Bioengineering Institute, University of Auckland, Auckland, New Zealand, [10]Insigneo Institute for in Silico Medicine and Department of Computer Science, University of Sheffield, Sheffield, United Kingdom

Background and Objective: Renewal theory is a statistical approach to model the formation and destruction of phase singularities (PS), which occur at the pivots of spiral waves. A common issue arising during observation of renewal processes is an inspection paradox, due to oversampling of longer events. The objective of this study was to characterise the effect of a potential inspection paradox on the perception of PS lifetimes in cardiac fibrillation.

Methods: A multisystem, multi-modality study was performed, examining computational simulations (Aliev-Panfilov (APV) model, Courtmanche-Nattel model), experimentally acquired optical mapping Atrial and Ventricular Fibrillation (AF/VF) data, and clinically acquired human AF and VF. Distributions of all PS lifetimes across full epochs of AF, VF, or computational simulations, were compared with distributions formed from lifetimes of PS existing at 10,000 simulated commencement timepoints.

Results: In all systems, an inspection paradox led towards oversampling of PS with longer lifetimes. In APV computational simulations there was a mean PS lifetime shift of +84.9% (95% CI, ± 0.3%) ($p < 0.001$ for observed vs overall), in Courtmanche-Nattel simulations of AF +692.9% (95% CI, ±57.7%) ($p < 0.001$), in optically mapped rat AF +374.6% (95% CI, ± 88.5%) ($p = 0.052$), in human AF mapped with basket catheters +129.2% (95% CI, ±4.1%) ($p < 0.05$), human AF-HD grid catheters 150.8% (95% CI, ± 9.0%) ($p < 0.001$), in optically mapped rat VF

Abbreviations: PS, Phase Singularities; AF, Atrial Fibrillation; VF, Ventricular Fibrillation; APV model, Aliev-Panfilov model.

+171.3% (95% CI, ±15.6%) ($p < 0.001$), in human epicardial VF 153.5% (95% CI, ±15.7%) ($p < 0.001$).

Conclusion: Visual inspection of phase movies has the potential to systematically oversample longer lasting PS, due to an inspection paradox. An inspection paradox is minimised by consideration of the overall distribution of PS lifetimes.

KEYWORDS

ventricular fibrillation, atrial fibrilation, renewal theory, inspection paradox, cardiac fibrillation, phase singularity

Introduction

The repetitive creation and annihilation of spiral vortices is a pattern observed in spatiotemporally turbulent nonequilibrium systems throughout nature (Lechleiter et al., 1991; Cross and Hohenberg, 1993; Ouyang and Flesselles, 1996; Cross and Greenside, 2009; Tan et al., 2020). In physical (Morris et al., 1993; Ouyang and Flesselles, 1996; Egolf et al., 2000), chemical (Beta et al., 2006; Qiao et al., 2009), and biological systems (Lechleiter et al., 1991; Tan et al., 2020), this motif, variously known as defect-mediated turbulence (Coullet et al., 1989; Ouyang and Flesselles, 1996) or spiral defect chaos (Morris et al., 1993; Egolf et al., 2000), is characterised by the repetitive creation and annihilation of topological defects called phase singularities (PS), which are located at the pivot of spiral waves (Winfree, 1980; Winfree, 1987).

A surprising finding is that the population dynamics of PS in these diverse systems appear to be governed by common statistical laws (Davidsen et al., 2008; Tan et al., 2020). Specifically, theoretical studies have predicted that due to the effective statistically independent nature of spiral nucleation and annihilation processes under conditions of spatiotemporal turbulence, PS populations should follow Poisson distributions (Gil et al., 1990; Wang, 2004), with the corollary being that PS lifetimes should be exponentially distributed (Tan et al., 2020; Quah et al., 2021). These statistical properties have empirically been subsequently demonstrated to apply to spiral vortex regeneration in fluid mechanics (Ecke and Hu, 1997; Egolf et al., 2000), chemical reactions (Beta et al., 2006), quantum fluids (Abo-Shaeer et al., 2002; Tan et al., 2020), as well as biologically in the brain (Huang et al., 2010) and cell membranes of living cells (Tan et al., 2020).

There are strong reasons to suggest that a similar process of regeneration of spiral vortices sustains fibrillation in the heart (Christoph et al., 2018). Unstable re-entrant circuits, are at present considered most likely to arise from spiral vortices, (Comtois et al., 2005) which has been observed in cardiac fibrillation for over a century (Comtois et al., 2005). Exponential distributions of PS lifetimes are observed in pre-clinical mapping data in both atrial (Chen et al., 2000a; Kuklik et al., 2016; Child et al., 2018) and ventricular fibrillation (Rogers et al., 1999; Chen et al., 2000b; Rogers, 2004; Kay and Rogers, 2006; Christoph et al., 2018) (AF/VF), computer simulations of AF and VF and in humans mapped with extracellular electrograms and optical mapping (Chen et al., 2000a; Chen et al., 2000b; Rogers, 2004; Kuklik et al., 2016; Child et al., 2018; Christoph et al., 2018; Schlemmer et al., 2018). Importantly, this principle has been shown to apply to both short-lasting PS and more sustained PS associated with rotors (Rogers et al., 1999; Kay et al., 2006; Dharmaprani et al., 2019b). Collectively, these results suggest, the statistical properties of PS in cardiac fibrillation are similar to those observed to other forms of defect-mediated turbulence in nature.

We have recently investigated spiral vortex regeneration population dynamics in AF and VF (Dharmaprani et al., 2019b; Dharmaprani et al., 2021; Dharmaprani et al., 2022). These studies have shown in cardiac fibrillation, similar to other natural systems, PS inter-formation times and lifetimes fit with an exponential distribution, consistent with the notion that PS creation and annihilation may be characterised as renewal processes (Dharmaprani et al., 2019b; Dharmaprani et al., 2021; Quah et al., 2021). By combining the renewal rate constants for PS formation (λf—pronounced 'lambda-f') and destruction (λd), we have shown that it is possible to explain the Poisson distribution of PS that is observed in both AF and VF (Dharmaprani et al., 2019b; Dharmaprani et al., 2021; Quah et al., 2021) (Jenkins et al., 2022).

The finding that PS formation and destruction may be characterised as renewal processes has important implications in the experimental evaluation of cardiac fibrillation. In this study, we consider the potential for an inspection paradox. The inspection paradox is a common issue observed with renewal processes (Angus, 1997; Ross, 2014). Inspection paradoxes occur in scenarios when a renewal process is randomly observed in time, giving rise for the tendency to observe an interval larger than that of an average interval (Ross, 2014). To be specific about what this would mean in AF or VF, this would give the tendency for recordings to commence during longer periods of re-entry, giving the potential to perceive that observed PS lifetimes are longer than the actual average PS lifetime (Angus, 1997; Ross, 2014). The inspection paradox could have the potential to influence the interpretation of mechanistic and clinical studies

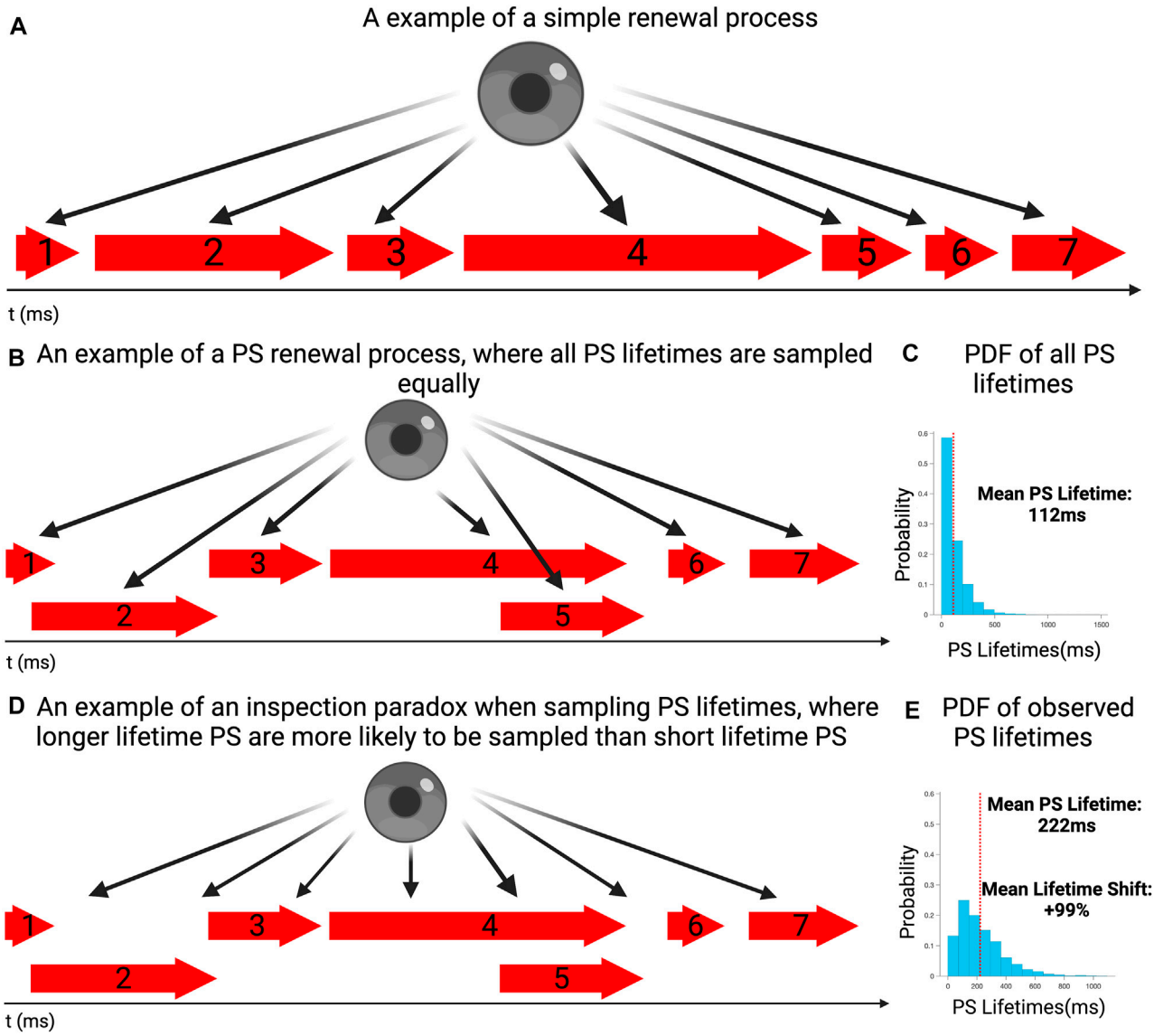

FIGURE 1
(A) An example of a simple renewal process in which event lasts for a period of time, before a new occurs. **(B)** An example of a PS renewal process, where at any given time either one event could be ongoing, multiple events can occur simultaneously or no events could be active. Each event is sampled equally and individually. **(C)** The probability distribution of event lifetimes for a simulated sequence of event lifetimes (PS), consistent with other renewal processes and our previous work. The mean PS lifetime is 112 ms. **(D)** An example where PS lifetimes are sampled according to the moment of observation, rather than properly examining the full distribution of lifetimes around it. Due to an inspection paradox, it is more likely for longer lasting events to be observed rather than short lasting ones. **(E)** To demonstrate how an inspection paradox can lead to a bias in favor of longer lasting events, 10,000 randomly chosen commencement timepoints where chosen, with the lifetimes of PS occurring at those timepoints sampled. The probability distribution demonstrates suggests that longer lasting events had a higher probability of occurring, compared with the overall distribution This is reflected in the mean lifetime of this distribution being 222 ms.

of cardiac fibrillation, by inadvertently emphasising the relative temporal significance of more sustained re-entrant circuits during the early stages of cardiac fibrillation recordings. This may be relevant, by contributing to the cognitive perception of temporal stability of re-entry.

In the following study, we sought to quantify the potential effect of an inspection paradox on the perception of PS lifetimes through sampling of the lifetimes at possible commencement points for fibrillation recordings. This involved comparing the statistical properties of PS lifetimes sampled across full epochs, with PS lifetimes present during potential commencement timepoints, and was performed across a wide range of experimental and clinical datasets, including computational simulations, animal, and human AF and VF.

Materials and methods

The potential influence of an inspection paradox is illustrated and examined in two parts. In Part 1–Theory, we demonstrate the effects of an inspection paradox on a simulated renewal process, to demonstrate to readers the operation of an inspection paradox. In Part 2, we simulate the effect of observations around randomly chosen commencement timepoints on PS lifetime distributions in a range of cardiac fibrillation data.

Part 1–theory

To illustrate how an inspection paradox works, we present data from a simple simulated renewal process generated as follows. Using MATLAB, two exponential probability distributions were generated, each defined by a rate constant, λ_f/ λ_d. Random draws from the probability distribution defined by λ_f were used to simulate inter-formation timings of theoretical events (theoretically identical to PS). Random draws from the distribution defined by λ_d were used to define event destruction timings. These timings were used to create a data table of event formation and destruction times, as a continuous sequence of events forming and being destroyed.

To demonstrate the effect of observation of events around a commencement point, a random time-point in the data-table between 0% and 90% of the final event formation time was selected. The lifetimes of events existing at the randomly chosen timepoint in the data selected were examined, Figures 1A,C.

To demonstrate the potential for a distorting influence, this was repeated many times to create a data set of sampled lifetimes, of events existing at the commencement timepoint. This was performed 10,000 times, to ensure that the distribution of sampled (observed) lifetimes could have a distinct shape. The justification for a 10,000-fold repetition was that a large sampling would ensure characterisation of the shape of the potential distribution developed by the inspection paradox.

In this example, the full distribution of lifetimes of all events is presented in Figure 1B, showing the exponential distribution of lifetimes, with a mean event lifetime of 112 ms. This distributional shape was in keeping with those we have previously identified with renewal processes (Dharmaprani et al., 2019b; Dharmaprani et al., 2021; Dharmaprani et al., 2022; Jenkins et al., 2022). Figure 1D presents the distribution of observed lifetimes, all sampled events, including potential repetitions of events. It can be seen that the mean lifetime in the observed distribution is shifted to the right, with a mean of 222 ms (+99% shift). This demonstrates the disproportionate likelihood of observing longer lifetime events, relative to the true distribution of lifetimes, when examined across a full epoch.

The MATLAB code used to perform this example is provided in the Supplementary Material S1.

Part 2–the effect of an inspection paradox in atrial and ventricular fibrillation

To examine the impact of an inspection paradox on the observed lifetimes of PS, we examined PS lifetimes. A multi-system, multi-modality study was performed in order to examine the potential influence of an inspection paradox in cardiac, independent of the mapping modality utilized. We first examined it in computational models (a model of spiral-defect turbulence; Aliev-Panfilov (APV) model, followed by more detailed models of AF in 2D and 3D) and then subsequently evaluated them in a range of experimentally and clinically acquired AF and VF data.

An overview of the computational models, fibrillation data used, and analytical approach is provided in Figure 2.

Computational models

Aliev-Panfilov model

A simulation of fibrillation-like spiral-defect chaos was generated using the APV model (Aliev and Panfilov, 1996). In this a spiral wave was generated on an map with an inhomogeneous surface, leading to break up and additional spiral waves and free wavelets. A 200 × 200-pixel simulation was computed. Ten simulations were developed using identical model parameters, but with different patterns of randomly distributed inhomogeneities, μ_1 . A full description of the model details are provided in Supplementary Material S2.

Atrial fibrillation models

Computational models of AF were also used to examine the influence of an inspection paradox. The computational models of AF were based on the Courtemanche-Ramirez-Nattel cell model (Courtemanche et al., 1998; Kneller et al., 2002; Aguilar et al., 2017) These models were developed as described during a previously published study (Dharmaprani et al., 2021) The full details of these models are further detailed in Supplementary Material S3.

Animal models of fibrillation

Optical mapping was performed as previously described in rat AF and VF models (Aguilar et al., 2015; Xiong et al., 2015; Nattel et al., 2017; Dharmaprani et al., 2019b).

For AF, the heart was excised and perfused with Krebs solution at 30 ml/min and 37°C for 30 min. Following electrical/mechanical decoupling with blebbistatin (15 μmol/L), the heart was loaded with di-4-ANEPPS (Biotium, Inc, Hayward, CA). RA free wall fluorescence was recorded at 1 kHz, using a charge coupled device (CardioCCD, RedShirtImaging, LLC, Decatur, Georgia). Recording duration was 1 s for n = 3 cases.

In VF, rat hearts were retrogradely perfused with oxygenated Tyrodes solution (37°C, perfusion pressure 60 mmHg). Recording duration was 2 s for n = 10 cases (Ilkan et al., 2018; Dharmaprani et al., 2019b; Strauss et al., 2019).

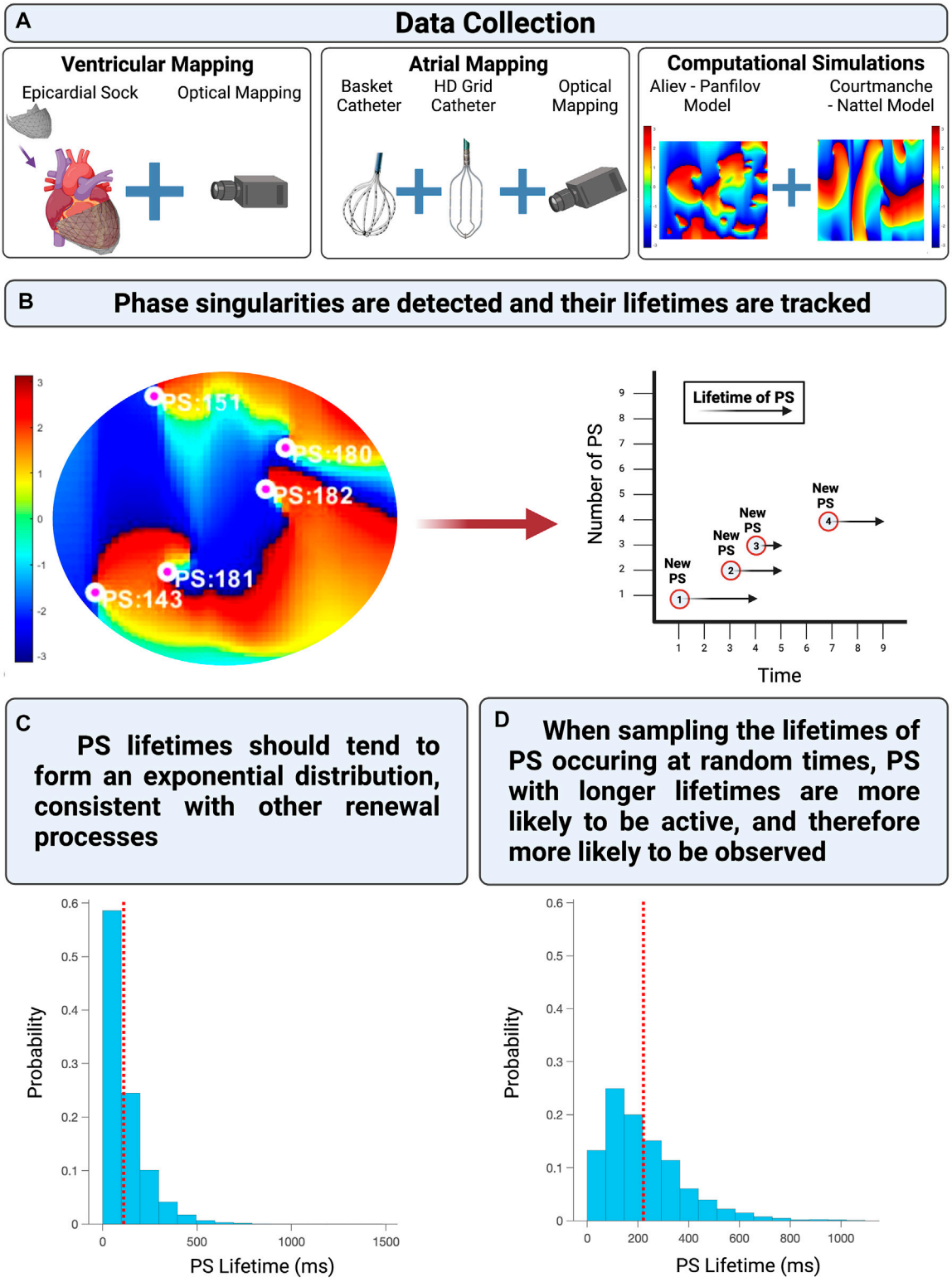

FIGURE 2
(A) The experimentally acquired data, clinically acquired data, and computational simulations utilized in this study. **(B)** Shows presents an example of PS detected and tracked on a phase map. **(C)** Demonstrates the distribution of PS lifetimes when all PS are properly sampled from an epoch of fibrillation. **(D)** Demonstrates the distribution of PS lifetimes when only PS present at a randomly chosen timepoint (such as the commencement of a recording) are observed.

Human fibrillation mapping

The study also included data from human AF and VF. Human AF data was mapped from previously analysed basket catheter and HD-grid recordings prior to AF ablation (Dharmaprani et al., 2019a; Dharmaprani et al., 2019b; Dharmaprani et al., 2021; Schopp et al., 2021) For the basket data, 64-electrode basket catheters were used [Constellation, Boston Scientific, 48 mm (4 mm spacing), 60 mm (5 mm spacing)]. Unipolar electrogram recordings were obtained from patient recordings [0.5–500 Hz, 2000 Hz sampling frequency]. For basket catheter recordings, n = 11 patients for the basket catheters (mean duration = 56.54 s, 95% CI = 1.74 s), and for HD-grid recordings n = 10 patients. Ethics approval was obtained (IRB approval number 110634). For HD-grid data, a 16-pole Advisor™-HD grid catheter (3 mm electrodes, 3 mm equidistant spacing) was used to obtain 1-min recordings from the left inferior pulmonary vein.

The human VF data utilised in this study was acquired as previously described (Nash et al., 2006) In brief, this data was obtained from patients undergoing cardiac surgery. A 256-electrode epicardial sock was placed around the ventricle, and VF was induced by electrical stimulation after cross-clamping the aorta. 2.5-min unipolar electrogram signals were recorded [1000Hz sampling frequency] with a UneMap recording system. Ethics approval was obtained (IRB approval number REC 01/0130).

Signal processing and phase singularity detection

Signal pre-processing was performed as in previous studies (Nash et al., 2006; Dharmaprani et al., 2019b; Dharmaprani et al., 2021). For human AF recordings, the unipolar electrograms and surface electrograms were exported from NavX. QRS subtraction was performed, followed by 4th order 1–30 Hz bandpass Butterworth filtering, 8th order 10 Hz lowpass Butterworth filtering, and sinusoidal recompositioning (Kuklik et al., 2014; Dharmaprani et al., 2021). For human VF unipolar epicardial signals from the 256 electrode epicardial sock were mapped onto a 2D grid, with the instantaneous phase calculated using the Hilbert Transform (Nash et al., 2006). Instantaneous phase was calculated by applying the Hilbert transform to sinusoidally reconstructed signals (Dharmaprani et al., 2021; Dharmaprani et al., 2022). PS tracking was performed as previously described, utilizing an algorithm to compare the locations of PS in order to create a continuous data-table of when a new PS occurs and when it has been destroyed (Dharmaprani et al., 2019b; Dharmaprani et al., 2021; Dharmaprani et al., 2022). This data-table was used to construct a distribution of PS lifetimes. This distribution was fit to an exponential distribution using maximum likelihood as previously described (Dharmaprani et al., 2021; Dharmaprani et al., 2022). Signal processing and PS detection techniques are further described in Supplementary Material S4 and S5

Simulating observation/recording at random times

To model the effect of observing an inspection paradox, 10,000 randomly selected commencement timepoints were selected across full recordings of fibrillation. These timepoints represent an instance of observation and demonstrate the potential impact of short-term observations around these points. The start times and end times of all PS active at the selected timepoints were used to create a list of lifetimes. The means of the overall PS lifetimes and the 10,000 samples were compared.

Statistical analysis

Distributional fitting was performed using maximum likelihood estimation. Distributional parameters were compared with a paired sample t-test, with significance α-value set at p = 0.05. An important consideration in the computational simulations is that of p-values, due to the fact that these can be replicated many times (Liberos et al., 2017). In the interests of interpretability to a wider scientific audience, we have presented findings with p-values and specified the number of replicates.

Sensitivity analysis

A sensitivity analysis was performed in order to confirm that the different statistics between the observed vs. overall PS lifetime distributions were due to an inspection paradox. To address this several approaches were taken, including 1) adjustment of grid sizes in the simulated data to confirm that the size of the observed field of view did not induce an inspection paradox, 2) use of a 3D model of fibrillation to confirm that it is not a feature of 2D mapping techniques.

For the n = 10 simulations generated using the Aliev-Panfilov computational simulations, the grid size was varied. The grid size was varied from 50 × 50 pixels to 200 × 200 pixels. This was performed through constraining the 200 × 200 grid, to 150 × 150 pixels, 100 × 100 pixels, 80 × 80 pixels, 50 × 50 pixels, 30 × 30 pixels, and 20 × 20 pixels.

A 3D computational simulation of AF using the Courtmanche-Ramirez-Nattel model was also examined (Courtemanche et al., 1998). The model was constructed from cardiac MRI data of an AF patient. This model was generated during a previously published study (Roney et al., 2020).

Results

We examined the potential for an inspection paradox in seven model systems: 1) two computational models; 2) two experimental models of AF and VF examined with optical mapping; and 3) three mapping modalities for human AF and VF data.

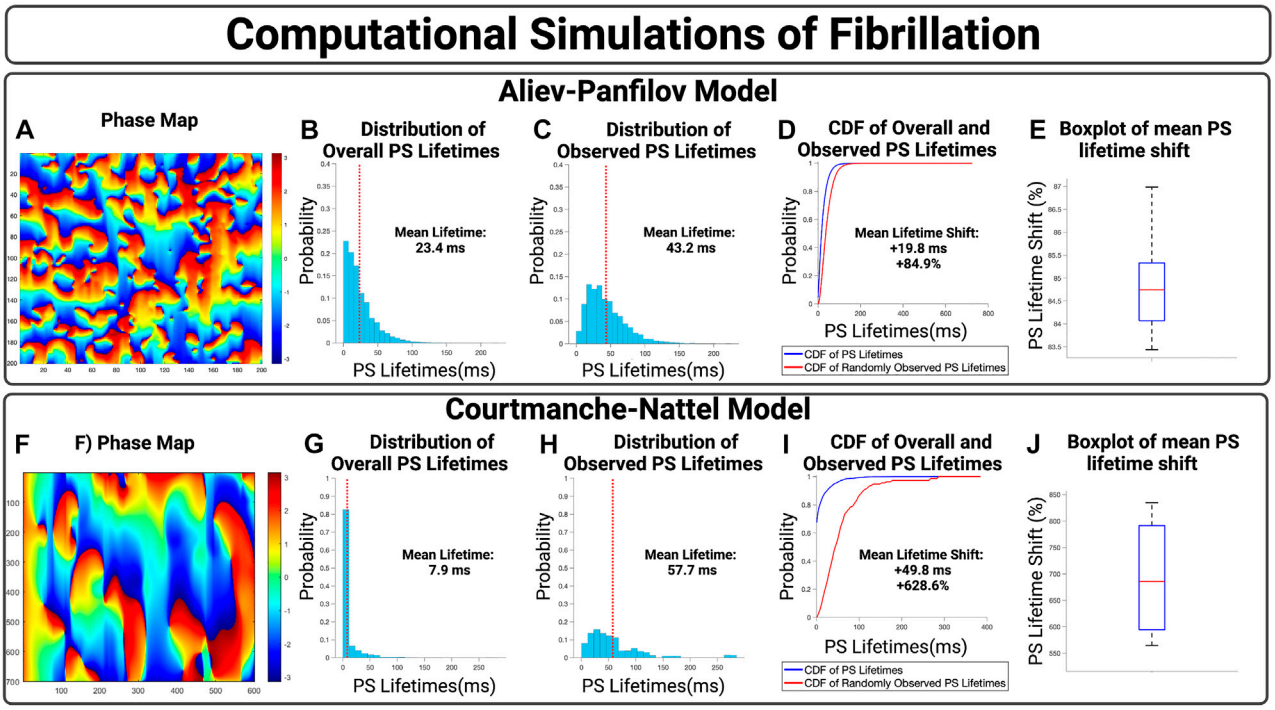

FIGURE 3
(A–D) Presents an example case of an APV simulation. **(B,G)** presents the overall distribution of PS lifetimes across a full epoch of their respective model systems. **(C,H)** Demonstrate the distribution of observed PS sampled at the 10,000 commencement timepoints. **(D,I)** Presents the cumulative distribution functions (CDF) of the overall and observed PS lifetimes. **(E)** shows the boxplot of mean lifetime shifts across n = 10 APV cases, with an increase in the mean PS lifetime of +19.7 ms (95% CI, ± 0.1 ms) and an overall lifetime shift of +84.9% (95% CI, ± 0.3%). ($p < 0.001$ for observed vs. overall). **(F–I)** presents an example case of a 2D computational model of fibrillation. **(J)** For n = 4 cases, there was an increase in mean PS lifetimes of +45.5 (95% CI, ± 1.9 ms) and an overall lifetime shift of +692.9% (95% CI, ± 57.7%). ($p < 0.001$ for observed vs. overall).

Computational simulations

We first show the effect of an inspection paradox in the APV model, Figures 3A–E. In Figures 3A–D, an example case is presented with an observed mean PS lifetime increase of +59.8 ms and overall lifetime shift of +115.3%. For n = 10 cases, the mean increase in PS lifetimes +19.7 ms (95% CI, ± 0.1 ms) and an overall mean lifetime shift of +84.9% (95% CI, ± 0.3%) ($p < 0.001$ for observed vs. overall).

The effect of an inspection paradox is next shown in 2D AF simulations are shown in Figures 3F–J. In Figures 3F–I, an example case is presented with an increase in mean PS lifetime of +49.8 ms and an overall lifetime shift of +628.6%. For n = 4 cases, there was an increase in mean PS lifetimes of +45.9 ms (95% CI, ± 1.9 ms) and a mean PS lifetime shift of +692.9% (95% CI, ± 57.7%) ($p < 0.001$ for observed vs. overall).

Atrial fibrillation

To examine the potential influence of an inspection paradox in experimentally acquired AF, we first examined optically mapped AF in rat models. A representative case is presented in Figures 4A–D, with a PS lifetime increase of +120.5 ms and a PS lifetime shift of +303.5%. For n = 3 cases, the mean increase in observed PS lifetimes was +122.6 ms (95% CI, ± 27.5 ms) and a mean PS lifetime shift was +374.6 (95% CI, ± 88.5%) (p = 0.052 for observed vs. overall).

The potential effect of an inspection paradox was next examined in human AF. For basket catheter recordings, a representative example case is shown in Figures 4F–I, with an observed PS lifetime increase of +86.6 ms and a PS lifetime shift of +126.0%. For n = 10 cases, the mean increase in PS lifetimes was 82.6 ms (95% CI, ± 7.1 ms) and a mean PS lifetimes shift of 135.3% (95% CI, ± 5.0%) ($p < 0.04$ for observed vs. overall).

Human AF recorded using HD Grid Catheters was also examined. From a sample of n = 10, a representative example is presented in Figure 4K–N, with an increase in mean observed PS lifetimes of +68.4 ms and an overall PS lifetime shift of +135.2%. For n = 10 cases, the mean increase in PS lifetimes was +64.3 ms (95% CI, ± 5.8 ms) and a mean PS lifetime shift of +150.8% (95% CI, ± 9.0%) ($p <$ 0.001 for observed vs. overall).

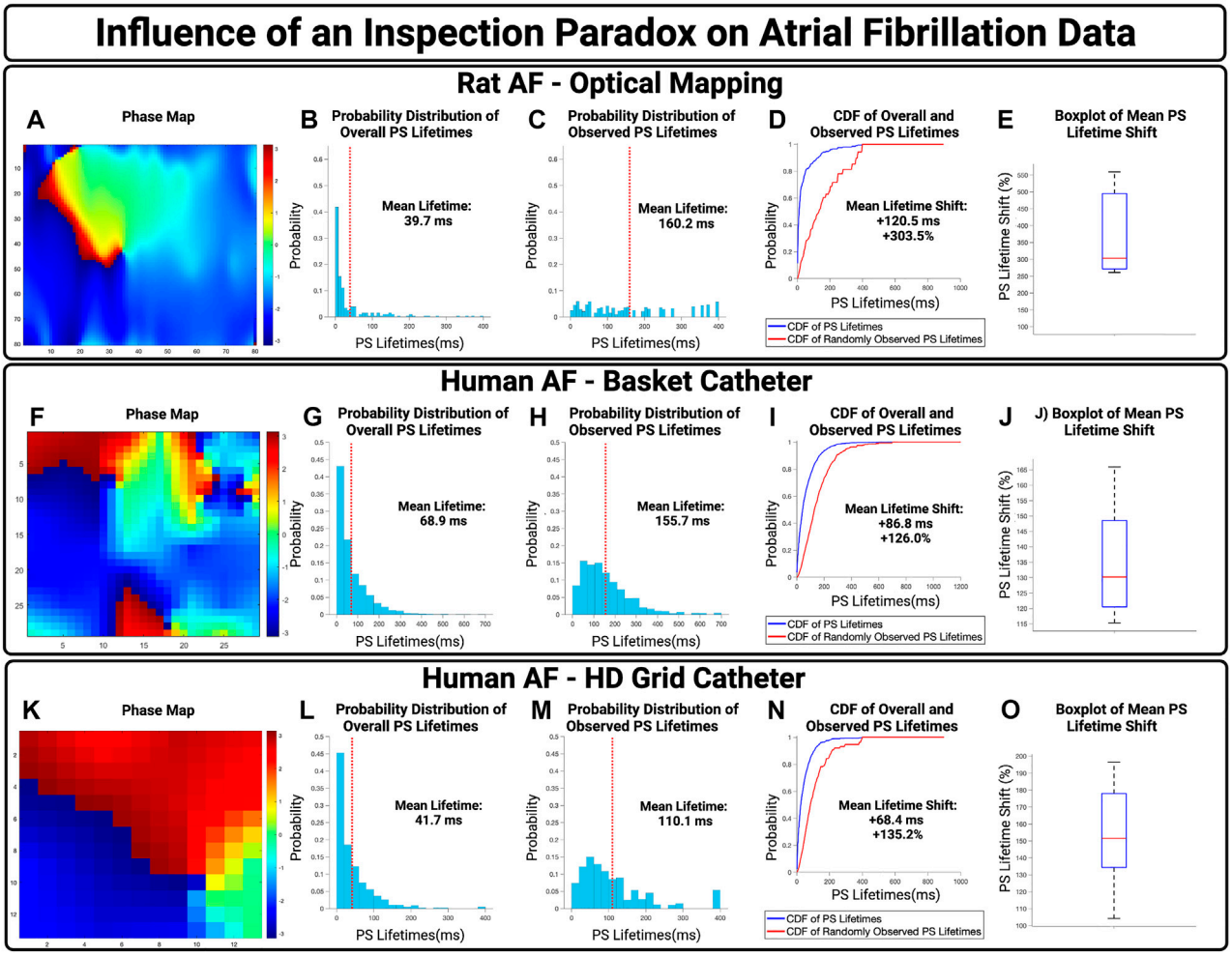

FIGURE 4
The influence of an inspection paradox on AF data. **(A–D)** Presents an example case of optically mapped rat AF, **(F–I)** presents an example case of basket catheter recorded human AF, **(K–N)** Presents an example case of HD grid recorded human AF. **(B,G,L)** Presents the overall distribution of PS lifetimes across full epochs of AF. **(C,H,M)** Demonstrates the distribution of observed PS sampled at the 10,000 commencement timepoints. **(D,I,M)** Presents the cumulative distribution functions (CDF) of the overall and observed PS lifetimes. **(E)** In n = 3 cases of optical mapping, the increase in mean PS lifetime was 122.6 ms (95% CI, ± 27.5 ms) and the overall mean PS lifetime shift was +374.6% (95% CI, ± 88.5%) (p = 0.052 for observed vs. overall). **(J)** In n = 10 cases, the increase in mean PS lifetime was 78.8 ms (95% CI, ± 9.2 ms) and the overall mean lifetime shift of PS was +129.2% (95% CI, ± 4.1%) (p = 0.04 for observed vs. overall). **(O)** In n = 10 cases, the increase in mean PS lifetime was 64.3 ms (95% CI, ± 5.8 ms) and the overall mean PS lifetime shift was +150.8 (95% CI, ± 9.0%) (p < 0.001 for observed vs. overall).

In basket catheter, HD-grid catheter, and optical recordings of AF, the probability distributions of observed PS lifetimes were shifted towards a higher probability of longer lifetimes.

Ventricular fibrillation

We next examined the influence of an inspection paradox in VF data. Optically mapped VF from rat models were first used, with an example case in Figures 5A–D. This example demonstrated a mean PS lifetime increase of +36.8 ms and an overall lifetime shift of +133.7% Across n = 10 cases, there was an increase in the mean PS lifetime of +40.0 ms (95% CI, ± 5.1 ms) and an overall shift in the mean PS lifetime shift of +171.3% (95% CI, ± 15.6%) (p < 0.001 for observed vs. overall).

We next evaluated the potential effect of an inspection paradox in human VF. A representative example is shown in Figures 5F–I, from patients with human VF, As summary box plot is shown in Figure 5D showing the range of mean PS lifetime

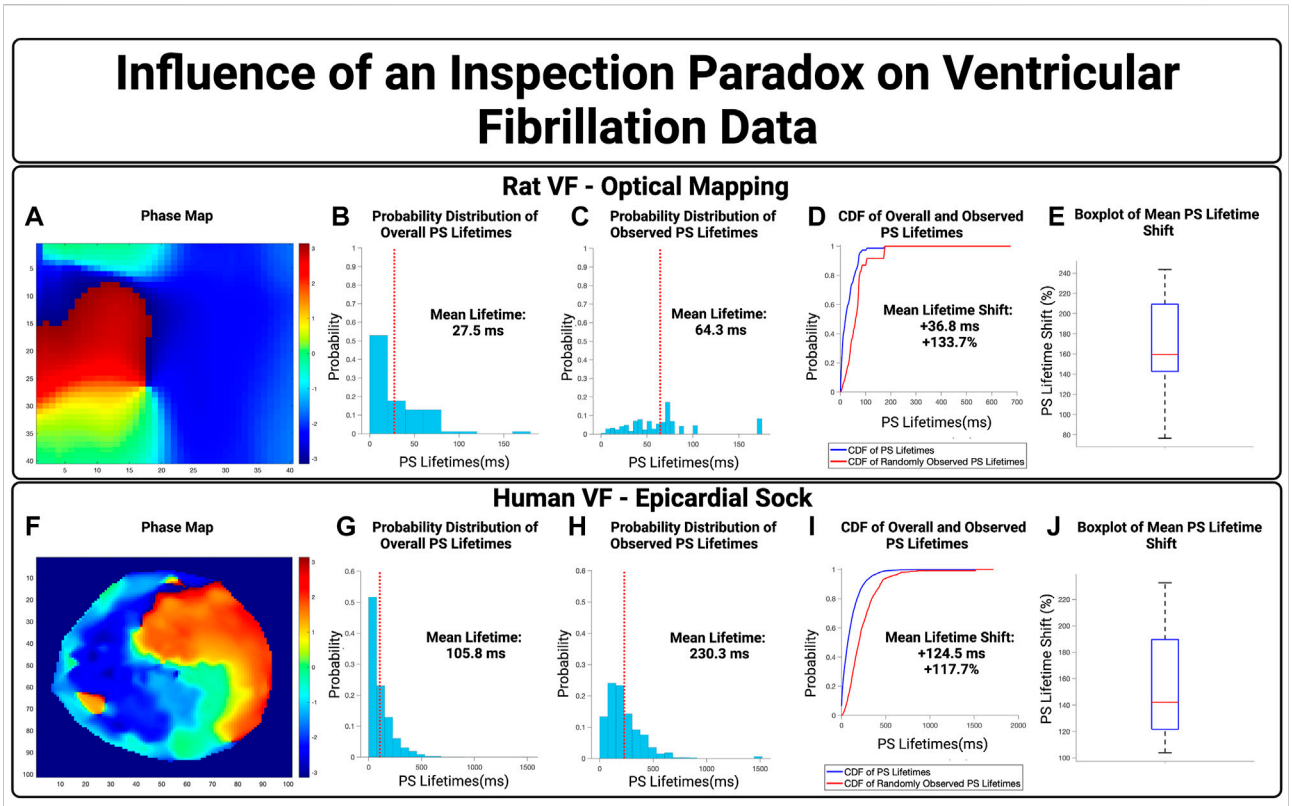

FIGURE 5
The Influence of an inspection paradox on VF data. **(A–D)** Show an example case of optically mapped rat VF, and **(F–I)** shows an example case of human VF recording through a 256 electrode epicardial sock. **(B,G)** Show the overall distribution of PS lifetimes across full epochs of VF. **(C,H)** Show the distribution of PS lifetimes observed across the 10,000 samples. **(D,I)** Presents the cumulative distribution functions (CDF) of the overall and observed PS lifetimes. **(E)** In optically mapped rat VF, there was an increase in the mean PS lifetime of +40.0 ms (95% CI, ±5.1 ms) and an overall mean lifetime shift of +171.3% (95% CI, ± 15.6%) ($p < 0.001$ for observed vs. overall). **(J)** In human VF, in n = 8 cases, there was an increase in the mean PS lifetime of +159.5 ms (95% CI, ±15.2 ms) and an overall mean lifetime shift of +153.5% (95% CI, ± 15.7%) ($p < 0.001$ for observed vs. overall).

shifts. In $n = 8$ cases examined, the increase in mean lifetime of PS was +159.5 ms (95% CI, ± 15.2 ms) and an overall shift in the mean lifetimes of PS +153.5% (95% CI, ± 15.7%) ($p < 0.001$ for observed vs. overall).

Overall, in both epicardial electrogram recordings of human VF and optically mapped rat VF, the probability distributions of observed PS lifetimes were shifted towards a higher probability of longer lifetimes.

Sensitivity analysis

As part of a sensitivity analysis, a 3D computational simulation of fibrillation in a detailed geometry was also examined. In this simulation, an inspection paradox could result in an increase in observed PS lifetimes of +791.7 ms and a mean lifetime shift of +691.7%.

An additional sensitivity analysis was performed examining whether the size of the system influenced the computational simulations. At different grid sizes, an inspection paradox led to increases in the mean lifetime observed. At 20 × 20 pixels a relative lifetime increase of +114.8% (+17.2 ms), at 30 × 30 pixels a relative increase of +105.2% (+18.0 ms), at 50 × 50 pixels a relative increase of +94.1% (+18.4 ms), at 80 × 80 pixels a relative increase of +87.9% (+18.6 ms), at 100 × 100 pixels a relative increase of +87.1% (+18.9 ms), at 150 × 150 = pixels a relative increase of +85.5% (+19.3 ms), at 200 × 200 pixels a relative increase of +84.9% (+19.7 ms).

Discussion

Spiral vortex regeneration is a feature of many spatiotemporally turbulent systems in nature. The statistical properties of topological defects known as phase singularities (PS), located at the pivot of spiral wave vortices, appear to be common, despite differences in underlying generating processes. Specifically, the populations of PS have been shown to adopt

Poisson-type distributions, (Gil et al., 1990; Wang, 2004) and the lifetimes of PS appear to be exponentially distributed (Tan et al., 2020). These statistical properties are important because they are consistent with a notion of effective statistical independence of creation and annihilation events.

It appears that cardiac fibrillation may share these statistical properties. A substantial body of evidence from multiple laboratories using multiple mapping approaches in AF and VF suggests that lifetimes of spiral vortices in AF and VF (and the more sustained spirals lasting more than one rotation) also adopt exponential-type distributions (Chen et al., 2000a; Chen et al., 2000b; Kay et al., 2006; Kuklik et al., 2016; Child et al., 2018; Christoph et al., 2018). We recently confirmed these data, with these studies of AF and VF suggesting the population dynamics of spirals in cardiac fibrillation analogous to spiral vortex regeneration in physical, chemical and biological systems in nature (Dharmaprani et al., 2019b; Dharmaprani et al., 2021; Dharmaprani et al., 2022).

Cardiac fibrillation is characterised by continuous regeneration of spiral waves (Dharmaprani et al., 2019b). Recently, we have shown that PS and wavelet regeneration can be modelled as renewal processes (Dharmaprani et al., 2019b; Dharmaprani et al., 2021). In a renewal process, individual events are effectively statistically independent, and over time may converge to a constant hazard rate (Ross, 2014). We have shown that the formation and destruction of PS and wavelets may adopt this property in human, experimental and simulated cardiac fibrillation (Dharmaprani et al., 2019b; Dharmaprani et al., 2021). The renewal theory approach has a number of key strengths: 1) It provides simple probabilistic models to analysing clinical and experimental arrhythmias; (Qu, 2022) 2) It connects fibrillatory dynamics to other spatiotemporally turbulent natural systems characterised by regeneration of spiral vortices—providing useful principles that may assist understanding challenging problems in AF and VF, such as the difficulty in reliable identification of driving rotors, and the origin of the critical mass hypothesis (Zipes et al., 1975; Kim et al., 1997; Vidmar and Rappel, 2019).

In this study, we sought to evaluate the impact of the renewal process on PS lifetime observation. We hypothesised that if PS lifetimes are modelled as renewal processes, there was a possibility that PS occurring around the commencement of a recording would have disproportionately longer lifetimes than the true mean PS lifetime, due to an inspection paradox. In periods of short observation, such as short recordings during optical mapping studies, there would a relative increase in the probability of oversampling prolonged PS lifetimes, in particular at the initiation of a recording.

We illustrated that the inspection paradox could lead to a relative emphasis on prolonged events in a theoretical simulated renewal process. To date, the possibility of an inspection paradox in recordings of cardiac fibrillation has not to our knowledge previously been established in prior published investigations. A strength of our study is the comprehensive approach to validation and quantitation of this effect in multiple settings. Specifically, we have shown that an inspection paradox has the potential to occur in both AF and VF, in simulated, and experimentally mapped AF and VF in animal models and humans, and that it was independent of the modality by which cardiac fibrillation is recorded. This suggests that the possibility of inspection paradoxes is a general property of fibrillatory dynamics that should be considered in both mechanistic and clinical studies of AF and VF.

The potential influence of an inspection paradox is particularly noticeable in systems which have not undergone long periods of recording, such as the optical mapping datasets utilized here. The distributions of observed lifetimes lack the distinctive shape present in systems with longer recordings (such as the basket catheter, HD-grid catheter, epicardial VF sock, and computational simulations utilized in this study), while still demonstrating that longer lifetime events are more probably to occur, as shown by the greater mean lifetime for observed PS lifetimes. This suggests that an inspection paradox can have a more distorting influence on shorter datasets, with a preference for long lifetime PS.

An inspection paradox is a potentially important consideration in efforts to ablate re-entrant circuits as potential “drivers” of AF, because purely visual inspection of AF recordings would tend to fall during periods of relatively sustained re-entry. It would therefore be important to examine the overall temporal distribution of re-entrant circuit lifetimes to avoid inadvertent over-sampling of longer lasting PS by chance.

Relationship to spatiotemporal turbulence in other natural systems

A fundamental property of nonequilibrium spatiotemporally turbulent systems throughout nature is the presence of the regeneration of spiral wave type vortices (Cross and Hohenberg, 1993; Cross and Greenside, 2009). This property of repetitive creation and annihilation of spiral defects have been shown to have common statistical laws, with an exponential distribution of defect lifetimes and Poisson distribution of PS population (Tan et al., 2020; Jenkins et al., 2022). These properties have been shown to apply in a variety of physical (Morris et al., 1993; Ouyang and Flesselles, 1996; Egolf et al., 2000), chemical (Beta et al., 2006; Qiao et al., 2009), and biological systems (Lechleiter et al., 1991; Tan et al., 2020) characterised by the repetitive creation and destruction spirals. These properties have recently been shown to apply to the comparably spatiotemporally turbulent biological process of cardiac fibrillation in the heart (Dharmaprani et al., 2019b; Dharmaprani et al., 2021;

Dharmaprani et al., 2022). The consistency of these statistical properties is evident in the visual distributions of PS lifetimes in cardiac fibrillation published by multiple laboratories around the world (Chen et al., 2000a; Chen et al., 2000b; Kay et al., 2006; Kuklik et al., 2016; Child et al., 2018; Christoph et al., 2018).

Given the consistency of these statistical laws across spatiotemporally turbulent systems in nature, their validation in the context of cardiac fibrillation is to be expected. Further, it would strongly suggest that the distributions of PS defect lifetimes observed in this study, and previous investigations of cardiac fibrillation, have not occurred due to the method of sampling or mapping, but are a fundamental and generic property of the spatiotemporal turbulence as a natural phenomenon. We have recently shown that the origin of these statistical properties arises in the effective statistical independence of consecutive formation and destruction events (Jenkins et al., 2022).

The current manuscript deals the inspection paradox in the context of cardiac fibrillation as an example of natural biological spatiotemporal turbulence, However, given the common statistical properties of topological defect dynamics in cardiac fibrillation and other systems in nature, the issue of an inspection paradox has the potential to have a broader occurrence in each of these other systems.

How to avoid the inspection paradox

The purpose of the current manuscript is to highlight the importance of considering the possibility of an inspection paradox arising in recordings of AF and VF. The keys to avoiding the inspection paradox are: 1) Focus on the overall distribution of PS lifetimes as opposed to the most-sustained PS lifetimes; 2) As far as possible use continuous recording modalities (e.g., with dyes that are resistant to photobleaching, or continuous electrogram recording), to enable the full distribution of PS lengths to be fully characterised. To understand the fibrillatory process, it may require a focus on the lifetimes of all lengths of PS, rather than consideration of only the longest re-entrant episodes. We would suggest in publications that examine PS lifetimes the overall PS lifetime distribution should be published, ideally not just the longest lasting re-entry episodes. If possible, renewal rate constants for the rate of formation and destruction of re-entrant circuits should be examined, as these metrics have the potential to be more statistically stable than the lifetime of individual re-entrant circuits (Dharmaprani et al., 2019b; Dharmaprani et al., 2021; Dharmaprani et al., 2022).

Conclusion

The inspection paradox can be a potential source of inadvertent error when observing AF or VF. Visual inspection of phase movies has the potential to systematically oversample prolonged longer-lasting PS, giving the impression of sustained rotors. The effect of the inspection paradox is minimised by careful consideration of the overall PS lifetime distribution over prolonged windows in cardiac fibrillation recordings.

Data availability statement

The original contributions presented in the study are included in the article/Supplementary Material, further inquiries about the data used to support conclusions of this article can be directed to the corresponding author.

Ethics statement

The studies involving human participants were reviewed and approved by The Hospital Ethics Committee and The Southern Adelaide Local Health Network. The patients/participants provided their written informed consent to participate in this study. The animal study was reviewed and approved by The Animal Ethics Committee of the Montreal Heart Institute and The Icahn School of Medicine Institutional Animal Care and Use Committee.

Author contributions

EJ contributed to the analysis and manuscript draft. DD contributed to the analysis and editorial input. MS contributed to the modelling. JQ and KT contributed to the data collection. LM contributed to the editorial input. MA contributed to the modelling. KP contributed to the editorial input. FA contributed to the data collection. CR, SAN, and SN contributed to the modelling. MN and RC contributed to the data collection. AG contributed to the concept, study design, data collection, and editorial supervision.

Funding

This work was supported by the National Health and Medical Research Council of Australia Ideas Grant (No. 2010522) and the National Heart Foundation of Australia (No. 101188).

Conflict of interest

The authors declare that the research was conducted in the absence of any commercial or financial relationships that could be construed as a potential conflict of interest.

Publisher's note

All claims expressed in this article are solely those of the authors and do not necessarily represent those of their affiliated organizations, or those of the publisher, the editors and the reviewers. Any product that may be evaluated in this article, or claim that may be made by its manufacturer, is not guaranteed or endorsed by the publisher.

Supplementary material

The Supplementary Material for this article can be found online at: https://www.frontiersin.org/articles/10.3389/fphys.2022.920788/full#supplementary-material

References

Abo-Shaeer, J. R., Raman, C., and Ketterle, W. (2002). formation and decay of vortex lattices in bose-einstein condensates at finite temperatures. *Phys. Rev. Lett.* 88 (7), 070409. doi:10.1103/PhysRevLett.88.070409

Aguilar, M., Feng, J., Vigmond, E., Comtois, P., and Nattel, S. (2017). Rate-dependent role of IKur in human atrial repolarization and atrial fibrillation maintenance. *Biophys. J.* 112 (9), 1997–2010. doi:10.1016/j.bpj.2017.03.022

Aguilar, M., Xiong, F., Qi, X. Y., Comtois, P., and Nattel, S. (2015). Potassium channel blockade enhances atrial fibrillation–selective antiarrhythmic effects of optimized state-dependent sodium channel blockade. *Circulation* 132 (23), 2203–2211. doi:10.1161/CIRCULATIONAHA.115.018016

Aliev, R. R., and Panfilov, A. V. (1996). A simple two-variable model of cardiac excitation. *Chaos, Solit. Fractals* 7 (3), 293–301. doi:10.1016/0960-0779(95)00089-5

Angus, J. E. (1997). Classroom note:the inspection paradox inequality. *SIAM Rev. Soc. Ind. Appl. Math.* 39 (1), 95–97. doi:10.1137/S003614459529298X

Beta, C., Mikhailov, A. S., Rotermund, H. H., and Ertl, G. (2006). Defect-mediated turbulence in a catalytic surface reaction. *Europhys. Lett.* 75 (6), 868–874. doi:10.1209/epl/i2006-10215-5

Chen, J., Mandapati, R., Berenfeld, O., Skanes, A. C., Gray, R. A., and Jalife, J. (2000a). Dynamics of wavelets and their role in atrial fibrillation in the isolated sheep heart. *Cardiovasc. Res.* 48 (2), 220–232. doi:10.1016/s0008-6363(00)00177-2

Chen, J., Mandapati, R., Berenfeld, O., Skanes, A. C., and Jalife, J. (2000b). High-frequency periodic sources underlie ventricular fibrillation in the isolated rabbit heart. *Circ. Res.* 86 (1), 86–93. doi:10.1161/01.res.86.1.86

Child, N., Clayton, R. H., Roney, C. R., Laughner, J. I., Shuros, A., Neuzil, P., et al. (2018). Unraveling the underlying arrhythmia mechanism in persistent atrial fibrillation: Results from the STARLIGHT study. *Circ. Arrhythm. Electrophysiol.* 11 (6), e005897. doi:10.1161/CIRCEP.117.005897

Christoph, J., Chebbok, M., Richter, C., Schröder-Schetelig, J., Bittihn, P., Stein, S., et al. (2018). Electromechanical vortex filaments during cardiac fibrillation. *Nature* 555 (7698), 667–672. doi:10.1038/nature26001

Comtois, P., Kneller, J., and Nattel, S. (2005). Of circles and spirals: Bridging the gap between the leading circle and spiral wave concepts of cardiac reentry. *Europace* 7, 10–20. doi:10.1016/j.eupc.2005.05.011

Coullet, P., Gil, L., and Lega, J. (1989). Defect-mediated turbulence. *Phys. Rev. Lett.* 62 (14), 1619–1622. doi:10.1103/PhysRevLett.62.1619

Courtemanche, M., Ramirez, R. J., and Nattel, S. (1998). Ionic mechanisms underlying human atrial action potential properties: Insights from a mathematical model. *Am. J. Physiol.* 275 (1), H301–H321. doi:10.1152/ajpheart.1998.275.1.H301

Cross, M. C., and Hohenberg, P. C. (1993). Pattern formation outside of equilibrium. *Rev. Mod. Phys.* 65 (3), 851–1112. doi:10.1103/revmodphys.65.851

Cross, M., and Greenside, H. (2009). *Pattern formation and dynamics in nonequilibrium systems*. Cambridge, UK: Cambridge University Press.

Davidsen, J., Zhan, M., and Kapral, R. (2008). Filament-induced surface spiral turbulence in three-dimensional excitable media. *Phys. Rev. Lett.* 101 (20), 208302. doi:10.1103/PhysRevLett.101.208302

Dharmaprani, D., Jenkins, E., Aguilar, M., Quah, J. X., Lahiri, A., Tiver, K., et al. (2021). M/M/Infinity birth-death processes–A quantitative representational framework to summarize and explain phase singularity and wavelet dynamics in atrial fibrillation. *Front. Physiol.* 11, 616866. doi:10.3389/fphys.2020.616866

Dharmaprani, D., Jenkins, E. V., Quah, J. X., Lahiri, A., Tiver, K., Mitchell, L., et al. (2022). A governing equation for rotor and wavelet number in human clinical ventricular fibrillation: Implications for sudden cardiac death. *Heart rhythm.* 19 (2), 295–305. doi:10.1016/j.hrthm.2021.10.008

Dharmaprani, D., McGavigan, A. D., Chapman, D., Kutlieh, R., Thanigaimani, S., Dykes, L., et al. (2019a). Temporal stability and specificity of high bipolar electrogram entropy regions in sustained atrial fibrillation: Implications for mapping. *J. Electrocardiol.* 53, 18–27. doi:10.1016/j.jelectrocard.2018.11.014

Dharmaprani, D., Schopp, M., Kuklik, P., Chapman, D., Lahiri, A., Dykes, L., et al. (2019b). Renewal theory as a universal quantitative framework to characterize phase singularity regeneration in mammalian cardiac fibrillation. *Circ. Arrhythm. Electrophysiol.* 12 (12), e007569. doi:10.1161/CIRCEP.119.007569

Ecke, R. E., and Hu, Y. (1997). Spiral defect chaos in Rayleigh-Be´ nard convection: Defect population statistics. *Phys. A Stat. Mech. its Appl.* 239 (1-3), 174–188. doi:10.1016/s0378-4371(97)00026-5

Egolf, D. A., Melnikov, I. V., Pesch, W., and Ecke, R. E. (2000). Mechanisms of extensive spatiotemporal chaos in Rayleigh–Bénard convection. *Nature* 404 (6779), 733–736. doi:10.1038/35008013

Gil, L., Lega, J., and Meunier, J. (1990). Statistical properties of defect-mediated turbulence. *Phys. Rev. A* 41 (2), 1138–1141. doi:10.1103/physreva.41.1138

Huang, X., Xu, W., Liang, J., Takagaki, K., Gao, X., and Wu, J.-y. (2010). Spiral wave dynamics in neocortex. *Neuron* 68 (5), 978–990. doi:10.1016/j.neuron.2010.11.007

Ilkan, Z., Strauss, B., Campana, C., and Akar, F. G. (2018). "Optical action potential mapping in acute models of ischemia–reperfusion injury: Probing the arrhythmogenic role of the mitochondrial translocator protein," in *Experimental models of cardiovascular Diseases* (Berlin, Germany: Springer), 133–143.

Jenkins, E. V., Dharmaprani, D., Schopp, M., Quah, J. X., Tiver, K., Mitchell, L., et al. (2022). Understanding the origins of the basic equations of statistical fibrillatory dynamics. *Chaos* 32 (3), 032101. doi:10.1063/5.0062095

Kay, M. W., and Rogers, J. M. (2006). Epicardial rotors in panoramic optical maps of fibrillating swine ventricles. *Conf. Proc. IEEE Eng. Med. Biol. Soc.*, 2268–2271. doi:10.1109/iembs.2006.260635

Kay, M. W., Walcott, G. P., Gladden, J. D., Melnick, S. B., and Rogers, J. M. (2006). Lifetimes of epicardial rotors in panoramic optical maps of fibrillating swine ventricles. *Am. J. Physiol. Heart Circ. Physiol.* 291 (4), H1935–H1941. doi:10.1152/ajpheart.00276.2006

Kim, Y. H., Garfinkel, A., Ikeda, T., Wu, T. J., Athill, C. A., Weiss, J. N., et al. (1997). Spatiotemporal complexity of ventricular fibrillation revealed by tissue mass reduction in isolated swine right ventricle: Further evidence for the quasiperiodic route to chaos hypothesis. *J. Clin. Invest.* 100 (10), 2486–2500. doi:10.1172/JCI119791

Kneller, J., Zou, R., Vigmond, E. J., Wang, Z., Leon, L. J., and Nattel, S. (2002). Cholinergic atrial fibrillation in a computer model of a two-dimensional sheet of canine atrial cells with realistic ionic properties. *Circ. Res.* 90 (9), e73–e87. doi:10.1161/01.res.0000019783.88094.ba

Kuklik, P., Zeemering, S., Maesen, B., Maessen, J., Crijns, H. J., Verheule, S., et al. (2014). Reconstruction of instantaneous phase of unipolar atrial contact electrogram using a concept of sinusoidal recomposition and Hilbert transform. *IEEE Trans. Biomed. Eng.* 62 (1), 296–302. doi:10.1109/TBME.2014.2350029

Kuklik, P., Zeemering, S., van Hunnik, A., Maesen, B., Pison, L., Lau, D. H., et al. (2016). Identification of rotors during human atrial fibrillation using contact

mapping and phase singularity detection: Technical considerations. *IEEE Trans. Biomed. Eng.* 64 (2), 310–318. doi:10.1109/TBME.2016.2554660

Lechleiter, J., Girard, S., Peralta, E., and Clapham, D. (1991). Spiral calcium wave propagation and annihilation in *Xenopus laevis* oocytes. *Science* 252 (5002), 123–126. doi:10.1126/science.2011747

Liberos, A., Bueno-Orovio, A., Rodrigo, M., Ravens, U., Hernandez-Romero, I., Fernandez-Aviles, F., et al. (2017). Reply to the editor—on misuse of null hypothesis testing: Analysis of biophysical model simulations. *Heart rhythm.* 14 (4), e50–e51. doi:10.1016/j.hrthm.2016.12.011

Morris, S. W., Bodenschatz, E., Cannell, D. S., and Ahlers, G. (1993). Spiral defect chaos in large aspect ratio Rayleigh-Bénard convection. *Phys. Rev. Lett.* 71 (13), 2026–2029. doi:10.1103/PhysRevLett.71.2026

Nash, M. P., Mourad, A., Clayton, R. H., Sutton, P. M., Bradley, C. P., Hayward, M., et al. (2006). Evidence for multiple mechanisms in human ventricular fibrillation. *Circulation* 114 (6), 536–542. doi:10.1161/CIRCULATIONAHA.105.602870

Nattel, S., Xiong, F., and Aguilar, M. (2017). Demystifying rotors and their place in clinical translation of atrial fibrillation mechanisms. *Nat. Rev. Cardiol.* 14 (9), 509–520. doi:10.1038/nrcardio.2017.37

Ouyang, Q., and Flesselles, J.-M. (1996). Transition from spirals to defect turbulence driven by a convective instability. *Nature* 379 (6561), 143–146. doi:10.1038/379143a0

Qiao, C., Wang, H., and Ouyang, Q. (2009). Defect-mediated turbulence in the Belousov-Zhabotinsky reaction. *Phys. Rev. E Stat. Nonlin. Soft Matter Phys.* 79 (1), 016212. doi:10.1103/PhysRevE.79.016212

Qu, Z. (2022). What is ventricular fibrillation? *Heart rhythm.* 19 (2), 306–307. doi:10.1016/j.hrthm.2021.10.021

Quah, J. X. D., Dharmaprani, D., Lahiri, A., Tiver, K., and Ganesan, A. N. (2021). Reconceptualising atrial fibrillation using renewal theory: A novel approach to the assessment of AF dynamics. *Arrhythmia Electrophysiol. Res. Rev.* 10 (2), 77–84. doi:10.15420/aer.2020.42

Rogers, J. M. (2004). Combined phase singularity and wavefront analysis for optical maps of ventricular fibrillation. *IEEE Trans. Biomed. Eng.* 51 (1), 56–65. doi:10.1109/TBME.2003.820341

Rogers, J. M., Huang, J., Smith, W. M., and Ideker, R. E. (1999). Incidence, evolution, and spatial distribution of functional reentry during ventricular fibrillation in pigs. *Circ. Res.* 84 (8), 945–954. doi:10.1161/01.res.84.8.945

Roney, C. H., Beach, M. L., Mehta, A. M., Sim, I., Corrado, C., Bendikas, R., et al. (2020). *In silico* comparison of left atrial ablation techniques that target the anatomical, structural, and electrical substrates of atrial fibrillation. *Front. Physiol.* 11, 1145. doi:10.3389/fphys.2020.572874

Ross, S. M. (2014). *Introduction to probability models*. Cambridge, Massachusetts, US: Academic Press.

Schlemmer, A., Berg, S., Lilienkamp, T., Luther, S., and Parlitz, U. (2018). Spatiotemporal permutation entropy as a measure for complexity of cardiac arrhythmia. *Front. Phys.* 6 (39). doi:10.3389/fphy.2018.00039

Schopp, M., Dharmaprani, D., Kuklik, P., Quah, J., Lahiri, A., Tiver, K., et al. (2021). Spatial concentration and distribution of phase singularities in human atrial fibrillation: Insights for the AF mechanism. *J. Arrhythm.* 37 (4), 922–930. doi:10.1002/joa3.12547

Strauss, B., Sassi, Y., Bueno-Beti, C., Ilkan, Z., Raad, N., Cacheux, M., et al. (2019). Intra-tracheal gene delivery of aerosolized SERCA2a to the lung suppresses ventricular arrhythmias in a model of pulmonary arterial hypertension. *J. Mol. Cell. Cardiol.* 127, 20–30. doi:10.1016/j.yjmcc.2018.11.017

Tan, T. H., Liu, J., Miller, P. W., Tekant, M., Dunkel, J., and Fakhri, N. (2020). Topological turbulence in the membrane of a living cell. *Nat. Phys.* 16 (6), 657–662. doi:10.1038/s41567-020-0841-9

Vidmar, D., and Rappel, W.-J. (2019). Extinction dynamics of spiral defect chaos012407. *Phys. Rev. E* 99 (1). doi:10.1103/PhysRevE.99.012407

Wang, H. (2004). Statistics of defect-mediated turbulence influenced by noise154101. *Phys. Rev. Lett.* 93 (15). doi:10.1103/PhysRevLett.93.154101

Winfree, A. T. (1980). "Excitable kinetics and excitable media," in *The geometry of biological time*. Editor A. T. Winfree, Berlin, Heidelberg: Springer, 231–257.

Winfree, A. T. (1987). When time breaks down: The three-dimensional dynamics of electrochemical waves and cardiac arrhythmias. Princeton, New Jersey, US: Princeton University Press.

Xiong, F., Qi, X., Nattel, S., and Comtois, P. (2015). Wavelet analysis of cardiac optical mapping data. *Comput. Biol. Med.* 65, 243–255. doi:10.1016/j.compbiomed.2015.06.022

Zipes, D. P., Fischer, J., King, R. M., deBNicoll, A., and Jolly, W. W. (1975). Termination of ventricular fibrillation in dogs by depolarizing a critical amount of myocardium. *Am. J. Cardiol.* 36 (1), 37–44. doi:10.1016/0002-9149(75)90865-6

frontiers | Frontiers in Physiology

TYPE Original Research
PUBLISHED 15 September 2022
DOI 10.3389/fphys.2022.966046

OPEN ACCESS

EDITED BY
Omer Berenfeld,
University of Michigan, United States

REVIEWED BY
Eric A. Sobie,
Icahn School of Medicine at Mount Sinai, United States
Wayne Rodney Giles,
University of Calgary, Canada

*CORRESPONDENCE
Blanca Rodriguez,
blanca.rodriguez@cs.ox.ac.uk
Albert Dasí,
albert.dasiimartinez@cs.ox.ac.uk

SPECIALTY SECTION
This article was submitted to Cardiac Electrophysiology, a section of the journal Frontiers in Physiology

RECEIVED 10 June 2022
ACCEPTED 23 August 2022
PUBLISHED 15 September 2022

CITATION
Dasí A, Roy A, Sachetto R, Camps J, Bueno-Orovio A and Rodriguez B (2022), *In-silico* drug trials for precision medicine in atrial fibrillation: From ionic mechanisms to electrocardiogram-based predictions in structurally-healthy human atria.
Front. Physiol. 13:966046.
doi: 10.3389/fphys.2022.966046

In-silico drug trials for precision medicine in atrial fibrillation: From ionic mechanisms to electrocardiogram-based predictions in structurally-healthy human atria

Albert Dasí[1]*, Aditi Roy[1], Rafael Sachetto[2], Julia Camps[1], Alfonso Bueno-Orovio[1] and Blanca Rodriguez[1]*

[1]Department of Computer Science, University of Oxford, Oxford, United Kingdom, [2]Departamento de Ciência da Computação, Universidade Federal De São João Del-Rei, São João del Rei, Brazil

Atrial fibrillation (AF) inducibility, sustainability and response to pharmacological treatment of individual patients are expected to be determined by their ionic current properties, especially in structurally-healthy atria. Mechanisms underlying AF and optimal cardioversion are however still unclear. In this study, in-silico drug trials were conducted using a population of human structurally-healthy atria models to 1) identify key ionic current properties determining AF inducibility, maintenance and pharmacological cardioversion, and 2) compare the prognostic value for predicting individual AF cardioversion of ionic current properties and electrocardiogram (ECG) metrics. In the population of structurally-healthy atria, 477 AF episodes were induced in ionic current profiles with both steep action potential duration (APD) restitution (eliciting APD alternans), and high excitability (enabling propagation at fast rates that transformed alternans into discordant). High excitability also favored 211 sustained AF episodes, so its decrease, through prolonged refractoriness, explained pharmacological cardioversion. In-silico trials over 200 AF episodes, 100 ionic profiles and 10 antiarrhythmic compounds were consistent with previous clinical trials, and identified optimal treatments for individual electrophysiological properties of the atria. Algorithms trained on 211 simulated AF episodes exhibited >70% accuracy in predictions of cardioversion for individual treatments using either ionic current profiles or ECG metrics. In structurally-healthy atria, AF inducibility and sustainability are enabled by discordant alternans, under high excitability and steep restitution conditions. Successful pharmacological cardioversion is predicted with 70% accuracy from either ionic or ECG properties, and it is optimal for treatments maximizing refractoriness (thus reducing excitability) for the given ionic current profile of the atria.

KEYWORDS
atrial fibrillation, *in-silico*, drug trials, cardioversion, electrocardiogram

1 Introduction

In-silico trials with human modeling and simulation represent an effective means for drug safety and efficacy assessment (Passini et al., 2017; Musuamba et al., 2021; Margara et al., 2022). Besides yielding accurate predictions of pro-arrhythmic toxicity, superior to that obtained through animal studies (Passini et al., 2017), they provide mechanistic explanations to potential adverse events. Accordingly, in-silico trials constitute a central paradigm for drug safety (Passini et al., 2021), with unexploited capabilities for drug efficacy evaluation at higher dimensional levels (i.e., whole-organ scale) (Margara et al., 2022). The latter could support the introduction of human-based multiscale modeling and simulation into precision medicine, as shown by Roney et al., 2022 for the prediction of atrial fibrillation (AF) recurrence after catheter ablation. Similarly, in-silico trials offer the possibility of identifying key modulators of successful pharmacological treatment, that could guide tailored AF therapies.

Recent studies of AF pathophysiology have highlighted the low incidence (i.e., 3% of cases) of AF in the absence of heart disease (Wyse et al., 2014). Newly identified forms of heart disease, however, coincide with the absence of atrial structural abnormalities. Channelopathies (Wyse et al., 2014), genetic variants (Ragab et al., 2020) metabolic disorders, imbalanced autonomic nervous system (Hanna et al., 2021), endocrine control (Aguilar et al., 2021) or the inflammatory response (Scott et al., 2021), might increase AF susceptibility by transiently altering the electrical substrate (Heijman, Linz and Schotten, 2021). These dynamic substrates, as opposed to static structural inhomogeneities, might underlie the high variability observed across AF paroxysms. While patients presenting the above-mentioned disorders cannot be categorized as healthy, they might have structurally-healthy atria, in which AF inducibility has proven to be common, especially in males (Kumar et al., 2012).

In-vivo studies conducted in human subjects (Kim et al., 2002; Narayan et al., 2008; Krummen et al., 2012) observed that dynamic substrates favoring AF initiation resulted from steep action potential duration (APD) restitution (APDR). Steep APDR favored APD alternans and dynamic heterogeneities in repolarization when the atria were paced at rapid rates. Simulation studies (Gong et al., 2007) showed that discordant APD alternans (i.e., APD alternating in a beat-to-beat short-long pattern, with opposing phase in neighboring regions) could derive from steep APDR and preceded AF initiation. While discordant alternans was only observed for elevated L-type Ca^{2+} current, the authors did not analyze further alterations. Thus, other ionic current properties, mechanisms or channel dysregulation, resulting from genetic polymorphisms (Ragab et al., 2020), imbalanced regulatory systems (Heijman, Linz and Schotten, 2021) or natural inter-subject variability in ionic densities (Muszkiewicz et al., 2018), may also engage with steep electrical restitution and facilitate AF induction in patients with structurally-healthy atria. The mechanisms are however unknown.

Early detection of AF in patients with structurally-healthy atria is crucial, given their higher eligibility for antiarrhythmic drug treatment (Andrade et al., 2020; Hindricks et al., 2021). Indeed, absence of structural heart disease and AF duration <24 h are independent predictors of successful pharmacological cardioversion to normal sinus rhythm (Boriani et al., 2004). Restoring sinus rhythm limits the atrial structural remodeling (Andrade et al., 2020) and reduces the risk of stroke and cardiovascular death compared to rate control strategies (Kirchhof et al., 2020). Nevertheless, the success rate of pharmacological treatment is currently suboptimal (Heijman, Linz and Schotten, 2021), and little is known about how inter-subject variability in channel densities (Muszkiewicz et al., 2018) determines the response of individual AF patients to antiarrhythmic drugs (Capucci et al., 2018).

This lack of knowledge might be attributed to the unfeasible, non-ethical and risky nature of studying the effect of inter-subject variability in human electrophysiology on drug efficacy. The latter would require the patient to undergo multiple treatments and invasive screening procedures. Modeling and simulation studies, on the other hand, can provide strong evidence under high spatio-temporal resolution and perfect control over the parameters of interest, avoiding all three barriers and overcoming experimental limitations (Heijman et al., 2021).

Therefore, the aim of this study is to exploit human-based multiscale modeling and simulation to 1) identify the ionic profiles that determine electrical restitution and excitability properties, and favor AF in structurally-healthy atria, 2) understand their relationship with pharmacological cardioversion, and 3) quantify the prognostic significance for successful pharmacological cardioversion of ionic current densities versus electrocardiogram (ECG) metrics. To address these goals, simulated AF episodes were induced in a population of human-based whole-atria models with varying ionic densities and steep electrical restitution properties, as observed *in-vivo*. Pharmacological cardioversion was subsequently attempted by simulating the effects of the antiarrhythmic drugs used clinically for restoring sinus rhythm. Simulation results were consistently evaluated against experimental and clinical data. Ultimately, predictive algorithms for AF cardioversion, in the form of clinical decision support systems, were built using the information obtained from ECG metrics and ionic current profiles.

2 Methods

2.1 Population of human atrial cardiomyocyte models

A population of human atrial cardiomyocyte models was generated as described in Muszkiewicz et al., 2018. The CRN model (Courtemanche, Ramirez and Nattel, 1998) was considered as baseline, since it reproduces the long plateau observed in paroxysmal AF patients with steep APDR (Narayan et al., 2008; Krummen et al., 2012) and it has been extensively used for developing and testing antiarrhythmic drug modeling (Loewe et al., 2014, 2015; Sutanto et al., 2019). Effects of drug modeling on the CRN model, moreover, were compared to the effects on the Grandi-Bers (Grandi et al., 2011) and Maleckar-Trayanova (Maleckar et al., 2009) models to assess model independence of key results.

Key conductances and permeabilities were sampled up to ±70% of their control ranges using Latin Hypercube sampling, including the ultrarapid, rapid and slow delayed-rectifier K^+ current density (G_{Kur}, G_{Kr} and G_{Ks}), transient outward K^+ current density (G_{to}), inward rectifier K^+ current density (G_{K1}), L-type Ca^{2+} current density (G_{CaL}), fast Na^+ current density (G_{Na}), Na^+/K^+ pump (G_{NaK}), Ca^{2+}/Na^+ exchanger (G_{NCX}) and the sarcoplasmic reticulum Ca^{2+} release (G_{rel}), leak (G_{leak}) and uptake (G_{up}) currents. Experimental calibration was subsequently applied using action potential characteristics obtained from human cells of patients in sinus rhythm (dataset and further explanation available in Sánchez et al., 2014; Table 1). No AF remodeling was applied to the calibrated population of atrial cardiomyocyte models.

The APDR curves of the experimentally-calibrated population were computed by both standard S1S2 and dynamic restitution protocols. The standard S1S2 protocol consisted of a train of stimuli applied at a fixed S1 cycle length (CL), followed by a single extrastimulus with coupling interval S2. For the dynamic restitution protocol, the train was applied until steady-state at constant S1, for decreasing CLs. Conduction velocity (CV) restitution (CVR) was measured for models yielding APDR slope greater than unity for both restitution protocols (Koller, Riccio and Gilmour, 1998; Watanabe et al., 2001), and an APDR slope greater than unity over a diastolic interval range (Qu, Weiss and Garfinkel, 1999) of at least 30 milliseconds (ms). A detailed explanation of the APDR and CVR calculation can be found in the Supplementary Material.

2.2 Populations of whole-atria models with homogeneous vs. heterogeneous ionic current properties

Ninety-seven atrial cardiomyocyte models presenting steep APDR and CVR were used to populate two human-based whole-atria models, one with homogeneous and one with heterogeneous ionic current properties (Supplementary Figure S1). The population of 97 homogeneous whole-atria models was constructed by assigning one atrial cardiomyocyte model to all regions of the atria (to isolate the contribution of ionic densities to AF). The population of 97 heterogeneous models was similarly constructed with each atrial cardiomyocyte model, but in this case, the ionic profile was modified in specific atrial regions, as previously detailed (Seemann et al., 2006; Tobón et al., 2013; Sánchez et al., 2017). Specifically, the single-cell properties of the cardiomyocyte model were assigned to the left atrial tissue, so that the restitution properties interfered with burst pacing at the pulmonary veins (see below), and scaled in the right atrium, crista terminalis, pectinate muscles, left atrial appendage and atrio-ventricular rings, as detailed in Supplementary Table S1.

Regional heterogeneities in CV and anisotropy ratio were included in both populations of whole-atria models as in (Tobón et al., 2013; Sánchez et al., 2017) (Detailed in Supplementary Table S1). Simulations of electrical propagation were conducted using the monodomain equation with the MonoAlg3D software (Sachetto Oliveira et al., 2018; available at https://github.com/rsachetto/MonoAlg3D_C).

2.3 Atrial fibrillation inducibility

The protocol for simulated AF induction mimicked the spontaneous ectopic beats reported in human patients with frequent episodes of AF (Haïssaguerre et al., 1999). As such, a burst of five periodic stimuli was applied at the left pulmonary veins, the most common foci origin site. To account for repetitive discharges with irregular CL, different CLs, ranging from 170 to 260 ms (Haïssaguerre et al., 1999; mean CL of focal discharges 175 ± 30 msec) with 10 ms increment, were tested for the burst. AF episodes longer than 3 s were considered sustained.

2.4 Atrial fibrillation pharmacological management: Drug modeling

Sustained AF episodes were subjected to 10 simulated pharmacological treatments: five drugs currently approved for restoring sinus rhythm (i.e., flecainide, propafenone, vernakalant, amiodarone, and ibutilide; Hindricks et al., 2021), dronedarone (an analogue of amiodarone), ranolazine (as a promising compound for sinus rhythm maintenance; Capucci et al., 2018) and digoxin (a rate control agent previously used for rhythm control; The Digitalis in Acute Atrial Fibrillation (DAAF) Trial Group, 1997). Drug action was simulated as simple pore-block models

according to previously reported effective plasma drug concentration, and their 50% inhibitory concentration and hill coefficient profiles (Supplementary Table S2, Supplementary Figure S2). For computational feasibility, considering the large number and complexity of the simulations and the deterministic nature of the models, drug administration was modelled 3 s from AF induction (Sánchez et al., 2017), and the episode was recorded for another 4 s. AF was considered successfully cardioverted by the drug if the atria were free of arrhythmic activity before the completion of the 7 s (Matene and Jacquemet, 2012). Drug efficacy was defined as the number of AF episodes cardioverted by a given drug over the total number of AF episodes.

Moreover, to evaluate whether pharmacological AF prevention and cardioversion followed the same restitution mechanisms, the AF-induction protocol was repeated in sinus rhythm after drug application. For this, only the two drugs that steepened/flattened the APDR curve the most were considered.

2.5 Simulated electrocardiogram

Simulated 8-lead (leads I, II, V1-V6) ECGs were computed for sustained fibrillation as in Gima and Rudy, 2002. The ECG was recorded during the 3-s AF episode prior to drug application. The resulting signals were standardized and processed using pass-band filtering with cut-off frequency of [0.5–50] Hz (Alcaraz et al., 2011). Five biomarkers, namely, dominant frequency, organization index, Shannon's spectral entropy, sample entropy and relative harmonic energy, were extracted from each lead as in (Alcaraz et al., 2011; Zeemering et al., 2018). These biomarkers provided a characterization of AF complexity in the frequency and temporal domain.

2.6 Clinical decision support systems

An algorithm for predicting the likelihood of pharmacological cardioversion (equivalent to a clinical decision support system) was built using ECG metrics, ionic current profiles and cellular electrophysiological properties as input. For this, a dataset was constructed for each antiarrhythmic drug, combining the information of the AF episodes and the outcome of drug application. Every AF episode was characterized by M = 55 features, including 15 derived from the electrophysiological properties of the atria (i.e., baseline CV, APD_{90}, resting membrane potential (RMP) and 12 ionic current densities) and 40 from the ECG analysis (i.e., 5 biomarkers from each lead, 8-lead ECG). Each episode was labelled either as 1, if AF was successfully cardioverted, or 0, otherwise.

The whole dataset was partitioned in sub-datasets to determine the predictive power of each set of biomarkers. Clinical decision support systems were built with each sub-dataset by elastic-net logistic regression (Zeemering et al., 2018), using the Glmnet toolbox (available at http://hastie.su.domains/glmnet_matlab/). Parameter selection was done by stepwise logistic regression with alpha equal 0.5 and 100 values for lambda. The performance of the predictive models was validated through 5-fold cross-validation, repeated 20 times, randomly allocating 70–30% of data for training and testing, respectively. Further details of the algorithms and the different sub-datasets can be found in the Supplementary Material.

3 Results

3.1 Evaluation of human atrial cardiomyocyte action potential models shows that steep restitution is associated with low triangulation and high cellular excitability

A calibrated subpopulation of human atrial cardiomyocyte models, matching experimental action potential characteristics, was selected from the initial candidate population. Four hundred fifty-one cardiomyocyte models in the calibrated subpopulation showed steep APDR for both restitution protocols, and 97 additionally presented steep CVR. Figure 1 illustrates action potential morphologies (Figure 1A), representative APDR and CVR curves of steep restitution properties (Figures 1B–E) and ionic density distribution (Figure 1F) of the subpopulations of atrial cardiomyocyte models considered.

Steep APDR curves occurred for longer plateau phases (triangulation (APD_{90}-APD_{50}) 72.6 ± 18.1 vs 126.9 ± 61.3 ms, steep vs flat APDR curves). Models additionally yielding steep CVR curves had a more negative resting membrane potential (RMP: 82.4 ± 1.7 vs. -74.5 ± 3.3 mV; steep APDR and CVR vs steep APDR alone) (Figure 1A, pink versus blue traces). The hyperpolarization of the RMP allowed propagation for shorter CLs (307 ± 15 vs 538 ± 152 ms; steep APDR and CVR vs steep APDR alone), increasing the magnitude of APD alternans (Figure 1B) and favoring a greater modulation of CV (Figure 1D).

Steep APDR alone was found in models with significantly high G_{CaL} and low G_{Kur} compared to flat restitution (Figure 1F, blue vs green boxes). Steep APDR and CVR curves (Figure 1F, pink boxes) were associated with even greater G_{CaL}, elevated G_{Na}, and high density of repolarization currents, especially G_{NaK}, G_{K1}, G_{Kr} and G_{to}. The 97 atrial cardiomyocyte models exhibiting steep APDR and CVR were used to develop the populations of human whole-atria models (Supplementary Figure S1).

10.3389/fphys.2022.966046

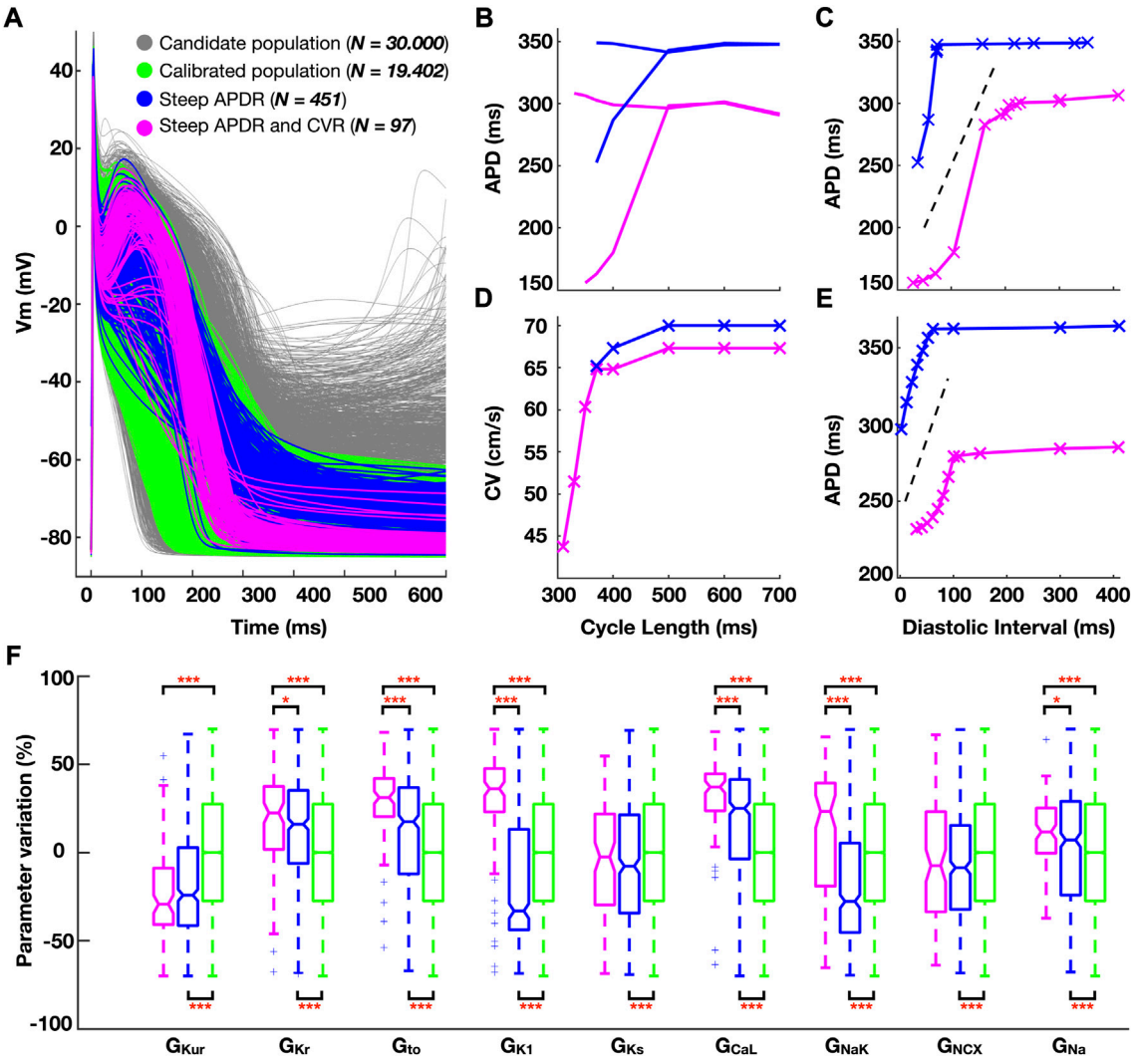

FIGURE 1
(A) Simulated action potential traces for human atrial cardiomyocyte models in the population before (grey) and after (green) experimental calibration. **(B–E)** Comparison of the electrical restitution between a representative cardiomyocyte model characterized by steep action potential duration restitution (APDR) alone (blue) and additional steep conduction velocity restitution (CVR, pink). **(B)** Dynamic APDR plotted against the cycle length, showing transient alternation, and **(C)** against the diastolic interval. **(D)** CVR. **(E)** Standard S1S2 APDR. **(F)** Ionic density distribution (color-code as per panel **(A)**. Data analyzed using Wilcoxon test. *$p < 0.05$, **$p < 0.01$, ***$p < 0.001$.

3.2 Atrial fibrillation is facilitated by discordant APD alternans enabled by propagation at fast rates due to high excitability, for high L-type Ca^{2+} and inward rectifier K^+ currents

212 and 265 AF episodes were induced in 75 out of the 97 homogeneous and heterogeneous whole-atria models, respectively, following burst stimulation at 10 different CLs. Whole-atria models with 22 ionic profiles failed to induce AF for both homogeneous and heterogeneous ionic current properties. Figure 2 illustrates a representative AF episode, showing multiple rotors in the whole-atria model (Figure 2A, left), the transmembrane voltage from 1 cell (Figure 2A, right), and similarities between the simulated ECG (atrial activity, Figure 2B) and the clinical ECG (atrial activity) obtained from a human AF patient (Figure 2C). More AF episodes were induced with the heterogeneous ionic substrate, but the 75 ionic profiles of the models ensuring AF inducibility were the same in both populations.

Figure 3 illustrates the distribution of ionic densities (Figure 3A), effective refractory period (ERP) (Figure 3B), and APDR curves (Figure 3C) between the 75 atrial cardiomyocyte models favoring AF and the 22 non-inducible models. The dynamic restitution curves in Figure 3C are plotted against the CLs used for

10.3389/fphys.2022.966046

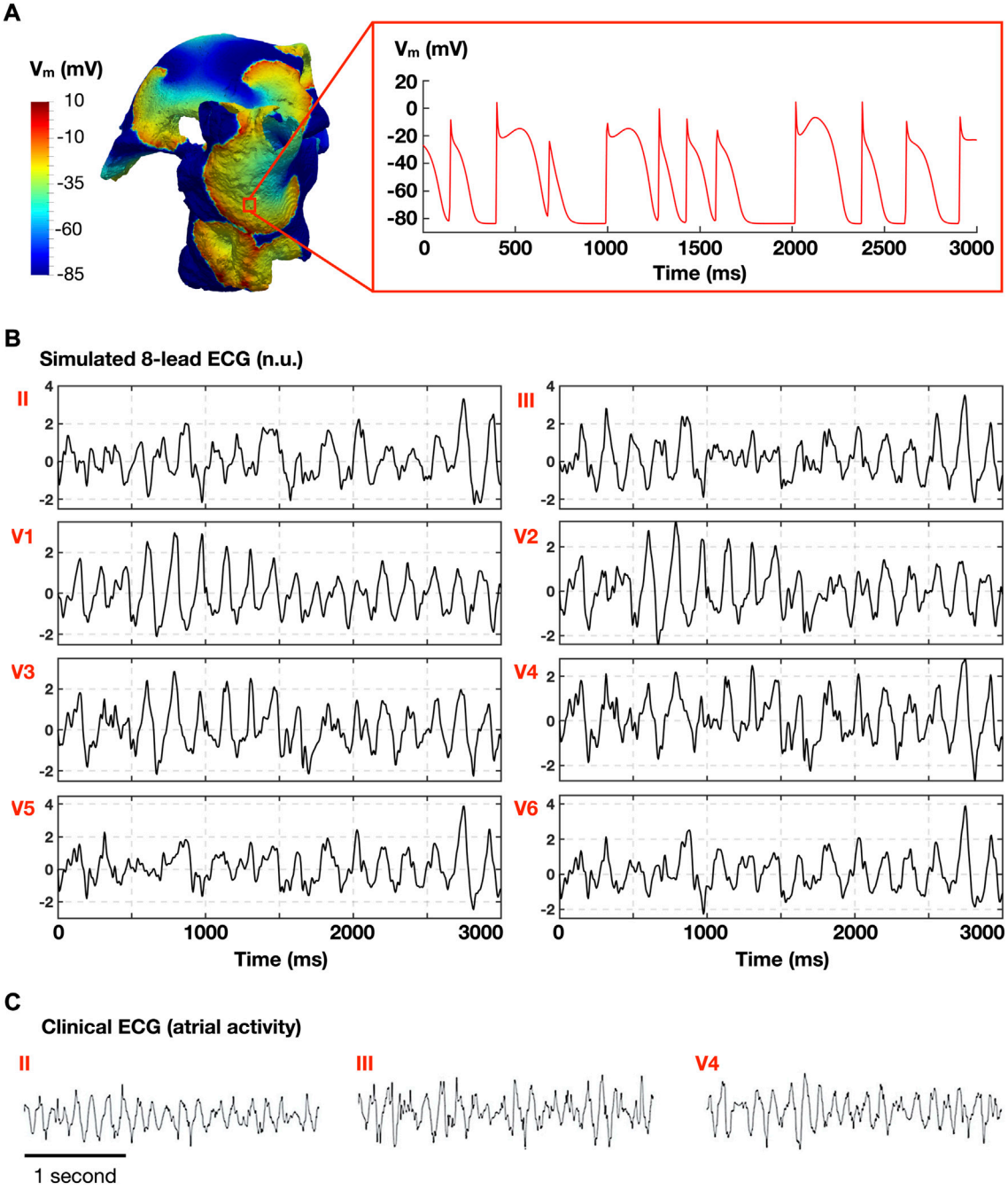

FIGURE 2
Representative atrial fibrillation (AF) episode. **(A)** Simulated AF in the whole atria model (left), and time course of the transmembrane voltage (V_m) in 1 cell (right). **(B)** Simulated atrial electrocardiogram (normalized ECG; no units). **(C)** Clinical ECG obtained in AF patient (adapted from Lankveld et al., 2016 under permission).

burst pacing (170–260 ms), for two consecutive beats to show magnitude of APD alternans (i.e., difference between long and short APD). Figures 3D,E compare the response of the whole-atria models to burst stimulation between AF inducible (Figure 3D, top and Figure 3E) and non-inducible models (Figure 3D, middle and bottom), to illustrate the dynamics underlying AF initiation. The analysis presented in Figure 3 considers the population with homogeneous ionic current properties.

Analysis of whole-atria simulations revealed AF inducibility for ionic profiles presenting high G_{CaL}, which increased APD alternans,

10.3389/fphys.2022.966046

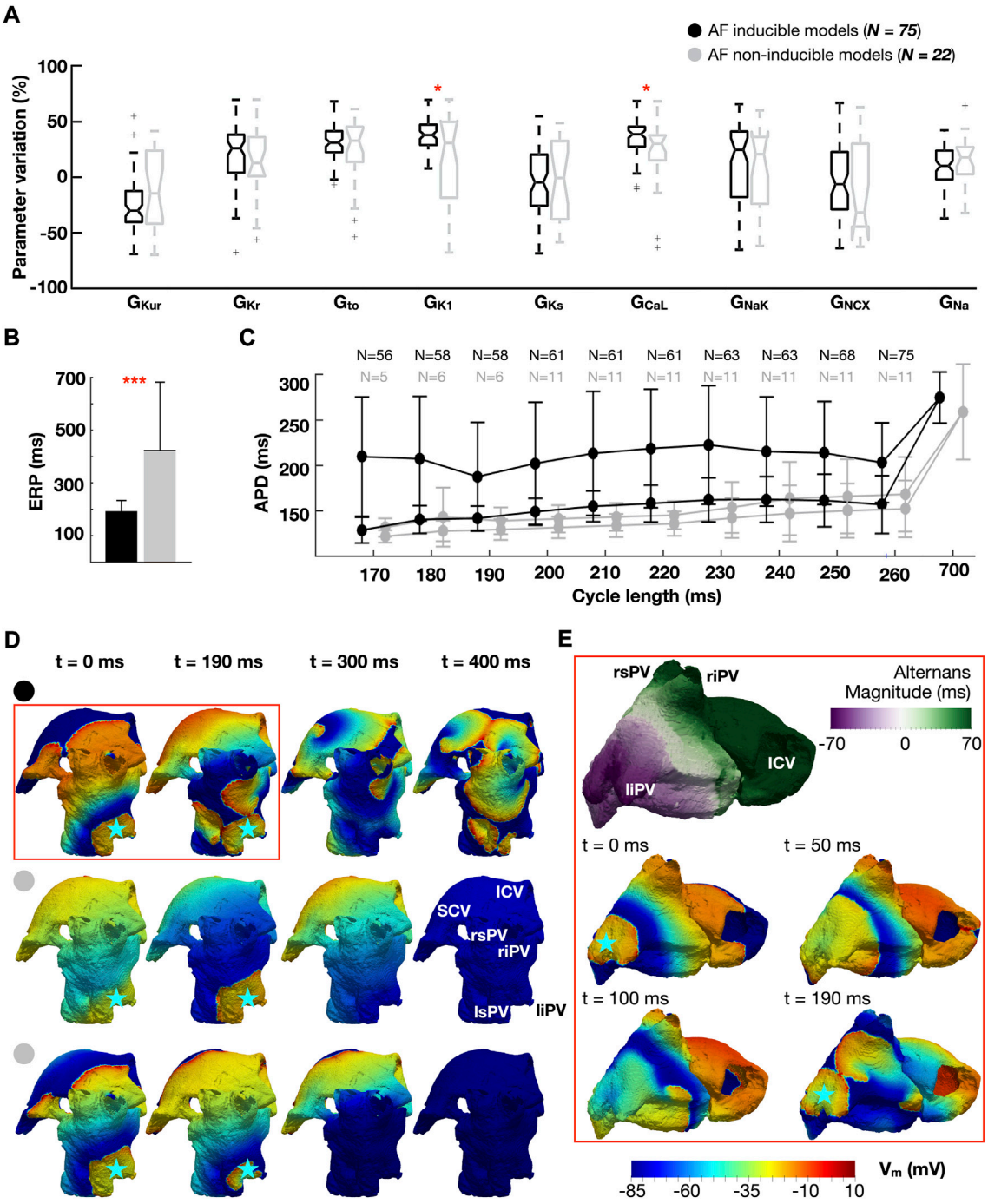

FIGURE 3
Ionic properties of AF-inducible (black) and non-inducible models (grey): **(A)** Ionic density distributions. **(B)** Effective refractory period (ERP). **(C)** Dynamic action potential duration (APD) restitution curves plotted against the cycle length used for burst pacing (170–260 ms). Two consecutive beats are considered (i.e., long and short APD), showing magnitude of APD alternans. Number (N) of models able to propagate all stimuli. **(D)** Comparison of propagation dynamics between an AF-inducible model (top), and two non-inducible models: one showing a 1:2 conduction pattern (middle row), the other propagating all stimuli without AF induction (bottom row). Burst stimulus applied at a cycle length of 190 ms. The blue star represents the location of the burst. **(E)** Discordant alternans favoring conduction block and re-entry. The snapshots in **(E)** are an expansion of the red box in **(D)**. Abbreviations. S-ICV: Superior and inferior cava vein; ri-rs-li-ls-PV: Right inferior, right superior, left inferior and left superior pulmonary veins. Data are expressed as medians and IQR and analyzed using Wilcoxon Test. *$p < 0.05$, **$p < 0.01$. ***$p < 0.001$.

and G_{K1}, which conferred high cellular excitability (Figures 3A–C). Indeed, all whole-atria models susceptible to AF exhibited propagation at CL = 260 ms, while this only occurred in 11 models (50%) free of arrhythmia (Figure 3C). Likewise, 56 (75%) AF inducible and 5 (23%) non-inducible whole-atria models enabled propagation at 170 ms (i.e., the shortest CL tested in the burst).

Figure 3D compares the response to burst stimulation between one whole-atria model susceptible to AF (top row) and two non-inducible models (one of them belonging to the 11 models that failed to propagate burst stimulation at CL = 260 ms (middle row), the other belonging to the 5 models that propagated at 170 ms without inducing AF (bottom row)). Whole-atria models unable to propagate all stimuli in the burst exhibited a 1:2 conduction pattern (i.e., propagation of one every two stimuli), which prevented engagement with the steep restitution properties, as illustrated in Figure 3D (middle): the stimulus at t = 190 ms propagates following propagation failure at t = 0 ms.

However, even when all burst stimuli propagated, some models were resistant to AF (Figure 3D, bottom). Analysis of their associated APDR curves revealed that AF-inducible models presented greater magnitude of APD alternans (67.3 ± 92.5 vs 8.9 ± 6.6 ms, AF-inducible vs non-inducible models) (Figure 3C). The latter developed into discordant alternans (i.e., APD alternating in a beat-to-beat short-long pattern, with opposing phase in neighboring regions) during the application of rapid burst stimulation, causing unidirectional block and re-entry at different sites of the left atrium (Figure 3E). An extensive explanation of discordant alternans formation after burst pacing is provided in the Supplementary Figure S3. Discordant alternans were not observed in whole-atria models free of AF.

Restoring the baseline density (i.e., ionic conductance) of the L-type Ca^{2+} current in AF-inducible models recapitulated the magnitude of APD alternans observed in non-inducible models (67.3 ± 92.5 vs 8.3 ± 6.0 ms, AF-inducible models with elevated vs control L-type Ca^{2+} current density). Similarly, alternans magnitude was reduced after decreasing the inward rectifier K^+ current density to control conditions (67.3 ± 92.5 vs 18.2 ± 12.1; AF-inducible models with elevated vs control inward rectifier K^+ current). The latter effect was due to a reduction in the number of models propagating at short CLs (explanation given in the Supplementary Figure S4).

3.3 Analysis of 477 AF episodes reveals atrial fibrillation sustainability supported by high excitability, with enhanced up-regulation of the inward rectifier K^+ current and elevated Na^+/K^+ pump

AF sustainability was evaluated in the 75 whole-atria models ensuring AF inducibility considering homogeneous versus heterogeneous ionic current properties, to compare the role of the ionic profile and spatial gradients. The heterogeneous ionic substrate favored AF maintenance: 154 (58%) of the 265 AF episodes induced in heterogeneous models were sustained for over 3 s, versus 57 (27%) of 212 AF episodes induced in homogeneous models. In the former, the left atrial appendage and atrioventricular rings had a shorter APD_{90} than the bulk tissue, which favored rotor stabilization. Together with the APD heterogeneities within the right atrium (i.e., crista terminalis, pectinate muscles and bulk tissue) and between the right and left atrium, the heterogeneous ionic substrate presented inhomogeneous restitution properties that reinforced AF maintenance.

Overall, 211 (44%) AF episodes sustained in both populations of whole-atria models. In order to isolate the role of ionic profile rather than gradients in AF sustainability, the properties of the homogeneous models yielding sustained (>3s) and un-sustained fibrillation were analyzed. Thus, Figure 4 shows ionic density distribution (Figure 4A), ERP (Figure 4B), APDR curves (Figure 4C), and Na^+ current dynamics (Figure 4D).

Higher G_{NaK} and G_{K1}, and lower G_{Na} were associated with models sustaining AF. Analysis of Na^+ inactivation gates revealed that, in spite of a lower G_{Na}, Na^+ availability was higher in the sustained AF group (Figure 4D, right). This was accentuated as the pacing rate increased: the maximum Na^+ current peak, which was greater in the un-sustained AF group for lower rates, became higher in models yielding sustained AF when stimulated at short CLs (Figure 4D, left). This was due to the higher G_{NaK} and G_{K1}, which hyperpolarized the RMP (-82.6 ± 0.7 vs. -81.5 ± 0.6 mV, sustained and un-sustained AF, respectively). Accordingly, these atrial cardiomyocyte models had higher cellular excitability (and shorter effective refractory period, Figure 4B).

At slow rates (CL = 700 ms), lower CVs were found in whole-atria models leading to sustained AF (60.3 ± 5.7 vs 62.5 ± 4.5 cm/s), as a result of lower G_{Na}. At fast rates (CL = 260 ms), however, the opposite trend was observed (56.4 ± 9.8 vs 50.7 ± 5.7 cm/s; sustained vs unsustained AF). The magnitude of APD alternans was similar across groups.

3.4 In-silico drug trials in over 200 atrial fibrillation episodes consistently reproduce cardioversion efficacy observed in clinical trials and identify key properties determining treatment success

Pharmacological cardioversion with 10 compounds was attempted in the 211 sustained AF episodes induced in both whole-atria populations (homogeneous, 58 episodes; heterogeneous, 153 episodes). Figure 5 displays the efficacy (Figure 5A) of each treatment obtained in-silico and reported

10.3389/fphys.2022.966046

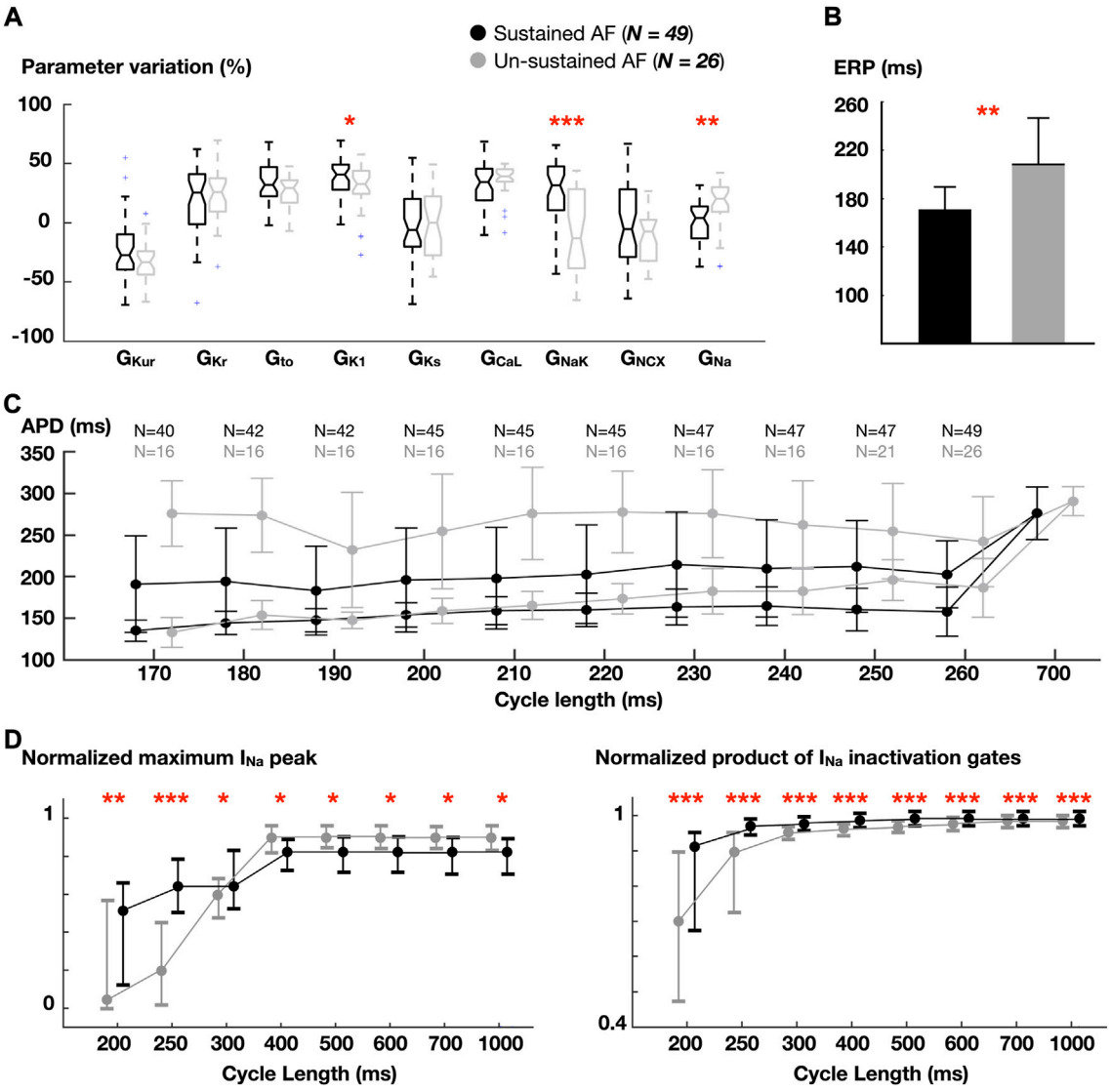

FIGURE 4
Comparison between atrial cardiomyocyte models favoring sustained vs un-sustained fibrillation in homogeneous whole-atria models. **(A)** Ionic density distribution. **(B)** Effective refractory period (ERP). **(C)** Dynamic action potential duration (APD) restitution (as in Figure 3C). Number (N) of models able to propagate all stimuli. **(D)** Normalized fast Na^+ current (I_{Na}) peak and normalized product of I_{Na} inactivation gates. Data are expressed as medians and IQR and analyzed using Wilcoxon Test. *$p < 0.05$, **$p < 0.01$, ***$p < 0.001$.

in human clinical trials. In-silico antiarrhythmic drugs are displayed according to their preferential ionic channel target. Cardioversion efficacy was higher for homogeneous versus heterogeneous whole-atria models as illustrated by dashed and solid bars, respectively in Figure 5A (described below). Figure 5B compares the percentage (%) of APD_{90} variation obtained after drug action with respect to control conditions in-silico and *in-vitro*. Corresponding results were obtained for APD_{90} change between simulated drug action and experimental data (Figure 5B), with further validation, illustrating rate-dependence alterations in APD, CV, and maximum upstroke velocity, provided in Supplementary Table S3.

Moreover, a comparison of APD_{90} variation after drug action between the CRN, Grandi-Bers and Maleckar-Trayanova models can be found in the Supplementary Figure S5). The latter models showed a higher sensitivity to I_{Kur} inhibition than the CRN model, which presented a greater APD prolongation after I_{Kr} block. Thus, repeating the whole-atria simulations with the Grandi-Bers or Maleckar-Trayanova models is expected to produce even

10.3389/fphys.2022.966046

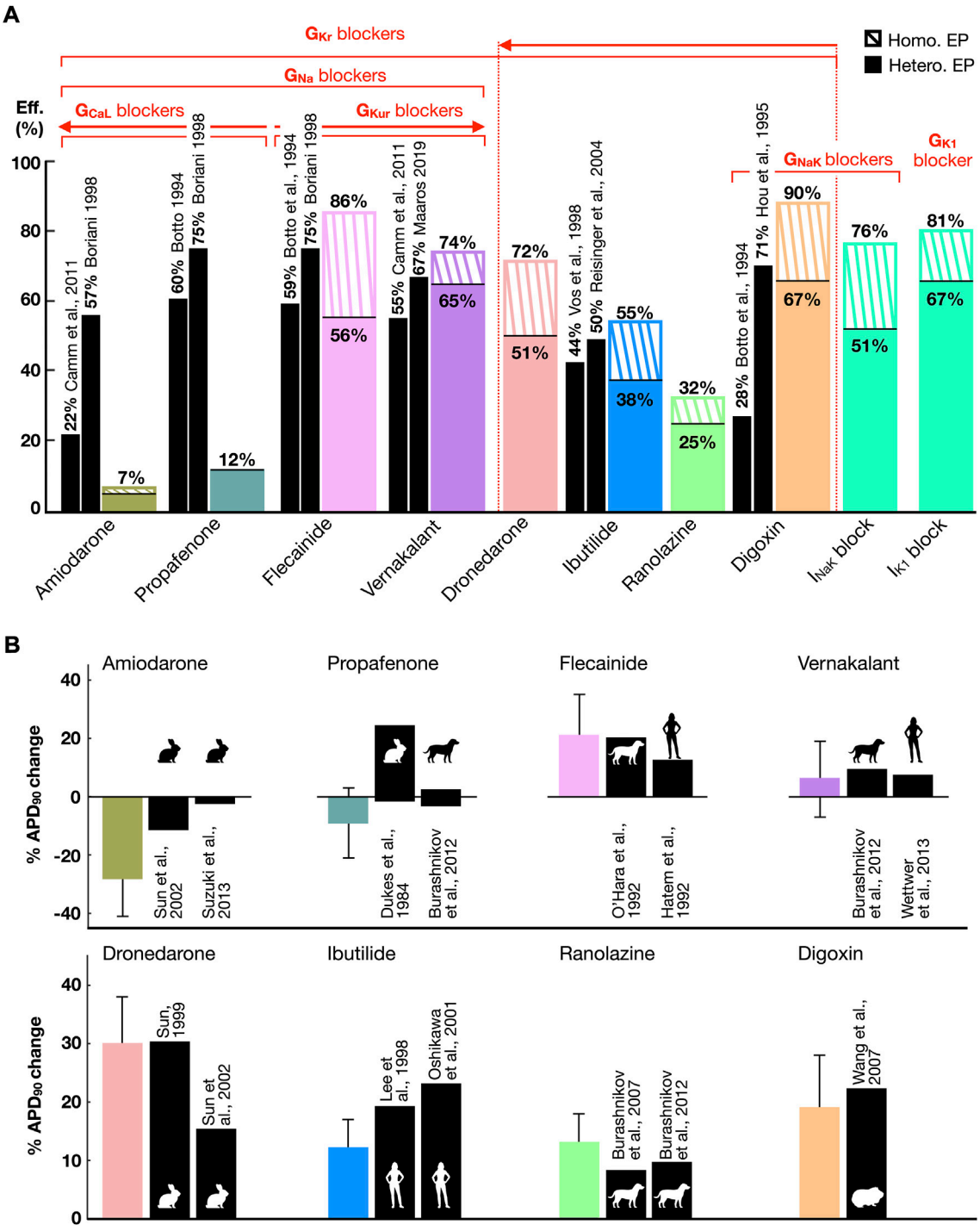

FIGURE 5
(A) Comparison between the cardioversion efficacy (Eff.) obtained in-silico (color bars) in whole-atria models with homogeneous (*Homo.*) and heterogeneous (Hete.) electrophysiology (EP) and human clinical trials (black bars). Drugs are grouped according to the ionic channels they target. A threshold of 25% block at therapeutic plasma concentration has been considered to denote ion current block. The arrows point towards greater ionic density block. **(B)** Percentage (%) of APD_{90} variation after drug modeling or administration with respect to control conditions, in-silico (color bars) and *in-vitro* (black bars, error bars *in-vitro* not available, see Supplementary Table S3). The animal silhouettes represent the species analyzed *in-vitro*.

10.3389/fphys.2022.966046

higher efficacy for I_{Kur} blockers than that already shown in Figure 5.

Higher cardioversion efficacy derived from class III (i.e., dronedarone and vernakalant) and class V (i.e., digoxin) antiarrhythmic drugs. Targeting I_{Kr}, I_{Kur}, I_{NaK} and I_{K1} yielded a greater prolongation of refractoriness than inward current block (Supplementary Figure S6). Antiarrhythmic drugs resulting in I_{Kr} inhibition (i.e, ranolazine, ibutilide, and dronedarone) showed an increase in cardioversion efficacy proportional to the extent of I_{Kr} block. However, higher success rates resulted from blocking multiple K^+ channels, even for lower percentages of I_{Kr} inhibition. For instance, a 25% I_{NaK} and 40% I_{Kr} block (i.e., digoxin) was far more effective than 45% I_{Kr} (i.e., ibutilide, efficacy in-silico matching clinical trials) or 70% I_{Kr} block (i.e., dronedarone).

The high efficacy of digoxin, in agreement with some clinical trials, owed to I_{NaK} inhibition. Blocking I_{NaK} or I_{K1} alone raised the RMP and decreased I_{Na} availability. The subsequent prolongation of post-repolarization refractoriness was sufficient to terminate AF regardless of a subtle APD change (Supplementary Figure S6). Indeed, single I_{K1} block and digoxin were the pharmacological approaches that provided the highest cardioversion rates.

Combined I_{Kr} and I_{Kur} block (i.e., flecainide and vernakalant, whose cardioversion efficacies matched the efficacy reported in clinical trials) was also more effective than I_{Kr} inhibition alone, especially in the population with heterogeneous ionic current properties. In general, the heterogeneous substrate hampered pharmacological cardioversion, since it facilitated AF maintenance (Section 3.3) and antiarrhythmic drugs had an inhomogeneous effect on different atrial regions. In particular, the heterogeneous ionic substrate was characterized by a lower G_{Kr} in the right atrium compared to the left atrium (Supplementary Table S1), so that I_{Kr} inhibition lost cardioversion efficacy in this setting. Thus, the efficacy of flecainide and dronedarone, but not of vernakalant, dropped significantly in the heterogeneous ionic substrate.

Low cardioversion rates stemmed from targeting the inward currents, as a result of drug-induced APD reduction (Figures 5A,B). I_{Na} block was effective when complemented with I_{Kur} and I_{Kr} inhibition (i.e., flecainide and vernakalant). However, combined I_{Na} and I_{CaL} block (i.e., amiodarone and propafenone) shortened the APD, yielding the formation of focal re-entrant sources (Supplementary Figures S7, S8). The cardioversion efficacy decreased proportionally to I_{CaL} block (equivalently, resulting in larger APD abbreviation, Figures 5A,B), with amiodarone (i.e., 50% I_{CaL} and 30% I_{Na} block) showing the lowest cardioversion rate. The efficacy of amiodarone, and especially of propafenone, differed from the efficacy reported in clinical trials (see Discussion).

Nevertheless, amiodarone-induced APD shortening significantly flattened the APDR curved (Supplementary Figure S6). Investigations on cardio-protection instead of cardioversion (i.e., inducing the AF-initiation protocol after in-silico drug application) showed that amiodarone prevented 100% of recurrent AF episodes, with only atrial flutter (i.e., regular and periodic activation) remaining in 2% of cases. In contrast, dronedarone prolonged the APD, steepening the APDR. Therefore, while effective in preventing AF induced at very short CLs (i.e., 170–200 ms), 49% of AF episodes were still inducible in dronedarone-pretreated substrates.

3.5 Optimal pharmacological treatments for individual ionic profiles are those that maximize prolonged refractoriness thus minimizing excitability

Forty-nine AF episodes, sustained by 40 whole-atria models, were only successfully cardioverted by a single drug. Eleven episodes sustained in 9 models were only cardioverted by dronedarone, 14 episodes in 13 models by flecainide, and 24 episodes in 18 models by vernakalant. Figure 6 illustrates the ionic density distribution of the whole-atrial models that only responded favorably to dronedarone, flecainide, or vernakalant, and how the ERP of these models, grouped according to successful treatment, was modified after applying each drug.

The extent of ERP prolongation caused by each treatment in a particular model explained the ability for AF cardioversion. Thus, models showing a favorable response to dronedarone (N = 9) also presented a greater ERP prolongation after dronedarone application. Similarly, flecainide prolonged the ERP more than dronedarone or vernakalant in whole-atria models only cardioverted by flecainide (N = 13), and the same applied for vernakalant (Figure 6B).

Analysis of the ionic current profiles revealed that atrial cardiomyocyte models showing greater ERP prolongation and thus, successful cardioversion after vernakalant application, had high G_{Kur} and low G_{Kr}. This agrees with vernakalant action, with the strongest I_{Kur} inhibitory profile within the tested antiarrhythmic drugs. By contrast, dronedarone cardioverted AF in models presenting the opposite situation: higher G_{Kr} and lower G_{Kur}. Flecainide resulted more effective for an intermediate scenario, since it blocked G_{Kur} and G_{Kr}, but to a lesser extent than vernakalant and dronedarone, respectively (Figure 6A). Whole-atrial models presenting high G_{K1} and G_{NaK}, and therefore high excitability (Figure 4), responded better to vernakalant and flecainide than to dronedarone. While none of them caused I_{NaK} or I_{K1} inhibition, the former yielded greater inward current block (Supplementary Table S2, Supplementary Figure S2). Thus, vernakalant- and flecainide-induced I_{Na} and I_{CaL} inhibition facilitated

10.3389/fphys.2022.966046

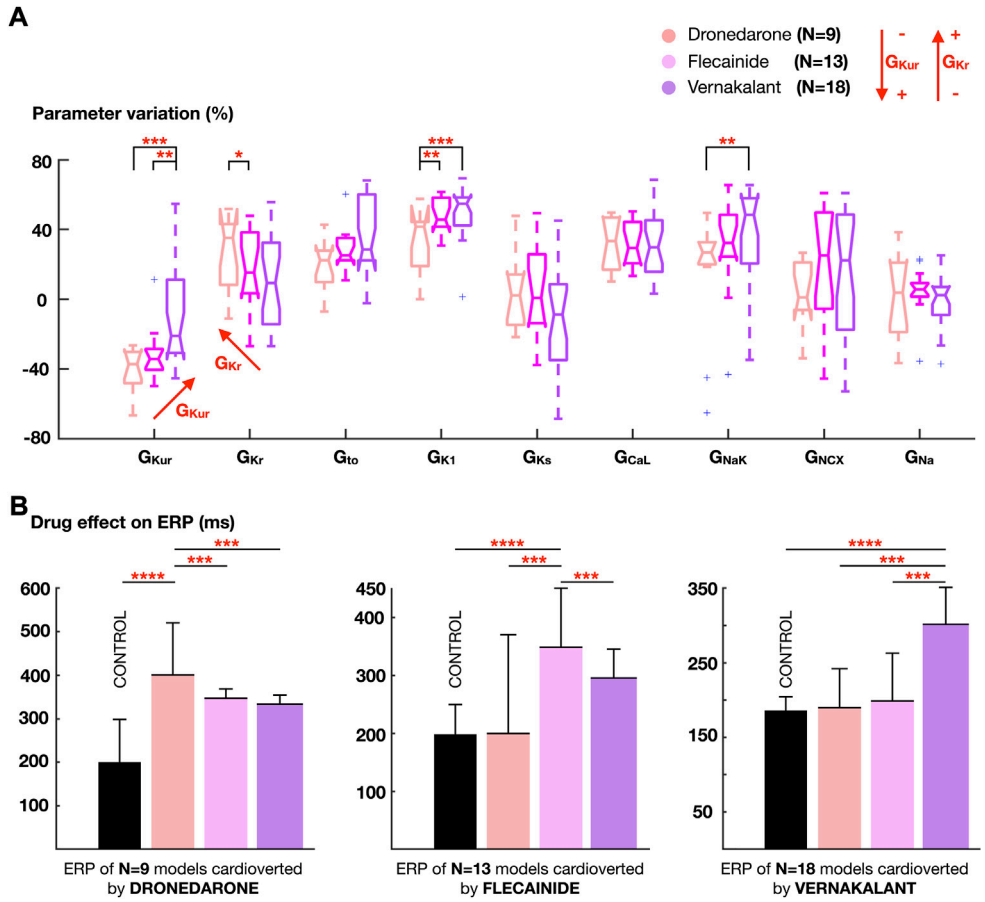

FIGURE 6
(A) Comparison of the ionic density distribution between atrial cardiomyocyte models showing favorable response only to dronedarone, flecainide or vernakalant. **(B)** Effect of the three antiarrhythmic drugs on the effective refractory period (ERP), stratifying the atrial cardiomyocyte models according to the pharmacological treatment that produced successful cardioversion. Colors on the bars as in **(A)**. Data are expressed as medians and IQR and analyzed using Wilcoxon Test. *$p < 0.1$, **$p < 0.05$, ***$p < 0.01$. ****$p < 0.001$.

pharmacological cardioversion in those models presenting higher excitability.

3.6 Accuracy of prediction of AF cardioversion with specific treatments is 70% using both electrocardiogram metrics and ionic current profiles

Clinical decision support systems were built based on the information of the atrial model sustaining AF (i.e., ionic current properties) and the ECG metrics obtained during AF. Figure 7 and Table 1 show the prediction accuracy and receiver operating characteristics (ROC) curves of successful cardioversion for the drugs illustrated in Figure 6.

Both the information of the ionic densities and the ECG biomarkers yielded high-accuracy predictions of successful AF cardioversion, with the former being slightly superior to the latter. Higher accuracies were obtained for dronedarone, due to a higher specificity (Figure 7). Dronedarone cardioverted around 50% of episodes, so that the dataset was more balanced (i.e., similar proportion of episodes cardioverted and not cardioverted). By contrast, the lowest specificity was obtained for vernakalant (70% cardioversion efficacy), with random oversampling slightly improving the prediction.

Three ionic densities were consistently selected as relevant features: G_{K1}, G_{Kur}, and G_{NaK}. As illustrated in Figure 6, these ionic densities differed to a greater extent in atrial cardiomyocyte models that responded better to flecainide, vernakalant or dronedarone, and thus, were revealing of the most favorable treatment for each episode. Conversely, the dominant frequency, sample entropy and the relative harmonic energy (directly related to the dominant frequency) were selected as relevant ECG

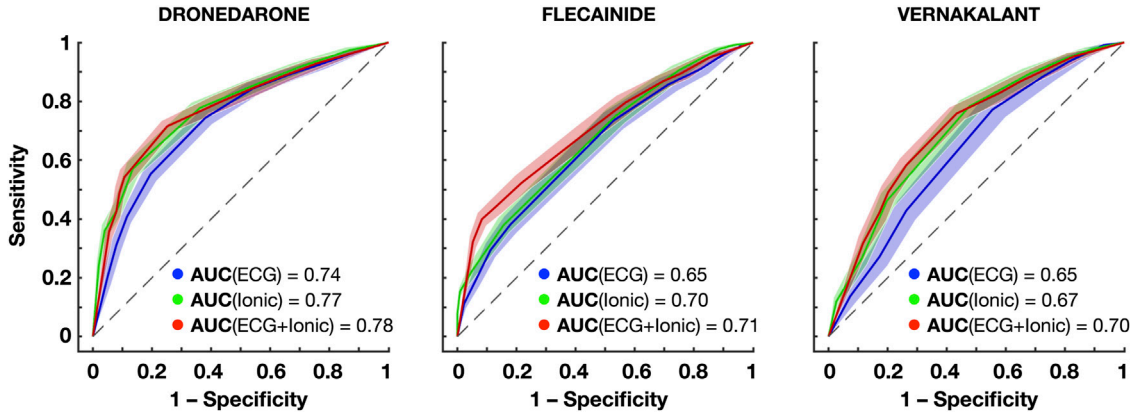

FIGURE 7
Receiver operating characteristics (ROC) curves for the prediction of successful cardioversion with dronedarone, flecainide and vernakalant using the ECG, ionic properties and both. The confidence interval around each ROC is obtained repeating 5-fold cross-validation 20 times. Abbreviations: AUC: Areas under the curve.

TABLE 1 Prediction accuracy (mean and confidence interval). Most relevant features selected by the elastic-net logistic regression. Abbreviations: DF: Dominant frequency; SaE: Sample entropy. RHE: Relative harmonic energy.

Drug	Data	Best predictive biomarkers	Accuracy (%)
Dronedarone	ECG	DF (Leads V2–V6), SaE (Leads V2, V6)	0.72 [0.70, 0.74]
	Ionic properties	GK1, GKur, GNaK, GNa, GKr, GCaL	0.76 [0.74, 0.78]
	ECG + Ionic	CV, DF (Leads V2, V4)	0.77 [0.75, 0.79]
Flecainide	ECG	SaE (Lead V1), RHE (Lead III), SaE (Lead III)	0.69 [0.67, 0.71]
	Ionic properties	GNaK, GK1, GKs, Gto	0.71 [0.69, 0.73]
	ECG + Ionic	Gto, GK1, GNaK, GKs, SaE (Lead V1)	0.72 [0.70, 0.74]
Vernakalant	ECG	RHE (Lead V4, V5), SaE (V6)	0.68 [0.66, 0.70]
	Ionic properties	Gto, GKur, GNaK	0.70 [0.68, 0.72]
	ECG + Ionic	Gto, GKur, SaE (Lead V6), RHE (Lead V4, V5)	0.70 [0.68, 0.72]

metrics, suggesting that AF dynamics also had a crucial role on cardioversion efficacy.

4 Discussion

Key features underlying AF inducibility, maintenance and pharmacological cardioversion are identified in a population of structurally-healthy atria with varying ionic current properties. In-silico trials for 10 antiarrhythmic treatments are consistent with previously-reported clinical trials, and identify mechanisms and predictors of successful cardioversion. Specific findings are: 1) AF inducibility in structurally-healthy atria might be explained by discordant APD alternans resulting from steep electrical restitution and high excitability (occurring for elevated L-type Ca^{2+} and inward rectifier K^+ currents); 2) AF maintenance is also enabled by high excitability, for profiles with high inward rectifier K^+ and Na^+/K^+ pump currents; 3) pharmacological cardioversion is optimal for treatments minimizing excitability, through maximal prolongation of refractoriness, which is dependent on individual ionic profiles; 4) successful pharmacological cardioversion is predicted in virtual human atria with >70% accuracy using both ionic current profiles or ECG metrics. Methodologically, our study demonstrates the power of in-silico drug trials conducted in human whole-atria models constructed based on hundreds of ionic current profiles, with perfect control over the parameters studied and high spatio-temporal resolution.

4.1 Precision medicine for atrial fibrillation management: *In-silico* drug trials

Currently, rhythm control therapy for AF follows a "one-size fits all" approach (Kany et al., 2021). However, the response of individual patients to rhythm control therapy is highly variable, and predicting its success is still a challenge (Kany et al., 2021). Previous studies have demonstrated that analyzing AF complexity through the ECG might help predicting flecainide cardioversion efficacy (Zeemering et al., 2018). Others assert that pharmacogenetics would bring the best tailored approach (Capucci et al., 2018). In our study, we have shown that pharmacological cardioversion can be predicted with over 70% accuracy using either ionic or ECG metrics in virtual human atria. This is important as it points towards the possibility of predicting the response of pharmacological treatment using both non-invasive markers and ionic current properties. Moreover, it highlights the integral part of multi-scale modeling and simulation for AF treatment personalization (Roney et al., 2022).

In our in-silico drug trial, G_{K1} was selected as one of the most informative properties for predicting AF cardioversion, together with G_{NaK} and G_{Kur}. Inhibiting the Na^+/K^+ pump reduced the cellular excitability and hampered AF maintenance, consistent with its potential for rhythm control (Bueno-Orovio et al., 2014) and rate control strategy (i.e., digoxin; Hindricks et al., 2021). Similarly, the importance of the inward rectifier K^+ current in regulating AF inducibility and maintenance has been proven by previous experimental and computational studies (Noujaim et al., 2007; Sánchez et al., 2017). Results obtained with the cellular model used, however, should be carefully interpreted, given the strong model-dependent effects. This is especially important when evaluating the antiarrhythmic efficacy of I_{K1} inhibition, since a higher sensitivity for I_{K1} block is reported for Courtemanche compared to other ionic models (Sánchez et al., 2014; Sutanto, 2022). Moreover, I_{K1} inhibition might have opposing effects on triggers and substrates. While effective in terminating fibrillatory activity, as shown in this study, blocking I_{K1} might promote triggered activity and focal excitations (Filgueiras-Rama et al., 2012). In this sense, safe restoration of sinus rhythm (i.e., absence of ventricular arrhythmias) resulted from I_{K1} inhibition in goats with persistent AF (Ji et al., 2017). Moreover, as in our simulations, higher cardioversion efficacies resulted from applying chloroquine (I_{K1} blocker, among others) than flecainide in sheep models (Filgueiras-Rama et al., 2012).

Flecainide cardioverted 56% of the simulated AF episodes, matching the efficacy observed in clinical trials with AF patients (Boriani et al., 1998; Reisinger et al., 2004). Compared to flecainide, a higher proportion of AF episodes (i.e., 65%) were terminated for vernakalant simulation. Similarly, a non-randomized retrospective study (Pohjantähti-Maaroos et al., 2019) observed higher number of patients cardioverted to sinus rhythm with vernakalant than flecainide (67 vs 46%, respectively).

Dronedarone also proved to be effective in terminating a great number of simulated AF episodes. Dronedarone has shown a positive impact on clinical endpoints for paroxysmal AF patients and compared to amiodarone, it delays and reduces AF occurrence (Singh et al., 2008). However, amiodarone has proven more effective than dronedarone in rhythm control (Hindricks et al., 2021).

In our study, amiodarone showed the lowest cardioversion efficacy. Nevertheless, cardioversion rates as high as 87% are observed after 24 h from its administration (Bash et al., 2012). Amiodarone inhibits multiple ionic channels, including I_{CaL} and I_{Na}. Blocking both channels reduces cellular excitability (Loewe et al., 2014; Liberos et al., 2016) and amiodarone-induced I_{Na} inhibition has been suggested as the main mechanism underlying rotor termination (Wilhelms et al., 2013). In our study, however, the baseline atrial cardiomyocyte models yielding AF presented increased G_{Na} and G_{CaL} compared to the baseline model. Consequently, the inward current block induced by amiodarone was not sufficient to reduce excitability and terminate AF. This is in agreement with previous simulations studies, that showed that the antiarrhythmic effects of I_{Na} and I_{CaL} block depended on their basal ionic densities (Liberos et al., 2016). Of note, amiodarone is primarily recommended in the context of severe heart failure (Andrade et al., 2020), in which I_{CaL} is expected to be down-regulated (Denham et al., 2018). Thus, amiodarone-induced I_{CaL} inhibition might have a lower impact on the APD and higher on excitability than in our study. It has been also suggested that amiodarone metabolites, such as desethylamiodarone, which accumulates after long-term therapy with amiodarone, might be the actual responsible for the increased atrial refractory period (Talajic, DeRoode and Nattel, 1987).

Furthermore, amiodarone-induced I_{CaL} inhibition flattened the APDR curve, reduced the frequency and amplitude of APD alternans and prevented AF inducibility in the structurally-healthy atria. Therefore, while ineffective for AF termination, amiodarone hindered the formation of dynamic substrates derived from steep electrical restitution.

4.2 Ionic current dysregulation and dynamic electrophysiological substrates in structurally-healthy atria

Steep electrical restitution was the mechanism adopted in this study to trigger dynamic substrates that facilitate AF, as observed in human AF patients (Narayan et al., 2008; Krummen et al., 2012). Unlike previous simulation works that changed single ionic currents (Garfinkel et al., 2000), steep electrical restitution in our study resulted from specific multivariate

ionic density distributions. These distributions were obtained by scaling uniformly all ionic densities of the cellular model, which mimicked inter-patient variability in ionic densities and preserved the high non-linearity between ion channel conductances and the action potential morphology (Elliott et al., 2021). Moreover, we considered a detailed atrial geometry with realistic anisotropy ratios and CV, as opposed to using monolayers (Virag et al., 2002) or isotropic conduction (Gong et al., 2007), and replicate accurate AF-initiation conditions.

As such, we observed that increased G_{CaL}, G_{K1} and G_{NaK} characterized those atrial cardiomyocyte models favoring AF inducibility and maintenance in structurally-healthy atria. Previous simulation studies observed that increasing G_{CaL} steepens the APD restitution slope, potentially leading to wave break-up and fibrillation (Garfinkel et al., 2000). In our study, however, we found that steep restitution was only engaged for high cellular excitability. The latter was enabled by G_{K1} up-regulation, and could be aggravated by increased acetylcholine-activated inward rectifier K^+ ($I_{K,ACh}$) current, not considered in the present study.

Likewise, elevated G_{K1} and G_{NaK} ensured AF maintenance. In agreement with our simulations, increased Na^+/K^+ pump was linked to higher susceptibility to postoperative AF (Tran et al., 2009). Increased inward rectifier K^+ current has been extensively associated with the AF-induced electrophysiological remodeling (Dobrev and Ravens, 2003) and proven essential for rotor stabilization in the electrically remodeled atria (Pandit et al., 2005). In our population of structurally-healthy atria, however, high G_{K1} was additionally required for AF inducibility. Similarly, other computational studies have observed that in the absence of fibrosis, the inhibition of the inward rectifier K^+ current considerably hindered AF initiation (Gharaviri et al., 2021). A genetic analysis performed in a population of kindreds (Xia et al., 2005) identified a gain-of-function mutation in KCNJ2, encoding the Kir2. x channels of the inward rectifier K^+ current, underlying familial AF. Missense mutations in KCNJ2 were also reported in human patients with paroxysmal AF (Deo et al., 2013). Therefore, as shown in this study, increased inward rectifier K^+ current constitutes an AF predisposing condition that additionally favors AF perpetuation.

4.3 Limitations and future perspectives

Drug action was simulated as simple pore-block models as the data required were available for the compounds investigated. However, it is possible that this might have increased the model sensitivity to repolarization prolonging effects, explaining the grater efficacy of class III antiarrhythmic drugs compared to class Ic. Neglecting the rate dependence of class Ic agents and thus, potentially underestimating I_{Na} inhibition, might explain the different results obtained for propafenone and flecainide. Similarly, increasing the resting membrane potential through I_{K1} inhibition, therefore hampering I_{Na} (in)activation, resulted more effective than direct I_{Na} block. This might reflect the importance of class Ic agents for binding with different affinities to the different states of the Na^+ channel, which was not considered in this study.

Moreover, pharmacological treatment and the performance of the predictive model should be further evaluated considering, not only electrophysiological, but also anatomical and structural variability. Even the electrophysiological variability considered was small. The 97 models selected, which presented the ionic current properties required to induce AF in structurally-healthy atria, had similar morphologies (i.e., a rapid phase 3 repolarization and relatively hyperpolarized resting membrane potential). Therefore, a wider range of action potentials has to be taken into account in future studies.

Restricting the study to similar action potential morphologies could also explain why the accuracy of the clinical decision support system was not higher than 70%. A better stratification of the ionic current properties that respond to specific antiarrhythmic drugs would result from considering a wider ionic current distribution in the first place (i.e., wider range of action potential morphologies). The latter could improve the prediction accuracy and boost associated prediction metrics. In this sense, employing other machine learning algorithms might also add extra predictive power.

In the clinic, obtaining the ionic density of the patient presents a challenge, especially without undertaking an invasive procedure (i.e., biopsy during surgery). However, the finding that similar accuracies are obtained with the ECG and ionic metrics for predicting successful AF cardioversion, suggests that the ECG already contain information of the ionic current properties. Thus, further studies should investigate whether the atrial ionic profile of a patient could be characterized non-invasively through the ECG.

5 Conclusion

In structurally-healthy atria, AF inducibility and sustainability are enabled by high excitability and steep restitution, due to elevated L-type Ca^{2+} and inward rectifier K^+ currents. Accordingly, decreasing excitability, through prolonged refractoriness, results in pharmacological cardioversion. However, maximal prolongation of refractoriness depends on the interaction between the ionic distribution of the atria and the ionic currents targeted by the antiarrhythmic drug, highlighting optimal pharmacological treatments for individual ionic current profiles. Therefore, successful cardioversion is predicted in virtual human atria with 70% accuracy from both ionic current and ECG properties.

Data availability statement

The original contributions presented in the study are included in the article/Supplementary Material, further inquiries can be directed to the corresponding authors.

Author contributions

All authors equally contributed to the conception of the work, revising it critically for important intellectual content, and final approval of the version to be published, ensuring that questions related to the accuracy or integrity of any part of the work were appropriately investigated and resolved. BR and AB-O acted as supervisors of the research, AR, RS and JC mainly contributed in methodological aspects, and AD was responsible for conducting all the simulations, analysis of results, and drafting the work.

Funding

This work was supported by a British Heart Foundation (BHF) Intermediate Fellowship (FS/17/22/32,644 to AB-O), a Wellcome Trust Senior Fellowship in Basic Biomedical Sciences (214290/Z/18/Z to BR), and the CompBioMed Centre of Excellence in Computational Biomedicine (European Union's Horizon 2020; grant agreements 675,451, 823,712). This project has also received funding from the European Union's Horizon 2020 research and innovation programme under the Marie Skłodowska-Curie grant agreement No.860974 (to AD). The authors acknowledge additional support from an Infrastructure for Impact Award from the National Centre for the Replacement, Refinement and Reduction of Animals in Research (NC/P001076/1), the Oxford BHF Centre of Research Excellence (RE/13/1/30,181), PRACE, Piz Daint at the Swiss National Supercomputing Centre, Switzerland (ICEI-PRACE grants icp005 and icp013) and Fapemig.

Conflict of interest

The authors declare that the research was conducted in the absence of any commercial or financial relationships that could be construed as a potential conflict of interest.

Publisher's note

Supplementary material

The Supplementary Material for this article can be found online at: https://www.frontiersin.org/articles/10.3389/fphys.2022.966046/full#supplementary-material

References

Aguilar, M., Rose, A., Takawale, S., Nattel, S., and Reilly, S. (2021). New aspects of endocrine control of atrial fibrillation and possibilities for clinical translation. *Cardiovasc. Res.* 117 (7), 1645–1661. doi:10.1093/cvr/cvab080

Alcaraz, R., Sandberg, L., Sörnmo, J. J., and Rieta, J. J. (2011). Classification of paroxysmal and persistent atrial fibrillation in ambulatory ECG recordings. *IEEE Trans. Biomed. Eng.* 58 (5), 1441–1449. doi:10.1109/TBME.2011.2112658

Andrade, J. G., Aguilar, M., Atzema, C., Bell, A., Cairns, J. A., Cheung, C. C., et al. (2020). The 2020 Canadian cardiovascular society/Canadian heart rhythm society comprehensive guidelines for the management of atrial fibrillation. *Can. J. Cardiol.* 36 (12), 1847–1948. doi:10.1016/j.cjca.2020.09.001

Bash, L. D., Buono, G. M., Davies, A., Martin, K., Fahrbach, H., et al. (2012). Systematic review and meta-analysis of the efficacy of cardioversion by vernakalant and comparators in patients with atrial fibrillation. *Cardiovasc. Drugs Ther.* 26 (2), 167–179. doi:10.1007/s10557-012-6374-4

Boriani, G., Bifft, A., Capucci, G., Botto, T., BroffoniM., T., et al. (1998). Conversion of recent-onset Atrial Fibrillation to sinus rhythm: Effects of different drug protocols. *Pacing Clin. Electro* 21 (11 II), 2470–2474. doi:10.1111/j.1540-8159.1998.tb01203.x

Boriani, G., Diemberger, M., Biffi, C., Martignani, A., and Branzi, A. (2004). Pharmacological cardioversion of atrial fibrillation. *Drugs* 64 (24), 2741–2762. doi:10.2165/00003495-200464240-00003

Bueno-Orovio, A., Sánchez, E., Pueyo, B., and Rodriguez, B. (2014). Na/K pump regulation of cardiac repolarization: Insights from a systems biology approach. *Pflugers Arch. - Eur. J. Physiol.* 466 (2), 183–193. doi:10.1007/s00424-013-1293-1

Capucci, A., Cipolletta, L., Guerra, F., and Giannini, I. (2018). Emerging pharmacotherapies for the treatment of atrial fibrillation. *Expert Opin. Emerg. Drugs* 23 (1), 25–36. doi:10.1080/14728214.2018.1446941

Courtemanche, M., Ramirez, R. J., and Nattel, S. (1998). Ionic mechanisms underlying human atrial action potential properties: Insights from a mathematical model. *Am. J. Physiology-Heart Circulatory Physiology* 275 (1 44-1), H301–H321. doi:10.1152/ajpheart.1998.275.1.h301

Denham, N. C., Pearman, J. L., Caldwell, G. W. P., Madders, D. A., Eisner, A. W., et al. (2018). Calcium in the pathophysiology of atrial fibrillation and heart failure. *Front. Physiol.* 9, 1380. doi:10.3389/fphys.2018.01380

Deo, M., Ruan, S. V., Pandit, K., Shah, O., Berenfeld, A., et al. (2013). KCNJ2 mutation in short QT syndrome 3 results in atrial fibrillation and ventricular proarrhythmia. *Proc. Natl. Acad. Sci. U.S.A.* 110 (11), 4291–4296. doi:10.1073/pnas.1218154110

Dobrev, D., and Ravens, U. (2003). Remodeling of cardiomyocyte ion channels in human atrial fibrillation. *Basic Res. Cardiol.* 98 (3), 137–148. doi:10.1007/s00395-003-0409-8

Elliott, J., Belen, L., Mainardi, J. F., and Rodriguez Matas, J. F. (2021). A comparison of regional classification strategies implemented for the population based approach to modelling atrial fibrillation. *Mathematics* 9 (14), 1686. doi:10.3390/math9141686

Filgueiras-Rama, D., Martins, S., Mironov, M., Yamazaki, C. J., Calvo, S. R., et al. (2012). Chloroquine terminates stretch-induced atrial fibrillation more effectively than flecainide in the sheep heart. *Circ Arrhythmia Electrophysiol.* 5 (3), 561–570. doi:10.1161/CIRCEP.111.966820

Garfinkel, A., Kim, Z., Voroshilovsky, J. R., Qu, M. H., et al. (2000). Preventing ventricular fibrillation by flattening cardiac restitution. *Proc. Natl. Acad. Sci. U.S.A.* 97 (11), 6061–6066. doi:10.1073/pnas.090492697

Gharaviri, A., Pezzuto, M., Potse, G., Conte, S., Zeemering, V., et al. (2021). Synergistic antiarrhythmic effect of inward rectifier current inhibition and pulmonary vein isolation in a 3D computer model for atrial fibrillation. *Europace.* 23, I161–I168. doi:10.1093/europace/euaa413

Gima, K., and Rudy, Y. (2002). Ionic current basis of electrocardiographic waveforms. *Circulation Res.* 90 (8), 889–896. doi:10.1161/01.RES.0000016960.61087.86

Gong, Y., Xie, K. M., Stein, A., Garfinkel, C. A., Culianu, B. B., et al. (2007). Mechanism underlying initiation of paroxysmal atrial flutter/atrial fibrillation by ectopic foci. *Circulation* 115 (16), 2094–2102. doi:10.1161/CIRCULATIONAHA.106.656504

Grandi, E., Pandit, N., Voigt, A. J., Workman, D., Dobrev, J., et al. (2011). Human atrial action potential and Ca 2+ model. *Circ. Res.* 109 (9), 1055–1066. doi:10.1161/CIRCRESAHA.111.253955

Haïssaguerre, M., Jaïs, P., Shah, D. C., Takahashi, A., Hocini, M., Quiniou, G., et al. (1999). Spontaneous initiation of atrial fibrillation by ectopic impulses originating in the pulmonary veins. *Cardiol. Rev.* 7 (2), 65. doi:10.1097/00045415-199903000-00006

Hanna, P., Buch, S., Stavrakis, C., Meyer, J. D., Tompkins, J. L., et al. (2021). Neuroscientific therapies for atrial fibrillation. *Cardiovasc. Res.* 117 (7), 1732–1745. doi:10.1093/cvr/cvab172

Heijman, J., Linz, D., and Schotten, U. (2021). Dynamics of atrial fibrillation mechanisms and comorbidities. *Annu. Rev. Physiol.* 83, 83–106. doi:10.1146/annurev-physiol-031720-085307

Hindricks, G., Potpara, N., Dagres, E., Arbelo, J. J., Bax, C., et al. (2021). 2020 ESC Guidelines for the diagnosis and management of atrial fibrillation developed in collaboration with the European Association for Cardio-Thoracic Surgery (EACTS): The Task Force for the diagnosis and management of atrial fibrillation of the European Society of Cardiology (ESC) Developed with the special contribution of the European Heart Rhythm Association (EHRA) of the ESC. *Eur. Heart J.* 42 (5), 373–498. doi:10.1093/eurheartj/ehaa612

Ji, Y., Varkevisser, D., Opacic, A., Bossu, M., Kuiper, J. D. M., et al. (2017). The inward rectifier current inhibitor PA-6 terminates atrial fibrillation and does not cause ventricular arrhythmias in goat and dog models. *Br. J. Pharmacol.* 174 (15), 2576–2590. doi:10.1111/bph.13869

Kany, S., Reissmann, A., Metzner, P., Kirchhof, D., Darbar, R. B., and Schnabel, R. B. (2021). Genetics of atrial fibrillation-practical applications for clinical management: If not now, when and how? *Cardiovasc. Res.* 117 (7), 1718–1731. doi:10.1093/cvr/cvab153

Kim, B. S., Kim, Y.-H., Hwang, G.-S., Pak, H.-N., Lee, S. C., Shim, W. J., et al. (2002). Action potential duration restitution kinetics in human atrial fibrillation. *J. Am. Coll. Cardiol.* 39 (8), 1329–1336. doi:10.1016/S0735-1097(02)01760-6

Kirchhof, P., Camm, A., Goette, A., Brandes, L., Eckardt, A., et al. (2020). Early rhythm-control therapy in patients with atrial fibrillation. *N. Engl. J. Med.* 383 (14), 1305–1316. doi:10.1056/nejmoa2019422

Koller, M. L., Riccio, M. L., and Jr., R. F. (1998). Dynamic restitution of action potential duration during electrical alternans and ventricular fibrillation. *Am. J. Physiology-Heart Circulatory Physiology* 275 (5 44-5), H1635–H1642. doi:10.1152/ajpheart.1998.275.5.h1635

Krummen, D. E., Bayer, J., Ho, G., Ho, M. R., Smetak, P., et al. (2012). Mechanisms of human atrial fibrillation initiation. *Circ Arrhythmia Electrophysiol.* 5 (6), 1149–1159. doi:10.1161/CIRCEP.111.969022

Kumar, S., Kalman, F., Sutherland, S. J., Spence, S., Finch, P. B., and Sparks, P. B. (2012). Atrial fibrillation inducibility in the absence of structural heart disease or clinical atrial fibrillation. *Circ Arrhythmia Electrophysiol.* 5 (3), 531–536. doi:10.1161/CIRCEP.111.968859

Lankveld, T., de Vos, C. B., Limantoro, I., Zeemering, S., Dudink, E., Crijns, H. J., et al. (2016). Systematic analysis of ECG predictors of sinus rhythm maintenance after electrical cardioversion for persistent atrial fibrillation. *Heart rhythm.* 13 (5), 1020–1027. doi:10.1016/j.hrthm.2016.01.004

Liberos, A., Bueno-Orovio, A., Rodrigo, M., Ravens, U., Hernandez-Romero, I., Fernandez-Aviles, F., et al. (2016). Balance between sodium and calcium currents underlying chronic atrial fibrillation termination: An *in silico* intersubject variability study. *Heart rhythm.* 13 (12), 2358–2365. doi:10.1016/j.hrthm.2016.08.028

Loewe, A., Lutz, M., Wilhelms, D., Sinnecker, P., Barthel, E. P., et al. (2014). *In-silico* assessment of the dynamic effects of amiodarone and dronedarone on human atrial patho-electrophysiology. *Europace* 16, iv30–iv38. doi:10.1093/europace/euu230

Loewe, A., Xu, E. P., Scholz, O., Dössel, G., and Seemann, G. (2015). Understanding the cellular mode of action of vernakalant using a computational model: Answers and new questions. *Curr. Dir. Biomed. Eng.* 1 (1), 418–422. doi:10.1515/cdbme-2015-0101

Maleckar, M. M., Greenstein, W. R., Giles, N. A., and Trayanova, N. A. (2009). K+current changes account for the rate dependence of the action potential in the human atrial myocyte. *Am. J. Physiology-Heart Circulatory Physiology* 297 (4), H1398–H1410. doi:10.1152/ajpheart.00411.2009

Margara, F., Psaras, Y., and Jenny Wang, Z. (2022). Human iPSC-CMs and *in-silico* technologies define mechanisms and accelerate targeted pharmacogenetics in hypertrophic cardiomyopathy. *bioRxiv* 2022, 495324. doi:10.1101/2022.06.08.495324

Matene, E., and Jacquemet, V. (2012). Fully automated initiation of simulated episodes of atrial arrhythmias. *Europace* 14 (5), v17–v24. doi:10.1093/europace/eus271

Musuamba, F. T., Skottheim Rusten, R., Lesage, G., Russo, R., Bursi, L., et al. (2021). Scientific and regulatory evaluation of mechanistic *in silico* drug and disease models in drug development: Building model credibility. *CPT Pharmacometrics Syst. Pharmacol.* 10 (8), 804–825. doi:10.1002/psp4.12669

Muszkiewicz, A., Liu, A., Bueno-Orovio, B. A. J., Lawson, K., Burrage, B., et al. (2018). From ionic to cellular variability in human atrial myocytes: An integrative computational and experimental study. *Am. J. Physiology-Heart Circulatory Physiology* 314 (5), H895–H916. doi:10.1152/ajpheart.00477.2017

Narayan, S. M., Kazi, D. E., Krummen, W. J., and Rappel, W.-J. (2008). Repolarization and activation restitution near human pulmonary veins and atrial fibrillation initiation. *J. Am. Coll. Cardiol.* 52 (15), 1222–1230. doi:10.1016/j.jacc.2008.07.012

Noujaim, S. F., Pandit, O., Berenfeld, K., Vikstrom, M., Cerrone, S., et al. (2007). Up-regulation of the inward rectifier K+current (Ik1) in the mouse heart accelerates and stabilizes rotors. *J. Physiol.* 578 (1), 315–326. doi:10.1113/jphysiol.2006.121475

Pandit, S. V., Berenfeld, J. M. B., Anumonwo, R. M., Zaritski, J., Kneller, S., et al. (2005). Ionic determinants of functional reentry in a 2-D model of human atrial cells during simulated chronic atrial fibrillation. *Biophysical J.* 88 (6), 3806–3821. doi:10.1529/biophysj.105.060459

Passini, E., Britton, H. R., Lu, J., Rohrbacher, A. N., Hermans, D. J., et al. (2017). Human *in silico* drug trials demonstrate higher accuracy than animal models in predicting clinical pro-arrhythmic cardiotoxicity. *Front. Physiol.* 8 (SEP), 668–715. doi:10.3389/fphys.2017.00668

Passini, E., Zhou, X., Trovato, C., Britton, O. J., Bueno-Orovio, A., and Rodriguez, B. (2021). The virtual assay software for human *in silico* drug trials to augment drug cardiac testing. *J. Comput. Sci.* 52, 101202. doi:10.1016/j.jocs.2020.101202

Pohjantähti-Maaroos, H., Hyppölä, M., Lekkala, E., Sinisalo, A., Heikkola, J., and Hartikainen, J. (2019). Intravenous vernakalant in comparison with intravenous flecainide in the cardioversion of recent-onset atrial fibrillation. *Eur. Heart J. Acute Cardiovasc. Care* 8 (2), 114–120. doi:10.1177/2048872617728558

Qu, Z., Weiss, J. N., and Garfinkel, A. (1999). Cardiac electrical restitution properties and stability of reentrant spiral waves: A simulation study. *Am. J. Physiology-Heart Circulatory Physiology* 276 (1 45-1), H269–H283. doi:10.1152/ajpheart.1999.276.1.h269

Ragab, A. A. Y., Sitorus, B. B. J. J. M., Brundel, N. M. S., and Groot, N. M. S. d. (2020). The genetic puzzle of familial atrial fibrillation. *Front. Cardiovasc. Med.* 7, 14–18. doi:10.3389/fcvm.2020.00014

Reisinger, J., Gatterer, E., Lang, W., Vanicek, T., Eisserer, G., Bachleitner, T., et al. (2004). Flecainide versus ibutilide for immediate cardioversion of atrial fibrillation of recent onset. *Eur. Heart J.* 25 (15), 1318–1324. doi:10.1016/j.ehj.2004.04.030

Roney, C. H., Sim, J., Yu, M., Beach, A., Mehta, J., et al. (2022). Predicting atrial fibrillation recurrence by combining population data and virtual cohorts of patient-specific left atrial models. *Circ Arrhythmia Electrophysiol.* 15 (2), e010253. doi:10.1161/CIRCEP.121.010253

Sachetto Oliveira, R., Martins Rocha, D., Burgarelli, W., Meira, C., Constantinides, R., and Weber dos Santos, R. (2018). Performance evaluation of GPU parallelization, space-time adaptive algorithms, and their combination for simulating cardiac electrophysiology. *Int. J. Numer. Meth Biomed. Engng* 34 (2), e2913–17. doi:10.1002/cnm.2913

Sánchez, C., Bueno-Orovio, E., Pueyo, B., and Rodríguez, B. (2017). Atrial fibrillation dynamics and ionic block effects in six Heterogeneous human 3D virtual atria with distinct repolarization dynamics. *Front. Bioeng. Biotechnol.* 5 (MAY), 29–13. doi:10.3389/fbioe.2017.00029

Sánchez, C., Bueno-Orovio, E., Wettwer, S., Loose, J., Simon, U., et al. (2014). Inter-subject variability in human atrial action potential in sinus rhythm versus chronic atrial fibrillation. *PLoS ONE* 9 (8), e105897. doi:10.1371/journal.pone.0105897

Scott Jr, L., Fender, A., Saljic, L., Li, X., Chen, X., et al. (2021). NLRP3 inflammasome is a key driver of obesity-induced atrial arrhythmias. *Cardiovasc. Res.* 117 (7), 1746–1759. doi:10.1093/cvr/cvab024

Seemann, G., Höper, F. B., Sachse, O., Dössel, A. V., Holden, H., and Zhang, H. (2006). Heterogeneous three-dimensional anatomical and electrophysiological model of human atria. *Phil. Trans. R. Soc. A* 364 (1843), 1465–1481. doi:10.1098/rsta.2006.1781

Singh, B. N., Connolly, S. J., Crijns, H. J., Roy, D., Kowey, P. R., Capucci, A., et al. (2008). Efficacy of dronedarone for maintenance of sinus rhythm in atrial fibrillation or flutter. Results of the EURIDIS and ADONIS. *Kardiologiia* 48 (7), 58–59.

Sutanto, H. (2022). Individual contributions of cardiac ion channels on atrial repolarization and reentrant waves: A multiscale in-silico study. *Jcdd* 9 (1), 28. doi:10.3390/jcdd9010028

Sutanto, H., Laudy, L., Clerx, M., Dobrev, D., Crijns, H. J. G. M., and Heijman, J. (2019). Maastricht antiarrhythmic drug evaluator (MANTA): A computational tool for better understanding of antiarrhythmic drugs. *Pharmacol. Res.* 148, 104444. doi:10.1016/j.phrs.2019.104444

Talajic, M., DeRoode, M. R., and Nattel, S. (1987). Comparative electrophysiologic effects of intravenous amiodarone and desethylamiodarone in dogs: Evidence for clinically relevant activity of the metabolite. *Circulation* 75 (1), 265–271. doi:10.1161/01.CIR.75.1.265

The Digitalis in Acute Atrial Fibrillation (DAAF) Trial Group (1997). Intravenous digoxin in acute atrial fibrillation: Results of a randomized, placebo-controlled multicentre trial in 239 patients. *European Heart Journal* 18 (4), 649–654. doi:10.1093/oxfordjournals.eurheartj.a015311

Tobón, C., Ruiz-Villa, E., Heidenreich, L., Romero, F., Hornero, J., and Saiz, J. (2013). A three-dimensional human atrial model with fiber orientation. Electrograms and arrhythmic activation patterns relationship. *PLoS ONE* 8 (2), e50883. doi:10.1371/journal.pone.0050883

Tran, C. T., Schmidt, J. B., Christensen, K., and Kjeldsen, K. (2009). Atrial Na,K-ATPase increase and potassium dysregulation accentuate the risk of postoperative atrial fibrillation. *Cardiology* 114 (1), 1–7. doi:10.1159/000209264

Virag, N., Jacquemet, C. S., Henriquez, S., Zozor, O., Blanc, J. M., et al. (2002). Study of atrial arrhythmias in a computer model based on magnetic resonance images of human atria. *Chaos* 12 (3), 754–763. doi:10.1063/1.1483935

Watanabe, M. A., Fenton, S. J., Evans, H. M., Hastings, A., and Karma, A. (2001). Mechanisms for discordant alternans. *J. Cardiovasc. Electrophysiol.* 12 (2), 196–206. doi:10.1046/j.1540-8167.2001.00196.x

Wilhelms, M., Hettmann, M. M., Maleckar, J. T., Koivumäki, O., Dössel, G., and Seemann, G. (2013). Benchmarking electrophysiological models of human atrial myocytes. *Front. Physio.* 3, 487–516. JAN(January). doi:10.3389/fphys.2012.00487

Wyse, D. G., Van Gelder, P. T., Ellinor, A. S., Go, J. M., Kalman, S. M., et al. (2014). Lone atrial fibrillation. *J. Am. Coll. Cardiol.* 63 (17), 1715–1723. doi:10.1016/j.jacc.2014.01.023

Xia, M., Jin, S., Bendahhou, Y., He, M. M., Larroque, Y., et al. (2005). A Kir2.1 gain-of-function mutation underlies familial atrial fibrillation. *Biochem. Biophysical Res. Commun.* 332 (4), 1012–1019. doi:10.1016/j.bbrc.2005.05.054

Zeemering, S., Lankveld, P., Bonizzi, I., Limantoro, S. C. A. M., Bekkers, H. J. G. M., et al. (2018). The electrocardiogram as a predictor of successful pharmacological cardioversion and progression of atrial fibrillation. *Europace* 20 (7), e96–e104. doi:10.1093/europace/eux234

frontiers | Frontiers in Physiology

TYPE Original Research
PUBLISHED 15 September 2022
DOI 10.3389/fphys.2022.976468

OPEN ACCESS

EDITED BY
Axel Loewe,
Karlsruhe Institute of Technology, Germany

REVIEWED BY
Jordi Heijman,
Maastricht University, Netherlands
Alberto Porta,
University of Milan, Italy

*CORRESPONDENCE
Felix Plappert,
felix.plappert@bme.lth.se

SPECIALTY SECTION
This article was submitted to Cardiac Electrophysiology, a section of the journal Frontiers in Physiology

RECEIVED 23 June 2022
ACCEPTED 10 August 2022
PUBLISHED 15 September 2022

CITATION
Plappert F, Wallman M, Abdollahpur M, Platonov PG, Östenson S and Sandberg F (2022), An atrioventricular node model incorporating autonomic tone.
Front. Physiol. 13:976468.
doi: 10.3389/fphys.2022.976468

An atrioventricular node model incorporating autonomic tone

Felix Plappert[1]*, Mikael Wallman[2], Mostafa Abdollahpur[1], Pyotr G. Platonov[3], Sten Östenson[4] and Frida Sandberg[1]

[1]Department of Biomedical Engineering, Lund University, Lund, Sweden, [2]Department of Systems and Data Analysis, Fraunhofer-Chalmers Centre, Gothenburg, Sweden, [3]Department of Cardiology, Clinical Sciences, Lund University, Lund, Sweden, [4]Department of Internal Medicine and Department of Clinical Physiology, Central Hospital Kristianstad, Kristianstad, Sweden

The response to atrial fibrillation (AF) treatment is differing widely among patients, and a better understanding of the factors that contribute to these differences is needed. One important factor may be differences in the autonomic nervous system (ANS) activity. The atrioventricular (AV) node plays an important role during AF in modulating heart rate. To study the effect of the ANS-induced activity on the AV nodal function in AF, mathematical modelling is a valuable tool. In this study, we present an extended AV node model that incorporates changes in autonomic tone. The extension was guided by a distribution-based sensitivity analysis and incorporates the ANS-induced changes in the refractoriness and conduction delay. Simulated RR series from the extended model driven by atrial impulse series obtained from clinical tilt test data were qualitatively evaluated against clinical RR series in terms of heart rate, RR series variability and RR series irregularity. The changes to the RR series characteristics during head-down tilt were replicated by a 10% decrease in conduction delay, while the changes during head-up tilt were replicated by a 5% decrease in the refractory period and a 10% decrease in the conduction delay. We demonstrate that the model extension is needed to replicate ANS-induced changes during tilt, indicating that the changes in RR series characteristics could not be explained by changes in atrial activity alone.

KEYWORDS

atrial fibrillation, atrioventricular node, autonomic tone, tilt test, mathematical modeling, ECG, RR series characteristics, sample entropy

1 Introduction

Atrial fibrillation (AF) is the most common supraventricular tachyarrhythmia (Hindricks et al., 2020). Characteristic for AF is an increased and irregular atrial activity that results in a rapid and irregular ventricular activation. Atrial fibrillation is linked to substantial morbidity and mortality, and is a significant burden to patients, physicians, and healthcare systems globally. Two main strategies of AF treatments are rate control and rhythm control. Rate control is one of the corner stones of AF management, however the effect of individual rate-control drugs are difficult to predict in advance. This is why the choice of a rate-control drug today remains empiric and driven largely by their

safety profile and contraindications rather than predicted efficacy. Therefore, the complex mechanisms of AF have to be better understood to personalize the treatment and reduce the burden of AF on the healthcare system.

It has been shown that the autonomic nervous system (ANS) is contributing to the initiation and maintenance of AF (Shen and Zipes, 2014). Either a predominance in sympathetic or in parasympathetic modulation has been observed to initiate an episode of paroxysmal atrial fibrillation (PAF); and in some patients, both the sympatho-vagal and vagal predominances have been observed to initiate PAF episodes (Lombardi et al., 2004). Hence, differences in the ANS activity among patients may be an important factor behind the inter-patient differences in response to treatment. To investigate the ANS-induced changes to the pathophysiology of AF, the effect of the ANS has to be quantified. One common method to quantify the autonomic tone during normal sinus rhythm (NSR) is by heart rate variability (HRV) (Sassi et al., 2015). In sinus rhythm, HRV can be used to obtain information about the function of the sinoatrial (SA) node. This information is valuable for the quantification of the autonomic tone, because the SA node is densely innervated by the ANS (Shen and Zipes, 2014; George et al., 2017). In AF, however, HRV cannot be used to quantify the autonomic tone, because the heart beats are not initiated in the SA node.

Instead, the ventricular rhythm during AF is determined by the atrial electrical activity and the subsequent AV nodal modulation. Since the AV node is densely innervated by the ANS, characterizing the AV nodal behavior during AF may give valuable information about the autonomic tone. Results from previous studies suggest that the heart rate, as well as the heart rate variability, quantified by RR rmssd, and heart rate irregularity, quantified by RR sample entropy, are affected by β-blocker induced changes in sympathetic response (Corino et al., 2015). We hypothesize that such changes in the heart rate and its variability and irregularity reflect ANS-induced changes in the AV node. The ANS-induced changes on the cardiac electrophysiology can be studied using head-up and head-down tilt test, which in a previous study was shown to affect electrophysiological properties of atrial myocardium during AF (Östenson et al., 2017). It is unclear if the changes in the heart rate and its variability and irregularity are explained by the changes in the atrial electrophysiology alone or also by changes in the AV nodal properties. Investigating how the ANS is modulating the heart rate during AF is a complex task and requires a model based analysis.

Previously, several AV node models have been proposed that incorporate important characteristics of the AV nodal structure and electrophysiology in their design. Characteristic for the AV node is its dual-pathway physiology enabling a parallel excitation propagation of impulses with different electrophysiological properties (George et al., 2017). For example, the slow pathway (SP) has a longer conduction delay and shorter refractory period compared to the fast pathway (FP) (George et al., 2017). Furthermore, the refractory period and conduction delay are dynamic and depend on the recent history of the conducted and blocked impulses in the AV nodal tissue (George et al., 2017; Billette and Tadros, 2019). Early models of the AV node did not account for the dual-pathway physiology (Cohen et al., 1983; Jørgensen et al., 2002; Rashidi and Khodarahmi, 2005; Mangin et al., 2005; Lian et al., 2006). Later models have incorporated this feature, represented by separate refractory periods (Corino et al., 2011; Henriksson et al., 2016; Inada et al., 2017; Wallman and Sandberg, 2018) and separate conduction delays (Climent et al., 2011b; Inada et al., 2017; Wallman and Sandberg, 2018). However, no models have explicitly incorporated ANS-induced changes in their model description.

Therefore, the aim of the present study is to incorporate ANS-induced changes into the AV node network model previously proposed by Wallman and Sandberg, (2018). The extension of the AV node model was guided by a distribution-based sensitivity analysis (Pianosi and Wagener 2018) and incorporates ANS-induced changes in the computation of the refractoriness and conduction delay. The extended model is evaluated with respect to its ability to replicate changes in heart rate and RR series variability and irregularity observed during head-up and head-down tilt test.

2 Materials and methods

First, the clinical tilt test data is described in Section 2.1. The RR series characteristics are defined in Section 2.2, followed by the description of a network model of the AV node (Section 2.3). A sensitivity analysis on the AV node model is described in Section 2.4, that identifies the influence of changes in model parameters on the RR series characteristics. Based on the sensitivity analysis, the AV node model is modified to account for ANS-induced changes in AV node characteristics (Section 2.5). The ability of the modified AV node model to replicate ANS induced changes in RR series characteristics observed during tilt-test is assessed in Section 2.6. Finally, the statistical analysis is described in Section 2.7, that is used to determine significant differences in AFR and RR series characteristics between tilt positions.

2.1 Tilt test study

The autonomic influence on the RR series characteristics was analysed using ECG data recorded during a tilt test study performed by Östenson et al. (2017). Recordings from 24 patients with persistent AF were considered of sufficient quality for analysis and were included in the present study; their age was 66 ± 9 (mean ± std), and 63% were men. None

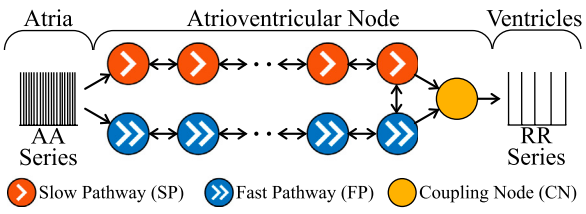

FIGURE 1
A schematic representation of the AV node model. Note that retrograde conduction is possible within the AV node model. For simplicity, only a subset of the ten nodes in each pathway is shown.

of the patients had abnormal levels of thyroid hormones, severe renal failure requiring dialysis, or heart valve disease. None of the patients were ablated for AF or on any of the Class I or Class III antiarrhythmic drugs. The tilt test was performed between 1 and 3 p.m. in a quiet study room. Standard 12-lead ECG was recorded during supine position, followed by head-down tilt (HDT, -30°) and then head-up tilt (HUT, +60°). The tilt table was manually operated and had hand grip and ankle support for HDT and foot board support for HUT; the patients remained in each position approximately 5 min. ECG preprocessing and R-peak detection was performed using the CardioLund ECG parser (www.cardiolund.com).

2.2 RR series characteristics

The RR series consists of the intervals between consecutive heartbeats, where the time of a heartbeat is determined by the corresponding R peak in the ECG signal. In this work, three statistical measures of the RR series characteristics were used, quantifying heart rate, heart rate variability and heart rate irregularity, respectively, defined according to Eqs. 1–3. The mean of the RR intervals ($\overline{RR}$) is computed as

$$\overline{RR} = \frac{1}{N}\sum_{i=1}^{N} RR_i, \tag{1}$$

where RR_i denotes the i:th RR interval in the RR series. The root mean square of successive RR interval differences (RR_V, variability) is computed as

$$RR_V = \sqrt{\frac{1}{N-1}\sum_{i=1}^{N-1}(RR_{i+1} - RR_i)^2}. \tag{2}$$

The sample entropy of the RR series (RR_I, irregularity) is computed as

$$RR_I = -\ln\left(\frac{\sum_{i=1}^{N-m}\sum_{j=1,j\neq i}^{N-m} b_{i,j}^{m+1}(r)}{\sum_{i=1}^{N-m}\sum_{j=1,j\neq i}^{N-m} b_{i,j}^{m}(r)}\right), \tag{3}$$

where the binary variable $b_{i,j}^{l}(r)$ with $l \in \{m, m+1\}$ has the value 1 if the maximum absolute distance between corresponding scalar elements in the vectors $V_i^l = \{RR_i, RR_{i+1}, \ldots, RR_{i+l-1}\}$ and V_j^l is below the tolerance r times the standard deviation of the RR interval series, otherwise the value is zero (Richman and Moorman, 2000). In this study, the parameters were set to $m = 2$ and $r = 0.2$.

2.3 Network model of the human atrioventricular node

The AV node is modelled by a network of 21 nodes (cf. Figure 1) (Wallman and Sandberg, 2018; Karlsson et al., 2021). The AV nodal dual-pathway physiology with a slow pathway (SP) and a fast pathway (FP) is represented with two chains of 10 nodes each. The last nodes of the two pathways are connected to each other and to an additional coupling node (CN). Impulses enter the AV node model simultaneously at the first node of each pathway and leave the model over the CN. Retrograde conduction is possible due to the bidirectional conduction within the pathways and between the last nodes of SP and FP.

Each node represents a section of the AV node and is described with an individual refractory period $R^P(\Delta t_k)$ and conduction delay $D^P(\Delta t_k)$ defined as

$$R^P(\Delta t_k) = R^P_{min} + \Delta R^P\left(1 - e^{-\Delta t_k/\tau_R^P}\right), \tag{4}$$

$$D^P(\Delta t_k) = D^P_{min} + \Delta D^P e^{-\Delta t_k/\tau_D^P}, \tag{5}$$

where P ∈ {*SP*, *FP*, *CN*} denotes the association to a pathway. The electrical excitation propagation through the AV node is modelled as a series of impulses that can either be passed on or blocked by a node. This decision is based on the interval Δt_k between the k:th impulse arrival time t_k and the end of the (k–1): th refractory period computed as

$$\Delta t_k = t_k - t_{k-1} - R^P(\Delta t_{k-1}). \tag{6}$$

If Δt_k is positive, the impulse is conducted to all adjacent nodes, otherwise the impulse is blocked due to the ongoing refractory period $R^P(\Delta t_{k-1})$. The conduction delay $D^P(\Delta t_k)$ describes the time delay between the arrival of an impulse at a node and its transmission to all adjacent nodes. If an impulse is conducted, $R^P(\Delta t_k)$ and $D^P(\Delta t_k)$ of the current node are updated according to Eqs. 4–6. For the computation of $R^P(\Delta t_k)$ and $D^P(\Delta t_k)$, the nodes in each pathway are characterized by six parameters, defining minimum refractory period, $R^P_{\min}$; maximum prolongation of refractory period, ΔR^P; time constant τ_R^P; minimum conduction delay, $D^P_{\min}$; maximum prolongation of conduction delay, ΔD^P; and the time constant τ_D^P. The SP, FP and CN are modelled with separate vectors $\boldsymbol{\theta}^P = [R^P_{\min}, \Delta R^P, \tau_R^P, D^P_{\min}, \Delta D^P, \tau_D^P]$, all with fixed values.

TABLE 1 Model parameters used for the sensitivity analysis.

Parameters	SP (ms)	FP (ms)	CN (ms)
$R_{\min}$	$\mathcal{U}[250, 600]$	$\mathcal{U}[250, 600]$	250
ΔR	$\mathcal{U}[0, 600]$	$\mathcal{U}[0, 600]$	0
τ_R	$\mathcal{U}[50, 300]$	$\mathcal{U}[50, 300]$	1
$D_{\min}$	$\mathcal{U}[0, 30]$	$\mathcal{U}[0, 30]$	0
ΔD	$\mathcal{U}[0, 75]$	$\mathcal{U}[0, 75]$	0
τ_D	$\mathcal{U}[50, 300]$	$\mathcal{U}[50, 300]$	1

The AV node model processes the impulse propagation chronologically and node by node, using a priority queue of nodes, sorted by impulse arrival time; details can be found in Wallman and Sandberg (2018). The input to the AV node model is a series of atrial impulses that is used to initialize the priority queue. As the impulses are conducted to adjacent nodes, new entries are added to the priority queue. The output of the AV node model is a series of impulses activating the ventricles.

In this study, the series of atrial impulses during AF is modelled as a point-process with independent inter-arrival times according to a Pearson Type IV distribution (Climent et al., 2011a). Hence, the atrial activation (AA) series is completely characterized by four parameters, namely the mean μ, standard deviation σ, skewness γ and kurtosis κ.

2.4 Distribution-based sensitivity analysis

The sensitivity of the three RR series characteristics $\boldsymbol{y} = [\overline{RR}, RR_V, RR_I]^\mathsf{T}$ to the AV node model and AA series parameters $\boldsymbol{x} = [\boldsymbol{\theta}^{SP}, \boldsymbol{\theta}^{FP}, \mu, \sigma]^\mathsf{T}$ is evaluated by applying a distribution-based sensitivity analysis, based on the work of Pianosi and Wagener, (2018). For the sensitivity analysis, cumulative distribution functions (CDF) are estimated using a dataset of $K = 250\,000$ randomly generated model parameter sets $\boldsymbol{x}$ and the characteristics $\boldsymbol{y}$ of the corresponding simulated RR series. For each simulation, an atrial impulse series with 60 000 AA intervals was generated using the Pearson Type IV distribution, with μ randomly drawn from $\mathcal{U}[100, 250]$ ms, σ randomly drawn from $\mathcal{U}[15, 30]$ ms, and γ and κ kept fixed to 1 and 6, respectively. The γ and κ were kept fixed since they cannot be estimated from the f-waves of the ECG. Negative AA intervals were excluded from the impulse series. The model parameters $\boldsymbol{\theta}^{SP}$ and $\boldsymbol{\theta}^{FP}$ were randomly drawn from bounded uniform distributions given in Table 1, as previously done in Karlsson et al. (2021). The $\boldsymbol{\theta}^{CN}$ were kept fixed according to Table 1, corresponding to $R^P(\Delta t_k)$ and $D^P(\Delta t_k)$ of the CN equal to 250 ms and 0 ms, respectively.

The RR series characteristics were computed using a series of 4000 RR intervals corresponding to the first impulses that left the AV node model through the CN. Two selection criteria were used to remove non-physiological parameter sets. First, a model parameter set was only included if the slow pathway had a lower refractory period $R^{SP}(\Delta t_k) < R^{FP}(\Delta t_k)$ and higher conduction delay $D^{SP}(\Delta t_k) > D^{FP}(\Delta t_k)$ than the fast pathway for all Δt_k. Second, the resulting $\overline{RR}$ was required to be in the range 300 ms $\leq \overline{RR} \leq$ 1000 ms, corresponding to heart rates between 60 bpm and 200 bpm. Heart rates below 60 bpm are disregarded, because the pacemaker function of the AV node, that becomes relevant in this case (George et al., 2017), is not incorporated in the AV node model. Heart rates above 200 bpm are disregarded based on a reported minimum refractory period in the bundle branches of around 300 ms (Denes et al., 1974).

A sensitivity coefficient $\mathcal{S}_{n,m}$ is computed for each pair of model parameter x_n and RR series characteristic y_m, where x_n is the n:th element in $\boldsymbol{x}$ and y_m is the m-th element in $\boldsymbol{y}$. The $\mathcal{S}_{n,m}$ indicates how much a change in model parameter x_n affects the distribution of y_m and is defined as

$$\mathcal{S}_{n,m} = \underset{c=1,\ldots,C}{\text{median}} \ \underset{d=1,\ldots,D}{\text{median}} \ \text{KS}\left(F_{y_m}^{(d)}(y_m), F_{y_m|x_n}(y_m|x_n \in \mathcal{I}_c)\right), \tag{7}$$

where $\text{KS}(F_{y_m}^{(d)}(y_m), F_{y_m|x_n}(y_m|x_n \in \mathcal{I}_c))$ is the Kolmogorov-Smirnov (KS) distance between the unconditional CDF $F_{y_m}^{(d)}(y_m)$ and the conditional CDF $F_{y_m|x_n}(y_m|x_n \in \mathcal{I}_c)$. When estimating $F_{y_m|x_n}(y_m|x_n \in \mathcal{I}_c)$, the range of variation of x_n is split into $C = 15$ equally spaced conditioning intervals $\mathcal{I}_c$, with $c = 1, \ldots, C$ (cf. Figure 2A). All samples within $\mathcal{I}_c$ are used to estimate the corresponding $F_{y_m|x_n}(y_m|x_n \in \mathcal{I}_c)$ (cf. Figure 2B). To generate the set of $F_{y_m}^{(d)}(y_m)$, with $d = 1, \ldots, D$, a subset of K/C samples are bootstrapped $D = 1000$ times (cf. Figures 2A,B). The KS distance is defined as

$$\text{KS}(F_1(y), F_2(y)) = \max_y |F_1(y) - F_2(y)|. \tag{8}$$

As the $F_{y_m}^{(d)}(y_m)$ and $F_{y_m|x_n}(y_m|x_n \in \mathcal{I}_c)$ are approximations based on a finite number of samples, parameters that have no influence on y_m can result in $\mathcal{S}_{n,m}$ above zero. The impact of approximation errors on $\mathcal{S}_{n,m}$ can be estimated for each y_m using a dummy parameter $\mathcal{D}_m$ defined as

$$\mathcal{D}_m = \underset{d=2,\ldots,D}{\text{median}} \ \text{KS}\left(F_{y_m}^{(d)}(y_m), F_{y_m}^{(1)}(y_m)\right), \tag{9}$$

A model parameter x_n is determined to have influence on y_m if and only if $\mathcal{S}_{n,m} > \mathcal{D}_m$.

2.5 Extended atrioventricular node model accounting for autonomic nervous system induced changes

The results from the sensitivity analysis (Section 3.1) indicate that changes in both the AV node model parameters and the AA

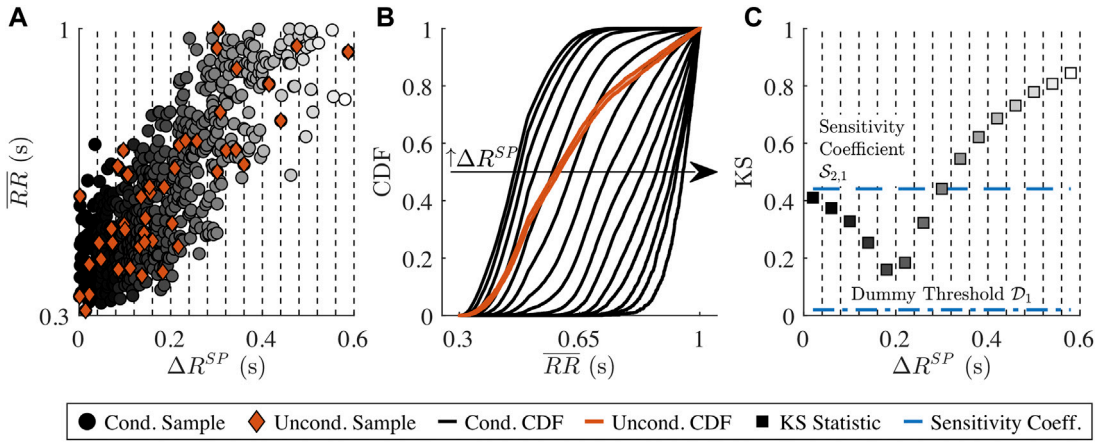

FIGURE 2
Illustration of the distribution-based sensitivity analysis. **(A)** $\overline{RR}$ plotted against one of the model parameters ΔR^{SP}. The samples that are used to estimate the conditional CDFs $F_{y_m|x_n}(y_m|x_n \in \mathcal{I}_c)$ are illustrated as circles and the conditioning intervals $\mathcal{I}_c$ are illustrated with vertical dotted lines. The samples that are used to estimate the unconditional CDF $F^{(d)}_{y_m}(y_m)$ are illustrated as diamonds. **(B)** $F_{y_m|x_n}(y_m|x_n \in \mathcal{I}_c)$ are illustrated as black lines, where the leftmost line corresponds to $F_{y_m|x_n}(y_m|x_n \in \mathcal{I}_1)$ with the lowest ΔR^{SP} values and the rightmost line corresponds to $F_{y_m|x_n}(y_m|x_n \in \mathcal{I}_{15})$. The 1,000 $F^{(d)}_{y_m}(y_m)$ lay all within the area illustrated by the red patch. **(C)** Each of the 15 squares correspond to $\underset{d=1,\ldots,D}{\text{median}}\ \text{KS}(F^{(d)}_{y_m}(y_m), F_{y_m|x_n}(y_m|x_n \in \mathcal{I}_c))$.

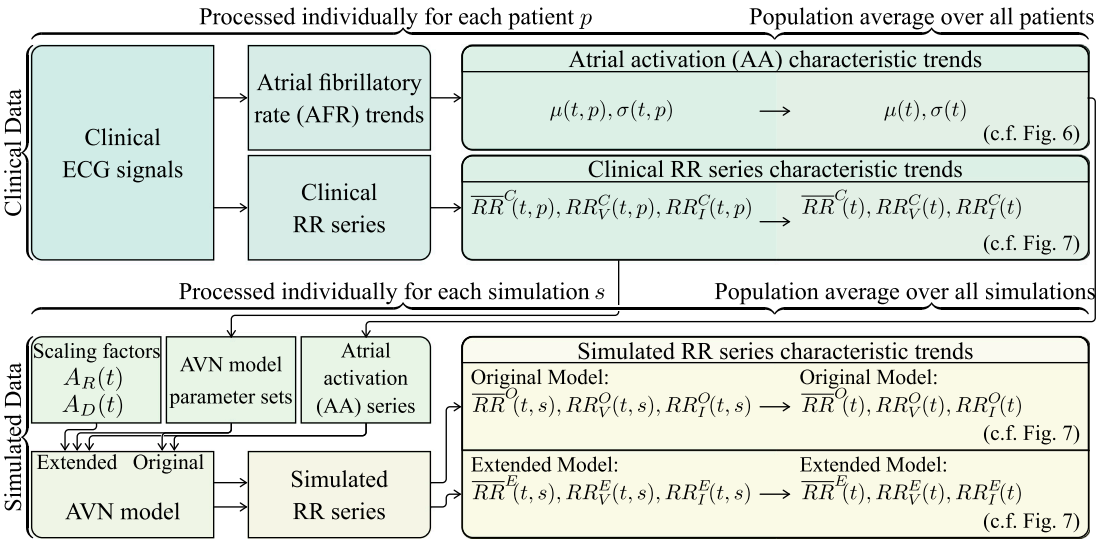

FIGURE 3
Schematic illustrating how the clinical and simulated RR series characteristic trends are computed.

series parameters have an influence on the RR series characteristics. Based on this, the AV node model described in Section 2.3 is extended to account for ANS-induced changes in the AA series by allowing $\mu(t)$ and $\sigma(t)$ of the Pearson Type IV distribution to vary over time. Moreover, the AV node model was extended by two scaling factors A_R and A_D, accounting for the effect of changes in autonomic tone on refractory period (A_R) and on conduction delay (A_D).

$$R^P(\Delta t_k, A_R) = A_R \cdot R^P(\Delta t_k) = A_R\left(R^P_{min} + \Delta R^P\left(1 - e^{-\Delta t_k/\tau^P_R}\right)\right) \tag{10}$$

$$D^P(\Delta t_k, A_D) = A_D \cdot D^P(\Delta t_k) = A_D\left(D^P_{min} + \Delta D^P e^{-\Delta t_k/\tau^P_D}\right) \tag{11}$$

The factors A_R and A_D model the combined effect of changes in sympathetic and parasympathetic activity and do not differ between the SP, FP and CN.

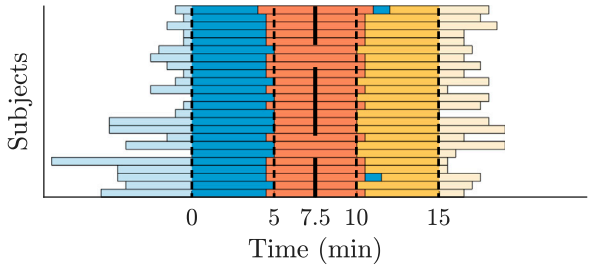

FIGURE 4
Tilt recordings of 24 patients divided into supine (blue), HDT (red) and HUT (yellow). The bars represent the length of the recorded ECG data. All recordings are centered along the middle of the HDT section.

2.6 Tilt-induced changes in extended atrioventricular node model

In this section, the extended AV node model proposed in Section 2.5 is investigated with respect to its ability to mimic tilt-induced changes in RR series characteristics.

The clinical ECG signals (cf. Section 2.1) are used to generate AA series for the AV node model input and to compare the characteristics of the simulated RR series to the clinical RR series (cf. Figure 3). For this purpose, a continuous 15-min ECG signal with 5 minutes per supine, HDT and HUT position was desired for each patient. In the clinical data, however, the length of the three tilt positions varied between patients with the supine position being between 5 and 13 min, HDT being between 5 and 7 min and HUT being between 5 and 9 min. For two patients, there was an additional minute in supine position between the HDT and HUT. The ECG signals were aligned to the middle of the HDT section and a 15-min long segment centered around the same midpoint was chosen for each patient (cf. Figure 4).

The clinical RR series characteristic trends $\overline{RR}^C(t,p)$, $RR_V^C(t,p)$ and $RR_I^C(t,p)$ for each patient p are computed from the RR intervals using a sliding window of length N according to Eqs. 1–3 (cf. Figure 3). For RR_V and RR_I, N is set to 200, because shorter RR interval series might lead to inaccuracies in the sample entropy computation (Yentes et al., 2013). For $\overline{RR}$, N is set to 100, as its computation is more robust than the computation of RR_V and RR_I and shorter RR interval series allow for a better temporal resolution. RR intervals in the clinical RR series preceding and following ectopic beats were excluded. For the computation of RR_I according to Eq. 3, vectors V_i^l with excluded RR intervals were omitted. The RR series characteristic trends of each patient $\overline{RR}^C(t,p)$, $RR_V^C(t,p)$ and $RR_I^C(t,p)$ were averaged over all 24 patients to obtain population-averaged clinical trends $\overline{RR}^C(t)$, $RR_V^C(t)$ and $RR_I^C(t)$ (cf. Figure 3).

TABLE 2 Ranges of the 240 model parameters used for the illustration (mean ± std).

Parameters	SP (ms)	FP (ms)	CN (ms)
$R_{\min}$	339 ± 77	493 ± 82	250 ± 0
ΔR	232 ± 112	369 ± 161	0 ± 0
τ_R	160 ± 77	162 ± 72	1 ± 0
$D_{\min}$	20 ± 7	7 ± 6	0 ± 0
ΔD	39 ± 20	23 ± 16	0 ± 0
τ_D	171 ± 71	163 ± 70	1 ± 0

For the generation of the AA series, first, an atrial fibrillatory rate (AFR) trend is estimated from each 15-min ECG segment (cf. Figure 3). The AFR is estimated by fitting a complex sinusoidal model to the f-waves of the ECG, following spatiotemporal QRST cancellation, as described in Henriksson et al. (2018). From each of the resulting AFR trends, the AA series parameters $\mu(t,p)$ and $\sigma(t,p)$ are estimated by the mean and standard deviation of 1/AFR using 1-min sliding windows; the resolution of the AFR trend is 0.02 s (cf. Figure 3). Then, $\mu(t,p)$ and $\sigma(t,p)$ are averaged over all 24 patients, resulting in the population-averaged trends $\mu(t)$ and $\sigma(t)$ (cf. Figure 3). Finally, the AA series is iteratively generated (cf. Figure 3). The first AA interval is drawn from the Pearson Type IV distribution with $\mu(0)$ and $\sigma(0)$, and each consecutive AA interval is drawn from the distribution with $\mu(t_i)$ and $\sigma(t_i)$ where t_i corresponds to the accumulated time of the previous AA intervals. The γ and κ of the Pearson Type IV distribution were kept fixed to 1 and 6, respectively.

For the simulations using the original and extended model, a set of 240 AV node model parameter vectors $\boldsymbol{x}' = [\boldsymbol{\theta}^{SP}, \boldsymbol{\theta}^{FP}, \boldsymbol{\theta}^{CN}]^\mathsf{T}$ were generated (cf. Figure 3). Ten parameter vectors per patient were selected from a set of randomly drawn parameter sets based on their ability to replicate the RR series characteristics of the 5-min long supine segment of the respective patient. A detailed description of the parameter sets and the selection process can be found in the Supplementary Section 1. The ranges of the model parameters in the 240 parameter sets are given in Table 2.

For the computation of simulated RR series characteristic trends using the original and the extended model, respectively, simulations were performed with each of the 240 parameter sets using 10 different realizations of the AA series generated from $\mu(t)$ and $\sigma(t)$. In the original model, the scaling factors A_R and A_D are not included, which is equivalent to the extended model using $A_R = 1$ and $A_D = 1$ (cf. Figure 3). In the extended model, A_R and A_D were allowed to change between supine and HDT and between HDT and HUT, respectively, but were assumed to remain constant within each position. Hence, for the extended model, A_R and A_D were set to 1 in the supine position, and different combinations of $A_R \in \{0.95, 1, 1.05\}$ and $A_D \in \{0.8, 1,$

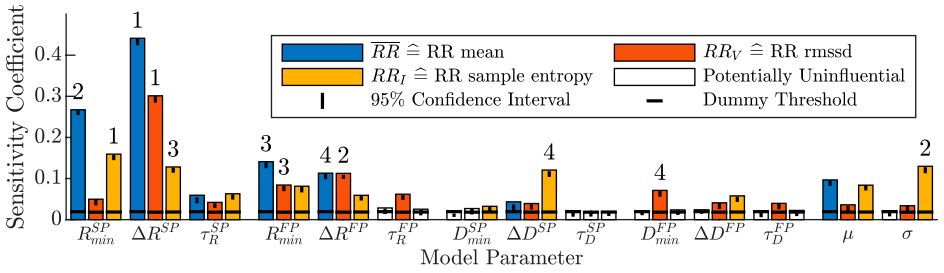

FIGURE 5
Distribution-based sensitivity indices describing the influence of changes in the 14 model parameters to changes in the three RR series characteristics. A model parameter is assumed to have influence on the RR series characteristics if the sensitivity coefficient is above the threshold of the dummy parameter (horizontal black line), otherwise it is not influential and illustrated with a white bar. The black vertical line illustrates the 95% confidence interval of the *t* bootstrapping iterations of the sensitivity coefficient. The ranking of the four most influential model parameters for each RR series characteristic is shown with the numbers above the bars.

1.2} were used for the simulations during HDT and HUT. For each simulation s, the mean RR interval trends $\overline{RR}^O(t,s)$ and $\overline{RR}^E(t,s)$ were computed from the RR interval series using a sliding window of length N = 100 (cf. Eq. 1). Whereas the RR variability and RR irregularity trends $RR^O_V(t,s)$ and $RR^O_I(t,s)$, as well as $RR^E_V(t,s)$ and $RR^E_I(t,s)$ were computed from the RR interval series using a sliding window of length N = 200 (cf. Eqs. 2 and 3). The simulated RR series characteristic trends were averaged over all parameter sets and realizations to obtain the population-averaged simulated trends $\overline{RR}^O(t)$, $RR^O_V(t)$ and $RR^O_I(t)$ for the original model and $\overline{RR}^E(t)$, $RR^E_V(t)$ and $RR^E_I(t)$ for the extended model (cf. Figure 3).

2.7 Statistical analysis

A Wilcoxon signed rank test was applied to determine if AFR, $\overline{RR}$, RR_V and RR_I differed significantly between supine, HDT and HUT. For the analysis, the AFR and RR series characteristics were computed for each patient and tilt position using the 5-min long ECG segments (cf. Figure 4). A p-value < 0.05 was considered significant.

3 Results

3.1 Sensitivity analysis

Results from the distribution-based sensitivity analysis (described in Section 2.4) with respect to the influence of the AV node model parameters on RR series characteristics are shown in Figure 5. Heart rate, quantified by $\overline{RR}$ is predominantly sensitive to changes in the refractory period parameters with the four largest contributors being the $R_{\min}$ and ΔR parameters of both pathways. In contrast, the changes in the conduction delay had little influence on the $\overline{RR}$, with ΔD^{SP} being the only conduction delay parameter that is slightly above the dummy threshold. Changes in the mean of the AA series μ were also influential on the $\overline{RR}$, while changes in the standard deviation σ of the AA series are not considered to have influence to changes in $\overline{RR}$.

For RR_V quantifying RR series variability, nearly all model parameters of the refractory period, conduction delay and AA series had sensitivity coefficients above the dummy threshold. The four largest contributors to changes in the RR_V were the ΔR parameters of both pathways, as well as the minimum refractory period and minimum conduction delay of the fast pathway, $R^{FP}_{\min}$ and $D^{FP}_{\min}$.

The RR_I quantifying RR series irregularity was also influenced by most model parameters of the refractory period, conduction delay and AA series. The four largest contributors were the minimum refractory period of the slow pathway $R^{SP}_{\min}$, the standard deviation σ of the AA series and the maximum prolongation of the refractory period and conduction delay of the slow pathway, ΔR^{SP} and ΔD^{SP}.

TABLE 3 Mean ± std of AFR and RR series characteristics of the 24 patients in the study population for each tilt position.

Tilt Position	Supine	HDT	HUT
AFR mean (Hz)	6.78 ± 0.64	6.62 ± 0.7**	6.84 ± 0.63*,†
$\overline{RR}$ (ms)	656 ± 126	642 ± 111*	613 ± 115**,†
RR_V (ms)	192 ± 54	182 ± 45	176 ± 51**
RR_I	2.09 ± 0.2	2.05 ± 0.28	1.95 ± 0.31**

HDT, head-down tilt; HUT, head-up tilt. *$p < 0.05$ vs Supine. **$p < 0.01$ vs Supine. $^{\dagger}p < 0.05$ vs HDT.

3.2 Clinical data

The AFR decreased significantly from the supine position to HDT and increased significantly from HDT to HUT, where the

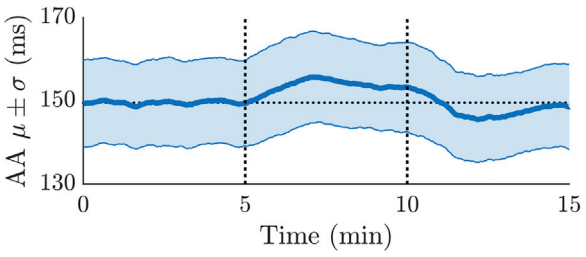

FIGURE 6
Averaged mean and standard deviation of the AA series estimated from ECG recordings of 24 patients. The first 5 min were during supine position, followed by 5 min of HDT and 5 min of HUT. The horizontal dotted line illustrates the average of the μ trend during the first 5 min.

AFR during HUT was significantly higher than during supine (Table 3). The heart rate increased during HDT and increased further during HUT (Table 3). The results align with the observations of Östenson et al. (2017). The variability and irregularity of the RR series decreased during HDT and decreased further during HUT (Table 3). For the variability and irregularity of the RR series, only the differences between supine and HUT were statistically significant.

3.3 Tilt-induced changes in atrioventricular node model

The average of $\mu(t)$ and $\sigma(t)$ over all 24 patients is illustrated in Figure 6. The $\mu(t)$ shows a clear variation during HDT and HUT, but not in supine position, where $\mu(t)$ was approximately constant around 150 ms. Compared to $\mu(t)$ during supine position, $\mu(t)$ increased during HDT and decreased during HUT (cf. Figure 6).

In Figure 7, the characteristics $\overline{RR}^C(t)$, $RR_V^C(t)$ and $RR_I^C(t)$ estimated from clinical data during tilt test are illustrated. It can be seen that $\overline{RR}^C(t)$, $RR_V^C(t)$ and $RR_I^C(t)$ are decreasing from supine to HDT and decreasing further from HDT to HUT. When performing the simulations with the original model, $\overline{RR}^O(t)$, $RR_V^O(t)$ and $RR_I^O(t)$ are decreasing from supine to HDT, but increasing from HDT to HUT. When performing the simulations with the extended model, $\overline{RR}^E(t)$, $RR_V^E(t)$ and $RR_I^E(t)$ are decreasing from supine to HDT and decreasing further from HDT to HUT. Comparing the clinical and simulated trends of $\overline{RR}(t)$ and $RR_V(t)$, it can be seen that the extended model accounting for ANS-induced changes can better replicate the observed changes to the clinical RR series characteristics compared to the original model. For $RR_I(t)$, both the original and extended model produce RR series that are more regular than the clinical RR series, as the irregularity quantified by the sample entropy is higher for the clinical RR series. For the simulated RR series characteristics of the extended model, the average of $\overline{RR}^E(t)$, $RR_V^E(t)$ and $RR_I^E(t)$ during the 5 min in HDT and HUT were illustrated for the nine different combinations of $A_R \in \{0.95, 1, 1.05\}$ and $A_D \in \{0.9, 1, 1.1\}$. For $\overline{RR}^E(t)$, $RR_V^E(t)$ and $RR_I^E(t)$, an increase in A_R causes an increase, and for $\overline{RR}^E(t)$ and $RR_V^E(t)$, an increase in A_D causes an increase. However, for $RR_I^E(t)$, an increase in A_D instead causes a decrease. The $\overline{RR}^E(t)$, $RR_V^E(t)$ and $RR_I^E(t)$ are obtained using $A_R = 1$ and $A_D = 0.9$ during HDT and $A_R = 0.95$ and $A_D = 0.9$ during HUT and are displayed in Figure 7; the scaling factors were chosen so that the resulting $\overline{RR}^E(t)$ and $RR_V^E(t)$ matches $\overline{RR}^C(t)$ and $RR_V^C(t)$.

4 Discussion

The aim of this study was to extend the AV node model (Wallman and Sandberg, 2018) to incorporate ANS-induced changes. The extension of the AV node model was guided by a distribution-based sensitivity analysis. The sensitivity analysis indicated that the refractory period and conduction delay parameters as well as the atrial impulse series had a significant influence on the heart rate as well as the variability and the irregularity of the RR series, while the most influential parameters were predominantly those describing the refractory period. Rather than modelling the effect of the sympathetic and parasympathetic activity separately, we describe the joint effects, i.e., the autonomic tone. We proposed an extension to the AV node model that accounts for the ANS-induced changes by introducing scaling factors for the refractory period and conduction delay. The capability of the extended AV node model to replicate ANS-induced changes was investigated by comparison to ECG data acquired during tilt test.

Our results (Figure 7) indicate that the extended model, but not the original, could replicate the observed changes in the clinical RR series characteristics during HUT and HDT, since the changes in RR series characteristics could not be explained by changes in atrial activity alone. The $\overline{RR}^E(t)$, $RR_V^E(t)$ and $RR_I^E(t)$ (Figure 7) show that a decrease in refractory period and conduction delay allow the model to replicate the decrease in $\overline{RR}^C(t)$, $RR_V^C(t)$ and $RR_I^C(t)$. Conversely, if the refractory period and conduction delay are kept fixed for $\overline{RR}^O(t)$, $RR_V^O(t)$ and $RR_I^O(t)$, all three RR series characteristics increase during HUT, which is the opposite direction of change of $\overline{RR}^C(t)$, $RR_V^C(t)$ and $RR_I^C(t)$. When comparing $RR_I^O(t)$ and $RR_I^E(t)$ with $RR_I^C(t)$, it can be seen that the sample entropy of the simulated RR series is lower than that of the clinical RR series. This highlights that the simulated RR series are more regular than the clinical RR series. One possible explanation for a lower irregularity in simulated RR series is the lack of short-term variations in AV node refractoriness and conduction delay. Such short-term variations may be induced by respiratory modulation in ANS activity. Thus, a natural next step in our model development will be to incorporate the respiratory modulation of the ANS, likely via periodical variations in the scaling factors A_R and A_D.

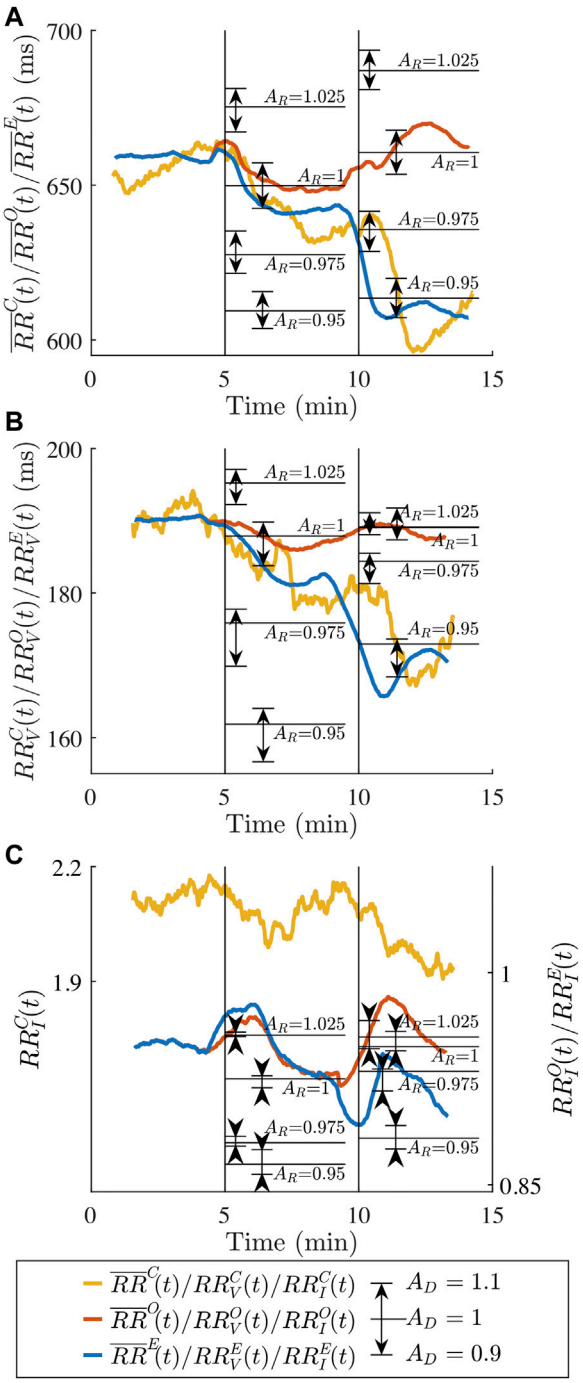

FIGURE 7
Average clinical RR series characteristics **(A)** $\overline{RR}^C(t)$ **(B)** $RR_V^C(t)$ and **(C)** $RR_I^C(t)$ (yellow) and average simulated RR series characteristics for the original model **(A)** $\overline{RR}^O(t)$ **(B)** $RR_V^O(t)$ and **(C)** $RR_I^O(t)$ (red) and average simulated RR series characteristics for the extended model **(A)** $\overline{RR}^E(t)$ **(B)** $RR_V^E(t)$ and **(C)** $RR_I^E(t)$ (blue). The dashed black lines mark the transition between the supine and HDT, and HDT and HUT, respectively. Horizontal black lines show 5-min averages of $\overline{RR}^E(t)$, $RR_V^E(t)$ and $RR_I^E(t)$ during HDT or HUT with A_R as indicated and A_D = 1. Arrows show the impact of perturbing A_D by +0.1 (arrow pointing up) or −0.1 (arrow pointing down).

Many electrophysiological (EP) studies have demonstrated that an increase in sympathetic activity is causing a decrease in the human AV nodal conduction delay (Lister et al., 1965; Dhingra et al., 1973; Morady et al., 1988; Cossú et al., 1997) and a decrease in the refractory period (Morady et al., 1988; Cossú et al., 1997). Moreover, a decrease in sympathetic activity in the human AV node is causing an increase in conduction delay and refractory period (Morady et al., 1988). Head-up tilt is associated with increased sympathetic tone, and it has been demonstrated that the AV nodal conduction delay and refractory period decrease when changing the posture from supine to standing (Hashimoto et al., 1991). The results in Figure 7 confirm that a reduction in the conduction delay using A_D = 0.9 and a reduction in the refractory period using A_R = 0.95 better replicate the observed changes in the clinical RR series characteristics than the original model during HUT. Decreases in refractory period and conduction delay of up to 30% in response to isoproterenol-induced increases in sympathetic activity have been reported (Lister et al., 1965; Dhingra et al., 1973; Cossú et al., 1997). However, when considering that the reported changes in heart rate due to the isoproterenol administration is larger than the observed changes in $\overline{RR}$ during tilt, the parameter choice of A_D = 0.9 and A_R = 0.95 are reasonable for the tilt test data used in this study.

Increased parasympathetic activity has been associated with an increased conduction delay (Martin, 1977); studies in dogs reported an increased conduction delay with acetylcholine administration (Priola et al., 1983; Bertrix et al., 1984) and vagal stimulation (Spear and Moore, 1973; Martin, 1975; Pirola and Potter, 1990). Moreover, there are indications that an increased parasympathetic activity is associated with an increased refractory period (Martin, 1977); experimental studies using rabbit hearts reported an increased AV-nodal refractory period (West and Toda, 1967) and occurrences of 2:1 AV nodal block (Cranefield et al., 1959) with acetylcholine administration, and studies in dogs reported occurrences of AV block with acetylcholine administration (Hageman et al., 1985) and vagal stimulation (Spear and Moore, 1973; Hageman et al., 1985).

It is unclear how the HDT affects the sympathetic and parasympathetic activity. The results in Figure 7 show that a reduction in the conduction delay using A_D = 0.9 and no modification of the refractory period using A_R = 1 better replicate the observed changes in the clinical RR series characteristics than the original model during HDT. These results are consistent with possible slight increase in sympathetic tone provoked by HDT. However, other interpretations are possible. Nagaya et al. (1995) postulated a diminished sympathetic activity in HDT. Under that hypothesis, the results in Figure 7 suggest a decrease in parasympathetic tone to revert the direction of change caused by a decreased sympathetic tone. It should be noted that the model presented here does not distinguish between these two possibilities, since

A_D and A_R are modelling the joint effect of changes in parasympathetic and sympathetic activity. Hence, the scale factor A_D = 0.9 during HDT could be reflecting either a slight increase in sympathetic activity, a slight decrease in parasympathetic activity, a larger increase in sympathetic activity combined with an increase in parasympathetic activity, or a large decrease in parasympathetic activity combined with a decrease in sympathetic activity.

The set of scaling factors A_R and A_D used to create $\overline{RR}^E(t)$, $RR_V^E(t)$ and $RR_I^E(t)$ in Figure 7 results in RR series characteristics similar to that observed during HDT and HUT. The results in Figure 7 show that a scaling factor A_R below 1, i.e., a decrease of the refractory period, causes a decrease in $\overline{RR}^E(t)$, $RR_V^E(t)$ and $RR_I^E(t)$. Conversely, a scaling factor A_R above 1, i.e., an increase of the refractory period, causes an increase in $\overline{RR}^E(t)$, $RR_V^E(t)$ and $RR_I^E(t)$. A scaling factor A_D below 1, i.e., a decrease in conduction delay, causes a decrease in $\overline{RR}^E(t)$, $RR_V^E(t)$ and vice versa. The opposite relationship can be seen for the RR series irregularity, where a scaling factor A_D below 1 causes an increase in $RR_I^E(t)$ and vice versa. Moreover, when considering one RR series characteristic at a time, it can be anticipated in Figure 7 that the same 5-min average value of the RR series characteristics can be achieved with different combinations of A_R and A_D. Hence, considering all three RR series characteristics simultaneously increases the likelihood of identifying a unique pair of scaling factors A_R and A_D that fits the observed data.

To reduce the complexity of the model, the refractoriness and conduction delay of the SP, FP and CN are modified with the same A_R and A_D. However, due to the structural and molecular heterogeneity of the different pathways, it is likely that the ANS-induced changes affect each pathway differently (George et al., 2017). In rabbit hearts, it was reported that acetylcholine strongly affects fibers of the atrionodal junction but does not show any effect in the lower part of the node or the bundle of His (Trautwein, 1963). In the description of the AV node model, the CN is merging the impulses from the SP and FP and its refractory period and conduction delay is independent of Δt_k. In contrast to Karlsson et al. (2021), $R_{\min}^{CN}$ was set to the minimum of the bounded uniform distributions for the $R_{\min}^{SP}$ and the $R_{\min}^{FP}$ given in Table 1. Further, the conduction delay of the CN was set to 0, as other choices of a constant conduction delay would not have changed the resulting RR series. In previous work on the network model (Wallman and Sandberg, 2018; Karlsson et al., 2021), the AA interval series was modelled as a Poisson process. However, based on results of Climent et al. (2011a), a Pearson Type IV distribution better reproduces the statistical properties of the AA interval series during AF and was therefore chosen in the present study. The mean and standard deviation of the Pearson Type IV distribution were determined from the mean and standard deviation of the AFR. However, the skewness and kurtosis were fixed, as their sensitivity coefficients were uninfluential (data not shown) and since there is no straight-forward way to estimate these parameters from the f-waves of the ECG.

In the present study, the ability of the extended model to mimic tilt-induced changes was investigated using data from a previous study (Östenson et al., 2017), with tilt angles fixed to -30° in HDT and 60° in HUT, respectively. Different tilt angles of the tilt, i.e., different magnitude of the orthostatic stimulus, may affect the ANS response and hence the resulting RR series characteristics. Previous results from patients in normal sinus rhythm show that the sample entropy of the RR series was decreasing during HUT from 0° to 60° but remained roughly constant from 60° to 90° (Porta et al., 2007). Based on these results, we assume that the tilt angle of 60° is sufficiently large to induce changes in autonomic tone. Access to data from patients with AF during other tilt-inclinations could potentially be used to refine the model to take the degree on inclination into account. The tilt-induced changes in RR series irregularity observed in the present study are in line with the results in Patel et al. (2018), where a decrease in RR sample entropy in response to HUT in patients with AF was reported. The tilt-induced changes in RR series irregularity observed in the present study are also in line with the changes reported for patients in normal sinus rhythm during HUT (Porta et al., 2007). Results from previous studies suggest that the RR series irregularity during normal sinus rhythm increase in response to HDT (Porta et al., 2015), whereas a slight but not significant decrease was observed in the present study with patients in AF. However, it should be noted that origin of RR series variability and irregularity during AF differs from that during normal sinus rhythm and hence, the interpretation of the results with respect to autonomic tone may be different.

The effect of the ANS-induced activity was investigated with respect to its ability to mimic the population-averaged changes observed during tilt test. The RMSSD and sample entropy were used to quantify RR series variability and irregularity, respectively, since these statistical measures have been used in previous studies to assess changes in RR series characteristics during AF in response to drugs (Corino et al., 2015) and tilt-test (Patel et al., 2018). Population-averaged trends were chosen over the trends of individual patients to reduce the uncertainty in the estimation of the clinical RR_V and RR_I trends. The parameter sets used for the simulations in Section 2.6 were selected to be representative of the patients in the present study based on their ability to replicate RR series characteristics observed during supine position. However, it should be noted that fitting of the model to individual patients is outside the scope of the present study. Due to the short measurement duration of the clinical data, a robust estimation of individual model parameters is not to be expected with the present methodology (Karlsson et al., 2021). Longer measurements from more patients will allow model development and evaluation on a patient-specific basis, forming an attractive next step.

A distribution-based sensitivity analysis was chosen over a variance-based method, because the distributions of the

simulated RR series characteristics are highly-skewed and multi-modal. Hence, variance alone cannot adequately represent the uncertainty (Pianosi and Wagener, 2018). Instead, a distribution-based method characterizes the uncertainty and sensitivity by investigating the entire distribution of the model outputs (Pianosi and Wagener, 2018). The results of the sensitivity analysis in Figure 5 indicate that τ_D^{SP} is the only model parameter that is uninfluential, since the sensitivity coefficients for all three RR series characteristics are below the dummy threshold. One important outcome of the sensitivity analysis therefore is that the refractory period and conduction delay of the AV node as well as the atrial input are influencing the RR series characteristics. For simplicity, we are proposing a linear scaling of refractory period and conduction delay parameters, but it would be interesting to refine this model description in the light of additional clinical data. It should be noted that the sensitivity coefficients $\mathcal{S}_{n,m}$ are quantifying sensitivity on a global scale, and that there may be large local variations. As a result, the extent of variation in $\overline{RR}(t)$, $RR_V(t)$ and $RR_I(t)$ for a set of scaling factors A_R and A_D depend on the model parameters. For example, in Figure 7, it is clear that the scaling factor A_D affects $\overline{RR}(t)$, while the sensitivity analysis (Figure 5) indicates that the influence of changes in conduction delay on $\overline{RR}(t)$ is very limited on a global scale.

In the present study, the estimates in $RR_V^E(t)$ and $RR_I^E(t)$ were based on sliding windows of $N = 200$ RR intervals. The choice of N is a tradeoff between estimation accuracy and time resolution. The sample entropy estimation is expected to stabilize with greater N and a minimum of $N \geq 200$ was recommended by Yentes et al. (2013). In the present study, N was chosen as short as possible in favour of time resolution to investigate the ANS-induced changes in the RR series characteristics during tilt. To accommodate the estimation uncertainty resulting from a small N, the simulated RR series characteristics trends were averaged over 10 repeated simulations for 240 different parameter sets. For the sensitivity analysis, N was chosen to be 4,000 in favour of estimation accuracy since the simulation was stationary.

While ANS modulation has been extensively studied during normal sinus rhythm (Porta et al., 2007; Porta et al., 2015; Sassi et al., 2015; Patel et al., 2018), no attempts have been made towards the estimation of ANS modulation during persistent AF. The present study is a first step towards developing a model of the AV node that will ultimately be used to quantify ANS modulation on a patient specific basis by fitting to RR interval series and information on atrial electrical activity obtained from clinical ECG recordings. The results (Figure 7) show that the proposed extended model of the AV node accounting for changes in autonomic tone can better replicate changes in RR series characteristics observed during tilt-test than the original model, implying that this is a viable approach to take. Further developments are needed to incorporate ANS modulation in the model and methodology for robust estimation of such modulation from clinical data.

5 Conclusion

We present an extended AV node model that incorporates ANS-induced changes. The extension was guided by a distribution-based sensitivity analysis showing that changes in refractoriness and conduction delay of the AV node as well as changes in atrial activity significantly influence the RR series characteristics. We demonstrate that the model extension is needed to replicate the changes in heart rate and RR series variability and irregularity observed during head-up and head-down tilt.

Data availability statement

The data analyzed in this study is subject to the following licenses/restrictions: The data is owned by the Department of Cardiology, Clinical Sciences, Lund University, Sweden. Requests to access these datasets should be directed to pyotr.platonov@med.lu.se. The code for the extended model together with a user example can be found in the Supplementary Material.

Ethics statement

The studies involving human participants were reviewed and approved by Regionala Etikprövningsnämnden i Lund. The patients/participants provided their written informed consent to participate in this study.

Author contributions

FP, MW, PP, and FS contributed to conception and design of the study. SÖ was responsible for the tilt test experiment. MA and FS were responsible for ECG processing. FP performed the distribution-based sensitivity analysis, designed and evaluated the extended AV node model, wrote the original draft of the manuscript and produced the figures, with supervision from MW and FS. MW, PP and FS contributed to the funding acquisition. PP and SÖ contributed to the clinical interpretation of the results. All authors contributed to manuscript revision, read, and approved the submitted version.

Funding

The research was supported by the Swedish Research Council (grant VR 2019–04272) and the Crafoord Foundation (grant 20200605).

Conflict of interest

The authors declare that the research was conducted in the absence of any commercial or financial relationships that could be construed as a potential conflict of interest.

Publisher's note

All claims expressed in this article are solely those of the authors and do not necessarily represent those of their affiliated organizations, or those of the publisher, the editors and the reviewers. Any product that may be evaluated in this article, or claim that may be made by its manufacturer, is not guaranteed or endorsed by the publisher.

Supplementary material

The Supplementary Material for this article can be found online at: https://www.frontiersin.org/articles/10.3389/fphys.2022.976468/full#supplementary-material

References

Bertrix, L., Bouzouita, K., Lang, J., Lakhal, M., Chah, Q. T., and Faucon, G. (1984). Potentiation by hypokalemia of the effects of acetylcholine on the canine heart *in situ*. *Naunyn. Schmiedeb. Arch. Pharmacol.* 326, 169–174. doi:10.1007/BF00517315

Billette, J., and Tadros, R. (2019). An integrated overview of av node physiology. *Pacing Clin. Electrophysiol.* 42, 805–820. doi:10.1111/pace.13734

Climent, A. M., Atienza, F., Millet, J., and Guillem, M. S. (2011a). Generation of realistic atrial to atrial interval series during atrial fibrillation. *Med. Biol. Eng. Comput.* 49, 1261–1268. doi:10.1007/s11517-011-0823-2

Climent, A. M., Guillem, M. S., Zhang, Y., Millet, J., and Mazgalev, T. N. (2011b). Functional mathematical model of dual pathway av nodal conduction. *Am. J. Physiol. Heart Circ. Physiol.* 300, 1393–1401. doi:10.1152/ajpheart.01175.2010

Cohen, R. J., Berger, R. D., and Dushane, T. E. (1983). A quantitative model for the ventricular response during atrial fibrillation. *IEEE Trans. Biomed. Eng.* 30, 769–781. doi:10.1109/TBME.1983.325077

Corino, V. D., Sandberg, F., Mainardi, L. T., and Sörnmo, L. (2011). An atrioventricular node model for analysis of the ventricular response during atrial fibrillation. *IEEE Trans. Biomed. Eng.* 58, 3386–3395. doi:10.1109/TBME.2011.2166262

Corino, V. D., Ulimoen, S. R., Enger, S., Mainardi, L. T., Tveit, A., and Platonov, P. G. (2015). Rate-control drugs affect variability and irregularity measures of RR intervals in patients with permanent atrial fibrillation. *J. Cardiovasc. Electrophysiol.* 26, 137–141. doi:10.1111/jce.12580

Cossú, S. F., Rothman, S. A., Chmielewski, I. L., Hsia, H. H., Vogel, R. L., Miller, J. M., et al. (1997). The effects of isoproterenol on the cardiac conduction system: Site-specific dose dependence. *J. Cardiovasc. Electrophysiol.* 8, 847–853. doi:10.1111/j.1540-8167.1997.tb00845.x

Cranefield, P. F., Hoffman, B. F., and Paes de Carvalho, A. (1959). Effects of acetylcholine on single fibers of the atrioventricular node. *Circ. Res.* 7, 19–23. doi:10.1161/01.RES.7.1.19

Denes, P., Wu, D., Dhingra, R., Pietras, R. J., and Rosen, K. M. (1974). The effects of cycle length on cardiac refractory periods in man. *Circulation* 49, 32–41. doi:10.1161/01.CIR.49.1.32

Dhingra, R. C., Winslow, E., Pouget, J. M., Rahimtoola, S. H., and Rosen, K. M. (1973). The effect of isoproterenol on atrioventricular and intraventricular conduction. *Am. J. Cardiol.* 32, 629–636. doi:10.1016/S0002-9149(73)80055-4

George, S. A., Faye, N. R., Murillo-Berlioz, A., Lee, K. B., Trachiotis, G. D., and Efimov, I. R. (2017). At the atrioventricular crossroads: Dual pathway electrophysiology in the atrioventricular node and its underlying heterogeneities. *Arrhythm. Electrophysiol. Rev.* 6, 179–185. doi:10.15420/aer.2017.30.1

Hageman, G. R., Neely, B. H., Urthaler, F., and James, T. N. (1985). Negative chronotropic and parasympatholytic effects of alinidine on canine sinus node and AV junction. *Am. J. Physiol.* 248, 324–330. doi:10.1152/ajpheart.1985.248.3.H324

Hashimoto, T., Fukatani, M., Mori, M., and Hashiba, K. (1991). Effects of standing on the induction of paroxysmal supraventricular tachycardia. *J. Am. Coll. Cardiol.* 17, 690–695. doi:10.1016/S0735-1097(10)80185-8

Henriksson, M., Corino, V. D., Sörnmo, L., and Sandberg, F. (2016). A statistical atrioventricular node model accounting for pathway switching during atrial fibrillation. *IEEE Trans. Biomed. Eng.* 63, 1842–1849. doi:10.1109/TBME.2015.2503562

Henriksson, M., Marozas, V., Sandberg, F., and Sörnmo, L. (2018). PetrnasModel-based assessment of f-wave signal quality in patients with atrial fibrillation. *IEEE Trans. Biomed. Eng.* 65, 2600–2611. doi:10.1109/TBME.2018.2810508

Hindricks, G., Potpara, T., Dagres, N., Arbelo, E., Bax, J. J., Blomström-Lundqvist, C., et al. (2020). 2020 ESC Guidelines for the diagnosis and management of atrial fibrillation developed in collaboration with the European Association for Cardio-Thoracic Surgery (EACTS): The Task Force for the diagnosis and management of atrial fibrillation of the European Society of Cardiology (ESC) Developed with the special contribution of the European Heart Rhythm Association (EHRA) of the ESC. *Eur. Heart J.* 42, 373–498. doi:10.1093/eurheartj/ehaa612

Inada, S., Shibata, N., Iwata, M., Haraguchi, R., Ashihara, T., Ikeda, T., et al. (2017). Simulation of ventricular rate control during atrial fibrillation using ionic channel blockers. *J. Arrhythm.* 33, 302–309. doi:10.1016/j.joa.2016.12.002

Jørgensen, P., Schäfer, C., Guerra, P. G., Talajic, M., Nattel, S., and Glass, L. (2002). A mathematical model of human atrioventricular nodal function incorporating concealed conduction. *Bull. Math. Biol.* 64, 1083–1099. doi:10.1006/bulm.2002.0313

Karlsson, M., Sandberg, F., Ulimoen, S. R., and Wallman, M. (2021). Non-invasive characterization of human AV-nodal conduction delay and refractory period during atrial fibrillation. *Front. Physiol.* 12, 728955. doi:10.3389/fphys.2021.728955

Lian, J., Müssig, D., and Lang, V. (2006). Computer modeling of ventricular rhythm during atrial fibrillation and ventricular pacing. *IEEE Trans. Biomed. Eng.* 53, 1512–1520. doi:10.1109/TBME.2006.876627

Lister, J. W., Stein, E., Kosowsky, B. D., Lau, S. H., and Damato, A. N. (1965). Atrioventricular conduction in man: Effect of rate, exercise, isoproterenol and atropine on the p-r interval. *Am. J. Cardiol.* 16, 516–523. doi:10.1016/0002-9149(65)90028-7

Lombardi, F., Tarricone, D., Tundo, F., Colombo, F., Belletti, S., and Fiorentini, C. (2004). Autonomic nervous system and paroxysmal atrial fibrillation: A study based on the analysis of RR interval changes before, during and after paroxysmal atrial fibrillation. *Eur. Heart J.* 25, 1242–1248. doi:10.1016/j.ehj.2004.05.016

Mangin, L., Vinet, A., Pagé, P., and Glass, L. (2005). Effects of antiarrhythmic drug therapy on atrioventricular nodal function during atrial fibrillation in humans. *Europace* 7, S71–S82. doi:10.1016/j.eupc.2005.03.016

Martin, P. (1975). Dynamic vagal control of atrial-ventricular condition: Theoretical and experimental studies. *Ann. Biomed. Eng.* 3, 275–295. doi:10.1007/BF02390973

Martin, P. (1977). The influence of the parasympathetic nervous system on atrioventricular conduction. *Circ. Res.* 41, 593–599. doi:10.1161/01.RES.41.5.593

Morady, F., Nelson, S. D., Kou, W. H., Pratley, R., Schmaltz, S., De Buitleir, M., et al. (1988). Electrophysiologic effects of epinephrine in humans. *J. Am. Coll. Cardiol.* 11, 1235–1244. doi:10.1016/0735-1097(88)90287-2

Nagaya, K., Wada, F., Nakamitsu, S., Sagawa, S., and Shiraki, K. (1995). Responses of the circulatory system and muscle sympathetic nerve activity to head-down tilt in humans. *Am. J. Physiol.* 268, R1289–R1294. doi:10.1152/ajpregu.1995.268.5.R1289

Östenson, S., Corino, V. D., Carlsson, J., and Platonov, P. G. (2017). Autonomic influence on atrial fibrillatory process: Head-up and head-down tilting. *Ann. Noninvasive Electrocardiol.* 22, e12405. doi:10.1111/anec.12405

Patel, H. C., Hayward, C., Wardle, A. J., Middleton, L., Lyon, A. R., Di Mario, C., et al. (2018). The effect of head-up tilt upon markers of heart rate variability in patients with atrial fibrillation. *Ann. Noninvasive Electrocardiol.* 23, e12511. doi:10.1111/anec.12511

Pianosi, F., and Wagener, T. (2018). Distribution-based sensitivity analysis from a generic input-output sample. *Environ. Model. Softw.* 108, 197–207. doi:10.1016/j.envsoft.2018.07.019

Pirola, F. T., and Potter, E. K. (1990). Vagal action on atrioventricular conduction and its inhibition by sympathetic stimulation and neuropeptide y in anaesthetised dogs. *J. Auton. Nerv. Syst.* 31, 1–12. doi:10.1016/0165-1838(90)90166-g

Porta, A., Gnecchi-Ruscone, T., Tobaldini, E., Guzzetti, S., Furlan, R., and Montano, N. (2007). Progressive decrease of heart period variability entropy-based complexity during graded head-up tilt. *J. Appl. Physiol.* 103, 1143–1149. doi:10.1152/japplphysiol.00293.2007

Porta, A., Faes, L., Marchi, A., Bari, V., De Maria, B., Guzzetti, S., et al. (2015). Disentangling cardiovascular control mechanisms during head-down tilt via joint transfer entropy and self-entropy decompositions. *Front. Physiol.* 6, 301. doi:10.3389/fphys.2015.00301

Priola, D. V., Curtis, M. B., Anagnostelis, C., and Martinez, E. (1983). Altered nicotinic sensitivity of AV node in surgically denervated canine hearts. *Am. J. Physiol.* 245, 27–32. doi:10.1152/ajpheart.1983.245.1.H27

Rashidi, A., and Khodarahmi, I. (2005). Nonlinear modeling of the atrioventricular node physiology in atrial fibrillation. *J. Theor. Biol.* 232, 545–549. doi:10.1016/j.jtbi.2004.08.033

Richman, J. S., and Moorman, J. R. (2000). Physiological time-series analysis using approximate entropy and sample entropy. *Am. J. Physiol. Heart Circ. Physiol.* 278, 2039–2049. doi:10.1152/ajpheart.2000.278.6.H2039

Sassi, R., Cerutti, S., Lombardi, F., Malik, M., Huikuri, H. V., Peng, C.-K., et al. (2015). Advances in heart rate variability signal analysis: Joint position statement by the e-cardiology ESC working group and the European heart rhythm association co-endorsed by the asia pacific heart rhythm society. *Europace* 17, 1341–1353. doi:10.1093/europace/euv015

Shen, M. J., and Zipes, D. P. (2014). Role of the autonomic nervous system in modulating cardiac arrhythmias. *Circ. Res.* 114, 1004–1021. doi:10.1161/CIRCRESAHA.113.302549

Spear, J. F., and Moore, E. N. (1973). Influence of brief vagal and stellate nerve stimulation on pacemaker activity and conduction within the atrioventricular conduction system of the dog. *Circ. Res.* 32, 27–41. doi:10.1161/01.RES.32.1.27

Trautwein, W. (1963). Generation and conduction of impulses in the heart as affected by drugs. *Pharmacol. Rev.* 15, 277–332.

Wallman, M., and Sandberg, F. (2018). Characterisation of human AV-nodal properties using a network model. *Med. Biol. Eng. Comput.* 56, 247–259. doi:10.1007/s11517-017-1684-0

West, T. C., and Toda, N. (1967). Response of the A-V node of the rabbit to stimulation of intracardiac cholinergic nerves. *Circ. Res.* 20, 18–31. doi:10.1161/01.res.20.1.18

Yentes, J. M., Hunt, N., Schmid, K. K., Kaipust, J. P., McGrath, D., and Stergiou, N. (2013). The appropriate use of approximate entropy and sample entropy with short data sets. *Ann. Biomed. Eng.* 41, 349–365. doi:10.1007/s10439-012-0668-3

frontiers | Frontiers in Physiology

TYPE Original Research
PUBLISHED 19 September 2022
DOI 10.3389/fphys.2022.976925

OPEN ACCESS

EDITED BY
Ruben Coronel,
University of Amsterdam, Netherlands

REVIEWED BY
Andrius Petrėnas,
Kaunas University of Technology, Lithuania
Marianna Meo,
EPD Solutions, a Philips company, Netherlands

*CORRESPONDENCE
Mostafa Abdollahpur,
mostafa.abdollahpur@bme.lth.se

SPECIALTY SECTION
This article was submitted to Cardiac Electrophysiology, a section of the journal Frontiers in Physiology

RECEIVED 01 July 2022
ACCEPTED 23 August 2022
PUBLISHED 19 September 2022

CITATION
Abdollahpur M, Engström G, Platonov PG and Sandberg F (2022), A subspace projection approach to quantify respiratory variations in the f-wave frequency trend.
Front. Physiol. 13:976925.
doi: 10.3389/fphys.2022.976925

A subspace projection approach to quantify respiratory variations in the f-wave frequency trend

Mostafa Abdollahpur[1]*, Gunnar Engström[2], Pyotr G. Platonov[3] and Frida Sandberg[1]

[1]Department of Biomedical Engineering, Lund University, Lund, Sweden, [2]Department of Clinical Sciences, Cardiovascular Research—Epidemiology, Malmö, Sweden, [3]Department of Cardiology, Clinical Sciences, Lund University, Lund, Sweden

Background: The autonomic nervous system (ANS) is known as a potent modulator of the initiation and perpetuation of atrial fibrillation (AF), hence information about ANS activity during AF may improve treatment strategy. Respiratory induced ANS variation in the f-waves of the ECG may provide such information.

Objective: This paper proposes a novel approach for improved estimation of such respiratory induced variations and investigates the impact of deep breathing on the f-wave frequency in AF patients.

Methods: A harmonic model is fitted to the f-wave signal to estimate a high-resolution f-wave frequency trend, and an orthogonal subspace projection approach is employed to quantify variations in the frequency trend that are linearly related to respiration using an ECG-derived respiration signal. The performance of the proposed approach is evaluated and compared to that of a previously proposed bandpass filtering approach using simulated f-wave signals. Further, the proposed approach is applied to analyze ECG data recorded for 5 min during baseline and 1 min deep breathing from 28 AF patients from the Swedish cardiopulmonary bioimage study (SCAPIS).

Results: The simulation results show that the estimates of respiratory variations obtained using the proposed approach are more accurate than estimates obtained using the previous approach. Results from the analysis of SCAPIS data show no significant differences between baseline and deep breathing in heart rate (75.5 $\pm$ 22.9 vs. 74 $\pm$ 22.3) bpm, atrial fibrillation rate (6.93 $\pm$ 1.18 vs. 6.94 $\pm$ 0.66) Hz and respiratory f-wave frequency variations (0.130 $\pm$ 0.042 vs. 0.130 $\pm$ 0.034) Hz. However, individual variations are large with changes in heart rate and atrial fibrillatory rate in response to deep breathing ranging from −9% to +5% and −8% to +6%, respectively and there is a weak correlation between changes in heart rate and changes in atrial fibrillatory rate (r = 0.38, p < 0.03).

Conclusion: Respiratory induced f-wave frequency variations were observed at baseline and during deep breathing. No significant changes in the magnitude of these variations in response to deep breathing was observed in the present study population.

10.3389/fphys.2022.976925

KEYWORDS

atrial fibrillation, autonomic nervous system, respiratory variation, f-wave frequency, ECG processing

1 Introduction

Atrial fibrillation is known as the most common heart arrhythmia and is a growing public health concern worldwide. Atrial fibrillation has been estimated to affect 10 million people in the United States by 2050 (Miyasaka et al., 2006) and 17.9 million in Europe by 2060, with more than half of these patients aged 80 years or older (Krijthe et al., 2013). Atrial fibrillation is associated with increased mortality and morbidity resulting from stroke and congestive heart failure, and increased hospitalization costs (Patel et al., 2014). Despite progression in AF treatment, including medications aimed at controlling heart rate, rhythm, or both, and ablative therapy, finding the most accurate therapy for an individual patient is still problematic (Crandall et al., 2009). Historically, research has shown that multiple etiological mechanisms, such as atrial fibrosis, ion-channel dysfunction, autonomic imbalance, and genetic background, likely drive the factors associated with the maintenance and progression of AF (Lip et al., 2010; Fabritz et al., 2016).

This study focuses on respiratory modulation in the atrial activity during AF. It is well established from a variety of studies that the refractory period of the atria during atrial fibrillation can be influenced by various underlying mechanisms, including pathological changes, electrophysiological dynamics, and an imbalanced autonomic tone (Waldo, 2003; Nitta et al., 2004; Saksena et al., 2005). The refractory period of the atria has been found to have linear correlation with f-waves frequency (Capucci et al., 1995). The frequency of the f-waves in the ECG, also referred to as the atrial fibrillatory rate (AFR) (Platonov et al., 2014), has previously been analyzed with respect to ANS induded changes during AF. For instance (Stridh et al., 2003; Holmqvist et al., 2005), have shown that variation in the f-wave frequency during controlled respiration can be linked to the parasympathetic activity. Östenson et al. studied changes in the f-wave frequency in response to changes in ANS tone induced by tilt-test in 40 patients with persistent AF, results showed f-wave frequency decreased during head-down tilt (HDT) compared to baseline and increased during head-up tilt (HUT) (Östenson et al., 2017). In a previous study, we investigated changes in f-wave frequency variations in response to controlled respiration (Abdollahpur et al., 2021). In a study population of eight pacemaker patients with permanent AF recorded at baseline, during controlled respiration, and during controlled respiration after injection of atropine. Briefly, a high-resolution f-wave frequency trend obtained using model-based approach was filtered using a narrow bandpass filter with center frequency corresponding to respiration rate and fixed bandwidth. The envelope of the filtered frequency trend served as an estimate of the magnitude of the respiratory variation; the results indicated that this magnitude was affected by parasympathetic regulation (Abdollahpur et al., 2021).

The present study addresses main weaknesses of our previous study. In contrast to the previous study, where the AF patients had pacemakers set at a fixed heart rate, the present study is based on AF patients without pacemaker whose heart rate varies over time. Such variations in heart rate may affect the ANS and hence the ANS induced variations in atrial electrical activity. Second, the previous approach to quantify respiratory variation in the f-wave frequency is sensitive to noise and cannot handle time-varying respiration rates. Hence, the objectives of the present study were twofold: 1) To propose a novel subspace projection approach to quantify respiratory variation in the f-wave frequency trend that is robust to noise and can handle time-varying respiration, and 2) to investigate the impacts of deep breathing on the f-wave frequency in a population of AF patients without a pacemaker.

2 Materials and methods

A schematic overview of the methodology is shown in Figure 1. The clinical data is described in Section 2.1, the ECG processing aiming to obtain an f-wave signal $x(n)$ is explained in Section 2.2. As follow, a model-based approach is applied to the extracted signal $x(n)$ to estimate an f-wave frequency trend $f(n)$ (Section 2.3). An ECG-derived respiration signal $r(n)$ is estimated using the slope range approach (Section 2.4). Respiratory variation in $f(n)$ is estimated using orthogonal subspace projection method (Section 2.5). Simulated f-wave signals are used to evaluate the performance of the proposed methodology (Section 2.6). Finally, statistical tests are applied to the results from analysis of clinical data to determine if there is a significant differences in heart rate, f-wave frequency, and respiratory variation in f-wave frequency trend between deep breathing phase and baseline (Section 2.7).

2.1 ECG data

The study population consists of a subset of 28 participants from the Swedish cardiopulmonary bioimage study (SCAPIS) (Bergström et al., 2015) that were diagnosed with AF. The clinical characteristics of the study population are summarized in Table 1. The subjects performed a deep breathing task. The task was 5-s inhalation and 5-s exhalation as deep-breathing (D) phase for 1 min, and as follows 5 min during baseline (B); the patients were in AF during the recordings. For further details on the study protocol, the reader is referred to (Engström et al.,

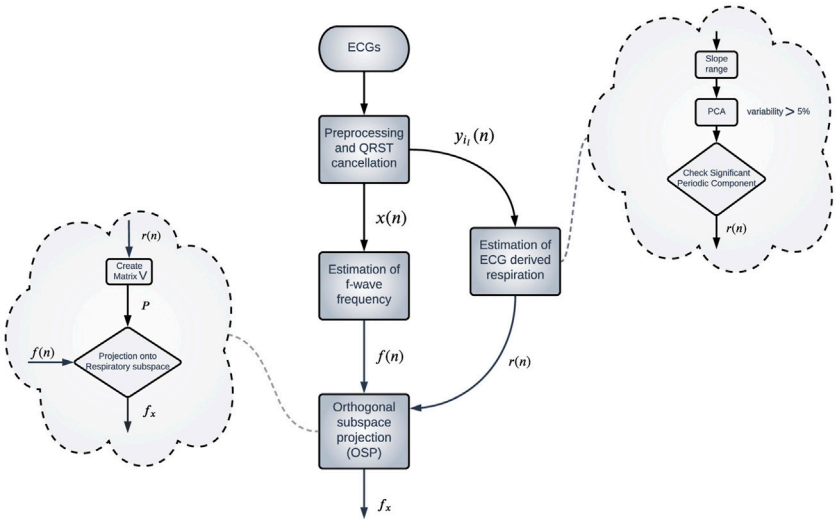

FIGURE 1
Schematic representation of the methodology.

TABLE 1 Clinical characteristics of patients.

	Number
Age (*mean* ± SD, range)	60.1 ± 4.0 [50.1–64.9]
Men (%)	23 (82)
BMI (*mean* ± SD, range)	31.8 ± 7.2 [18.8–50.8]
Systolic BP	124 ± 23 [90–188]
Diastolic BP	79.9 ± 11 [61–104]
Hypertension*(%)	17 (61)
Diabetes (%)	2 (7)
Never smokers (%)	9 (32)
Heart failure (%)	2 (7)
Previous AMI or angina (%)	2 (7)
Treatment	
Beta blocker (%)	15 (54)
Ca-antagonist (%)	6 (21)
Antiarrhythmic drug (%)	4 (14)

* ≥140/90 mmHg or treatment for hypertension.

2022). A standard 12-lead ECG at 500 Hz sampling rate was recorded throughout the protocol.

2.2 ECG processing

The CardioLund ECG parser (CardioLund Research AB, Lund, Sweden) is used for preprocessing, beat-detection, and beat classification and QRST cancellation. Briefly, in this software, a linear-phase high-pass filter is applied to the ECG to eliminate baseline wander, and fiducial points in the QRS complexes are detected; also, the QRS complexes are classified based on their morphology. The ectopic beats were identified based on correlation to template beats and were clustered and treated as a separate class for the QRST-cancellation. The QRS interval $\boldsymbol{y_{i_l}(n)}$ is set to 140 ms, starting 110 ms before the end of the S wave and finishing 30 ms after the end of the S wave, where i and l denotes beat-number and lead, respectively. A spatiotemporal QRST cancellation approach (Stridh and Sörnmo, 2001) is employed to extract f-wave signals from the ECG. This average beat subtraction method compensates for minor morphological variations in the QRST complex by combining beat averages from different leads. For each beat class, one beat average is calculated and used for QRST cancellation in the corresponded beats in the ECG leads. The extracted f-wave signal is downsampled from 1 kHz to 50 Hz using appropriate low-pass filtering and decimation since such signals have negligible frequency content above 25 Hz. In the present study, the extracted f-wave signal from lead V1 denoted $x(n)$, is subjected to analysis. For further analysis, the ECG data was divided into 1-min segments, resulting in five segments at baseline and one segment during deep breathing. The AFR and respiratory f-wave modulation was estimated from each 1-min segment of $x(n)$ as described in Section 2.3 and Section 2.5, respectively. A respiration signal, which is required for estimation of respiratory f-wave modulation, was obtained from the corresponding QRS intervals $y_{i_l}(n)$ as described in Section 2.4; ectopic beats were removed for this analysis. For each patient, results from the 1-min segments recorded at baseline were averaged to obtain the heart rate (HR^B), atrial fibrillatory rate

(AFR^B), and respiratory f-wave frequency modulation ($\Delta f_{OSP}{}^B$), respectively. The corresponding estimates during deep breathing (HR^D, AFR^D, $\Delta f_{OSP}{}^D$) were based on one segment.

2.3 Estimation of f-wave frequency trend

For the estimation of a high-resolution f-wave frequency trend, a harmonic f-wave model (Henriksson et al., 2018) is employed. The model f-wave signal is defined as the sum of a complex exponential signal with fundamental frequency f and its second harmonic,

$$s(n;\boldsymbol{\theta}) = \sum_{m=1}^{2} A_m e^{j\left(m2\pi\frac{f}{f_s}n+\phi_m\right)}, \tag{1}$$

where A_m and ϕ_m denote the amplitude and phase of m:th harmonic, respectively, and f_s is sampling frequency. The use of two harmonics in the model is motivated by the observations in (Henriksson et al., 2018), that additional harmonic results in more noise due to the additional degrees of freedom of this model. The parameters $\boldsymbol{\theta} = [f \quad A_1 \quad A_2 \quad \phi_1 \quad \phi_2]^T$, are estimated by fitting the harmonic model $s(n;\boldsymbol{\theta})$ to the analytic equivalent of $x(n)$, denoted $x_a(n)$, using maximum likelihood approach.

$$\hat{\boldsymbol{\theta}} = \arg\min_{\boldsymbol{\theta}} \|x_a(n) - s(n;\boldsymbol{\theta})\|^2, \tag{2}$$

The model is fitted to 20 ms overlapping 0.5-second segments of $x_a(n)$. For this fitting, f is constrained to the interval $[f_0 \pm 1.5]$ Hz, where global frequency estimate (f_0) is the maximum peak in the interval [4,12] Hz of the Welch periodogram of the whole $x(n)$. The estimates of f result in an f-wave frequency trend $f(n)$ sampled at 50 Hz. Then, correspond to the sampling rate of the respiration signal (cf. Section 2.4), $f(n)$ is resampled to 5Hz. To quantify accuracy of the fitted model, a signal quality index, denoted $\mathcal{S}$, is computed

$$\mathcal{S} = 1 - \frac{\sigma_{\hat{e}}}{\sigma_{x_a}}, \tag{3}$$

where $\sigma_{\hat{e}}$ and σ_{x_a} denote the standard deviation of the model error ($\hat{e}(n) = x_a(n) - s(n;\hat{\theta})$) and $x_a(n)$, respectively. In this study, $\mathcal{S}$ is computed for non-overlappning 5 s segments. $\mathcal{S}$ ranges from 0 to 1, where a higher value corresponds to a better fit. Only segments with $\mathcal{S} > 0.3$ is considered for further analysis, since previous studies has shown that $\mathcal{S}$ larger than 0.3 was sufficient for accurate estimation of $f(n)$ (Henriksson et al., 2018). The atrial fibrillatory rate (AFR) is estimated by the median of $f(n)$.

2.4 Estimation of ECG-derived respiration

The slope range method (Kontaxis et al., 2019) is applied to each lead of the ECG separately to obtain a respiratory signal. The method quantifies variations in the QRS morphology, which are assumed to reflect respiratory activity, using the difference between the maximum and minimum derivative in the QRS interval,

$$r_l(i) = \max_n\left\{y'_{i_l}(n)\right\} - \min_n\left\{y'_{i_l}(n)\right\}, \tag{4}$$

where i and l denotes beat-number and lead, respectively, and $y'_{i_l}(n) = y_{i_l}(n) - y_{i_l}(n-1)$. The resulting signal $r_l(i)$ is resampled to 5Hz using cubic spline interpolation to obtain a uniformly sampled signal $r_l(n)$. Principal component analysis (PCA) is applied to the set of $r_l(n)$ to derive a joint respiratory signal from all leads. The principal component that has the greatest variance and a significant periodic component in the respiratory interval ([0.1 0.5] Hz) is selected as the respiratory signal, denoted as $r(n)$. A principal component is considered to have a significant periodic component if the magnitude of the largest peak in the respiratory interval of its spectrum is at least 85% of the largest peak in the whole spectrum. The spectra are estimated by Welch periodograms based on 30 s sliding 25 s overlapping segments of PCA components. If none of the principal component accounting for more than 5% of the total variance has a significant periodic component in the respiration interval, no respiration signal is extracted.

2.5 Orthogonal subspace projection

To extract variations in the f-wave frequency trend that are linearly related to the respiration, an orthogonal subspace projection approach is employed (Chang, 2005). The demeaned $f(n)$ denoted as $\tilde{f}(n)$ is projected onto a subspace defined by the matrix $\boldsymbol{V}$, constructed using the respiratory signal $r(n)$,

$$\boldsymbol{V} = [\boldsymbol{r}_0, \boldsymbol{r}_1, \ldots, \boldsymbol{r}_d, \ldots, \boldsymbol{r}_m], \tag{5}$$

$$\boldsymbol{r}_d = \{r(1+d), r(2+d), \ldots, r(N-m+d)\}^T, \tag{6}$$

The model order m is determined by analysis of the simulated data (cf. Section 3.1). After creating the matrix $\boldsymbol{V}$, the signal $\tilde{f}(n)$ is projected onto the respiratory subspace using

$$\boldsymbol{f_x} = \boldsymbol{V}(\boldsymbol{V}^T\boldsymbol{V})^{-1}\boldsymbol{V}^T\boldsymbol{f} = \boldsymbol{P}\boldsymbol{f}, \tag{7}$$

where $\boldsymbol{f}$ is a length N vector of $\tilde{f}(n)$, $\boldsymbol{P}$ is the projection matrix of size $N-m \times N-m$, and $\boldsymbol{f_x}$ is the component of $\boldsymbol{f}$ that is linearly related to respiration. The power of the variations linearly related to respiration ($\boldsymbol{f_x}^\top\boldsymbol{f_x}$) is a fraction of the total power of the variations ($\boldsymbol{f}^\top\boldsymbol{f}$). Assuming that the variations in $\boldsymbol{f_x}$ are sinusoidal, the peak-to-peak amplitude is given by

$$\Delta\bar{f}_{OSP} = \sqrt{\frac{2\cdot(\boldsymbol{f_x}^\top\boldsymbol{f_x})}{N}}, \tag{8}$$

In the present study, $\Delta\bar{f}_{OSP}$ serves as an estimate of the magnitude of the respiratory induced f-wave frequency variations.

2.6 Performance evaluation

Simulated f-wave signals were used in order to assess the performance of the orthogonal subspace projection approach and its dependence on model order m (Section 2.5), signal quality $\mathcal{S}$ (Section 2.3) and characteristics of the f-wave signals. The f-wave signals were simulated by a modified version of the saw-tooth model proposed by (Stridh and Sörnmo, 2001). The f-wave signal is the sum of a sinusoid and its harmonic with time-varying frequency

$$x_{sim}(n) = \sum_{k=1}^{2} A_k(n)\sin(2\pi k F(n) n) + v(n), \tag{9}$$

$$F(n) = \frac{F}{F_s} + \frac{\Delta F}{2\pi F_r n}\sin\left(2\pi n \frac{F_r}{F_s}\right) + \frac{\Phi(n)}{2\pi k n}, \tag{10}$$

where F defines the average fundamental frequency, and respiratory f-wave frequency variation is quantified by F_r and ΔF, defining the variation frequency and the variation magnitude, respectively. To incorporate other forms of variation in the f-wave frequency, random phase variation, $\Phi(n)$, is added; it is modeled as white Gaussian noise with standard deviation σ_Φ. The amplitude of the k:th harmonic is given by

$$A_k(n) = \frac{2}{k\pi}(A + \Delta A(n)), \tag{11}$$

where A is the average f-wave amplitude, and $\Delta A(n)$ quantifies random amplitude variation and is assumed to have a Gaussian distribution with mean zero and standard deviation $A/5$; the parameter A was chosen to obtain a signal standard deviation of signal σ_x equal to 50. The following parameters were used for simulating one minute-long f-wave signals: $F = \{4, 5, 6, 7, 8, 9, 10\}$ Hz, $F_r = \{0.1, 0.15, 0.20, 0.25, 0.30\}$ Hz, $\Delta F = \{0, 0.025, 0.05, \ldots, 0.3\}$ Hz, $\sigma_\Phi = \{0.27, 0.40, 0.55, 0.67, 0.80\}$. White Gaussian noise $v(n)$ with $\sigma_v = \{0.1A, 0.2A, 0.3A, 0.4A, 0.5A\}$ is added to form realistic f-wave signals and the sampling frequency was set to F_s = 50 Hz. Ten realizations of $x_{sim}(n)$ for each parameter setting were considered, resulting in a total of 113,750 simulated signals.

Through these simulated signals, the accuracy of $\Delta\bar{f}_{OSP}$ as an estimate of ΔF is compared to our previously proposed band-pass filtering approach to quantify respiratory induced variations in the f-wave frequency trend (Abdollahpur et al., 2021). In that method, respiratory variation is estimated by applying a narrow band-pass filter with a fixed bandwidth of 0.06 Hz and a center frequency corresponding to the F_r. The f-wave frequency trend $f(n)$ obtained as described in Section 2.3. The average envelope of the filtered $f(n)$, denoted $\Delta\bar{f}_{BP}$, is used to quantify the magnitude of the respiratory variation. The absolute difference between ΔF and $\Delta\bar{f}_{BP}$, denoted as ϵ_{BP}, and the absolute difference between ΔF and $\Delta\bar{f}_{OSP}$ denoted as ϵ_{OSP} are used to assess the performance of the methods.

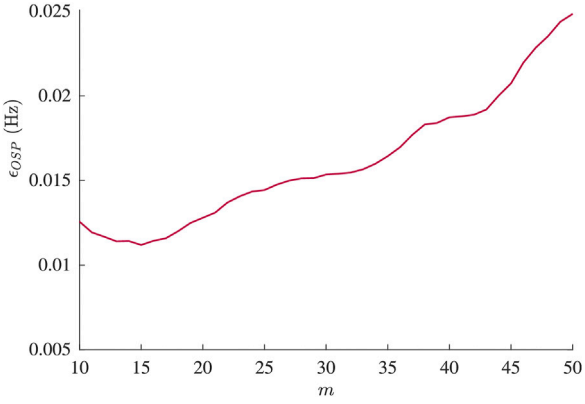

FIGURE 2
Mean estimation error ϵ_{OSP} from simulation plotted versus model order m.

2.7 Statistical analysis

Results are presented as mean ± std, and as median (range) for Gaussian and non-gaussian variables, respectively; the Lilliefors test is used to test for gaussianity. Student's t-test and Wilcoxon signed-rank test are applied to determine if differences are significant for Gaussian and non-gaussian variables, respectively. Hence, a paired t-test is applied to evaluate the difference between ϵ_{OSP} and ϵ_{BP}, and a Wilcoxon signed-rank test is applied to determine whether differences in HR, AFR, and Δf_{OSP} between baseline and deep breathing are significant. Further, Spearman rank correlation is used to evaluate the relationship between changes in HR, AFR, and Δf_{OSP} in response to deep breathing. The level of statistical significance is considered $p < 0.05$.

3 Results

3.1 Simulations

Results from the analysis of simulated data are presented in Figures 2–5. From Figure 2, it is apparent that the smallest ϵ_{OSP} was achieved for m = 15, and hence, m was set to 15 for the remaining analysis. The effect of the time-varying respiration is illustrated in Figure 3 where F_r changes from 0.1 to 0.3 Hz during 1 minute. As shown in Figure 3, the

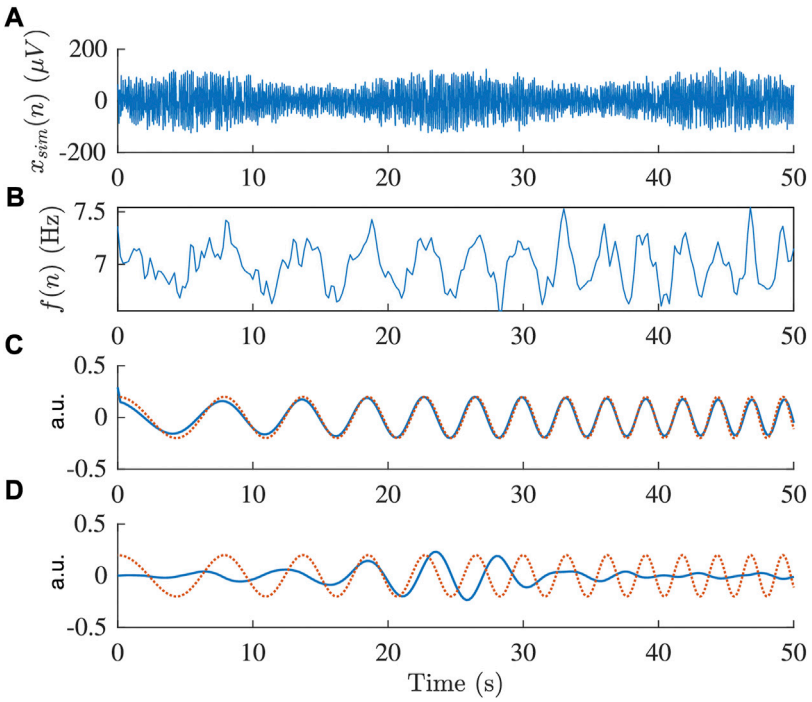

FIGURE 3
(A) Simulated signal $x_{sim}(n)$ and **(B)** corresponding estimated frequency trend $f(n)$, respectively. **(C,D)** Modeled respiration signal (red) and extracted respiratory component (blue) obtained using **(C)** orthogonal subspace projection and **(D)** bandpass filtering.

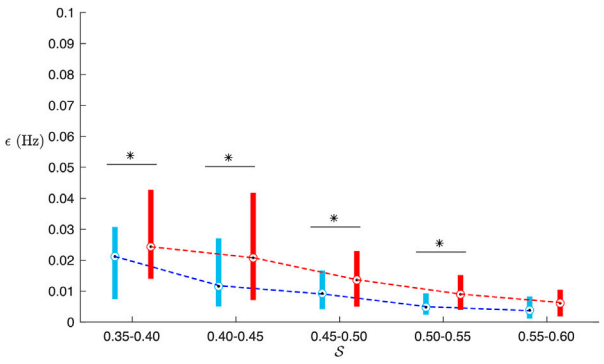

FIGURE 4
Box-plot of ϵ_{BP} (red) and ϵ_{OSP} (blue) from simulation as a function of signal quality $\mathcal{S}$. (*) denotes significant differences (p <0.05).

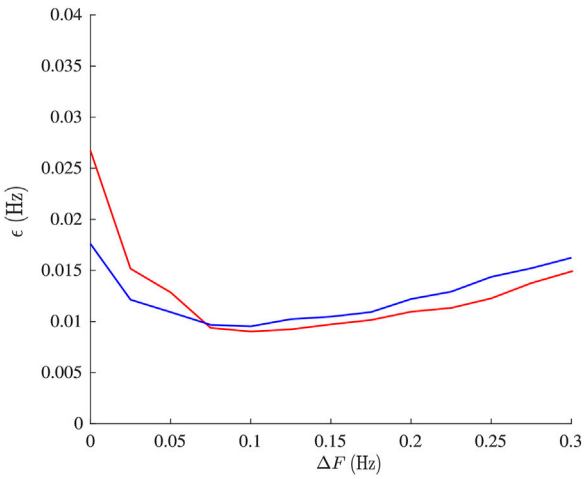

FIGURE 5
Mean estimation error ϵ_{OSP} (red) and ϵ_{BP} (blue) from simulations plotted versus the magnitude of respiratory modulation ΔF.

respiratory variations can be accurately extracted using the orthogonal subspace projection approach, while the previously proposed bandpass filtering approach fails. The ϵ_{OSP} was significantly smaller than ϵ_{BP} (0.017 ± 0.012 vs. 0.021 ± 0.015, $p < 0.001$). The improved accuracy obtained with the orthogonal subspace projection approach is more prominent for lower values of S, corresponding to higher noise levels, cf. Figure 4. The accuracy of the estimates was

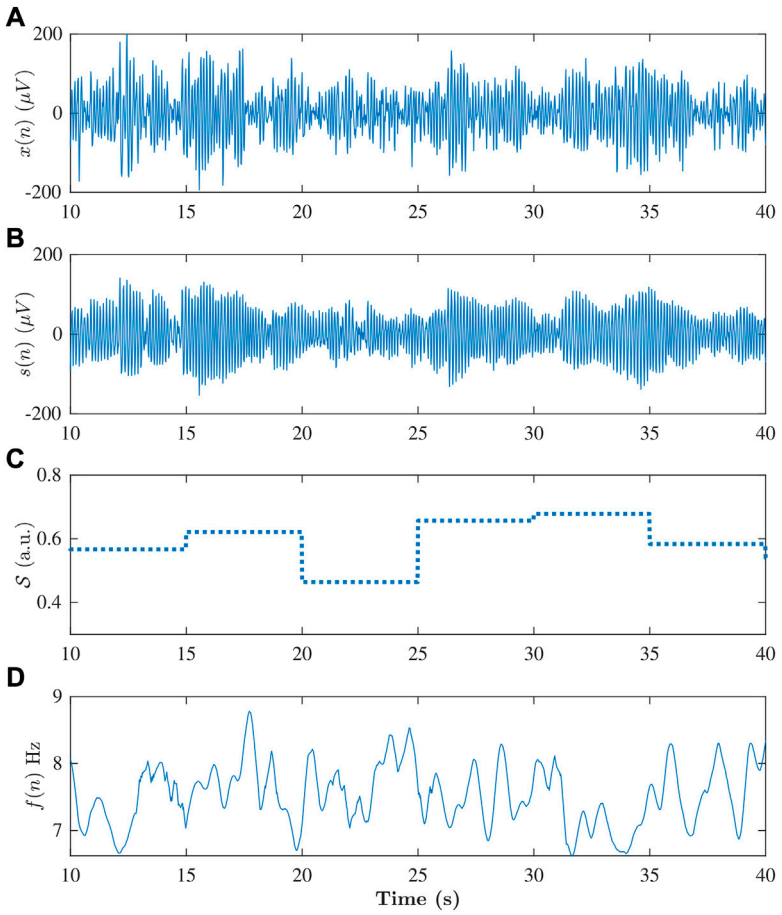

FIGURE 6
(A) Extracted f-wave signal $x(n)$, and **(B)** corresponding modeled signal $s(n)$, **(C)** signal quality index $\mathcal{S}$ and **(D)** extracted f-wave frequency trend $f(n)$ obtained from a 30 s ECG segment from one of the patient at baseline.

not affected by the f-wave frequency and the respiration rate (results not shown). However, for both approaches the estimates were less accurate for respiratory variations of small magnitudes ($\Delta f < 0.075$ Hz), cf. Figure 5.

3.2 Heart rate and f-wave frequency

An example of a 30-second f-wave signal $x(n)$ and the corresponding model signal $s\ (n; \boldsymbol{\theta})$, signal quality index $\mathcal{S}$, and extracted f-wave frequency trend $f(n)$ is displayed in Figure 6. The signal quality was sufficient ($\mathcal{S} > 0.3$) for estimation of $f(n)$ in 98% of the data. The AFR^B was 6.93 (4.65–6.97) Hz and AFR^D was 6.94 (4.56–6.99) Hz, a paired t-test showed no significant difference between baseline and deep breathing. The HR^B was 75.5 (37–150) bpm and HR^D was 74 (37–146) bpm; there were no significant differences between baseline and deep breathing. The changes in AFR versus changes in HR are displayed in Figure 7. The changes in AFR range between −8 and 6%, and the changes in HR range between −9 and 5%. There was a weak correlation between changes in HR and changes in AFR ($r = 0.38$, $p < 0.03$). The linear dependence between changes in HR and changes in AFR appears to be more pronounced for patients where the heart rate decreases in response to deep breathing, cf. Figure 7.

3.3 Respiration

Figure 8 gives an example of extracted respiratory signals $r_l(n)$ and the corresponding principal components for one patient during deep breathing. In this example, both $r_{PC_1}(n)$ and $r_{PC_2}(n)$ have a significant periodic component according to definition in Section 2.4. The $r_{PC_1}(n)$ is selected as respiration signal ($r(n)$) since it has the largest variance. Respiration signals $r(n)$ could be obtained from 118 out of 168 (70%) of the analyzed 1-min segments. The estimated respiration rate F_r was

10.3389/fphys.2022.976925

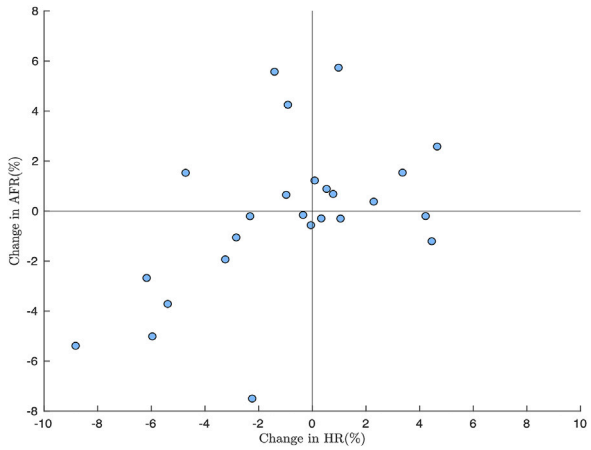

FIGURE 7
Relative changes between AFR^D and AFR^B plotted versus relative between HR^D and HR^B

significantly higher at baseline (0.20 ± 0.06) Hz than during deep breathing (0.10 ± 0.01) Hz; the F_r estimated during deep breathing corresponded to the respiration frequency in controlled of the study protocol.

3.4 Respiratory f-wave variation

The $\Delta\bar{f}_{OSP}$ could be obtained from all 1-min segments with a valid respiration signal, i.e., 118 out of 168.; these estimates are displayed in Figure 9. The ${\Delta f_{OSP}}^B$ was 0.130 (0.045–0.260) Hz and ${\Delta f_{OSP}}^D$ was 0.130 (0.056–0.230) Hz. A paired *t*-test showed no significant differences between baseline and deep breathing. The changes in $\Delta\bar{f}_{OSP}$ from phase from baseline to deep breathing plotted versus the corresponding changes in the *AFR* in Figure 10. The changes ranged from −100 to 100% for $\Delta\bar{f}_{OSP}$. The Spearman method showed no correlation between changes in $\Delta\bar{f}_{OSP}$ and changes in the *AFR*.

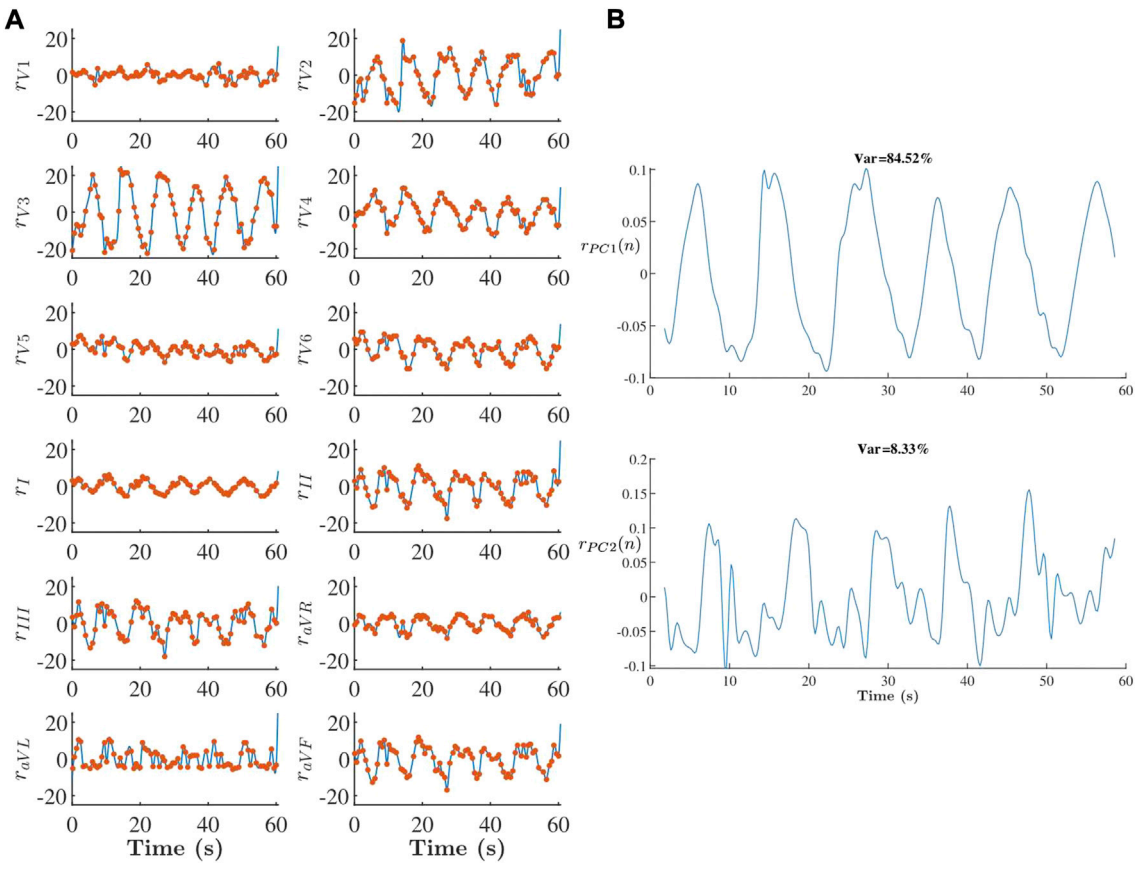

FIGURE 8
(A) Respiration signals $r_l(n)$ (blue line) and $r_l(i)$ (red dots) derived from 1-min ECG during deep breathing and **(B)** corresponding PCA components. In this example $r(n)$ is set to $r_{PC_1}(n)$ since it has a significant periodic component and accounts for most of the total variance.

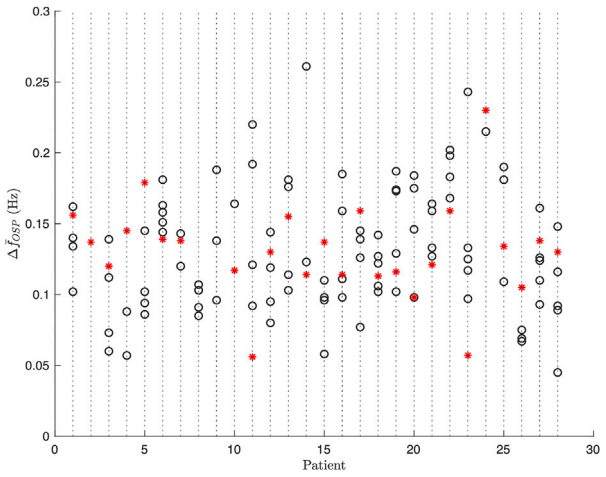

FIGURE 9
Estimates of respiratory f-wave frequency variations $\Delta f_{OSP}{}^{B}$ (black circle) and $\Delta f_{OSP}{}^{D}$ (red ∗) from all 1-min segments for each patient.

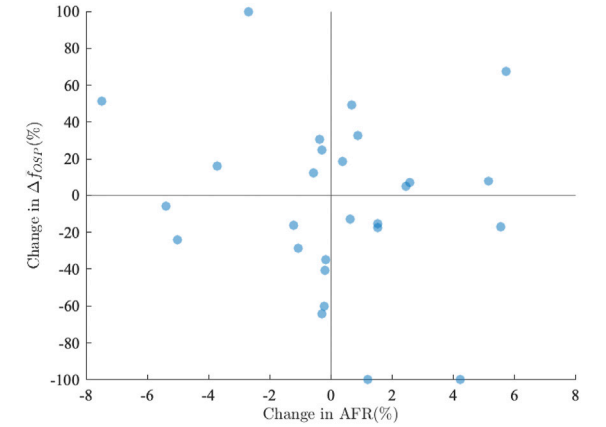

FIGURE 10
Relative change between $\Delta f_{OSP}{}^{B}$ and $\Delta f_{OSP}{}^{D}$ plotted versus relative change between AFR^{B} and AFR^{D}.

4 Discussion

In the present study, we propose a novel methodology, based on orthogonal subspace projection, for quantifying respiratory variations in the f-wave frequency trend. Results from analysis of simulated data show that the estimation accuracy of the proposed approach is comparable to that of our previously proposed bandpass filtering approach (Abdollahpur et al., 2021). However, the proposed approach is better suited for analysis of standard ECG recordings since it can handle time-varying respiration (Figure 3) and provides more accurate estimates of respiratory variations at low SNR (Figure 4).

Orthogonal subspace projection has previously been proposed for removing respiratory influences in heart rate variability signal for improved estimation of sympathovagal balance (Varon et al., 2018). In contrast, in this study we aimed to keep variations in f-wave frequency trend that were linearly related to respiration and remove other variations. Such respiratory–induced f-wave frequency variations have previously been shown to be affected by parasympatetic regulation in a cohort of AF patients with complete AV block and pacemaker set at a fixed pacing rate (Abdollahpur et al., 2021).

The orthogonal subspace projection relies on an ECG-derived respiration (EDR) signal. It should be noted that standard RR interval-based algorithms for ECG-derived respiration (Widjaja et al., 2014) are not applicable during AF since variations in heart rate during AF do not originate from the sinus node. Hence, the slope range method was selected for this since previous studies (Kontaxis et al., 2019) has shown that this method is robust during AF and provides more accurate estimates compared to QRS loop rotation angle (Bailón et al., 2006) and the R-wave angle (Lázaro et al., 2014). In the slope range method f-wave suppression is not needed and its performance is less affected by the presence of f-waves (Kontaxis et al., 2019). An EDR signal is derived from each lead separately, and PCA is employed to merge respiratory information from EDR signals from different leads. It is assumed that the PCA component that has a significant periodicity in the 0.1–0.4 Hz interval and accounts for the largest part of the variations in the EDR signals contains the respiratory information. Respiration signals couldn't be obtained from 30% of the analyzed 1-min segments due to criteria defined in Section 2.4. Since this methodology aimed for the effect of time-varying respiration on the f-wave frequency, we used PCA to find respiration signal. The PCA uses a maximum-variance criteria to separate respiration signal and noise into orthogonal subspaces. Its components are sensitive to the high variance noise, which may not be the best way to find respiration signals. An alternative solution would be to use periodic component analysis (Saul and Allen, 2000), which has previously been proposed for decomposition of multilead ECG (Sameni et al., 2008) and applied for analysis of, e.g., t-wave alternans (Monasterio et al., 2010; Palmieri et al., 2021). Whereas PCA uses a maximum-variance criteria to decompose signals, periodic component analysis maximizes the periodic structure. Periodic component analysis has the advantage of being less sensitive to large amplitude noise, however, it is requires prior knowledge on the periodicity of the desired signal.

Respiratory induced f-wave frequency variations has previously been shown to be affected by parasympathetic regulation. In our previous study, (Abdollahpur et al., 2021), 5-min ECGs recorded from eight patients during controlled respiration before and after full vagal blockade were analyzed; in 50% of the patients, respiratory variation was significantly reduced after the vagal blockade. Moreover, results from computational simulations of human

atrial tissues confirmed that the pattern of the parasympathetic neurotransmitter acetylcholine release could be an important factor involved in f-wave frequency variation (Celotto et al., 2020). These results suggest that respiratory f-wave frequency variations can potentially be used to quantify ANS activity, which is of clinical interest since ANS activity is an important factor on the maintenance and progression of AF (Linz et al., 2019). For example, vagus nerve stimulation has been shown to shorten the atrial effective refractory period and suppress autonomic remodeling in dogs with obstructive apnea induced AF (Yu et al., 2017). Further, it has been shown that AF progression through cellular remodeling could be reduced by minimizing sympathetic or increasing parasympathetic tone (Bashir et al., 2019). In a recent study (Sohinki et al., 2021), investigated the impact of low-level electromagnetic fields (LL-EMF) which is specifically targeted for vagal stimulation, on AF inducibility in humans.

In present study no significant differences were found between f-wave frequency variations at baseline and during deep breathing. Several factors could contribute to this observation. Firstly, the duration of the deep breathing task was just 1 min which may not be sufficient time to observe the effect of changes in autonomic tone on the f-wave frequency trend. Further, considering the large variation of $\Delta\bar{f}_{OSP}$ from the 1-min segments at baseline (cf Figure 9), recordings of longer duration during deep breathing are desired for robust estimation. Secondly, the heterogeneous behavior of changes in $\Delta\bar{f}_{OSP}$ in response to deep breathing may be due to individual differences in AF progression which may effect the ANS regulation (Linz et al., 2019). The patients in the present study have paroxysmal and persistent AF with unknown duration. However, due to the small study population subgroup analysis is not possible. Thirdly, the fluctuations in intrathoracic pressure as a result of respiration have an important effect on the heart rate during normal sinus rhythm. The effect of these fluctuations on the heart rate during AF are largely unknown. It is possible that variations in heart rate counteract the impact of respiration on the fluctuations in acetylcholine level in the atrial tissues and, as a result, the f-wave frequency variation. In the previous study, the effect of the parasympathetic activity was investigated in a cohort of AF patients with complete AV block and fixed-rate (60 beat/min) pacemaker (Abdollahpur et al., 2021) and hence the effect of changes in ANS activity induced by variations in heart rate was eliminated. In contrast, the present dataset consists of patients without a pacemaker. Finally, it should be noted that the estimation accuracy of the proposed methodology sets a lower bound for changes that can be detected (cf. Section 3.1), and we cannot exclude the possibility that there are changes below this limit that remain undetected.

5 Conclusion

We propose a novel orthogonal subspace projection approach to quantify respiratory variations in the f-wave frequency trend obtained from the ECG during AF. Results from simulated f-wave signals show that the proposed approach offers more robust performance in respiratory variation estimation compared to the previously proposed bandpass filtering approach. Results from analysis of clinical data were heterogeneous and no significant differences in HR, AFR and respiratory f-wave frequency variations $\Delta\bar{f}_{OSP}$ between baseline and deep breathing were found in SCAPIS dataset.

Data availability statement

The data analyzed in this study is subject to the following licenses/restrictions: The data is owned by Lund University. Requests to access these datasets should be directed to the steering committee of SCAPIS. Requests to access these datasets should be directed to scapis@scapis.org.

Ethics statement

The studies involving human participants were reviewed and approved by the Written informed consent was obtained from all SCAPIS participants. The project was approved by the ethics committee at Lund University (2016/1031). The patients/participants provided their written informed consent to participate in this study.

Author contributions

FS devised the project and the main conceptual ideas and was responsible for overseeing the research and providing critical insight and recommendations regarding the focus, structure, and content of the paper. MA processed the data, performed the analysis, drafted the manuscript and designed the figures. GE was responsible for the clinical data acquisition protocol. PP helped supervise the project focusing on clinical aspects. All authors contributed to the final version of the manuscript.

Funding

This work was supported by the European Union's Horizon 2020 research and innovation programme under the Marie Sklodowska-Curie Grant Agreement No. 766082, the Swedish Research Council (Grant VR2019-04272) and the Crafoord Foundation (Grant 20200605). The main funding body of SCAPIS is the Swedish Heart and Lung Foundation. The study was also supported by grants from Swedish Research Council (2019-01236), Swedish Heart Lung Foundation (20200173) and grant from the Swedish state under the

agreement between the Swedish government and the county councils (ALF-project 2018-0030).

Conflict of interest

The authors declare that the research was conducted in the absence of any commercial or financial relationships that could be construed as a potential conflict of interest.

Publisher's note

All claims expressed in this article are solely those of the authors and do not necessarily represent those of their affiliated organizations, or those of the publisher, the editors and the reviewers. Any product that may be evaluated in this article, or claim that may be made by its manufacturer, is not guaranteed or endorsed by the publisher.

References

Abdollahpur, M., Holmqvist, F., Platonov, P., and Sandberg, F. (2021). Respiratory induced modulation in f-wave characteristics during atrial fibrillation. *Front. Physiol.* 12, 653492. doi:10.3389/fphys.2021.653492

Bailón, R., Sornmo, L., and Laguna, P. (2006). A robust method for ecg-based estimation of the respiratory frequency during stress testing. *IEEE Trans. Biomed. Eng.* 53, 1273–1285. doi:10.1109/TBME.2006.871888

Bashir, M. U., Bhagra, A., Kapa, S., and McLeod, C. J. (2019). Modulation of the autonomic nervous system through mind and body practices as a treatment for atrial fibrillation. *Rev. Cardiovasc. Med.* 20, 129–137. doi:10.31083/j.rcm.2019.03.517

Bergström, G., Berglund, G., Blomberg, A., Brandberg, J., Engström, G., Engvall, J., et al. (2015). The Swedish cardiopulmonary bioimage study: Objectives and design. *J. Intern. Med.* 278, 645–659. doi:10.1111/joim.12384

Capucci, A., Biffi, M., Boriani, G., Ravelli, F., Nollo, G., Sabbatani, P., et al. (1995). Dynamic electrophysiological behavior of human atria during paroxysmal atrial fibrillation. *Circulation* 92, 1193–1202. doi:10.1161/01.cir.92.5.1193

Celotto, C., Sánchez, C., Mountris, K. A., Abdollahpur, M., Sandberg, F., Laguna, P., et al. (2020). Relationship between atrial oscillatory acetylcholine release pattern and f-wave frequency modulation: A computational and experimental study. *Comput. Cardiol.*, 1–4.

Chang, C.-I. (2005). Orthogonal subspace projection (osp) revisited: A comprehensive study and analysis. *IEEE Trans. Geosci. Remote Sens.* 43, 502–518. doi:10.1109/tgrs.2004.839543

Crandall, M. A., Bradley, D. J., Packer, D. L., and Asirvatham, S. J. (2009). Contemporary management of atrial fibrillation: Update on anticoagulation and invasive management strategies. *Mayo Clin. Proc.* 84, 643–662.

Engström, G., Hamrefors, V., Fedorowski, A., Persson, A., Johansson, M. E., Ostenfeld, E., et al. (2022). Cardiovagal function measured by the deep breathing test: Relationships with coronary atherosclerosis. *J. Am. Heart Assoc.* 11, e024053. doi:10.1161/JAHA.121.024053

Fabritz, L., Guasch, E., Antoniades, C., Bardinet, I., Benninger, G., Betts, T. R., et al. (2016). Expert consensus document: Defining the major health modifiers causing atrial fibrillation: A roadmap to underpin personalized prevention and treatment. *Nat. Rev. Cardiol.* 13, 230–237. doi:10.1038/nrcardio.2015.194

Henriksson, M., Petrenas, A., Marozas, V., Sandberg, F., and Sornmo, L. (2018). Model-based assessment of f-wave signal quality in patients with atrial fibrillation. *IEEE Trans. Biomed. Eng.* 65, 2600–2611. doi:10.1109/TBME.2018.2810508

Holmqvist, F., Stridh, M., Waktare, J. E. P., Brandt, J., Sörnmo, L., Roijer, A., et al. (2005). Rapid fluctuations in atrial fibrillatory electrophysiology detected during controlled respiration. *Am. J. Physiol. Heart Circ. Physiol.* 289, H754–H760. doi:10.1152/ajpheart.00075.2005

Kontaxis, S., Lázaro, J., Corino, V. D., Sandberg, F., Bailón, R., Laguna, P., et al. (2019). Ecg-derived respiratory rate in atrial fibrillation. *IEEE Trans. Biomed. Eng.* 67, 905–914. doi:10.1109/TBME.2019.2923587

Krijthe, B. P., Kunst, A., Benjamin, E. J., Lip, G. Y., Franco, O. H., Hofman, A., et al. (2013). Projections on the number of individuals with atrial fibrillation in the European Union, from 2000 to 2060. *Eur. Heart J.* 34, 2746–2751. doi:10.1093/eurheartj/eht280

Lázaro, J., Alcaine, A., Romero, D., Gil, E., Laguna, P., Pueyo, E., et al. (2014). Electrocardiogram derived respiratory rate from qrs slopes and r-wave angle. *Ann. Biomed. Eng.* 42, 2072–2083. doi:10.1007/s10439-014-1073-x

Linz, D., Elliott, A. D., Hohl, M., Malik, V., Schotten, U., Dobrev, D., et al. (2019). Role of autonomic nervous system in atrial fibrillation. *Int. J. Cardiol.* 287, 181–188. doi:10.1016/j.ijcard.2018.11.091

Lip, G. Y., Nieuwlaat, R., Pisters, R., Lane, D. A., and Crijns, H. J. (2010). Refining clinical risk stratification for predicting stroke and thromboembolism in atrial fibrillation using a novel risk factor-based approach: The euro heart survey on atrial fibrillation. *Chest* 137, 263–272. doi:10.1378/chest.09-1584

Miyasaka, Y., Barnes, M. E., Gersh, B. J., Cha, S. S., Bailey, K. R., Abhayaratna, W. P., et al. (2006). Secular trends in incidence of atrial fibrillation in olmsted county, Minnesota, 1980 to 2000, and implications on the projections for future prevalence. *Circulation* 114, 119–125. doi:10.1161/CIRCULATIONAHA.105.595140

Monasterio, V., Clifford, G. D., Laguna, P., and MARTInez, J. P. (2010). A multilead scheme based on periodic component analysis for t-wave alternans analysis in the ecg. *Ann. Biomed. Eng.* 38, 2532–2541. doi:10.1007/s10439-010-0029-z

Nitta, T., Ishii, Y., Miyagi, Y., Ohmori, H., Sakamoto, S.-i., and Tanaka, S. (2004). Concurrent multiple left atrial focal activations with fibrillatory conduction and right atrial focal or reentrant activation as the mechanism in atrial fibrillation. *J. Thorac. Cardiovasc. Surg.* 127, 770–778. doi:10.1016/j.jtcvs.2003.05.001

Östenson, S., Corino, V. D. A., Carlsson, J., and Platonov, P. G. (2017). Autonomic influence on atrial fibrillatory process: Head-up and head-down tilting. *Ann. Noninvasive Electrocardiol.* 22, e12405. doi:10.1111/anec.12405

Palmieri, F., Gomis, P., Ruiz, J. E., Ferreira, D., Martín-Yebra, A., Pueyo, E., et al. (2021). Ecg-based monitoring of blood potassium concentration: Periodic versus principal component as lead transformation for biomarker robustness. *Biomed. Signal Process. Control* 68, 102719. doi:10.1016/j.bspc.2021.102719

Patel, N. J., Deshmukh, A., Pant, S., Singh, V., Patel, N., Arora, S., et al. (2014). Contemporary trends of hospitalization for atrial fibrillation in the United States, 2000 through 2010: Implications for healthcare planning. *Circulation* 129, 2371–2379. doi:10.1161/CIRCULATIONAHA.114.008201

Platonov, P. G., Corino, V. D., Seifert, M., Holmqvist, F., and Sörnmo, L. (2014). Atrial fibrillatory rate in the clinical context: Natural course and prediction of intervention outcome. *Europace* 16, iv110–iv119. iv110–iv119. doi:10.1093/europace/euu249

Saksena, S., Skadsberg, N. D., Rao, H. B., and Filipecki, A. (2005). Biatrial and three-dimensional mapping of spontaneous atrial arrhythmias in patients with refractory atrial fibrillation. *J. Cardiovasc. Electrophysiol.* 16, 494–504. doi:10.1111/j.1540-8167.2005.40531.x

Sameni, R., Jutten, C., and Shamsollahi, M. B. (2008). Multichannel electrocardiogram decomposition using periodic component analysis. *IEEE Trans. Biomed. Eng.* 55, 1935–1940. doi:10.1109/TBME.2008.919714

Saul, L., and Allen, J. (2000). Periodic component analysis: An eigenvalue method for representing periodic structure in speech. *Adv. Neural Inf. Process. Syst.* 13.

Sohinki, D., Thomas, J., Scherlag, B., Stavrakis, S., Yousif, A., Po, S., et al. (2021). Impact of low-level electromagnetic fields on the inducibility of atrial fibrillation in the electrophysiology laboratory. *Heart Rhythm O2* 2, 239–246. doi:10.1016/j.hroo.2021.04.004

Stridh, M., Meurling, C., Olsson, B., and Sörnmo, L. (2003). Detection of autonomic modulation in permanent atrial fibrillation. *Med. Biol. Eng. Comput.* 41, 625–629. doi:10.1007/bf02349969

Stridh, M., and Sörnmo, L. (2001). Spatiotemporal QRST cancellation techniques for analysis of atrial fibrillation. *IEEE Trans. Biomed. Eng.* 48, 105–111. doi:10.1109/10.900266

Varon, C., Lázaro, J., Bolea, J., Hernando, A., Aguiló, J., Gil, E., et al. (2018). Unconstrained estimation of hrv indices after removing respiratory influences from heart rate. *IEEE J. Biomed. Health Inf.* 23, 2386–2397. doi:10.1109/JBHI.2018.2884644

Waldo, A. L. (2003). Mechanisms of atrial fibrillation. *J. Cardiovasc. Electrophysiol.* 14, S267–S274. doi:10.1046/j.1540-8167.2003.90401.x

Widjaja, D., Caicedo, A., Vlemincx, E., Van Diest, I., and Van Huffel, S. (2014). Separation of respiratory influences from the tachogram: A methodological evaluation. *PloS one* 9, e101713. doi:10.1371/journal.pone.0101713

Yu, L., Li, X., Huang, B., Zhou, X., Wang, M., Zhou, L., et al. (2017). Impacts of renal sympathetic activation on atrial fibrillation: The potential role of the autonomic cross talk between kidney and heart. *J. Am. Heart Assoc.* 6, e004716. doi:10.1161/JAHA.116.004716

frontiers | Frontiers in Cardiovascular Medicine

TYPE Original Research
PUBLISHED 23 September 2022
DOI 10.3389/fcvm.2022.1001883

OPEN ACCESS

EDITED BY
Enyi Shi,
China Medical University, China

REVIEWED BY
Sivaraman Jayaraman,
National Institute of Technology Rourkela, India
Mustafa Begenc Tascanov,
Harran University, Turkey

*CORRESPONDENCE
Zhong Wu
wuzhong71@scu.edu.cn

†These authors share first authorship

SPECIALTY SECTION
This article was submitted to Heart Surgery, a section of the journal Frontiers in Cardiovascular Medicine

RECEIVED 24 July 2022
ACCEPTED 05 September 2022
PUBLISHED 23 September 2022

CITATION
He K, Liang W, Liu S, Bian L, Xu Y, Luo C, Li Y, Yue H, Yang C and Wu Z (2022) Long-term single-lead electrocardiogram monitoring to detect new-onset postoperative atrial fibrillation in patients after cardiac surgery.
Front. Cardiovasc. Med. 9:1001883.
doi: 10.3389/fcvm.2022.1001883

Long-term single-lead electrocardiogram monitoring to detect new-onset postoperative atrial fibrillation in patients after cardiac surgery

Kang He[1†], Weitao Liang[1†], Sen Liu[2†], Longrong Bian[1], Yi Xu[1], Cong Luo[1], Yifan Li[1], Honghua Yue[1], Cuiwei Yang[2] and Zhong Wu[1*]

[1]Department of Cardiovascular Surgery, West China Hospital of Sichuan University, Chengdu, China, [2]Center for Biomedical Engineering, School of Information Science and Technology, Fudan University, Shanghai, China

Background: Postoperative atrial fibrillation (POAF) is often associated with serious complications. In this study, we collected long-term single-lead electrocardiograms (ECGs) of patients with preoperative sinus rhythm to build statistical models and machine learning models to predict POAF.

Methods: All patients with preoperative sinus rhythm who underwent cardiac surgery were enrolled and we collected long-term ECG data 24 h before surgery and 7 days after surgery by single-lead ECG. The patients were divided into a POAF group a no-POAF group. A clinical model and a clinical + ECG model were constructed. The ECG parameters were designed and support vector machine (SVM) was selected to build a machine learning model and evaluate its prediction efficiency.

Results: A total of 100 patients were included. The detection rate of POAF in long-term ECG monitoring was 31% and that in conventional monitoring was 19%. We calculated 7 P-wave parameters, Pmax (167 ± 31 ms vs. 184 ± 37 ms, $P = 0.018$), Pstd (15 ± 7 vs. 19 ± 11, $P = 0.031$), and PWd (62 ± 28 ms vs. 80 ± 35 ms, $P = 0.008$) were significantly different. The AUC of the clinical model (sex, age, LA diameter, GFR, mechanical ventilation time) was 0.86. Clinical + ECG model (sex, age, LA diameter, GFR, mechanical ventilation time, Pmax, Pstd, PWd), AUC was 0.89. In the machine learning model, the accuracy (Ac) of the train set and test set was above 80 and 60%, respectively.

Conclusion: Long-term ECG monitoring could significantly improve the detection rate of POAF. The clinical + ECG model and the machine learning model based on P-wave parameters can predict POAF.

KEYWORDS

postoperative new-onset atrial fibrillation, long-term ECG monitoring, P wave characteristics, machine learning, support vector machine

Introduction

Postoperative atrial fibrillation (POAF) after cardiac surgery was defined as a new episode of atrial fibrillation or flutter requiring treatment after surgery. A more specific definition is a new episode of atrial fibrillation with duration $\geq$ 5 min detected on any monitoring instrument, including rhythm monitor/telemetry/electrocardiogram, and requiring treatment. POAF is the most common complication after cardiac surgery and is a challenge for cardiac surgeons (1). Patients with POAF are often associated with serious early complications, including hemodynamic instability, acute heart failure and stroke. The incidence of long-term atrial fibrillation and stroke risk is 2 or 3 times that of patients without POAF, accompanied by a significantly increased incidence of heart failure, rehospitalization rate, etc.

Studies have shown that there may be minimal fibrillation, despite a normal sinus rhythm on ECG, which cannot reflect atrial function (2, 3). The electrophysiology and structural reconstruction of the heart occurs before the appearance of the characteristic ECG waveform change in patients prone to AF (4, 5). However, it's difficult for humans to recognize non-sinus electrical activity, which has become the basis for the prediction of AF.

The rapid development of mobile medical techniques and wearable ECG technology provides a cheap choice for AF detection and assessment. Convenient intermittent or systematic monitoring of elderly patients with specific risk factors can improve the detection of AF (6). The advent of the era of big data makes artificial intelligence applications in medicine possible. Due to its powerful predictive potential, machine learning and deep learning can identify individuals likely to develop AF from their sinus rhythm records (7), which can make clinical practice more effective, convenient and personalized for the identification and prediction of atrial fibrillation.

In conclusion, the purpose of this study was to build a statistical model and machine learning model to predict POAF in patients with preoperative sinus rhythm after cardiac surgery using portable long-term ECG monitoring.

Patients and methods

This study was approved by the West China Hospital of Sichuan University ethics committee. This study adheres to the Strengthening the Report of Observation Studies in Epidemiology (STROBE) guidelines.

Patients

Patients with preoperative sinus rhythm undergoing cardiac surgery from September 2020 to December 2021 in the Department of Cardiovascular, West China Hospital of Sichuan University were included. Eligible patients underwent ECG recording 24 h or more before surgery and 7 days or more after surgery by long-term single-lead electrocardiogram. Patients were excluded if they underwent emergency surgery or had paroxysmal atrial fibrillation.

Electrocardiogram monitoring

The main equipment used in this study is the long-term single-lead electrocardiogram. It is a patch with 2 electrodes 10 cm apart placed over the patients' precordium at an angle of 45°. The device can continuously record and collect ECG data dynamically for up to 14 days.

Electrocardiograms

All raw data were processed by Ecglab software developed by Shanghai Yuanxin Medical (**Figure 1**). Blinded to the patient outcomes, two readers (KH and SL) labeled and measured the required ECG fragments.

The original data were low-pass filtered by Ecglab software and then high-pass filtered to remove noise and correct filter delay. The second step was to smooth the ECG curve and facilitate the algorithm selection. Then, P wave localization (including the start point, first peak point, and end point) was performed based on the ECG waveform localization algorithm provided in a previous study (8), and the positioning results were manually verified. The measurement of the start point was taken at the intersection of the start point of the P wave and the iso-potential line, and the measurement of the end point was taken at the intersection of the end point of the P wave and the iso-potential line. Based on the results of P-wave localization and combined with the reports in the literature (8), 7 P-wave characteristics were calculated: Pmax, Pmin, Pmean, Pstd, P wave dispersion (PWd), Pptmean, and Pptstd. Pmax was defined as the widest P-wave in the selected segment. Pmin was defined as the minimum p-wave time in the fragment. Pmean was defined as the mean p-wave time of all fragments. Pstd was defined as the standard deviation (SD) of P-wave time. PWd was defined as the difference between the maximum and minimum P-wave times. Pptmean was defined as the mean time interval from the start point of the P wave to the peak point. Pptstd was defined as the SD of the p-wave peak time (**Figure 2**).

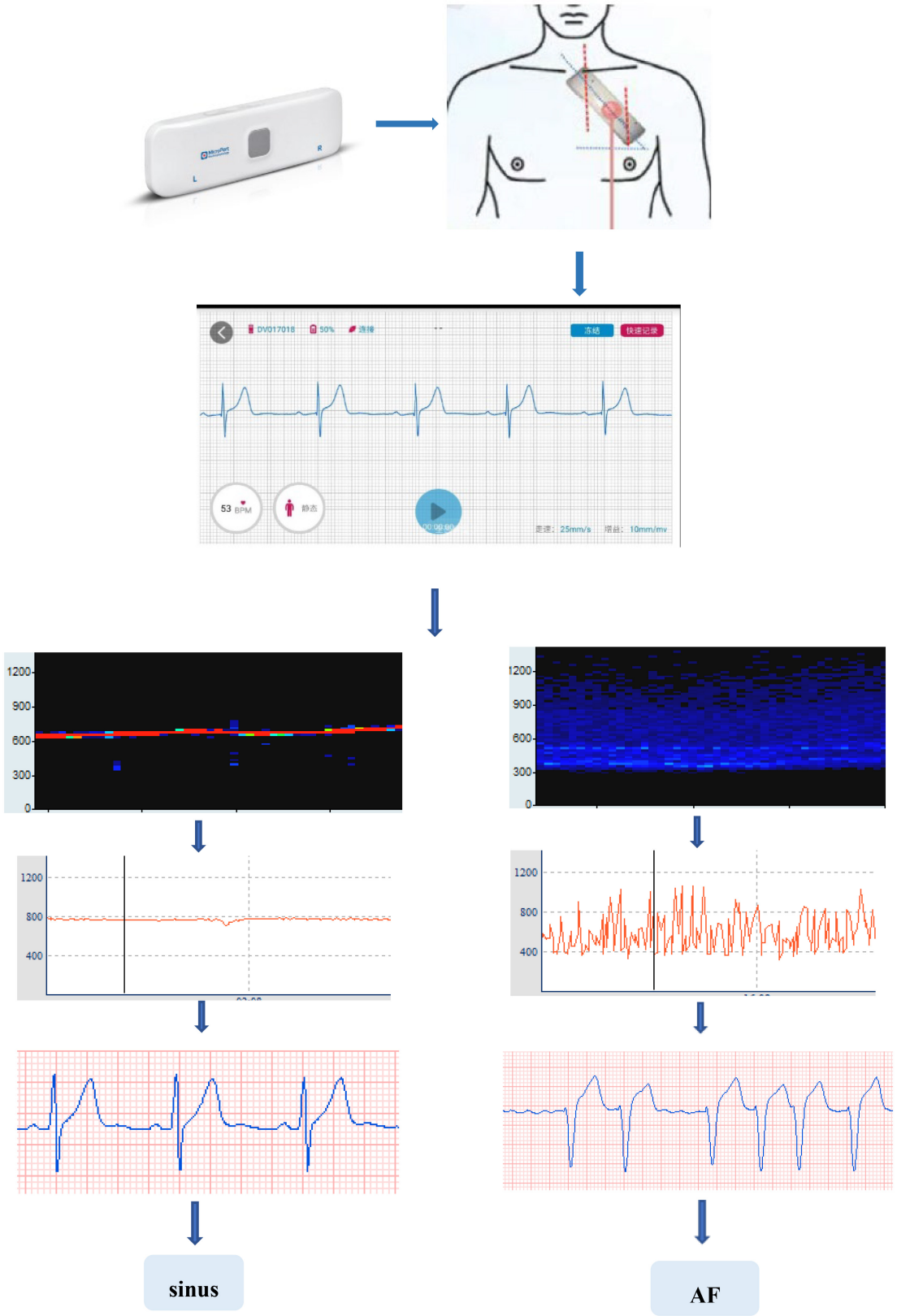

FIGURE 1
Work flow of portable long-time single-lead ECG monitor and Ecglab.

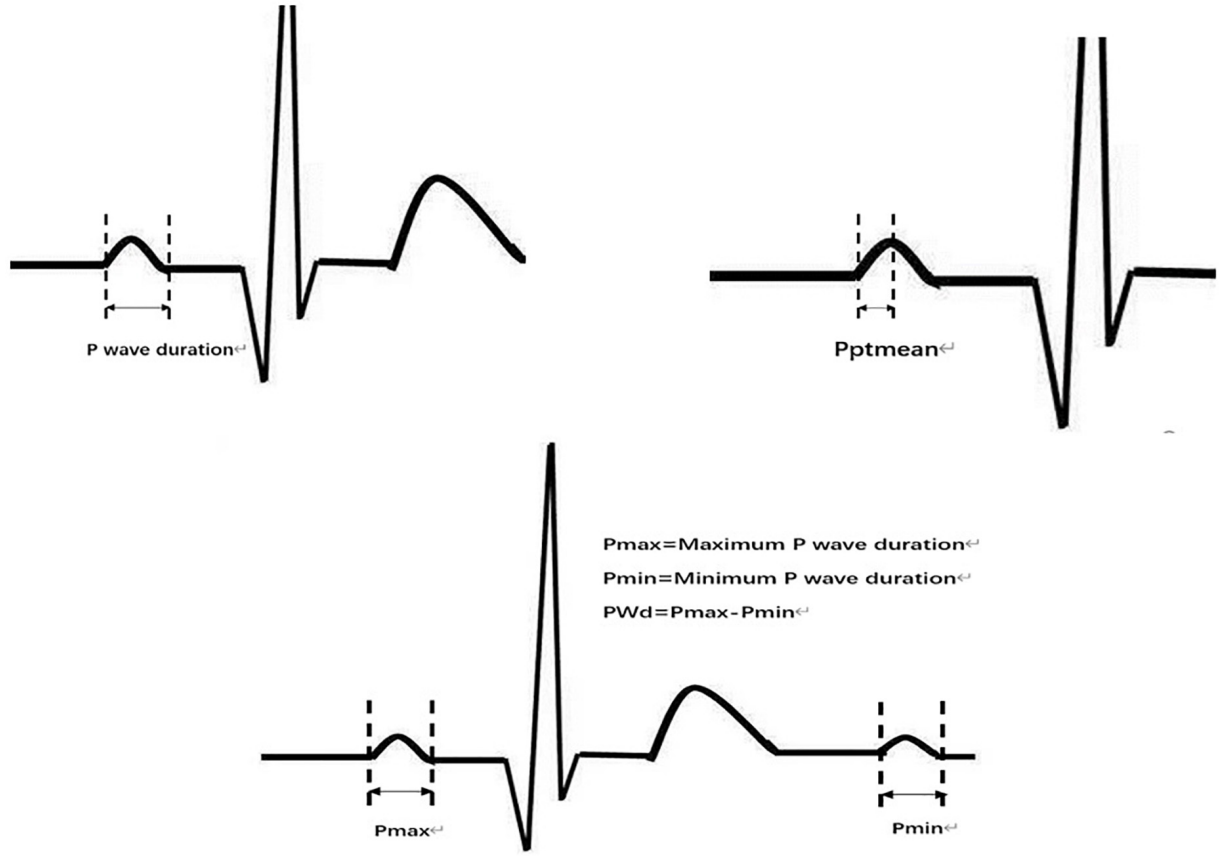

FIGURE 2
Part of P-wave parameters. P wave duration, Pmax, Pmin, Pptmean, PWd.

Statistical analysis and machine learning

Statistical analysis

All statistical analyses were performed using SPSS 25.0 software. All continuous data with a normal distribution are expressed as the mean ± *SD*, which were assessed by two independent sample *t*-tests. Non-normally distributed continuous data were represented by the median and interquartile range (IQR) and compared with the Mann–Whitney *U*-test. Categorical data are reported as an absolute number and percentage and compared using the chi-square test or Fisher's exact test. The association between predictors and POAF was assessed by univariate logistic regression separately and combined by multivariate logistic regression. Clinical data and ECG parameters were used to construct prediction models, which were evaluated by receiver operating characteristic curves (ROCs) and areas under the curve (AUCs). All results were two-tailed statistically significant with $P < 0.05$, and confidence intervals (CIs) were calculated at the 95% level.

Machine learning

Seven P-wave features were calculated, and a few patients' ECGs that were difficult to recognize by computer were excluded. A total of 94 patients' data feature matrices (94 × 7) were incorporated into the machine learning model. There were 28 cases in POAF group (Class 1) and 66 cases in no-POAF group (Class 0).

19 cases in Class 1 were randomly selected as the training set, and 9 cases were selected as the test set at a ratio of 7:3. To reduce the overlearning of one group, 19 patients in Class 0 were also randomly selected as the training set, and the remaining 47 patients were selected as the test set. Two schemes were adopted: Scheme A: all patient data were used, training set: 19 cases (0) + 19 cases (1); test set: 47 cases (0) + 9 cases (1); Scheme B: partial patient data were randomly used to ensure data balance as far as possible, training set: 19 cases (0) + 19 cases (1); test set: 9 cases (0) + 9 cases (1).

Support vector machine (SVM) was selected in this experiment. Based on the training set, the optimal hyperparameters of the model (C-penalty factor, gamma-kernel

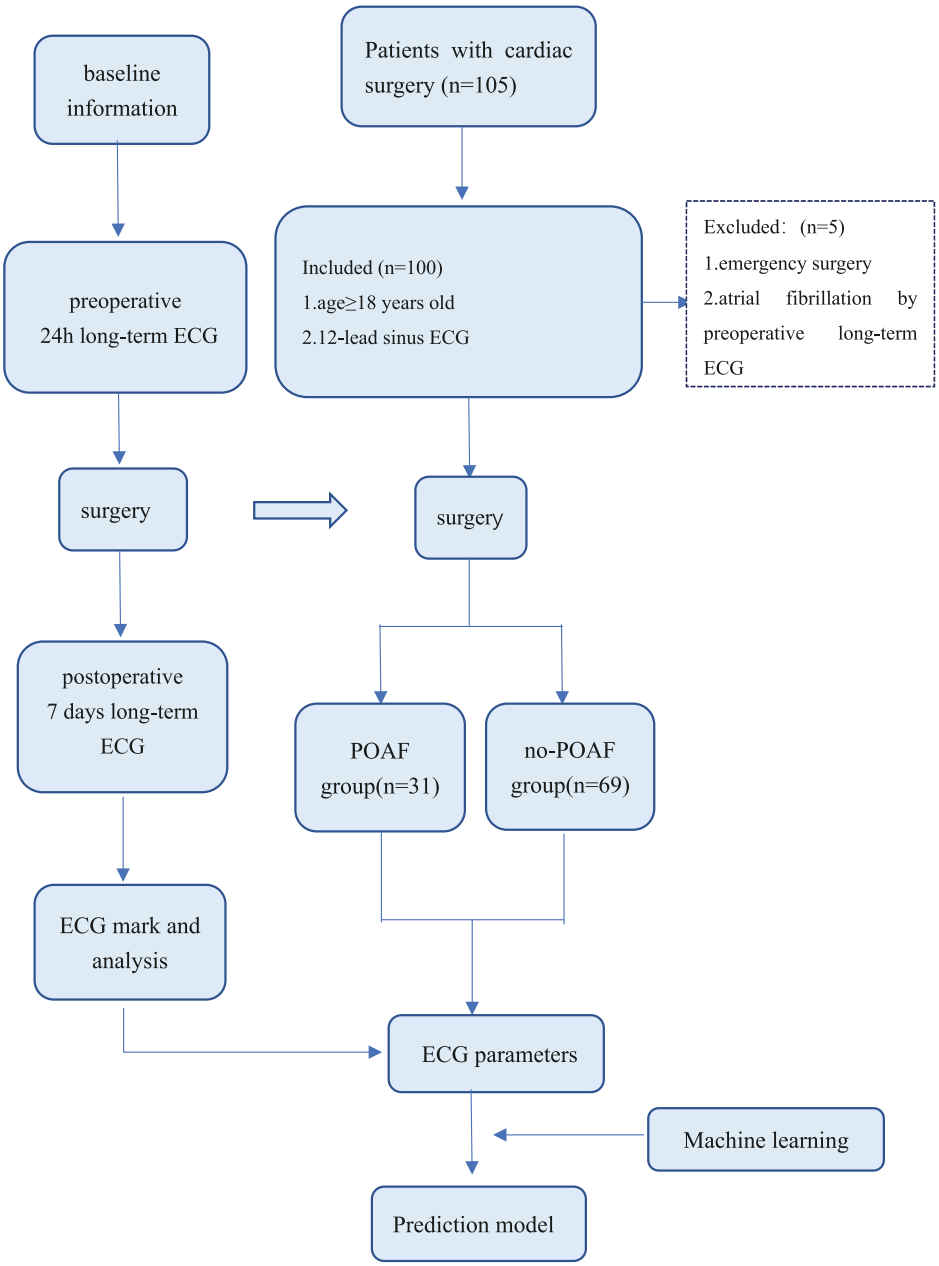

FIGURE 3
Study flowchart. ECG, electrocardiogram; POAF, postoperative atrial fibrillation.

function) were determined by fivefold cross-validation and grid search. The confusion matrix was used to calculate the accuracy (Ac), sensitivity (Sen), and specificity (Spe) of the training set and test set.

Results

The preoperative ECG of 105 patients was monitored; however, 5 patients were excluded because paroxysmal atrial fibrillation was detected by preoperative long-term monitoring. A total of 100 patients entered this study (Figure 3). After processing the long-term ECG of 100 patients, we found that POAF occurred in 31 patients, with a detection rate of 31%. Among the 31 patients with POAF, 12 were not identified in the intensive care unit (ICU) or ward, and the detection rate of POAF in routine care was 19%.

The patients' demographics and information about the operative procedures are shown in Table 1. Of the 100 patients included, 51.6 and 62.3% were males in the POAF and no-POAF

TABLE 1 Patient demographic, clinicopathologic, and operative characteristics.

Variable	no-POAF ($n = 69$)	POAF ($n = 31$)	*P*-value
Gender, male (%)	43 (62.3%)	16 (51.6%)	0.314
Age (y)	50.43 ± 10.59	55.97 ± 8.49	0.012
Height (cm)	163.44 ± 8.0	162.42 ± 8.5	0.562
Weight (kg)	64.28 ± 10.41	63.42 ± 9.0	0.693
BMI	23.96 ± 2.65	23.99 ± 2.44	0.971
DM	3 (4.3%)	0	0.550
CHD	5 (7.2%)	5 (16.1%)	0.277
RF	2 (2.9%)	0	1.000
Hypertension	16 (23.2%)	11 (35.5%)	0.200
Stroke	0	1 (3.2%)	0.310
Hyperlipidemia	2 (2.9%)	3 (9.7%)	0.171
Preoperative medication			
ß- receptor blocker	11 (15.9%)	9 (29%)	0.130
CCB	12 (17.4%)	3 (9.7%)	0.381
Statin	4 (5.8%)	3 (9.7%)	0.674
Anticoagulant	3 (4.3%)	3 (9.7%)	0.371
Amiodarone	0	0	/
Digoxin	4 (5.8%)	1 (1.6%)	1.000
ACEI, ARB	12 (17.4%)	4 (12.9%)	0.770
Diuretics	38 (55.1%)	20 (64.5%)	0.376
Preoperative TTE			
LA (mm)	40.06 ± 7.63	46 ± 11.94	0.015
RA (mm)	35.32 ± 5.54	37.48 ± 11.15	0.312
LVEF (%)	62.57 ± 9.35	59.97 ± 12.45	0.251
CRE (μmol/L)	76.59 ± 15.12	81.87 ± 12.89	0.123
GFR (ml/min/1.73 m^2)	93.00 ± 13.81	82.02 ± 14.94	0.001
Urea (mmol/L)	5.59 ± 1.32	6.40 ± 1.75	0.012
ALT (IU/L)	21.64 ± 16.16	21.23 ± 9.87	0.896
AST (IU/L)	20.90 ± 9.10	22.00 ± 5.25	0.532
ALP (IU/L)	78.91 ± 34.31	83.42 ± 30.71	0.532
TG (mmol/L)	1.47 ± 1.01	1.55 ± 1.04	0.715
CHO (mmol/L)	4.58 ± 1.04	4.39 ± 0.82	0.352
Operative details			
Surgery time (h)	4 (3,4.5)	4 (3,4.5)	0.634
CPB (min)	110 (85,133.5)	110 (96,137)	0.474
Acc (min)	73 (60,103.5)	78 (59,108)	0.864
Mechanical ventilation time (h)	33 (18.5,47)	52 (34,88)	0.001
Surgery procedures			
Single valve	34 (49.3%)	7 (22.6%)	0.012
Multiple valve	15 (21.7%)	17 (54.9%)	0.001
CABG	4 (5.8%)	3 (9.7%)	0.674
Aortic replacement	17 (24.6%)	4 (12.9%)	0.183

BMI, body mass index; DM, diabetes mellitus; CHD, coronary heart disease; RF, renal failure; CCB, calcium channel blockers; ACEI, angiotensin converting enzyme inhibitor; ARB, angiotensin-II receptor blocker; TTE, transthoracic echocardiography; LA, left atrium; RA, right atrium; LVEF, left ventricular ejection fraction; CRE, creatinine; GFR, glomerular filtration rate; ALT, glutamate pyruvate transaminase; AST, aspartate aminotransferase; ALP, alkaline phosphatase; TG, triglyceride; CHO cholesterol. CPB, cardiopulmonary bypass; Acc, aortic cross-clamp. CABG, coronary artery bypass graft.

groups, respectively. The mean age was 55.97 ± 8.49 years and 50.43 ± 10.59 years in the two groups. Preoperative transthoracic echocardiography (TTE) showed that the left atrium diameter (LAD) in the POAF group was significantly larger than that in the no-POAF group [55.97 ± 8.49 y vs. 50.43 ± 10.59 y, 95% CI (1.25, 9.82), $P = 0.012$]. In addition, the glomerular filtration rate (GFR) (82.02 ± 14.94 ml/min/1.73 m2 vs. 93.00 ± 13.81 ml/min/1.73 m2, $P < 0.001$) and blood urea

TABLE 2 Comparison of preoperative ECG P-wave characteristic.

Parameters	no-POAF	POAF	*P*-value
Pmax (ms)	167 ± 31	184 ± 37	0.018
Pmin (ms)	105 ± 22	104 ± 19	0.872
Pmean (ms)	133 ± 23	141 ± 25	0.162
Pstd	15 ± 7	19 ± 11	0.031
PWd (ms)	62 ± 28	80 ± 35	0.008
Pptmean (ms)	72 ± 16	73 ± 18	0.923
Pptstd	13 ± 6	14 ± 8	0.432

level (6.40 ± 1.75 mmol/L vs. 5.59 ± 1.32 mmol/L, $P = 0.012$) were significantly different.

In the preoperative ECG of patients in the two groups, there was a significant difference in the maximum time of the P-wave (167 ± 31 ms vs. 184 ± 37 ms, $P = 0.018$), the SD of the P-wave time (15 ± 7 vs. 19 ± 11, $P = 0.031$), and the PWd (62 ± 28 ms vs. 80 ± 35 ms, $P = 0.008$). However, the minimum time of the P-wave, the average time of the P-wave, the average peak time of the P-wave and the SD of the peak time of the P wave were not different (Table 2).

Two multivariate prediction models: (model 1) clinical model with the five selected variables age, sex, LAD, GFR, and mechanical ventilation; and (model 2) ECG and clinical models with eight variables Pmax, Pstd, PWd, age, sex, LAD, GFR, and mechanical ventilation. The AUCs for the two models were 0.86 (95% CI 0.78–0.94) and 0.89 (95% CI 0.82–0.96), respectively (Figure 4).

In scheme A, all patient data were included, and after the hyperparameters of the SVM model were adjusted (penalty Factor C = 0.58, gamma = 3.59), the Ac of the training set was 84%, and the Ac, sensitivity and specificity of the test set were 66, 22, and 74%, respectively. In scheme B, the Ac of the training set was 86%, while the Ac, sensitivity and specificity of the test set were 67, 56, and 78%, respectively, with the penalty Factor C = 95.6 and gamma = 0.83 (Table 3).

Discussion

Differences between wearable long-term electrocardiogram monitoring and conventional monitoring

We found that the detection rate of POAF by wearable long-term ECG monitoring was 31%, while the rate was only

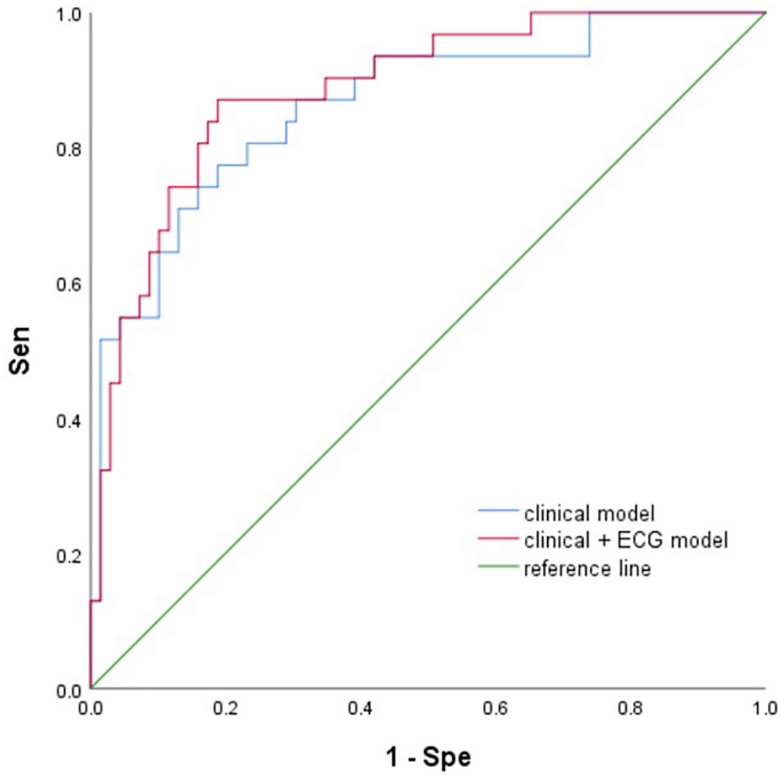

FIGURE 4
The ROC of two models. Sen, sensitivity; Spe, specificity; ECG, electrocardiogram.

TABLE 3 The results and parameters of machine learning model.

Scheme	Hyperparameter		Train (0:1)	Test (0:1)	Train set	Test set		
	C	gamma			Ac	Ac	Sen	Spe
A	0.58	3.59	19:19	47:9	0.84	0.66	0.22	0.74
B	95.6	0.83	19:19	9:9	0.86	0.67	0.56	0.78

C, penalty-factor C; Ac, accuracy; Sen, sensitivity; Spe, specificity.

19% through conventional ECG monitoring (Conventional ECG monitoring means 12-lead ECG or continues ECG monitoring after surgery in ICU). Compared with routine clinical monitoring, long-term ECG can significantly improve the detection rate of POAF. Ha et al. (9) found that enhanced rhythm monitoring in patients with a high risk of stroke could improve the detection rate of POAF by continuous ECG monitoring for 30 days after cardiac surgery, which was 10 times higher than that of routine follow-up. Due to the short time of ECG monitoring during postoperative hospitalization, routine methods cannot capture the occurrence of transient POAF.

The 2020 ESC Guidelines suggested that convenient intermittent or systematic monitoring for elderly patients could improve the detection rate of paroxysmal AF. It noted that advances in wearable technology, single-lead electrocardiogram devices and smart devices, could provide a cheap and practical option for AF detection and evaluation (6). The mSToPS (10) results showed that the detection rate of new atrial fibrillation at 4 months through a wearable ECG device was obviously increased, with a reduction in the incidence of clinical end-point events.

At present, the clinical monitoring of POAF is still intermittent and fragmented. The high detection rate and convenience of long-term ECG can greatly capture all kinds of ECG events within 7 days, 30 days or even longer without any obvious burden on patients. Not only can patients with paroxysmal AF and a high risk of POAF be identified preoperatively, but transient POAF can also be timely and accurately screened, which makes it more convenient to adopt targeted prevention and treatment.

Occurrence mechanism and influencing factors of postoperative atrial fibrillation

Previous studies had proposed a mechanism of POAF, which environmental triggers interact with substrates. When transient postoperative factors act on the sensitive atrial, due to preoperative factors and surgical induction, POAF is triggered (11). Preoperative factors such as age, sex, and underlying diseases may lead to atrial fibrosis and electrophysiological remodeling, thereby increasing sensitivity. Atrial incision and cardiopulmonary bypass can improve the sensitivity of atrial and approach the threshold of POAF. POAF is triggered by the combination of transient autonomic nervous system, immune inflammation response and oxidative stress. Inflammation plays a crucial role in cardiovascular disease (12). Tascanov et al. found that total oxidant status and DNA damage levels were significantly higher in patients with atrial fibrillation. Structural and electrophysiological changes play an important role in the development of AF. Atrial remodeling begins in sinus rhythm long before the onset of AF in patients with recurrent PAF. This is a time-dependent process that can be explained as adaptive changes of myocytes to protect the atrium from external stress. It is therefore important to identify patients with PAF at an early stage (13). Ocak and Tascanov (14). Combined use of troponin I and P-wave dispersion for predicting AF recurrence.

Comparing the baseline data of the two groups, the POAF group was significantly older than the no-POAF group. Most studies (15, 16) reported that the older the patients were, the more obvious their cardiovascular structural and electrophysiological abnormalities were, leading to a non-linear increase in the incidence of POAF. The incidence was significantly higher in patients over 55 years.

LA diameter has been identified as an important risk factor for AF (17, 18). AF is rare when the LA diameter is less than 40 mm, and the risk of AF increases by 39% for each 5 mm increase (18, 19). A gradual increase in LA diameter is associated with the transition from sinus rhythm to paroxysmal AF to permanent AF (19).

Our study found that poor preoperative renal function is associated with the occurrence of POAF. The mechanism of AF induced by renal insufficiency is not completely clear. Myocardial fibrosis may be aggravated by hypertension, volume overload and activation of the renin-angiotensin-aldosterone system (RAAS) (20). In patients undergoing cardiac surgery, the high level of acute systemic inflammation and oxidative stress leads to renal hypoperfusion, which activates the autonomic nervous system and RAAS system and leads to arrhythmias (21, 22).

Relationship between P-wave and postoperative atrial fibrillation in preoperative sinus electrocardiogram

Even apparently normal hearts have undergone structural and electrical conduction changes as they progressed from sinus rhythm to AF (23). Changes in atrial structure, such as

myocardial hypertrophy, fibrosis and enlargement, occur before the occurrence of AF, which all lead to weak electrocardiogram changes in the atria (2). Sinus rhythm cannot completely represent the function of the atria (3). The insignificant changes in the P-wave on ECG reflect local non-sinus atrial electrical activity. These subtle changes can be detected by various algorithms and serve as important factors in predicting the occurrence of AF (7, 24). Many ECG characteristics have been regarded as important predictors, especially P waves.

P wave duration is an important reference for the occurrence of POAF. A shortened atrial refractory period and reduced atrial conduction rate lead to atrial conduction block and a prolonged conduction time, resulting in a prolonged P wave duration (25). PWd has gradually been recognized an important predictor of atrial fibrillation after cardiac surgery and electrical cardioversion (26). The heterogeneity of atrial structure or electrophysiology in the early stage of AF plays an important role in reentry and affects the P wave duration at different times, which is more accurate than using P wave duration alone (27). An increase in PWd suggests that there is heterogeneous electrical activity in different parts of the atria. Chandy et al. (26) analyzed 300 patients who underwent CABG and found that an increase in postoperative PWd compared to preoperative PWd was an independent predictor. Lazzeroni et al. (28) compared the postoperative PWd and P wave duration after CABG and valve surgery, which showed that both had good predictive ability and the PWd variation was higher in the POAF group.

The area of the P wave is also considered to be a marker of atrial structural abnormalities (29).

Besides, under the premise of sinus rhythm, the product of the amplitude depth, and duration of the negative part of the P wave is calculated when the P wave of the V1 lead is bidirectional (30, 31). P wave negative terminal force (PtfV1) is a sensitive marker for judging left atrial enlargement (32). Atrial fibrosis and scarring can indirectly lead to abnormal PtfV1.

Most of the ECGs in previous studies were from public databases or 12-lead ECGs of patients who were retrospectively collected. There are many problems with these approaches, such as whether the routine ECG of several seconds can completely represent the preoperative ECG changes and trends of patients; retrospective collection and database ECG may have omission and bias, which can lead to large errors in ECG feature calculation. Studies on long-term ECG are mostly limited to the screening of events such as AF, and there are few reports on the analysis of its waveform characteristics. Although the long-term data may be affected due to the patient's wearing mode and various noises, its validity may avoid the problems of short-term conventional ECG, so feature calculation can be carried out more accurately.

In our study, only the P wave characteristics were calculated. Pft is a bidirectional waveform, which requires high signal quality. In actual detection, we found that the long-term ECG data were not very clean, so it was difficult to detect and calculate this feature. The absence of such features may also limit the results. The heart rate variability has become one of the most excellent points to predict the POAF base on 12-lead ECG in the previous studies. In the process of labeling all preoperative ECG data, we found that there was variability in P waveform at different time periods. First of all, it may be because of the inconsistent activity state and autonomic nerve excitability at different times. At night, the sleep state and parasympathetic dominance of the patient lead to negative chronotropic and negative metamorphosis of the heart. During the day, the increased activity of the patient and the sympathetic nerve lead to the increased heart rate, and the increased conductivity of excitement in the heart. Secondly, the patient's posture change and wearing problems will also lead to the change of waveform, obvious interference or even false performance. In our study, P-wave signs were selected to analyze, however, heart rate variability requires dynamic analysis of patients' ECG data for 24 h or more, which is more affected by signal quality. Therefore, basing on the advantages and disadvantages of long-term ECG, the current study only calculates the characteristics of part of P waves, and has not introduced dynamic analysis and heart rate variability. In the future research, we will deal with different types of feature group computation and model building.

Our results showed that a model incorporating baseline clinical data and ECG parameters is more effective in predicting POAF than a model using clinical characteristics alone. The model 2 included 5 kinds of clinical information (gender, age, LA, GFR, mechanical ventilation time) and 3 kinds of P wave parameters (Pmax, Pstd, PWd). The AUC was 0.89, and the predictive performance of the model was significantly better than that of a previous study with multiple clinical variables. Preoperative changes in the P wave are important factors for predicting the occurrence of POAF.

With our model, we could identify patients who may be prone to POAF by preoperative ECG. For these patients, it is necessary to strengthen their perioperative management, such as more rhythm monitoring, maintaining the balance of the internal environment, strengthening anti-infection treatment, and appropriately increasing the duration of mechanical ventilation, which can prevent POAF from being triggered by a series of postoperative factors.

Prediction of postoperative atrial fibrillation by artificial intelligence and machine learning

Artificial intelligence and machine learning can simulate or realize human learning behavior to require new knowledge and skills and reorganizes its existing knowledge structure to continuously improve its performance. In previous studies, ECG data obtained by traditional monitoring methods were analyzed by artificial intelligence and machine learning, but

long-term ECG data were used in our study. The larger amount of data and the larger time span make the analysis more specific.

There are many traditional machine learning models, including naïve Bayes, K nearest neighbor, logistic regression, decision making Tree, random forest, XGboosting algorithm, and SVM. Different models have different applications and advantages and disadvantages. SVM was used in our study. SVM is a widely used binary classifier using supervised learning. It is based on the theory of computational learning and structural risk minimization and has obvious advantages in theoretical methods. It has many unique advantages in solving small sample, non-linear and high-dimensional pattern recognition problems and can overcome the curse of dimensionality to a large extent (33, 34). In a binary problem, it mainly introduces the samples that need to be classified into a high-dimensional space and attempts to create an optimal hyperplane to divide the samples into two categories so that the hyperplane can ensure the classification Ac and maximize the area on both sides of the hyperplane. It can ensure that the extremum is the optimal solution, which makes it have good generalization ability.

The penalty factor C and Gamma kernel function are two important hyperparameters in SVM. The parameters set manually before machine learning. The value of the penalty factor C balances the empirical risk (the ability to fit the sample) and the structural risk (the ability to predict the test sample). Although the number of people in the two training sets is the same, the hyperparameter values will change according to the different samples randomly sampled. In scheme A, the model is prone to underfitting if the value of C is small; In scheme B, if C is large, the model is prone to overfitting. Although there is little difference in Ac between the test set and training set of the two groups, the sensitivity in the test set of scheme A is low, which affects the Ac to a certain extent. However, in the more rigorous scheme B, the sensitivity and specificity of the test set are higher, and the test effect is better.

However, the performance of our model is not very good for POAF detection, showing low Ac and a low positive prediction rate. The reason may be as follows: (1) the sample size is small, and the classifier cannot learn the overall distribution of various categories well, so the classification effect is not good. The results of AI and machine learning depend on the quality and quantity of data. Although traditional machine learning can analyze the characteristics of hundreds of ECGs, the results were not as good as those of previous large studies that included exponentially more data points. (2) The types of data were relatively complex. Although all signals were manually calibrated, some parts of the signal were still of poor quality, which affected the results of P wave detection and feature calculation. (3) Current feature analysis was insufficient. Although atrial waves play an important role in the judgment of atrial fibrillation, in fact, waves are susceptible to noise, so additional research on atrial waves in long-term monitoring environments may be beneficial.

Karri et al. (35) compared the predictive performance of 6 machine learning models (random forest, decision tree, logistic regression, K-nearest neighbor, SVM, gradient boosting) and the POAF score for the occurrence of POAF in the ICU after cardiac surgery and found that according to the preoperative clinical data, the performance of machine learning was better than that of the clinical score. The use of AI-equipped medical apps and tools on wearable devices can reduce the dependence on expert care and the cost to the health care system. Perez et al. (36) evaluated the monitoring algorithm of Apple Watch. They found that 34% of patients were confirmed to have atrial fibrillation, and the positive predictive value was 0.84. In addition to smartwatches, photoplethysmography (PPG) measurements of contactless faces and fingertips using a smartphone camera also showed excellent potential for screening and diagnosing atrial fibrillation. Yan et al. (37) used a digital camera and a deep convolutional neural network to prospectively evaluate the feasibility of high-throughput atrial fibrillation detection. Therefore, with the advent of the era of mobile technology, wearable devices with AI would be sensitive to the detection and evaluation of AF, which will be a cheap, non-invasive monitoring method in the future (38).

Innovation and limitation

The innovation of this study is that there are still few applications of long-term ECG monitoring for POAF. The study explored the use of portable long-term ECG monitoring and machine learning model to predict the occurrence of POAF after cardiopulmonary bypass in patients with preoperative sinus rhythm.

Of course, the limitations of this study are as follows: 1. The included sample size is relatively small, which may affect the results. 2. ECG signal quality limits the effective of machine learning model.

Conclusion

This prospective, observational study analyzed the differences in long-term ECG parameters in patients undergoing cardiac surgery with preoperative sinus rhythm and evaluated the performance of a machine learning model constructed with P wave characteristics to predict POAF. The results of this study showed that long-term ECG monitoring could significantly improve the detection rate of POAF. The model combining P wave parameters and clinical data performed better in predicting POAF. Machine learning based on P wave parameters can predict the occurrence of POAF.

Data availability statement

The raw data supporting the conclusions of this article will be made available by the authors, without undue reservation.

Ethics statement

The studies involving human participants were reviewed and approved by West China hospital. The patients/participants provided their written informed consent to participate in this study. Written informed consent was obtained from the individual(s) for the publication of any potentially identifiable images or data included in this article.

Author contributions

ZW and CY: methodology. KH, WL, and SL: analysis and writing original draft. LB and CL: data gathering. YX, YL, and HY: review. All authors have read and approved the final version of the manuscript.

Funding

This study was supported by the National Natural Science Foundation of China (Project No. 82172060) "Assessment of sensitivity and early warning effect of atrial fibrillation with sinus rhythm based on ECG variability and atrial fibrosis."

Acknowledgments

The technical and device assistance was supported by the Shanghai Yuanxin Medical Technology Company.

Conflict of interest

The authors declare that the research was conducted in the absence of any commercial or financial relationships that could be construed as a potential conflict of interest.

Publisher's note

All claims expressed in this article are solely those of the authors and do not necessarily represent those of their affiliated organizations, or those of the publisher, the editors and the reviewers. Any product that may be evaluated in this article, or claim that may be made by its manufacturer, is not guaranteed or endorsed by the publisher.

References

1. Gudbjartsson T, Helgadottir S, Sigurdsson MI, Taha A, Jeppsson A, Christensen TD, et al. New-onset postoperative atrial fibrillation after heart surgery. *Acta Anaesthesiol Scand.* (2020) 64:145–55. doi: 10.1111/aas.13507

2. Bellotti P, Spirito P, Lupi G, Vecchio C. Left atrial appendage function assessed by transesophageal echocardiography before and on the day after elective cardioversion for nonvalvular atrial fibrillation. *Am J Cardiol.* (1998) 81:1199–202. doi: 10.1016/s0002-9149(98)00089-7

3. Warraich HJ, Gandhavadi M, Manning WJ. Mechanical discordance of the left atrium and appendage: a novel mechanism of stroke in paroxysmal atrial fibrillation. *Stroke.* (2014) 45:1481–4. doi: 10.1161/STROKEAHA.114.004800

4. Nattel S, Harada M. Atrial remodeling and atrial fibrillation: recent advances and translational perspectives. *J Am Coll Cardiol.* (2014) 63:2335–45. doi: 10.1016/j.jacc.2014.02.555

5. Nattel S, Dobrev D. Electrophysiological and molecular mechanisms of paroxysmal atrial fibrillation. *Nat Rev Cardiol.* (2016) 13:575–90. doi: 10.1038/nrcardio.2016.118

6. Hindricks G, Potpara T, Dagres N, Arbelo E, Bax JJ, Blomström-Lundqvist C, et al. ESC scientific document group. 2020 ESC guidelines for the diagnosis and management of atrial fibrillation developed in collaboration with the European association for cardio-thoracic surgery (EACTS): the task force for the diagnosis and management of atrial fibrillation of the European society of cardiology (ESC) developed with the special contribution of the European heart rhythm association (EHRA) of the ESC. *Eur Heart J.* (2021) 42:373–498. doi: 10.1093/eurheartj/ehaa612

7. Attia ZI, Noseworthy PA, Lopez-Jimenez F, Asirvatham SJ, Deshmukh AJ, Gersh BJ, et al. An artificial intelligence-enabled ECG algorithm for the identification of patients with atrial fibrillation during sinus rhythm: a retrospective analysis of outcome prediction. *Lancet.* (2019) 394:861–7. doi: 10.1016/S0140-6736(19)31721-0

8. Martínez JP, Almeida R, Olmos S, Rocha AP, Laguna P. A wavelet-based ECG delineator: evaluation on standard databases. *IEEE Trans Biomed Eng.* (2004) 51:570–81. doi: 10.1109/TBME.2003.821031

9. Ha ACT, Verma S, Mazer CD, Quan A, Yanagawa B, Latter DA, et al. SEARCH AF CardioLink-1 investigators. Effect of continuous electrocardiogram monitoring on detection of undiagnosed atrial fibrillation after hospitalization for cardiac surgery: a randomized clinical trial. *JAMA Netw Open.* (2021) 4:e2121867. doi: 10.1001/jamanetworkopen.2021.21867

10. Steinhubl SR, Waalen J, Edwards AM, Ariniello LM, Mehta RR, Ebner GS, et al. Effect of a home-based wearable continuous ECG monitoring patch on detection of undiagnosed atrial fibrillation: the mSToPS randomized clinical trial. *JAMA.* (2018) 320:146–55. doi: 10.1001/jama.2018.8102

11. Nattel S. New ideas about atrial fibrillation 50 years on. *Nature.* (2002) 415:219–26. doi: 10.1038/415219a

12. Hartman J, Frishman WH. Inflammation and atherosclerosis: a review of the role of interleukin-6 in the development of atherosclerosis and the potential for targeted drug therapy. *Cardiol Rev.* (2014) 22:147–51. doi: 10.1097/CRD.0000000000000021

13. Tascanov MB, Tanriverdi Z, Gungoren F, Besli F, Erkus ME, Altiparmak IH, et al. Relationships between paroxysmal atrial fibrillation, total oxidant status, and DNA damage. *Rev Port Cardiol.* (2021) 40:5–10. doi: 10.1016/j.repc.2020.05.011

14. Ocak M, Tascanov MB. Clinical value of the combined use of P-wave dispersion and troponin values to predict atrial fibrillation recurrence in patients with paroxysmal atrial fibrillation. *Rev Port Cardiol.* (2021) 40:679–84. doi: 10.1016/j.repce.2020.10.022

15. Spach MS, Dolber PC. Relating extracellular potentials and their derivatives to anisotropic propagation at a microscopic level in human cardiac muscle. Evidence for electrical uncoupling of side-to-side fiber connections with increasing age. *Circ Res.* (1986) 58:356–71. doi: 10.1161/01.res.58.3.356

16. Shen J, Lall S, Zheng V, Buckley P, Damiano RJ Jr., Schuessler RB. The persistent problem of new-onset postoperative atrial fibrillation: a single-institution experience over two decades. *J Thorac Cardiovasc Surg.* (2011) 141:559–70. doi: 10.1016/j.jtcvs.2010.03.011

17. Psaty BM, Manolio TA, Kuller LH, Kronmal RA, Cushman M, Fried LP, et al. Incidence of and risk factors for atrial fibrillation in older adults. *Circulation.* (1997) 96:2455–61. doi: 10.1161/01.cir.96.7.2455

18. Vaziri SM, Larson MG, Benjamin EJ, Levy D. Echocardiographic predictors of nonrheumatic atrial fibrillation. The Framingham heart study. *Circulation.* (1994) 89:724–30. doi: 10.1161/01.cir.89.2.724

19. Henry WL, Morganroth J, Pearlman AS, Clark CE, Redwood DR, Itscoitz SB, et al. Relation between echocardiographically determined left atrial size and atrial fibrillation. *Circulation.* (1976) 53:273–9. doi: 10.1161/01.cir.53.2.273

20. Chua SK, Shyu KG, Lu MJ, Hung HF, Cheng JJ, Chiu CZ, et al. Renal dysfunction and the risk of postoperative atrial fibrillation after cardiac surgery: role beyond the CHA2DS2-VASc score. *Europace.* (2015) 17:1363–70. doi: 10.1093/europace/euu360

21. Chua SK, Shyu KG, Lu MJ, Hung HF, Cheng JJ, Lee SH, et al. Association between renal function, diastolic dysfunction, and postoperative atrial fibrillation following cardiac surgery. *Circ J.* (2013) 77:2303–10.

22. Limite LR, Magnoni M, Berteotti M, Peretto G, Durante A, Cristell N, et al. The predictive role of renal function and systemic inflammation on the onset of de novo atrial fibrillation after cardiac surgery. *Eur J Prev Cardiol.* (2016) 23:206–13. doi: 10.1177/2047487314564896

23. Kottkamp H. Human atrial fibrillation substrate: towards a specific fibrotic atrial cardiomyopathy. *Eur Heart J.* (2013) 34:2731–8. doi: 10.1093/eurheartj/eht194

24. Steinberg JS, Zelenkofske S, Wong SC, Gelernt M, Sciacca R, Menchavez E. Value of the P wave signal-averaged ECG for predicting atrial fibrillation after cardiac surgery. *Circulation.* (1993) 88:2618–22. doi: 10.1161/01.cir.88.6.2618

25. Janse MJ. Why does atrial fibrillation occur?. *Eur Heart J.* (1997) 18:12–8. doi: 10.1093/eurheartj/18.suppl_c.12

26. Chandy J, Nakai T, Lee RJ, Bellows WH, Dzankic S, Leung JM. Increases in P-wave dispersion predict postoperative atrial fibrillation after coronary artery bypass graft surgery. *Anesth Analg.* (2004) 98:303–10. doi: 10.1213/01

27. Boriani G, Diemberger I, Biffi M, Camanini C, Valzania C, Corazza I, et al. P wave dispersion and short-term vs. late atrial fibrillation recurrences after cardioversion. *Int J Cardiol.* (2005) 101:355–61. doi: 10.1016/j.ijcard.2004.03.039

28. Lazzeroni D, Parati G, Bini M, Piazza P, Ugolotti PT, Camaiora U, et al. P-wave dispersion predicts atrial fibrillation following cardiac surgery. *Int J Cardiol.* (2016) 203:131–3. doi: 10.1016/j.ijcard.2015.10.143

29. Tse G, Lakhani I, Zhou J, Li KHC, Lee S, Liu Y, et al. P-wave area predicts new onset atrial fibrillation in mitral stenosis: a machine learning approach. *Front Bioeng Biotechnol.* (2020) 8:479. doi: 10.3389/fbioe.2020.00479

30. Tiffany Win T, Ambale Venkatesh B, Volpe GJ, Mewton N, Rizzi P, Sharma RK, et al. Associations of electrocardiographic P-wave characteristics with left atrial function, and diffuse left ventricular fibrosis defined by cardiac magnetic resonance: the PRIMERI Study. *Heart Rhythm.* (2015) 12:155–62. doi: 10.1016/j.hrthm.2014.09.044

31. Huang Z, Zheng Z, Wu B, Tang L, Xie X, Dong R, et al. Predictive value of P wave terminal force in lead V1 for atrial fibrillation: a meta-analysis. *Ann Noninvasive Electrocardiol.* (2020) 25:e12739. doi: 10.1111/anec.12739

32. Eranti A, Aro AL, Kerola T, Anttonen O, Rissanen HA, Tikkanen JT, et al. Prevalence and prognostic significance of abnormal P terminal force in lead V1 of the ECG in the general population. *Circ Arrhythm Electrophysiol.* (2014) 7:1116–21. doi: 10.1161/CIRCEP.114.001557

33. Deo RC. Machine learning in medicine. *Circulation.* (2015) 132:1920–30. doi: 10.1161/CIRCULATIONAHA.115.001593

34. Johnson KW, Torres Soto J, Glicksberg BS, Shameer K, Miotto R, Ali M, et al. Artificial intelligence in cardiology. *J Am Coll Cardiol.* (2018) 71:2668–79. doi: 10.1016/j.jacc.2018.03.521

35. Karri R, Kawai A, Thong YJ, Ramson DM, Perry LA, Segal R, et al. Machine learning outperforms existing clinical scoring tools in the prediction of postoperative atrial fibrillation during intensive care unit admission after cardiac surgery. *Heart Lung Circ.* (2021) 30:1929–37. doi: 10.1016/j.hlc.2021.05.101

36. Perez MV, Mahaffey KW, Hedlin H, Rumsfeld JS, Garcia A, Ferris T, et al. Apple Heart Study Investigators. Large-scale assessment of a smartwatch to identify atrial fibrillation. *N Engl J Med.* (2019) 381:1909–17. doi: 10.1056/NEJMoa1901183

37. Yan BP, Lai WHS, Chan CKY, Au ACK, Freedman B, Poh YC, et al. High-throughput, contact-free detection of atrial fibrillation from video with deep learning. *JAMA Cardiol.* (2020) 5:105–7. doi: 10.1001/jamacardio.2019.4004

38. Wasserlauf J, You C, Patel R, Valys A, Albert D, Passman R. Smartwatch performance for the detection and quantification of atrial fibrillation. *Circ Arrhythm Electrophysiol.* (2019) 12:e006834. doi: 10.1161/CIRCEP.118.006834

frontiers | Frontiers in Physiology

TYPE Original Research
PUBLISHED 29 September 2022
DOI 10.3389/fphys.2022.1001060

OPEN ACCESS

EDITED BY
Jose F. Rodriguez Matas,
Politecnico di Milano, Italy

REVIEWED BY
Laura Martinez-Mateu,
Rey Juan Carlos University, Spain
Matthijs Cluitmans,
Maastricht University, Netherlands

*CORRESPONDENCE
Anna McCann,
anna.mccann@epfl.ch

SPECIALTY SECTION
This article was submitted to Cardiac Electrophysiology, a section of the journal Frontiers in Physiology

RECEIVED 22 July 2022
ACCEPTED 08 September 2022
PUBLISHED 29 September 2022

CITATION
McCann A, Luca A, Pascale P, Pruvot E and Vesin J-M (2022), Novel spatiotemporal processing tools for body-surface potential map signals for the prediction of catheter ablation outcome in persistent atrial fibrillation. *Front. Physiol.* 13:1001060. doi: 10.3389/fphys.2022.1001060

Novel spatiotemporal processing tools for body-surface potential map signals for the prediction of catheter ablation outcome in persistent atrial fibrillation

Anna McCann[1]*, Adrian Luca[2], Patrizio Pascale[2], Etienne Pruvot[2] and Jean-Marc Vesin[1]

[1]Applied Signal Processing Group, Department of Electrical Engineering, Swiss Federal Institute of Technology, Lausanne, Switzerland, [2]Service of Cardiology, Lausanne University Hospital, Lausanne, Switzerland

Background: Signal processing tools are required to efficiently analyze data collected in body-surface-potential map (BSPM) recordings. A limited number of such tools exist for studying persistent atrial fibrillation (persAF). We propose two novel, spatiotemporal indices for processing BSPM data and test their clinical applicability through a comparison with the recently proposed non-dipolar component index (NDI) for prediction of single-procedure catheter ablation (CA) success rate in persAF patients.

Methods: BSPM recordings were obtained with a 252-lead vest in 13 persAF patients (8 men, 63 ± 8 years, 11 ± 13 months sustained AF duration) before undergoing CA. Each recording was divided into seven 1-min segments of high signal quality. Spatiotemporal ventricular activity (VA) cancellation was applied to each segment to isolate atrial activity (AA). The two novel indices, called error-ratio, normalized root-mean-square error (ER_{NRMSE}) and error-ratio, mean-absolute error (ER_{ABSE}), were calculated. These indices quantify the capacity of a subset of BSPM vest electrodes to accurately represent the AA, and AA dominant frequency (DF), respectively, on all BSPM electrodes over time, compared to the optimal principal component analysis (PCA) representation. The NDI, quantifying the fraction of energy retained after removal of the three largest PCs, was also calculated. The two novel indices and the NDI were statistically compared between patient groups based on single-procedure clinical CA outcome. Finally, their predictive power for univariate CA outcome classification was assessed using receiver operating characteristic (ROC) analysis with cross-validation for a logistic regression classifier.

Results: Patient clinical outcomes were recorded 6 months following procedures, and those who had an arrhythmia recurrence at least 2 months post-CA were defined as having a negative outcome. Clinical outcome information was available for 11 patients, 6 with arrhythmia recurrence. Therefore, a total of 77 1-min AA-BSPM segments were available for analysis. Significant differences were found in the values of the novel indices and NDI between patients with arrhythmia recurrence post-ablation and those

without. ROC analysis showed the best CA outcome predictive performance for ER_{NRMSE} (AUC = 0.77 ± 0.08, sensitivity = 76.2%, specificity = 84.8%).

Conclusion: Significant association was found between the novel indices and CA success or failure. The novel index ER_{NRMSE} additionally shows good predictive power for single-procedure CA outcome.

KEYWORDS

atrial fibrillation, catheter ablation, body surface potential mapping, spatiotemporal analysis, outcome stratification

1 Introduction

In contrast to the many studies that have analyzed the 12-lead electrocardiogram (ECG) for the study of atrial fibrillation (AF), relatively few have developed AF analysis tools for body-surface potential map (BSPM) signals. Despite the development of these 12-lead ECG based indices, to our knowledge, the use of ECG for AF in clinical practice is still limited to its diagnosis (Lankveld et al., 2014). The traditional 12-lead ECG was designed to capture mainly ventricular activity (VA), therefore, BSPM signals could harbor additional information from the atrial activity (AA) relevant for AF analysis.

Various studies have performed analyses of BSPM data for the study of AF. For example (Bonizzi et al., 2010), applied principal component analysis (PCA) to BSPM data and proposed two novel parameters derived from the resulting PCA mixing matrices to quantify complexity and stationarity in BSPM recordings, finding a significant inverse correlation between the two. It was additionally found that these parameters formed clusters for organized vs. disorganized AF, but no further clinical application was proposed by the authors. The study in (Di Marco et al., 2012) proposed four parameters to quantify spatial organization, variability, spectral concentration, and spectral variability of BSPM signals. They found that greater spatial organization was associated with reduced variability of spatial organization over time, and that lower spectral variability was associated with increased spectral concentration. However, the clinical impact of the parameters was not assessed. Later (Meo et al., 2018), proposed the non-dipolar component index (NDI), which was calculated as the residual variance not accounted for by the first three principal components (PCs) of concatenated TQ segments of BSPM signals. It was found that the NDI correlated with AF complexity and AF termination at the end of catheter ablation (CA) procedures. However, correlation with clinical CA outcome was not reported, and the NDI leaves unexploited the temporal variability of BSPM signals found to be indicative of AF organization in (Bonizzi et al., 2010; Di Marco et al., 2012). These parameters do however show promise for capturing information from BSPM signals relevant for the computational analysis of AF signals. Additionally, they are all linked in that they use PCA in the computation of their indices. However, insufficient attention has been paid to the temporal aspect of the data, with most of the parameters using concatenated TQ segments. While this method has merit as it eliminates the possibility of interfering VA, it precludes a temporal analysis, and we aim to address this with our novel indices.

Despite the above research, the use of BSPM for persAF treatment remains limited in clinical practice, and there are not many tools available for its efficient analysis. Apart from its use in electrocardiographic imaging (ECGI), the clinical advantage of BSPM over 12-lead ECG signal analysis for AF remains unclear. In this study, we draw on the above research to propose two novel indices also employing PCA: error ratio, normalized root-mean square error (ER_{NRMSE}) and error ratio, mean absolute error (ER_{ABSE}), which exploit spatiotemporal information in BSPM recordings. The indices make use of the full set of BSPM electrodes by measuring how well only a subset of electrodes can represent AA on all BSPM electrodes compared to the optimal PCA-representation. The indices also encapsulate the temporal variability of the AA using long-duration BSPM recordings. We hypothesized that when subsets can represent AA nearly as well as the optimal PCA-representation, the AF is more organized and stable with time, and thus more likely to respond well to CA treatment. When the optimal PCA representation is much better than the electrode subset representation, we hypothesized that this could be indicative of a disorganized AF that is more variable over time, manifested as greater spatial variability in the recorded AA on the BSPM vest. In this way, we aim to provide additional tools which efficiently utilize the large amount of data incurred when working with BSPM recordings and show their clinical relevance for persAF disease quantification through correlation with and prediction of single-procedure CA outcome. We first discuss the study population and BSPM signal acquisition and pre-processing. An overview of the novel indices and BSPM vest electrode subset selection required for their calculation is then given. The statistical cross-validation protocol used to evaluate their clinical relevance is then presented. Finally, the results, implications, and limitations of the study are discussed.

10.3389/fphys.2022.1001060

TABLE 1 Study population baseline characteristics.

	$n = 13$
Sex (M/F)	8/5
Age, mean ± std, years	63 ± 8
Hypertension, *n*	6
Coronary artery disease, *n*	2
Heart Failure, *n*	3
Valvular Disease, *n*	3
Diabetes, *n*	2
Left ventricular ejection fraction, mean ± std, %	51 ± 13
Sustained AF duration, mean ± std, months	11 ± 13

std, standard deviation.

FIGURE 1
CardioInsight™ BSPM vest with 252 unipolar electrodes. The reference electrode is not shown. **(A)** Anterior part of vest with 126 electrodes. **(B)** Posterior part of vest with 126 electrodes.

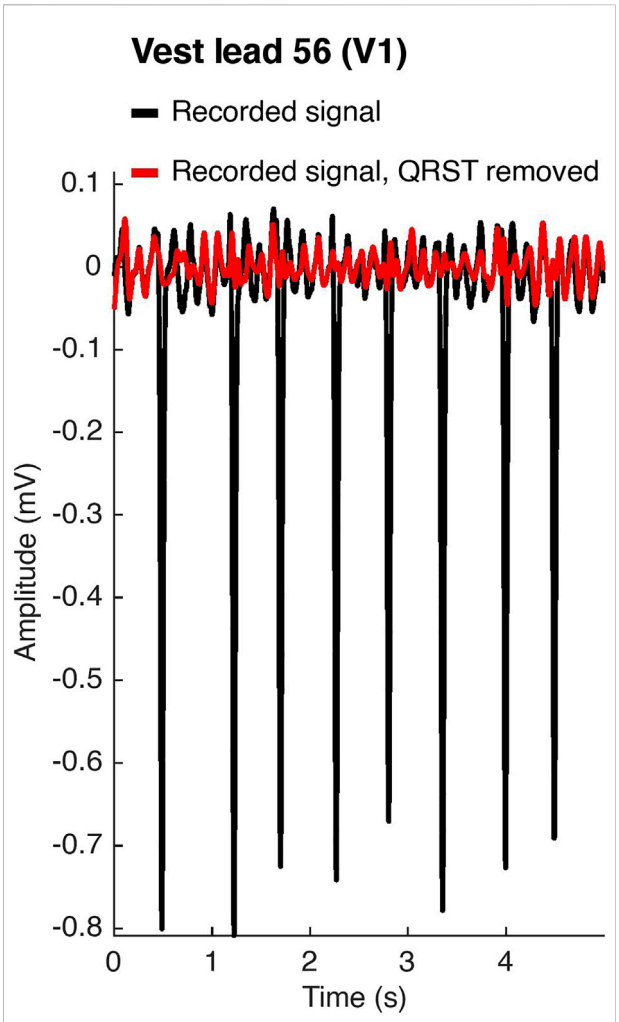

FIGURE 2
Atrial activity extraction. In black, the original recorded signal on vest lead 56, which corresponds to lead V_1 of the standard 12-lead ECG configuration. In red, the signal after spatiotemporal QRST cancellation.

2 Methods

2.1 Study population

We studied a total of 13 patients admitted for CA of drug-refractory persAF. Their baseline characteristics are reported in Table 1. The CA endpoint was complete pulmonary vein isolation (PVI). Electrical cardioversion was performed on patients still in AF after PVI completion to restore sinus rhythm (SR). Patients were then monitored throughout a follow up period and divided into two groups: 1) SR and arrhythmia recurrence (AR), according to whether they experienced an AR within 6 months, but at least 2 months after undergoing CA. The study protocol was approved by the

Lausanne University Hospital Human Research Ethics Committee, and all patients provided written informed consent.

2.2 BSPM signal acquisition and preprocessing

BSPMs were recorded with a 252-lead vest (CardioInsight™, Medtronic, MN, United States) at a sampling frequency of 1 kHz in persAF patients the day before undergoing CA at Lausanne University Hospital in Switzerland. A schematic of the vest is shown in Figure 1. Mean signal recording duration was 17 ± 4 min. Electrode contact and signal quality varied considerably over the course of the recording duration. Recordings were therefore visually inspected, and 1-min segments with good signal quality were extracted from the long duration recordings for further analysis. Remaining leads with poor signal quality were removed (up to 30 leads), and signals from high quality leads were used to estimate BSPM signals at the removed locations using interpolation. Recordings were then processed for removing baseline drift and high frequency noise (bandpass filter 1–30 Hz). R-peaks were detected and QRST delineation was performed in each lead using an open source ECG delineation toolbox (Pilia et al., 2021). In order to evaluate BSPM signals free of ventricular interference and enable a temporal analysis, the spatiotemporal method for QRST cancellation was applied (Stridh and Sornmo, 2001). This method, which operates on a single-beat, multi-lead basis, was chosen due to its exploitation of multiple leads and its tested performance (Langley et al., 2006). Clustering was applied to QRST complexes across all leads, so that the complexes used in each ensemble average had similar shapes. The extracted 1-min atrial activity BSPM segments (AA-BSPM) devoid of VA were then further normalized to have zero mean and unit variance, and low-pass filtered by a 10th order Butterworth filter with a cutoff frequency of 30 Hz to eliminate signal discontinuities introduced by spatiotemporal VA cancellation. An example of a BSPM signal before and after AA extraction is shown in Figure 2.

The power spectral densities (PSD) of all AA-BSPM segments were computed using a Welch periodogram (2-s Hamming window with a 4,096 Fast Fourier transform per window and 50% window overlap) to determine the body surface distribution of the atrial DF. The DF was defined as the highest peak in the power spectrum.

2.3 AA-BSPM reconstruction using a subset of BSPM electrodes

The purpose of this section is to describe how only a subset of vest electrode signals may be used to reconstruct the signals on all vest electrodes, as this is an important concept in the development of the novel indices ER_{NRMSE} and ER_{ABSE} (elaborated in Section 2.5). Each AA-BSPM segment may be represented by a matrix $X \in \mathbb{R}^{m\times n}$, with m consecutive samples in the rows, and n synchronously recorded signals in the columns, one from each BSPM vest electrode. Given an arbitrary subset of signals recorded on k vest electrodes, $S \in \mathbb{R}^{m\times k}$, $k < n$, the minimum least-squares transformation of the subset matrix S to approximate the full BSPM signal matrix X is given by:

$$\underset{A}{\operatorname{argmin}} \|X - SA\|_F^2 \tag{1}$$

whose known solution is $A = S^+X$, where $(\cdot)^+$ and $\|\cdot\|_F$ denote the Moore-Penrose pseudoinverse and the Frobenius norm of a matrix, respectively. Then, to represent the full BSPM signal matrix X as accurately as possible, one should aim to find a subset S of vest electrode signals such that the AA-BSPM segment X is best represented by S, most commonly in terms of the Frobenius norm:

$$\underset{S}{\operatorname{argmin}} \|X - SS^+X\|_F^2 \tag{2}$$

Finding the subset S is thought to be an NP-hard problem, with $\binom{n}{k}$ solutions, (Civril, 2014; Altschuler et al., 2016). Therefore, finding the optimal solution would involve searching the $\binom{n}{k}$ solutions, which for n and k of reasonable size is not feasible. The goal for electrode subset selection is then to find good, but not necessarily optimal subsets, and this will be discussed in the next section. An upper limit on the performance of a subset of k electrode signals for reconstructing the signals on all n electrodes is given by reconstruction using the first k principal components (PCs), since the explicit goal of PCA is to minimize the Frobenius reconstruction criterion. The PCs may be obtained efficiently by singular value decomposition (SVD) of X, $X = U\Sigma V^T$. The first k PCs are the columns of the matrix $U_k\Sigma_k$, where U_k contains the first k columns of U, and Σ_k contains the $k \times k$ upper-left portion of Σ. The corresponding rank-k reconstruction of X is given by:

$$X_k = U_k\Sigma_k V_k^T \tag{3}$$

where V_k contains the first k columns of V. Then the minimum approximation error $\|X - Q\|_F^2$ which can be attained by an arbitrary rank-k matrix is achieved when $Q = X_k$. Note that each PC is a linear combination of the signals on all n electrodes of X. Therefore, the rank-k PCA solution X_k is distinct from reconstruction using a subset S of k vest electrode signals and serves only as an upper bound to compare how well a given S captures the information on all BSPM electrodes.

2.4 Electrode subset selection and comparison

The purpose of this section is to describe the different subsets of vest electrodes we used for the calculation of the novel indices

ER_{NRMSE} and ER_{ABSE}, which will be elaborated in the next section. We also describe the characterization of the vest electrode subsets in terms of their capacity to accurately represent AA-BSPM signal information on all vest electrodes and compare this to the optimal PCA representation, as this is an important concept for the understanding of the novel indices.

1) Sequential: This algorithm was first proposed by (Lux et al., 1978) and later used by (Guillem et al., 2008, 2009) for selecting electrode subsets from a wider array of body vest electrodes. As its name suggests, this sequential approach greedily chooses electrodes one after the other, at each step picking the column containing the electrode signal which minimizes the reconstruction error, i.e., Eq. 2. This algorithm is in no way guaranteed to be optimal, since at each step it only considers that one additional electrode must be selected, rather than considering the entire subset. However, it can be relatively efficient (Farahat et al., 2011; Altschuler et al., 2016) and in general has had good performance for electrode selection. Therefore, it was chosen for use in this study. We call SEQ_k the subset of k vest electrodes (columns) chosen sequentially from the BSPM signal matrix X, for $k = 8:30$ electrodes. The lower limit of $k = 8$ electrodes was chosen to equal the number of independent leads used in the standard ECG, and the upper limit of $k = 30$ electrodes was chosen as a result of suggestions that roughly 30 electrodes are necessary to accurately represent AA in AF (Guillem et al., 2009).

2) Standard ECG: A subset of BSPM vest electrodes closest to the positions of the six precordial leads plus two limb leads used in the standard 12-lead ECG was extracted. We refer to this subset, which contains eight electrodes, as ECG_8.

3) Augmented ECG: Additionally, there have been suggestions that posterior electrodes may be desirable to better capture left atrial activity in AF. Therefore, a subset of vest electrodes closest to the augmented ECG suggested in (Petrutiu et al., 2009) consisting of the eight electrodes in the ECG_8 subset plus three posterior electrodes, V_8, V_9, and V_{10} in the same horizontal plane as V_6, was tested. We refer to this subset, which contains 11 electrodes, as ECG_{11}.

Subsets were compared regarding how well they could represent the full BSPM signal matrix as follows. $SEQ_{8:30}$, ECG_8, ECG_{11}, and $PCA_{8:30}$ subset reconstructions were calculated for 5-s windows of each AA-BSPM segment. Given $\hat{X}$ the reconstruction (Eq. 2) and X the full BSPM signal matrix for a window, two error measures were calculated and averaged over all windows in a segment. The first was the normalized root-mean square reconstruction error (NRMSE), given by:

$$\text{NRMSE} = \frac{\| X - \hat{X} \|_F}{\| X \|_F} \tag{4}$$

The second was the mean absolute difference (ABSE) across all electrodes between the atrial DF on each vest electrode signal of X and $\hat{X}$, where the DF was obtained as described at the end of the previous section:

$$\text{ABSE} = \frac{1}{L} \sum_{l=1}^{l=L} |DF(X(:,l)) - DF\left(\hat{X}(:,l)\right)| \tag{5}$$

where $L = 252$ vest electrodes in our case. The above measures were calculated on 5-s windows of the 1-min AA-BSPM segments extracted from each patient and then averaged over all windows, for $\hat{X}$ found for the ECG_8, ECG_{11}, and $SEQ_{8:30}$ subsets determined for each window. Finally, for comparison, the above measures were calculated for $\hat{X} = X_k$, the rank-k PCA reconstruction as described in Eq. 3 for $k = 8:30$.

2.5 Novel spatiotemporal indices ER_{NRMSE} and ER_{ABSE}

The purpose of this section is to combine the concepts discussed in Sections 2.3, 2.4 to introduce the novel indices ER_{NRMSE} and ER_{ABSE}. These indices quantify the capacity of a subset of BSPM vest electrodes to accurately represent the AA, and the atrial DF, respectively, on all BSPM electrodes over time, compared to the optimal PCA representation of the same rank as the electrode subset.

For the calculation of the indices, the 1-min AA-BSPM segments were divided into windows of 5-s as in Section 2.4. The SEQ_8 and SEQ_{11} subsets were obtained for the first window, and reconstructions were obtained on subsequent windows using these subsets and the corresponding matrices A from Eq. 1 determined for the first window. Concretely, for the first 5-s window, the solution to Eq. 1 is $A^1 = S_k^1 X^1$, where X^1 is the full BSPM signal matrix for the first window, and S_k^1 contains the signals on a subset of k vest electrodes. The reconstruction for the i^{th} window X^i is given by $\hat{X}^i = S_k^i A^1$, where S_k^i contains the signals of X^i on the SEQ_8/SEQ_{11} subset electrodes determined for the first 5-s window X^1, or the ECG_8/ECG_{11} subset electrodes. In addition, the optimal rank-k ($k = 8, 11$) PCA reconstruction for each window, X_k^i, was determined as previously described, using the first k PCs, which we refer to as PCA_k. Then, the first index, ER_{NRMSE}, is given by the ratio of the reconstruction error obtained using SEQ_8, SEQ_{11}, ECG_8, or ECG_{11}, and the optimal same-rank reconstruction obtained with PCA_8 or PCA_{11}:

$$ER_{NRMSE_i} = \frac{\| X^i - \hat{X}^i \|_F}{\| X^i - X_k^i \|_F} \tag{6}$$

The second index, ER_{ABSE}, is given by the ratio of the mean-absolute error between the atrial DFs extracted on each electrode of the subset vs. PCA reconstructions:

$$ER_{ABSE_i} = \frac{\sum_{l=1}^{l=L} |DF(X^i(:,l)) - DF(\hat{X}^i(:,l))}{\sum_{l=1}^{l=L} |DF(X^i(:,l)) - DF(X^i_k(:,l))} \quad (7)$$

The above indices were calculated on each 5-s window following the first window of the 1-min AA-BSPM segments, then averaged across all windows, for one value per 1-min AA-BSPM segment. We chose to calculate these indices for the SEQ_8 and SEQ_{11} subsets to allow a direct comparison with the standard and augmented ECG subsets, ECG_8 and ECG_{11}.

We hypothesized more organized, easier to treat forms of AF should have lower error ratios (ER), indicating stability in the AF dynamics between windows. This is because for lower ERs, the subset of electrodes chosen for the first window and A^1 permit a reconstruction of the i^{th} window that is closer to the optimal PCA reconstruction of the same rank. As a comparison to another BSPM index utilizing PCA for AF analysis, we calculated the NDI proposed by (Meo et al., 2018), which was found to be useful for quantifying AF complexity, choosing patients eligible for AF ablation and assessing therapy impact. The NDI was calculated as the residual variance not accounted for by the first three PCs of each AA-BSPM window. Note also that this index uses only PCA and therefore is not dependent on any particular subset of electrodes.

2.6 Performance metrics and statistical analysis

The purpose of this section is to describe how the different electrode subsets introduced in Section 2.4 were compared in terms of their capacity to accurately represent AA-BSPM signal information on all vest electrodes compared to the optimal PCA representation. We also describe the methods used to quantify the relationship between the indices ER_{NRMSE}, ER_{ABSE} and NDI, and single-procedure CA success rate.

Calculated values of continuous parameters are expressed as mean ± standard deviation. The statistical distributions of all parameters were checked using a Lilliefors test. Statistical inter-group differences were calculated as mean *p*-values across 3-folds, with 20% of the parameter values left out of each fold. One-way analysis of variance (ANOVA) was used for normally distributed data, or Wilcoxon's rank sum test was used for non-normally distributed data. Statistical tests were performed across folds to reduce the likelihood of chance group differences due to a small data set, and statistical significance was considered for *p*-values less than 0.05. For comparing the different electrode subsets in terms of their capacity to accurately represent AA-BSPM segments, we checked for statistical differences of the NRMSE and ABSE parameters calculated using the different electrode subsets (SEQ_k, ECG_8, ECG_{11}), or using the corresponding number of PCs (PCA_k). For comparing the relationships between single-procedure CA outcome and ER_{NRMSE}, ER_{ABSE}, and NDI, we checked for statistical differences between these indices calculated for AA-BSPM segments associated with AR and SR outcome groups.

For indices ER_{NRMSE}, ER_{ABSE}, and NDI displaying statistically significant differences between groups, univariate logistic regression classifiers were used to test their predictive power for single-procedure CA outcome. We used group-wise 3-fold cross-validation (CV) to ensure that indices calculated from different AA-BSPM segments of the same patient were only assigned to either the train or test set (80/20) for each fold. The resulting receiver operating curves (ROC) were analyzed to obtain area under the curve (AUC) to compare the predictive power of each index. We reported the AUC for AA-BSPM segment-wise classification as mean ± standard deviation over all CV folds, and the sensitivity and specificity were reported for the optimal classification threshold value determined through ROC analysis. The sensitivity and specificity were the fraction of true positive and true negative cases correctly identified, respectively, where AR was considered a positive case, and SR was considered a negative case.

3 Results

3.1 Study population

At the time of this study, clinical outcome information was available for 11 patients, six of whom experienced an AR (55%) (3.4 ± 0.9 months post-CA). Therefore, only BSPM data from 11 patients were available for the part of the study associating the novel indices to CA outcome. Patients experiencing an AR were offered repeat procedures, however, in this study, only signals recorded prior to the first procedure and associated clinical outcomes were analyzed. Seven high quality 1-min AA-BSPM segments were extracted from the long duration BSPM recordings of each patient. Therefore, 91 1-min AA-BSPM segments were available for the analysis with results described in Section 3.2, and 77 AA-BSPM segments for the results described in Sections 3.3, 3.4, with each segment associated with an SR or AR outcome.

3.2 AA-BSPM reconstruction with BSPM electrode subsets

A representation of the spatial distributions of the SEQ_8, SEQ_{11}, ECG_8, and ECG_{11} subsets used for AA-BSPM reconstruction is shown in Figure 3. For each subset type, the color of each electrode represents its occurrence in all the subsets used to calculate NRMSE and ABSE, that is, in what ratio of the tested subsets the electrode was included. It can be seen in Figures 3A,B, that for SEQ subsets, both anterior and posterior electrodes were included in the subsets, with certain torso regions (upper and lower) being less represented in the subsets, while the mid-section regions were in general more represented. For the ECG

10.3389/fphys.2022.1001060

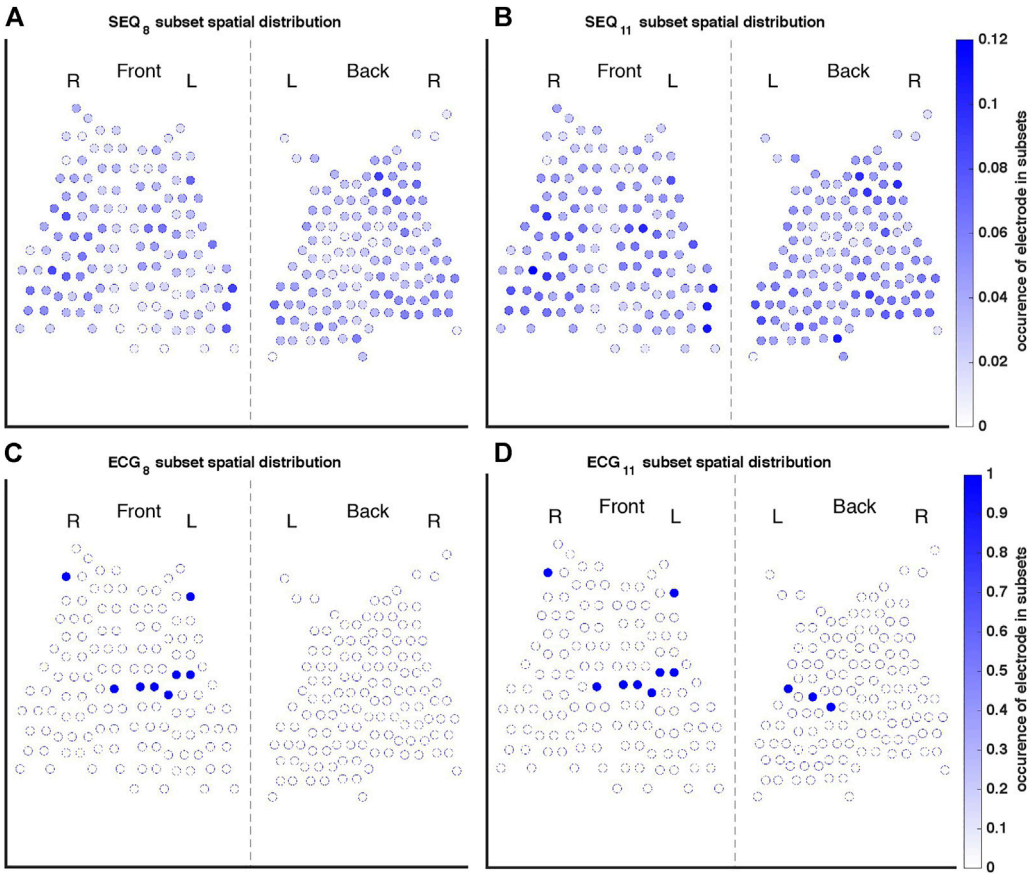

FIGURE 3
Occurrence of each electrode in the **(A)** SEQ_8, **(B)** SEQ_{11}, **(C)** ECG_8, and **(D)** ECG_{11} subsets. The color of each electrode indicates its occurrence in all of the subsets used to calculate reconstruction performance measures, where, for example, one indicates the electrode was present in every subset tested, and 0.1 indicates the electrode was present in 10% of subsets.

subsets, the same subset of electrodes was applied to each 5-s window of AA-BSPM data, as seen in Figures 3C,D.

The similarity between reconstructed and original BSPM signals is shown in Figure 4. A 5-s window of a signal recorded on vest lead 57, close to the position of precordial lead V_1, as well as its optimal least-squares reconstructions using the ECG_8 and SEQ_8 subsets associated with the window and its PCA_8 reconstruction are demonstrated in Figure 4A. It can be seen that morphological characteristics of the signal were mostly captured in the reconstructed signals, however, the amplitude of the recorded signal was not perfectly reconstructed. The power spectral densities of the original and reconstructed signals are shown in Figure 4B. It can be seen that the DF was correctly captured on this electrode. The NRMSE and ABSE as a function of number of electrodes included in the subsets are shown in Figures 4C,D, taken as a mean across all patients, with error bars representing the 95% confidence interval. In addition, the PCA_k reconstruction obtained for k PCs equaling the number of electrodes is shown. As expected, reconstructions using ECG_8 and ECG_{11} subsets had higher NRMSE and ABSE values than reconstructions using SEQ_8 and SEQ_{11}, and this difference was statistically significant ($p < 0.01$). In addition, it can be seen that PCA_k reconstruction consistently performed better than SEQ_k reconstruction, and this difference was also statistically significant for $k = 8 : 30$, ($p < 0.01$). An example showing the DF of each electrode for original recorded AA-BSPM and AA-BSPM using ECG_8, SEQ_8, and PCA_8 reconstruction is shown in the Supplementary Materials, where it can be seen that spatial differences in the original DFs at different parts of torso were mostly captured by SEQ_8 and PCA_8 reconstruction, and to a lesser extent by ECG_8 reconstruction.

3.3 BSPM AF spatiotemporal indices and CA outcome

For the analysis of ER_{NRMSE} and ER_{ABSE}, only the indices calculated using SEQ_8, SEQ_{11}, PCA_8, and PCA_{11} were used, to

10.3389/fphys.2022.1001060

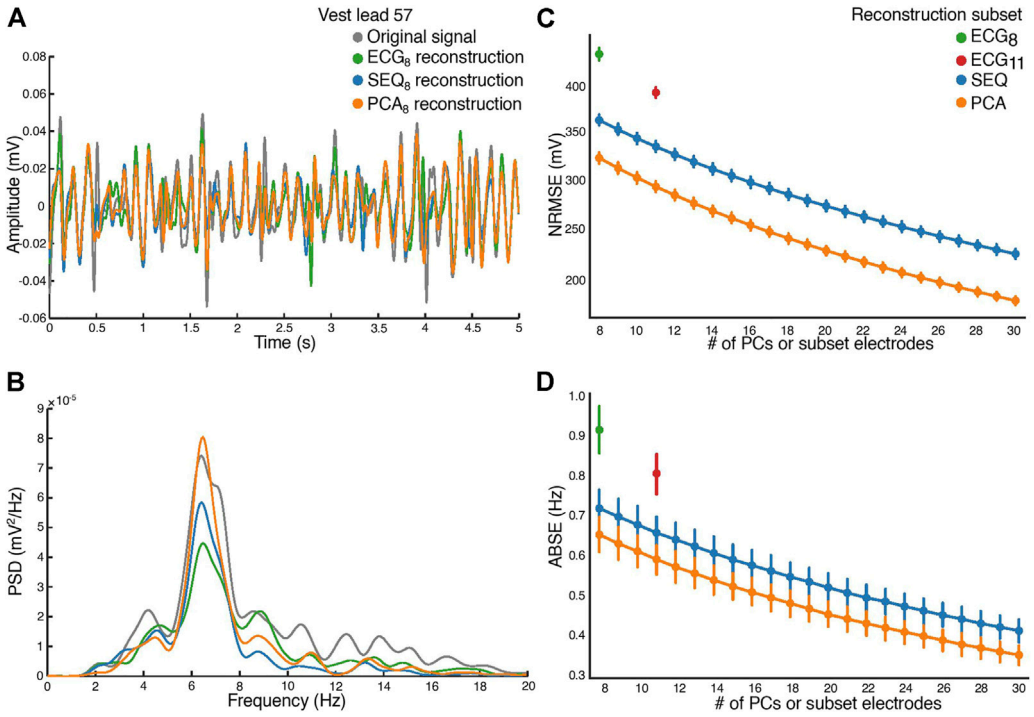

FIGURE 4
Atrial activity reconstruction. **(A)** A 5-s window of the original recorded (in grey) and reconstructed signals, for vest electrode 57, close to V_1. Reconstruction with the ECG_8 subset (green), SEQ_8 subset (blue), and PCA_8 (orange). **(B)** The corresponding power spectral densities (PSD) of the original recorded and reconstructed signals. **(C)** Normalized root-mean square reconstruction error (NRMSE), and **(D)** mean absolute error (ABSE), as a function of number of principal components or vest electrodes used in subset for reconstruction.

allow for comparison with ECG_8 and ECG_{11}. Shown in Figure 5 are the (A) ER_{NRMSE}, (B) ER_{ABSE}, and (C) NDI values according to CA outcome. The associated mean ± standard deviation values of the indices are shown in Table 2. There was a statistically significant difference in the NDI value between the SR and AR groups, with NDI greater in the SR group. Greater ER_{NRMSE} values were associated with AR following single-procedure CA, while lower ER_{NRMSE} values were associated with SR, for all electrode subsets tested. Finally, for ER_{ABSE}, greater values were again observed for AR than SR, with statistical significance only for the ECG_8 and SEQ_{11} subsets.

3.4 Predictive power of spatiotemporal indices for single-procedure CA outcome classification

A summary of the ROC analysis of the NDI, ER_{NRMSE}, and ER_{ABSE} parameters for prediction of CA outcome is shown in Table 3. Note that sensitivity and specificity values are shown for segment-wise classification. It can be seen that ER_{NRMSE} displayed the most consistent performance across folds and electrode subsets, with AUC = 0.77 ± 0.08, sensitivity = 76.2%, and specificity = 84.8% for ER_{NRMSE} calculated with the SEQ_{11} electrode subset. Despite the associations between NDI and ER_{ABSE} and CA outcome, the predictive performances of these indices were not as consistent as for ER_{NRMSE}. The ROC curves associated with ER_{NRMSE} calculated for each subset are shown in Figure 6. The ROC curves associated with NDI and ER_{ABSE} (for statistically significant subsets) are shown in the Supplementary Materials.

To further test the efficacy of ER_{NRMSE}, we repeated the statistical comparison and predictive performance analysis for SEQ subsets with 8–30 electrodes, to see whether performance changed for different numbers of electrodes included in the SEQ subset. The results are shown in Figures 7, 8. It can be seen in Figure 7A that the ER_{NRMSE} was greater in the AR group than SR group when calculated with all $SEQ_{8:30}$ subsets. However, this difference was only statistically significant for ER_{NRMSE} calculated with $SEQ_{8:24}$ subsets, as shown in Figure 7B, with the p-values from significance testing transformed as $\frac{-log10(p)}{max(-log10(p))}$ to allow for a graphical representation. In Figure 8 are shown AUC values associated with the ROC analysis of the ER_{NRMSE} calculated with $SEQ_{8:30}$ subsets. It can be seen that the AUC increased,

10.3389/fphys.2022.1001060

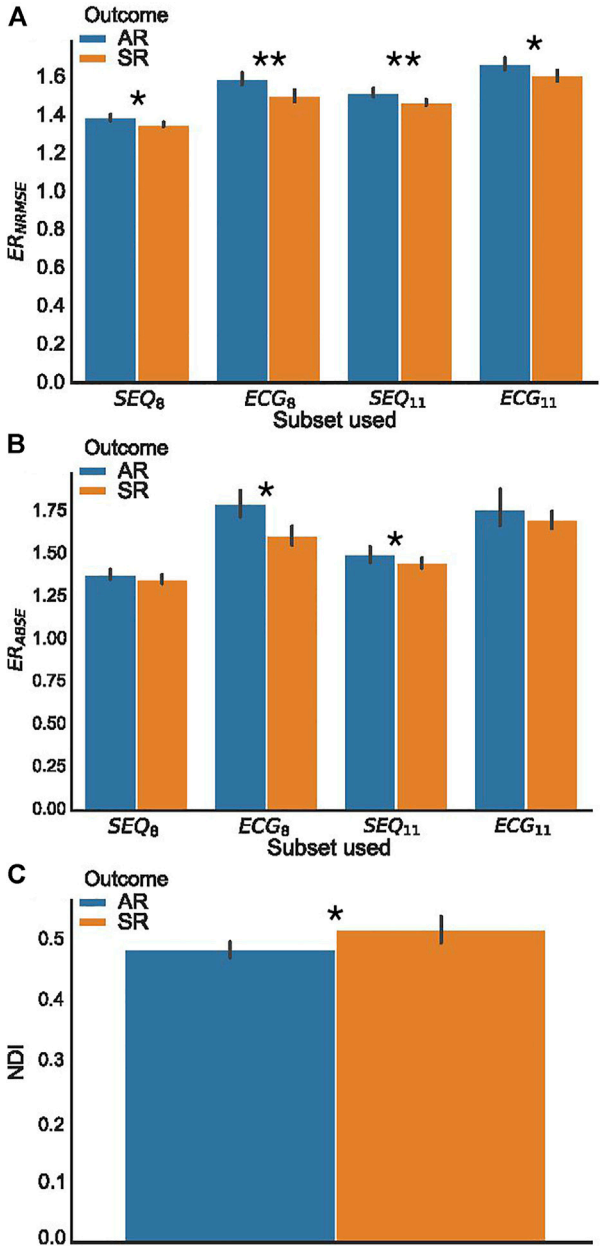

FIGURE 5
BSPM analysis indices, grouped according to clinical outcome. **(A)** Error ratio NRMSE to PCA (ER_{NRMSE}); **(B)** Error ratio ABSE to PCA (ER_{ABSE}); **(C)** Non-dipolar component index (NDI). Significant differences between AR and SR outcome means are indicated by asterisks. (*$p < 0.05$, **$p < 0.01$.).

and variance of the AUC decreased, for up to 15 electrodes included in the SEQ subset. For more than 15 electrodes, the AUC generally decreased, and variance of the AUC increased.

4 Discussion

In this study, we developed two novel, fully spatiotemporal indices for the efficient processing of long-duration BSPM signals collected from patients with persAF. The use of spatiotemporal ventricular activity cancellation rather than short, nonconsecutive TQ segments allowed the incorporation of a temporal component in the analysis. By combining PCA and the temporal component, a true spatiotemporal characterization was achieved. To the best of our knowledge, this is the first study to propose indices exploiting temporal irregularity in long-duration BSPM recordings for persAF analysis, with a view to predicting AR following single procedure CA. The selection of which electrodes to use for the calculation of the novel indices can be automatically performed using the sequential subset selection method, or can be adapted for different subsets of electrodes, such as the standard or augmented ECG lead configurations. Finally, in our study, we have investigated the relationship between the proposed novel indices and their correlation with and predictive power for CA outcome. We found that a mean AUC of up to 0.8 may be achieved for predicting arrhythmia recurrence in persAF patients who underwent single-procedure CA for the novel index ER_{NRMSE}.

4.1 Electrode subset capacity to represent AA-BSPM

PCA-based indices have been used extensively in ECG signal processing (Castells et al., 2007), with applications including extraction of atrial fibrillatory waves, quantification of AF spatial complexity and organization, and efficient analysis of BSPM data. In this study, we have included a framework for understanding how PCA-based reconstruction of AA-BSPM signals compares to reconstruction using a subset of vest electrode signals. The use of vest electrode reconstruction was based on previous studies, which have demonstrated that the full BSPM signal matrix may be projected onto a smaller matrix containing only a subset of BSPM vest electrode signals (Lux et al., 1978; Guillem et al., 2008, 2009; Feng et al., 2019). The resulting reconstruction error between the original and projected matrices has been shown to depend on the number of electrodes included in the subset, as well as the type of BSPM signals. For example, in (Guillem et al., 2009), it was found that with the same number of electrodes, reconstruction error was lower for ventricular than atrial activity. In our study, as the number of electrodes included in the ECG or SEQ subsets increased, the NRMSE and ABSE both decreased, in line with results from (Guillem et al., 2009). We also showed for the first time in our study the same trend for optimal PCA reconstruction. It can be noted that for all numbers of electrodes tested, there is a greater overlap between the ABSE values than NRMSE values between the different subset types. This could be

TABLE 2 ER_{NRMSE}, ER_{ABSE}, and NDI values by vest electrode subset (not applicable for NDI) and single procedure CA outcome, expressed as mean ± standard deviation. *p*-values were computed as means across three folds of data, in which a *p*-value for the statistical significance between index values by outcome was computed using 80% of the AA-BSPM segments in each fold.

Subset	Outcome	ER_{NRMSE}	*p*-value	ER_{ABSE}	*p*-value	NDI	*p*-value
SEQ_8	SR	1.349 ± 0.034	0.010	1.352 ± 0.078	0.294	0.517 ± 0.070	0.018
	AR	1.385 ± 0.053		1.38 ± 0.096		0.484 ± 0.041	
ECG_8	SR	1.499 ± 0.091	0.008	1.607 ± 0.171	0.045		
	AR	1.589 ± 0.102		1.796 ± 0.253			
SEQ_{11}	SR	1.464 ± 0.041	0.002	1.448 ± 0.093	0.033		
	AR	1.515 ± 0.075		1.497 ± 0.159			
ECG_{11}	SR	1.605 ± 0.082	0.037	1.700 ± 0.150	0.107		
	AR	1.667 ± 0.100		1.760 ± 0.351			

TABLE 3 Predictive power of BSPM indices for CA outcome, for each of the tested subsets. Sensitivity and specificity indicate the rate of detection of arrhythmia recurrence and sinus rhythm 6 months post single-procedure CA, respectively. AUC, area under the curve.

	AUC (mean ± std)		Sensitivity (%)		Specificity (%)	
NDI	0.37 ± 0.45		33		98.9	
	ER_{NRMSE}	ER_{ABSE}	ER_{NRMSE}	ER_{ABSE}	ER_{NRMSE}	ER_{ABSE}
SEQ_8	0.72 ± 0.09	-	61.9	-	84.8	-
ECG_8	0.81 ± 0.26	0.76 ± 0.23	64.3	57.1	98.9	98.9
SEQ_{11}	0.77 ± 0.08	0.52 ± 0.29	76.2	28.6	84.8	98.9
ECG_{11}	0.69 ± 0.28	-	57.1	-	84.8	-

because the reconstruction method used optimizes for NRMSE, and not ABSE.

Regarding the comparison of different BSPM electrode subsets, it was found that SEQ subsets more accurately represent BSPM signal data than standard and augmented ECG subsets in both signal domains, manifested through lower NRMSE and ABSE values for both $k = 8$ and $k = 11$ electrodes included in the vest subset. This reinforces the idea that standard ECG electrode configurations are not optimal in terms of accurately representing the full BSPM signal matrix. Since results from previous works have suggested that the addition of posterior electrodes may be useful to better reflect left atrial activity in AF (Ihara et al., 2007; Petrutiu et al., 2009; Buttu et al., 2013; Guillem et al., 2013), we did include the augmented ECG_{11} subset. Interestingly, it was found that the decrease in reconstruction error between the ECG_8 and ECG_{11} subsets was greater than the decrease in error between the SEQ_8 and SEQ_{11} subsets, lending support to the argument that the addition of carefully positioned posterior electrodes may indeed be beneficial for representing AA-BSPM data. Additionally, it was found that PCA-based reconstruction performs better than electrode subset based reconstruction, in both the temporal and frequency domains. This is to be expected, since PCA explicitly optimizes for the reconstruction criterion. However, this remains an important result since to our knowledge, the gap between electrode subset and PCA reconstruction had not been previously investigated. We hypothesized that this gap may contain useful information related to AF signal analysis.

4.2 Statistical comparison of novel indices

The finding in our study that ER_{NRMSE}, ER_{ABSE}, and NDI all show statistically significant differences between AA-BSPM segments associated with AR or SR outcomes demonstrates that each of these indices shows some potential to be used as computational tools for AF disease management. Since calculation of ER_{NRMSE} and ER_{ABSE} required selection of a subset of vest electrodes, these indices were calculated for standard and augmented ECG subsets (ECG_8 and ECG_{11}, respectively), as well as for sequentially chosen subsets (SEQ_8 and SEQ_{11}), which differ between AA-BSPM segments, to test the robustness of the indices with respect to both which and how many electrodes were included in the subsets.

Many previous studies have investigated capturing AF information using surface recorded ECG signals, however, most often using a single or limited number of leads. This prevents the exploitation of the spatial diversity of multi-lead ECGs and is dependent on the available electrode signal containing information representative of the underlying AF. Since electrode placement cannot be exact, and patient anatomy varies widely, this is not always guaranteed. Further, it has already been shown that inclusion of multiple leads is beneficial, leading to greater correlation between calculated 12-lead ECG indices and AF complexity and

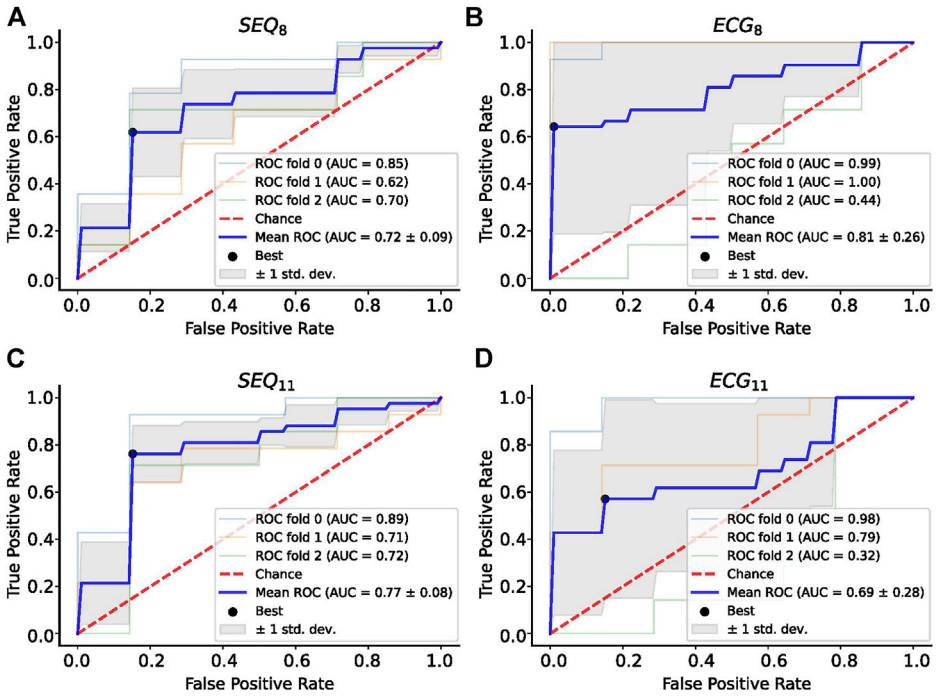

FIGURE 6
ROC Analysis for ER_{NRMSE} for predicting CA outcome calculated with **(A)** SEQ_8; **(B)** ECG_8; **(C)** SEQ_{11}; and **(D)** ECG_{11} vest electrode subsets. The optimal tradeoff between true positive rate and false positive rate is indicated by a black dot.

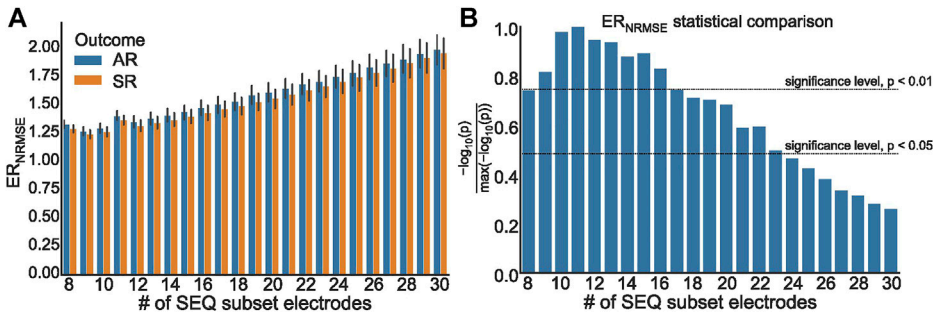

FIGURE 7
(A) ER_{NRMSE} values grouped according to clinical outcome, calculated with $SEQ_{8:30}$ subsets; **(B)** Representation of p values associated with statistical comparison of ER_{NRMSE} mean values for AR and SR patient groups. The $p = 0.05$ and $p = 0.01$ significance levels are indicated by dashed lines.

outcomes in (Meo et al., 2013; Zarzoso et al., 2016). The idea in this study was therefore to add to the limited number of BSPM indices for AF analysis, integrating both temporal and spatial information.

In (Bonizzi et al., 2010), it was shown that reconstruction error using the PCA rank-3 approximation of TQ segments of BSPM signals recorded during AF was capable of separating AA signals into clusters based on levels of AF organization, with greater reconstruction error corresponding to higher AF complexity and lower stationarity. Later, (Di Marco et al., 2012), using PCA-based indices, found that higher spatial organization, indicating easier to treat forms of AF, was correlated with more temporally stable atrial activation patterns. We hypothesized that lower ER_{NRMSE} values would therefore be observed among SR patients, indicating more stability in the AF dynamics between BSPM windows, and this was indeed the case. The finding that ER_{NRMSE} displayed greater values in AR AA-BSPM segments than SR segments for all four electrode

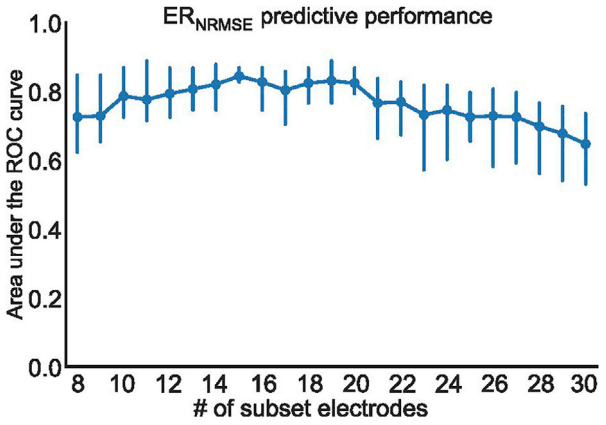

FIGURE 8
Mean and standard deviation of the area under the ROC curve (AUC) computed using three cross-validation folds, for ER_{NRMSE} performance for predicting CA outcome when calculated with $SEQ_{8:30}$ electrodes.

subsets lends support to its use as a robust index for predicting single-procedure AF outcome. Further, also in (Di Marco et al., 2012), it was found that greater temporal variability was associated with lower spectral concentration. Therefore, we hypothesized again that lower ER_{ABSE} values would be observed for SR patients. While the ER_{ABSE} calculated for AR patients was greater than that for SR patients, this difference was only statistically significant for two of the electrode subsets tested, potentially making it less robust than ER_{NRMSE}. This lower robustness could relate to the finding discussed above that there was a greater overlap in ABSE values calculated for subset vs. PCA reconstruction.

The NDI was unexpectedly found to be greater for SR segments than AR segments, meaning that the remaining variance unexplained by the first three PCs of the BSPM signal data was on average greater for SR segments than AR segments. This is contrary to the result in (Meo et al., 2018), which found smaller NDI values in concatenated TQ segments of BSPM data collected from patients with successful procedural CA outcome. Several key differences in our study could explain the contradictory results, including our use of longer duration AA-BSPM segments rather than concatenated TQ segments. Additionally, the study in (Meo et al., 2018) compared NDI values calculated for procedural outcomes, while in this study we used single-procedure clinical outcomes. Future studies testing the NDI may shed light on this discrepancy.

4.3 Assessment of clinical impact of novel indices

The clinical impact of the indices tested in this study depends not only on their association with CA outcomes but also their ability to predict CA outcomes. Therefore, we tested classification performance of univariate logistic regression classifiers for ER_{NRMSE}, ER_{ABSE}, and NDI. The use of group-wise CV was important to ensure AA-BSPM segments extracted from the same patient were included only in either the train or test set of each fold. Reporting both mean and standard deviation values of the AUC for each classifier also gave an indication of the CA outcome prediction model variance for different folds of the data. These were important features of our methodology considering the small-size of our data set.

Importantly, only ER_{NRMSE} displayed consistent results in predictive power across tested vest electrode subsets. The AUCs for this index calculated with each subset (SEQ_8: 0.72 ± 0.09, ECG_8: 0.81 ± 0.26, SEQ_{11}: 0.77 ± 0.08, ECG_{11}: 0.69 ± 0.28) were as good or better than the AUC associated with NDI (0.69), found in (Meo et al., 2018), and the model variance was not reported in their study. Additionally, the (Meo et al., 2018) study also tested prediction performance for NDI combined with clinical parameters, achieving an AUC of 0.7. Our results were also as good or better than those described in (Lankveld et al., 2016), in which predictive performance varied from AUC = 0.76 ± 0.15 for 12-lead ECG derived complexity parameters alone to AUC = 0.79 ± 0.13 for ECG plus clinical parameters. Additionally, the results were in line with those obtained in (Zeemering et al., 2018), for which an AUC of 0.66, 95% confidence interval [0.64–0.67] was obtained for the best ECG parameter studied (dominant atrial frequency in lead II). The study also reported better performance when several ECG parameters were combined (AUC 0.78 [0.76–0.79]), and best performance for combining ECG plus clinical parameters (AUC = 0.81 [0.79–0.82]). It is important to note that the variance across CV folds was less for ER_{NRMSE} calculated with SEQ subsets compared to ECG subsets, and in general lower than model variances reported in other studies. This result was also found to be true in our additional analysis calculating ER_{NRMSE} with $SEQ_{8:30}$ electrodes, finding high predictive performance for nearly all numbers of electrodes included in the subset. That ER_{NRMSE} showed the best results and lowest variance when calculated with SEQ electrode subsets could indicate that when working with BSPM signals, an informed patient or segment specific selection of subset electrodes may be useful, for example using the sequential algorithm. This is logical given the nonstationary nature of BSPM recordings in AF. This was further supported by the lack of a clear pattern of specific electrodes included in the SEQ subsets as seen in Figure 3; rather, certain regions of the vest contain electrodes picked by the sequential algorithm more often than other regions. The finding that specificity was generally higher than sensitivity across all indices tested could indicate that this index would be more useful for selecting which patients would be most likely to benefit from CA, as opposed to selecting those least likely to benefit. Note

that specificity was also higher than sensitivity for the NDI in the original study (Meo et al., 2018). The other two indices appear less robust to predict CA outcome, with low AUC and sensitivity values for NDI. For ER_{ABSE}, the results appear more promising, but still displaying relatively low sensitivity and more variable AUC values across CV folds than ER_{NRMSE}.

These results all point towards the potential value of ER_{NRMSE} as a clinically useful tool that could be used to analyze BSPM data in persAF. If confirmed by future studies, the use of ER_{NRMSE} could be important in assisting in prediction of successful CA outcomes, which would be useful for improving informed decision making regarding treatment for persAF. This would be particularly important given the low success rate of CA for treating persAF. Finally, the added clinical value of using BSPM data in AF remains unclear, as evidenced by its being largely limited to research use (Salinet et al., 2021). However, if indices calculated using BSPM data, such as ER_{NRMSE}, could be shown to be consistently associated with and good predictors of CA outcomes, this could confirm the validity of using BSPM data for AF analysis.

4.4 Limitations

The study population, at 13 patients, and 11 patients with clinical outcome data, was small; however, the effort in obtaining BSPM recordings is considerable, due to the high number of electrodes which are used. The use of group-wise CV on segments of data extracted from each patient did however permit a robust analysis using this data set. In addition, the randomized inclusion criteria enhances our conclusions on BSPM AF characterization, though this may not be representative of the general characteristics of a wider population. Given the variation in experimental set up and parameters used, comparing with parameters from previous studies was challenging, and a more systematic study would be required for integration of the contributions of this work into clinical practice. Further, the small size of the population precluded the analysis of correlation with clinical indices, or whether the proposed indices could be combined with clinical indices for predicting CA outcome, as it has been shown previously in several studies that combining ECG-based indices with clinical parameters yields the best clinical performance (Lankveld et al., 2016; Meo et al., 2018; Zeemering et al., 2018). Additionally, the follow-up duration was relatively limited, and again due to the small study size, the impact of anti-arrhythmic medications could not be assessed since these were used by most patients. Finally, while we have shown the usefulness of the proposed indices for predicting CA outcome, we were unable to examine these indices for quantifying AF complexity due to a lack of available simultaneous intracardiac recordings.

4.5 Conclusion

In this study, we have proposed two novel indices for AF analysis with BSPM signals, ER_{NRMSE} and ER_{ABSE}. We have shown clinical applicability by demonstrating correlation between the novel indices and single-procedure CA outcome and also promising outcome prediction performance. However, only ER_{NRMSE} values were found to be statistically greater for the AR patient group than SR patient group, and demonstrate consistently high CA outcome predictive performance when calculated with ECG subsets, and independent of the number of electrodes included in the SEQ subset used for its calculation. These results, combined with previous studies also employing PCA-based methods, suggest that continued study of BSPM signals for AF analysis is warranted.

Data availability statement

The original contributions presented in the study are included in the article/Supplementary Materials, further inquiries can be directed to the corresponding author.

Ethics statement

The studies involving human participants were reviewed and approved by Lausanne University Hospital Human Research Ethics Committee. The patients/participants provided their written informed consent to participate in this study.

Author contributions

AM, AL, EP, and J-MV conceived and designed the study and were in charge of manuscript writing. AM, AL, and J-MV performed the analyses. EP and PP performed CA procedures, provided a clinical interpretation of the results, and both contributed to data acquisition. All authors contributed to the article and approved the submitted version.

Funding

This study was supported in part by grant 2018-322 of the Personalized Health and Related Technologies (PHRT) initiative of the Swiss ETH domain.

Acknowledgments

The authors would like to thank Medtronic Switzerland for their technical assistance with data collection.

Conflict of interest

The authors declare that the research was conducted in the absence of any commercial or financial relationships that could be construed as a potential conflict of interest.

Publisher's note

All claims expressed in this article are solely those of the authors and do not necessarily represent those of their affiliated organizations, or those of the publisher, the editors and the reviewers. Any product that may be evaluated in this article, or claim that may be made by its manufacturer, is not guaranteed or endorsed by the publisher.

Supplementary material

The Supplementary Material for this article can be found online at: https://www.frontiersin.org/articles/10.3389/fphys.2022.1001060/full#supplementary-material

References

Altschuler, J., Bhaskara, A., Fu, G., Mirrokni, V., Rostamizadeh, A., and Zadimoghaddam, M. (2016). "Greedy column subset selection: New bounds and distributed algorithms," in *Proc. Int. Conf. Mach. Learn. (PMLR)*, 2539–2548. doi:10.5555/3045390.3045658

Bonizzi, P., de la Salud Guillem, M., Climent, A. M., Millet, J., Zarzoso, V., Castells, F., et al. (2010). Noninvasive assessment of the complexity and stationarity of the atrial wavefront patterns during atrial fibrillation. *IEEE Trans. Biomed. Eng.* 57, 2147–2157. doi:10.1109/TBME.2010.2052619

Buttu, A., Pruvot, E., Van Zaen, J., Viso, A., Forclaz, A., Pascale, P., et al. (2013). Adaptive frequency tracking of the baseline ECG identifies the site of atrial fibrillation termination by catheter ablation. *Biomed. Signal Process. Control* 8, 969–980. doi:10.1016/j.bspc.2013.02.005

Castells, F., Laguna, P., Sörnmo, L., Bollmann, A., and Roig, J. M. (2007). Principal component analysis in ECG signal processing. *EURASIP J. Adv. Signal Process.* 2007, 1–16. doi:10.1155/2007/74580

Civril, A. (2014). Column subset selection problem is UG-hard. *J. Comput. Syst. Sci.* 80, 849–859. doi:10.1016/j.jcss.2014.01.004

Di Marco, L. Y., Bourke, J. P., and Langley, P. (2012). Spatial complexity and spectral distribution variability of atrial activity in surface ECG recordings of atrial fibrillation. *Med. Biol. Eng. Comput.* 50, 439–446. doi:10.1007/s11517-012-0878-8

Farahat, A. K., Ghodsi, A., and Kamel, M. S. (2011). "An efficient greedy method for unsupervised feature selection," in *Proc. IEEE int. Conf. Data min. (IEEE)*, 161–170. doi:10.1109/ICDM.2011.22

Feng, X., Bai, B., Wu, Z., Yang, C., and Wu, Z. (2019). Leads selection of body surface potential mapping during atrial fibrillation: A sequential selection based on adapted botteron's approach. *IEEE Access* 7, 158064–158074. doi:10.1109/ACCESS.2019.2949999

Guillem, M. S., Bollmann, A., Climent, A. M., Husser, D., Millet-Roig, J., and Castells, F. (2009). How many leads are necessary for a reliable reconstruction of surface potentials during atrial fibrillation? *IEEE Trans. Inf. Technol. Biomed.* 13, 330–340. doi:10.1109/TITB.2008.2011894

Guillem, M. S., Castells, F., Climent, A. M., Bodí, V., Chorro, F. J., and Millet, J. (2008). Evaluation of lead selection methods for optimal reconstruction of body surface potentials. *J. Electrocardiol.* 41, 26–34. doi:10.1016/j.jelectrocard.2007.07.001

Guillem, M. S., Climent, A. M., Millet, J., Arenal, Á., Fernández-Avilés, F., Jalife, J., et al. (2013). Noninvasive localization of maximal frequency sites of atrial fibrillation by body surface potential mapping. *Circ. Arrhythm. Electrophysiol.* 6, 294–301. doi:10.1161/CIRCEP.112.000167

Ihara, Z., van Oosterom, A., Jacquemet, V., and Hoekema, R. (2007). Adaptation of the standard 12-lead electrocardiogram system dedicated to the analysis of atrial fibrillation. *J. Electrocardiol.* 40, e1–e8. doi:10.1016/j.jelectrocard.2006.04.006

Langley, P., Rieta, J. J., Stridh, M., Millet, J., Sornmo, L., and Murray, A. (2006). Comparison of atrial signal extraction algorithms in 12-lead ECGs with atrial fibrillation. *IEEE Trans. Biomed. Eng.* 53, 343–346. doi:10.1109/TBME.2005.862567

Lankveld, T. A., Zeemering, S., Crijns, H. J., and Schotten, U. (2014). The ECG as a tool to determine atrial fibrillation complexity. *Heart* 100, 1077–1084. doi:10.1136/heartjnl-2013-305149

Lankveld, T., Zeemering, S., Scherr, D., Kuklik, P., Hoffmann, B. A., Willems, S., et al. (2016). Atrial fibrillation complexity parameters derived from surface ECGs predict procedural outcome and long-term follow-up of stepwise catheter ablation for atrial fibrillation. *Circ. Arrhythm. Electrophysiol.* 9, e003354. doi:10.1161/CIRCEP.115.003354

Lux, R. L., Smith, C. R., Wyatt, R. F., and Abildskov, J. (1978). Limited lead selection for estimation of body surface potential maps in electrocardiography. *IEEE Trans. Biomed. Eng.* 270, 270–276. doi:10.1109/TBME.1978.326332

Meo, M., Pambrun, T., Derval, N., Dumas-Pomier, C., Puyo, S., Duchateau, J., et al. (2018). Noninvasive assessment of atrial fibrillation complexity in relation to ablation characteristics and outcome. *Front. Physiol.* 9, 929. doi:10.3389/fphys.2018.00929

Meo, M., Zarzoso, V., Meste, O., Latcu, D. G., and Saoudi, N. (2013). Catheter ablation outcome prediction in persistent atrial fibrillation using weighted principal component analysis. *Biomed. Signal Process. Control* 8, 958–968. doi:10.1016/j.bspc.2013.02.002

Petrutiu, S., Sahakian, A. V., Fisher, W., and Swiryn, S. (2009). Manifestation of left atrial events and interatrial frequency gradients in the surface electrocardiogram during atrial fibrillation: Contributions from posterior leads. *J. Cardiovasc. Electrophysiol.* 20, 1231–1236. doi:10.1111/j.1540-8167.2009.01523.x

Pilia, N., Nagel, C., Lenis, G., Becker, S., Dössel, O., and Loewe, A. (2021). ECGdeli-an open source ECG delineation toolbox for MATLAB. *SoftwareX* 13, 100639. doi:10.1016/j.softx.2020.100639

Salinet, J., Molero, R., Schlindwein, F. S., Karel, J., Rodrigo, M., Rojo-Álvarez, J. L., et al. (2021). Electrocardiographic imaging for atrial fibrillation: A perspective from computer models and animal experiments to clinical value. *Front. Physiol.* 12, 653013. doi:10.3389/fphys.2021.653013

Stridh, M., and Sornmo, L. (2001). Spatiotemporal QRST cancellation techniques for analysis of atrial fibrillation. *IEEE Trans. Biomed. Eng.* 48, 105–111. doi:10.1109/10.900266

Zarzoso, V., Latcu, D. G., Hidalgo-Muñoz, A. R., Meo, M., Meste, O., Popescu, I., et al. (2016). Non-invasive prediction of catheter ablation outcome in persistent atrial fibrillation by fibrillatory wave amplitude computation in multiple electrocardiogram leads. *Arch. Cardiovasc. Dis.* 109, 679–688. doi:10.1016/j.acvd.2016.03.002

Zeemering, S., Lankveld, T. A., Bonizzi, P., Limantoro, I., Bekkers, S. C., Crijns, H. J., et al. (2018). The electrocardiogram as a predictor of successful pharmacological cardioversion and progression of atrial fibrillation. *Europace* 20, e96–e104. doi:10.1093/europace/eux234

frontiers | Frontiers in Physiology

TYPE Original Research
PUBLISHED 04 October 2022
DOI 10.3389/fphys.2022.976526

OPEN ACCESS

EDITED BY
Axel Loewe,
Karlsruhe Institute of Technology,
Germany

REVIEWED BY
Haibo Ni,
University of California, Davis,
United States
Michela Masè,
Institute of Mountain Emergency
Medicine, Eurac Research, Italy

*CORRESPONDENCE
Frida Sandberg,
frida.sandberg@bme.lth.se

SPECIALTY SECTION
This article was submitted to Cardiac Electrophysiology,
a section of the journal
Frontiers in Physiology

RECEIVED 23 June 2022
ACCEPTED 05 September 2022
PUBLISHED 04 October 2022

CITATION
Karlsson M, Wallman M, Platonov PG, Ulimoen SR and Sandberg F (2022), ECG based assessment of circadian variation in AV-nodal conduction during AF—Influence of rate control drugs. *Front. Physiol.* 13:976526. doi: 10.3389/fphys.2022.976526

ECG based assessment of circadian variation in AV-nodal conduction during AF—Influence of rate control drugs

Mattias Karlsson[1,2], Mikael Wallman[1], Pyotr G. Platonov[3], Sara R. Ulimoen[4] and Frida Sandberg[2]*

[1]Department of Systems and Data Analysis, Fraunhofer-Chalmers Centre, Gothenburg, Sweden, [2]Department of Biomedical Engineering, Lund University, Lund, Sweden, [3]Department of Cardiology, Clinical Sciences, Lund University, Lund, Sweden, [4]Vestre Viken Hospital Trust, Department of Medical Research, Bærum Hospital, Drammen, Norway

The heart rate during atrial fibrillation (AF) is highly dependent on the conduction properties of the atrioventricular (AV) node. These properties can be affected using β-blockers or calcium channel blockers, mainly chosen empirically. Characterization of individual AV-nodal conduction could assist in personalized treatment selection during AF. Individual AV nodal refractory periods and conduction delays were characterized based on 24-hour ambulatory ECGs from 60 patients with permanent AF. This was done by estimating model parameters from a previously created mathematical network model of the AV node using a problem-specific genetic algorithm. Based on the estimated model parameters, the circadian variation and its drug-dependent difference between treatment with two β-blockers and two calcium channel blockers were quantified on a population level by means of cosinor analysis using a linear mixed-effect approach. The mixed-effects analysis indicated increased refractoriness relative to baseline for all drugs. An additional decrease in circadian variation for parameters representing conduction delay was observed for the β-blockers. This indicates that the two drug types have quantifiable differences in their effects on AV-nodal conduction properties. These differences could be important in treatment outcome, and thus quantifying them could assist in treatment selection.

KEYWORDS

atrial fibrillation, atrioventricular node, circadian variation, mathematical modeling, genetic algorithm, mixed effect modeling, ECG, rate control drugs

1 Introduction

Atrial fibrillation (AF) is the most common arrhythmia in the world, with a prevalence of 2–4% in the adult population Benjamin et al. (2019), reaching 7% for those aged 65 and above Di Carlo et al. (2019). It is characterized by rapid and irregular contraction of the atria, originating from highly disorganized electrical activity, and associated with an increased risk of mortality, mainly due to stroke or heart failure Hindricks et al. (2021).

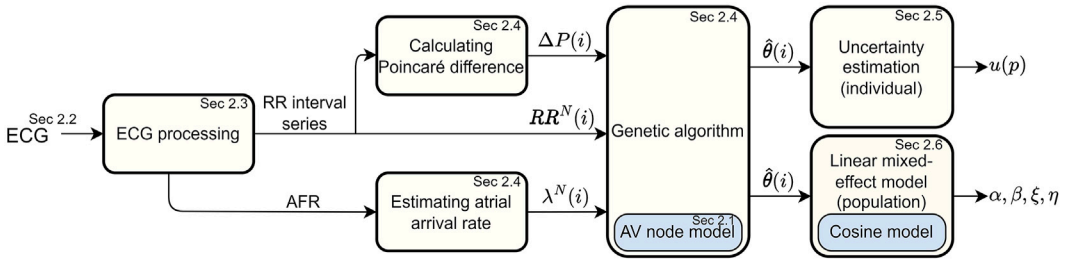

FIGURE 1
A flowchart of the overall framework for estimating AV node conduction properties on an individual and a population level.

The electrical impulses in the atria are conducted via the atrioventricular (AV) node to reach and activate the ventricles. The AV node can block and delay incoming impulses based on its refractory period and conduction delay properties. During AF - when the AV node is bombarded with impulses from the atria - blocking of impulses prevents the heart from racing, but may not be sufficient to maintain a normal heart rate and will still result in significant beat-to-beat variability in the ventricular activation Corino et al. (2015b); Mase et al. (2017).

To remedy this, rate control drugs can be used in order to modify the conduction properties of the AV node. There are two main types of rate control drugs used for AF treatment; β-blockers and calcium channel blockers Hindricks et al. (2021). As the name suggests, β-blockers block the β-receptors in AV node cells, decreasing the effect of the sympathetic nervous system, whereas calcium channel blockers prevent the L-type calcium channels from opening, thereby reducing the conduction in the AV node cells. Both types of drugs have been shown effective in reducing the heart rate during AF Ulimoen et al. (2013). However, the optimal treatment for a given patient is often chosen empirically. Since the two drug types have different physiological effects on the AV node conduction properties, assessing the drug-induced changes in these AV node properties could provide an important step toward personalized treatment. One of the main differences between the two drug types is the effect on the sympathetic nervous system, which can be quantified by the circadian variation in the AV node conduction properties. Furthermore, previous studies have shown a significant difference in the predominant RR interval between day and night, without a difference in dominant atrial cycle length, suggesting circadian variation in the AV node conduction properties Climent et al. (2010).

Conduction properties of the AV node have previously been characterized using mathematical models based on measurements of the electrical activity in the heart Shrier et al. (1987); Billette and Nattel (1994); Sun et al. (1995). Several models of the AV node during AF have been proposed; both based on invasive data from rabbits Inada et al. (2009); Climent et al. (2011) and humans Jørgensen et al. (2002); Mangin et al. (2005); Masè et al. (2012, 2015), and on non-invasive data from humans Corino et al. (2011, 2013); Henriksson et al. (2015). We have previously presented a network model of the AV node capable of assessing the refractory period and the conduction delay of the AV node from 20-min ECG segments Karlsson et al. (2021). However, continuous assessment of AV conduction delay and refractoriness from 24-hour ECG recordings has not previously been performed; such assessment enables analysis of long-term variations in AV conduction properties.

The aim of the present study is to develop a framework for long-term ECG-based assessment of conduction properties in the AV node, and to utilize this framework for analysis of circadian variation and its drug-induced changes in a cohort of 60 patients with persistent AF Ulimoen et al. (2013). To accomplish this, we propose a problem-specific optimization algorithm able to continuously estimate the model parameters from the previously presented network model Karlsson et al. (2021). Furthermore, the uncertainty of the parameter estimates is assessed using a variant of Sobol's method Sobol (2001), and the drug-induced differences in circadian variation between β-blockers and calcium channel blockers on a population level are quantified using a linear mixed-effect model.

2 Materials and methods

A schematic overview of the methodology is given in Figure 1. The ECG data (Section 2.2) is first processed in order to extract a RR interval series and an atrial fibrillatory rate (AFR) trend, as described in Section 2.3. The RR interval series is then divided into segments of length N, and the AFR trend is used to estimate the atrial arrival rate in the corresponding time interval. The AV node model (Section 2.1) is fitted to the ECG-derived data using a tailored optimization algorithm, as described in Section 2.4, in order to obtain model parameter estimates. Furthermore, the Poincaré plot difference, which quantifies the rate of change of RR series characteristics, is used to tune hyper-parameters in the optimization algorithm during parameter estimation. The uncertainty of the estimated model

parameters is investigated using a variant of Sobol's method, as described in Section 2.5. Finally, cosinor analysis is used to quantify circadian variation in the model parameter trends, and a linear mixed effects modeling approach is used to investigate drug-dependent differences on a population level, as described in Section 2.6.

2.1 AV node model

A network model of the human AV node, shown in Figure 2, is used to characterize the conduction delay and refractory period. A brief description of the model is given here, for more details, see Karlsson et al. (2021). The model describes the AV node as an interconnected network of nodes, each capable of transmitting incoming impulses. The model consists of 21 nodes; divided into a fast pathway (FP) with ten nodes, a slow pathway (SP) with ten nodes, and a coupling node. The nodes can react to an incoming impulse either by blocking - if the node is in its refractory state - or by conducting it to all adjacent nodes after adding a conduction delay, after which the node returns to its refractory state. The refractory period ($R_j(n)$) and the conduction delay ($D_j(n)$) of node j following an impulse n are given by,

$$R_j(n) = R_{min} + \Delta R\left(1 - e^{\frac{-\tilde{t}_j(n)}{\tau_R}}\right) \quad (1)$$

$$D_j(n) = D_{min} + \Delta D e^{\frac{-\tilde{t}_j(n)}{\tau_D}}, \quad (2)$$

where $\tilde{t}_j(n)$ is the diastolic interval preceding impulse n,

$$\tilde{t}_j(n) = t_j(n) - t_j(n-1) - R_j(n-1), \quad (3)$$

and $t_j(n)$ is the arrival time of impulse n at node j. When $\tilde{t}_j(n)$ is negative, the impulse will be blocked since the node is in its refractory state. The parameters $R_{\min}$, ΔR, τ_R, $D_{\min}$, ΔD, and τ_D are fixed for all nodes in the SP and the FP, respectively. This results in the 12 model parameters

TABLE 1 The interpretation of the model parameters. Superscripts indicating the pathway (SP, FP) are omitted to avoid redundancy.

Parameter	Parameter description
$R_{\min}$	Minimum refractory period, attained for short diastolic intervals
ΔR	Maximum prolongation of the refractory period, attained for long diastolic intervals.
τ_R	Time constant for the refractory period, determining the impact of the diastolic interval
$D_{\min}$	Minimum conduction delay, attained for short diastolic intervals
ΔD	Maximum prolongation of the conduction delay, attained for long diastolic intervals.
τ_D	Time constant for the conduction delay, determining the impact of the diastolic interval

$\boldsymbol{\theta} = [R^{FP}_{\min}, \Delta R^{FP}, \tau^{FP}_R, R^{SP}_{\min}, \Delta R^{SP}, \tau^{SP}_R, D^{FP}_{\min}, \Delta D^{FP}, \tau^{FP}_D, D^{SP}_{\min}, \Delta D^{SP}, \tau^{SP}_D]$. For convenience, the interpretation of the model parameters are given in Table 1. For the coupling node, the delay is fixed to 60 ms, and the refractory period is fixed to the mean of the ten shortest RR intervals in the data used for model parameter estimation, $RR_{\min}$.

The input to the model - representing impulses arriving from the atria - is created using a Poisson process with mean arrival rate λ. The output of the model represents the time points for ventricular activation, and thus the differences between adjacent elements in the output vector represent the RR intervals.

2.2 ECG data

The RATe control in Atrial Fibrillation (RATAF) study Ulimoen et al. (2013) acquired 24-hour ambulatory ECGs during baseline and under the influence of four rate control drugs; the two calcium channel blockers verapamil and diltiazem, and the two β-blockers metoprolol and carvedilol. The study population consists of 60 patients with permanent AF, no heart failure, or symptomatic ischemic heart disease. The study was approved by the regional ethics

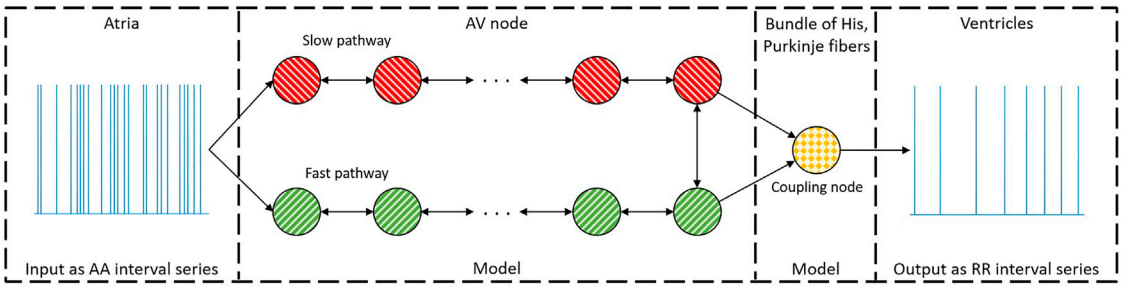

FIGURE 2
A schematic representation of the network model where the yellow node represents the coupling node, the red nodes the SP, the green nodes the FP, and arrows the direction for impulse conduction. For readability, only a subset of the 21 nodes is shown.

committee and the Norwegian Medicines Agency and conducted in accordance with the Helsinki Declaration. The trend in the AV node refractory period and conduction delay from these five 24-hour ECG recordings per patient is assessed by estimations of the trends in $\boldsymbol{\theta}$.

2.3 ECG processing

The RR interval series is extracted from the ECG, where RR intervals following and preceding QRS-complexes with deviating morphology are excluded from the series Lagerholm et al. (2000). Due to excessive noise in the ECGs, some RR intervals are missed, leading to an unrealistically low heart rate. Thus, the data are divided into minute-long non-overlapping segments, and all segments with a heart rate lower than 20 bpm are removed, occasionally resulting in gaps in the signals. The signals with a total duration shorter than 12 h or with less than 20 h between start and end are excluded from further analysis. After excluding data according to these criteria, data from 59 patients remained for inclusion in this study. The number of patients with data considered to be of sufficient duration for analysis and the average duration of these recordings for the different treatments are shown in Table 2.

The f-waves in the ECG are extracted using spatiotemporal QRST cancellation Stridh and Sornmo (2001). The AFR trends are then estimated by tracking the fundamental frequency of the extracted f-wave signal using a hidden Markov model-based approach Sandberg et al. (2008); resulting in a resolution for the AFR trends of one minute.

2.4 Parameter estimation

The atrial arrival rate, λ, is estimated by correcting the AFR trend, taking the atrial depolarization time into account Corino et al. (2013). Outliers in the estimated λ trends are excluded based on visual inspection guided by cluster analysis. The resulting trends are low-pass filtered using a sliding triangular window filter with a width equal to 70.

The model parameters $\boldsymbol{\theta}$ are assumed to vary over time, making this a dynamic optimization problem. Thus, the data are first divided into overlapping data segments of $N = 1000$ RR intervals; where N is chosen to give a good balance between resolution and robustness of the estimates. Each data segment contains one segment-specific mean arrival rate $\lambda^N(i)$ calculated as the mean of the λ trend in the segment starting at RR interval i, as well as one RR interval series, $\boldsymbol{RR}^N(i)$. The estimated parameters of a data segment starting at RR interval i is denoted by $\hat{\boldsymbol{\theta}}(i)$.

A fitness function based on the Poincaré plot - a scatter plot of successive pairs of RR intervals - is used to quantify the difference between observed and simulated RR series. The Poincaré plots are binned into two-dimensional bins with a width of 50 m, centered between 250 and 1800 m, forming a two-dimensional histogram. The error function (ϵ), i.e., the inverse fitness function, is then calculated from the number of samples in the bins according to Eq. 4,

$$\epsilon = \frac{1}{K}\sum_{k=1}^{K}\frac{\left(x_k^N - \frac{N}{N_{sim}}\tilde{x}_k^{N_{sim}}\right)^2}{\sqrt{\frac{N}{N_{sim}}\tilde{x}_k^{N_{sim}}}}, \tag{4}$$

where K is the number of bins, N_{sim} is the number of RR intervals simulated with the model, and x_k^N and $\tilde{x}_k^{N_{sim}}$ are the numbers of RR intervals in the k-th bin of the observed data and model output, respectively.

A genetic algorithm (GA) is used to search for the values of $\boldsymbol{\theta}$ yielding the minimum ϵ. A GA consists of a population of individuals that evolves based on their fitness value towards a solution using selection, crossover, and mutation Wahde (2008).

By assuming that a large change in the Poincaré plot relates to a large change in parameter values, it is possible before starting the optimization to decide when the optimization algorithm should focus on exploration or exploitation. As a heuristic for this, we introduce the difference in the Poincaré plots ($\Delta P(i)$), according to Eq. 5,

TABLE 2 The number of recordings and recording length (mean ± std) analyzed in this study following exclusion of recordings with insufficient signal quality, as described in Section 2.3.

Drug	Number of recordings	Recordings length (h)
Baseline	51	20.88 ± 2.85
Verapamil	53	21.92 ± 2.39
Diltiazem	56	21.71 ± 2.44
Metoprolol	53	21.87 ± 1.98
Carvedilol	57	21.23 ± 2.65
Total	270	21.52 ± 2.59

$$\Delta P(i) = \frac{1}{K}\sum_{k=1}^{K}\left(x_k^{N_{\Delta P}}(i) - x_k^{N_{\Delta P}}(i+1000)\right)^2, \quad (5)$$

where $x_k^{N_{\Delta P}}(i)$ and $x_k^{N_{\Delta P}}(i+1000)$ are the number of RR intervals in the k-th bin of the Poincaré plot for the RR interval series starting at interval i and i + 1000, respectively. Moreover, the segment length $N_{\Delta P}$ is set to 2000. The Poincaré plot difference, $\Delta P(i)$, is used to tune hyper-parameters in the optimization algorithm.

The GA used for estimating $\hat{\boldsymbol{\theta}}(i)$ has a population size of 400 individuals - where each individual is a vector of values for $\boldsymbol{\theta}$ - and uses tournament selection, a two-point crossover, and creep mutation Wahde (2008). The number of generations the GA runs before switching to the next data segment varies from 1 when $\Delta P(i) < 800$; to 2 when $800 \leq \Delta P(i) < 2000$; to 3 when $\Delta P(i) \geq 2000$. The step size for the sliding windows is determined by the trade-off between the resolution and the computing cost, and is set to 108 s; resulting in 800 steps for full 24-hour measurements. Thus, there will be 800 estimated $\hat{\boldsymbol{\theta}}(i)$ for a 24-hour measurement. As noted previously, there are also gaps in the data. Thus, the step size will partly vary to match the start and end of the RR segments, to ensure that all data are used. For reference, estimating the $\hat{\boldsymbol{\theta}}(i)$ trend from a 24-hour RR and λ series using a single core on a standard desktop computer (Intel® Core™ i7-6600U Processor, @ 2.60 GHz) requires on average 4 hours.

Since the Poisson process used to create the model input is stochastic, ϵ varies between realizations. This variation is dependent on the number of RR intervals generated from the model, where more RR intervals reduce the variation but require more computing power. To have a good balance between computing power and stability, N_{sim} is set to 1500. However, the ten fittest individuals in each generation are re-evaluated, with N_{sim} = 5000, before the individual with the best fit for each data segment, $\hat{\boldsymbol{\theta}}(i)$, is saved.

The individuals for the first generation are randomly initialized using a latin hypercube sampling in the ranges: $\{R_{\min}^{SP}, R_{\min}^{FP}\} \in [150, 650]$ *ms*; $\{\Delta R^{SP}, \Delta R^{FP}\} \in [0, 700]$ *ms*; $\{\tau_R^{SP}, \tau_R^{FP}\} \in [40, 300]$ *ms*; $\{D_{\min}^{SP}, D_{\min}^{FP}\} \in [0, 30]$ *ms*; $\{\Delta D^{SP}, \Delta D^{FP}\} \in [0, 75]$ *ms*; $\{\tau_D^{SP}, \tau_D^{FP}\} \in [40, 300]$ *ms*. These values are also used as boundaries for the model parameters. Hence, the difference between the upper bound and the lower bound for the parameters is the range that the parameters can vary within, here denoted $r(p)$ and in vector form $\boldsymbol{r}$, where p is the parameter index ordered as in $\boldsymbol{\theta}$.

To reduce the risk of premature convergence and to maintain a good diversity in the population, immigrants - individuals not created from the current population - are used. These immigrants are created using three different methods; 1) by saving and then re-using the ten most fit individuals and their model output per generation; 2) by running eight computationally faster GA, using only 16 individuals and N_{sim} = 750, simultaneously; and 3), by random sampling. The number of immigrants is dependent on $\Delta P(i)$ and is created in equal proportion using the three different creation methods. These new individuals are then introduced into the population at the start of every new data segment by replacing the individuals with the lowest fitness. More specific details about the GA are found in Supplementary Material, Section 1.

2.5 Parameter uncertainty estimation

A variant of Sobol's method Sobol (2001) is used to derive the uncertainty for each estimated parameter set $\hat{\boldsymbol{\theta}}(i)$. The contribution to the output variance ($v(p)$) for a parameter p, including the variation caused by its interaction with all the other parameters, is estimated by the following procedure. Firstly, two 30 x 12 matrices ($\boldsymbol{A}$ and $\boldsymbol{B}$), where 30 is the number of sampled parameter vectors, are generated by samples from a quasi Monte Carlo procedure based on the Latin hypercube design. Unlike Sobol's method - which samples in the whole parameter range - these samples are generated within $\hat{\boldsymbol{\theta}}(i) \pm 0.075\boldsymbol{r}$, hence within a hyper-rectangle covering 15% of the total range of each parameter. Secondly, 12 new matrices, $\boldsymbol{AB}_p$ are created by replacing the p-th column in $\boldsymbol{A}$ with the p-th from $\boldsymbol{B}$. Thirdly, ϵ is calculated for each parameter set in the matrices by running the model, before the expected value of the contribution to the output variance is estimated according to Eq. 6 Sobol (2001).

$$\hat{v}(p) = \frac{1}{2\cdot 30}\sum_{q=1}^{30}\left(\epsilon_{A_q} - \epsilon_{AB_{pq}}\right)^2. \quad (6)$$

Here ϵ_{A_q} and $\epsilon_{AB_{pq}}$ quantifies the difference between the observed RR series and the model output as given in Eq. 4, for the parameter sets in $\boldsymbol{A}$ and $\boldsymbol{AB}_p$, respectively.

The estimated $\hat{v}(p)$ are then, together with the mean ($\bar{\epsilon}$) and standard deviation (σ_ϵ) of the 30 realizations of $\hat{\boldsymbol{\theta}}(i)$, used to calculate a parameter uncertainty estimate according to Eq. 7.

$$u(p) = \frac{0.15r(p)}{\sqrt{\hat{v}(p)} - \sigma_\epsilon}0.1\bar{\epsilon}. \quad (7)$$

Here $0.15r(p)$ originates from the distance between $\hat{\boldsymbol{\theta}}(i)$ and the border of the sampled hyper-space, and $\sqrt{\hat{v}(p)} - \sigma_\epsilon$ from the difference between the error variation inside the hyper-space and at $\hat{\boldsymbol{\theta}}(i)$. Hence, the fraction relates to the slope-intercept between the parameter distance and the uncertainty. The remaining product relates this slope to 10% of the mean error for $\hat{\boldsymbol{\theta}}(i)$. Thus, the interpretation of $u(p)$ is: 'Assuming interaction between all model parameters, how large a step can be taken for parameter p before the contribution to ϵ for $\hat{\boldsymbol{\theta}}(i)$ is increased by 10%'. This was then repeated for all $\hat{\boldsymbol{\theta}}(i)$ for all patients and drugs.

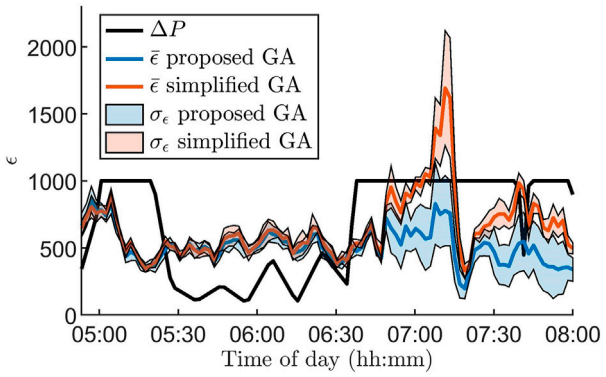

FIGURE 3
Mean (colored lines) and standard deviation (colored areas) of the error ϵ for 100 segments for the proposed genetic algorithm (blue) and a standard genetic algorithm (red) together with the Poincare difference $\Delta P(i)$ (black line), defined in Eq. 5, for data from one patient at baseline during 3 hours. The standard deviation and mean are based on ten runs of the algorithms. Note that $\Delta P(i)$ is scaled with $\frac{1}{5}$ for readability.

2.6 Circadian variation

The drug-dependent circadian variation for the estimated AV node parameters is quantified using linear mixed-effect modeling, i.e., using a statistical model comprising both fixed effects and random effects. The model used consists of a 24-hour periodic cosine with mean $\boldsymbol{m}$, amplitude $\boldsymbol{a}$, and phase $\boldsymbol{\phi}$, as seen in Eqs. 8, 9, and 10.

$$\boldsymbol{y}_{pat,m}(t) = \boldsymbol{m}_{pat,m} + \boldsymbol{a}_{pat,m} \cos\left(\frac{2\pi}{24}t + \boldsymbol{\phi}\right) \tag{8}$$

$$\boldsymbol{m}_{pat,m} = \boldsymbol{\alpha} + \boldsymbol{\alpha}_m + \boldsymbol{\eta}_{pat} + \boldsymbol{\eta}_{pat,m} \tag{9}$$

$$\boldsymbol{a}_{pat,m} = \boldsymbol{\beta} + \boldsymbol{\beta}_m + \boldsymbol{\xi}_{pat} + \boldsymbol{\xi}_{pat,m} \tag{10}$$

Here $\boldsymbol{y}_{pat,m}(t)$ represents the estimated parameter trends of patient *pat* during treatment $m \in$ {Baseline, Verapamil, Diltiazem, Metoprolol, Carvedilol}. Moreover, t corresponds to the time of the day, in hours, of the RR interval i that the estimated $\hat{\boldsymbol{\theta}}(i)$ relates to. Furthermore, $\boldsymbol{\alpha}$, $\boldsymbol{\alpha}_m$, $\boldsymbol{\beta}$, and $\boldsymbol{\beta}_m$ represent the fixed-effects; with $\boldsymbol{\alpha}$ and $\boldsymbol{\beta}$ corresponding to the mean value for the mean and amplitude during baseline, and $\boldsymbol{\alpha}_m$ and $\boldsymbol{\beta}_m$ to the average deviation from the baseline values, caused by the drugs. The random effects $\boldsymbol{\eta}_{pat}$, $\boldsymbol{\eta}_{pat,m}$, $\boldsymbol{\xi}_{pat}$, and $\boldsymbol{\xi}_{pat,m}$ correspond to the individual deviation from the fixed-effects, and are assumed to be sampled from a zero-mean gaussian distribution. During baseline, $\boldsymbol{\alpha}_m$, $\boldsymbol{\beta}_m$ and $\boldsymbol{\eta}_{pat,m}$, $\boldsymbol{\xi}_{pat,m}$ are assumed to be zero. For a given individual, $\boldsymbol{\phi}$ is assumed to be equal for all 12 model parameters and is estimated by means of principal component analysis of the $\hat{\boldsymbol{\theta}}(i)$ trends. The 12 vectors created by projecting the data onto the 12 principal components are fitted to a cosine with mean m_c, amplitude a_c, and phase ϕ_c, where c indicates the c-th principal component, using the simplex search method Lagarias et al. (1998). The phase, ϕ, is set equal to the ϕ_c associated with the highest a_c. Moreover, for cases where $\boldsymbol{a}_{pat,m}$ is negative, a phase-shift of π is added to ensure that all the amplitudes are positive.

With $\boldsymbol{\phi}$ estimated, $\boldsymbol{\alpha}$, $\boldsymbol{\alpha}_m$, $\boldsymbol{\beta}$, $\boldsymbol{\beta}_m$, $\boldsymbol{\eta}_{pat}$, $\boldsymbol{\eta}_{pat,m}$, $\boldsymbol{\xi}_{pat}$, and $\boldsymbol{\xi}_{pat,m}$ are fitted using the linear mixed-effects model function 'fitlme ()' in MATLAB (The MathWorks Inc. Version R2019b); using the full covariance matrix with the Cholesky parameterization and the maximum likelihood for estimating parameters of the linear mixed-effects model with trust region based quasi-Newton optimizer as settings.

An assessment of the goodness of fit for the linear mixed-effect model is calculated as the RMSE between the modeled cosine and the estimated parameters. For easier comparison between parameters, the RMSE for each parameter is weighted by their respective range, $r(p)$.

2.7 Statistic analysis

The estimated parameters $\hat{\boldsymbol{\theta}}(i)$, as well as AFR and HR, were averaged for each recording, and significant difference between the averages at baseline and under the four drugs were assessed one-by-one using the paired two-sided Wilcoxon signed rank test Woolson (2007) with the Benjamini–Hochberg correction Benjamini and Hochberg (1995). Patients with missing recordings (cf. Table 2) at baseline or the drug in question were excluded from the analysis. A p-value below 0.05 after correction was considered significant.

3 Results

Figure 3 illustrates the advantages of using the GA proposed in Section 2.4 for parameter estimation by comparing it to a standard version of the GA. For the standard GA, all hyper-parameters, as well as the number of generations per data segment, are fixed and thus do not take advantage of $\Delta P(i)$. To highlight the differences between the algorithms, we zoom in on a three hour long segment where the RR series characteristics change rapidly. It is clear that ϵ increases along with $\Delta P(i)$ for the standard GA, in contrast to the proposed GA.

From the GA we acquire one estimate per data segment, for all 59 patients and all drugs, resulting in a total of 175,640 $\hat{\boldsymbol{\theta}}(i)$. To give the reader a sense of the match between the model output and RR interval series obtained from the ECG, we present two examples of Poincaré plots and histograms together with the associated RR interval series. One corresponds to the median ϵ, and one where ϵ is higher than 95% of all ϵ, as shown in Figure 4. It is evident that the histograms and Poincaré plots from the model output and data are similar for both cases, indicating a good match to data in most data segments. However, there is a considerable difference on a beat-to-beat level, as indicated by the RR interval series. Moreover, $\hat{\boldsymbol{\theta}}(i)$ for one patient at baseline is shown in Figure 5, where clear changes over time can be seen.

TABLE 3 Recording averages of estimated model parameters, AFR, and HR at baseline and during treatment with the four different drugs (mean ± standard deviation). Differences from baseline are evaluated using the Wilcoxon signed rank test with the Benjamini–Hochberg correction; significant difference from baseline for the drugs, with false discovery rate at 0.05, is indicated with *.

Parameter	Baseline	Verapamil	Diltiazem	Metoprolol	Carvedilol
$R_{\min}^{FP}$ (ms)	435 ± 139	488 ± 134*	518 ± 118*	489 ± 126*	476 ± 123*
ΔR^{FP} (ms)	403 ± 195	478 ± 190*	488 ± 202*	495 ± 180*	483 ± 172*
τ_R^{FP} (ms)	175 ± 59	165 ± 63	163 ± 64	162 ± 58	167 ± 57
$R_{\min}^{SP}$ (ms)	241 ± 102	280 ± 125*	287 ± 124*	260 ± 114	269 ± 123
ΔR^{SP} (ms)	231 ± 176	274 ± 201	301 ± 215*	312 ± 187*	274 ± 186*
τ_R^{SP} (ms)	180 ± 60	183 ± 62	171 ± 63	176 ± 62	176 ± 63
$D_{\min}^{FP}$ (ms)	5.3 ± 4.5	5.4 ± 4.8	5.4 ± 4.7	5.9 ± 4.5	5.3 ± 4.5
ΔD^{FP} (ms)	18.9 ± 16.9	21.7 ± 17.2	22.1 ± 17.3	21.8 ± 16.7	21.4 ± 16.9
τ_D^{FP} (ms)	141 ± 54	144 ± 50	145 ± 53	149 ± 50	142 ± 53
$D_{\min}^{SP}$ (ms)	21.0 ± 5.3	21.6 ± 5.1	22.5 ± 5.2*	21.7 ± 4.8	21 ± 5.2
ΔD^{SP} (ms)	26.3 ± 21.4	23.8 ± 20.9	19.6 ± 20.7*	22.6 ± 21.2	21.5 ± 20.8
τ_D^{SP} (ms)	185 ± 68	184 ± 57	183 ± 65	186 ± 58	180 ± 65
HR (bpm)	95 ± 13	80 ± 12*	74 ± 10*	81 ± 10*	84 ± 11*
AFR (Hz)	4.96 ± 0.34	4.56 ± 0.45*	4.71 ± 0.44*	4.86 ± 0.40*	4.81 ± 0.51*

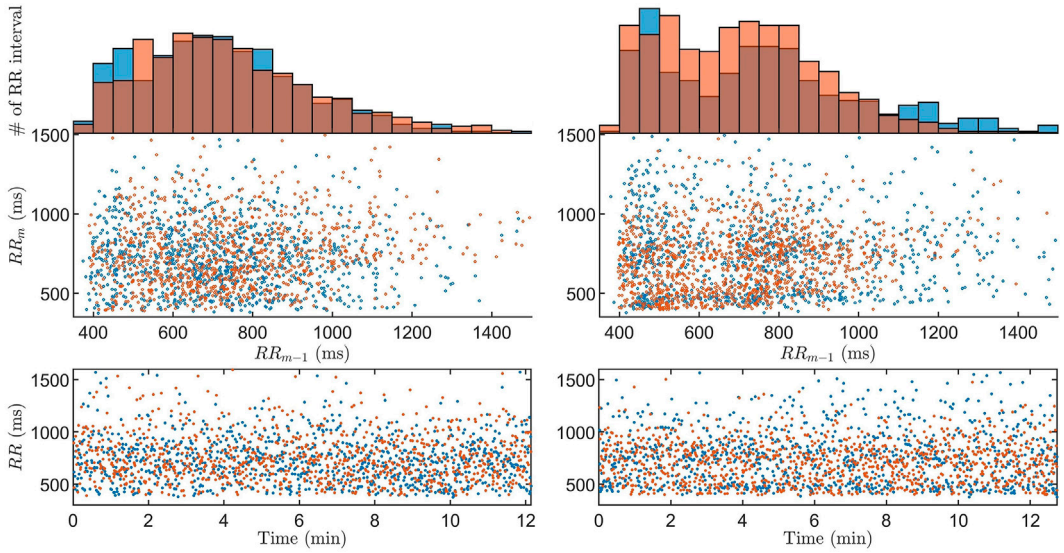

FIGURE 4
The Poincaré plot with associated histogram and RR interval series of data (blue) and model output (orange) for the $\hat{\theta}(i)$ corresponding to the median ϵ (left) and to the $\hat{\theta}(i)$ which ϵ is higher than 95% of all ϵ (right).

Recording averages of estimated model parameters, AFR, and HR at baseline and during treatment with the four different drugs are shown in Table 3. Significant differences, as described in Section 2.7, are indicated in the table by '*'. This shows a significant increase in the refractory period in the FP for all drugs, as well as a significant decrease in heart rate and AFR for all drugs.

3.1 Uncertainty estimation

The average $u(p)$, as explained in Eq. 7, normalized with $r(p)$, are shown in Figure 6. From this, it is evident that the model parameters relating to the SP are more robustly estimated than their FP counterpart, and that the model parameters relating to the

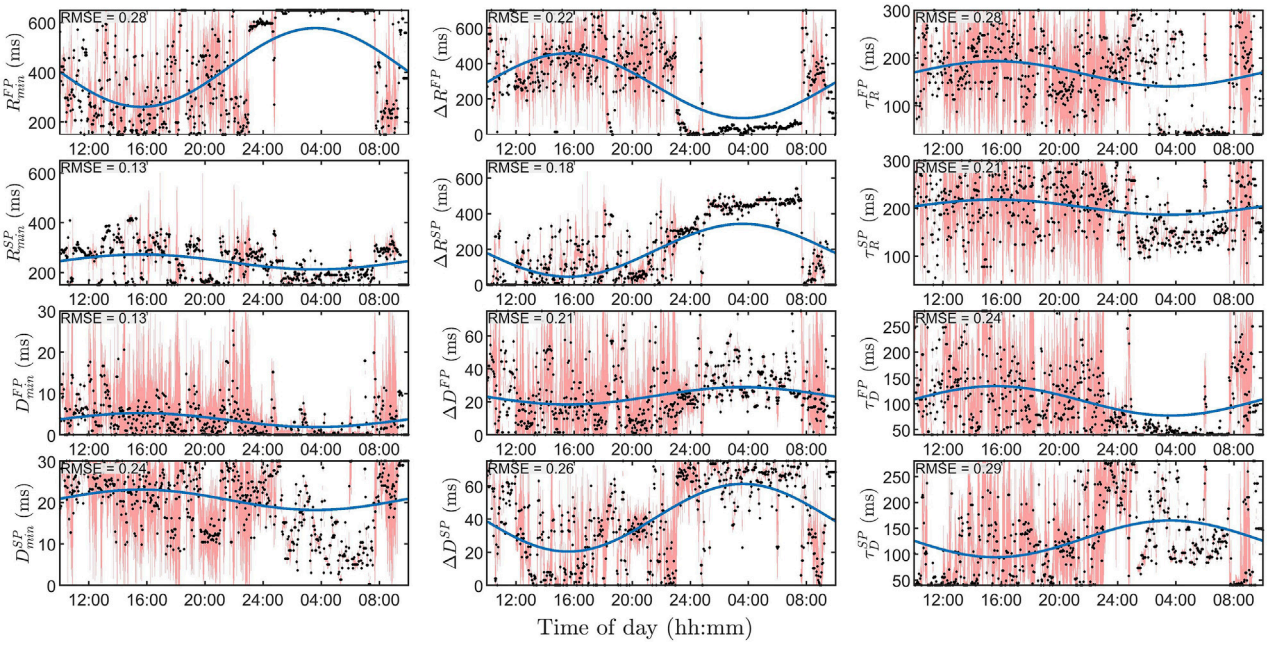

FIGURE 5
Estimated model parameters $\hat{\boldsymbol{\theta}}(i)$ (black dots), with corresponding uncertainty estimates *PU* (red areas), along with the fitted cosine (blue lines) used for the circadian variation, for one patient during baseline. In each panel, the RMSE is reported as a measure of goodness of fit between $\hat{\boldsymbol{\theta}}(i)$ and the fitted cosine. Left column shows the parameters relating to the minimum conduction delay or refractory period, the middle column the parameters relating to the maximum prolongation, and the right column to the time constants. For further explanation of the model parameters, see Table 1.

refractory period are more robustly estimated than their conduction delay counterpart. Most noteworthy is the lower uncertainty for R^{SP}_{min} and ΔR^{SP}, suggesting a higher impact on the output of the model.

The uncertainty estimates, $u(p)$, for one patient are shown as red background for each $\hat{\boldsymbol{\theta}}(i)$ in Figure 5, where again $u(p)$ for the refractory parameters in the SP is lower. There is also a clear difference in $u(p)$ between nighttime and daytime, where the uncertainty is much lower at night.

3.2 Circadian variation

In Figure 5 we also show an example of the circadian variation (blue lines) for the aforementioned patient, as explained in Eqs. 8, 9, and 10, where a clear distinction between night and day can be seen for most parameters. The average RMSE for the 12 model parameters seen in Figure 5 is 0.22, which can be compared with the average RMSE for all patients and treatment of 0.16 ± 0.03 (mean ± std).

The mean and standard deviation of the circadian variation phase ϕ was 1.03 ± 0.74 rad; corresponding to an extreme value at approximately 04:00 am ± 2.8 h.

The fixed-effects $\boldsymbol{\alpha}_m$ and $\boldsymbol{\beta}_m$ and their respective 95% confidence interval, normalized with $r(p)$, are shown in Figure 7, where the fixed-effects represent the average difference in effect with respect to baseline that the drugs have on the population. It is evident from $\boldsymbol{\alpha}_m$ in Figure 7 (top panel) that all rate control drugs on average increase the refractory period in both pathways; with a significant increase ($p < 0.05$) in R^{FP}_{min} and Δ^{FP} for all drugs, in R^{SP}_{min} for all but metoprolol, and in ΔR^{SP} for all but verapamil. Moreover, differences between the β-blockers and the calcium channel blockers can be observed. Most noticeably for the amplitude ($\boldsymbol{\beta}_m$) of ΔD^{FP} and ΔD^{SP}, where the two β-blockers have a distinctly negative effect in comparison with the two calcium channel blockers.

Detailed results for the estimated fixed and random effects can be found in the Supplementary Material, Section 2.

4 Discussion

In this study, we have presented a mathematical framework able to continuously estimate model parameters representing the conduction delay and refractory period of the AV node during 24 h for patients with permanent AF from ECG data. Trends in the estimated model parameters were analyzed using a mixed-effects model to study the circadian variation, where drug-dependent differences could be seen.

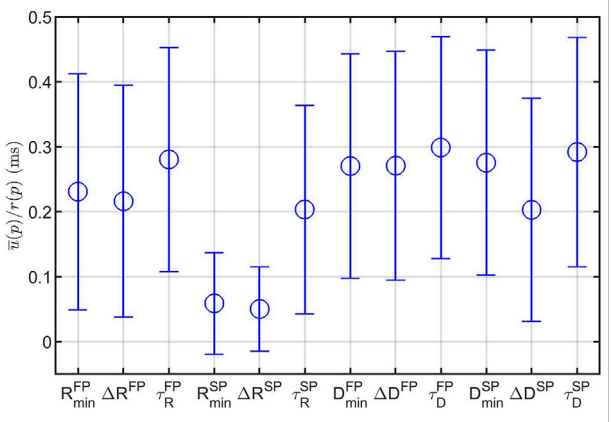

FIGURE 6
Mean (circles) ± one standard deviation (bars) of the parameter uncertainty estimates $u(p)$ over all recordings and all patients, normalized with the parameter ranges $r(p)$. Note that the model parameters R^{SP}_{min} and ΔR^{SP} have a lower uncertainty, indicating a higher impact on the resulting model outcome.

The model has previously been shown to be able to represent measured data in the form of histograms and Poincaré plots for 20-min long segments Karlsson et al. (2021). However, continuously estimating model parameters representing the refractory period and conduction delay in the AV node has previously not been possible. A previous study of the RR interval series has indicated that one interval delay in the autocorrelation gives sufficient information to replicate the dynamics of the RR interval series Karlsson et al. (2021). Hence, the Poincaré plot was chosen as a basis for the fitness function in order to take the one interval delay of the RR interval series into account, something that is not possible with an one-dimensional distribution representation such as the histogram. Moreover, since the model describes the impulses from the atria as a stochastic process, it is not possible to have a beat-to-beat level of detail in the fitness function, as evident by the RR interval series in Figure 4.

The choice of segment length N is a trade-off between robustness and time-resolution. The segment length N was set to 1000 RR intervals, corresponding to a time duration of 11 : 53 ± 03 : 28 (mm:ss), to capture changes in RR series characteristics on this time-scale while allowing sufficient estimation accuracy. As a consequence of the choice of N = 1000, the bin size of 50 m was used for the Poincaré plot-based error function. A smaller bin size would allow a more detailed match between model output and data, but would require more RR intervals.

From Figure 4, it is evident that the model and workflow can replicate the histogram and Poincaré plot of obtained RR interval series even for the case with the 95% highest ϵ. This was made possible by using the problem-specific GA presented in Section 2.4. Evolutionary algorithms - such as GA - and particle swarm optimization are the most common optimization algorithms used for solving dynamic optimization problems Yazdani et al. (2021); Mavrovouniotis et al. (2017).

One of the main challenges with dynamic optimization problems is the balance between exploration and exploitation, i.e., between searching for different promising regions of the search space, or searching for the optimal solutions within an already promising region. To keep a good level of exploration, the diversity in the population - usually defined as the average Euclidean distance between the individuals in the population - is often monitored. Thus, diversity loss is one of the most critical challenges Yazdani et al. (2021). A great number of methods have been developed to address this diversity loss, often based on randomizing individuals in the population that are too similar to others. For example, crowding - letting new individuals replace

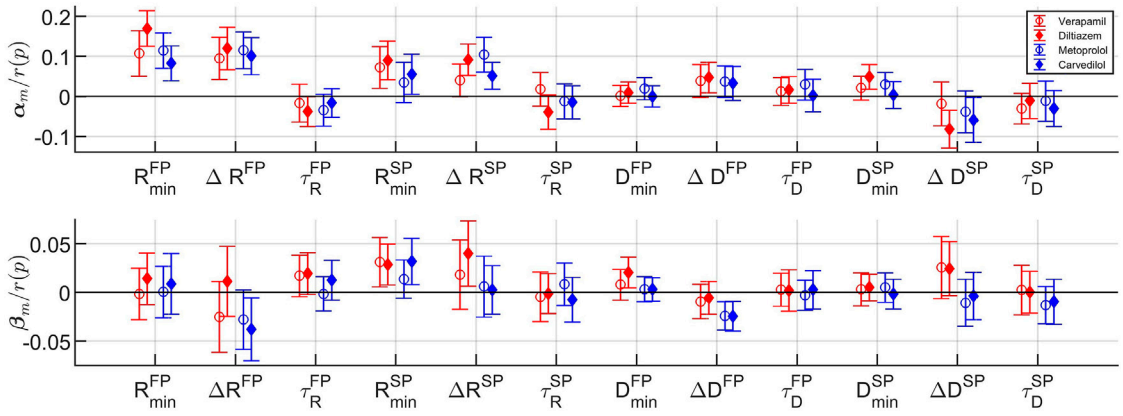

FIGURE 7
The fixed effects with corresponding 95% confidence intervals for the cosinor mean ***m*** (top) and cosinor amplitude ***a*** (bottom) for each model parameter (cf. Table 1) and drug. Confidence intervals not overlapping zero indicate significant difference from baseline (p <0.05).

the most similar individual in the population Kordestani et al. (2014) - or based on the age of the individuals Das et al. (2013). For GA, it is also possible to combat diversity loss by regulating the mutation rate. However, maintaining a good level of exploration using diversity does not take any information about the data into account. In contrast, changing the mutation rate, the number of immigrants, and the number of generations per segment using $\Delta P(i)$ - as was done in this study - takes information about the data directly into account. Additionally, the number of immigrants in the proposed GA ranges from 10–70%, which limits the initialization's effect on the overall results. Moreover, the results in Figure 3 indicate that the proposed problem-specific optimization method yields a better fit compared to the standard approach when the characteristics of the data change rapidly. On the other hand, when the characteristics of the data change slowly, the performance is similar even though the proposed algorithm is using fewer generations per segment. The number of RR intervals simulated with the model for each parameter set, N_{sim}, was set to 1500 in the GA based on a trade-off between computational complexity and variation based on the stochastic input sequence to the model. A simulation study relating the variation in ϵ and N_{sim} which was used to guide the decision is shown in the Supplementary Material, Section 1. Moreover, the thresholds for ΔP to determine how many generations are to be run per data segment were set so that approximately 55% are run for 1 generation, 30% are run for 2 generations, and the remaining 15% are run for 3.

A variation of Sobol's method was used to estimate the contribution to output variance for each model parameter, which was related to an increase in error by 10%. This more complex methodology was preferred over a one-at-a-time approach due to the large effect that interaction between model parameters has on the model output. Note that, unlike more traditional uncertainty estimates, this is not directly connected to a probability, since the error function used does not have a proper probabilistic interpretation. Thus, the uncertainty shall only be interpreted as a relative measure between the model parameters, between patients, and between the time of day. For example, it is evident in Figure 5 that the uncertainty for this patient is much lower during nighttime than daytime.

A linear mixed-effect model based on a cosinor analysis was used to derive the circadian variations. This method was used to quantify the circadian variation for the different drugs over the whole population, as well as the individual response to the drugs. The focus of this study is on the population effects of the different drug types in order to understand the drug-dependent differences in the conduction properties, something that needs to be understood before the method could be applicable on an individual level. Even though the focus of this study is on the population level, the individual responses are still of interest, especially for future work. For example, to predict individual responses to different drugs. As shown in Figure 5, the individual match is not optimal, thus a better tool for capturing the circadian variation is believed to be needed before robust analysis on an individual level is feasible. However, the cosinor analysis is an established model for characterizing circadian variation and has previously been used on the RATAF data-set to study heart rate variation Corino et al. (2015a).

From Table 3, in the parameters $R^{FP}_{\min}$ and ΔR^{FP}, we see a significantly increased refractory period relative to baseline in the FP for all four drugs. In addition, a significant increase in the SP for either $R^{SP}_{\min}$, or ΔR^{SP} could also be seen for all drugs. This increase is also visible in the fixed effect parameters $\boldsymbol{\alpha}_m$ in Figure 7, top panel. Electrophysiological studies of the two calcium channel blockers verapamil and diltiazem as well as the β-blocker metoprolol have shown that the drugs increase the refractoriness in the AV node Leboeuf et al. (1989); Talajic et al. (1992); Rizzon et al. (1978). Moreover, carvedilol has been shown to increase the effective refractory period in the atria during AF Kanoupakis et al. (2004). However, to the best of our knowledge, no studies have been conducted to determine the effect of carvedilol specifically for the refractory period in the AV node. Furthermore, conduction properties in the atria influence the model through the mean arrival rate λ, and thus affect the estimated parameters.

In addition, from Figure 7 bottom panel, it is shown that the two β-blockers reduce the circadian variation of the conduction delay more than the calcium channel blockers, as evident by ΔD^{FP} and ΔD^{SP}. Stimulation of the β_1-receptors - regulated by the autonomic nervous system - have been shown to increase the conduction velocity in the AV node Gordan et al. (2015). Hence, blocking this receptor using β-blocking drugs might decrease the autonomic nervous system effect, and thus reduce the circadian variation, yielding the presented results.

Also seen in Figure 7, the model parameters for the two β-blockers often behave similarly. However, the model parameters for the calcium channel blockers verapamil and diltiazem do not always align. In fact, the values for $\boldsymbol{\alpha}_m$ and $\boldsymbol{\beta}_m$ for verapamil are in several cases - most noticeably for $R^{FP}_{\min}$ for $\boldsymbol{\alpha}_m$ and ΔR^{FP}, ΔR^{SP}, and $D^{FP}_{\min}$ for $\boldsymbol{\beta}_m$ - similar to those of the two β-blockers. Interestingly, it has previously been proposed that the pharmacological effects of verapamil may partly be due to some degree of β-blockade Drici et al. (1993).

Moreover, the large confidence intervals in Figure 7, where the majority includes zero, are most likely due to the high inter-patient variability in parameter values. A confidence interval that includes zero would indicate that there is no significant difference from baseline. The high inertia and simplicity of the cosine are other factors in this. For example, some patients have more than one section with parameter values close to those during the night - possibly due to periods of sleep during the day - which a cosine with a period of 24 h could not capture.

4.1 Study limitations and future perspectives

The present model of the AV node accounts for dual pathway physiology and rate dependent changes in conduction delay and refractoriness and can simulate retrograde conduction. However, it is not able to simulate some physiological interesting phenomena such as AV node re-entry.

A limited range for the model parameters was used to make the optimization more efficient. The choice of the boundaries was guided by electrophysiological measurements from previous clinical studies while keeping a conservative range to not exclude realistic values. The maximal refractory period for the model - given as the sum of R_{min} and ΔR - lies in the range [150, 1350] ms and was set to include the effective refractory period of the AV node, which has been reported as 361 ± 57 and 283 ± 48 m for the FP and SP, respectively Natale et al. (1994). Furthermore, the conduction delay of the whole model is given by the sum of D_{min} and ΔD multiplied by the number of nodes, which lies in the range [0, 1050] ms. Thus, it includes all realistic PR intervals, which rarely exceed 200 m Schumacher et al. (2017). Even though the boundaries were conservatively chosen, we cannot exclude the possibility that a different choice would have affected the resulting parameter values. Moreover, since the parameters might be hard to interpret, combining the model parameters associated with the same conduction property, i.e., the two refractory periods and the two conduction delays, to create more interpretable representations, is interesting.

As mentioned before, high inertia and simplicity of the cosine are limiting factors for the assessment of circadian variation. However, the cosinor analysis is an established model for characterizing circadian variation and is thus important for clear and interpretable results. Using the estimated uncertainty to weight the estimated parameters is one possible approach to make the cosine fit the estimates better. Other methods to capture the differences in the AV node parameters over time, such as time-frequency analysis of the estimated parameter trends, should also be investigated.

It should be noted that the estimated model parameters are not clinically validated for assessment of AV node refractoriness and conduction delay. Hence, the clinical significance of the results should be interpreted with caution. However, the overall findings for the different drugs on the whole population are, as discussed above, in accordance with electrophysiological studies. Another limitation is the sample size of 60 patients in combination with the high inter-patient variability in parameter values, as seen in the large standard deviation in Table 3. This makes the population estimates more uncertain, partly causing the large confidence intervals seen in Figure 7.

A natural continuation of this work is to analyze the estimated model parameters during baseline, possible in combinations with other factors such as age or gender, to predict the mean heart rate under the influence of the different drugs. This in turn could be used to assist in personalized treatment selection during AF.

5 Conclusion

We have presented a framework - including a mathematical model and a genetic algorithm - which for the first time enables characterization of the refractory period and the conduction delay of the AV node during 24 h for patients with permanent AF, solely based on non-invasive data.

With ECG from AF patients during baseline and under the influence of different rate control drugs, a mixed-model framework was used on the estimated model parameters to compare the impact on circadian variation between drugs. From this, differences in conduction delay could be identified between β-blockers and calcium channel blockers, which was previously unknown.

Data availability statement

The data analyzed in this study is subject to the following licenses/restrictions: The estimated model parameters $\boldsymbol{\theta}_{(i)}$ and associated uncertainty estimate u(p) supporting the conclusions for this article will be available from MK upon request. The ECG data are owned by Vestre Viken Hospital Trust, and requests for access can be made to SU. The code for the model together with an user example can be found at https://github.com/FraunhoferChalmersCentre/AV-node-model.

Ethics statement

The studies involving human participants were reviewed and approved by Regional ethics committee and the Norwegian Medicines Agency. The patients/participants provided their written informed consent to participate in this study.

Author contributions

MK, FS, and MW contributed to the conception and design of the study. SU was responsible for the clinical study. FS was responsible for the ECG pre-processing and estimation of the RR interval series and AFR trends. MK wrote the manuscript and designed the genetic algorithm, the method for the uncertainty estimation, and the circadian variation model, with advice, suggestions, and supervision from FS and MW. PP and SU analyzed and gave medical interpretations of the results. FS and MW supervised the project and reviewed the manuscript during the whole writing process. All authors contributed to manuscript revision, read, and approved the submitted version.

Funding

This work was supported by the Swedish Foundation for Strategic Research (Grant FID18-0023), the Swedish Research Council (Grant VR 2019–04272), and the Crafoord Foundation (Grant 20200605).

Conflict of interest

The authors declare that the research was conducted in the absence of any commercial or financial relationships that could be construed as a potential conflict of interest.

Publisher's note

All claims expressed in this article are solely those of the authors and do not necessarily represent those of their affiliated organizations, or those of the publisher, the editors and the reviewers. Any product that may be evaluated in this article, or claim that may be made by its manufacturer, is not guaranteed or endorsed by the publisher.

Supplementary material

The Supplementary Material for this article can be found online at: https://www.frontiersin.org/articles/10.3389/fphys.2022.976526/full#supplementary-material

References

Benjamin, E. J., Muntner, P., Alonso, A., Bittencourt, M. S., Callaway, C. W., Carson, A. P., et al. (2019). Heart disease and stroke statistics-2019 update a report from the American heart association. *Circulation* 139, e56–e528. doi:10.1161/CIR.0000000000000659

Benjamini, Y., and Hochberg, Y. (1995). Controlling the false discovery rate: A practical and powerful approach to multiple testing. *J. R. Stat. Soc. Ser. B Methodol.* 57, 289–300. doi:10.1111/j.2517-6161.1995.tb02031.x

Billette, J., and Nattel, S. (1994). Dynamic behavior of the atrioventricular node: A functional model of interaction between recovery, facilitation, and fatigue. *J. Cardiovasc. Electrophysiol.* 5, 90–102. doi:10.1111/j.1540-8167.1994.tb01117.x

Climent, A. M., Guillem, M. S., Husser, D., Castells, F., Millet, J., and Bollmann, A. (2010). Role of the atrial rate as a factor modulating ventricular response during atrial fibrillation. *Pacing Clin. Electrophysiol.* 33, 1510–1517. doi:10.1111/j.1540-8159.2010.02837.x

Climent, A. M., Guillem, M. S., Zhang, Y., Millet, J., and Mazgalev, T. (2011). Functional mathematical model of dual pathway av nodal conduction. *Am. J. Physiol. Heart Circ. Physiol.* 300, H1393–H1401. doi:10.1152/ajpheart.01175.2010

Corino, V. D., Platonov, P. G., Enger, S., Tveit, A., and Ulimoen, S. R. (2015a). Circadian variation of variability and irregularity of heart rate in patients with permanent atrial fibrillation: Relation to symptoms and rate control drugs. *Am. J. Physiol. Heart Circ. Physiol.* 309, H2152–H2157. doi:10.1152/ajpheart.00300.2015

Corino, V. D., Sandberg, F., Lombardi, F., Mainardi, L. T., and Sörnmo, L. (2013). Atrioventricular nodal function during atrial fibrillation: Model building and robust estimation. *Biomed. Signal Process. Control* 8, 1017–1025. doi:10.1016/j.bspc.2012.10.006

Corino, V. D., Sandberg, F., Mainardi, L. T., and Sornmo, L. (2011). An atrioventricular node model for analysis of the ventricular response during atrial fibrillation. *IEEE Trans. Biomed. Eng.* 58, 3386–3395. doi:10.1109/TBME.2011.2166262

Corino, V. D., Ulimoen, S. R., Enger, S., Mainardi, L. T., Tveit, A., and Platonov, P. G. (2015b). Rate-control drugs affect variability and irregularity measures of rr intervals in patients with permanent atrial fibrillation. *J. Cardiovasc. Electrophysiol.* 26, 137–141. doi:10.1111/jce.12580

Das, S., Mandal, A., and Mukherjee, R. (2013). An adaptive differential evolution algorithm for global optimization in dynamic environments. *IEEE Trans. Cybern.* 44, 966–978. doi:10.1109/TCYB.2013.2278188

Di Carlo, A., Bellino, L., Consoli, D., Mori, F., Zaninelli, A., Baldereschi, M., et al. (2019). Prevalence of atrial fibrillation in the Italian elderly population and projections from 2020 to 2060 for Italy and the European Union: The fai project. *Europace* 21, 1468–1475. doi:10.1093/europace/euz141

Drici, M., Jacomet, Y., Iacono, P., and Lapalus, P. (1993). Is verapamil also a non-selective beta blocker? *Int. J. Clin. Pharmacol. Ther. Toxicol.* 31, 27–30.

Gordan, R., Gwathmey, J. K., and Xie, L.-H. (2015). Autonomic and endocrine control of cardiovascular function. *World J. Cardiol.* 7, 204–214. doi:10.4330/wjc.v7.i4.204

Henriksson, M., Corino, V. D., Sörnmo, L., and Sandberg, F. (2015). A statistical atrioventricular node model accounting for pathway switching during atrial fibrillation. *IEEE Trans. Biomed. Eng.* 63, 1842–1849. doi:10.1109/TBME.2015.2503562

Hindricks, G., Potpara, T., Dagres, N., Arbelo, E., Bax, J. J., Blomström-Lundqvist, C., et al. (2021). 2020 ESC guidelines for the diagnosis and management of atrial fibrillation developed in collaboration with the European association for cardio-thoracic surgery (EACTS) the task force for the diagnosis and management of atrial fibrillation of the European society of cardiology (ESC) developed with the special contribution of the European heart rhythm association (EHRA) of the ESC. *Eur. Heart J.* 42, 373–498. doi:10.1093/eurheartj/ehaa612

Inada, S., Hancox, J., Zhang, H., and Boyett, M. (2009). One-dimensional mathematical model of the atrioventricular node including atrio-nodal, nodal, and nodal-his cells. *Biophys. J.* 97, 2117–2127. doi:10.1016/j.bpj.2009.06.056

Jørgensen, P., Schäfer, C., Guerra, P. G., Talajic, M., Nattel, S., and Glass, L. (2002). A mathematical model of human atrioventricular nodal function incorporating concealed conduction. *Bull. Math. Biol.* 64, 1083–1099. doi:10.1006/bulm.2002.0313

Kanoupakis, E. M., Manios, E. G., Mavrakis, H. E., Tzerakis, P. G., Mouloudi, H. K., and Vardas, P. E. (2004). Comparative effects of carvedilol and amiodarone on conversion and recurrence rates of persistent atrial fibrillation. *Am. J. Cardiol.* 94, 659–662. doi:10.1016/j.amjcard.2004.05.037

Karlsson, M., Sandberg, F., Ulimoen, S. R., and Wallman, M. (2021). Non-invasive characterization of human av-nodal conduction delay and refractory period during atrial fibrillation. *Front. Physiol.* 12, 728955. doi:10.3389/fphys.2021.728955

Kordestani, J. K., Rezvanian, A., and Meybodi, M. R. (2014). Cdepso: A bi-population hybrid approach for dynamic optimization problems. *Appl. Intell. (Dordr).* 40, 682–694. doi:10.1007/s10489-013-0483-z

Lagarias, J. C., Reeds, J. A., Wright, M. H., and Wright, P. E. (1998). Convergence properties of the Nelder–Mead simplex method in low dimensions. *SIAM J. Optim.* 9, 112–147. doi:10.1137/s1052623496303470

Lagerholm, M., Peterson, C., Braccini, G., Edenbrandt, L., and Sornmo, L. (2000). Clustering ecg complexes using hermite functions and self-organizing maps. *IEEE Trans. Biomed. Eng.* 47, 838–848. doi:10.1109/10.846677

Leboeuf, J., Lamar, J., Massingham, R., and Ponsonnaille, J. (1989). Electrophysiological effects of bepridil and its quaternary derivative cerm 11888 in closed chest anaesthetized dogs: A comparison with verapamil and diltiazem. *Br. J. Pharmacol.* 98, 1351–1359. doi:10.1111/j.1476-5381.1989.tb12684.x

Mangin, L., Vinet, A., Pagé, P., and Glass, L. (2005). Effects of antiarrhythmic drug therapy on atrioventricular nodal function during atrial fibrillation in humans. *Europace* 7, S71–S82. doi:10.1016/j.eupc.2005.03.016

Mase, M., Disertori, M., Marini, M., and Ravelli, F. (2017). Characterization of rate and regularity of ventricular response during atrial tachyarrhythmias. insight on atrial and nodal determinants. *Physiol. Meas.* 38, 800–818. doi:10.1088/1361-6579/aa6388

Masè, M., Glass, L., Disertori, M., and Ravelli, F. (2012). Nodal recovery, dual pathway physiology, and concealed conduction determine complex av dynamics in human atrial tachyarrhythmias. *Am. J. Physiol. Heart Circ. Physiol.* 303, H1219–H1228. doi:10.1152/ajpheart.00228.2012

Masè, M., Marini, M., Disertori, M., and Ravelli, F. (2015). Dynamics of av coupling during human atrial fibrillation: Role of atrial rate. *Am. J. Physiol. Heart Circ. Physiol.* 309, H198–H205. doi:10.1152/ajpheart.00726.2014

Mavrovouniotis, M., Li, C., and Yang, S. (2017). A survey of swarm intelligence for dynamic optimization: Algorithms and applications. *Swarm Evol. Comput.* 33, 1–17. doi:10.1016/j.swevo.2016.12.005

Natale, A., Klein, G., Yee, R., and Thakur, R. (1994). Shortening of fast pathway refractoriness after slow pathway ablation. effects of autonomic blockade. *Circulation* 89, 1103–1108. doi:10.1161/01.cir.89.3.1103

Rizzon, P., Di Biase, M., Chiddo, A., Mastrangelo, D., and Sorgente, L. (1978). Electrophysiological properties of intravenous metoprolol in man. *Br. Heart J.* 40, 650–655. doi:10.1136/hrt.40.6.650

Sandberg, F., Stridh, M., and Sornmo, L. (2008). Frequency tracking of atrial fibrillation using hidden markov models. *IEEE Trans. Biomed. Eng.* 55, 502–511. doi:10.1109/TBME.2007.905488

Schumacher, K., Dagres, N., Hindricks, G., Husser, D., Bollmann, A., and Kornej, J. (2017). Characteristics of pr interval as predictor for atrial fibrillation: Association with biomarkers and outcomes. *Clin. Res. Cardiol.* 106, 767–775. doi:10.1007/s00392-017-1109-y

Shrier, A., Dubarsky, H., Rosengarten, M., Guevara, M. R., Nattel, S., and Glass, L. (1987). Prediction of complex atrioventricular conduction rhythms in humans with use of the atrioventricular nodal recovery curve. *Circulation* 76, 1196–1205. doi:10.1161/01.cir.76.6.1196

Sobol, I. M. (2001). Global sensitivity indices for nonlinear mathematical models and their Monte Carlo estimates. *Math. Comput. Simul.* 55, 271–280. doi:10.1016/s0378-4754(00)00270-6

Stridh, M., and Sornmo, L. (2001). Spatiotemporal qrst cancellation techniques for analysis of atrial fibrillation. *IEEE Trans. Biomed. Eng.* 48, 105–111. doi:10.1109/10.900266

Sun, J., Amellal, F., Glass, L., and Billette, J. (1995). Alternans and period-doubling bifurcations in atrioventricular nodal conduction. *J. Theor. Biol.* 173, 79–91. doi:10.1006/jtbi.1995.0045

Talajic, M., Lemery, R., Roy, D., Villemaire, C., Cartier, R., Coutu, B., et al. (1992). Rate-dependent effects of diltiazem on human atrioventricular nodal properties. *Circulation* 86, 870–877. doi:10.1161/01.cir.86.3.870

Ulimoen, S. R., Enger, S., Carlson, J., Platonov, P. G., Pripp, A. H., Abdelnoor, M., et al. (2013). Comparison of four single-drug regimens on ventricular rate and arrhythmia-related symptoms in patients with permanent atrial fibrillation. *Am. J. Cardiol.* 111, 225–230. doi:10.1016/j.amjcard.2012.09.020

Wahde, M. (2008). *Biologically inspired optimization methods: An introduction*. Southampton: WIT press.

Woolson, R. F. (2007). *Wilcoxon signed-rank test*. Wiley encyclopedia of clinical trials, 1–3.

Yazdani, D., Cheng, R., Yazdani, D., Branke, J., Jin, Y., and Yao, X. (2021). A survey of evolutionary continuous dynamic optimization over two decades—Part a. *IEEE Trans. Evol. Comput.* 25, 609–629. doi:10.1109/tevc.2021.3060014

frontiers | Frontiers in Physiology

TYPE Original Research
PUBLISHED 06 October 2022
DOI 10.3389/fphys.2022.1030025

OPEN ACCESS

EDITED BY
Juan Pablo Martínez,
University of Zaragoza, Spain

REVIEWED BY
Vincent Jacquemet,
Université de Montréal, Canada
Fa-Po Chung,
Taipei Veterans General Hospital, Taiwan
Ali Gharaviri,
University of Edinburgh, United Kingdom

*CORRESPONDENCE
Natasja M. S. De Groot,
n.m.s.degroot@erasmusmc.nl

SPECIALTY SECTION
This article was submitted to Cardiac Electrophysiology, a section of the journal Frontiers in Physiology

RECEIVED 28 August 2022
ACCEPTED 22 September 2022
PUBLISHED 06 October 2022

CITATION
Van Schie MS, Knops P, Zhang L, Van Schaagen FRN, Taverne YJJ and De Groot NMS (2022), Detection of endo-epicardial atrial low-voltage areas using unipolar and omnipolar voltage mapping.
Front. Physiol. 13:1030025.
doi: 10.3389/fphys.2022.1030025

Detection of endo-epicardial atrial low-voltage areas using unipolar and omnipolar voltage mapping

Mathijs S. Van Schie[1], Paul Knops[1], Lu Zhang[1], Frank R. N. Van Schaagen[2], Yannick J. H. J. Taverne[2] and Natasja M. S. De Groot[1]*

[1]Department of Cardiology, Erasmus Medical Center, Rotterdam, Netherlands, [2]Department of Cardiothoracic Surgery, Erasmus Medical Center, Rotterdam, Netherlands

Background: Low-voltage areas (LVA) can be located exclusively at either the endocardium or epicardium. This has only been demonstrated for bipolar voltages, but the value of unipolar and omnipolar voltages recorded from either the endocardium and epicardium in predicting LVAs at the opposite layer remains unknown. The goal of this study was therefore to compare simultaneously recorded endo-epicardial unipolar and omnipolar potentials and to determine whether their voltage characteristics are predictive for opposite LVAs.

Methods: Intra-operative simultaneous endo-epicardial mapping (256 electrodes, interelectrode distances 2 mm) was performed during sinus rhythm at the right atrium in 93 patients (67 ± 9 years, 73 male). Cliques of four electrodes (2 × 2 mm) were used to define maximal omnipolar ($V_{omni,max}$) and unipolar ($V_{uni,max}$) voltages. LVAs were defined as $V_{omni,max}$ ≤0.5 mV or $V_{uni,max}$ ≤1.0 mV.

Results: The majority of both unipolar and omnipolar LVAs were located at only the endocardium (74.2% and 82.0% respectively) or epicardium (52.7% and 47.6% respectively). Of the endocardial unipolar LVAs, 25.8% were also located at the opposite layer and 47.3% vice-versa. In omnipolar LVAs, 18.0% of the endocardial LVAs were also located at the epicardium and 52.4% vice-versa. The combination of epicardial $V_{uni,max}$ and $V_{omni,max}$ was most accurate in identifying dual-layer LVAs (50.4%).

Conclusion: Unipolar and omnipolar LVAs are frequently located exclusively at either the endocardium or epicardium. Endo-epicardial LVAs are most accurately identified using combined epicardial unipolar and omnipolar voltages. Therefore, a combined endo-epicardial unipolar and omnipolar mapping approach is favoured as it may be more indicative of possible arrhythmogenic substrates.

KEYWORDS

voltage mapping, unipolar voltage, omnipolar mapping, low-voltage areas, endo-epicardial mapping, atrial fibillation, sinus rhythm

Introduction

Endocardial bipolar voltage mapping has emerged as an invasive tool for defining potential target sites for ablation therapy of atrial tachyarrhythmia such as atrial fibrillation (AF). Low-voltage areas (LVA) are commonly considered surrogate markers for areas of conduction disorders, which play a key role in perpetuation of AF (Kottkamp et al., 2015; Knops et al., 2016). However, the efficacy of such bipolar voltage-guided ablation strategies remains controversial. Especially in patients with persistent AF, the presence of intramural or epicardial substrate limits the efficacy of endocardial ablation strategies (De Martino et al., 2021). Recently, Piorkowski et al. (2018)) showed that bipolar LVAs can also be located exclusively at either the endocardium or epicardium, therefore favoring an endo-epicardial ablation approach.

We demonstrated that identification of LVAs was considerably directional dependent when using bipolar voltages (van Schie et al., 2021a). Bipolar LVAs could also contain large unipolar voltages. In addition, there were not solely conduction disorders within LVAs, but also high conduction velocities (CV). It could therefore be that the bipolar low-voltage threshold overestimates the size of dense scar and still harbors islets and channels of viable tissue (Chopra et al., 2014).

Endocardial bipolar recordings are still mainly used to detect scar tissue areas as it represents more local activity. In the ventricles it has been demonstrated that unipolar voltage mapping is preferred to identify intramural or epicardial substrates as unipolar electrograms (EGM) comprise a larger region of myocardial electrical activity (Sim et al., 2019). On the other hand, omnipolar voltage mapping can be used to extract maximal bipolar voltage from a collection of EGMs in order to minimize directional differences of bipolar voltages. A combination of unipolar and omnipolar voltage may therefore provide additional information on the underlying tissue and it may also be more indicative of transmural substrates (Chopra et al., 2014; van Schie et al., 2021a).

It, however, remains unknown whether simultaneously recorded atrial endo- and epicardial unipolar and omnipolar voltages are complementary or contradictory on identifying LVAs at the opposite layer. We therefore performed simultaneously endo-epicardial high-density mapping to 1) examine endo- and epicardial characteristics of unipolar and omnipolar voltages, 2) explore the relation between various types of voltages in identification of LVAs from an endocardial and epicardial point of view, and 3) examine whether characteristics of LVAs can be predictive for LVAs at the opposite layer.

Materials and methods

Study population

The study population consisted of 93 successive adult patients undergoing elective open heart coronary artery bypass grafting, aortic or mitral valve surgery or a combination of valvular surgery and bypass grafting in the Erasmus Medical Center Rotterdam. This study was approved by the institutional medical ethical committee (MEC 2015-373). Written informed consent was obtained from all patients and patient characteristics (e.g., age, medical history and cardiovascular risk factors) were obtained from the patient's medical record.

Simultaneous endo-epicardial mapping procedure

An overview of the methodology is provided in Figure 1A and previously described in detail (Knops et al., 2016). Two electrode arrays, each containing 128 (8 × 16) unipolar electrodes with a diameter of 0.45 mm and 2 mm interelectrode spacing, were secured on two bendable spatulas and were located on the exact opposite side of each other. A temporally bipolar epicardial pacemaker wire attached to the right atrial (RA) free wall served as a reference electrode and the indifferent electrode consisted of a steel wire fixed to subcutaneous tissue of the thoracic cavity. Simultaneous endo- and epicardial mapping was performed after heparinization and arterial cannulation but before commencement of extracorporeal circulation. One spatula (marked as the endocardial electrode array) was introduced in the RA after incising the RA appendage and closed with the purse-string suture. To prevent overlap of recording areas near the right atrial incision, the endocardial electrode array was introduced into the RA for at least 1.5 cm extra after introducing the last row of electrodes. Unipolar EGMs were recorded for 5 s during stable sinus rhythm at the superior, middle and inferior RA free wall (Figure 1A), including a surface ECG lead I, a calibration signal of 2 mV and 1,000 ms and a bipolar reference EGM. Data were stored on a hard disk after amplification (gain 1,000), filtering (bandwidth 0.5–400 Hz), sampling (1 kHz) and analogue to digital conversion (16 bits).

Omnipolar voltage mapping

In order to create omnipolar EGMs, bipolar EGMs were first created by subtracting two neighboring unipolar EGMs in horizontal (bipolar-x) and vertical direction (bipolar-y) and subsequently filtered (bandwidth 30–400 Hz) as demonstrated in Figure 1A. Omnipolar EGMs were then created from these

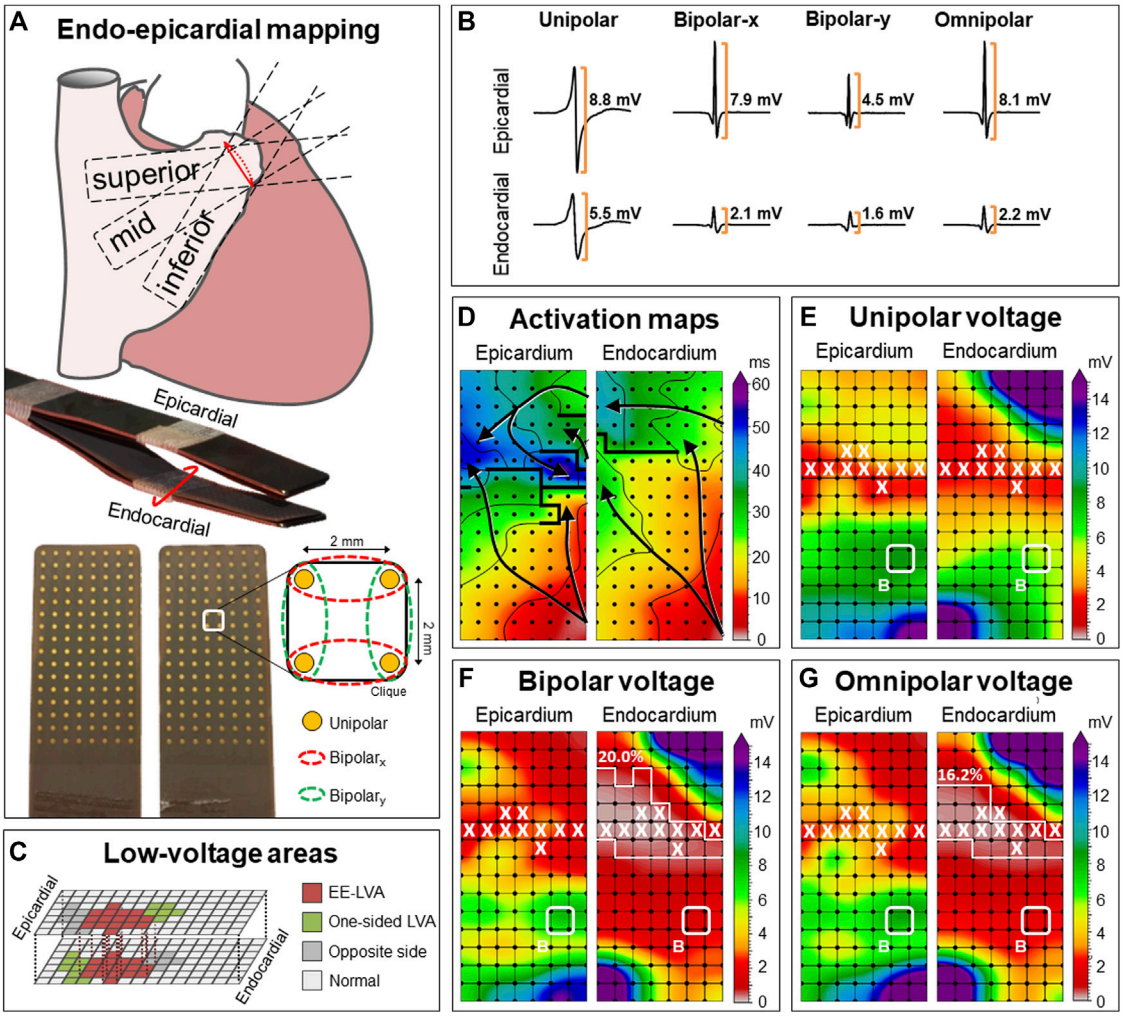

FIGURE 1
Construction of unipolar, bipolar and omnipolar voltages in 2 × 2 mm cliques. **(A)** Two high-density electrode arrays consisting of 128 unipolar electrodes are fixed together. One array was placed on the epicardium and one array is introduced into the RA using the incision for venous cannulation to map the endocardium and epicardium simultaneously. The RA was mapped with the tip of the electrode arrays toward the inferior vena cava (inferior), the superior vena cava (superior) and in between, toward the terminal crest (mid). For each square area, enclosed by four electrodes, four unipolar EGMs and matched bipolar and omnipolar EGMs were derived from two electrode orientations [along the vertical *y*-axis (green) and horizontal *x*-axis (red)] as indicated by the dotted lines. **(B)** Examples of a unipolar, horizontal bipolar-x, vertical bipolar-y and omnipolar EGM recorded from both the epicardium (upper) and endocardium (lower). The two bipolar EGMs differed considerably, illustrating the electrode orientation dependence of bipolar mapping. Omnipolar mapping provides electrode orientation-independent voltages that are larger than the bipolar with the largest measurable peak-to-peak voltage, in both cases the horizontal bipolar-x EGMs. **(C)** LVAs can be either located at solely the endocardium or epicardium (green) or at both sides (red). The corresponding clique at the exact opposite side is highlighted (grey). The other cliques are then indicated as normal voltage (light grey). **(D)** Example of endo-epicardial activation time maps with isochrones drawn at every 10 ms. Arrows indicate the main direction of the propagation wavefront and thick black lines indicate areas of conduction block (time difference between adjacent electrodes ≥12 ms). **(E–G)** Peak-to-peak voltages of corresponding EGMs are used to create different voltage maps. Bipolar voltage map illustrates the maximal bipolar voltage in both horizontal and vertical orientations within one clique. LVAs are highlighted by a white line and areas of EEA are indicated by a white X. In this example, endocardial bipolar and omnipolar LVA are present in respectively 20.0% and 16.2% of the cliques. EEA was present in 9.5% of the cliques at both the endocardium and epicardium. EEA = endo-epicardial asynchrony; EGM = electrogram; (EE-) LVA = (endo-epicardial-) low-voltage area.

bipolar EGMs as previously described (Deno et al., 2017; van Schie et al., 2021a). Within a square area defined by four adjacent electrodes (a *clique*), omnipolar EGMs were used to mathematically obtain bipolar EGMs in any direction without physically rotating the sensing electrodes of the bipolar pair. Within a clique, a 2-dimensional voltage vector $\vec{v}(t)$ is derived from an electric field of a passing activation wavefront from which the maximal extent of two orthogonal bipolar EGMs is calculated over the interval (T) containing one SR beat (Haldar et al., 2017):

$$V_{max} = \max_{t_i,t_j \in T} \left\{ \left| \vec{v}(t_i) - \vec{v}(t_j) \right| \right\}$$

V_{max} corresponds to the peak-to-peak amplitude of a bipolar voltage signal obtained along the unit vector direction $\hat{m}$ where t_i and t_j are now the times associated with V_{max} in which $t_i > t_j$

$$\hat{m} = \frac{\vec{v}(t_i) - \vec{v}(t_j)}{V_{max}}$$

V_{max} provides an objective measure of the largest possible bipolar EGM within a clique without the ambiguity of electrode orientation and is used to describe omnipolar EGM voltages.

Data analysis

Unipolar and omnipolar EGMs were semi-automatically analyzed using custom-made software. The steepest negative slope of a unipolar atrial potential was marked as the local activation time (LAT), providing that the amplitude of the deflection was at least two times the estimated noise level of the unipolar EGM (de Groot et al., 2016). In case of fractionated potentials, the deflection with the steepest slope was taken as LAT. All annotations were manually checked with a consensus of two investigators. CV was computed at each electrode from LATs using discrete velocity vectors (DVV) as previously described (van Schie et al., 2021b). The DVV method uses all eight neighboring electrodes to compute an average local propagation velocity for the center electrode. Endo-epicardial LAT differences were determined by selecting the median of the LAT differences within the exact opposite electrode and its eight surrounding electrodes (Kharbanda et al., 2020). Potential voltage was defined as the peak-to-peak amplitude of the steepest deflection (unipolar) or highest peak (omnipolar) as demonstrated in Figure 1B.

As omnipolar EGMs can only be derived in square areas, unipolar potentials were correlated to each other in areas of 2 × 2 mm -a *clique*- which contain four unipolar EGMs and the corresponding omnipolar EGMs (Figure 1A). Subsequently, the maximal potential voltage of the unipolar and omnipolar EGMs pertaining to that area were computed, resulting in two values ($V_{uni,max}$ and $V_{omni,max}$). In addition, the mean of the magnitudes of the four CV estimates derived from the four unipolar LATs was used as indication of the CV within the 2 × 2 mm area. Areas corresponding to a mean CV of 0 cm/s were excluded to avoid inclusion of far field potentials. To calculate endo-epicardial asynchrony (EEA), the minimum of endo-epicardial LAT differences within a clique was taken. EEA was then defined as a transmural difference in electrical activation of ≥15 ms (de Groot et al., 2016). As a unipolar voltage cut-off of ≤1.0 mV and bipolar voltage cut-off of ≤0.5 mV are most frequently used in daily clinical practice to identify LVAs, we also used these values as the "golden standard" to identify low-voltage cliques (Sanders et al., 2003; Kharbanda et al., 2021; van Schie et al., 2021c). Endo-epicardial LVAs (EE-LVA) are defined as LVA cliques located at both the endocardium and epicardial at the exact same site (Figure 1C).

TABLE 1 Baseline characteristics.

Patients	93
Male	73 (78.5%)
Age (years)	67 [61–72]
BMI (kg/m^2)	28.0 [24.6–31.1]
Underlying heart disease	
- iHD	47 (50.5%)
- vHD	24 (25.8%)
- cHD	21 (22.6%)
History of AF	37 (39.8%)
- Paroxysmal	31 (33.3%)
- Persistent	4 (4.3%)
- Longstanding persistent	2 (2.2%)
Cardiovascular risk factors	
Hypertension	56 (60.2%)
Diabetes mellitus	32 (34.4%)
Hypercholesterolemia	50 (53.8%)
Left ventricular ejection fraction <40%	12 (12.9%)
Antiarrhythmic drugs	
- Class I	1 (1.1%)
- Class II	64 (68.8%)
- Class III	6 (6.5%)
- Class IV	7 (7.5%)

Values are presented as N (%) or median [interquartile ranges].
BMI, body mass index; iHD, ischemic heart disease; vHD, valvular heart disease; cHD, combined heart disease; AF, atrial fibrillation; LVEF, left ventricular ejection fraction.

Statistical analysis

Normally distributed data are expressed as mean ± SD, whereas skewed data are expressed as median [25th–75th percentile]. Clinical characteristics were compared using Student's *t*-test or Mann-Whitney *U* test when appropriate. Categorical data are expressed as numbers (percentages) and analyzed with a $\chi 2$ or Fisher exact test. Paired voltage and velocity data were analyzed between the endo- and epicardium using a paired *t*-test or Wilcoxon signed-rank test. Correlation was determined by ordinary least squares regression. A *p*-value <0.05 was considered statistically significant.

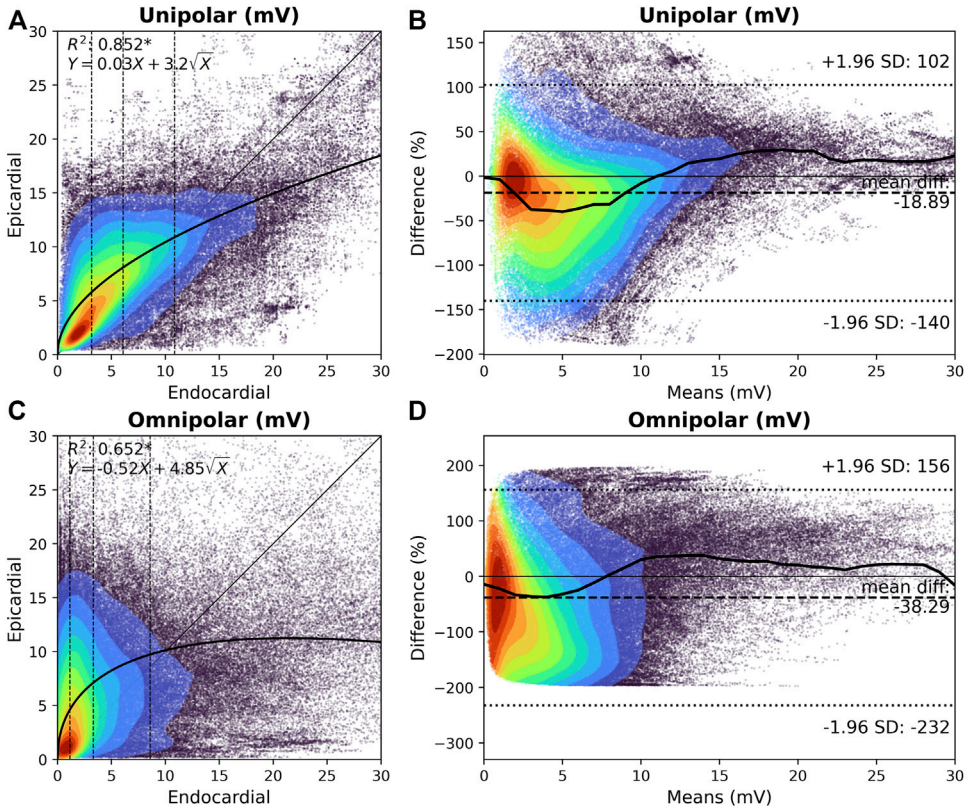

FIGURE 2
Relation between endocardial and epicardial unipolar and omnipolar voltage. **(A)** and **(C)** Kernel density plots of $V_{uni,max}$ **(A)** and $V_{omni,max}$ **(C)** voltages between the endocardium and epicardium. The colors indicate the data density. A black line indicates the ordinary least squares prediction. Statistical significance is indicated by an asterisk ($p < 0.001$). $V_{uni,max}$ and $V_{omni,max}$ are subdivided according to the 25th, 50th, and 75th percentiles of the endocardial voltages, and are indicated by dashed vertical lines. **(B)** and **(D)** Bland-Altman plots of endocardial *versus* epicardial $V_{uni,max}$ **(B)** and $V_{omni,max}$ **(D)** voltages. The colors indicate the data density. A black line indicates the median per one means mV. The mean difference and 95% confidence intervals are indicated by the dashed lines. $V_{omni,max}$ = omnipolar clique voltage; $V_{uni,max}$ = unipolar clique voltage.

Results

Study population

Clinical characteristics of the study population [$N = 93$, age 67 (61–72) years, 73 male (78.5%)] are summarized in Table 1. A history of AF was present in 37 (39.8%) patients. Ischemic- or valvular heart disease or combined heart diseases were present in 47 (50.5%), 24 (25.8%), and 21 (22.6%) patients respectively. Most patients used class II antiarrhythmic drugs ($N = 64$, 68.8%).

Clique characteristics

In the entire study population, a total of 281 mapping locations resulted in 406,571 unipolar and 723,695 bipolar potentials from which 164,704 cliques were created for both the endocardium and epicardium (329,408 cliques in total; 3,542 ± 1,610 per patient). The mean CV of each clique was 83.6 [62.3–103.4] cm/s at the endocardium and 84.4 [67.0–100.5] cm/s at the epicardium ($p < 0.001$, $R^2 = 0.853$, $CV_{epi} = 0.91 \cdot CV_{endo}$). EEA was present in 2.9% of all cliques. An example of differences in activation and voltage maps constructed by using unipolar and corresponding bipolar and omnipolar EGMs are illustrated in Figures 1D–G.

Relation between endo-and epicardial voltages

The upper panel of Figure 2 demonstrates the relationship between endocardial and the corresponding epicardial $V_{uni,max}$. In 61% of the cliques, $V_{uni,max}$ at the epicardium was larger than the corresponding $V_{uni,max}$ at the endocardium (8.2 [4.9–11.6] mV vs. 6.1 [3.2–10.9] mV, $p < 0.001$). When $V_{uni,max}$ was subdivided into four quartiles, $V_{uni,max}$ at the epicardium was especially larger at the lower $V_{uni,max}$ values at the endocardium (p0-p25: 83.7%; p25-p50: 79.8%; p50-p75: 61.7%; p75-p100: 18.6%). As a consequence, there was a strong inversely quadratic relation with linear component ($R^2 =$

TABLE 2 Characteristics of low-voltage areas.

	Unipolar		Omnipolar	
	Normal	**LVA (≤1.0 mV)**	**Normal**	**LVA (≤0.5 mV)**
Endocardial	96.9%	3.1%	88.3%	11.7%
Unipolar (mV)	6.3 [3.4–11.1]	0.8 [0.6–0.9]	6.9 [4.1–11.8]	1.5 [1.1–2.0]
Omnipolar (mV)	3.5 [1.3–8.9]	0.2 [0.2–0.4]	4.2 [1.7–9.7]	0.3 [0.2–0.4]
CV (cm/s)	84.3 [63.3–103.8]	52.0 [28.6–79.2]	86.3 [66.4–105.2]	55.7 [34.2–80.6]
EEA (%)	2.4%	18.3%	2.1%	8.8%
Epicardial	98.3%	1.7%	96.0%	4.0%
Unipolar (mV)	8.3 [5.1–11.7]	0.8 [0.7–0.9]	8.5 [5.3–11.8]	1.3 [0.9–1.8]
Omnipolar (mV)	6.8 [3.4–11.0]	0.3 [0.2–0.5]	7.0 [3.6–11.1]	0.3 [0.2–0.4]
CV (cm/s)	84.7 [67.6–100.7]	53.5 [31.9–79.2]	85.0 [68.3–100.9]	57.2 [35.0–82.8]
EEA (%)	2.7%	14.2%	2.6%	10.5%

Values are presented as median [interquartile ranges] or incidence (distribution of parameter). Sum of the normal and LVA, values correspond to the total number of cliques ($N = 164{,}704$) per parameter.
CV, conduction velocity; EEA, endo-epicardial asynchrony; LVA, low-voltage area.

0.852, $Y = 0.03X + 3.2\sqrt{X}$) between $V_{uni,max}$ at the endocardium and epicardium. As illustrated in Figure 2B, $V_{uni,max}$ up to 12 mV were particularly larger at the epicardium than the endocardium, although there was a large variation in the differences. Epicardial $V_{uni,max}$ were on average 19% larger than endocardial $V_{uni,max}$.

The lower panel of Figure 2 demonstrates the relationship between endocardial and the corresponding epicardial $V_{omni,max}$. In 64% of the cliques, $V_{omni,max}$ at the epicardium was larger compared to the corresponding endocardial cliques (6.7 [3.2–10.9] mV vs. 3.3 [1.1–8.6] mV, $p < 0.001$, respectively). When $V_{omni,max}$ was subdivided into four quartiles, $V_{omni,max}$ at the epicardium was especially larger at the lower $V_{omni,max}$ values at the endocardium (p0-p25: 91.3%; p25-p50: 86.5%; p50-p75: 62.2%; p75-p100: 15.5%). However, there was no clear relationship between the endocardial and epicardial $V_{omni,max}$, although lower endocardial voltages were associated with a larger range of epicardial voltages. As illustrated in Figure 2D, $V_{omni,max}$ up to 8 mV were particularly larger at the epicardium than the endocardium. Epicardial $V_{omni,max}$ were on average 38% larger than endocardial $V_{omni,max}$.

Endo-epicardial differences in low-voltage areas

Characteristics of unipolar and omnipolar LVAs at the endo- and epicardium are listed in Table 2. Endocardial and epicardial unipolar LVAs were present at respectively 3.1% and 1.7% of the mapping area. At the endo- and epicardium, unipolar LVAs corresponded to respectively 86.8% and 73.3% of the omnipolar LVA.

Omnipolar LVAs were present at 11.7% of the endocardium and 4.0% of the epicardium. However, only 22.7% and 30.6% of omnipolar LVAs corresponded to unipolar LVAs at respectively the endo- and epicardial side.

As demonstrated in Table 2, CV was lower and EEA was more pronounced in both unipolar and omnipolar LVAs compared to the non-LVAs. The difference in CV and EEA between LVAs and non-LVAs was smaller in omnipolar LVAs than in unipolar LVAs ($p < 0.001$).

Prediction of unipolar opposite LVAs

To determine the predictive value of endocardial or epicardial LVAs for the opposite layer, all cliques were subdivided into cliques with either LVA in only one layer (*endo/epi*-LVA) or cliques with LVAs present at both layers (EE-LVA). Characteristics of these clique categories are listed in Table 3. Of all endocardial LVA cliques, 25.8% corresponded to an epicardial LVA and 47.3% of the epicardial LVA cliques corresponded to an endocardial LVA. Therefore, 0.8% of all cliques were identified as EE-LVA, 0.9% as *epi*-LVA and 2.3% as *endo*-LVA. At the opposite site of unipolar *endo*- and *epi*-LVAs, "normal" cliques were characterized by lower $V_{uni,max}$, $V_{omni,max}$, lower CV and enhanced EEA compared to the other non-LVA cliques ($p < 0.001$). Most EEA was found at *endo*-LVA cliques.

Prediction of omnipolar opposite LVAs

Of all endocardial omnipolar LVA cliques, 18.0% corresponded to an epicardial LVA and 52.4% of the epicardial LVA cliques corresponded to an endocardial

TABLE 3 Characteristics of low-voltage areas at the opposite side (*N* = 164,704 per parameter).

Endocardial	Unipolar			Omnipolar		
	Normal	*Epi*-LVA	EE-LVA	Normal	*Epi*-LVA	EE-LVA
N (%)	96.0%	0.9%	0.8%	86.3%	1.9%	2.1%
Unipolar (mV)	6.3 [3.4–11.1]	2.2 [1.4–5.0]	0.8 [0.6–0.9]	7.0 [4.2–11.9]	3.2 [1.8–6.2]	1.2 [0.8–1.6]
Omnipolar (mV)	3.5 [1.3–8.9]	1.6 [0.6–4.8]	0.2 [0.2–0.3]	4.2 [1.7–9.8]	2.1 [0.9–6.2]	0.3 [0.2–0.4]
CV (cm/s)	84.4 [63.5–104.0]	68.4 [48.6–89.0]	53.9 [29.2–81.6]	86.7 [66.8–105.4]	70.0 [50.0–91.4]	54.6 [32.7–82.0]
EEA (%)	2.2%	18.3%	9.3%	1.8%	14.0%	7.2%
Epicardial	**Normal**	***Endo*-LVA**	**EE-LVA**	**Normal**	***Endo*-LVA**	**EE-LVA**
N (%)	96.0%	2.3%	0.8%	86.3%	9.6%	2.1%
Unipolar (mV)	8.4 [5.2–11.8]	3.8 [2.0–6.5]	8.8 [5.7–12.1]	8.8 [5.7–12.1]	5.6 [3.2–8.8]	1.2 [0.9–1.6]
Omnipolar (mV)	6.9 [3.4–11.0]	3.5 [1.3–7.0]	0.2 [0.2–0.4]	7.1 [3.8–11.3]	5.2 [2.1–9.2]	0.3 [0.2–0.4]
CV (cm/s)	84.8 [67.8–100.8]	78.8 [59.1–98.4]	57.5 [32.7–84.2]	85.7 [69.1–101.4]	78.9 [62.0–95.5]	55.9 [34.2–81.3]
EEA (%)	2.2%	21.3%	9.5%	1.8%	9.2%	7.3%

Values are presented as median [interquartile ranges] or incidence (distribution of parameter).
CV, conduction velocity; EEA, endo-epicardial asynchrony; EE-LVA, endo-epicardial low-voltage area; *Endo*-LVA, endocardial low-voltage area; *Epi*-LVA, epicardial low-voltage area.

TABLE 4 Characteristics of low-voltage areas at the opposite side using combined unipolar and omnipolar voltage mapping (*N* = 164,704 per parameter).

Endocardial	Normal	*Epi*-LVA	EE-LVA
N (%)	96.7%	0.6%	0.6%
Unipolar (mV)	6.3 [3.4–11.1]	2.2 [1.2–5.8]	0.8 [0.6–0.9]
Omnipolar (mV)	3.5 [1.3–8.8]	1.6 [0.5–5.7]	0.2 [0.1–0.3]
CV (cm/s)	84.3 [63.3–103.9]	69.5 [49.2–90.3]	54.6 [29.2–82.6]
EEA (%)	2.4%	20.1%	6.8%
Epicardial	**Normal**	***Endo*-LVA**	**EE-LVA**
N (%)	96.7%	2.0%	0.6%
Unipolar (mV)	8.4 [5.1–11.7]	3.9 [2.0–6.6]	0.8 [0.6–0.9]
Omnipolar (mV)	6.8 [3.4–11.0]	3.8 [1.2–7.3]	0.2 [0.2–0.3]
CV (cm/s)	84.7 [67.6–100.7]	79.3 [59.2–98.8]	56.3 [30.6–84.2]
EEA (%)	2.4%	20.9%	6.9%

Values are presented as median [interquartile ranges] or incidence (distribution of parameter).
CV, conduction velocity; EEA, endo-epicardial asynchrony; EE-LVA, endo-epicardial low-voltage area; *Endo*-LVA, endocardial low-voltage area; *Epi*-LVA, epicardial low-voltage area.

LVA. Therefore, 2.1% of all cliques were identified as EE-LVA, 1.9% as *epi*-LVA and 9.6% as *endo*-LVA. At the opposite site of omnipolar *endo*- and *epi*-LVAs, "normal" cliques were characterized by lower $V_{uni,max}$, $V_{omni,max}$, lower CV and enhanced EEA compared to the other non-LVA cliques ($p < 0.001$). Only 7.6% of these cliques corresponded to unipolar LVAs.

Identification of LVAs by combined unipolar and omnipolar voltage mapping

Cliques containing both unipolar and omnipolar LVAs were identified. Characteristics of these overlapping LVAs are listed in Table 4. At the endocardium, overlapping LVAs consisted of 86.8% of $V_{uni,max}$ and 22.7% of $V_{omni,max}$ compared to 73.7% of $V_{uni,max}$ and 30.6% of $V_{omni,max}$ at the epicardium.

In total, 2.6% overlapping endocardial LVAs were identified, compared to 1.2% at the epicardium; 0.6% were identified as EE-LVAs. These EE-LVAs consisted of 23.3% of all endocardial overlapping LVAs and 50.4% at the epicardium. At the opposite site of overlapping *endo*- and *epi*-LVAs, "normal" cliques were characterized by lower $V_{uni,max}$, $V_{omni,max}$, lower CV and enhanced EEA compared to the other non-LVA cliques ($p < 0.001$).

Figure 3 demonstrates ROC-curves of the accuracy of identifying overlapping endocardial and epicardial LVAs based on all parameters recorded at the opposite layer. Combined unipolar and omnipolar voltages were most accurate in identifying overlapping LVAs at the opposite layer (endocardial LVAs: AUC = 0.83; epicardial LVAs: AUC = 0.89).

Discussion

Key findings

In most clinical settings, endocardial bipolar voltage mapping is mainly used to identify LVAs, which are considered surrogate markers for areas of diseased tissue.

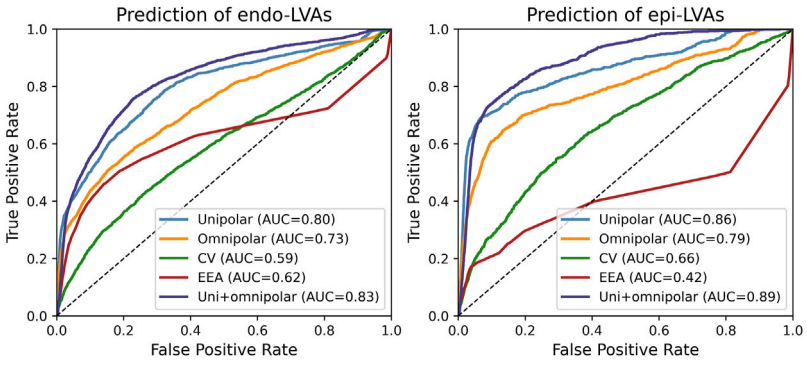

FIGURE 3
ROC-curves of the prediction of overlapping endocardial (left) and epicardial (right) LVAs based on all parameters recorded from the opposite layer. AUC = area under the curve; CV = conduction velocity; EEA = endo-epicardial asynchrony.

However, in recent perspective, it has become clear that bipolar LVAs can also be located exclusively at the epicardium (Piorkowski et al., 2018). Our study demonstrated that also by using unipolar and omnipolar EGMs, the majority of unipolar and omnipolar LVAs are also located exclusively at either the endocardium or epicardium. More importantly, we have shown that the most accurate methodology to identify EE-LVAs is to combine epicardial unipolar and omnipolar voltages. When using either unipolar or omnipolar voltages separately, epicardial LVAs still corresponded well with endocardial LVAs, but not vice-versa. Within the same layer, only unipolar LVAs corresponded well with omnipolar LVAs. Furthermore, there was a clear relationship between endo-epicardial unipolar voltages, but not between endo-epicardial omnipolar voltages.

Endo-epicardial voltage mapping

Data on the relationship between atrial endocardial and epicardial voltages is lacking, although it has been studied in the ventricles (Hutchinson et al., 2011; Tokuda et al., 2013). In the atria, van der Does et al. (2018) demonstrated a linear relationship between unipolar endocardial and epicardial voltage in which epicardial voltages were larger than endocardial voltages. Other studies also reported higher mean voltage values in the epicardium compared to mean endocardial voltage, in both atria and ventricles (Lemery et al., 2007; Hutchinson et al., 2011; Tokuda et al., 2013; van der Does et al., 2021). Using our clique voltages, we demonstrated a clear inverse quadratic relation with linear component between endocardial and epicardial unipolar clique voltages. Therefore, unipolar voltages recorded at the endocardium are predictive for epicardial unipolar voltages. In contrast, we found no relationship between endocardial and epicardial omnipolar voltages. This could likely be caused by the limited field-of-view of omnipolar voltages. Consequently, omnipolar voltages recorded at the endocardium are a poor predictor for voltages at the other layer.

Anatomy of the right atrium

Variations between endocardial and epicardial voltages can also be explained by the anatomical structure of the RA. The surface of the endocardium is very irregular due to the presence of the pectinate muscles and terminal crest, in contrast to the smooth epicardium. Diameters and therefore cardiac mass of the pectinate muscles may vary considerably (Sanchez-Quintana et al., 2002). In addition, the arrangement of pectinate muscles causes variation in the level of contact with the electrodes. Furthermore, due to atrial remodeling and varying wall stress, the atria and therefore the pectinate muscles may elongate resulting in alternation of the bundle density (Schuessler et al., 1993). This results in a non-uniform spread of activation and can consequently also considerably affect omnipolar voltages. Moreover, Kharbanda et al. (2020) demonstrated that conduction disorders occur more frequently at the endocardium. These features could explain the large discrepancies in unipolar and omnipolar voltages at endocardial LVAs. As the epicardial surface is more smooth, proper tissue contact with the entire electrode array can be achieved more easily. Therefore, epicardial LVAs could be more likely indicative of structural abnormalities and hence EE-LVAs.

Identification of endo-epicardial substrate

The arrhythmogenic substrate can be located either subendocardially, subepicardially, intramurally or transmurally (Tokuda et al., 2013; Chen et al., 2018; Gharaviri et al., 2020).

Piorkowski et al. (2018) recently demonstrated by bipolar endo-epicardial mapping in the left and RA that LVAs were present in 44 patients with history of AF in either both layers ($N = 33$, 75%) or in solely the endocardium ($N = 6$, 14%) or epicardium ($N = 6$, 14%). However, all patients already had (multiple) ablation procedures. Our study population consisted of patients without previous ablation therapy and we demonstrated that the majority of the LVAs at the RA were exclusively located at either the endocardium or epicardium. These findings demonstrate that the arrhythmogenic substrates may not necessarily be transmural present. Verheule et al. (2013) also demonstrated in a goat model of AF that formation of endomysial fibrosis located within the outer millimeter of the epicardial layer accompanied the transition from persistent to permanent AF, while endocardial bundles remained unaffected. Hence, as structural remodeling can occur locally within one layer, the presence of a LVA can also be confined to either the endocardial or epicardial layer. This could in turn lead to increased EEA due to progressive uncoupling between the epicardial layer and the endocardial bundles, which also has been proposed as an important mechanism for AF (de Groot et al., 2016).

On the other hand, as omnipolar voltages represent more local activity, this recording modality is more likely to only detect LVAs representing substrate located either (sub) endocardially or (sub) epicardially depending on the recording location. Several studies have shown an added value of combining unipolar and bipolar voltages to detect intramural or transmural substrates (Spears et al., 2012; Casella et al., 2015; Yalin et al., 2015). Hutchinson et al. (2011) demonstrated that epicardial bipolar LVAs can be identified in most patients with left ventricular cardiomyopathy using endocardial unipolar voltage mapping. However, Tokuda et al. (2013) observed discrepancies in the accuracy of epicardial bipolar LVA identification using endocardial unipolar voltages between patients with nonischemic and ischemic cardiomyopathy. In our present study, we demonstrated that endocardial LVAs at the atria frequently did not correspond to LVAs at the epicardium, independently of the recording technique used. Even by combining unipolar and omnipolar voltages, only 23.3% of the endocardial LVAs corresponded to epicardial LVAs, favoring a combined endocardial and epicardial mapping approach.

Endo-epicardial ablation therapy

Especially in patients with persistent AF, the presence of complex 3-dimensional arrhythmogenic substrates limits the efficacy of endocardial ablation strategies. Minimally invasive surgical ablation of AF is therefore increasingly combined with the endocardial transcatheter procedures in so-called hybrid procedures, showing promising results (Edgerton et al., 2016; Piorkowski et al., 2018; De Martino et al., 2021; Zheng et al., 2021). In the study of Piorkowski et al. (2018), 73% of complex AF patients remained free from AF during 2 years of follow-up, although other studies encountered higher recurrence rates (Gehi et al., 2013; Edgerton et al., 2016; Jiang et al., 2019). However, LVAs frequently occur at either the endocardium or epicardium alone and the opposite areas could contain normal voltages. These areas are therefore "invisible" when recording from only one side. Diseased tissue could then consequently be missed using a one-sided approach. In addition, epicardial mapping provides more often accurate identification of EE-LVAs and the role of epicardial structures, such as Bachmann's bundle, become more recognized in the pathogenesis of AF (Teuwen et al., 2016; De Martino et al., 2021). This suggests that a strategy of combined endo-epicardial access for mapping and ablation may provide superior efficacy to an endocardial-only approach.

Study limitations

Intraoperative simultaneous endo-epicardial mapping in humans can only be safely performed during cardiac surgical procedures. Therefore, as endo-epicardial mapping was only performed on a limited area of the RA free wall, we could not evaluate the relation of endocardial and epicardial voltages in the complete atria, specifically not in the left atrium. The recorded potentials might be influenced by the presence of epicardial fat as previous studies demonstrated that the presence of thick epicardial fat is associated with attenuated bipolar voltage (Saba et al., 2009; Desjardins et al., 2010). Although we did not experience any large effects of visually present epicardial fat at the RA, we cannot ascertain that the presence of epicardial fat has influenced our results. In addition, the underlying anatomy such as variability in atrial wall thickness and the degree of trabeculation cannot be retrieved, and exact tissue histology could not be performed. Therefore, we were unable to correlate the exact underlying anatomy and histology with the mapping data. This study focused on the comparison of the different voltage mapping methodologies and identification of LVAs without interventions. The next step will be to incorporate the results of this study with ablation targeting EE-LVAs in order to determine whether the combination of low unipolar and low omnipolar voltage can improve ablation outcomes.

Conclusion

When using unipolar and omnipolar EGMs, LVAs are frequently located exclusively at either the endocardium or epicardium and could be undetectable when measuring from

the opposite layer only. An endo-epicardial mapping approach is therefore favored to accurately identify LVAs. EE-LVAs are most accurately identified using combined epicardial unipolar and omnipolar voltages. Therefore, a combination of simultaneously recorded endo-epicardial low unipolar *and* low omnipolar voltage may be more indicative of dual-layer LVAs and probably arrhythmogenic substrates.

Data availability statement

The datasets presented in this article are not readily available because of EU privacy law. Requests to access the datasets should be directed to NG, n.m.s.degroot@erasmusmc.nl.

Ethics statement

The studies involving human participants were reviewed and approved by METC Erasmus MC. The patients/participants provided their written informed consent to participate in this study.

Author contributions

MS contributed to data acquisition and analysis, manuscript drafting and conceptual thinking. PK, LZ, FS, and YT contributed to data acquisition and critically revising the manuscript. NG contributed to manuscript drafting and conceptual thinking. All authors contributed to the article and approved the submitted version.

Funding

NG is supported by funding grants from CVON-AFFIP [grant number 914728], NWO-Vidi [grant number 91717339], Biosense Webster USA [ICD 783454] and Medical Delta.

Acknowledgments

The authors would like to kindly thank J. A. Bekkers; C. Kik: W. J. Van Leeuwen; F. B. S. Oei; P. C. Van de Woestijne; A. Yaksh; E. A. H. Lanters; C. P. Teuwen; E. M. J. P. Mouws; J. M. E. Van Der Does; C. A. Houck; R. Starreveld; C. S. Serban; L. N. Van Staveren; A. Heida; W. F. B. Van Der Does; M. C. Roos-Serote; for their contribution to this work.

Conflict of interest

The authors declare that the research was conducted in the absence of any commercial or financial relationships that could be construed as a potential conflict of interest.

Publisher's note

All claims expressed in this article are solely those of the authors and do not necessarily represent those of their affiliated organizations, or those of the publisher, the editors and the reviewers. Any product that may be evaluated in this article, or claim that may be made by its manufacturer, is not guaranteed or endorsed by the publisher.

References

Casella, M., Pizzamiglio, F., Dello Russo, A., Carbucicchio, C., Al-Mohani, G., Russo, E., et al. (2015). Feasibility of combined unipolar and bipolar voltage maps to improve sensitivity of endomyocardial biopsy. *Circ. Arrhythm. Electrophysiol.* 8, 625–632. doi:10.1161/CIRCEP.114.002216

Chen, R., Wen, C., Fu, R., Li, J., and Wu, J. (2018). The effect of complex intramural microstructure caused by structural remodeling on the stability of atrial fibrillation: Insights from a three-dimensional multi-layer modeling study. *PLoS One* 13, e0208029. doi:10.1371/journal.pone.0208029

Chopra, N., Tokuda, M., Ng, J., Reichlin, T., Nof, E., John, R. M., et al. (2014). Relation of the unipolar low-voltage penumbra surrounding the endocardial low-voltage scar to ventricular tachycardia circuit sites and ablation outcomes in ischemic cardiomyopathy. *J. Cardiovasc. Electrophysiol.* 25, 602–608. doi:10.1111/jce.12393

de Groot, N., van der Does, L., Yaksh, A., Lanters, E., Teuwen, C., Knops, P., et al. (2016). Direct proof of endo-epicardial asynchrony of the atrial wall during atrial fibrillation in humans. *Circ. Arrhythm. Electrophysiol.* 9, e003648. doi:10.1161/CIRCEP.115.003648

De Martino, G., Compagnucci, P., Mancusi, C., Vassallo, E., Calvanese, C., Della Ratta, G., et al. (2021). Stepwise endo-/epicardial catheter ablation for atrial fibrillation: The Mediterranea approach. *J. Cardiovasc. Electrophysiol.* 32, 2107–2115. doi:10.1111/jce.15151

Deno, D. C., Balachandran, R., Morgan, D., Ahmad, F., Masse, S., and Nanthakumar, K. (2017). Orientation-independent catheter-based characterization of myocardial activation. *IEEE Trans. Biomed. Eng.* 64, 1067–1077. doi:10.1109/TBME.2016.2589158

Desjardins, B., Morady, F., and Bogun, F. (2010). Effect of epicardial fat on electroanatomical mapping and epicardial catheter ablation. *J. Am. Coll. Cardiol.* 56, 1320–1327. doi:10.1016/j.jacc.2010.04.054

Edgerton, Z., Perini, A. P., Horton, R., Trivedi, C., Santangeli, P., Bai, R., et al. (2016). Hybrid procedure (Endo/Epicardial) versus standard manual ablation in patients undergoing ablation of longstanding persistent atrial fibrillation: Results from a single center. *J. Cardiovasc. Electrophysiol.* 27, 524–530. doi:10.1111/jce.12926

Gehi, A. K., Mounsey, J. P., Pursell, I., Landers, M., Boyce, K., Chung, E. H., et al. (2013). Hybrid epicardial-endocardial ablation using a pericardioscopic technique for the treatment of atrial fibrillation. *Heart rhythm.* 10, 22–28. doi:10.1016/j.hrthm.2012.08.044

Gharaviri, A., Bidar, E., Potse, M., Zeemering, S., Verheule, S., Pezzuto, S., et al. (2020). Epicardial fibrosis explains increased endo-epicardial dissociation and epicardial breakthroughs in human atrial fibrillation. *Front. Physiol.* 11, 68. doi:10.3389/fphys.2020.00068

Haldar, S. K., Magtibay, K., Porta-Sanchez, A., Masse, S., Mitsakakis, N., Lai, P. F. H., et al. (2017). Resolving bipolar electrogram voltages during atrial fibrillation using omnipolar mapping. *Circ. Arrhythm. Electrophysiol.* 10, e005018. doi:10.1161/CIRCEP.117.005018

Hutchinson, M. D., Gerstenfeld, E. P., Desjardins, B., Bala, R., Riley, M. P., Garcia, F. C., et al. (2011). Endocardial unipolar voltage mapping to detect epicardial ventricular tachycardia substrate in patients with nonischemic left ventricular cardiomyopathy. *Circ. Arrhythm. Electrophysiol.* 4, 49–55. doi:10.1161/CIRCEP.110.959957

Jiang, R., Buch, E., Gima, J., Upadhyay, G. A., Nayak, H. M., Beaser, A. D., et al. (2019). Feasibility of percutaneous epicardial mapping and ablation for refractory atrial fibrillation: Insights into substrate and lesion transmurality. *Heart rhythm.* 16, 1151–1159. doi:10.1016/j.hrthm.2019.02.018

Kharbanda, R. K., Knops, P., van der Does, L., Kik, C., Taverne, Y., Roos-Serote, M. C., et al. (2020). Simultaneous endo-epicardial mapping of the human right atrium: Unraveling atrial excitation. *J. Am. Heart Assoc.* 9, e017069. doi:10.1161/JAHA.120.017069

Kharbanda, R. K., Wesselius, F. J., van Schie, M. S., Taverne, Y., Bogers, A., and de Groot, N. M. S. (2021). Endo-epicardial mapping of *in vivo* human sinoatrial node activity. *JACC. Clin. Electrophysiol.* 7, 693–702. doi:10.1016/j.jacep.2020.11.017

Knops, P., Kik, C., Bogers, A. J., and de Groot, N. M. (2016). Simultaneous endocardial and epicardial high-resolution mapping of the human right atrial wall. *J. Thorac. Cardiovasc. Surg.* 152, 929–931. doi:10.1016/j.jtcvs.2016.05.026

Kottkamp, H., Bender, R., and Berg, J. (2015). Catheter ablation of atrial fibrillation: How to modify the substrate? *J. Am. Coll. Cardiol.* 65, 196–206. doi:10.1016/j.jacc.2014.10.034

Lemery, R., Birnie, D., Tang, A. S., Green, M., Gollob, M., Hendry, M., et al. (2007). Normal atrial activation and voltage during sinus rhythm in the human heart: An endocardial and epicardial mapping study in patients with a history of atrial fibrillation. *J. Cardiovasc. Electrophysiol.* 18, 402–408. doi:10.1111/j.1540-8167.2007.00762.x

Piorkowski, C., Kronborg, M., Hourdain, J., Piorkowski, J., Kirstein, B., Neudeck, S., et al. (2018). Endo-/Epicardial catheter ablation of atrial fibrillation: Feasibility, outcome, and insights into arrhythmia mechanisms. *Circ. Arrhythm. Electrophysiol.* 11, e005748. doi:10.1161/CIRCEP.117.005748

Saba, M. M., Akella, J., Gammie, J., Poston, R., Johnson, A., Hood, R. E., et al. (2009). The influence of fat thickness on the human epicardial bipolar electrogram characteristics: Measurements on patients undergoing open-heart surgery. *Europace* 11, 949–953. doi:10.1093/europace/eup156

Sanchez-Quintana, D., Anderson, R. H., Cabrera, J. A., Climent, V., Martin, R., Farre, J., et al. (2002). The terminal crest: Morphological features relevant to electrophysiology. *Heart* 88, 406–411. doi:10.1136/heart.88.4.406

Sanders, P., Morton, J. B., Davidson, N. C., Spence, S. J., Vohra, J. K., Sparks, P. B., et al. (2003). Electrical remodeling of the atria in congestive heart failure: Electrophysiological and electroanatomic mapping in humans. *Circulation* 108, 1461–1468. doi:10.1161/01.CIR.0000090688.49283.67

Schuessler, R. B., Kawamoto, T., Hand, D. E., Mitsuno, M., Bromberg, B. I., Cox, J. L., et al. (1993). Simultaneous epicardial and endocardial activation sequence mapping in the isolated canine right atrium. *Circulation* 88, 250–263. doi:10.1161/01.cir.88.1.250

Sim, I., Bishop, M., O'Neill, M., and Williams, S. E. (2019). Left atrial voltage mapping: Defining and targeting the atrial fibrillation substrate. *J. Interv. Card. Electrophysiol.* 56, 213–227. doi:10.1007/s10840-019-00537-8

Spears, D. A., Suszko, A. M., Dalvi, R., Crean, A. M., Ivanov, J., Nanthakumar, K., et al. (2012). Relationship of bipolar and unipolar electrogram voltage to scar transmurality and composition derived by magnetic resonance imaging in patients with nonischemic cardiomyopathy undergoing VT ablation. *Heart rhythm.* 9, 1837–1846. doi:10.1016/j.hrthm.2012.07.022

Teuwen, C. P., Yaksh, A., Lanters, E. A., Kik, C., van der Does, L. J., Knops, P., et al. (2016). Relevance of conduction disorders in bachmann's bundle during sinus rhythm in humans. *Circ. Arrhythm. Electrophysiol.* 9, e003972. doi:10.1161/CIRCEP.115.003972

Tokuda, M., Tedrow, U. B., Inada, K., Reichlin, T., Michaud, G. F., John, R. M., et al. (2013). Direct comparison of adjacent endocardial and epicardial electrograms: Implications for substrate mapping. *J. Am. Heart Assoc.* 2, e000215. doi:10.1161/JAHA.113.000215

van der Does, L., Knops, P., Teuwen, C. P., Serban, C., Starreveld, R., Lanters, E. A. H., et al. (2018). Unipolar atrial electrogram morphology from an epicardial and endocardial perspective. *Heart rhythm.* 15, 879–887. doi:10.1016/j.hrthm.2018.02.020

van der Does, L., Starreveld, R., Kharbanda, R. K., Knops, P., Kik, C., Bogers, A., et al. (2021). Detection of endo-epicardial asynchrony in the atrial wall using one-sided unipolar and bipolar electrograms. *J. Cardiovasc. Transl. Res.* 14, 902–911. doi:10.1007/s12265-021-10111-1

van Schie, M. S., Heida, A., Taverne, Y., Bogers, A., and de Groot, N. M. S. (2021b). Identification of local atrial conduction heterogeneities using high-density conduction velocity estimation. *Europace.* 23, 1815–1825. doi:10.1093/europace/euab088

van Schie, M. S., Kharbanda, R. K., Houck, C. A., Lanters, E. A. H., Taverne, Y., Bogers, A., et al. (2021a). Identification of low-voltage areas: A unipolar, bipolar, and omnipolar perspective. *Circ. Arrhythmia Electrophysiol.* 14, e009912. doi:10.1161/circep.121.009912

van Schie, M. S., Starreveld, R., Bogers, J. J. C., and de Groot, N. M. S. (2021c). Sinus rhythm voltage fingerprinting in patients with mitral valve disease using a high-density epicardial mapping approach. *Europace.* 23 (3), 469–478. doi:10.1093/europace/euaa336

Verheule, S., Tuyls, E., Gharaviri, A., Hulsmans, S., van Hunnik, A., Kuiper, M., et al. (2013). Loss of continuity in the thin epicardial layer because of endomysial fibrosis increases the complexity of atrial fibrillatory conduction. *Circ. Arrhythm. Electrophysiol.* 6, 202–211. doi:10.1161/CIRCEP.112.975144

Yalin, K., Golcuk, E., Bilge, A. K., Aksu, T., Buyukbayrak, H., Tiryakioglu, S. K., et al. (2015). Combined analysis of unipolar and bipolar voltage mapping identifies recurrences after unmappable scar-related ventricular tachycardia ablation. *Europace* 17, 1580–1586. doi:10.1093/europace/euv013

Zheng, Z., Yao, Y., Li, H., Zheng, L., Liu, S., Lin, H., et al. (2021). Simultaneous hybrid maze procedure for long-standing persistent atrial fibrillation with dilated atrium. *JTCVS Tech.* 5, 34–42. doi:10.1016/j.xjtc.2020.10.015

frontiers | Frontiers in Physiology

TYPE Original Research
PUBLISHED 12 October 2022
DOI 10.3389/fphys.2022.1025430

OPEN ACCESS

EDITED BY
Zhenhui Chen,
Indiana University, United States

REVIEWED BY
Jieyun Bai,
Jinan University, China
Seth H Weinberg,
The Ohio State University, United States

*CORRESPONDENCE
Felipe Atienza,
felipe.atienza@salud.madrid.org

†These authors have contributed equally to this work and share first authorship

‡These authors have contributed equally to this work and share senior authorship

SPECIALTY SECTION
This article was submitted to Cardiac Electrophysiology, a section of the journal Frontiers in Physiology

RECEIVED 22 August 2022
ACCEPTED 28 September 2022
PUBLISHED 12 October 2022

CITATION
Sánchez de la Nava AM, Gómez-Cid L, Domínguez-Sobrino A, Fernández-Avilés F, Berenfeld O and Atienza F (2022), Artificial intelligence analysis of the impact of fibrosis in arrhythmogenesis and drug response. *Front. Physiol.* 13:1025430. doi: 10.3389/fphys.2022.1025430

Artificial intelligence analysis of the impact of fibrosis in arrhythmogenesis and drug response

Ana María Sánchez de la Nava[1,2†], Lidia Gómez-Cid[1,2†], Alonso Domínguez-Sobrino[1], Francisco Fernández-Avilés[1,2,3], Omer Berenfeld[4‡] and Felipe Atienza[1,2,3*‡]

[1]Department of Cardiology, Hospital General Universitario Gregorio Marañón, Instituto de Investigación Sanitaria Gregorio Marañón (IISGM), Madrid, Spain, [2]Centro de Investigación Biomédica en Red de Enfermedades Cardiovasculares (CIBERCV), Madrid, Spain, [3]Universidad Complutense de Madrid, Madrid, Spain, [4]Center for Arrhythmia Research, University of Michigan, Ann Arbor, MI, United States

Background: Cardiac fibrosis has been identified as a major factor in conduction alterations leading to atrial arrhythmias and modification of drug treatment response.

Objective: To perform an *in silico* proof-of-concept study of Artificial Intelligence (AI) ability to identify susceptibility for conduction blocks in simulations on a population of models with diffused fibrotic atrial tissue and anti-arrhythmic drugs.

Methods: Activity in 2D cardiac tissue planes were simulated on a population of variable electrophysiological and anatomical profiles using the Koivumaki model for the atrial cardiomyocytes and the Maleckar model for the diffused fibroblasts (0%, 5% and 10% fibrosis area). Tissue sheets were of 2 cm side and the effect of amiodarone, dofetilide and sotalol was simulated to assess the conduction of the electrical impulse across the planes. Four different AI algorithms (Quadratic Support Vector Machine, QSVM, Cubic Support Vector Machine, CSVM, decision trees, DT, and K-Nearest Neighbors, KNN) were evaluated in predicting conduction of a stimulated electrical impulse.

Results: Overall, fibrosis implementation lowered conduction velocity (CV) for the conducting profiles (0% fibrosis: 67.52 ± 7.3 cm/s; 5%: 58.81 ± 14.04 cm/s; 10%: 57.56 ± 14.78 cm/s; $p < 0.001$) in combination with a reduced 90% action potential duration (0% fibrosis: 187.77 ± 37.62 ms; 5%: 93.29 ± 82.69 ms; 10%: 106.37 ± 85.15 ms; $p < 0.001$) and peak membrane potential (0% fibrosis: 89.16 ± 16.01 mV; 5%: 70.06 ± 17.08 mV; 10%: 82.21 ± 19.90 mV; $p < 0.001$). When the antiarrhythmic drugs were present, a total block was observed in most of the profiles. In those profiles in which electrical conduction was preserved, a decrease in CV was observed when simulations were performed in the 0% fibrosis tissue patch (Amiodarone ΔCV: −3.59 ± 1.52 cm/s; Dofetilide ΔCV: −13.43 ± 4.07 cm/s; Sotalol ΔCV: −0.023 ± 0.24 cm/s). This effect was preserved for amiodarone in the 5% fibrosis patch (Amiodarone ΔCV: −4.96 ± 2.15 cm/s; Dofetilide ΔCV: 0.14 ± 1.87 cm/s;

Sotalol ΔCV: 0.30 ± 4.69 cm/s). 10% fibrosis simulations showed that part of the profiles increased CV while others showed a decrease in this variable (Amiodarone ΔCV: 0.62 ± 9.56 cm/s; Dofetilide ΔCV: 0.05 ± 1.16 cm/s; Sotalol ΔCV: 0.22 ± 1.39 cm/s). Finally, when the AI algorithms were tested for predicting conduction on input of variables from the population of modelled, Cubic SVM showed the best performance with AUC = 0.95.

Conclusion: *In silico* proof-of-concept study demonstrates that fibrosis can alter the expected behavior of antiarrhythmic drugs in a minority of atrial population models and AI can assist in revealing the profiles that will respond differently.

KEYWORDS

atrial fibrillation, cardiac fibrosis, machine learning, population of models, support vector machines

Introduction

Cardiac fibrosis has been identified as a major pro-arrhythmic factor associated with impaired electrical conductance and reentries. Two different mechanisms have been proposed to underlie the possible reentrant patterns: reentry due to an anatomical obstacle or functional reentry (Yeo et al., 2017). Contrary to cardiomyocytes, fibroblasts are non-excitable cells. Therefore, the increased presence of cardiac fibrosis or fibroblasts can form areas of reduced conduction velocity in the anatomy of the cardiac tissue that increase the susceptibility to initiation and maintenance of cardiac arrhythmias (Krul et al., 2015). Overall, the combination of cardiac fibrosis in the presence of atrial fibrillation (AF), represents a synergetic proarrhythmic framework relative to patients suffering AF without cardiac fibrosis (Marrouche et al., 2014). As the fibrotic AF scenario is biologically and electrophysiologically more complex than AF alone, the effects of therapies such as antiarrhythmic drugs (AADs) would benefit from evaluation on relevant population models.

AADs are a group of pharmacological compounds that modify the rhythm of the heart by blocking one or several ionic channels controlling the electrical activation of the excitable cells of the heart (Sanguinetti and Bennett, 2003). While AADs may be particularly helpful in the treatment of AF caused by functional reentries or reentries caused by hyper-excitability of the cardiac tissue, in the presence of fibrosis and low conduction velocity of the cardiac tissue, AADs may cause undesired effects and actually exacerbate proarrhythmic factors. Among the most common AADs used for AF treatment in clinical practice we can find amiodarone, dofetilide, sotalol, flecainide or verapamil (Zimetbaum, 2012). The use of antiarrhythmic drugs in scenarios with fibrosis has been previously described (Zimetbaum, 2012; Saljic and Heijman, 2022) as proarrhythmic due to heterogeneous conduction (Cox et al., 1995), however a systematic evaluation of arrhythmogenicity produced by the many possible combinations of electrophysiological and fibrosis factors in AF is lacking.

Artificial Intelligence (AI), on the other hand, has been rapidly incorporated in biomedical applications to analyze and detect possible patterns or associations in large datasets that enable identification of mechanistic relationships and predict outcomes (Sánchez de la Nava et al., 2021b). Previous studies using population of models have underscored the importance of different ionic profiles on drug effect (Sanchez de la Nava et al., 2021a) and the potential proarrhythmic role of fibrosis (Kazbanov et al., 2016). Therefore, in this study we explore the effects of different AADs on the electrical impulse propagation using a population of different atrial models with diffused fibrosis distribution, and test the ability of AI algorithms to predict conduction patterns relevant to initiation and maintenance of AF.

Materials and methods

Cellular models and tissue connection

Two different models were implemented to simulate cardiac tissue with different levels of fibrosis. The cardiomyocyte model was the Koivumaki Model with Skibsbye modifications that mimick AF remodelling (Skibsbye et al., 2016) and described the electrophysiological behavior of human atrial cardiomyocyte, as previously presented by our group (Sanchez de la Nava et al., 2021a). The fibroblast model implemented in this study corresponded to the Maleckar model (Maleckar et al., 2009) that emulates the behavior of active fibroblasts along the atrial tissue based on the model developed by MacCannell (MacCannell et al., 2007). In total, four different currents were modeled, including the time and voltage dependent fibroblast K^+ current (I_{kv}), the time-independent inward-rectifier current (I_{K1}), the fibroblast Na^+-K^+ pump current (I_{NaK}) and the fibroblast background Na^+ current ($I_{Na\text{-}b}$) and

10.3389/fphys.2022.1025430

adapted to atrial electrophysiology. Then, heterogeneous coupling was simulated through Na^+ and K^+ movement through gap junctions (I_{Gap}), which assumed these two species as independent. This I_{Gap} current depends on the transmembrane voltage difference between the cardiomyocyte and the neighboring fibroblast, and on the gap conductance which was fixed (G_{gap} = 0.5 nS, taking into account both $G_{gap\text{-}Na}$ and $G_{gap\text{-}K}$). This I_{Gap} current contributed to the term I_{ion} in the equation below, when a communication among a cardiomyocyte and a fibroblast was simulated. Initial conditions were applied according to the stablished protocol as follows: resting membrane potential (RMP) was set to -47.75 mV for fibroblasts and -79.83 mV for cardiomyocytes, the capacitance of the cell membrane (C_m) was set to 6.3 pF for fibroblasts and 66 pF for cardiomyocytes, $[K^+]_i$ and $[Na^+]_i$ were set to 129.43 mM and 8.5547 mM, respectively. Main parameters used for the cardiomyocyte and the fibroblast model are shown in Supplementary Tables S1,2.

Diffused fibrosis was modeled using planes of the same size where the fibroblasts were randomly located considering two different distributions that differed in the percentage: 0%, 5% and 10% of fibrotic cells, percentages similar to those in other studies (Kazbanov et al., 2016; Palacio et al., 2021). Simulation protocols were performed on 2D planes mimicking a sheet of cardiac tissue of 200 x 200 nodes (2 cm side plane) that constitute around 20–25% of the total area of a human atria (Sachse, 2004). No-flux boundary condition was implemented at the edges. To connect the cells within the plane, the monodomain reaction-diffusion equation was implemented, assuming that tissue behaves as a functional syncytium where membrane voltage is propagated smoothly (Clayton and Panfilov, 2008):

$$\frac{\partial V_m}{\partial t} = \nabla \cdot (D \nabla V_m) - \frac{I_{ion} + I_{applied}}{C_m}$$

Where V_m is the transmembrane potential, t is the time, ∇ corresponds to the gradient operator and D a diffusion coefficient with units distance^2 time^{-1}, I_{ion} is the sum of all modeled transmembrane ionic currents, $I_{applied}$ is the externally applied stimulus current, and C_m is the capacitance of the cell membrane. By using this monodomain simplification, the tissue is considered to have an unlimited extracellular medium, so the extracellular resistivity can be neglected. The extracellular medium is isopotential and equal to zero for simplicity. Consequently, the membrane potential is the same as the intracellular potential. Planes were fully connected not including structures such as the pulmonary veins.

Electrophysiological variability: Population of models approach

The equations included in the aforementioned cellular models depend on constants such as channel conductivities, ionic concentrations and diffusion factors. A population of models allows mathematical computations to consider variations of the initial variables introduced in the model to account for the genetic variability present in real patients. In this case, a population of 127 ionic profiles was used including the variability present in a set of human data (Liberos et al., 2016; Simon et al., 2017).

Briefly, experimental data to calibrate the population was obtained by patch clamp techniques on myocardium atrial tissue of 149 AF patients (Sánchez et al., 2014). From these experiments, nine specific electrophysiological variables were measured to account for variation: g_{Na}, I_{NaK}, g_{K1}, g_{CaL}, g_{Kur}, I_{KCa}, diffusion (D), extracellular potassium concentration and extracellular sodium concentration. Action potential biomarkers were measured (Sánchez et al., 2014) and later used as reference (Supplementary Tables S3) to ensure that simulations were within physiological ranges. From the electrophysiological variables measured, Latin Hypercubic Sampling (LHS) was run to amplify the set of combinations to a final number of 500. These 500 combinations were included in an *in silico* tissue model of 8x256 cells in which electrophysiological properties were measured (Simon et al., 2017), Action potential biomarkers were evaluated to ensure that simulations were within physiological ranges and only the combinations within these ranges (Supplementary Tables S3) were included in the final population. A complete description of the calibration of this population can be consulted in previous publications of the group (Simon et al., 2017; Sanchez de la Nava et al., 2021a). The modification of the values (in percentage with respect to the baseline cardiomyocyte model) for each parameter in the different profiles in the population of models is shown in Supplementary Table S1, and the distribution of the range of parameter variation (-50% to +100%) is shown in Supplementary Figure S1.

Drug implementation

All antiarrhythmic drugs were evaluated in the electrophysiological population of models in order to characterize the effect according to the fibrosis percentage. The Single Pore Channel Model was implemented to analyze the effect of three different drugs (amiodarone, dofetilide and sotalol). This model inhibits the current by decreasing the conductance of the channel as described in the following equation:

$$G_i = G_0 \cdot \frac{1}{1 + \frac{[C_d]_i}{IC_{50}}}$$

Where G_0 corresponds to the initial conductance of the channel, G_i corresponds to the final conductance of the channel, $[C_d]_i$ is the concentration of the drug and IC_{50} is the

10.3389/fphys.2022.1025430

TABLE 1 Constants for drug modelling.

Drug	$[C_d]i$ (μM)	IC50 IKr (μM)	IC50 ICaL (μM)	IC50 INa (μM)
Amiodarone	0.8	0.9	1.3	4.6
Dofetilide	0.005	0.002	0.006	0.006
Sotalol	86.3	2100	2100	2.1

concentration of the drug that reduces by 50% the channel current. The values of IC_{50} and drug concentration can be observed in Table 1, and were obtained from (Patel et al., 2019).

Simulation protocols

Simulations were performed by implementing partial differential equations for the transmembrane potential models of all cells computed with a time step of 1 μs in the forward Euler scheme using in-house C++ code with CUDA parallelization solved on an NVIDIA TESLA C2057 GPU (NVIDIA Corporation, Santa Clara, CA). The Rush-Larsen scheme (Rush and Larsen, 1978) was used for gating variables in cell models of the form

$$\frac{dw_i}{dt} = \alpha_{w_i}(1 - w_i) - \beta_{w_i} w_i$$

where w is the corresponding gating variable and $\alpha_{w_i} = \alpha_{w_i}(V)$ and $\beta_{w_i} = \beta_{w_i}(V)$ are the voltage dependent rate constants. The Rush-Larsen method provides a stable temporal solution for the gating variables by relaying on the exact exponential solution implemented in the following expression (Perego and Veneziani, 2009) for each cell:

$$w_{i+1}^j = e^{a_{w_i}(V)h}\left(w_i^j + \frac{b_{w_i}(V)}{a_{w_i}(V)}\right) - \frac{b_{w_i}(V)}{a_{w_i}(V)}$$

where $a_{w_i} = -(\alpha_{w_i} + \beta_{w_i})$, $b_i = \alpha_{w_i}$, j corresponds to each individual cell, and h is the time step for the forward time index i integration.

Planes were simulated for a total of four impulses (S1) of magnitude 4000 pA/pF and duration 3 ms applied at the left edge of the planes in 200 cells at a frequency of 1 Hz. From the complete set of simulations, four different biomarkers were evaluated considering the last two S1 pulses: the Action Potential Duration at 90% repolarization (APD90, measured in ms), the conduction velocity (CV, measured in cm/s), the resting membrane potential (RMP, measured in mV) and peak voltage value (Peak, measured in mV). APD90, RMP and Peak were calculated by averaging the values of all the cardiomyocytes present in the plane. Cell activation time was marked at the time of highest voltage time derivative (Simon et al., 2017). For CV propagation measurements, the distance between two points at coordinates (0.5 mm, 10 mm) and (19.5 mm, 10 mm) in the 2D plane was divided by the activation time differences between these points. Absence of conduction was considered when the cell in the second coordinate (right side of the plane) did not activate (depolarize and repolarize) after the application of the last stimulus in the left side of the plane. This included some profiles that failed to repolarize, some profiles that failed to conduct and some profiles that failed to be stimulated. All measurements reported in this study are the average value of each biomarker during the last two S1 pulses. To evaluate the effect of a drug, the difference in value of the aforementioned biomarkers was computed to quantify and increase or decrease relative to a basal value as:

$$\Delta Biomarker = Biomarker_{Drug} - Biomarker_{Basal}$$

Artificial intelligence algorithm: Pattern recognition for non-conducting and conducting profiles

A total of 1032 simulations were computed in this study corresponding to all different combinations of the population of models with different fibrosis degree (0% fibrosis, 5% fibrosis and 10% fibrosis) under the effect of different antiarrhythmic drugs (amiodarone, dofetilide and sotalol), simulated in sheets of cardiac tissue.

Several supervised models were trained to evaluate the algorithm that better described the behavior of the population including Quadratic Support Vector Machine (QSVM), Cubic Support Vector Machine (CSVM), decision trees (DT), K-Nearest Neighbors (KNN) with 10k-fold cross validation. The input of the algorithms corresponded to a combination of the variables from the population of models: g_{Na}, I_{NaK}, g_{K1}, g_{CaL}, g_{Kur}, I_{KCa}, diffusion (D), extracellular potassium concentration ($[K]_o$) and extracellular sodium concentration ($[Na]_o$), including the variation induced in the final conductance of the channel (G_i) by the different antiarrhythmic drugs tested (amiodarone, dofetilide or sotalol), and the percentage of fibrosis (0, 5% or 10%). AI algorithms were trained to predict a binary outcome: conduction along the plane (labeled as 1) or absence of conduction (labeled as 0). An example of a conducting and non-conducting profile both with 10% fibrosis and in the absence of drugs are shown in Figure 1. Figure 1A shows how two consecutive impulses propagate in each profile across the

10.3389/fphys.2022.1025430

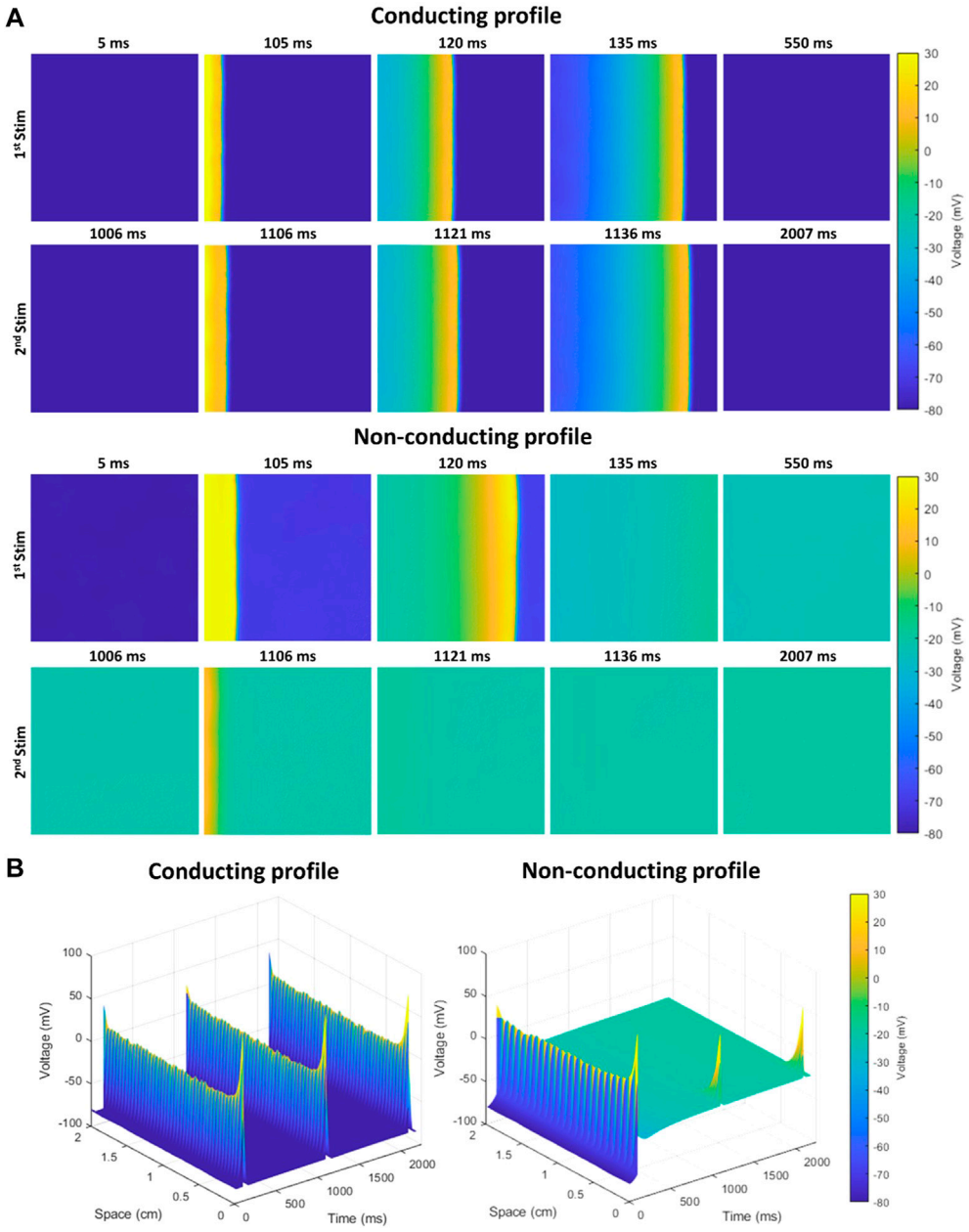

FIGURE 1
Example of conducting and non-conducting profiles both with 10% of fibrosis, in the absence of the effect of any antiarrhythmic drug. **(A)** Propagation of two stimuli in each profile across the simulated tissue (2 cm x 2 cm) from left to right, with no-flux boundary conditions. While the second impulse propagates in the first profile, it does not in the second profile as the simulated tissue is failing to repolarize to initial membrane potential. **(B)** Time-space plot along the propagation direction in both profiles, showing effective propagation in the first profile and the blockade in the second profile.

simulated tissue and Figure 1B the time-space plot along the propagation direction. While at 10% fibrosis the combination of variables in the cardiomyocytes of the first profile allow to conduct both impulses, in the second profile, the different combination of variables produces a conduction block for the second stimulus. The cardiomyocyte variables in the conducting profile shown in Figure 1 correspond to the baseline reference Koivumaki Model with Skibsbye modifications (Skibsbye et al., 2016), and the variables in the non-conducting profile are: $g_{Na=+73.13\%}$, $I_{NaK=+76.95\%}$, $g_{K1=-38.37\%}$, $g_{CaL=+92.17\%}$, $g_{Kur=+77.18\%}$, $I_{KCa=-47.2\%}$, $D_{=-30.64\%}$, $[K]_{o=+94.93\%}$ and $[Na]_{o=+89.34\%}$ relative to the baseline cardiomyocyte model. Algorithms were trained

10.3389/fphys.2022.1025430

using the variable parameters for the population of models while the output for prediction was if propagation was possible along the plane or not. Training testing ratio was set 80:20 as in previous experiments by the group (Sanchez de la Nava et al., 2021a).

The algorithms were evaluated by means of specificity, sensitivity, positive predictive value, negative predictive value and accuracy, as follows:

$$Sensitivity = \frac{Number\ of\ true\ positives}{Number\ of\ true\ positives + Number\ of\ false\ negatives}$$

$$Specificity = \frac{Number\ of\ true\ negatives}{Number\ of\ false\ positives + Number\ of\ true\ negatives}$$

$$Positive\ Predictive\ Value = \frac{Number\ of\ true\ positives}{Number\ of\ true\ positives + Number\ of\ false\ positives}$$

$$Negative\ Predictive\ Value = \frac{Number\ of\ true\ negatives}{Number\ of\ true\ negatives + Number\ of\ false\ negatives}$$

$$Accuracy = \frac{Number\ of\ correct\ predictions}{Total\ number\ of\ predictions}$$

Variability on the simulated models: Validation of the protocol

In order to evaluate the potential applicability of this technology into different fields, and specially for translating the results into the clinic, we evaluated small variations on the population of models to quantify changes in propagation of the electrical impulse.

Statistical analysis

The *t*-test was used to evaluate the statistical significance between continuous paired or unpaired variables. One-way ANOVA, Kruskal Wallis test calculator and Chi Square test were calculated to evaluate differences among the three studied groups (0% fibrosis, 5% fibrosis and 10% fibrosis) in continuous and binary variables, respectively. Statistical significance was considered for p <0.05 in all cases.

Results

Construction and calibration of the model population

From the complete population consisting on 127 different electrophysiological profiles that conducted the electrical impulse along the plane in 0% fibrosis conditions, 58 profiles conducted for the 5% condition and 32 for the 10% fibrosis (Figure 2). In addition, when the drugs were added, the number of conductive profiles diminished for all cases due to the antiarrhythmic effect of the compound (Figure 2). The distribution of the variables of the population of models that present propagation during simulations at three different fibrosis concentrations in basal conditions (no drugs) presented no significant differences and are shown in Supplementary Figure S1. All the subsequent results are presented for the profiles that did conduct the electrical impulse at 5% or at 10% fibrosis level.

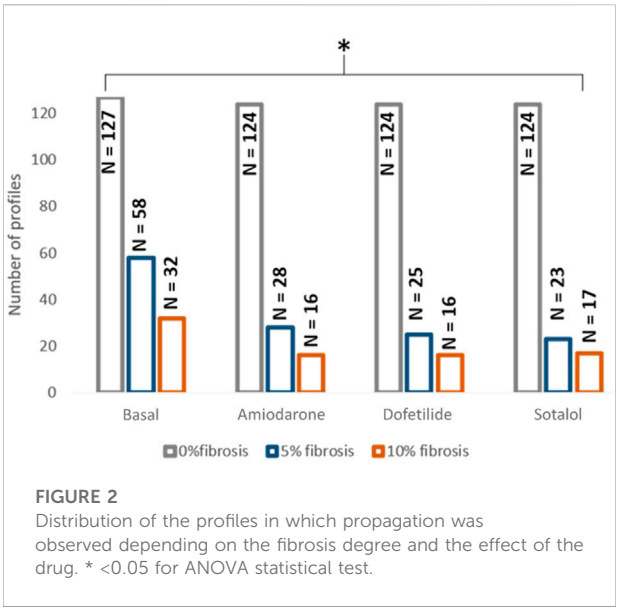

FIGURE 2
Distribution of the profiles in which propagation was observed depending on the fibrosis degree and the effect of the drug. * <0.05 for ANOVA statistical test.

The effects of fibrosis on the electrophysiological measurements in the simulations are shown in Figure 3. At the electrophysiological level, the presence of fibrosis produced a shortening of the APD90 (0% fibrosis: 187.77 ± 37.62 ms; 5% fibrosis: 93.29 ± 82.69 ms; 10% fibrosis: 106.37 ± 85.15 ms; p-value<0.001) on the simulated cardiomyocytes. Conduction velocity was significantly reduced for higher presence of fibrosis (0% fibrosis: 67.52 ± 7.3 cm/s; 5% fibrosis: 58.81 ± 14.04 cm/s; 10% fibrosis: 57.56 ± 14.78 cm/s; p-value<0.001). Both RMP (0% fibrosis: −78.63 ± 4.63 mV; 5% fibrosis: −79.46 ± 5.46 mV; 10% fibrosis: −77.35 ± 5.43 mV; p-value: >0.1) and peak membrane potential value in the cardiomyocytes (0% fibrosis: 89.16 ± 16.01 mV; 5% fibrosis: 70.06 ± 17.08 mV; 10% fibrosis: 82.21 ± 19.90 mV; p-value<0.001) presented a decrease for 5% fibrosis and an increase for 10% fibrosis planes (Figure 3).

Drug implementation on the stable ionic profiles

All drugs were studied at two different levels on the conducting profiles at basal conditions: first, regarding the variations on the ionic conductances present at the population

10.3389/fphys.2022.1025430

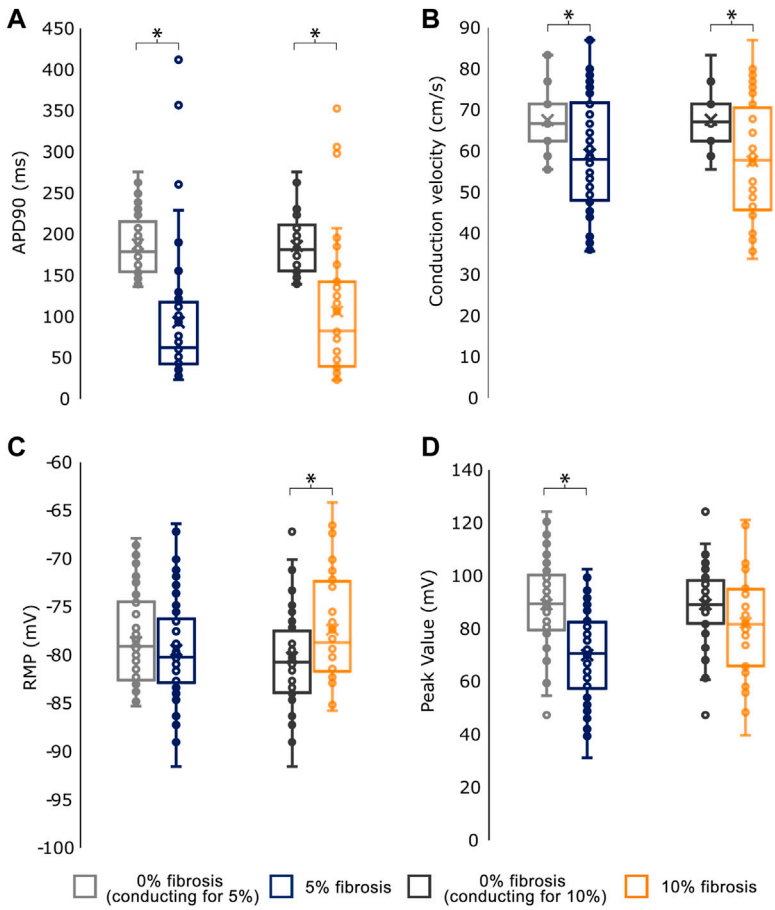

FIGURE 3
Mean values for the electrophysiological characterization of simulations conducting for the different fibroblast concentrations. **(A)** Action Potential Duration at 90% repolarization (APD90) **(B)** Conduction velocity **(C)** Resting Membrane Potential (RMP) and **(D)** Peak Transmembrane Value. As the number of profiles conducting in each group (0%, 5% and 10% fibrosis) differ, each group is compared against the basal (0% fibrosis) electrophysiological values of the same profiles.* <.05 for *t*-test statistical test.

TABLE 2 Change in conduction velocity for the studied antiarrhythmic drugs under the effect of fibrosis (number of profiles and percentage).

	0% Fibrosis		5% Fibrosis		10% Fibrosis	
	Increase in CV	Decrease in CV	Increase in CV	Decrease in CV	Increase in CV	Decrease in CV
Amiodarone	0	124 (100%)	0	28 (100%)	5 (31.25%)	11 (68.75%)
Dofetilide	0	124 (100%)	7 (28%)	13 (52%)	6 (37.5%)	3 (18.8%)
Sotalol	0	124 (100%)	15 (65.21%)	6 (26.08%)	7 (43.75%)	2 (12.5%)

of models and secondly, based on the clinical biomarkers extracted from the simulations.

Figure 2 shows the distribution of the profiles conducting the electrical impulse for each scenario and Table 2 contains the proportion of profiles with conduction velocity modifications in the population with respect to the corresponding control population (0%, 5% or 10% fibrosis without drug). An example of a conducting profile and non-conducting profile for 10% fibrosis can be consulted in Figure 1. Interestingly, in the absence of fibrosis (0% fibrosis simulations), all the profiles presented a decrease in conduction velocity under the effect of all drugs, in accordance to what is described and expected for AADs.

10.3389/fphys.2022.1025430

TABLE 3 Change in conduction velocity for the studied antiarrhythmic drugs under the effect of fibrosis.

		ΔCV (cm/s)	*p*-value	ΔAPD90 (ms)	*p*-value	ΔRMP (mV)	*p*-value	ΔPeak value (mV)	*p*-value
Amiodarone	0% fibrosis	−3.59 ± 1.52	0.24	−49.42 ± 96.72	0.06	0.14 ± 0.43	<0.01	−4.76 ± 0.98	0.01
	5% fibrosis	−4.96 ± 2.15		−16.32 ± 93.05		−1.97 ± 3.15		−7.34 ± 3.61	
	10% fibrosis	0.62 ± 9.56		−28.79 ± 142.98		−5.39 ± 7.29		−1.97 ± 22.96	
Dofetilide	0% fibrosis	−13.43 ± 4.07	<0.01	−29.51 ± 71.67	0.92	1.78 ± 9.83	0.04	−18.85 ± 9.47	<0.01
	5% fibrosis	0.14 ± 1.87		5.73 ± 136.26		4.75 ± 27.58		−0.96 ± 3.83	
	10% fibrosis	0.05 ± 1.16		−18.92 ± 129.98		−1.94 ± 4.29		3.59 ± 11.31	
Sotalol	0% fibrosis	−0.023 ± 0.24	<0.01	−15.83 ± 43.76	0.06	0.18 ± 0.16	<0.01	−0.04 ± 0.16	<0.01
	5% fibrosis	0.30 ± 4.69		3.80 ± 135.56		−0.46 ± 3.34		−0.41 ± 3.12	
	10% fibrosis	0.22 ± 1.39		−40.28 ± 106.18		−1.93 ± 4.28		3.49 ± 11.49	

However, the simulations with fibrosis showed a different effect of some drugs: dofetilide and sotalol simulations exhibited part of the profiles in which the conduction velocity was increased (dofetilide: 28% of profiles; sotalol: 65.21%). Finally, when simulations were repeated with a higher percentage of fibrosis (i.e. 10% fibrosis) a dispersed effect on the conduction velocity was observed under the effect of all the tested drugs (increased conduction velocity of 31.25% for amiodarone profiles, 37.5% for dofetilide profiles and 43.75% for sotalol profiles).

In addition, the electrophysiological characterization of the simulations can be observed in Table 3, where the variation of four electrophysiological biomarkers (change in CV, APD90, RMP and peak value) induced by the different drugs is shown. Regarding the electrophysiological characterization, an average decrease or maintenance in CV was observed with respect to the corresponding control population, but the effect was more variable when fibrosis was present. The effect or drugs tended to reduce APD90 in most cases when measuring the variables in the cardiomyocytes except for the 5% fibrosis simulations. However, high variability in APD90 changes was observed among the different profiles. In the case of RMP, an average increase was observed on the 0% fibrosis under the effects of drugs, however, drugs tended to have the opposite effect and reduce RMP in the different profiles in the presence of fibrosis. The effect on RMP was highly variable for the different profiles, and in particular in the presence of dofetilide. Finally, the peak value tended to reduce in all cases except for the 10% fibrosis under the effect of dofetilide and sotalol.

In Silico models and artificial intelligence

Comparing the prediction accuracy of the different AI methods tested in this work, Cubic SVM showed the best performance for the tested dataset. As it can be observed from Table 4; Figure 4, the Area Under the Curve (AUC) was 0.95, the accuracy of the algorithm was 90.4% (C.I. 88.83%–91.85%) with a sensitivity of 90.43% (C.I. 88.20%–92.36%), specificity 90.41% (88.00%–92.48%), positive predictive value of 91.55% (C.I. 89.62%–93.15%) and negative predictive value of 89.15% (C.I. 86.92%–91.04%). All the other tested methods (QSVM, DT and KNN) showed an accuracy above 80% and an AUC larger than 0.89, but lower in comparison with CSVM.

The CSVM algorithm (Cristianini and Shawe-Taylor, 2000) includes an analysis to evaluate how important are the input features in outcome prediction. In particular, Sequential Minimal Optimization (Platt, 1998) that was implemented to solve the nonlinear problem during the algorithm training, enabled the identification and posterior optimization of the variables included in the final CSVM prediction algorithm. Once the problem has been solved, the kernel calculated for the support vector machines can reveal the relative importance of contributions during calibration by each of the input parameters. That is, their contribution to minimizing the error when predicting the outcome can be ranked based on quantifying their support vector magnitude. Utilizing such approach the CSVM algorithm revealed that the most important features for evaluating the block or conduction of the action potential in the tissue were in decreasing order: (i) the type of drug added, (ii) the values of the sodium currents (INak and gNa) and (iii) the values of the potassium currents (gK1 and gKur).

Discussion

In this study, we present a new methodology to identify and predict the propagation of the electrical impulse in the presence of electrophysiological variability, the presence of different

TABLE 4 Evaluation metrics for the different AI algorithms trained including sensitivity, specificity and accuracy expressed in percentage and respective confidence interval in brackets, and Area Under the Curve (AUC).

	Sensitivity	Specificity	Accuracy	AUC
QSVM	84.67% [82.14%–86.96%]	93.11% [90.83%–94.97%]	88.12% [86.39%–89.71%]	0.94
CSVM	90.43% [88.20%–92.36%]	90.41% [88.00%–92.48%]	90.40% [88.83%–91.85%]	0.95
DT	79.85% [77.17%–82.35%]	92.93% [90.50%–94.90%]	84.71% [82.81%–86.48%]	0.89
KNN	78.65% [75.91%–81.22%]	90.05% [87.30%–92.38%]	82.94% [80.96%–84.80%]	0.92

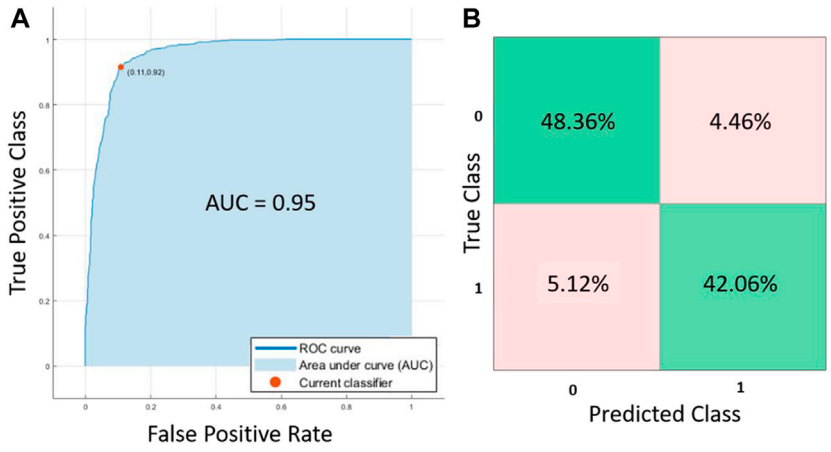

FIGURE 4
(A) ROC curves and **(B)** confusion matrix for the Cubic SVM trained algorithm.

degrees of fibrosis and the effect of antiarrhythmic drugs. Several algorithms were trained and cubic SVM showed the best performance using the *in silico* data from the simulations. These simulations included: (i) electrophysiological variability using a population of models, (ii) substrate variability using different percentages of fibrosis, and (iii) drug effect variability, introduced by the implementation of the effect of three different antiarrhythmic drugs used in the clinical practice for AF treatment. The main result of the study showed that, depending on the percentage of fibrosis and the effect of the drug, the modifications of the conduction velocity of the substrate could lead to proarrhythmic scenarios in specific subgroups.

Electrical conduction in 2D cardiac tissue: Effect of ionic profile and fibrosis presence

To our knowledge, this study is the first one that explores 2D tissue simulations combining a population of atrial cardiomyocytes with different percentages of diffused fibrosis. Previous studies have shown the effect of diffused fibrosis on the electrophysiological properties of the tissue, in line with the results presented in this publication (King et al., 2013; Palacio et al., 2021; Rios-Munoz et al., 2021). Our results are in agreement with studies that evaluated the effect of fibrosis in the electrophysiological characteristics of cardiac tissue showing a decrease in conduction velocity (Spencer et al., 2017).

Drug effect on fibrotic tissue behaviour: Electrophysiological implications

Populations of models have been implemented in the cardiac scenario for the prediction of drug effect on cardiac tissue (Britton et al., 2013; Muszkiewicz et al., 2016; Sanchez de la Nava et al., 2021a; Peirlinck et al., 2021). Here, the 2D fibrotic tissue simulations were not only evaluated at basal conditions but also under the effect of different antiarrhythmic drugs, including amiodarone, dofetilide and sotalol. Overall, these antiarrhythmic drugs showed a total block in the majority of the profiles. In those in which electrical conduction was preserved, a decrease on conduction velocity was observed when simulations were performed in the 0% fibrosis tissue patch. This effect was preserved for amiodarone in the 5%

fibrosis patch. Finally, 10% fibrosis simulations showed that part of the profiles increased CV while others showed a decrease in this variable.

This confirms our hypothesis that the expected effect of the drug can be altered due to the presence of fibrosis and that, for higher percentage of fibrosis, the effect is less predictable and more frequent to present unexpected effects. Furthermore, we observed that the antiarrhythmic drug that showed less variability of the effect among the different profiles was amiodarone, causing a decrease in the conduction velocity (CV) in most of the profiles with and without fibrosis. In contrast, the long-term use of amiodarone in porcine animal models with myocardial fibrosis showed no adverse effects (Zagorianou et al., 2016).

Reduced and more heterogeneous CV in the myocardium increases the probability of arrhythmia and can be caused by a single or combined effect of structural changes, alterations in electrical coupling in the tissue, or the effect of different drugs. In our study, the different profiles showed variability in the ionic current values and action potential morphology, leading to modifications of fibroblasts conduction velocity and arrhythmogenicity. Our results may help to further interpret the drug-induced modifications of CV in prior studies. Angiotensin converting enzyme inhibitors, angiotensin II type 1 receptor antagonists and pirfenidone have been shown to be effective in attenuating arrhythmogenic atrial remodeling, resulting in a marked reduction in atrial fibrosis, with reduced conduction heterogeneity and AF vulnerability (Li et al., 2001; Kumagai et al., 2003; Lee et al., 2006). On the other hand, the effects of drugs designed to enhance gap-junctional coupling on cardiac CV may depend on the presence of fibrotic changes. Rotigaptide showed that in the absence of fibroblasts, CV increases monotonically with gap junctional coupling (Lin et al., 2008). However, the presence of fibroblasts, resulted in a biphasic effect on CV, as showed in both experimental and computational studies (Miragoli et al., 2006; Zlochiver et al., 2008; Tveito et al., 2012). Additionally, the relative expression of Cx40 and Cx43 may either increase or decrease CV in experiments and humans (Bagwe et al., 2005; Dhillon et al., 2014). Finally, while acetylcholine induced APD shortening was able to induce an spiral wave AF episode in healthy canine hearts (Schuessler et al., 1992), shortening the APD using pinacidil induced AF was driven by intramural reentry anchored to atrial bundles insulated by fibrosis (Hansen et al., 2015). Therefore, we expect that using mathematical models such as used here may help to improve the understanding of the complex relationship of cardiac electrical substrate, electrical conduction and drugs effects on propagation and arrhythmogenicity.

Artificial intelligence for the evaluation of tissue conduction

In silico simulations allow to produce a significant number of scenarios that is suitable for the application of AI algorithms that enable to better analyze and extract patterns. The use of this technology has increased exponentially in the last years with the aim of better predicting and identifying new biomarkers.

In this case, these algorithms were implemented with the main objective of identifying the capabilities of the tissue to conduct the electrical signal. Lack of conduction of a small patch in the heart has been proved to cause arrhythmia, described as anatomical reentry, where the anatomical pathway is fixed (Arenal et al., 2012). Among the algorithms explored in this study, all showed an accuracy above 80%. However, Cubic SVM showed the best performance compared to QSVM, DT and KNN, with an accuracy of 90.4% and an AUC of 0.95. This high accuracy highlights the potential of these techniques as collaborative and predictive tools in the clinic. Using this methodology in more patient-specific complex scenarios is more likely to predict the potential benefit of an antiarrhythmic drug on a specific patient by avoiding the occurrence of conduction blocks. For example, after further validation, using patient specific 3D geometry and fibrosis distribution obtained by MRI and combining it with this *in silico* model, the CSVM algorithm could be applied to help in the decision of which antiarrhythmic drug may be more appropriate.

Limitations

The main limitations of this study include the high computational cost associated to obtain a broad number of profiles. In the same line, simulations were performed in 2D planes to reduce the overall computational cost, but the study will benefit to include more complex structures in the model such as the pulmonary veins, different CV areas (Sánchez et al., 2019) or a 3D configuration.

Although we considered the variability of the cardiomyocyte population, new approaches should explore the possibility of developing a population for human fibroblasts to be included in the model, as for this study variability was only introduced in the cardiomyocyte model.

Finally, regarding the diffused fibrosis that has been studied, the percentage of fibroblasts was varied from 0% to 5% and 10%, but the distribution of the fibroblast was determined randomly for each percentage and kept constant for all the profiles. Running the different profiles with the same percentage of fibrosis, but different distributions should be further tested in order to corroborate the obtained results.

Clinical implications

The identification of specific scenarios and combination of variables that present proarrhythmic effects can be of great importance in the understanding and development of new tools for future pharmacological treatments in the concepts of personalized medicine and optimizing treatment efficacy.

Conclusion

Cardiac fibrosis can alter the expected behavior of antiarrhythmic drugs in a minority of the population and data analysis using artificial intelligence can reveal the profiles that will respond differently.

Data availability statement

The code for the cardiomyocyte model, the fibroblast model, and the population of models are provided in the Supplementary Figure S1 (Supplementary Data S1, S2). The rest of the raw data supporting the conclusion of this article will be made available by the authors, without undue reservation.

Author contributions

AS, LG-C, FA, and AD-S designed and performed the experiments. AS, LG-C, AD-S, and FA analysed and evaluated the results. All authors contributed to the drafting and final approval of the manuscript.

Funding

This work was supported in part by the Instituto de Salud Carlos III (PI16/01123, DTS16/0160, PI17/01059, PI19/00161, PI20/01618, and PI18/01895), Spanish Ministry of Science and Innovation (CIBERCV), and European Union's H2020 Program under grant agreement No. 874827 (BRAVE), and cofunded by Fondo Europeo de Desarrollo Regional (FEDER), EIT Health 19600 AFFINE. Also supported in part by National Institutes of Health grants R01-HL118304, R21-HL153694, R21-EB032661 and R01-HL156961 (Berenfeld).

Conflict of interest

FA and FF-A have equity from Corify Care SL. FA served on the advisory board of Medtronic. OB is a co-founder and Member of Cor-Dx LLC and received research grants from Medtronic and CoreMap.

The remaining authors declare that the research was conducted in the absence of any commercial of financial relationships that could be construed as a potential conflict of interest.

Publisher's note

All claims expressed in this article are solely those of the authors and do not necessarily represent those of their affiliated organizations, or those of the publisher, the editors and the reviewers. Any product that may be evaluated in this article, or claim that may be made by its manufacturer, is not guaranteed or endorsed by the publisher.

Supplementary material

The Supplementary Material for this article can be found online at: https://www.frontiersin.org/articles/10.3389/fphys.2022.1025430/full#supplementary-material

References

Arenal, Á., Hernández, J., Pérez-David, E., Rubio-Guivernau, J. L., Ledesma-Carbayo, M. J., and Fernández-Avilés, F. (2012). Do the spatial characteristics of myocardial scar tissue determine the risk of ventricular arrhythmias? *Cardiovasc. Res.* 94, 324–332. doi:10.1093/cvr/cvs113

Bagwe, S., Berenfeld, O., Vaidya, D., Morley, G. E., and Jalife, J. (2005). Altered right atrial excitation and propagation in connexin40 knockout mice. *Circulation* 112, 2245–2253. doi:10.1161/CIRCULATIONAHA.104.527325

Britton, O. J., Bueno-Orovio, A., Van Ammel, K., Lu, H. R., Towart, R., Gallacher, D. J., et al. (2013). Experimentally calibrated population of models predicts and explains intersubject variability in cardiac cellular electrophysiology. *Proc. Natl. Acad. Sci. U. S. A.* 110, E2098–E2105. doi:10.1073/pnas.1304382110

Clayton, R. H., and Panfilov, A. V. (2008). A guide to modelling cardiac electrical activity in anatomically detailed ventricles. *Prog. Biophys. Mol. Biol.* 96, 19–43. doi:10.1016/j.pbiomolbio.2007.07.004

Cox, J. L., Boineau, J. P., Schuessler, R. B., Kater, K. M., Ferguson, T. B. J., Cain, M. E., et al. (1995). Electrophysiologic basis, surgical development, and clinical results of the maze procedure for atrial flutter and atrial fibrillation. *Adv. Card. Surg.* 6, 1–67.

Cristianini, N., and Shawe-Taylor, J. (2000). *An Introduction to Support Vector Machines and Other Kernel-Based Learning Methods*. doi:10.1017/CBO9780511801389

Dhillon, P. S., Chowdhury, R. A., Patel, P. M., Jabr, R., Momin, A. U., Vecht, J., et al. (2014). Relationship between connexin expression and gap-junction resistivity in human atrial myocardium. *Circ. Arrhythm. Electrophysiol.* 7, 321–329. doi:10.1161/CIRCEP.113.000606

Hansen, B. J., Zhao, J., Csepe, T. A., Moore, B. T., Li, N., Jayne, L. A., et al. (2015). Atrial fibrillation driven by micro-anatomic intramural re-entry revealed by simultaneous sub-epicardial and sub-endocardial optical mapping in explanted human hearts. *Eur. Heart J.* 36, 2390–2401. doi:10.1093/EURHEARTJ/EHV233

Kazbanov, I. V., Ten Tusscher, K. H. W. J., and Panfilov, A. V. (2016). Effects of heterogeneous diffuse fibrosis on arrhythmia dynamics and mechanism. *Sci. Rep.* 6, 20835. doi:10.1038/srep20835

King, J. H., Huang, C. L.-H., and Fraser, J. A. (2013). Determinants of myocardial conduction velocity: implications for arrhythmogenesis. *Front. Physiol.* 4, 154. doi:10.3389/FPHYS.2013.00154

Krul, S. P. J., Berger, W. R., Smit, N. W., Van Amersfoorth, S. C. M., Driessen, A. H. G., Van Boven, W. J., et al. (2015). Atrial fibrosis and conduction slowing in the left atrial appendage of patients undergoing thoracoscopic surgical pulmonary vein isolation for atrial fibrillation. *Circ. Arrhythm. Electrophysiol.* 8, 288–295. doi:10.1161/CIRCEP.114.001752

Kumagai, K., Nakashima, H., Urata, H., Gondo, N., Arakawa, K., and Saku, K. (2003). Effects of angiotensin II type 1 receptor antagonist on electrical and

structural remodeling in atrial fibrillation. *J. Am. Coll. Cardiol.* 41, 2197–2204. doi:10.1016/S0735-1097(03)00464-9

Lee, K. W., Everett IV, T. H., Rahmutula, D., Guerra, J. M., Wilson, E., Ding, C., et al. (2006). Pirfenidone prevents the development of a vulnerable substrate for atrial fibrillation in a canine model of heart failure. *Circulation* 114, 1703–1712. doi:10.1161/CIRCULATIONAHA.106.624320

Li, D., Shinagawa, K., Pang, L., Leung, T. K., Cardin, S., Wang, Z., et al. (2001). Effects of angiotensin-converting enzyme inhibition on the development of the atrial fibrillation substrate in dogs with ventricular tachypacing-induced congestive heart failure. *Circulation* 104, 2608–2614. doi:10.1161/HC4601.099402

Liberos, A., Bueno-Orovio, A., Rodrigo, M., Ravens, U., Hernandez-Romero, I., Fernandez-Aviles, F., et al. (2016). Balance between sodium and calcium currents underlying chronic atrial fibrillation termination: an *in silico* intersubject variability study. *Heart Rhythm* 13, 2358–2365. doi:10.1016/j.hrthm.2016.08.028

Lin, X., Zemlin, C., Hennan, J. K., Petersen, J. S., and Veenstra, R. D. (2008). Enhancement of ventricular gap-junction coupling by rotigaptide. *Cardiovasc. Res.* 79, 416–426. doi:10.1093/CVR/CVN100

MacCannell, K. A., Bazzazi, H., Chilton, L., Shibukawa, Y., Clark, R. B., and Giles, W. R. (2007). A mathematical model of electrotonic interactions between ventricular myocytes and fibroblasts. *Biophys. J.* 92, 4121–4132. doi:10.1529/BIOPHYSJ.106.101410

Maleckar, M. M., Greenstein, J. L., Giles, W. R., and Trayanova, N. A. (2009). Electrotonic coupling between human atrial myocytes and fibroblasts alters myocyte excitability and repolarization. *Biophys. J.* 97, 2179–2190. doi:10.1016/j.bpj.2009.07.054

Marrouche, N. F., Wilber, D., Hindricks, G., Jais, P., Akoum, N., Marchlinski, F., et al. (2014). Association of atrial tissue fibrosis identified by delayed enhancement MRI and atrial fibrillation catheter ablation: The DECAAF study. *JAMA - J. Am. Med. Assoc.* 311, 498–506. doi:10.1001/jama.2014.3

Miragoli, M., Gaudesius, G., and Rohr, S. (2006). Electrotonic modulation of cardiac impulse conduction by myofibroblasts. *Circ. Res.* 98, 801–810. doi:10.1161/01.RES.0000214537.44195.A3

Muszkiewicz, A., Britton, O. J., Gemmell, P., Passini, E., Sanchez, C., Zhou, X., et al. (2016). Variability in cardiac electrophysiology: Using experimentally-calibrated populations of models to move beyond the single virtual physiological human paradigm. *Prog. Biophys. Mol. Biol.* 120, 115–127. doi:10.1016/j.pbiomolbio.2015.12.002

Palacio, L. C., Ugarte, J. P., Saiz, J., and Tobón, C. (2021). The effects of fibrotic cell type and its density on atrial fibrillation dynamics: An *in silico* study. *Cells* 10, 2769. doi:10.3390/cells10102769

Patel, D., Stohlman, J., Dang, Q., Strauss, D. G., and Blinova, K. (2019). Assessment of proarrhythmic potential of drugs in optogenetically paced induced pluripotent stem cell-derived cardiomyocytes. *Toxicol. Sci.* 170, 167–179. doi:10.1093/toxsci/kfz076

Peirlinck, M., Costabal, F. S., Yao, J., Guccione, J. M., Tripathy, S., Wang, Y., et al. (2021). Precision medicine in human heart modeling: Perspectives, challenges, and opportunities. *Biomech. Model. Mechanobiol.* 20, 803–831. doi:10.1007/S10237-021-01421-Z

Perego, M., and Veneziani, A. (2009). An efficient generalization of the rush-Larsen method for solving electro-physiology membrane equations. *Electron. Trans. Numer. Anal.* 35, 234–257. Available at: https://go.gale.com/ps/i.do?p=AONE&sw=w&issn=10689613&v=2.1&it=r&id=GALE%7CA230063916&sid=googleScholar&linkaccess=fulltext (Accessed September 16, 2022).

Platt, J. C. (1998). *Sequential Minimal Optimization: A Fast Algorithm for Training Support Vector Machines*.

Rios-Munoz, G. R., Sanchez De La Nava, A. M., Gomez-Cid, L., Grigorian-Shamagian, L., Fernandez-Santos, M. E., Atienza, F., et al. (2021). Unveiling the impact of fibrosis presence in fibrillatory electrograms. *Eur. Heart J.* 42, ehab724.0417. doi:10.1093/eurheartj/ehab724.0417

Rush, S., and Larsen, H. (1978). A practical algorithm for solving dynamic membrane equations. *IEEE Trans. Biomed. Eng.* 25, 389–392. doi:10.1109/TBME.1978.326270

Sachse, F. B. (2004). *Computational cardiology : modeling of anatomy, electrophysiology, and mechanics*. Germany: Springer.

Saljic, A., and Heijman, J. (2022). Emerging antiarrhythmic drugs for atrial fibrillation. *Int. J. Mol. Sci.* 23, 4096. doi:10.3390/ijms23084096

Sánchez, C., Bueno-Orovio, A., Wettwer, E., Loose, S., Simon, J., Ravens, U., et al. (2014). Inter-subject variability in human atrial action potential in sinus rhythm versus chronic atrial fibrillation. *PLoS One* 9, e105897. doi:10.1371/journal.pone.0105897

Sanchez de la Nava, A. M., Arenal, Á., Fernández-Avilés, F., and Atienza, F. (2021a). Artificial intelligence-driven algorithm for drug effect prediction on atrial fibrillation: An *in silico* population of models approach. *Front. Physiol.* 0, 768468. doi:10.3389/FPHYS.2021.768468

Sánchez de la Nava, A. M., Atienza, F., Bermejo, J., and Fernández-Avilés, F. (2021b). Artificial intelligence for a personalized diagnosis and treatment of atrial fibrillation. *Am. J. Physiol. Heart Circ. Physiol.* 320, H1337–H1347. doi:10.1152/ajpheart.00764.2020

Sánchez, J., Gomez, J. F., Martinez-Mateu, L., Romero, L., Saiz, J., and Trenor, B. (2019). Heterogeneous effects of fibroblast-myocyte coupling in different regions of the human atria under conditions of atrial fibrillation. *Front. Physiol.* 10, 847–913. doi:10.3389/fphys.2019.00847

Sanguinetti, M. C., and Bennett, P. B. (2003). Antiarrhythmic drug target choices and screening. *Circ. Res.* 93, 491–499. doi:10.1161/01.RES.0000091829.63501.A8

Schuessler, R. B., Grayson, T. M., Bromberg, B. I., Cox, J. L., and Boineau, J. P. (1992). Cholinergically mediated tachyarrhythmias induced by a single extrastimulus in the isolated canine right atrium. *Circ. Res.* 71, 1254–1267. doi:10.1161/01.RES.71.5.1254

Simon, A., Liberos, A., Hernandez-Romero, I., Bueno Orovio, A., Rodrigo, M., Guillem, S., et al. (2017). "Electrophysiological parameters in the electrical propagation during atrial fibrillation: a population of models study," in 2017 Computing in Cardiology (CinC), Rennes, France, 24-27 September 2017, 1–4. doi:10.22489/CinC.2017.018-358

Skibsbye, L., Jespersen, T., Christ, T., Maleckar, M. M., van den Brink, J., Tavi, P., et al. (2016). Refractoriness in human atria: Time and voltage dependence of sodium channel availability. *J. Mol. Cell. Cardiol.* 101, 26–34. doi:10.1016/j.yjmcc.2016.10.009

Spencer, T. M., Blumenstein, R. F., PryseSheng, K. M., Lee, S. L., Glaubke, D. A., Carlson, B. E., et al. (2017). Fibroblasts slow conduction velocity in a reconstituted tissue model of fibrotic cardiomyopathy. *ACS Biomater. Sci. Eng.* 3, 3022–3028. doi:10.1021/acsbiomaterials.6b00576

Tveito, A., Lines, G. T., and Maleckar, M. M. (2012). Note on a possible proarrhythmic property of antiarrhythmic drugs aimed at improving gap-junction coupling. *Biophys. J.* 102, 231–237. doi:10.1016/J.BPJ.2011.11.4015

Yeo, J. M., Tse, V., Kung, J., Lin, H. Y., Lee, Y. T., Kwan, J., et al. (2017). Isolated heart models for studying cardiac electrophysiology: A historical perspective and recent advances. *J. Basic Clin. Physiol. Pharmacol.* 28, 191–200. doi:10.1515/jbcpp-2016-0110

Zagorianou, A., Marougkas, M., Drakos, S. G., Diakos, N., Konstantopoulos, P., Perrea, D. N., et al. (2016). The effect of long-term amiodarone administration on myocardial fibrosis and evolution of left ventricular remodeling in a porcine model of ischemic cardiomyopathy. *Springerplus* 5, 1568. doi:10.1186/s40064-016-3249-3

Zimetbaum, P. (2012). Antiarrhythmic drug therapy for atrial fibrillation. *Circulation* 125, 381–389. doi:10.1161/CIRCULATIONAHA.111.019927

Zlochiver, S., Muñoz, V., Vikstrom, K. L., Taffet, S. M., Berenfeld, O., and Jalife, J. (2008). Electrotonic myofibroblast-to-myocyte coupling increases propensity to reentrant arrhythmias in two-dimensional cardiac monolayers. *Biophys. J.* 95, 4469–4480. doi:10.1529/biophysj.108.136473

frontiers | Frontiers in Physiology

TYPE Brief Research Report
PUBLISHED 13 October 2022
DOI 10.3389/fphys.2022.1001719

OPEN ACCESS

EDITED BY
Axel Loewe,
Karlsruhe Institute of Technology (KIT), Germany

REVIEWED BY
Laura Anna Unger,
Essen University Hospital, Germany
David Edward Krummen,
University of California, San Diego, United States
Gregory Sands,
University of Auckland, New Zealand

*CORRESPONDENCE
Christian Meyer,
c.mey@web.de

SPECIALTY SECTION
This article was submitted to Cardiac Electrophysiology, a section of the journal Frontiers in Physiology

RECEIVED 23 July 2022
ACCEPTED 21 September 2022
PUBLISHED 13 October 2022

CITATION
Alken F-A, Scherschel K, Kahle A-K, Masjedi M and Meyer C (2022), Combined contact force and local impedance dynamics during repeat atrial fibrillation catheter ablation. *Front. Physiol.* 13:1001719. doi: 10.3389/fphys.2022.1001719

Combined contact force and local impedance dynamics during repeat atrial fibrillation catheter ablation

Fares-Alexander Alken[1], Katharina Scherschel[1,2], Ann-Kathrin Kahle[1,3], Mustafa Masjedi[1,2] and Christian Meyer[1,2]*

[1]Division of Cardiology, Angiology and Intensive Care, cNEP, Cardiac Neuro- and Electrophysiology Research Group, EVK Düsseldorf, Düsseldorf, Germany, [2]Department of Neurophysiology, Heinrich-Heine-University Düsseldorf, Medical Faculty, cNEP, Cardiac Neuro- and Electrophysiology Research Consortium, Düsseldorf, Germany, [3]Department of Cardiology, Pulmonology and Vascular Medicine, Medical Faculty, University Hospital Düsseldorf, Düsseldorf, Germany

Background: Optimal lesion formation during catheter-based radiofrequency current (RFC) ablation depends on electro-mechanical tip-tissue coupling measurable *via* contact force (CF) and local impedance (LI) monitoring. We aimed to investigate CF and LI dynamics in patients with previous atrial fibrillation (AF) ablation who frequently present with heterogenous arrhythmia substrate.

Methods: Data from consecutive patients presenting for repeat AF or atrial tachycardia ablation using a novel open-irrigated single-tip ablation catheter were studied. RFC applications were investigated regarding CF, LI and the maximum LI drop (ΔLI) for evaluation of ablation efficacy. ΔLI > 20 Ω was defined as a successful RFC application.

Results: A total of 730 RFC applications in 20 patients were analyzed. Baseline CF was not associated with baseline LI (R = 0.06, $p = 0.17$). A mean CF < 8 g during ablation resulted in lower ΔLI (<8 g: 13 Ω vs. ≥ 8 g: 16 Ω, $p < 0.001$). Baseline LI showed a better correlation with ΔLI (R = 0.35, $p < 0.001$) compared to mean CF (R = 0.17, $p < 0.001$). Mean CF correlated better with ΔLI in regions of low (R = 0.31, $p < 0.001$) compared to high (R = 0.21, $p = 0.02$) and intermediate voltage (R = 0.17, $p = 0.004$). Combined CF and baseline LI predicted ΔLI > 20 Ω (area under the receiver operating characteristic curve (AUC) 0.75) better compared to baseline LI (AUC 0.72), mean CF (AUC 0.60), force-time integral (AUC 0.59) and local bipolar voltage (0.55).

Conclusion: Combination of CF and LI may aid monitoring real-time catheter-tissue electro-mechanical coupling and lesion formation within heterogenous atrial arrhythmia substrate in patients with repeat AF or atrial tachycardia ablation.

Abbreviations: AF, Atrial fibrillation; AT, Atrial tachycardia; AUC, Area under the curve; ΔBaseline LI, Difference of baseline and blood pool local impedance; CF, Contact force; CI, Confidence interval; LI, Local impedance; RFC, Radiofrequency current; ΔLI, Maximum local impedance drop during ablation; ΔLI%, Percentage of maximum local impedance drop compared to baseline local impedance.

KEYWORDS

atrial fibrillation, contact force, local impedance, atrial arrhythmia, catheter ablation, myocardial scar

Introduction

Optimal lesion formation during catheter-based radiofrequency current (RFC) ablation has been known to depend on sufficient mechanical contact and electrical coupling for more than two decades (Ariyarathna et al., 2018). Measurement of beat-to-beat tip-tissue contact force (CF) is widely implemented today as a surrogate parameter for catheter stability (Calkins et al., 2018). However, as a physical parameter CF does not give insights into tissue response during ablation.

The applied electrical current inducing tissue heating is dependent on the resistive load during catheter tip-tissue contact, with measurement attempted *via* impedance by different technologies: classical transthoracic impedance measurement by RFC generators (between catheter tip and indifferent surface electrodes) is limited by significant inter-patient variability regarding torso impedance as well as intra-patient variability subject to the respiratory phase (Borganelli et al., 1992; Barkagan et al., 2018; Chu et al., 2022). Measurement of local impedance (LI) is conducted by driving a non-stimulatory current between a distal and proximal electrode. It has gained interest as it resembles the resistive load at the catheter tip which is proportional to the tissue-catheter contact (Barkagan et al., 2018; Sulkin et al., 2018). Therefore, when compared to generator impedance, baseline LI shows greater variation between blood pool and tissue (Sulkin et al., 2018; Gunawardene et al., 2019). A strong relationship between the LI drop during ablation (ΔLI) and efficacy of lesion formation has been demonstrated (Gunawardene et al., 2019; Garrott et al., 2020; Das et al., 2021; Solimene et al., 2021), with a ΔLI > 20 Ω being proposed to result in sufficient lesion formation according to previous clinical and experimental studies (Garrott et al., 2020; Szegedi et al., 2021; Ikenouchi et al., 2022; Sasaki et al., 2022).

Low voltage zones indicate fibrofatty infiltration and contribute to initiation and maintenance of atrial fibrillation (AF) and atrial tachycardia (AT). This is especially of interest in repeat ablation procedures, where reconnected pulmonary veins as well as reconduction of previously ablated or new low voltage zones are frequently encountered due to myocardial scarring (De Pooter et al., 2019; Huo et al., 2020). Creating durable ablation lesions in these low voltage zones remains of importance for ablation success but is challenged by several factors: Scar tissue offers heterogenous thermodynamic properties affecting resistive and conductive heating. Lower resistivity of collagen results in reduced heating as well as shunting of electrical current to blood, while adipose tissue is often present in scar areas providing higher electrical resistivity (Barkagan et al., 2019; Tao et al., 2019). We therefore aimed to investigate how CF correlates with changes in LI during repeat AF or AT ablation within heterogenous arrhythmia substrate.

Methods

Clinical cohort

In this explorative single-center series, consecutive patients presenting for catheter ablation due to continuous symptomatic atrial arrhythmia (AF or AT) after previous AF ablation were analyzed retrospectively. This analysis was approved by the local ethics committee (Ärztekammer Nordrhein, 201/2022) and written informed consent was obtained from all patients.

Electrophysiological study setup and catheter ablation procedure

The procedures were carried out in accordance to existing consensus statements as well as previously published protocols (Calkins et al., 2018; Alken et al., 2019). In short, patients underwent the procedure in a fasting state under conscious sedation using propofol or midazolam and fentanyl. Hemodynamic monitoring consisted of continuous assessment of saturation, non-invasive blood pressure as well as surface and intracardiac electrocardiogram recordings. A single transseptal puncture was conducted with fluoroscopic guidance and catheters were introduced into the left atrium using a fixed curve long sheath (SL0, 8-F; St. Jude Medical, for ablation catheter) and a long steerable sheath (Zurpaz™, medium curl, 8.5-F, Boston Scientific, for mini basket catheter). The catheter setting consisted of a steerable 6F decapolar catheter (Inquiry™, 5 mm spacing; St. Jude Medical, Saint Paul, MN, United States) positioned in the coronary sinus and serving as the reference of the Rhythmia™ 3-D electroanatomical mapping system (Boston Scientific Corporation, Marlborough, MA, United States) as well as an expandable, open-irrigated 64-pole mini basket mapping catheter (IntellaMap Orion™, Boston Scientific) comprising 8 splines with 8 electrodes for creation of ultra-high density maps. Furthermore, a novel open-irrigated single-tip ablation catheter (IntellaNav StablePoint™, Boston Scientific, Marlborough, MA, United States) capable of continuously assessing CF (translation of force to inductive sensors *via* a spring) and LI (non-stimulatory alternating current between tip and proximal ring electrode) was introduced (Garrott et al., 2020). Activated clotting time was monitored after first access of the left atrium, targeting a level >300 s.

A blood pool reference value was established without tissue contact for both CF and LI before ablation onset. In general, persistence of pulmonary vein isolation as well as previously set linear lesions was checked and discovered gaps were ablated. RFC applications were delivered with a standard power of 30 W, while adjusting power to 25 W at the posterior left atrial wall and 40 W

TABLE 1 Baseline patient parameters.

Variable	Total (n = 20)
Age [years]	66±11
Female sex, n (%)	8 (40)
Time since atrial fibrillation diagnosis [years]	8±6
Paroxysmal atrial fibrillation, n (%)	9 (45)
Persistent atrial fibrillation, n (%)	11 (55)
Atrial tachycardia, n (%)	10 (50)
Prior ablation procedures [n]	1.7±0.9
CHA_2DS_2-VASc-Score [n]	3 (2-4)
Arterial hypertension, n (%)	18 (90)
Diabetes mellitus, n (%)	2 (10)
Hyperlipidemia, n (%)	6 (30)
Prior stroke / transient ischemic attack, n (%)	1 (5)
Coronary artery disease, n (%)	7 (35)
Heart failure, n (%)	8 (40)
Left ventricular ejection fraction [%]	49 (43-60)
Ischemic cardiomyopathy, n (%)	2 (10)
Dilated cardiomyopathy, n (%)	1 (5)
Hypertrophic cardiomyopathy, n (%)	1 (5)
Tachymyopathy, n (%)	4 (20)
Prior revascularization, n (%)	4 (20)

Variables are expressed as absolute values with percentages, mean with standard deviation or median with interquartile ranges.

at the cavotricuspid isthmus where applicable. The irrigation rate was maintained at 17–30 ml/min for up to 120 s and the upper temperature limit was set at 48°C. Additional substrate modification *via* ablation of complex fractionated atrial electrograms was conducted at the operator's discretion. In macro-reentrant AT the critical isthmus was detected and ablated consecutively. In case of localized or focal AT, the site of earliest activation was targeted. Pacing maneuvers and pharmacological provocation were performed repeatedly to test for arrhythmia non-inducibility. A bidirectional block was confirmed whenever linear lesions were generated. Acute ablation success was defined as non-inducibility of atrial arrhythmias at the end of the procedure.

Postprocedural radiofrequency current application analysis

To study the biophysics of lesion formation, point-by-point RFC applications were analyzed regarding applied CF, force-time integral and detected LI before onset and during ablation. An automatized export software integrated into the Rhythmia™ system was used to export CF and LI data, while full-length procedure recordings and generated voltage maps were reviewed complementing analysis. Baseline, minimum, maximum and mean CF/LI values as well as the absolute and relative difference between baseline and minimum LI during ablation (maximum absolute LI drop, ΔLI; maximum LI drop in percent, ΔLI%) were measured. To account for inter-patient variability of blood pool LI, the difference between baseline tissue LI and blood pool LI (Δbaseline LI) was measured in all patients. Sufficient lesion formation was defined as a ΔLI > 20 Ω according to previous preclinical findings (Garrott et al., 2020; Szegedi et al., 2021; Ikenouchi et al., 2022; Sasaki et al., 2022). CF and LI dynamics were further analyzed considering local bipolar voltage for each RFC application, differentiating between high (>0.5 mV), intermediate (0.1–0.5 mV) and low (<0.1 mV) voltage (Frontera et al., 2018). RFC applications with a duration <10 s, poor signal quality, instable catheter contact or dragged ablation points were excluded from analysis for parameter standardization.

Statistical analysis

Continuous variables are expressed as mean ± standard deviation or absolute numbers and percentages. In case of non-parametric data, results are provided as medians with interquartile ranges. All analyses were performed using Graphpad Prism 9 (Graphpad Inc., La Jolla, CA, United States), MedCalc (MedCalc Software Ltd., Ostend, Belgium) and Microsoft Excel. For determination of normal distribution, the Shapiro-Wilk test was conducted. In case of paired datasets, a paired t-test was conducted for normally distributed and a Wilcoxon signed-rank test for non-normally distributed datasets. For comparison of unpaired datasets, an unpaired t-test was conducted in case of normal and the Mann-Whitney U test in case of non-normal distribution. A Kruskal–Wallis test was applied for unpaired comparison of more than two groups in case of non-normal distribution and an one-way analysis of variance (ANOVA) in case of normal distribution of datasets.

Correlation analysis was conducted to investigate the relationship of baseline LI to ΔLI and mean CF using Pearson correlation coefficients for normally distributed and Spearman correlation for non-normally distributed datasets. A Pearson R or Spearman R coefficient was calculated, where a positive value indicates a positive and a negative value a negative linear relation. Linear regression analysis was conducted to determine a fitted regression graph with 95% confidence bands. Simple and multiple logistic regression analysis was performed for prediction of a ΔLI > 20 Ω which has been described to result in sufficient lesion formation (Garrott et al., 2020). A p-value <0.05 was considered statistically significant.

Results

Baseline contact force and local impedance characteristics

Baseline patient as well as procedural characteristics are displayed in Table 1, 2. Out of 1488 RFC applications in 20

TABLE 2 Procedure characteristics.

Variable	Total (n = 20)
Procedure time [min]	225 (128-270)
Fluoroscopy time [min]	17 (7-26)
Dose area product [cGy*cm^2]	75 (47-117)
Number of radiofrequency deliveries analyzed per patient [n]	35 (22-46)
Total ablation time per patient [min]	20 (11-34)
Ablation duration per radiofrequency delivery [s]	20 (14-29)
Repeat pulmonary vein isolation, n (%)	15 (75)
Left atrial tachycardia ablation, n (%)	11 (55)
Right atrial tachycardia ablation, n (%)	4 (20)

Variables are expressed as absolute values with percentages or median with interquartile ranges.

consecutive patients, 730 (49%) were eligible for analysis, of which 93 % were located in the left atrium. Ablation was conducted at the pulmonary veins (54%), left atrial anterior wall (15%), left atrial roof (9%), mitral isthmus (6%), interatrial septum (5%), left atrial posterior wall (3%), left atrial appendage (1%), cavotricuspid isthmus (6%), coronary sinus and superior vena cava (1%). Acute procedural success was achieved in all patients and no catheter-related periprocedural complications were observed.

Baseline blood pool LI serving as a non-contact reference was similar compared to left and right atrial baseline LI (blood pool: median 146 (interquartile range 138-156) Ω vs left atrial: 147 (136-163) Ω and right atrial: 146 (132-165) Ω, Kruskal-Wallis test, p = 0.95). Median baseline LI was 146 (132-165) Ω and applied baseline CF was 9 (5-15) Ω. Baseline CF and LI did not show a significant correlation in the overall cohort (Spearman correlation, R = 0.06, p = 0.17) as well as when distinguishing between high (Spearman correlation, R = 0.17, p = 0.23), intermediate (Spearman correlation, R = −0.18, p = 0.054) and low voltage zones (Spearman correlation, R = 0.19, p = 0.23). ΔBaseline LI was not associated with baseline CF (Spearman correlation, R = 0.04, p = 0.39), while 45% of analyzed RFC applications displayed lower baseline LI compared to blood pool LI.

Impact of contact force and baseline local impedance on the local impedance drop

The median ΔLI per RFC application displayed at 15 (interquartile range 11–21) Ω and ΔLI% at 11 (8–14) %. High baseline LI predicted an increased δLI and correlated better with ΔLI (Spearman correlation, R = 0.35, p < 0.001) compared to ΔLI% (Spearman correlation, R = 0.12, p = 0.001, Figures 1A,B). ΔLI increased by 1 Ω with every 6.5 Ω baseline LI gain.

The median value of mean CF per RFC application was 11 (7–19) g. Transient catheter-tissue contact loss due to respiratory motion was reflected by low CF and simultaneous LI increases ultimately resulting in reduced ΔLI (Figure 2A). Mean CF and force-time integral showed a weaker correlation with ΔLI (Spearman correlation, CF: R = 0.17, p < 0.001; force-time integral: R = 0.16, p < 0.001) and with ΔLI% (Spearman correlation, CF: R = 0.24, p < 0.001; force-time integral: R = 0.21, p < 0.001, Figure 2B) compared to baseline LI.

For determination of the optimal mean CF cut-off value to achieve a ΔLI > 20 Ω, receiver operating characteristic analysis was conducted and revealed a mean CF level ≥8 g as the best predictor with overall limited sensitivity (0.75) and specificity (0.39). RFC applications with a mean CF < 8 g displayed lower ΔLI (< 8 g: 13 (9-18) Ω vs. <8 g: 16 (11-22) Ω, Mann-Whitney test, p < 0.001). However, mean CF rises beyond 8 g did not further alter ΔLI (8-16 g: 16 (11-21) Ω vs. > 16 g: 17 (12-22) Ω, Mann-Whitney test, p = 0.24, Figure 2C). A force-time integral <400 gs was also associated with lower ΔLI (<400 gs: 14 (10-20) Ω vs. <400 gs: 18 (12-24) Ω, Mann-Whitney test, p < 0.00).

Influence of underlying myocardial substrate on force-impedance dynamics

A subset of 547 RFC applications was analyzed regarding underlying local bipolar voltage. Baseline LI was higher in regions of high vs intermediate or low voltage (high: 152 (136-163) Ω vs. intermediate: 143 (132-155) Ω vs. low: 142 (131-156) Ω, Kruskal-Wallis test, pp < 0.0001), with applied baseline CF being higher in the high compared to the low voltage group (high: 12 (7-19) g vs. intermediate: 9 (6-16) g vs low: 8 (4-15) g, Kruskal-Wallis test, p = 0.02). Baseline CF did not correlate to baseline LI in high/low voltage regions and displayed a weak negative correlation in intermediate voltage regions (Spearman correlation, high: R = 0.06, p = 0.53; intermediate: R = −0.13, p = 0.04; low: R = 0.08, p = 0.41, Figure 3A).

Overall median ΔLI was higher in regions of high compared to intermediate voltage and was similar compared low voltage regions (high: 17 (11-24) Ω vs. intermediate: 15 (11-20) Ω vs. low: 16 (10-22) Ω, Kruskal-Wallis test, p = 0.02). Applied mean CF was greater in regions of high compared to low voltage (high: 13 (8-21) g vs. intermediate: 11 (7-18) vs. low: 10 (6-16) g, Kruskal-Wallis test, p = 0.007). Mean CF correlated better with ΔLI in regions of low compared to high and intermediate voltage (Spearman correlation, high: R = 0.21, p = 0.02; intermediate: R = 0.17, p = 0.004; low: R = 0.31, p < 0.001). When applying a mean CF cut-off level of 8 g, ΔLI was higher in regions of high compared with intermediate voltage with CF levels ≥8 g (high: 18 (12-25) Ω vs. intermediate: 16 (12-21) Ω vs. low: 17 (11-23) Ω, Kruskal-Wallis test, p = 0.04). However, no differences were observed for a mean CF < 8 g between regions (high: 12 (9-19) Ω vs. intermediate: 13 (9-18) Ω vs. low: 14 (9-19) Ω, Kruskal-Wallis test, p = 0.72, Figure 3B). When analyzing for underlying baseline

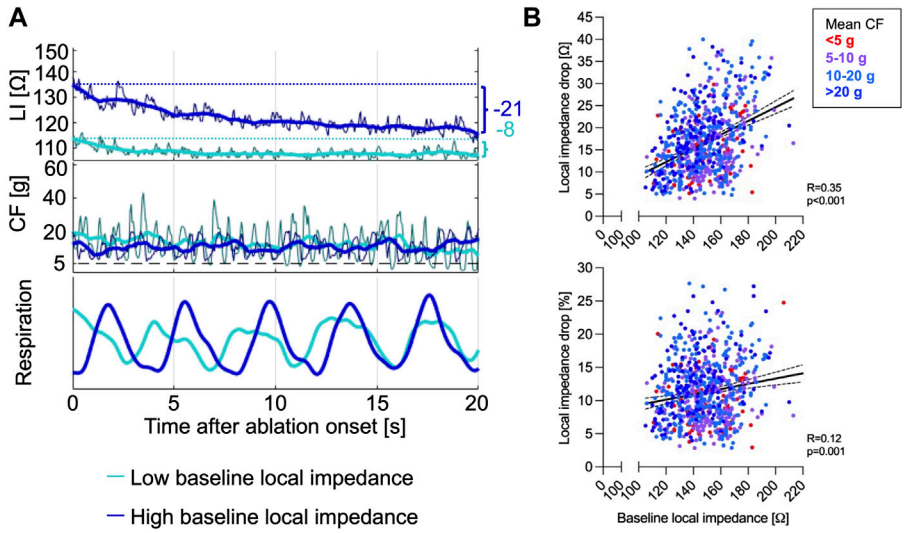

FIGURE 1
(A) Representative CF and LI raw as well as time-smoothed averaged recordings in a single patient during ablation are displayed. High baseline LI (dark blue) predicted increased ΔLI, while lower baseline LI (light blue) resulted in low δLI despite similar energy output of 30 W and adequate CF levels ≥8 g. **(B)** Baseline LI correlated better with ΔLI (upper panel) compared to the ΔLI% (lower panel). CF, contact force; LI, local impedance; ΔLI, absolute local impedance drop; ΔLI%, relative local impedance drop.

LI, mean CF correlated better to ΔLI in the high (158 - 220 Ω) and intermediate baseline LI tercile (140-158 Ω) compared to the low tercile (106-140 Ω, Figure 3C). While mean CF was higher in the low compared to the intermediate and high baseline LI tercile (high: 10 (6-16) g vs. intermediate: 10 (7-17) g vs. low: 11 (8-20) g, Kruskal-Wallis test, $p < 0.001$), ΔLI was elevated the most in the high baseline LI tercile (high: 18 (13-25) Ω vs. intermediate: 16 (12-22) Ω vs. low: 14 (10-18) Ω, Kruskal-Wallis test, $p < 0.001$).

Prediction of a local impedance drop >20 Ω

A ΔLI > 20 Ω was reached in 29.8% of RFC applications. Receiver operating characteristic analysis displayed combined CF and baseline LI as the best predictor for ΔLI > 20 Ω (area under the receiver operating characteristic curve (AUC) 0.75 [confidence interval (CI) 0.71–0.79], negative/positive predictive value 0.76/0.66, $p < 0.001$) compared to baseline LI [AUC 0.72 (CI 0.68–0.76), negative/positive predictive value 0.84/0.44, $p < 0.001$], Δbaseline LI [AUC 0.69 (CI 0.65–0.73), negative/positive predictive value 0.80/0.50, $p < 0.001$], mean CF (AUC 0.60 (0.55–0.64), negative/positive predictive value 0.79/0.35, $p < 0.001$), force-time integral [AUC 0.59 (CI 0.54–0.63), negative/positive predictive value 0.75/0.35], $p = 0.001$) and bipolar voltage [AUC 0.55 (CI 0.49–0.60), negative/positive predictive value 0.64/0.53, $p = 0.01$, Figure 4].

Discussion

In this single-center retrospective explorative study, we present for the first time an initial experience of combined CF and LI dynamics in patients undergoing repeat AF or AT ablation. The major findings consist of the following: 1) Applied baseline CF is not significantly associated with baseline LI levels. 2) A minimum mean CF level of 8 g increases ΔLI resembling stable contact, while further CF increases beyond 8 g do not additionally affect ΔLI. 3) Combined mean CF during ablation and baseline LI predicts ΔLI as a surrogate for lesion formation, with the highest ΔLI being observed in regions of high voltage and high baseline LI.

Biophysical rationale of combined force and impedance assessment

The relevance of sufficient tip-tissue contact for effective lesion formation has been described more than two decades ago (Organ, 1976; Haines, 1991, 2004). CF provides physical feedback on mechanical tip-tissue contact and cardiac as well as respiratory motion (Ariyarathna et al., 2018). Multidimensional indices incorporating parameters additional to CF were introduced aiming for real-time lesion formation estimation during ablation, while lacking information on tissue response (Hussein et al., 2018; Taghji et al., 2018). Here, LI

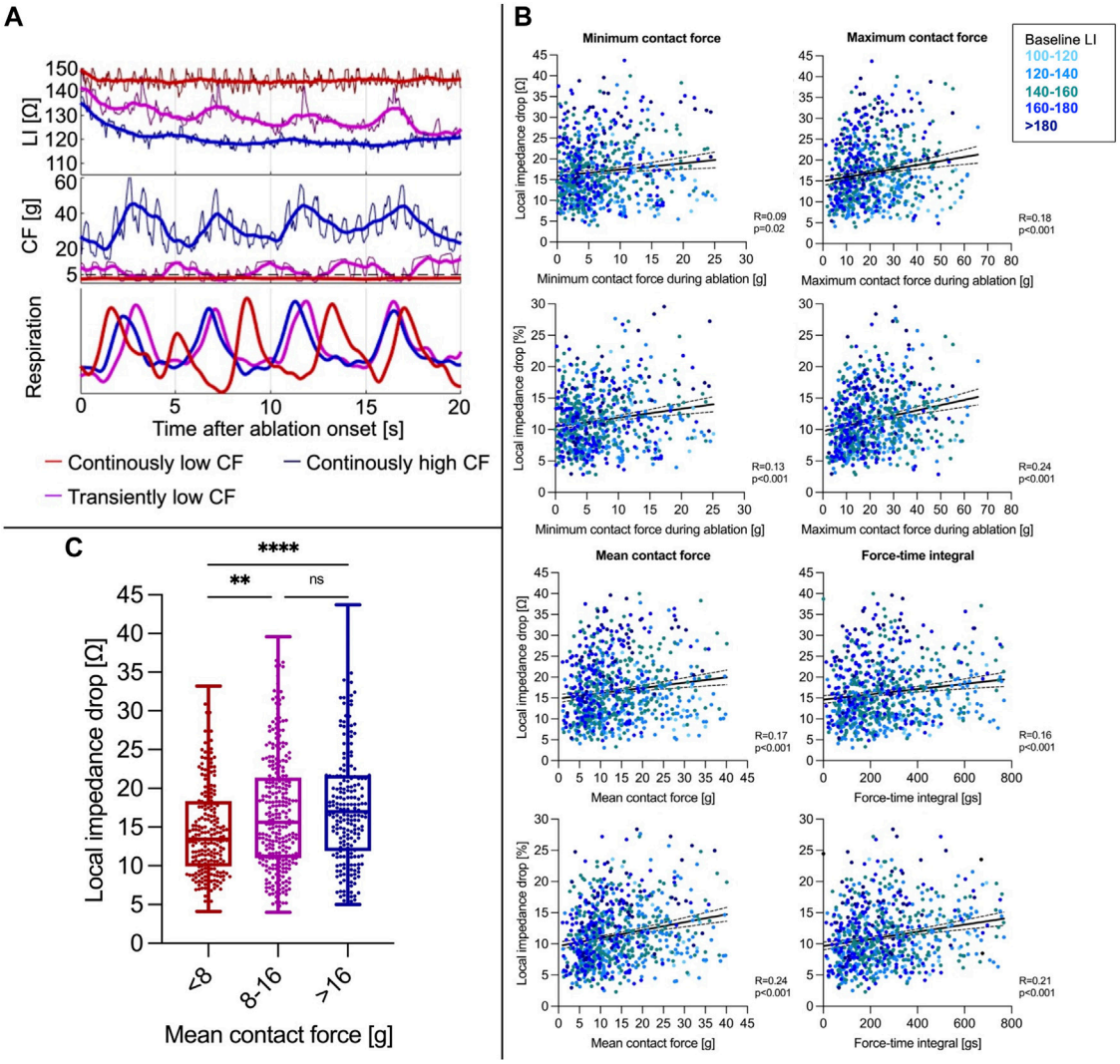

FIGURE 2
(A) Representative CF and LI raw as well as time-smoothed averaged recordings in a single patient during ablation are displayed. In regions of similar baseline LI, high constant CF (blue curve) resulted in a rapid δLI after approximately 4 s, whereas intermittent decreases of CF to 0 g due to inspiration (violet) went along with LI increases reflecting transient catheter-tissue contact loss with overall similar δLI. Continuously low CF (red) resulted in a reduced ΔLI. **(B)** Correlation of minimum/maximum/mean CF during ablation and force-time integral with ΔLI (upper panel) and ΔLI % (lower panel). **(C)** A mean CF < 8 g was concomitant with a reduced LI drop, whereas increases beyond 8 g did not further increase the LI drop. $^{**}p \leq 0.01$; $^{****}p \leq 0.0001$. For abbreviations see Figure 1.

measurement can complement CF: According to Ohm's law, transmitted current density relies on the electrical field and local tissue resistivity (Garrott et al., 2020; Chu et al., 2022). As power output is fixed by many ablation generators, baseline LI reflects resistive heating potential (Shapira-Daniels et al., 2019) and the degree of ΔLI mirrors volumetric tissue heating during ablation (Barkagan et al., 2018; Sulkin et al., 2018; Garrott et al., 2020). Therefore, combining CF and LI may improve real-time evaluation of lesion formation as electro-mechanical tip-tissue coupling can be assessed simultaneously. This may also contribute to improved safety, as avoiding high mechanical force as well as myocardial tissue heating *via* CF and ΔLI assessment may reduce the risk of steam pops or cardiac perforation (Ariyarathna et al., 2018; Gunawardene et al., 2019; Garrott et al., 2020). In our analysis, a minimum level of 8 g mean CF during ablation ensured sufficient mechanical tip-tissue catheter contact and resulted in increased ΔLI. This is in accordance with previous experimental and clinical studies on other catheter systems measuring CF only, which proposed cut-off values of 5–20 g (Ariyarathna et al., 2018). Excessive CF application may even lower lesion dimensions as it can impair catheter irrigation and result in excessive catheter-tip heating and

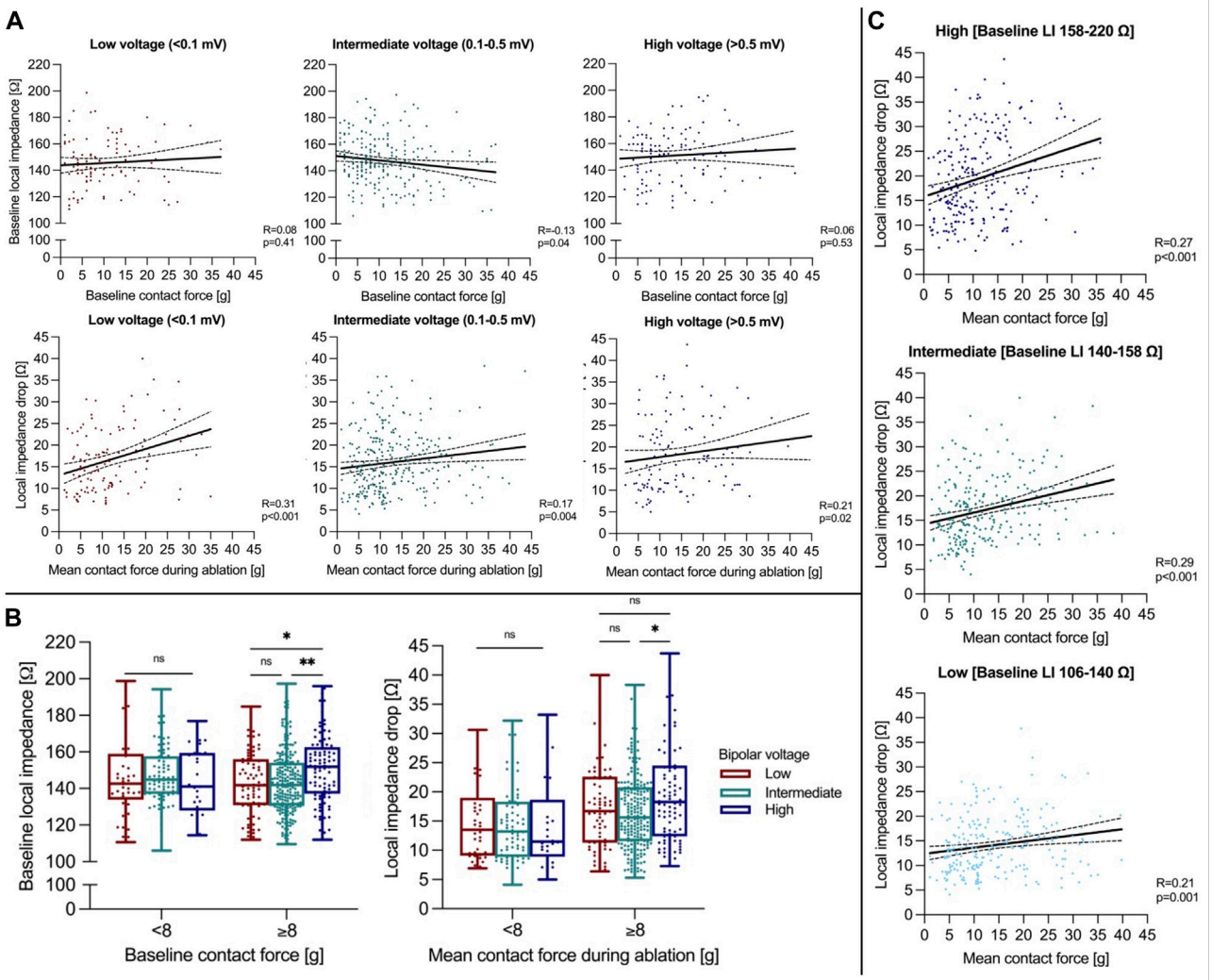

FIGURE 3
(A) Correlation analysis of baseline CF to LI (upper panel) and mean CF to the ΔLI (lower panel) is shown. **(B)** Baseline LI and ΔLI during ablation are displayed depending on local bipolar voltage and applied CF classified by the estimated mean CF cut-off of 8 g. **(C)** Correlation analysis of mean CF to ΔLI depending on underlying baseline LI terciles. *$p \leq 0.05$; ***$p \leq 0.001$. For abbreviations see Figure 1.

charring marked by an impedance increase (Ring et al., 1989; Makimoto et al., 2018). High baseline LI guaranteed electrical coupling and may aid catheter positioning additional to CF in challenging regions such as the coronary sinus (Sulkin et al., 2018).

Baseline LI showed the highest correlation to ΔLI which is in line with recently published experimental (Garrott et al., 2020; Gutbrod et al., 2022) and clinical studies (Martin et al., 2018; Gunawardene et al., 2019; Szegedi et al., 2021; Matsuura et al., 2022; Solimene et al., 2022). Furthermore, according to our results combined mean CF and baseline LI was the best predictor for a ΔLI > 20 Ω in comparison to applied mean CF or baseline LI alone. Therefore, maintaining a mean CF level ≥8 g may be valuable in ensuring sufficient tip-tissue contact, while LI provides information on the degree of electrical coupling and real-time tissue response to RFC applications.

Value of combined force and impedance assessment during repeat atrial arrhythmia ablation

Several experimental and clinical studies have recently been published reporting experiences of combined CF and LI assessment during index AF ablation (Szegedi et al., 2021; Gutbrod et al., 2022; Solimene et al., 2022; Yasumoto et al.,

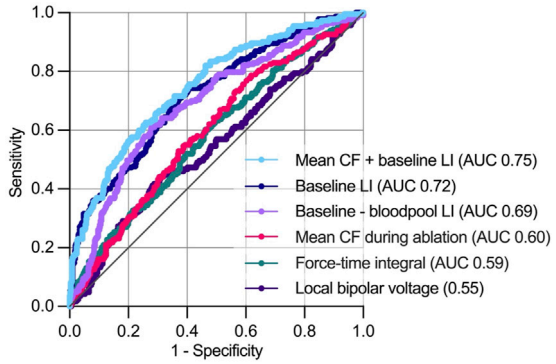

FIGURE 4
Predictors of a local impedance drop >20 Ω during ablation. During receiver operating characteristics analysis, combined mean CF and baseline LI showed the highest area under the receiver operating characteristics curve for predicting a >20 Ω. AUC, area under curve. For further abbreviations see Figure 1.

2022). Single-shot devices have seen increased usage for index AF ablations in recent years (Mulder et al., 2021). Therefore, the strength of combining CF and LI monitoring may lie in repeat AF and AT procedures: Here, previously conducted pulmonary vein isolation may show reconnection in up to 70% of cases (Hindricks et al., 2020). Adjunctive ablation strategies additional to pulmonary vein isolation including linear lesions, posterior wall isolation, ablation of non-pulmonary vein triggers and complex fractionated atrial electrograms may be required (Calkins et al., 2018). Reconduction over previous linear or substrate ablation and development of new low voltage areas are frequent findings during repeat AF ablation, while persistent conduction blocks have been reported to be present in only 21% using conventional ablation setups (Huo et al., 2020).

Therefore, index and repeat ablation procedures as well as ablation within healthy compared to impaired myocardium need to be distinguished when evaluating LI and CF dynamics: In our analysis, baseline LI was lower compared to previous results on index AF procedures, but LI correlated better with ΔLI compared to CF which is in line with published data (Szegedi et al., 2021; Ikenouchi et al., 2022; Solimene et al., 2022; Yasumoto et al., 2022). Furthermore, baseline LI was lower compared to blood pool LI in 45% of RFC applications, whereas an elevation of tissue baseline LI beyond blood pool LI was observed in index AF procedures (Solimene et al., 2022). Median ΔLI was lower at 15 Ω compared to index AF procedures reporting ΔLI ranges between 19–27 Ω. These observations may be explained by two central aspects: First, in our cohort with a mean of 2 prior ablation procedures per patient, 60% of RFC applications were located in areas of low voltage where baseline LI was reduced according to our current and previous results (Gunawardene et al., 2019). Second, lesion formation within scarred myocardial tissue results in irregular and lowered tissue injury due to altered thermodynamic characteristics compared to healthy myocardium (Barkagan et al., 2019; Tao et al., 2019). The target ΔLI of >20 Ω chosen in our analysis was only reached in 30% of RFC applications. Currently proposed target ΔLI values are based on experimental and clinical index AF/atrial flutter procedures aiming for healthy myocardium in most cases. Target ΔLI also differs depending on the ablation location within the left atrium (Chu et al., 2022). Therefore, currently proposed target ΔLI levels using this catheter system may not be appropriate in repeat ablation cohorts but rather may be lower due to more extensive regions of low voltage and low baseline LI.

Combination of CF and LI monitoring may allow to improve ablation procedures in regions of low voltage: 1) LI mapping may complement electrogram-based substrate maps potentially facilitating selection of optimal ablation sites within previously ablated areas (Unger et al., 2021). This is supported by our findings confirming baseline LI as a better predictor for a ΔLI > 20 Ω compared to local voltage. 2) When ablating in areas of low voltage and encountering low baseline LI and ΔLI, combined CF and LI monitoring allows to discriminate between insufficient contact and low electrical coupling due to myocardial scar. A study analyzing conduction gaps acutely after index cavotricuspid isthmus ablation proposed that gaps could not be distinguished by baseline LI, whereas effective lesions showed higher ΔLI (Sasaki et al., 2020). Therefore, algorithms incorporating both CF and LI may enhance ablation efficacy (Schreieck et al., 2021), while combining CF and baseline LI may improve prediction of a sufficient ΔLI according to our analysis. Further studies are needed to investigate advanced ablation strategies incorporating individualized ΔLI and CF targets depending on anatomical region, baseline LI and local voltage.

Limitations

The following limitations need to be addressed: First, this study reports an initial single-center experience with a relatively small sample size. Guidance of ablation using LI measurement was not performed prospectively. However, the amount of >700 analyzed RFC applications allowed to evaluate CF and LI dynamics. Second, as heterogenous regions of healthy and impaired myocardium were targeted during ablation, target ΔLI may vary from levels proposed in previous experimental and clinical studies investigating index procedures (Garrott et al., 2020; Szegedi et al., 2021; Ikenouchi et al., 2022; Sasaki et al., 2022) depending on local myocardial thickness, regional anatomical structures such as pouches and vessels as well as degree of fibrosis. Lastly, as follow-up data were not yet available, the impact of combined CF and LI assessment on long-term arrhythmia outcomes during repeat AF/AT ablation needs to be determined in future studies.

Conclusion

Taken together, the present findings suggest that combining CF and LI may be useful to monitor real-time catheter-tissue electro-mechanical coupling and lesion formation within heterogenous atrial arrhythmia substrate in patients with repeat AF or AT ablation. Further studies are needed to assess the value for long-term outcome especially in challenging patient cohorts.

Data availability statement

The raw data supporting the conclusions of this article will be made available by the authors, without undue reservation.

Ethics statement

The analysis involving human participants were reviewed and approved by Ärztekammer Nordrhein, Düsseldorf, Germany. The patients provided their written informed consent to participate in this analysis.

Author contributions

Conception and design: FA and CM. Performance of procedures: CM. Collection and assembly of data: FA and CM. Data analysis and interpretation: All authors. Manuscript writing: FA, KS, and CM. Final approval of manuscript: All authors.

Acknowledgments

We thank Lydia Merbold and Tobias Oesterlein for excellent postprocedural data processing.

Conflict of interest

FAA: Invited fellow of the Boston Scientific Cardiac Electrophysiology training program, travel grants from Bayer Pharmaceuticals and Boston Scientific; CM: speaker and consulting: Abbott, Boston Scientific; speaker: Biosense Webster.

The remaining authors declare that the research was conducted in the absence of any commercial or financial relationships that could be construed as a potential conflict of interest.

Publisher's note

All claims expressed in this article are solely those of the authors and do not necessarily represent those of their affiliated organizations, or those of the publisher, the editors and the reviewers. Any product that may be evaluated in this article, or claim that may be made by its manufacturer, is not guaranteed or endorsed by the publisher.

References

Alken, F.-A., Klatt, N., Muenkler, P., Scherschel, K., Jungen, C., Oezge Akbulak, R., et al. (2019). Advanced mapping strategies for ablation therapy in adults with congenital heart disease. *Cardiovasc. Diagn. Ther.* 9 (S2), S247–S263. doi:10.21037/cdt.2019.10.02

Ariyarathna, N., Kumar, S., Thomas, S. P., Stevenson, W. G., and Michaud, G. F. (2018). Role of contact force sensing in catheter ablation of cardiac arrhythmias: Evolution or history repeating itself? *JACC. Clin. Electrophysiol.* 4 (6), 707–723. doi:10.1016/j.jacep.2018.03.014

Barkagan, M., Leshem, E., Shapira-Daniels, A., Sroubek, J., Buxton, A. E., Saffitz, J. E., et al. (2019). Histopathological characterization of radiofrequency ablation in ventricular scar tissue. *JACC. Clin. Electrophysiol.* 5 (8), 920–931. doi:10.1016/j.jacep.2019.05.011

Barkagan, M., Rottmann, M., Leshem, E., Shen, C., Buxton, A. E., and Anter, E. (2018). Effect of baseline impedance on ablation lesion dimensions: A multimodality concept validation from physics to clinical experience. *Circ. Arrhythm. Electrophysiol.* 11 (10), e006690. doi:10.1161/circep.118.006690

Borganelli, M., el-Atassi, R., Leon, A., Kalbfleisch, S. J., Calkins, H., Morady, F., et al. (1992). Determinants of impedance during radiofrequency catheter ablation in humans. *Am. J. Cardiol.* 69 (12), 1095–1097. doi:10.1016/0002-9149(92)90873-w

Calkins, H., Hindricks, G., Cappato, R., Kim, Y.-H., Saad, E. B., Aguinaga, L., et al. (2018). 2017 HRS/EHRA/ECAS/APHRS/SOLAECE expert consensus statement on catheter and surgical ablation of atrial fibrillation. *Europace* 20 (1), e1–e160. doi:10.1093/europace/eux274

Chu, G. S., Calvert, P., Futyma, P., Ding, W. Y., Snowdon, R., and Gupta, D. (2022). Local impedance for the optimization of radiofrequency lesion delivery: A review of bench and clinical data. *J. Cardiovasc. Electrophysiol.* 33 (3), 389–400. doi:10.1111/jce.15335

Das, M., Luik, A., Shepherd, E., Sulkin, M., Laughner, J., Oesterlein, T., et al. (2021). Local catheter impedance drop during pulmonary vein isolation predicts acute conduction block in patients with paroxysmal atrial fibrillation: Initial results of the LOCALIZE clinical trial. *Europace.* 23, 1042–1051. doi:10.1093/europace/euab004

De Pooter, J., Strisciuglio, T., El Haddad, M., Wolf, M., Phlips, T., Vandekerckhove, Y., et al. (2019). Pulmonary vein reconnection No longer occurs in the majority of patients after a single pulmonary vein isolation procedure. *JACC. Clin. Electrophysiol.* 5 (3), 295–305. doi:10.1016/j.jacep.2018.11.020

Frontera, A., Takigawa, M., Martin, R., Thompson, N., Cheniti, G., Massoullié, G., et al. (2018). Electrogram signature of specific activation patterns: Analysis of atrial tachycardias at high-density endocardial mapping. *Heart rhythm.* 15 (1), 28–37. doi:10.1016/j.hrthm.2017.08.001

Garrott, K., Laughner, J., Gutbrod, S., Sugrue, A., Shuros, A., Sulkin, M., et al. (2020). Combined local impedance and contact force for radiofrequency ablation assessment. *Heart rhythm.* 17 (8), 1371–1380. doi:10.1016/j.hrthm.2020.03.016

Gunawardene, M., Munkler, P., Eickholt, C., Akbulak, R. O., Jularic, M., Klatt, N., et al. (2019). A novel assessment of local impedance during catheter ablation: Initial experience in humans comparing local and generator measurements. *Europace* 21 i34–i42. doi:10.1093/europace/euy273

Gutbrod, S. R., Shuros, A., Koya, V., Alexander-Curtis, M., Lehn, L., Miklos, K., et al. (2022). Improved ablation efficiency in PVI guided by contact force and local

impedance: Chronic canine model. *Front. Physiol.* 12, 808541. doi:10.3389/fphys.2021.808541

Haines, D. E. (2004). Biophysics of ablation: Application to technology. *J. Cardiovasc. Electrophysiol.* 15 S2–S11. doi:10.1046/j.1540-8167.2004.15102.x

Haines, D. E. (1991). Determinants of lesion size during radiofrequency catheter ablation: The role of electrode-tissue contact pressure and duration of energy delivery. *J. Cardiovasc. Electrophysiol.* 2 (6), 509–515. doi:10.1111/j.1540-8167.1991.tb01353.x

Hindricks, G., Potpara, T., Dagres, N., Arbelo, E., Bax, J. J., Blomström-Lundqvist, C., et al. (2020). 2020 ESC Guidelines for the diagnosis and management of atrial fibrillation developed in collaboration with the European Association for Cardio-Thoracic Surgery (EACTS). *Eur. Heart J.* 42, 373–498. doi:10.1093/eurheartj/ehaa612

Huo, Y., Kronborg, M. B., Richter, U., Guo, J., Ulbrich, S., Zedda, A. M., et al. (2020). Electrophysiological findings during atrial fibrillation reablation: Extending from pulmonary vein reconnection to sequential bipolar voltage map information. *J. Cardiovasc. Electrophysiol.* 31 (4), 885–894. doi:10.1111/jce.14387

Hussein, A., Das, M., Riva, S., Morgan, M., Ronayne, C., Sahni, A., et al. (2018). Use of ablation index-guided ablation results in high rates of durable pulmonary vein isolation and freedom from arrhythmia in persistent atrial fibrillation patients: The PRAISE study results. *Circ. Arrhythm. Electrophysiol.* 11 (9), e006576. doi:10.1161/circep.118.006576

Ikenouchi, T., Takigawa, M., Goya, M., Martin, C. A., Takahashi, Y., Shimizu, Y., et al. (2022). Requirement of larger local impedance reduction for successful lesion formation at carinal area during pulmonary vein isolation. *J. Interv. Card. Electrophysiol.* doi:10.1007/s10840-022-01282-1

Makimoto, H., Metzner, A., Tilz, R. R., Lin, T., Heeger, C. H., Rillig, A., et al. (2018). Higher contact force, energy setting, and impedance rise during radiofrequency ablation predicts charring: New insights from contact force-guided *in vivo* ablation. *J. Cardiovasc. Electrophysiol.* 29 (2), 227–235. doi:10.1111/jce.13383

Martin, C. A., Martin, R., Gajendragadkar, P. R., Maury, P., Takigawa, M., Cheniti, G., et al. (2018). First clinical use of novel ablation catheter incorporating local impedance data. *J. Cardiovasc. Electrophysiol.* 29 (9), 1197–1206. doi:10.1111/jce.13654

Matsuura, G., Fukaya, H., Ogawa, E., Kawakami, S., Mori, H., Saito, D., et al. (2022). Catheter contact angle influences local impedance drop during radiofrequency catheter ablation: Insight from a porcine experimental study with 2 different LI-sensing catheters. *J. Cardiovasc. Electrophysiol.* 33, 380–388. doi:10.1111/jce.15356

Mulder, B. A., Luermans, J. G. L. M., Hindricks, G., and Blaauw, Y. (2021). Innovations and paradigm shifts in atrial fibrillation ablation. *Europace.* 23, ii23–ii27. doi:10.1093/europace/euaa418

Organ, L. W. (1976). Electrophysiologic principles of radiofrequency lesion making. *Appl. Neurophysiol.* 39 (2), 69–76. doi:10.1159/000102478

Ring, M. E., Huang, S. K. S., Gorman, G., and Graham, A. R. (1989). Determinants of impedance rise during catheter ablation of bovine myocardium with radiofrequency energy. *Pacing Clin. Electrophysiol.* 12 (9), 1502–1513. doi:10.1111/j.1540-8159.1989.tb06155.x

Sasaki, T., Nakamura, K., Inoue, M., Minami, K., Miki, Y., Goto, K., et al. (2020). Optimal local impedance drops for an effective radiofrequency ablation during cavo-tricuspid isthmus ablation. *J. Arrhythm.* 36 (5), 905–911. doi:10.1002/joa3.12403

Sasaki, T., Nakamura, K., Minami, K., Take, Y., Nakatani, Y., Miki, Y., et al. (2022). Local impedance measurements during contact force-guided cavotricuspid isthmus ablation for predicting an effective radiofrequency ablation. *J. Arrhythm.* 38 (2), 245–252. doi:10.1002/joa3.12680

Schreieck, J., Heinzmann, D., Scheckenbach, C., Gawaz, M., and Duckheim, M. (2021). A novel local impedance algorithm and contact force sensing to guide high power short duration radiofrequency ablation is efficient and safe for circumferential pulmonary vein isolation. *EP Eur.* 23. doi:10.1093/europace/euab116.240

Shapira-Daniels, A., Barkagan, M., Rottmann, M., Sroubek, J., Tugal, D., Carlozzi, M. A., et al. (2019). Modulating the baseline impedance: An adjunctive technique for maximizing radiofrequency lesion dimensions in deep and intramural ventricular substrate: An adjunctive technique for maximizing radiofrequency lesion dimensions in deep and intramural ventricular substrate. *Circ. Arrhythm. Electrophysiol.* 12 (6), e007336. doi:10.1161/circep.119.007336

Solimene, F., De Sanctis, V., Maggio, R., Malacrida, M., Segreti, L., Anselmino, M., et al. (2022). When local impedance meets contact force: Preliminary experience from the CHARISMA registry. *J. Interv. Card. Electrophysiol.* 63, 749–758. doi:10.1007/s10840-022-01163-7

Solimene, F., Giannotti Santoro, M., De Simone, A., Malacrida, M., Stabile, G., Pandozi, C., et al. (2021). Pulmonary vein isolation in atrial fibrillation patients guided by a novel local impedance algorithm: 1-year outcome from the CHARISMA study. *J. Cardiovasc. Electrophysiol.* 32 (6), 1540–1548. doi:10.1111/jce.15041

Sulkin, M. S., Laughner, J. I., Hilbert, S., Kapa, S., Kosiuk, J., Younan, P., et al. (2018). Novel measure of local impedance predicts catheter–tissue contact and lesion formation. *Circ. Arrhythm. Electrophysiol.* 11 (4), e005831. doi:10.1161/circep.117.005831

Szegedi, N., Salló, Z., Perge, P., Piros, K., Nagy, V. K., Osztheimer, I., et al. (2021). The role of local impedance drop in the acute lesion efficacy during pulmonary vein isolation performed with a new contact force sensing catheter—a pilot study. *PLOS ONE* 16 (9), e0257050. doi:10.1371/journal.pone.0257050

Taghji, P., El Haddad, M., Phlips, T., Wolf, M., Knecht, S., Vandekerckhove, Y., et al. (2018). Evaluation of a strategy aiming to enclose the pulmonary veins with contiguous and optimized radiofrequency lesions in paroxysmal atrial fibrillation: A pilot study. *JACC. Clin. Electrophysiol.* 4 (1), 99–108. doi:10.1016/j.jacep.2017.06.023

Tao, S., Guttman, M. A., Fink, S., Elahi, H., Patil, K. D., Ashikaga, H., et al. (2019). Ablation lesion characterization in scarred substrate assessed using cardiac magnetic resonance. *JACC. Clin. Electrophysiol.* 5 (1), 91–100. doi:10.1016/j.jacep.2018.11.001

Unger, L. A., Schicketanz, L., Oesterlein, T., Stritt, M., Haas, A., Martínez Antón, C., et al. (2021). Local electrical impedance mapping of the atria: Conclusions on substrate properties and confounding factors. *Front. Physiol.* 12, 788885. doi:10.3389/fphys.2021.788885

Yasumoto, K., Egami, Y., Kawanami, S., Sugae, H., Ukita, K., Kawamura, A., et al. (2022). The correlation between local impedance drop and catheter contact in clinical pulmonary vein isolation use. *Pacing Clin. Electrophysiol.* 45, 984–992. doi:10.1111/pace.14500

frontiers | Frontiers in Physiology

TYPE Original Research
PUBLISHED 02 November 2022
DOI 10.3389/fphys.2022.999900

OPEN ACCESS

EDITED BY
Valentina Corino,
Politecnico di Milano, Italy

REVIEWED BY
Marianna Meo,
EPD Solutions, a Philips company, Netherlands
Mostafa Bendahmane,
Université de Bordeaux, France

*CORRESPONDENCE
Wu Jian,
wuj@sz.tsinghua.edu.cn

SPECIALTY SECTION
This article was submitted to Cardiac Electrophysiology, a section of the journal Frontiers in Physiology

RECEIVED 21 July 2022
ACCEPTED 18 October 2022
PUBLISHED 02 November 2022

CITATION
Yadan Z, Xin L and Jian W (2022), Solving the inverse problem in electrocardiography imaging for atrial fibrillation using various time-frequency decomposition techniques based on empirical mode decomposition: A comparative study.
Front. Physiol. 13:999900.
doi: 10.3389/fphys.2022.999900

Solving the inverse problem in electrocardiography imaging for atrial fibrillation using various time-frequency decomposition techniques based on empirical mode decomposition: A comparative study

Zhang Yadan, Lian Xin and Wu Jian*

Research Center of Biomedical Engineering, Institute of Biopharmaceutical and Health Engineering, Tsinghua Shenzhen International Graduate School, Shenzhen, China

Electrocardiographic imaging (ECGI) can aid in identifying the driving sources that cause and sustain atrial fibrillation (AF). Traditional regularization strategies for addressing the ECGI inverse problem are not currently concerned about the multi-scale analysis of the inverse problem, and these techniques are not clinically reliable. We have previously investigated the solution based on uniform phase mode decomposition (UPEMD-based) to the ECGI inverse problem. Numerous other methods for the time-frequency analysis derived from empirical mode decomposition (EMD-based) have not been applied to the inverse problem in ECGI. By applying many EMD-based solutions to the ECGI inverse problem and evaluating the performance of these solutions, we hope to find a more efficient EMD-based solution to the ECGI inverse problem. In this study, five AF simulation datasets and two real datasets from AF patients derived from a clinical ablation procedure are employed to evaluate the operating efficiency of several EMD-based solutions. The Pearson's correlation coefficient (CC), the relative difference measurement star (RDMS) of the computed epicardial dominant frequency (DF) map and driver probability (DP) map, and the distance (Dis) between the estimated and referenced most probable driving sources are used to evaluate the application of various EMD-based solutions in ECGI. The results show that for DF maps on all simulation datasets, the CC of UPEMD-based and improved UPEMD (IUPEMD)-based techniques are both greater than 0.95 and the CC of the empirical wavelet transform (EWT)-based solution is greater than 0.889, and the RDMS of UPEMD-based and IUPEMD-based approaches is less than 0.3 overall and the RDMS of EWT-based method is less than 0.48, performing better than other EMD-based solutions; for DP maps, the CC of UPEMD-based and IUPEMD-based techniques are close to 0.5, the CC of EWT-based is 0.449, and the CC of the remaining EMD-based techniques on the SAF and CAF is all below 0.1; the RDMS of UPEMD-based and IUPEMD-based are 0.06~0.9 less than that of other EMD-based methods for all the simulation datasets overall. On two authentic AF datasets, the Dis

between the first 10 real and estimated maximum DF positions of UPEMD-based and EWT-based methods are 212~1440 less than that of others, demonstrating these two EMD-based solutions are superior and are suggested for clinical application in solving the ECGI inverse problem. On all datasets, EWT-based algorithms deconstruct the signal in the shortest time (no more than 0.12s), followed by UPEMD-based solutions (less than 0.81s), showing that these two schemes are more efficient than others.

KEYWORDS

electrocardiography imaging, inverse problem, EMD-based solutions, time-frequency decomposition, atrial fibrillation

1 Introduction

The recurrence of atrial fibrillation (AF) after ablation, particularly persistent AF, remains a great challenge (Hussein, 2020). The location of the drivers that triggers and maintains AF has not been accurately identified (Pellman and Sheikh, 2015). As a result, improving the efficiency and accuracy of source mapping of AF driving sources is a pressing issue that must be addressed (Dubois et al., 2015).

Electrocardiographic imaging (ECGI) can non-invasively reconstruct epicardial potential from body surface electrocardiographic signals (ECGs) based on geometric structural data of the heart and torso (Cluitmans et al., 2018). By further calculating the isochronous map, domain frequency (DF) map, and driver probability (DP) map on the atria surface, the location of AF drivers can be more intuitively presented (Dubois et al., 2015; Figuera et al., 2016; Salinet et al., 2021). However, due to the limited number of body surface signals, there is an ill-posed problem in solving the ECGI inverse problem (Cluitmans et al., 2015).

Numerous regularization solutions have been proposed to solve this ill-posed problem at present. A pioneering solution for the ill-posed problem is the Tikhonov regularization, which is strongly developed as a motivation for the regularization theory (Wang, 2012; Benning and Burger, 2018). Besides, the truncated singular value decomposition (TSVD) and its modified version based on a singular value decomposition process are gradually popular (Caulier-Cisterna et al., 2018). However, these techniques have not yet achieved reliable and stable epicardial potential reconstructions. These techniques do not screen the different components of the ECGs from the perspective of multiscale time-frequency decomposition, which could skew the reconstruction of the epicardial potential. In our previous study, we performed multi-scale decomposition of body surface signals using the Uniform Phase Mode Decomposition (UPEMD) technique (Zhang et al., 2022), which was derived from Empirical Mode Decomposition (EMD) (Wang et al., 2018). Then, based on the various time-frequency domain features of the decomposed signal, alternative regularization techniques are implemented for the portions comprising various ECG information. Different weights are then assigned to the regularization findings of each component, which substantially increases the accuracy and robustness of the inverse issue solution. Please reference (Zhang et al., 2022) for a more thorough explanation of this technique.

Although we have studied the solution to the inverse problem based on UPEMD in ECGI, various other methods for multi-scale decomposition of signals developed based on EMD have not yet been applied to the inverse problem solving, which is worthy of further exploration.

EMD can decompose ECGs into several parts in the time-frequency domain, but there will be mode mixing and residual noise. In order to solve the above problems, many improved algorithms based on EMD (EMD-based) have been proposed. Among them, in recent years, multivariate empirical mode decomposition (MEMD) (Zheng and Xu, 2019), noise-assisted MEMD (NAMEMD) (Ahrabian et al., 2012), variational mode decomposition (VMD) (Dragomiretskiy and Zosso, 2014), successive variational mode decomposition (SVMD) (Nazari and Sakhaei, 2020), empirical wavelet transform (EWT) (Gilles, 2013; Hurat, 2020), UPEMD (Wang et al., 2018), improved UPEMD (IUPEMD) (Hurat, 2020; Ying et al., 2021; Zheng et al., 2021) have been proposed successively. The effectiveness of the above methods has been verified in mechanical fault detection, voice signal, ECG signal, and seismic signal processing (Lal et al., 2018; Zeng and Yuan, 2021; Liu et al., 2022). In order to study the influence of different EMD-based solutions on the accuracy and reliability of ECGI inverse operation, firstly, the ECGs were decomposed using the various EMD-based solutions mentioned above in this paper. Secondly, the truly useful components for the inverse operation were then screened out using the same principle. Finally, the same post-processing was carried out on the various parts screened out using the various EMD-based solutions to obtain the final epicardial potential.

The remaining of the study is organized as follows. Section 2 describes the principle of the inverse problem, the algorithm principles of various EMD-based technologies, the research process of this paper, and the solutions to the inverse problem based on EMD-based solutions. Section 3 focuses on introducing the data source used in the experiment, the parameter selection of the algorithm, the evaluation index of the algorithm, and the

experimental results of various EMD-based technologies. Section 4 is a discussion of the results. The conclusion is presented in section 5.

2 Methods

2.1 Inverse problem

ECGI can non-invasively reconstruct the electrical signal on the heart surface based on the high-density ECGs (Borras and Chamorro-Servent, 2021; Salinet et al., 2021). The mathematical mechanism of the ECGI inverse problem can be expressed as follows.

$$\Phi_H = A^{-1} * \Phi_B \tag{1}$$

Where $\mathbf{A}$ is the transfer matrix, indicating the conduction of electrical signals from the epicardium to the body surface, and $\boldsymbol{\Phi_B}$ is the ECGs, $\boldsymbol{\Phi_H}$ is the epicardial potential (Potyagaylo et al., 2021). The transfer matrix is determined by geometric models of the atrium and torso in this study (Zhou et al., 2018).

Even though the measurement error in the inverse problem's solution for $\boldsymbol{\Phi_B}$ is minimal, the inverse problem's ill-posedness results in a substantial calculation deviation on $\boldsymbol{\Phi_H}$. The Tikhonov regularization is a typical remedy for this issue, which can be mathematically represented as follows (Tikhonov, 1963).

$$\Phi_{\mathrm{H}} = \mathrm{argmin}\{\|\Phi_{\mathrm{B}} - \mathrm{A}\Phi_{\mathrm{H}}\|_2 + \lambda\|\Lambda\Phi_{\mathrm{H}}\|_2\} \tag{2}$$

Among them, $\mathbf{\Lambda}$ is the regularization operator, and λ is the regularization parameter, which is typically determined by the L-curve method (Orozco Rodríguez, 2011; Aster et al., 2018). (Chen et al., 2019) presents a novel L-curve technique based on bilateral accumulative area detector (L-BAA). BAA is a curve feature point identification operator that offers superior anti-interference capabilities. Tikhonov regularization can improve the smoothness and stability of the inverse operation. TSVD regularization, on the other hand, has a greater ability to suppress noise. The mathematical principle underlying TSVD is given as follows (Wu et al., 2013).

$$\Phi_H = \mathrm{argmin}\|A_k\Phi_H - \Phi_B\| \tag{3}$$

k is the truncation parameter, and like Tikhonov, it may be found using the L-BAA method. In addition to the influence of the regularization method on the result of the inverse operation, $\boldsymbol{\Phi_B}$ has a direct effect on $\boldsymbol{\Phi_H}$.

2.2 EMD-based signal decomposition solutions

To improve the accuracy of $\boldsymbol{\Phi_H}$, EMD-based technology can sieve the different time-frequency components of the ECGs $\boldsymbol{\Phi_B}$, assist in extracting specific components from $\boldsymbol{\Phi_B}$ to participate in the inverse operation and suppress the other part that has a little positive effect on the inverse operation. Currently, developed EMD-based technologies primarily include the following.

2.2.1 Variational mode decomposition

VMD decomposes the raw signal into narrowband signals with separate bands squeezed around different center frequencies in a non-recursive manner (Dragomiretskiy and Zosso, 2014; Zosso et al., 2017). In VMD, the setting of the optimal number of modes k, and weight factor α are two key parameters. The larger k, the heavier the computational burden the method has. The smaller the k, the more severe the mode aliasing may be. The smaller α, the larger the bandwidth of each component. VMD defines intrinsic mode function (IMF) as a limited bandwidth amplitude-modulation-frequency-modulation (AM-FM) signal, requiring that the sum of each IMF's estimated bandwidths is the smallest, and that the sum of all IMFs is equal to the original signal (Isham et al., 2019). For more detailed mathematical principles and implementation steps of the algorithm (Dragomiretskiy and Zosso, 2014), please refer to the appendix.

2.2.2 Successive variational mode decomposition

(Nazari and Sakhaei, 2020) presented SVMD to discover the optimal k with the use of a heuristic method to adaptively select the best number of modes k and the weighting factor in VMD. In contrast to VMD, SVMD incorporates a new penalty function to lessen spectral overlap (Guo et al., 2022).

VMD extracts modes concurrently whereas SVMD extracts all IMFs sequentially. SVMD has lower computational complexity than VMD. SVMD operates by constantly applying VMD to the signal until the decomposition error reaches a certain threshold; this succession aids in accelerating convergence and avoiding the extraction of undesired modes. In SVMD, just an initial and maximum weighting factor is required to be established in advance (Wang and Zhou, 2021). Please see the appendix for further information on the algorithm's implementation steps and more precise mathematical foundations.

2.2.3 Multivariate empirical mode decomposition

When employing an EMD-based technique for multivariate signal decomposition, the amount of IMFs decomposed from various channel signals may vary, impeding the subsequent synchronization analysis of decomposed multichannel signals. MEMD was suggested by (Rehman and Mandic, 2010) as a solution to the issue based on EMD. Using a low discrepancy Hammersley sequence, the raw multivariate signal is first projected into n-dimensional space in MEMD, and the projection signal is then decomposed by EMD to generate the same number of IMFs for multichannel signals. (Rehman and Mandic, 2010; Bussett, 2021). The appendix has more

information about the algorithm and how to put them into practice.

2.2.4 Noise-assisted multivariate empirical mode decomposition

Rehman and Mandic (Rehman et al., 2013) also proposed that NAMEMD can also decompose multi-channel signals into the same number of modes. Compared with MEMD, NAMEMD adds independent white noise to the signal to be decomposed to improve the problems of modal aliasing and residual noise (Zhao et al., 2022). Appendix contains the algorithm implementation procedures.

2.2.5 Uniform phase empirical mode decomposition

In order to get rid of the modal splitting and margin noise present in noise-assisted EMD, UPEMD adds a sinusoidal signal with a uniform phase (Wang et al., 2018). There will be some empirical mistakes introduced since the sinusoidal signal added to UPEMD's magnitude and phase are governed by subjective experience. See appendix for algorithm implementation details.

2.2.6 Improved uniform phase empirical mode decomposition

To acquire the added sinusoidal signal's ideal amplitude and to increase the decomposition's accuracy, IUPEMD applies an orthogonality index to choose the optimal amplitude from numerous decomposition results under various amplitudes. Moreover, the mean curve is not able to be completely isolated from the signal unless the iterative residual signal has been updated, while IUPEMD employs minimum orthogonality as an ideal weight selection criterion to make the mean curve separated from the signal to reduce the residual (Ying et al., 2021; Zheng et al., 2021). Appendix contains algorithm implementation steps.

2.2.7 Empirical wavelet transform

The wavelet transform approach has a positive impact on multi-resolution signal analysis. By merging EMD and wavelet analysis theory, some researchers have developed EWT. EWT generates an adaptive wavelet to extract AM and FM components. First, previous knowledge is extracted from the original signal's Fourier spectrum, and the signal spectrum is adaptively subdivided based on the distribution of extreme points in the frequency domain; next, a wavelet filter bank is formed. Finally, the empirical wavelet transform, i.e. band-pass filtering, is implemented in the divided spectrum range in order to separate individual FM and AM components, and the spectrum of these components is supported firmly (Gilles, 2013; Kedadouche et al., 2016; Liu et al., 2016). Please refer to the appendix for a more comprehensive description of the algorithm's implementation procedure.

The comparative study on EMD-based solutions to the inverse problem.

In this comparative study, various EMD-based solutions are first employed to accomplish multi-scale decomposition on N ECG signals in the EMD-based solution of the inverse issue. The N decomposed signal groups are represented as $\mathbf{S_1}, \mathbf{S_2}, \ldots, \mathbf{S}_n$, and each $\mathbf{S}$ comprises m decomposed signals.

Secondly, the decomposed signal will be screened. The m signals are separated into two parts, the valuable part $\mathbf{P_1}$ and the less valuable signals $\mathbf{P_2}$, where the decomposed signals with a higher variance contribution rate and the correlation coefficient are treated as valuable parts and the rest of the decomposed signals are taken as the less valuable signals. Then, the $\mathbf{P_1}$ parts of the N decomposed signals are then combined to form $\mathbf{\Phi_{B1}}$, and the $\mathbf{P_2}$ parts are combined to form $\mathbf{\Phi_{B2}}$.

Thirdly, utilizing Tikhonov and TSVD regularization for the two parts $\mathbf{\Phi_{B1}}$ and $\mathbf{\Phi_{B2}}$ to produce the inverse solutions $\mathbf{\Phi_{H1}}$ and $\mathbf{\Phi_{H2}}$.

$$\Phi_{H1} = \text{argmin}\{\|\Phi_{B1} - A\Phi_{H1}\|_2 + \lambda\|\Lambda\Phi_{H1}\|_2\} \quad (4)$$

$$\Phi_{H2} = \text{argmin}\|A_k\Phi_{H2} - \Phi_{B2}\| \quad (5)$$

$$\Phi_H = \alpha^*\Phi_{H1} + (1-\alpha)^*\Phi_{H2} \quad (6)$$

Finally, weighting and averaging $\mathbf{\Phi_{H1}}$ and $\mathbf{\Phi_{H2}}$ to obtain the potential signal on the epicardium, $\mathbf{\Phi_H}$. The literature (Yadan et al., 2022) contains more detailed description about these steps. The entire procedure is depicted in Figure 1.

The EMD-based technologies in ECGI are evaluated based on the computational efficiency and precision of inverse solutions.

3 Results

3.1 Datasets

To compare and test several proposed EMD-based solutions for the inverse problem in ECGI, two simulation datasets containing a total of five different AF types and two datasets from real AF patients were used in this study. One of the simulated datasets is from (Figuera et al., 2016; Pedron-Torrecilla et al., 2016), including two different AF propagation patterns, simple AF (SAF) and complex AF (CAF) on the atrial surface. The other simulated dataset from the EDGAR project[1] (Aras et al., 2015) contains realistic mathematical models of the two atria and the torso with different AF impulse propagation patterns. AF was simulated by a driving rotor on either the left atrium (LA) or right atrium (RA) and fibrillatory conduction to the rest of the atria, and in the case of LA driver, with and without

1 This simulation dataset can be found in the [EDGAR] https://edgar.sci.utah.edu/human-cardiac-mapping.html.

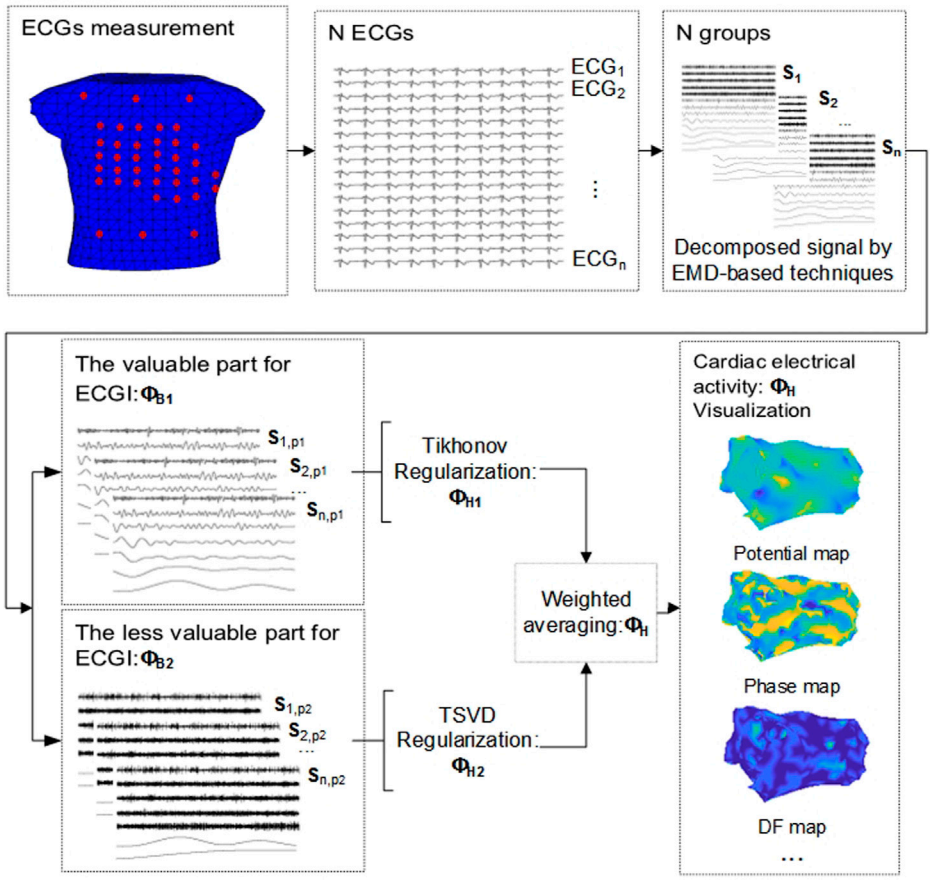

FIGURE 1
EMD-based solution to the inverse problem in ECGI.

fibrotic conduction (LA_normal and LA_fibrotic); The dataset is called RA_normal where the driver is located in RA without fibrotic conduction. Torso potentials were computed by solving the forward problem of electrocardiography (Pedron-Torrecilla et al., 2016).

The real AF dataset from the EDGAR project consists of the signals and geometrical meshes from two AF patients (Patient one# and Patient 2#) derived for an ablation procedure. ECGs were recorded simultaneously with the endocardial recordings with high-resolution multipolar catheters. This genuine AF dataset consists of 62-channel (Patient 1#) and 72-channel (Patient 2#) intracardiac catheter mapping signals from two AF patients, 54-lead body surface ECGs, atrial torso geometry, and transmission matrix A.

3.2 Parameters selection

We determined the initial values of various parameters by comprehensive tests, together with the sampling frequency and features of ECGs. The ECGs are decomposed into 10 layers respectively in VMD, i.e. k = 10. In SVMD, the number of decomposition layers of ECGs totally depends on the different datasets, ranging from 5 to 19. All ECGs in MEMD are adaptively decomposed into 11 layers. In NAMEMD, when the added white noise standard deviation is 1, the decomposition layers of ECGs are shown in Table 1 for different datasets. Furthermore, the ECGs are split into 10 layers using EWT. The amplitude of the sinusoidal signal added in UPEMD is set to one for all datasets, and the optimal number of phases is 18. In general, IUPEMD determines the number of phases between 4 and 32, and the optimal amplitude of the sinusoidal signal is set between 0.15 and 0.4. Table 2 shows the optimal signal amplitude and phase quantity selected adaptively by IUPEMD for various datasets.

After the ECGs have been decomposed using the aforementioned time-frequency decomposition solutions, the decomposed signals are divided into two parts based on the variance contribution rate and the correlation coefficient: one containing a large amount of irrelevant information and the

TABLE 1 The decomposition layers of ECGs for different datasets in NAMEMD.

Dataset	SAF	CAF	LA_fibrotic	LA_normal	RA_normal	Patient #1	Patient #2
Decomposition layers	12	11	11	12	11	13	14

TABLE 2 The optimal signal amplitude and phase quantity selected by IUPEMD for different datasets.

Dataset	SAF	CAF	LA_fibrotic	LA_normal	RA_normal	Patient #1	Patient #2
Amplitude	0.17	0.17	0.15	0.15	0.2	0.15	0.25
Phase Quantity	4	4	8	8	4	4	4

other containing more useful information. In all of the inverse problem solutions shown in this work, the processing that follows is identical.

3.3 Evaluation index

In this study, Pearson's correlation coefficient CC (Puth et al., 2014; Liu et al., 2021; Cui et al., 2022)and relative difference measurement star (RDMS) (Figuera et al., 2016) are used to quantify the similarity between the calculated and actual DF and the DP maps, thereby evaluating several EMD-based solutions to the inverse problem.

$$CC = \frac{\sum_{i=1}^{m}(x_i - \bar{x})(y_i - \bar{y})}{\sqrt{\sum_{i=1}^{m}(x_i - \bar{x})^2}\sqrt{\sum_{i=1}^{m}(y_i - \bar{y})^2}} \tag{4a}$$

$$RDMS = \sqrt{\sum_j \left(\frac{x_k}{\|x^2\|} - \frac{\hat{x_k}}{\|\hat{x}^2\|}\right)^2} \tag{5a}$$

In addition, to quantify the accuracy of the calculated DF or DP from many perspectives, the Euclidean distance (denoted by Dis) has also been employed (Etal, 2021). The calculated and referenced numbered positions of the n greatest DF or DP points will be processed as an n-dimensional vector, respectively. Dis measures the distance between these two vectors, that is, the similarity between the n biggest estimated DF or DP sites and their references.

$$Dis = \sqrt{\sum_{i=1}^{n}(x_i - y_i)^2} \tag{6a}$$

n denotes the number of sites. x_i and y_i are the calculated and referenced numbered positions of the n greatest DF or DP points, respectively. If n = 10, the Dis between the estimated and reference first 10 greatest DP location or the DF position will be calculated, representing the index distance between the estimated and the reference driving sources.

3.4 Experimental results

The DF and DP maps on the epicardium are constructed, and potential AF drivers are identified using several EMD-based solutions in this study.

3.4.1 Results on the simulation datasets

Figure 2 shows the DF maps of seven different EMD-based solutions for five simulation datasets. Among them, the DF maps generated by the UPEMD-based and IUPEMD-based solutions are the most comparable to the real maps in all datasets; the DF under the EWT-based solution also exhibits a good resemblance to the real one for SAF and CAF. From the perspective of CC, for the UPEMD-based, IUPEMD-based, and EWT-based methods, the CC is higher than other methods. The CC of UPEMD-based and IUPEMD-based techniques are both greater than 0.95 for five distinct simulation datasets, while the CC of the EWT-based solution is greater than 0.915 for all simulation datasets excluding the LA_fibrotic dataset (CC on the LA_fibrotic: 0.889). The aforementioned three solutions have distinct advantages over other EMD-based technologies.

On these five simulation datasets, the RDMS of UPEMD-based and IUPEMD-based approaches is less than 0.3 overall. On the datasets SAF, CAF, and RA normal, the RDMS of EWT-based method is less than 0.4; however, on the datasets LA_normal and LA_fibrotic, the RDMS is 0.413 and 0.471, respectively. Both the RDMS of VMD-based and SVMD-based are more than 0.5. There is little difference between the DF maps for MEMD-based and NAMEMD-based solutions, whereas CC and RDMS for MEMD-based solutions are slightly better than those for NAMEMD-based solutions, indicating that when MEMD is used to decompose ECGs, the addition of white noise cannot improve the inverse results; the SVMD-based inverse solution is superior to VMD overall.

This paper calculates the DP maps for each algorithm and identifies ten drivers with the highest probability as well. The relevant details are shown in Figure 3. In general, DP maps of

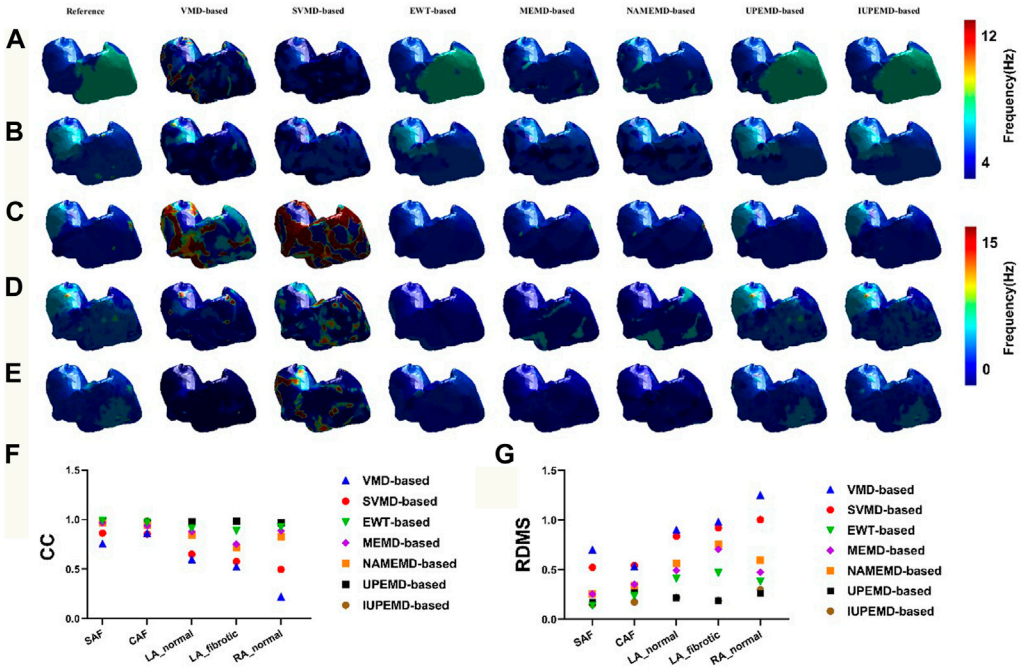

FIGURE 2
The DF maps using various EMD-based methods under the datasets SAF, CAF, LA_normal, LA_fibrotic, and RA_normal are represented by **(A–E)**, respectively. For each separate dataset, the reference DF map is in the first column, followed by the DF maps for the VMD-based, SVMD-based, EWT-based, MEMD-based, NAMEMD-based, UPEMD-based, and IUPEMD-based solutions, starting with the second column. On each model, a distinct color denotes the DF at that place. The RDMS **(G)** and CC **(F)** between the computed EMD-based algorithm and the real DF map for each EMD-based solution are shown as well.

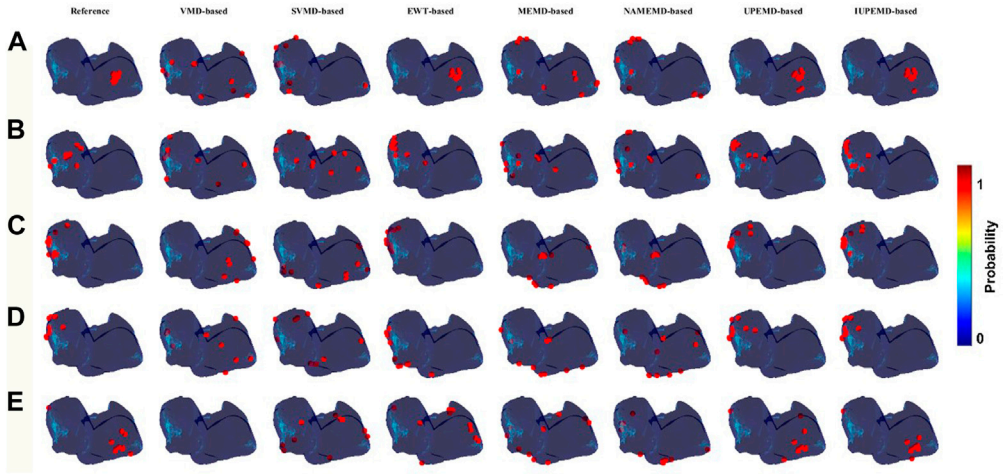

FIGURE 3
DP maps (red circles mark the 10 locations with the highest probability of driver location). Among them **(A–E)** represent the DP maps generated by various EMD-based algorithms for SAF, CAF, LA_normal, LA_fibrotic, and RA_normal, which from left to right correspond to the DP maps for VMD-based, SVMD-based, EWT-based, MEMD-based, NAMEMD-based, UPEMD-based, and IUPEMD-based solutions.

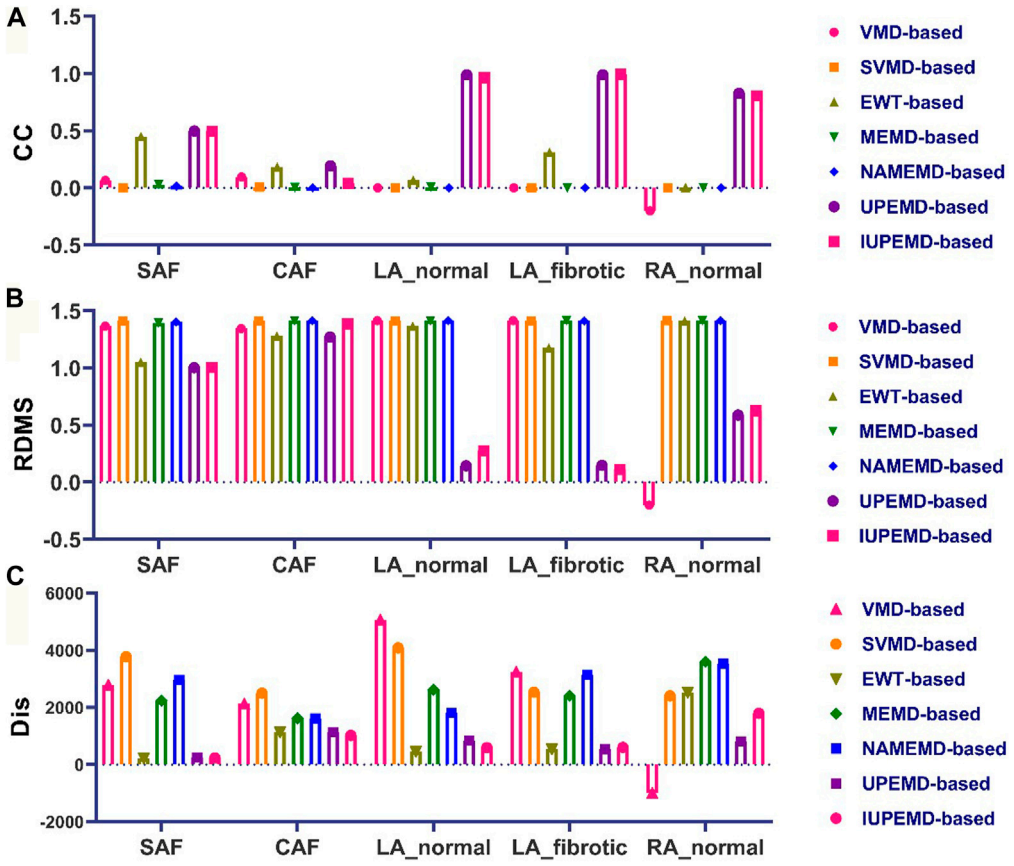

FIGURE 4
Quantitative evaluation of the DP map: **(A)** CC **(B)** RDMS **(C)** Dis (top 10 greatest possible drivers). The horizontal axis displays, from left to right, the quantitative indications of VMD-based, SVMD-based, EWT-based, MEMD-based, NAMEMD-based, UPEMD-based, and IUPEMD-based solutions for every dataset.

UPEMD-based and IUPEMD-based solutions are the most accurate, followed by EWT and other algorithms that have varying degrees of false detection. Compared to VMD-based and MEMD-based solutions, the inverse operation of the upgraded algorithms, SVMD-based and MEMD-based solutions, are not significantly enhanced. In the VMD-based scheme for the RA _normal, the VMD-based solution does not detect the driver, hence no driver position is marked in the VMD-based inverse solution in (E).

Meanwhile, Figure 4 depicts the CC, RDMS, and the Dis between the calculated drivers and the reference drivers on the DP maps. If no driving source is discovered, its CC, RDMS, and Dis are manually set to negative values. For DP maps, the CC of UPEMD-based (CC = 0.498) and IUPEMD-based (0.496) techniques are close to 0.5, the CC of EWT-based is 0.449, and the CC of the remaining EMD-based techniques on the SAF and CAF is all below 0.1; the RDMS of UPEMD-based and IUPEMD-based solutions are lower 0.3 on LA_normal and LA_fibrotic, while other EMD-based methods' RDMS is more than 1.2. On the SAF and CAF datasets, the RDMS of UPEMD-based, IUPEMD-based, and EWT-based methods is likewise less than that of other EMD-based methods. These results show that the UPEMD-based, EWT-based and IUPEMD-based solutions outperform other algorithms in the CC and RDMS of DP.

As for the Dis between estimated and reference driving sources, in general, the drivers calculated by EWT-based, UPEMD-based, and IUPEMD-based solutions are the closest to the reference drivers; For all the datasets, the Dis for VMD-based and SVMD-based solutions show no noticeable advantages or disadvantages, as do MEMD-based and NAMEND-based solutions, indicating that these algorithms have limited efficacy in solving ECGI inverse problems.

3.4.2 Results on the real datasets

This paper analyzes the DF maps of the epicardial potential generated by various EMD-based solutions on two authentic AF datasets and identified the 10 sites with the maximum DF, as shown in Figure 5 ((A) for patient one# and (B) for patient 2#).

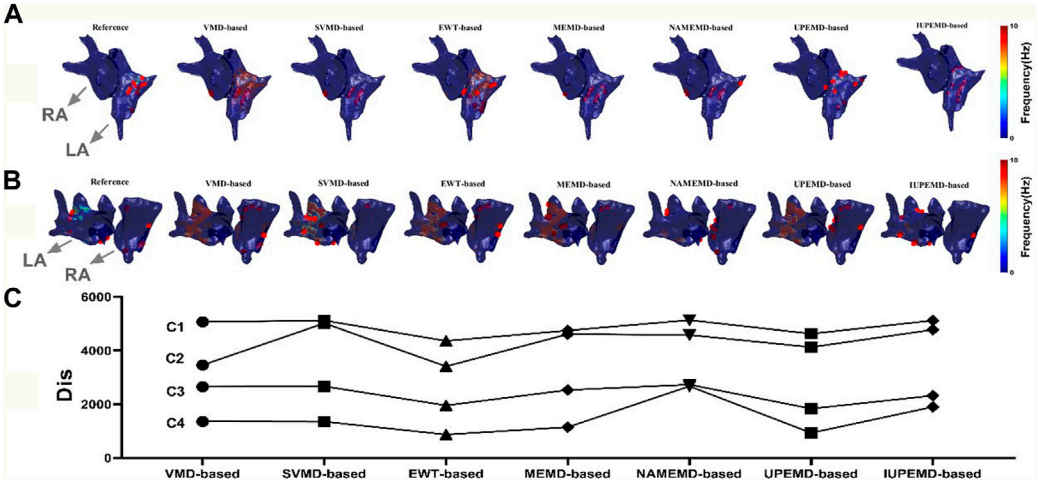

FIGURE 5
DF maps of two real patients with AF (red dots mark the 10 locations with the highest DF; both patients' LA and RA are indicated by grey arrows). **(A)** DF maps for Patient 1#; **(B)** DF maps for Patient 2#; **(C)** The Dis between the computed and actual DF maps: C1, for Patient 1#, the Dis between the estimated and actual 62 maximum DF positions for various EMD-based solutions; C2, for Patient 2#, the Dis between the estimated and actual 73 maximum DF positions; C3, for Patient 1#, the Dis between the first 10 real and estimated maximum DF positions; C4, for Patient 2#, the Dis between the first 10 real and inversely calculated maximum DF positions.

Figure 5A demonstrates that UPEMD-based and EWT-based solutions identified multiple maximum DF sites in the left atrium of patient 1#. Although these points were slightly dispersed in regard to the 10 maximum DF spots on the reference left atrium, the recognition results of UPEMD-based and EWT-based algorithms are more accurate than those of other EMD-based algorithms. For patient 2# (Figure 5B), both UPEMD-based and EWT-based algorithms recognized multiple highest DF spots in the RA. The maximum DF positions discovered by SVMD-based and IUPEMD-based approaches are mostly situated in the LA, which is much more than that of the reference LA, and they are definitely absent in the RA.

To analyze the aforementioned DF maps' findings quantitatively, the Dis between the actual and measured maximum DF was determined (62 locations for patient one# and 73 sites for patient 2#). Also given is the disparity between the projected and actual top 10 maximum DF positions. In general, the Dis between the first 10 real and estimated maximum DF positions of UPEMD-based and EWT-based methods are less than 1960 for patient 1#, while that of other EMD-based techniques are all more than 2300; for patient 2#, the Dis between the first 10 real and inversely calculated maximum DF positions of UPEMD-based (Dis = 934) and EWT-based (Dis = 875) techniques are lower to 935, less than that of others (more than 1147). The UPEMD-based and EWT-based are superior to others even for the Dis between the actual and measured maximum DF (62 locations for patient one# and 73 sites for patient 2#), showing that the estimated epicardial abnormal area by the UPEMD-based and EWT-based solutions is closer to the reference one.

3.4.3 The execution efficiency of EMD-based solutions

We counted the time taken by various EMD-based approaches for the decomposition of ECGs to assess the operational efficacy of various EMD-based solutions. The effect of datasets and methods on decomposition time is summarized in Figure 6.

On all datasets, EWT-based algorithms deconstruct the signal in the shortest time (no more than 0.12s), followed by UPEMD-based solutions (less than 0.81s), showing that these two schemes are more efficient than others. Due to the adaptive decomposition layers of the SVMD approach in different data sets, the SVMD-based method is not consistently more efficient than the VMD-based method in different simulated data sets. If the number of decomposition layers is greater than that of the VMD method, the length of time required will be greater. In contrast, if the number of adaptive decomposition layers is less than the predetermined value of the VMD method, the VMD method will consume less time. Due to the addition of a particular amount of white noise to the original signal in the NAMEMD-based solution (Rehman and Mandic, 2011), the time-frequency components of the signal become more diverse. Hence, more decomposed layers are required to get the final monotonic residual signal (Table 1). In comparison to the UPEMD-based solution, the IUPEMD-based solution must iteratively decompose the ECGs under various

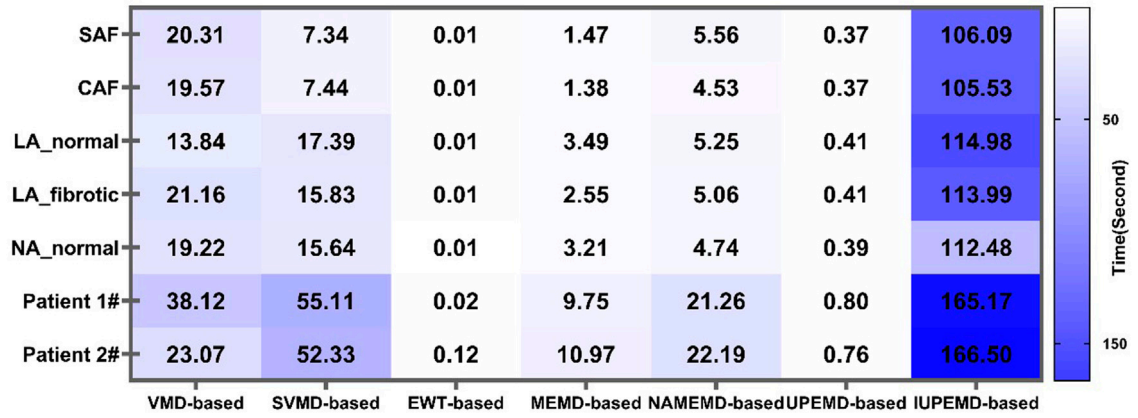

FIGURE 6
Decomposition time of ECGs by various EMD-based solutions for diverse datasets.

parameters (amplitude and phase number) using UPEMD and then determine the current optimal amplitude and the number of phases based on the principle of minimum orthogonality. Consequently, this method requires more time.

4 Discussion

This study employed five A F simulation datasets and two real AF patient datasets to evaluate the effect of various EMD-based solutions in ECGI. We obtain the Dis between the calculated and actual maximum DF, and maximum DP sites. What's more, the CC and RDMS of the estimated DF and DP maps for different inverse operation methods are investigated for simulated AF datasets as well.

UPEMD-based IUPEMD-based and EWT-based solutions perform better than other EMD-based solutions on simulated datasets from the CC and RDMS of DF and DP maps, and their Dis between estimated and actual top 10 most probable driving sources is shorter.

In comparison to the IUPEMD-based solution, the UPEMD-based solution simply decompose ECGs with the assistance of a sinusoidal signal whose amplitude and phase are pre-determined (Wang et al., 2018), hence lowering the number of iterations and saving calculation time. The IUPEMD-based solution is inferior to the UPEMD-based solution, indicating that adding sinusoidal signals with the phases and amplitudes adaptively determined by the principle of minimum orthogonality to ECGs does not significantly improve the solution of the ECGI inverse problem. In real AF datasets, the maximum DF calculated by the UPEMD-based solution and the EWT-based solution are the closest to the actual maximum DF, indicating that the detected drivers are more precise using UPEMD-based and EWT-based solutions.

VMD-based and SVMD-based solutions are less satisfactory when compared to UPEMD-based and EWT-based technology. It demonstrates that the hypothesis that decomposition of the ECGs is translated into a variational problem is not conducive to the ECGI inverse problem (Dragomiretskiy and Zosso, 2014; Wei et al., 2021). In these two decomposition methods, the screened IMFs cannot distinguish the valuable components for the ECGI inverse problem well. Although the SVMD-based solution, as an improved version of the VMD-based solution, adds constraints when solving variational problems (Liu et al., 2022), it is not better than the VMD-based solution, in fact, it is marginally worse. Dependent on the different ECGs, the execution efficiency of VMD-based and SVMD-based solutions differs.

Similarly, neither the NAMEMD-based solution nor the MEMD-based solution show any advantages, indicating that the method of first mapping ECGs to a high-dimensional space and then performing multi-scale decomposition of their projected signals may not be appropriate for multi-scale solutions of ECGI. The Dis calculated by the NAMEMD-based solution is greater than that of the MEMD-based solution in the SAF, LA_fibrotic, and genuine AF datasets, demonstrating that NAMEMD-based, an enhanced MEMD-based solution, does not solve ECGI inverse problems more effectively. The execution efficiency of the NAMEMD-based solution is lower than that of the MEMD-based solution.

5 Limitations

In this paper, only a small amount of data was used to test these EMD-based approaches, and when these open data sets were collected, they may have had mistakes because of the limits of the measurement environment or the simulation environment.

We did not evaluate the effect of the geometric errors of the atrium and torso models on the performance of various EMD-based solutions. When AF occurs, not only does the electrical activity of the atrium change, but so does the atrial structure to a certain extent. The reconstructed portion of the structure, such as fibrosis, must be distinguished from the normal portion during the construction of the atrial geometric model and mesh division; moreover, the static atrial model is utilized in this study. Using a dynamic atrial model that incorporates the natural systolic and diastolic activities of the atrium may increase the accuracy of inverse calculations.

How the number of electrodes and electrode placements affect the outcomes of various EMD-based inverse methods has not been properly investigated. The two real AF datasets used have a limited number of surface electrodes. Although some researchers disagree that more surface electrodes make it more conducive to study the inverse problem (Bear et al., 2018; Gharbalchi No et al., 2020; Parreira et al., 2020), the degree of inaccuracy brought on by 54 electrodes in the study of the ECGI inverse problem deserves further in-depth investigation.

In conclusion, this study disregards the influence of the defects caused by the aforementioned challenges on the inverse solutions and focuses solely on the application of various EMD-based solutions to constrained datasets. To some extent, the findings are useful; however, a large number of clinical data have not confirmed them.

6 Conclusion

In conclusion, we study the application of different EMD-based solutions in ECGI, and the results have strong regularity. Considering the efficiency of algorithm execution, UPEMD-based and EWT-based solutions have prominent advantages and are easier to meet the needs of ECGI in clinical applications. The UPEMD-based solution, IUPEMD-based solution, and EWT-based solution are superior to others for distinct datasets. However, the IUPEMD-based solution's running time is significantly longer than that of the UPEMD-based solution and EWT-based solution, causing the latter two more appropriate for clinical applications. This paper can serve as a reference for future researchers addressing relevant ECGI inverse problems by examining the use of various EMD-based solutions in ECGI.

Data availability statement

The original contributions presented in the study are included in the article/Supplementary Material, further inquiries can be directed to the corresponding author/s.

Author contributions

ZY conceived the technique and conducted computational simulations; ZY and WJ analyzed the results; ZY drafted the manuscript and WJ modified some spelling mistakes and corrected inappropriate formulation; LX contributed to the manuscript preparation.

Funding

Work supported by the Knowledge Innovation Program of Basic Research Projects of Shenzhen [JCY20200109142805928,JCYJ20160428182053361], in part by National Key R&D Program of China (2019YFC0119500).

Conflict of interest

The authors declare that the research was conducted in the absence of any commercial or financial relationships that could be construed as a potential conflict of interest.

Publisher's note

Supplementary material

The Supplementary Material for this article can be found online at: https://www.frontiersin.org/articles/10.3389/fphys.2022.999900/full#supplementary-material

References

Ahrabian, A., Looney, D., Tobar, F. A., Hallatt, J., and Mandic, D. P. (2012). *Noise assisted multivariate empirical mode decomposition applied to Doppler radar data.* London: Sensor Signal Processing for Defence SSPD 2012IET,

Aras, K., Good, W., Tate, J., Burton, B., Brooks, D., Coll-Font, J., et al. (2015). Experimental data and geometric analysis repository—Edgar. *J. Electrocardiol.* 48, 975–981. doi:10.1016/j.jelectrocard.2015.08.008

Aster, R. C., Borchers, B., and Thurber, C. H. (2018). *Parameter estimation and inverse problems*. Elsevier.

Bear, L. R., Dogrusoz, Y. S., Svehlikova, J., Coll-Font, J., Good, W., van Dam, E., et al. (2018). Effects of ECG signal processing on the inverse problem of electrocardiography. Proceedings of the 2018 Computing in Cardiology Conference (CinC) 45 Maastricht, Netherlands(September 2018).doi:10.22489/CinC.2018.070

Benning, M., and Burger, M. (2018). Modern regularization methods for inverse problems. *Acta Numer.* 27, 1–111. doi:10.1017/s0962492918000016

Borras, M., and Chamorro-Servent, J. (2021). Electrocardiographic imaging: A comparison of iterative solvers. *Front. Physiol.* 12, 620250. doi:10.3389/fphys.2021.620250

Bussett, N. T. (2021). *Hardware implementation of multivariate empirical mode decomposition*. San Diego(CA): San Diego State University.

Caulier-Cisterna, R., Munoz-Romero, S., Sanroman-Junquera, M., Garcia-Alberola, A., and Rojo-Alvarez, J. L. (2018). A new approach to the intracardiac inverse problem using Laplacian distance kernel. *Biomed. Eng. Online* 17, 86. doi:10.1186/s12938-018-0519-z

Chen, R., Li, J., and Wu, J. (2019). A robust algorithm for selecting optimal regularization parameter based on bilateral accumulative area, Proceedings of the 2019 41st Annual International Conference of the IEEE Engineering in Medicine and Biology Society (EMBC), Berlin, Germany: July 2019, IEEE, 4893.

Cluitmans, M., Brooks, D. H., MacLeod, R., Dossel, O., Guillem, M. S., van Dam, P. M., et al. (2018). Validation and opportunities of electrocardiographic imaging: From technical achievements to clinical applications. *Front. Physiol.* 9, 1305. doi:10.3389/fphys.2018.01305

Cluitmans, M. J. M., Peeters, R. L. M., Westra, R. L., and Volders, P. G. A. (2015). Noninvasive reconstruction of cardiac electrical activity: Update on current methods, applications and challenges. *Neth. Heart J.* 23, 301–311. doi:10.1007/s12471-015-0690-9

Cui, Y., Zhang, H., Zhu, J., Liao, Z., Wang, S., and Liu, W. (2022). Correlations of salivary and blood glucose levels among six saliva collection methods. *Int. J. Environ. Res. Public Health* 19, 4122. doi:10.3390/ijerph19074122

Dragomiretskiy, K., and Zosso, D. (2014). Variational mode decomposition. *IEEE Trans. Signal Process.* 62, 531–544. doi:10.1109/tsp.2013.2288675

Dubois, R., Shah, A. J., Hocini, M., Denis, A., Derval, N., Cochet, H., et al. (2015). Non-invasive cardiac mapping in clinical practice: Application to the ablation of cardiac arrhythmias. *J. Electrocardiol.* 48, 966–974. doi:10.1016/j.jelectrocard.2015.08.028

Etal, S. M. (2021). Euclidean distance based similarity measurement and ensuing ranking scheme for document search from outsourced cloud data. *Turkish J. Comput. Math. Educ.* 12, 4386–4395. doi:10.17762/turcomat.v12i3.1817

Figuera, C., Suarez-Gutierrez, V., Hernandez-Romero, I., Rodrigo, M., Liberos, A., Atienza, F., et al. (2016). Regularization techniques for ECG imaging during atrial fibrillation: A computational study. *Front. Physiol.* 7, 466. doi:10.3389/fphys.2016.00466

Gharbalchi No, F., Serinagaoglu Dogrusoz, Y., Onak, O. N., and Weber, G. W. (2020). Reduced leadset selection and performance evaluation in the inverse problem of electrocardiography for reconstructing the ventricularly paced electrograms. *J. Electrocardiol.* 60, 44–53. doi:10.1016/j.jelectrocard.2020.02.017

Gilles, J. (2013). Empirical wavelet transform. *IEEE Trans. Signal Process.* 61, 3999–4010. doi:10.1109/tsp.2013.2265222

Guo, Y. J., Yang, Y. D., Jiang, S. F., Jin, X. H., and Wei, Y. D. (2022). Rolling bearing fault diagnosis based on successive variational mode decomposition and the EP index. *Sensors* 22, 3889. doi:10.3390/s22103889

Hurat, B. (2020). *A fully adaptive 2D empirical wavelet transform using watersheds*. San Diego(CA): San Diego State University.

Hussein, A. (2020). *Evaluation of arrhythmia recurrence and electrical reconnection of the pulmonary veins following ablation index guided pulmonary vein isolation for persistent atrial fibrillation*. Liverpool(ENG): Institute of Life Courses and Medical Sciences, Faculty of Health and Life Sciences, University of Liverpool.

Isham, M. F. b., Leong, M., Lim, M., and Zakaria, M. K. (2019). A review on variational mode decomposition for rotating machinery diagnosis. *MATEC Web Conf.* 255, 02017. doi:10.1051/matecconf/201925502017

Kedadouche, M., Thomas, M., and Tahan, A. (2016). A comparative study between empirical wavelet transforms and empirical mode decomposition methods: Application to bearing defect diagnosis. *Mech. Syst. Signal Process.* 81, 88–107. doi:10.1016/j.ymssp.2016.02.049

Lal, G. J., Gopalakrishnan, E. A., and Govind, D. (2018). Epoch estimation from emotional speech signals using variational mode decomposition. *Circuits Syst. Signal Process.* 37, 3245–3274. doi:10.1007/s00034-018-0804-x

Liu, W., Cao, S. Y., and Chen, Y. K. (2016). Seismic time-frequency analysis via empirical wavelet transform. *IEEE Geosci. Remote Sens. Lett.* 13, 28–32. doi:10.1109/lgrs.2015.2493198

Liu, W., Zhang, H., Zhu, J., Peng, L., Duan, Z., Liu, T., et al. (2021). Unstimulated parotid saliva is a better method for blood glucose prediction. *Appl. Sci.* 11, 11367. doi:10.3390/app112311367

Liu, X. Y., Yan, Y., Hu, K. B., Zhang, S., Li, H. J., Zhang, Z., et al. (2022). Fault diagnosis of rotor broken bar in induction motor based on successive variational mode decomposition. *Energies* 15, 1196. doi:10.3390/en15031196

Nazari, M., and Sakhaei, S. M. (2020). Successive variational mode decomposition. *Signal Process.* 174, 107610. doi:10.1016/j.sigpro.2020.107610

Orozco Rodríguez, J. e. A. (2011). *Regularization methods for inverse problems*. Twin Cities (MN): University of Minnesota.

Parreira, L., Carmo, P., Adragao, P., Nunes, S., Soares, A., Marinheiro, R., et al. (2020). Electrocardiographic imaging (ECGI): What is the minimal number of leads needed to obtain a good spatial resolution? *J. Electrocardiol.* 62, 86–93. doi:10.1016/j.jelectrocard.2020.07.004

Pedron-Torrecilla, J., Rodrigo, M., Climent, A. M., Liberos, A., Perez-David, E., Bermejo, J., et al. (2016). Noninvasive estimation of epicardial dominant high-frequency regions during atrial fibrillation. *J. Cardiovasc. Electrophysiol.* 27, 435–442. doi:10.1111/jce.12931

Pellman, J., and Sheikh, F. (2015). Atrial fibrillation: Mechanisms, therapeutics, and future directions. *Compr. Physiol.* 5, 649–665. doi:10.1002/cphy.c140047

Potyagaylo, D., Chmelevsky, M., Budanova, M., Zubarev, S., Treshkur, T., and Lebedev, D. (2021). Combination of lead-field theory with cardiac vector direction: ECG imaging of septal ventricular activation. *J. Electrocardiol.* 69, S40-S44. doi:10.1016/j.jelectrocard.2019.08.003

Puth, M. T., Neuhauser, M., and Ruxton, G. D. (2014). Effective use of Pearson's product–moment correlation coefficient. *Anim. Behav.* 93, 183–189. doi:10.1016/j.anbehav.2014.05.003

Rehman, N., and Mandic, D. P. (2010). Multivariate empirical mode decomposition. *Proc. R. Soc. A* 466, 1291–1302. doi:10.1098/rspa.2009.0502

Rehman, N. U., and Mandic, D. P. (2011). filter bank property of multivariate empirical mode decomposition. *IEEE Trans. Signal Process.* 59, 2421–2426. doi:10.1109/tsp.2011.2106779

Rehman, N. U., Park, C., Huang, N. E., and Mandic, D. P. (2013). Emd via memd: Multivariate noise-aided computation of standard emd. *Adv. Adapt. Data Anal.* 5, 1350007. doi:10.1142/s1793536913500076

Salinet, J., Molero, R., Schlindwein, F. S., Karel, J., Rodrigo, M., Rojo-Alvarez, J. L., et al. (2021). Electrocardiographic imaging for atrial fibrillation: A perspective from computer models and animal experiments to clinical value. *Front. Physiol.* 12, 653013. doi:10.3389/fphys.2021.653013

Tikhonov, A. N. (1963). Regularization of incorrectly posed problems. *Dokl. Akad. Nauk. Sssr+* 153, 49

Wang, L. (2012). *Applications of sparse regularization to inverse problem of electrocardiography*. Hong Kong: The Chinese University of Hong Kong.

Wang, Y. H., Hu, K., and Lo, M. T. (2018). Uniform phase empirical mode decomposition: An optimal hybridization of masking signal and ensemble approaches. *IEEE Access* 6, 34819–34833. doi:10.1109/ACCESS.2018.2847634

Wang, Y. J., and Zhou, G. G. (2021). The novel successive variational mode decomposition and weighted regularized extreme learning machine for fault diagnosis of automobile gearbox. *Shock Vib.* 2021, 1–7. doi:10.1155/2021/5544031

Wei, H. R., Qi, T. Y., Feng, G. R., and Jiang, H. N. (2021). Comparative research on noise reduction of transient electromagnetic signals based on empirical mode decomposition and variational mode decomposition. *Radio Sci.* 56, e2020RS007135. doi:10.1029/2020rs007135

Wu, Z. M., Bian, S. F., Xiang, C. B., and Tong, Y. D. (2013) A new method for TSVD regularization truncated parameter selection. *Math. Probl. Eng.* 2013, 1–9. doi:10.1155/2013161834

Yadan, Z., Jian, W., Yifu, L., Haiying, L., Jie, L., and Hairui, L. (2022). Solving the inverse problem based on UPEMD for electrocardiographic imaging. *Biomed. Signal Process. Control* 76, 103665. doi:10.1016/j.bspc.2022.103665

Ying, W. M., Zheng, J. D., Pan, H. Y., and Liu, Q. Y. (2021). Permutation entropy-based improved uniform phase empirical mode decomposition for mechanical fault diagnosis. *Digit. Signal Process.* 117, 103167. doi:10.1016/j.dsp.2021.103167

Zeng, W., and Yuan, C. Z. (2021). ECG arrhythmia classification based on variational mode decomposition, Shannon energy envelope and deterministic learning. *Int. J. Mach. Learn. Cybern.* 12, 2963–2988. doi:10.1007/s13042-021-01389-3

Zheng, J. D., Su, M. X., Ying, W. M., Tong, J. Y., and Pan, Z. W. (2021). Improved uniform phase empirical mode decomposition and its application in machinery fault diagnosis. *Measurement* 179, 109425. doi:10.1016/j.measurement.2021.109425

Zhang, Y. D., Wu, J., Li, Y. F., Li, H. Y., Lin, J., and Li, H. R. (2022). Solving the inverse problem based on UPEMD for electrocardiographic imaging. *Biomed. Signal Process. Control* 76, 103665. doi:10.1016/j.bspc.2022.103665

Zhao, L. F., Siahpour, S., Yazdi, M. R. H., Ayati, M., and Zhao, T. Y. (2022). Intelligent monitoring system based on noise-assisted multivariate empirical mode decomposition feature extraction and neural networks. *Comput. Intell. Neurosci.* 2022, 2698498. doi:10.1155/2022/2698498

Zheng, Y., and Xu, G. (2019). Quantifying mode mixing and leakage in multivariate empirical mode decomposition and application in motor imagery–based brain-computer interface system. *Med. Biol. Eng. Comput.* 57, 1297–1311. doi:10.1007/s11517-019-01960-9

Zhou, S. J., Horacek, B. M., Warren, J. W., AbdelWahab, A., and Sapp, J. L. (2018). Rapid 12-lead automated localization method: Comparison to electrocardiographic imaging (ECGI) in patient-specific geometry. *J. Electrocardiol.* 51, S92-S97–S97. doi:10.1016/j.jelectrocard.2018.07.022

Zosso, D., Dragomiretskiy, K., Bertozzi, A. L., and Weiss, P. S. (2017). Two-dimensional compact variational mode decomposition. *J. Math. Imaging Vis.* 58, 294–320. doi:10.1007/s10851-017-0710-z

frontiers | Frontiers in Medicine

TYPE Original Research
PUBLISHED 10 January 2023
DOI 10.3389/fmed.2022.983330

OPEN ACCESS

EDITED BY
Valentina Corino,
Politecnico di Milano, Italy

REVIEWED BY
Hiroshi Morimatsu,
Okayama University, Japan
Nikolaos Papagiannakis,
Eginition Hospital, Greece
Massimo Walter Rivolta,
University of Milan, Italy

*CORRESPONDENCE
Seung-Hwa Lee
✉ shua9999@gmail.com

†These authors have contributed equally to this work

SPECIALTY SECTION
This article was submitted to Intensive Care Medicine and Anesthesiology, a section of the journal Frontiers in Medicine

RECEIVED 10 August 2022
ACCEPTED 20 December 2022
PUBLISHED 10 January 2023

CITATION
Oh AR, Park J, Shin SJ, Choi B, Lee J-H, Yang K, Kim HY, Sung JD and Lee S-H (2023) Prediction model for postoperative atrial fibrillation in non-cardiac surgery using machine learning.
Front. Med. 9:983330.
doi: 10.3389/fmed.2022.983330

Prediction model for postoperative atrial fibrillation in non-cardiac surgery using machine learning

Ah Ran Oh[1,2†], Jungchan Park[1,3†], Seo Jeong Shin[4], Byungjin Choi[3], Jong-Hwan Lee[1], Kwangmo Yang[3,5], Ha Yeon Kim[6], Ji Dong Sung[7] and Seung-Hwa Lee[7,8*]

[1]Samsung Medical Center, Department of Anesthesiology and Pain Medicine, School of Medicine, Sungkyunkwan University, Seoul, Republic of Korea, [2]Department of Anesthesiology and Pain Medicine, Kangwon National University Hospital, Chuncheon, Republic of Korea, [3]Department of Biomedical Sciences, Graduate School of Medicine, Ajou University, Suwon, Republic of Korea, [4]Institute for Innovation in Digital Healthcare, Yonsei University, Seoul, Republic of Korea, [5]Center for Health Promotion, Samsung Medical Center, School of Medicine, Sungkyunkwan University, Seoul, Republic of Korea, [6]Department of Anesthesiology and Pain Medicine, School of Medicine, Ajou University, Suwon, Republic of Korea, [7]Rehabilitation and Prevention Center, Samsung Medical Center, School of Medicine, Heart Vascular Stroke Institute, Sungkyunkwan University, Seoul, Republic of Korea, [8]Department of Biomedical Engineering, Seoul National University College of Medicine, Seoul, Republic of Korea

Some patients with postoperative atrial fibrillation (POAF) after non-cardiac surgery need treatment, and a predictive model for these patients is clinically useful. Here, we developed a predictive model for POAF in non-cardiac surgery based on machine learning techniques. In a total of 201,864 patients who underwent non-cardiac surgery between January 2011 and June 2019 at our institution, 5,725 (2.8%) were treated for POAF. We used machine learning with an extreme gradient boosting algorithm to evaluate the effects of variables on POAF. Using the top five variables from this algorithm, we generated a predictive model for POAF and conducted an external validation. The top five variables selected for the POAF model were age, lung operation, operation duration, history of coronary artery disease, and hypertension. The optimal threshold of probability in this model was estimated to be 0.1, and the area under the receiver operating characteristic (AUROC) curve was 0.80 with a 95% confidence interval of 0.78–0.81. Accuracy of the model using the estimated threshold was 0.95, with sensitivity and specificity values of 0.28 and 0.97, respectively. In an external validation, the AUROC was 0.80 (0.78–0.81). The working predictive model for POAF requiring treatment in non-cardiac surgery based on machine learning techniques is provided online (https://sjshin.shinyapps.io/afib_predictor_0913/). The model needs further verification among other populations.

KEYWORDS

cardiac event, atrial fibrillation, non-cardiac surgery, machine learning, prediction model

Introduction

Postoperative atrial fibrillation (POAF) is defined as new onset atrial fibrillation following surgery in patients without prior history of atrial fibrillation (1). PAOF is the most common complication following cardiac surgery and is associated with increased morbidity, mortality, length of hospital stay, and long-term risk of stroke (2, 3). In non-cardiac surgery where the heart is not manipulated directly, the incidence of POAF is reported to be lower and to vary by surgery type (4, 5). Although the majority of POAF converts spontaneously to sinus rhythm, POAF in non-cardiac surgery is known to affect long-term consequences (6). Moreover, current guidelines indicate that a certain portion of POAF patients need immediate medication treatment for heart rate or rhythm control (1, 4, 7). Considering the large number of patients who undergo non-cardiac surgery and their risks as they age, prediction of these events would be helpful in daily clinical practice (8).

Previous studies have attempted to identify risk factors for POAF in non-cardiac surgery (4, 5, 9). Reported risk factors include age, male sex, history of cardiovascular disease, and preoperative heart rate (10). There are limitations in applying individual risk factors in clinical practice because existing studies on these risk factors are heterogeneous and show inconsistent results. Moreover, these studies have been conducted with small numbers of patients or in specific groups with select surgical procedures or diagnoses (4, 5, 9). Here, we aimed to investigate risk factors of non-cardiac surgery in a comprehensive manner and to generate a predictive model of POAF that can be used in clinical practice. We used a large real-world data set of consecutive adult patients and identified those who needed interventional treatment for POAF during the first postoperative 30 days. Based on machine learning techniques, we developed a predictive model that can be applied conveniently in clinical practice and conducted an external validation. For further verification, we provided the model online.

Materials and methods

Approval for this study was waived by the Institutional Review Board of Samsung Medical Center (SMC 2021-06-078) because the study registry was curated in a de-identified form. The requirement for written informed consent from participants was also waived. Using data for external validation was approved by the Institutional Review Board of Ajou University Hospital (AJIRB-MED-MDB-21-662). The validation cohort was also curated in a de-identified form, so written informed consent was waived. We followed the Declaration of Helsinki and reported according to the guidelines for Strengthening the Reporting of Observational Studies in Epidemiology.

Abbreviations: POAF, postoperative atrial fibrillation; XGB, extreme gradient boosting.

Data curation and study population

We utilized data from the Samsung Medical Center-Non-Cardiac operation (SMC-NoCop) registry (KCT 0006363), a single-center de-identified cohort of 203,787 consecutive adult patients who underwent non-cardiac surgery under general or regional anesthesia at Samsung Medical Center, Seoul, Korea, between January 2011 and June 2019. The registry is based on the institutional electronic archive system, which contains medical information from electronic hospital records of over 4 million patients with more than 900 million laboratory findings and 200 million prescriptions. Raw data were extracted using "Clinical Data Warehouse Darwin-C," an electronic system for investigators to search and retrieve de-identified medical records. In this system, mortality is updated consistently and confirmed with the National Population Registry of the Korea National Statistical Office using a unique personal identification number for mortalities following hospital discharge.

After obtaining a preoperative evaluation sheet, investigators independent from this study organized relevant preoperative variables including demographic data, underlying diseases, and information from blood laboratory tests. We also estimated preoperative Charlson Comorbidity Index for patients using preoperative diagnoses based on International Classification of Diseases-10 (ICD-10) codes (11). Postoperative diagnoses were organized based on in-hospital progress notes, nursing charts, discharge notes, results of examinations, and drug prescriptions. For analysis, we excluded patients who experienced preoperative atrial fibrillation.

For external validation, we extracted data from patient records who underwent non-cardiac surgery at Ajou University Medical Center between January 2011 and October 2021. Through the same recruitment criteria, 91,576 patients were included in the external validation set.

Definitions and study endpoints

Risks in surgical procedures were stratified following the European Society of Cardiology (ESC)/European Society of Anesthesiology (ESA) guidelines on non-cardiac surgery (12). For the predictive model, we included newly-developed POAF events within 30 days following surgery and requiring interventions such as intravenous administration of antiarrhythmic agents such as propafenone, flecainide, amiodarone, diltiazem, or verapamil. We also included patients who required electrical cardioversion for rhythm or rate control.

The primary endpoint was POAF requiring interventional treatment during hospital stay within 30 days after non-cardiac

TABLE 1 Preoperative variables in patients with and without postoperative atrial fibrillation.

	No atrial fibrillation (*N* = 196,139)	Atrial fibrillation (*N* = 5,725)	*P*-value
Male	83,392 (42.5)	3,512 (61.3)	<0.001
Age	52.3 (±15.1)	64.1 (±12.5)	<0.001
Hypertension	48,033 (24.5)	2,645 (46.2)	<0.001
Diabetes	21,819 (11.1)	1,324 (23.1)	<0.001
Current alcohol	39,590 (20.2)	704 (12.3)	<0.001
Current smoking	15,203 (7.8)	310 (5.4)	<0.001
Chronic kidney disease	3,040 (1.5)	236 (4.1)	<0.001
Dialysis	866 (0.4)	68 (1.2)	–
Previous disease			
Charlson comorbidity index	0.1 (±0.5)	0.4 (±1.1)	<0.001
Stroke	3,812 (1.9)	309 (5.4)	<0.001
Coronary artery disease	3,181 (1.6)	821 (14.3)	<0.001
Myocardial infarction	809 (0.4)	89 (1.6)	<0.001
Coronary revascularization			
Percutaneous intervention	2,510 (1.3)	439 (7.7)	<0.001
Bypass graft	354 (0.2)	58 (1.0)	<0.001
Heart failure	380 (0.2)	108 (1.9)	<0.001
Arrhythmia	906 (0.5)	184 (3.2)	<0.001
Peripheral artery disease	508 (0.3)	45 (0.8)	<0.001
Aortic disease	603 (0.3)	80 (1.4)	<0.001
Valvular heart disease	211 (0.1)	35 (0.6)	<0.001
Chronic obstructive pulmonary disease	3,216 (1.6)	307 (5.4)	<0.001
Preoperative blood laboratory tests			
Hemoglobin, g/dl	13.3 (±1.8)	12.9 (±2.0)	<0.001
Creatinine, mg/dl	0.9 (±0.8)	1.0 (±1.0)	<0.001
Preoperative vital signs			
Heart rate, bpm	68.2 (±11.6)	71.0 (±15.2)	<0.001
Systolic blood pressure, mmHg	119.2 (±16.6)	122.6 (±17.9)	<0.001
Diastolic blood pressure, mmHg	70.7 (±10.9)	71.6 (±11.1)	<0.001
Mean blood pressure, mmHg	86.9 (±11.7)	88.6 (±12.0)	<0.001

Data are presented as *n* (%) or mean (±standard deviation).

surgery. From a total of 201,864 patients, newly developed POAF occurred in 7,757 (3.8%), and 5,725 (2.8%) required interventional treatment. We quantified and compared the effects of each variable on the predictive performance of the model. After conducting feature elimination, we developed a calculator for POAF prediction.

Development of the predictive model

A total of 50 predictor variables obtained from a preoperative evaluation sheet was provided as input to each model (**Supplementary Table 1**). We applied machine learning techniques with an extreme gradient boosting (XGB) algorithm, which is a decision tree-based ensemble model using a gradient boosting framework and the Shapley value framework (13, 14). The hyper-parameters were optimized based on a grid search using the area under the receiver operating characteristic (AUROC) curve, and 5-fold cross-validation was employed during model development. We divided the data into training and test sets. A stratified random split of the data was conducted while maintaining a constant ratio of an event, POAF in this study, and 80% of the data were reserved for creating

TABLE 2 Operative variables in patients with and without postoperative atrial fibrillation.

	No atrial fibrillation (*N* = 196,139)	Atrial fibrillation (*N* = 5,725)	*P*-value
General anesthesia	169,710 (86.5)	5,170 (90.3)	<0.001
Emergency operation	13,602 (6.9)	629 (11.0)	<0.001
Operation duration, min	130.8 (±100.3)	170.8 (± 118.9)	<0.001
Surgical risk	–	–	<0.001
Mild	77,427 (39.5)	1,280 (22.4)	–
Intermediate	107,282 (54.7)	3,518 (61.4)	–
High	11,430 (5.8)	927 (16.2)	–
Inotropic drug infusion	15,762 (8.0)	1,534 (26.8)	<0.001
Blood transfusion	6,321 (3.2)	560 (9.8)	<0.001
Red blood cell	6,129 (3.1)	531 (9.3)	<0.001
Cryoprecipitate	365 (0.2)	40 (0.7)	<0.001
Fresh frozen plasma	1,262 (0.6)	151 (2.6)	<0.001
Platelet concentrate	229 (0.1)	37 (0.6)	<0.001
Surgery types	–	–	–
Neuroendocrine	12,889 (6.6)	136 (2.4)	<0.001
Lung	10,682 (5.4)	1,277 (22.3)	<0.001
Head and neck	30,129 (15.4)	702 (12.3)	<0.001
Breast	17,477 (8.9)	159 (2.8)	<0.001
Stomach	12,200 (6.2)	279 (4.9)	<0.001
Hepatobiliary	16,566 (8.4)	485 (8.5)	0.97
Colorectal	13,331 (6.8)	409 (7.1)	0.32
Urology	17,942 (9.1)	445 (7.8)	<0.001
Gynecology	24,348 (12.4)	156 (2.7)	<0.001
Bone and skin etc.	40,575 (20.7)	1,677 (29.3)	<0.001

Data are presented as *n* (%) or mean (±standard deviation). Surgical risk was stratified according to the 2014 European Society of Cardiology (ESC)/European Society of Anesthesiology (ESA) guidelines.

the machine learning model, and the remaining 20% was for the testing model.

Feature interpretation was presented in a SHapley Additive exPlanations (SHAP) summary plot. The impact of each feature on POAF was presented as a SHAP value, which represents the characteristic of deriving a marginal distribution and weighted average by fixing all variables except one and predicting that one to determine its importance (14). In the SHAP summary plot, features are sorted in descending order by effect on POAF, and each patient is represented by one dot on each variable line. The horizontal location of each dot indicates the level of association between the feature and outcome. The area shown on the right side is the point where the SHAP value is greater than zero. Variable-specific SHAP values >0 indicate increased risk.

For practical use in clinical practice, we eliminated variables and developed a predictive model for POAF with the fewest number of variables. We also leveraged Shiny, an application-building package from R, which users can access gratis *via* a public link. Our model was developed based on our observed top five patient features. Using an estimated threshold for probability, AUROC, accuracy, sensitivity, and specificity were computed. For further validation, we generated a case-balanced dataset within an internal dataset and also conducted an external validation.

Statistical analysis

We compared differences between patients who developed POAF following non-cardiac surgery and patients who did not. Continuous features are presented as mean ± standard deviation or median with interquartile range, and comparisons were conducted by *t*-test or Mann-Whitney test, as applicable. Categorical features are presented as number and percentage,

and differences were evaluated using Chi-square or Fisher's exact test. Analysis was performed using R 4.1.0 (Vienna, Austria)[1].

Results

Baseline characteristics and mortality

We excluded 1,923 patients with preoperative atrial fibrillation. The baseline characteristics of patients with and without POAF are presented in **Table 1**. Patients with POAF were older, predominantly male, and had a higher incidence of underlying disease. In patients with POAF, preoperative hemoglobin level was significantly lower and creatinine level was higher. Large differences in operative variables were observed between patients with and without POAF (**Table 2**).

Predictive models for POAF

The SHAP summary plot for results of the XGB model is shown in **Figure 1**, with features shown in descending order of contribution to PAOF development. The horizontal line comprised of dots presents variable effects on POAF. Representing patient characteristics, SHAP values greater than zero (presented on the right side) indicate increased risk, while values on the left side indicate lower risk for POAF. The top five variables with SHAP values greater than 0.1 were age (0.559), lung operation (0.190), operation duration (0.154), history of coronary artery disease (0.138), and hypertension (0.113).

To apply our findings to clinical practice, we eliminated a number of variables in the predictive model, as the predictive models based on 10 and seven variables showed similar power (**Supplementary Figure 1**). Finally, we developed the predictive model based on the top five variables, which is simpler and more convenient for clinical use. A functioning version of the model is provided online at https://sjshin.shinyapps.io/afib_predictor_0913/ (**Figure 2**). When values for each of the top five variables for target patients are entered, the probability for POAF is shown as an output. An optimal threshold of probability in this model was estimated based on the maximal Youden index (**Supplementary Table 2**). We also estimated the correlation matrix of the selected features (**Supplementary Figure 2**). They were all below 0.2 except for the one between hypertension and age, indicating that there was a correlation only between hypertension and age among the top five variables. The receiver operating characteristic curve of the model is shown in **Figure 3**. Applying 0.1 as a threshold, the AUROC was 0.80 with a 95% confidence interval of 0.78–0.81. Accuracy of this threshold was 0.95, with sensitivity and specificity values of 0.28 and 0.97, respectively. The F1 score was 0.222, and precision was 0.185. In a case-balanced dataset, the AUROC was 0.77 with sensitivity and specificity values of 0.85 and 0.68, respectively. The F1 score was 0.785, and precision was 0.727.

External validation of the predictive model

The external validation dataset consisted of 91,576 patients. POAF developed in 1,977 (2.2%) patients, and 790 (0.9%) required interventional treatments. Based on the top five variables, our predictive model achieved an AUROC of 0.80 (0.78–0.81) in an external validation dataset (**Figure 3**). Using the same threshold of 0.1, the sensitivity and specificity values were 0.21 and 0.89, respectively.

Discussion

In this study, we used machine learning techniques with an XGB algorithm to identify variables associated with POAF requiring treatment in non-cardiac surgery and created a predictive model. The incidence of POAF was 2.8%, and the top five variables retained in our predictive model were age, lung operation, operation duration, history of coronary artery disease, and hypertension. Our predictive model achieved an AUROC value of 0.80 (95% confidence interval 0.78–0.81) at a threshold of 0.1.

Postoperative atrial fibrillation in non-cardiac surgery is typically considered to be a transient and reversible phenomenon of minor clinical significance. However, recent studies have revealed that POAF in non-cardiac surgery is associated with increased risk of long-term complications such as ischemic stroke (15–17). In addition, some POAF patients demonstrate instability in vital signs. Immediate treatment to control heart rate or rhythm can be urgent for these patients. In this regard, a predictive model for POAF requiring interventional treatment can be useful in postoperative care. Accordingly, we aimed to develop a predictive model that can be used in non-cardiac surgery to identify potentially high-risk patients and to adjust care and treatment at the individual level.

When applying artificial intelligence such as machine learning techniques in a field of medicine, interpretability should be primarily considered (18). We chose variables based on SHAP feature importance, and those that were clinically explainable. Age, which ranked as the first variable, has consistently been reported as a predictor of POAF in previous studies (4, 5, 9). This association is well-explained by age-associated structural changes and fibrosis in the atrium that provide substrate for arrhythmias (19). Another explanation could be the higher incidence of cardiovascular comorbidities in older patients. Comorbidities such as hypertension and coronary artery disease

1 http://www.R-project.org/

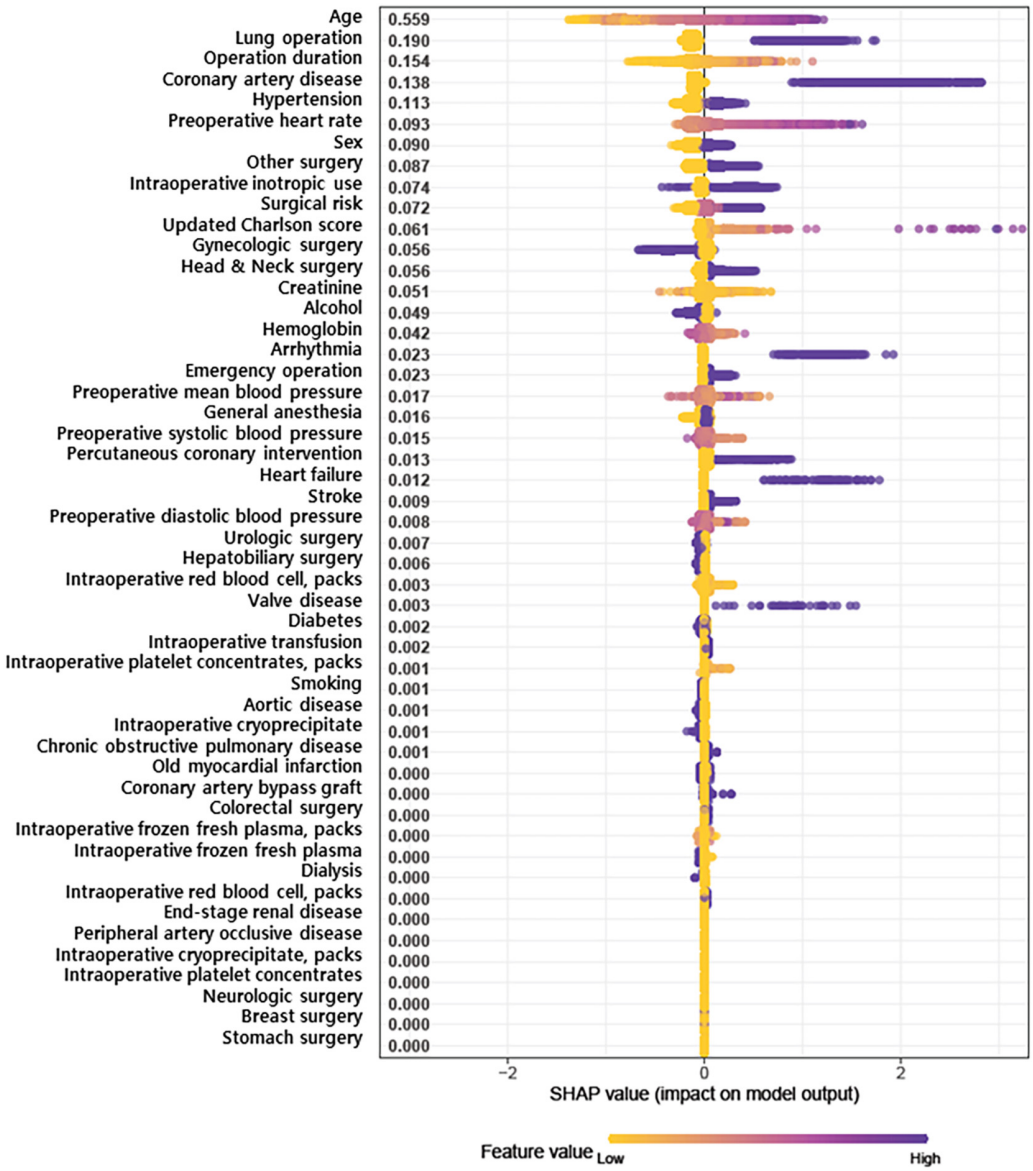

FIGURE 1
SHapley Additive exPlanations (SHAP) summary plot representing the results of a machine learning-based extreme gradient boosting (XGB) algorithm.

are also used in our predictive model. In hypertensive patients, the renin angiotensin aldosterone system and sympathetic outflow are activated, resulting in left ventricular hypertrophy, diastolic dysfunction, and atrial stiffness—all of which induce atrial fibrillation (20). Coronary artery disease contributes to POAF with a bidirectional relationship (21). The pro-inflammatory condition of coronary artery disease can cause myocardial inflammation exacerbated by a supply-demand mismatch, which triggers atrial fibrillation by altering cardiac conduction (22). In addition, myocardial infarction leads to left ventricular remodeling that can predispose patients to atrial fibrillation. Similar processes can occur in hypoxic patients, and coronary artery disease might lower the threshold for POAF development (10).

Among operative variables, thoracic surgery is well-known to result in a high incidence of POAF, ranging from 6.4 to 19% in various patient samples (23, 24). The atrial stretching induced by pulmonary vasoconstriction and local inflammation of pulmonary veins can contribute to POAF (10). In thoracic surgery, aspects of the procedure are known to affect the incidence of POAF (24). According to our SHAP summary plot, a short operation time had a definite negative impact on POAF, but a long operation time did not have a clear positive impact. Numerous studies have demonstrated that operation

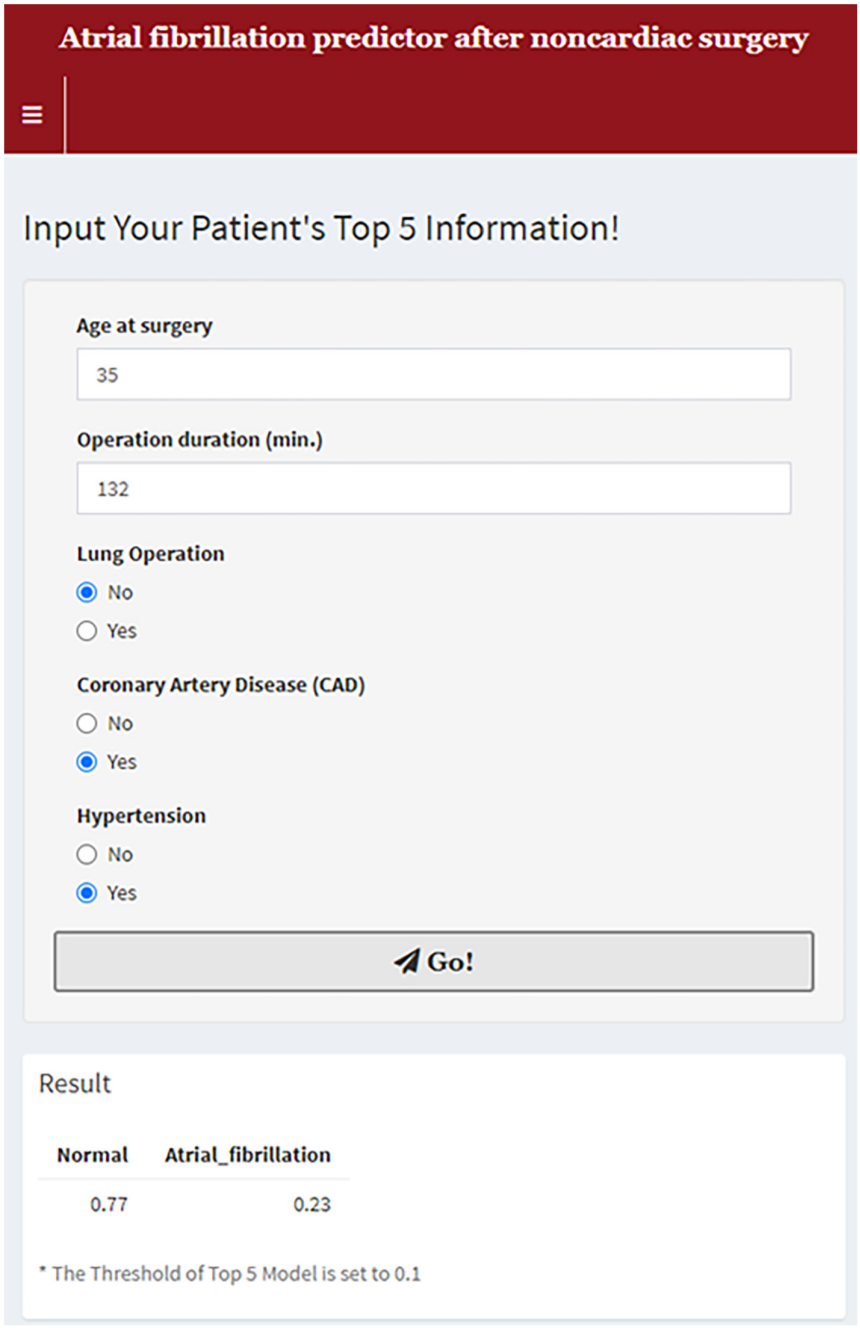

FIGURE 2
An online predictive model for postoperative atrial fibrillation.

duration is associated with postoperative outcomes (25), but an association with POAF has rarely been reported. This might be due to limitations in traditional regression models that implicitly assume a linear relationship between each risk factor and outcomes (26).

In the present study, XGB algorithms were used for machine learning techniques to evaluate the broad spectrum of non-cardiac surgical procedures with various diagnoses. XGB algorithms are known for superior performance in comparison to traditional algorithms and have been used to develop effective prediction models in a wide range of applications (13). We relied on SHAP feature importance based on Shapley values because they are computationally fast and have good theoretical properties (14). A Shapley value is defined as the average marginal contribution of a feature across all possible feature coalitions. Under this definition, Shapley values are affected by

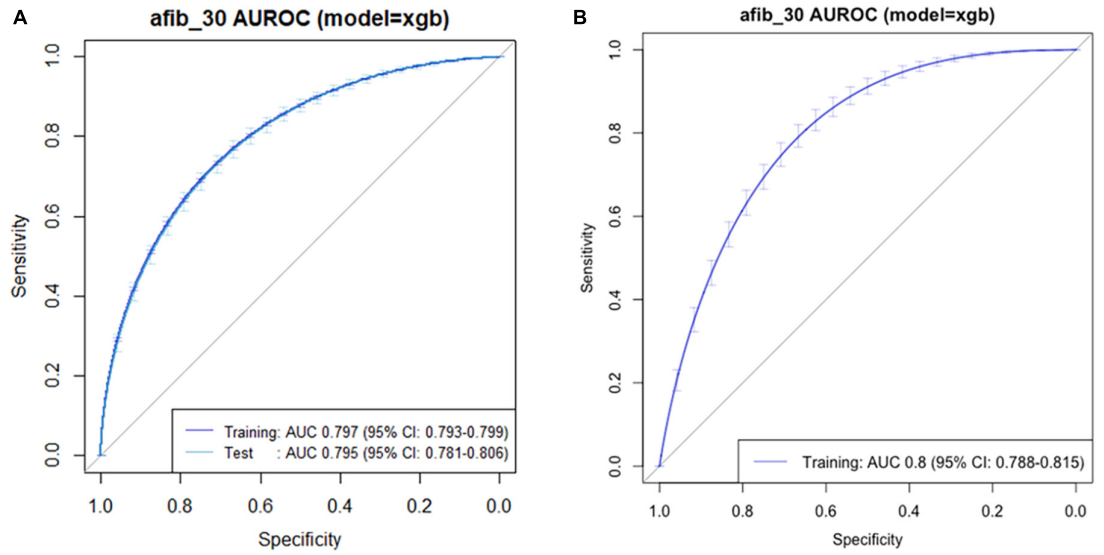

FIGURE 3
Receiver operating characteristic curve of the predictive model for postoperative atrial fibrillation in **(A)** original and **(B)** external validation datasets.

incidence, and the positions of dots on the y-axis should be considered in interpreting SHAP summary plots. Our results show the relatively low importance of valvular heart disease, which is a well-known risk factor for POAF (27), and this might be related to the low prevalence of valvular heart disease in our cohort. Traditional methods can ignore complex relationships among a large number of risk factors with non-linear interactions (26). By applying an advanced model that considers multiple risk factors, we aimed to overcome the conventional drawbacks of traditional statistical models.

An additional strength is that our predictive model can be applied widely. It was based on heterogeneous patients undergoing a broad spectrum of surgical procedures, and the generated model was further validated with an external dataset. In the external validation, our model achieved similar predictive power, despite lower incidence of POAF. The incidence of POAF has been reported to vary widely in previous studies, and our results suggest that our model can be applied in groups of patients with different characteristics. Furthermore, our predictive model is available to the public for further verification or clinical application.

Study strengths and limitations

There are several study limitations that need to be considered. First, due to the nature of the retrospective data, causality cannot be confirmed in the current study. Moreover, we could not evaluate the difference between self-limited POAF and POAF requiring intervention due to the nature of the dataset. The presence of underlying disease as variables was all self-reported. Second, perioperative care was not controlled during the long period of study. Despite the presence of an institutional protocol based on current guidelines, decisions were often made at the discretion of attending clinicians. Third, we cannot generalize our results to other patient groups due to the limitations of a single-center study, and ethnic differences were not considered. In addition, our model could not be compared with pre-existing predictive models for POAF in cardiac surgery because our study aimed to develop a predictive model in non-cardiac surgery. Detailed preoperative cardiac evaluations, including findings such as left ventricular ejection fraction or coronary artery angiograms, were not available for all patients in our sample. Fourth, the causality-based feature selection is not guaranteed in our model. To be specific, SHAP values are a measure of the importance of a feature related to the model which is different from the importance of a feature for the outcome. Last, factors retained in our model were mostly non-modifiable, and additional prevention or treatment strategies could not be established. Despite these limitations, this is the first study to identify risk factors for POAF in non-cardiac surgery using a machine learning algorithm and a proven predictive model.

Conclusion

Using five variables identified by machine learning techniques, we developed a predictive model for POAF requiring treatment with good predictive power in patients undergoing non-cardiac surgery. The predictive model is

available online, with the model in need of further verification among other populations.

Data availability statement

The raw data supporting the conclusions of this article will be made available by the authors, without undue reservation.

Ethics statement

Approval for this study was waived by the Institutional Review Board of Samsung Medical Center (SMC 2021-06-078) because the study registry was curated in a de-identified form. The requirement for written informed consent from participants was also waived. Using data for an external validation was approved by the Institutional Review Board of Ajou University Hospital (AJIRB-MED-MDB-21-87 662). The validation cohort was also curated in a de-identified form, so the written informed consent was waived.

Author contributions

S-HL: conceptualization. AO, JP, and HK: data curation. SS and BC: formal analysis. J-HL, KY, and JS: supervision. AO and JP: first draft. All authors contributed to article, revision of manuscript, and approved the submitted version.

Conflict of interest

The authors declare that the research was conducted in the absence of any commercial or financial relationships that could be construed as a potential conflict of interest.

Publisher's note

All claims expressed in this article are solely those of the authors and do not necessarily represent those of their affiliated organizations, or those of the publisher, the editors and the reviewers. Any product that may be evaluated in this article, or claim that may be made by its manufacturer, is not guaranteed or endorsed by the publisher.

Supplementary material

The Supplementary Material for this article can be found online at: https://www.frontiersin.org/articles/10.3389/fmed.2022.983330/full#supplementary-material

References

1. Kirchhof P, Benussi S, Kotecha D, Ahlsson A, Atar D, Casadei B, et al. 2016 ESC Guidelines for the management of atrial fibrillation developed in collaboration with EACTS. *Eur Heart J.* (2016) 37:2893–962. doi: 10.1093/eurheartj/ehw210

2. Hravnak M, Hoffman L, Saul M, Zullo T, Whitman G, Griffith B. Predictors and impact of atrial fibrillation after isolated coronary artery bypass grafting. *Crit Care Med.* (2002) 30:330–7. doi: 10.1097/00003246-200202000-00011

3. Mariscalco G, Klersy C, Zanobini M, Banach M, Ferrarese S, Borsani P, et al. Atrial fibrillation after isolated coronary surgery affects late survival. *Circulation.* (2008) 118:1612–8. doi: 10.1161/CIRCULATIONAHA.108.777789

4. Bhave P, Goldman L, Vittinghoff E, Maselli J, Auerbach A. Incidence, predictors, and outcomes associated with postoperative atrial fibrillation after major noncardiac surgery. *Am Heart J.* (2012) 164:918–24. doi: 10.1016/j.ahj.2012.09.004

5. Polanczyk C, Goldman L, Marcantonio E, Orav E, Lee T. Supraventricular arrhythmia in patients having noncardiac surgery: clinical correlates and effect on length of stay. *Ann Intern Med.* (1998) 129:279–85. doi: 10.7326/0003-4819-129-4-199808150-00003

6. Walsh S, Tang T, Gaunt M, Schneider H. New arrhythmias after non-cardiothoracic surgery. *BMJ.* (2006) 333:715. doi: 10.1136/bmj.333.7571.715

7. Danelich I, Lose J, Wright S, Asirvatham S, Ballinger B, Larson D, et al. Practical management of postoperative atrial fibrillation after noncardiac surgery. *J Am Coll Surg.* (2014) 219:831–41. doi: 10.1016/j.jamcollsurg.2014.02.038

8. Bartels K, Karhausen J, Clambey E, Grenz A, Eltzschig H. Perioperative organ injury. *Anesthesiology.* (2013) 119:1474–89. doi: 10.1097/ALN.0000000000000022

9. Vaporciyan A, Correa A, Rice D, Roth J, Smythe W, Swisher S, et al. Risk factors associated with atrial fibrillation after noncardiac thoracic surgery: analysis of 2588 patients. *J Thorac Cardiovasc Surg.* (2004) 127:779–86. doi: 10.1016/j.jtcvs.2003.07.011

10. Bessissow A, Khan J, Devereaux P, Alvarez-Garcia J, Alonso-Coello P. Postoperative atrial fibrillation in non-cardiac and cardiac surgery: an overview. *J Thromb Haemost.* (2015) 13(Suppl. 1):S304–12. doi: 10.1111/jth.12974

11. Sundararajan V, Henderson T, Perry C, Muggivan A, Quan H, Ghali W. New ICD-10 version of the Charlson comorbidity index predicted in-hospital mortality. *J Clin Epidemiol.* (2004) 57:1288–94. doi: 10.1016/j.jclinepi.2004.03.012

12. Kristensen S, Knuuti J. New ESC/ESA Guidelines on non-cardiac surgery: cardiovascular assessment and management. *Eur Heart J.* (2014) 35:2344–5. doi: 10.1093/eurheartj/ehu285

13. Chen T, Guestrin C. XGBoost. In: *proceedings of the 22nd ACM SIGKDD international conference on knowledge discovery and data mining*. New York, NY: ACM (2016) 785–94. doi: 10.1145/2939672.2939785

14. Aas K, Jullum M, Løland A. Explaining individual predictions when features are dependent: more accurate approximations to shapley values. *Artif Intell.* (2021) 298:103052. doi: 10.1016/j.artint.2021.103502

15. Gialdini G, Nearing K, Bhave P, Bonuccelli U, Iadecola C, Healey J, et al. Perioperative atrial fibrillation and the long-term risk of ischemic stroke. *JAMA.* (2014) 312:616–22. doi: 10.1001/jama.2014.9143

16. Conen D, Alonso-Coello P, Douketis J, Chan M, Kurz A, Sigamani A, et al. Risk of stroke and other adverse outcomes in patients with perioperative atrial fibrillation 1 year after non-cardiac surgery. *Eur Heart J.* (2020) 41:645–51. doi: 10.1093/eurheartj/ehz431

17. Butt J, Olesen J, Havers-Borgersen E, Gundlund A, Andersson C, Gislason G, et al. Risk of thromboembolism associated with atrial fibrillation following noncardiac surgery. *J Am Coll Cardiol.* (2018) 72:2027–36. doi: 10.1016/j.jacc.2018.07.088

18. Kundu S. AI in medicine must be explainable. *Nat Med.* (2021) 27:1328. doi: 10.1038/s41591-021-01461-z

19. Sezai A, Hata M, Niino T, Kasamaki Y, Nakai T, Hirayama A, et al. Study of the factors related to atrial fibrillation after coronary artery bypass grafting: a search for a marker to predict the occurrence of atrial fibrillation before surgical intervention. *J Thorac Cardiovasc Surg.* (2009) 137:895–900. doi: 10.1016/j.jtcvs.2008.10.003

20. Higuchi S, Kabeya Y, Matsushita K, Arai N, Tachibana K, Tanaka R, et al. Perioperative atrial fibrillation in noncardiac surgeries for malignancies and one-year recurrence. *Can J Cardiol.* (2019) 35:1449–56.

21. Staerk L, Sherer J, Ko D, Benjamin E, Helm R. Atrial fibrillation: epidemiology, pathophysiology, and clinical outcomes. *Circ Res.* (2017) 120:1501–17. doi: 10.1161/CIRCRESAHA.117.309732

22. Butler J, Parker D, Pillai R, Westaby S, Shale D, Rocker G. Effect of cardiopulmonary bypass on systemic release of neutrophil elastase and tumor necrosis factor. *J Thorac Cardiovasc Surg.* (1993) 105:25–30.

23. Roselli E, Murthy S, Rice T, Houghtaling P, Pierce C, Karchmer D, et al. Atrial fibrillation complicating lung cancer resection. *J Thorac Cardiovasc Surg.* (2005) 130:438–44. doi: 10.1016/j.jtcvs.2005.02.010

24. Muranishi Y, Sonobe M, Menju T, Aoyama A, Chen-Yoshikawa T, Sato T, et al. Atrial fibrillation after lung cancer surgery: incidence, severity, and risk factors. *Surg Today.* (2017) 47:252–8. doi: 10.1007/s00595-016-1380-y

25. Procter L, Davenport D, Bernard A, Zwischenberger J. General surgical operative duration is associated with increased risk-adjusted infectious complication rates and length of hospital stay. *J Am Coll Surg.* (2010) 210:60–5.e1–2. doi: 10.1016/j.jamcollsurg.2009.09.034

26. Nusinovici S, Tham Y, Chak Yan M, Wei Ting D, Li J, Sabanayagam C, et al. Logistic regression was as good as machine learning for predicting major chronic diseases. *J Clin Epidemiol.* (2020) 122:56–69. doi: 10.1016/j.jclinepi.2020.03.002

27. Butt J, Olesen J, Gundlund A, Kumler T, Olsen P, Havers-Borgersen E, et al. Long-term thromboembolic risk in patients with postoperative atrial fibrillation after left-sided heart valve surgery. *JAMA Cardiol.* (2019) 4:1139–47. doi: 10.1001/jamacardio.2019.3649

frontiers | Frontiers in Physiology

TYPE Original Research
PUBLISHED 30 January 2023
DOI 10.3389/fphys.2023.1057700

OPEN ACCESS

EDITED BY
Juan Pablo Martínez,
University of Zaragoza, Spain

REVIEWED BY
Masateru Takigawa,
Tokyo Medical and Dental University, Japan
Richard H. Clayton,
The University of Sheffield, United Kingdom

*CORRESPONDENCE
Carlos Fambuena-Santos,
carfamsa@upvnet.upv.es

SPECIALTY SECTION
This article was submitted to Cardiac Electrophysiology, a section of the journal Frontiers in Physiology

RECEIVED 29 September 2022
ACCEPTED 10 January 2023
PUBLISHED 30 January 2023

CITATION
Fambuena-Santos C, Hernández-Romero I, Molero R, Atienza F, Climent AM and Guillem MS (2023), AF driver detection in pulmonary vein area by electropcardiographic imaging: Relation with a favorable outcome of pulmonary vein isolation.
Front. Physiol. 14:1057700.
doi: 10.3389/fphys.2023.1057700

AF driver detection in pulmonary vein area by electropcardiographic imaging: Relation with a favorable outcome of pulmonary vein isolation

Carlos Fambuena-Santos[1]*, Ismael Hernández-Romero[1], Rubén Molero[1], Felipe Atienza[2,3], Andreu M. Climent[1] and M S. Guillem[1]

[1]COR Laboratory, ITACA Institute, Universitat Politècnica de València, Valencia, Spain, [2]Department of Cardiology, Hospital General Universitario Gregorio Marañón, Instituto de Investigación Sanitaria Gregorio Marañón (IISGM), Madrid, Spain, [3]Centro de Investigación Biomédica en Red de Enfermedades Cardiovasculares (CIBERCV), Madrid, Spain

Pulmonary vein isolation (PVI) is the most successful treatment for atrial fibrillation (AF) nowadays. However, not all AF patients benefit from PVI. In this study, we evaluate the use of ECGI to identify reentries and relate rotor density in the pulmonary vein (PV) area as an indicator of PVI outcome. Rotor maps were computed in a set of 29 AF patients using a new rotor detection algorithm. The relationship between the distribution of reentrant activity and the clinical outcome after PVI was studied. The number of rotors and proportion of PSs in different atrial regions were computed and compared retrospectively in two groups of patients: patients that remained in sinus rhythm 6 months after PVI and patients with arrhythmia recurrence. The total number of rotors obtained was higher in patients returning to arrhythmia after the ablation (4.31 $\pm$ 2.77 vs. 3.58 $\pm$ 2.67%, p = 0.018). However, a significantly higher concentration of PSs in the pulmonary veins was found in patients that remained in sinus rhythm (10.20 $\pm$ 12.40% vs. 5.19 $\pm$ 9.13%, p = 0.011) 6 months after PVI. The results obtained show a direct relationship between the expected AF mechanism and the electrophysiological parameters provided by ECGI, suggesting that this technology offers relevant information to predict the clinical outcome after PVI in AF patients.

KEYWORDS

atrial fibillation, ECGI, pulmonary vein isolation, clinical outcome, rotors

1 Introduction

Pulmonary vein isolation (PVI) is the most successful treatment for atrial fibrillation (AF) nowadays. Disoite this, 62 months after the intervention only 59% of patients remain free from AF (Kis et al., 2017). The main reason explaining this poor management of AF is the lack of understanding behind the mechanisms that originate and maintain this arrhythmia.

In the last years, many theories supporting localized drivers as the cause of atrial fibrillation (AF) have gained relevance (Guillem et al., 2016; Narayan et al., 2012). Rotors, or functional reentries, are a well-described type of local driver consisting in rotational activation patterns that perpetuate an asynchronous electrical propagation in the heart. Rotors have been theorized and implemented in many *in silico* models (Rodrigo et al., 2017a), as well as observed *in vitro*. However, their

TABLE 1 Description of the population used in the study.

		All patients (n = 29)	Non-recurrence (n = 15)	Recurrence (n = 14)
Male (%)		7 (24.14%)	6 (40.00%)	1 (7.14%)
Age (Years)		62.63 ± 14.26	58.13 ± 15.06	64.57 ± 13.18
Paroxysmal AF (%)		16	11 (73.33%)	5 (35.71%)
Valvuloplasty (%)		14	8 (53.33%)	6 (42.86%)
Medical Therapy	Beta-blockers	1	1	0
	Flecainide	1	1	0
	Amiodarone	6	3	3
Medical Therapy After Ablation	Beta-blockers	15	5	10
	Flecainide	2	2	0
	Amiodarone	12	5	7
Patients with Previous Ablation		27 (93.10%)	14 (93.33%)	13 (92.86%)
Ablations Per Patient		1.14 ± 0.51	1.13 ± 0.52	1.14 ± 0.53

identification in the clinics remains elusive. Several factors may hamper rotor identification in the EP lab, like their movement in the atria or the presence of transmural reentrant circuits. However, the main limitation to be faced nowadays is technological. Current sequential mapping systems do not allow for global characterization of the atria, making the identification and tracking of rotors very challenging.

Electrocardiographic Imaging (ECGI) is a non-invasive mapping technology that allows panoramic visualization of the atria, posing it as an interesting tool to understand the presence of rotors in the pulmonary veins (PPVV). This understanding may help to stratify non-invasively patients that may benefit from PVI from those who will return to arrhythmia after the intervention, saving resources and minimizing unnecessary risks for some patients. The most extended methodology used nowadays to localize rotors using ECGI is based on the detection of phase singularities (PSs) in phase maps (Li et al., 2020; Rodrigo et al., 2017b; Molero et al., 2021). Many strategies have been developed so far to identify PSs automatically (Li et al., 2020). However, the lack of standardized postprocessing techniques to identify PSs in phase maps obtained from ECGI and technological limitations associated to ECGI validation have raised skepticism on the use of phase maps and confusion about the electrophysiological interpretation of phase singularities (PS) (Podziemski et al., 2018; Cluitmans et al., 2018).

In this context, the main objective of this article is to develop and validate a methodology to identify reentries in AF patients using ECGI data. Additionally, the capacity of ECGI to find differences between patients in which the pulmonary veins region plays a relevant role in the maintenance of AF, and those in whom other atrial zones could be responsible of AF maintenance was studied.

2 Materials and methods

2.1 Study population

The data acquisition protocol used in this study was approved by the ethics committee of Hospital Gregorio Marañón, Madrid, Spain (reference 475/14) and all patients provided informed consent of the procedure. A total of 29 AF patients participated in the study with a subpopulation of 7 men and 22 women (mean age of 62.63 ± 14.26). The number of patients presenting paroxysmal and persistent AF numbered 16 and 13, respectively. Antiarrhythmic drugs were taken by a set of 6 patients before PVI procedure (for more details, see Table 1).

Patients were split into 2 groups attending to their clinical outcome 6 months after PVI. Those who remained in sinus rhythm were labelled as "Non-recurrence" patients (n = 15) and those that presented any kind of arrhythmia (i.e., AF or Atrial flutter) were classified as "recurrence" (n = 14). Clinical validation of the cardiac rhythms 6 months after the procedure was performed with a standard 12 lead ECG and quality-of-life questionnaires (Molero et al., 2021).

2.2 Ablation and electroanatomical mapping

Circumferential PVI was performed in all 29 patients point by point using irrigated catheters (Cool-Flex/TactiCath/Sapphire-Blue, St. Jude Medical). Energies ranging 25–35 W were delivered *via* conventional ablation in both pairs of pulmonary veins. Additionally, FIRMap 64-poles mapping catheters were consecutively placed in the right and left atrium for 3-dimensional electroanatomic imaging (NavX, St. Jude Medical). Cather placement was achieved *via* vein access through the femoral vein reaching the right atrium and later to the left atrium through transeptal punction. In patients arriving in sinus rhythm electrical burst pacing was used to induce AF (Rodrigo et al., 2020).

2.3 Data acquisition and preprocessing

Body Surface Potential Maps (BSPM) were recorded in all the patients during AF right before circumferential PVI. A set of 57 electrodes were employed to record the signals. The acquisition and preprocessing protocols employed in this study were already presented previously (Molero et al., 2021; Rodrigo et al., 2020). As an overview, BSPM signals were recorded with a 1 kHz sampling

frequency and filtered using a 0.05–500 Hz bandpass filter. The geometry of the torso and electrode positions were determined using photogrammetry and the anatomy of the atria was segmented from MRI/CT images. A total of 57 segments with similar durations (4.06 ± 0.311 s) were included in the analysis. Additionally, other 57 segments were recorded during adenosine injection in order to compare the clinical results obtained from adenosine-free signals (see Supplementary Material S1). Regarding signal processing, the baseline was removed using a low-frequency polynomial fitting. The signal was then filtered using a 10th Butterworth band-pass filter with cut-off frequencies of 2 and 45 Hz. In order to remove the ventricular activity, QRS cancellation was performed following a temporal PCA separation approach (Castells et al., 2005). The inverse problem was then computed using the boundary element method formulation, and zero-order Tikhonov regularization with L-curve optimization methods for matrix inversion. Once the 3D voltage maps were obtained, these were transformed into 2D squared images using a Teichmüller external mapping approach, guaranteeing a uniform conformal distortion of the 3D point cloud surface (Meng et al., 2016) (See Supplementary Material S1 for more information). Finally, phase maps were computed from 2D voltage maps by means of the Hilbert transform.

2.4 Rotors and phase singularities detection

The details on the proposed rotor detection algorithm are explained in Supplementary Material S1 but the general workflow of the algorithm is described in this section. The first stage on the detection algorithm consists on the identification of the center of rotation of rotors, namely phase singularities (PSs), on a given time instant. In this study, PS are defined as locations in the atria surrounded by the whole activation cycle, or equivalently, the full range of phases [-π,π] obtained by applying the Hilbert transform on inverse computed electrograms. PSs are identified by the topological charge (Bray and Wikswo, 2002). Then, PSs non-complying with a gradual spatial progression of phases between -π and π in their surroundings (Rodrigo et al., 2017b) were discarded. After having identified PSs we then connect them spatiotemporally into rotors and through filaments in order to both discard transient PSs that appear for a short period of time most likely corresponding to changes in direction of the propagation front- and connect PSs whose tracking is transiently lost. Rotors filaments were then dilated using a prism-shaped kernel in the direction of the trajectory, and skeletonized in order to cluster and identify the trajectories. Finally, the number of turns is quantified in each rotor and PSs belonging rotors that spin for less than a given number of turns are discarded for further analysis.

2.5 Rotor metrics and clinical outcome study

Two different parameters were calculated to study the relationship between the detected reentrant activity, and the clinical outcome of the patients after PVI. The first parameter was the number of rotors or clusters in the whole atria per unit time. The second set of parameters was the percentage of PSs at 9 different atrial regions. This percentage was calculated as the number of PSs detected at a particular atrial region over the total number of PS detected. After clustering PSs into rotors, the mentioned metrics were obtained in two different conditions: Considering all the detected rotors and PS, or keeping only those rotors (and correspondent PSs) that spin for at least 1 turn. These two implementations were applied to recordings obtained with and without adenosine injection. Finally, Mann-Whitney U test was used in order to compare the number of rotors detected in 'Non-recurrence' and "Recurrence" groups. The same test was used to study statistical differences in the percentage of PS obtained in the 9 different atrial regions. An independent test was used to evaluate differences between 'Recurrence' and "Non-recurrence" groups in each region using only values obtained from different recordings, assuring in this way, independency between samples.

2.6 Validation dataset

The proposed methodology for rotor detection in ECGI data was evaluated both, using recordings from patients and simulated data. Specifically, two mathematical models with well-defined location of reentries were employed. To identify the reentries maintaining the arrhythmia, we performed a virtual ablation in the middle of the fibrillatory episode. Then we solved the inverse problem and applied the rotor detections algorithm presented in this study to compare the pre- and post-ablation scenarios (see Supplementary Material S1 for further details on the simulations).

Regarding the validation in patients, a dataset of 9 ECGI segments where reentrant patterns could be visually identified were selected from the main database of patients. The algorithm was applied in these recordings in order to detect rotors, which were blindly labelled in the validation dataset according to two conditions: rotors spin for at least 1 turn and there was linear progression of the phase around the detected singularities. These conditions were visually checked by the operator labelling the data. The detected and manually labelled set of detections were then compared.

2.7 Evaluation metrics

The performance of the algorithm was evaluated using the precision (P) and recall (R), defined in Eqs 1, 2:

$$P = \frac{TP}{TP + FP} \tag{1}$$

$$R = \frac{TP}{TP + FN} \tag{2}$$

Where TP are the true positive detections, FP the false positive and FN the false negative. Precision (P) is a measure of how much the proposed algorithm overestimates the presence of PSs. On the other hand, recall (R) measures how often PSs are undetected. All the PSs detected within a tolerance distance of 5 mm from a manually labelled PS were considered true positives. In contrast, false positives were annotated when more than one PS was detected in the 5 mm surrounding area of a labelled PS. False negatives were identified as the absence of any detected PS withing a 5 mm distance from a labelled PS. In order to include the precision and recall information in only one parameter, the Fβ score was also computed [5] (see Eq. 3). This parameter allows to weight the relevance of the precision and recall in the final score through the constant β. In this study the same value presented in the literature of β = 2 was used for better comparison.

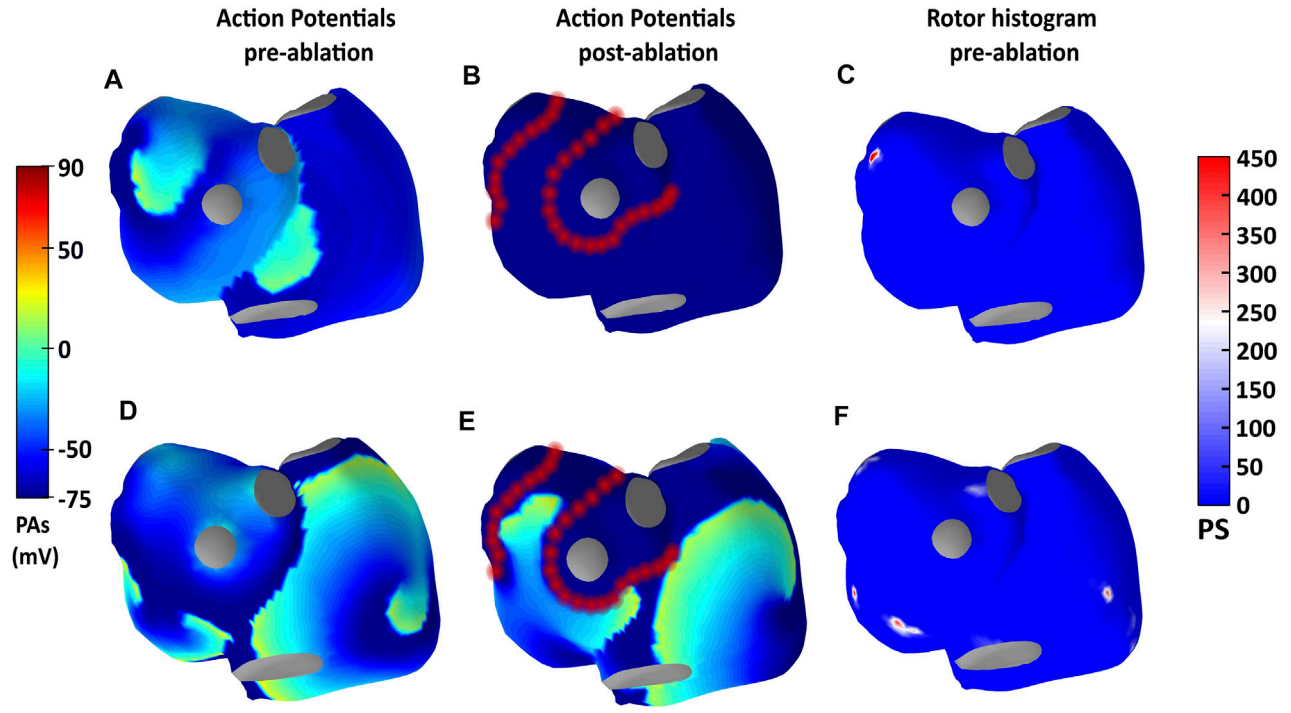

FIGURE 1
Information about simulations 1 and 2 is presented in the first and second panel rows. Panels **(A, D)** show the simulated action potentials in an instant previous to the ablation, while panels **(B, E)** show the action potentials after ablation. In **(C, F)**, ECGI-derived rotor histograms of the pre-ablation periods are shown.

$$F_\beta = \left(1+\beta^2\right)\cdot\frac{P\cdot R}{\beta^2\cdot P+R} \tag{3}$$

Finally, the regional accuracy of the algorithm was also evaluated. For that, the atrial geometries of all the patients were divided into 9 different regions depicted in Figure 3. The number of PS manually labelled in the validation data set was then compared to the number of PS detected by the algorithm in every region. The mean absolute error between these two quantities and the relative error were calculated. This last was defined as the ratio between the mean absolute error and the mean number of PSs labelled in each region.

3 Results

3.1 Validation of the rotor detection algorithm in simulations

The simulated AF episodes are illustrated in Figure 1. In the first AF episode (Figures 1A–C), a reentry driving the arrhythmia was localized near the left pair of PPVVs. In Figures 1A, B the transmembrane potentials of two different pre- and post-ablation instants in this episode are presented. The reentry was identified in ECGI signals by using our rotor detection algorithm after forward and inverse propagations. The rotor histograms summarizing the whole reentrant activity in the pre-ablation period is shown in Figure 1B. We can observe how most of the reentrant activity is located near the left pair of pulmonary veins. A virtual ablation in the PPVV area was able to stop the arrhythmia (Figure 1C). In contrast, in the second episode (Figures D–F) reentrant activity is spread throughout different atrial locations far from the PPVV. When applying PVI, the electrical activity is prevented from entering in the PPVV area and the dynamics of the arrhythmia are modified (see Figure 1F). However, PVI is not able to eliminate rotors present in the right atrial posterior wall, leaving some pro-arrhythmic mechanisms intact outside the PPVV and, thus the arrhythmia is not terminated.

3.2 Validation of the rotor detection algorithm in patients

In Figure 2A the global recall, precision and F-score values obtained for all the recordings in the validation dataset are represented. The mean F-score, precision and recall values of all these recordings were 0.84, 0.84 and 0.85 respectively. The lowest recall was found in recording 3 with a value of 0.66, and the lowest precision was found in the recording number 5 with also a value of 0.66. In Figures 2B, C a comparison of the rotor histograms obtained in two different recordings are presented: recording 9 with a high recall value (0.87), and recording 3 with a low value (0.66). In this example, it is shown how, in spite of missing some of the reentry areas (mostly in the right pair of PPVV), a map with very similar locations of the main reentrant activity is obtained.

The accuracy of the algorithm was also evaluated regionally. The proposed division for the atria is shown in Figures 3A, B. Regarding the local accuracy in each of these regions, the mean number of detected and annotated PSs along with the mean absolute error

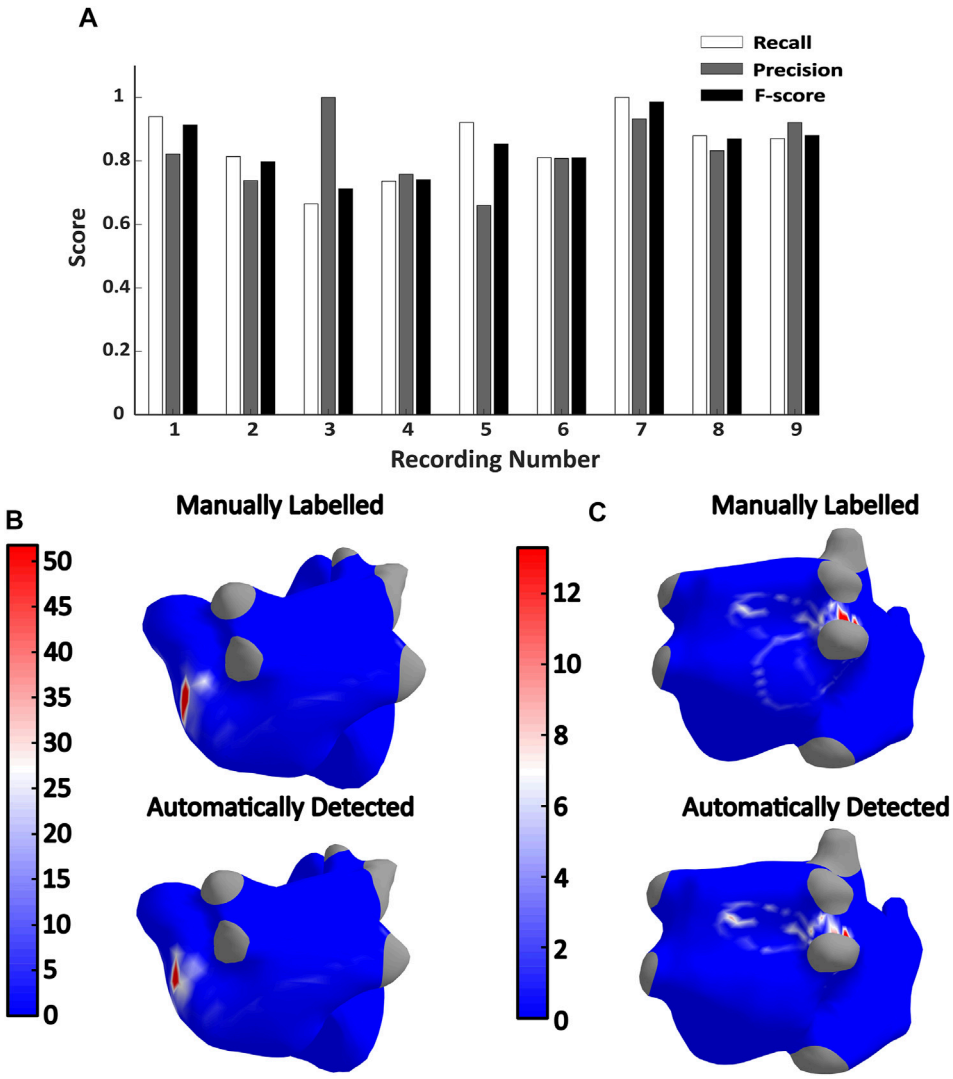

FIGURE 2
(A) Recall, precision and F-score values obtained in the validation dataset. **(B,C)**, Manually labelled and automatically detected rotor histograms obtained from recordings 9 (top) and 3 (bottom) respectively. The recall, precision and F-score values calculated in recording 9 were 0.87, 0.92, and 0.87 while the recall, precision and F-score values of recording 3 are 0.66, 1, and 0.7 respectively.

between these two magnitudes are presented in Figure 3E. In general, it can be observed a good correspondence between the annotated and detected PSs with a mean absolute error of 7.9 PS across all the regions. The areas with higher absolute errors were the RB (23,22 PSs) followed by the LB (18,11) which are also the largest regions in the proposed atrial segmentation. Regarding the relative error, it ranged between 0% and 67% with a mean value of 16.11%. The SVC is the atrial structure with lower relative error and RAPP the one with the largest. The distribution of the relative errors in the rest of atrial regions is presented in Figures 3C, D.

3.3 Relation between rotors and PVI outcome

In Figure 4 the number of rotors per second obtained in the whole atrium is presented for both studied groups: patients that remained in sinus rhythm and patients that returned to arrythmia 6 months after PVI (AF-recurrence). The number of rotors was quantified in two different ways: including all the rotors detected (any turns, Figure 4A) and discarding those rotors spinning for less than 1 turn (Figure 4B). Patients with an unsuccessful PVI had more rotors in the whole atria than patients remaining in sinus rhythm 6 months after the ablation. This difference was more noticeable when all the rotors detected were considered in the analysis, median values 54.83 ± 10.43 vs. 70.92 ± 27.77 ($p < 0.01$, Figure 4A). However, when keeping only rotors that spin for at least 1 turn, the difference is still preserved although the significance lowers down (3.59 ± 2.67 vs. 4.31 ± 2.78, $p < 0.05$, Figure 5B).

In both groups, higher concentrations of PS are found in the regions located in the left atria. This result is in line with the general belief that most of the initiation mechanisms of AF are present in the left atrium. In a regional level, a larger proportion of PS in the PPVV was always found in the non-recurrence group. This last finding is expected given the assumption that the mechanisms driving AF are

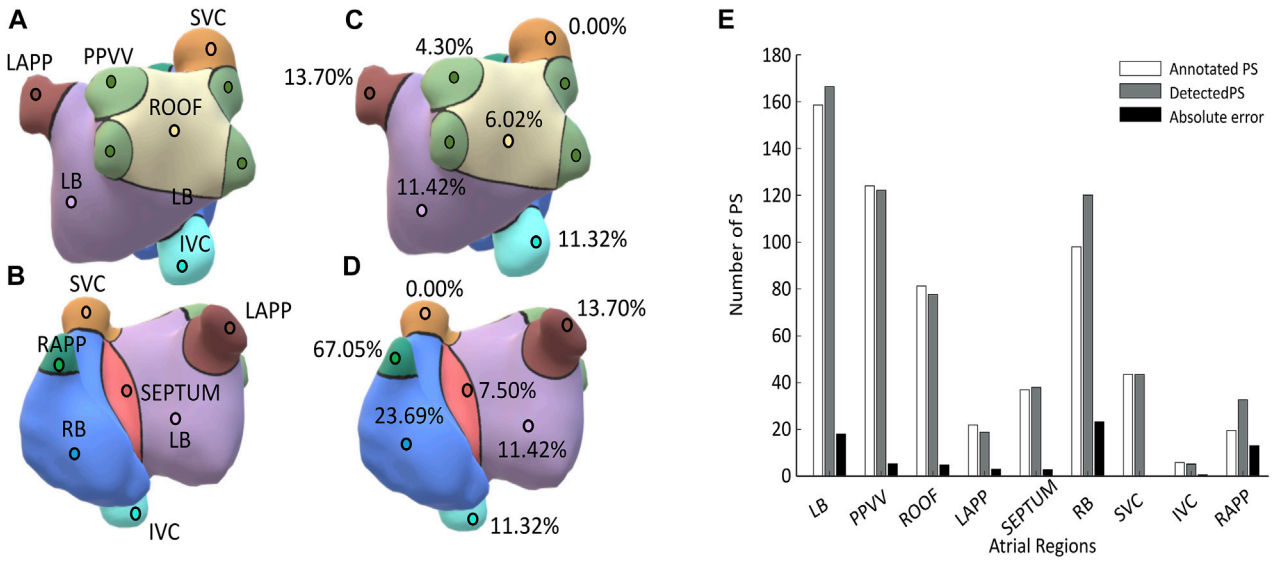

FIGURE 3
(A) and **(B)** Illustration of the regional anatomical division of the atria; **(C)** and **(D)** relative errors obtained in each of the atrial regions; **(E)** Mean number of annotated and detected PSs in different atrial regions across the validation dataset. The mean absolute error between these two magnitudes is also presented in black.

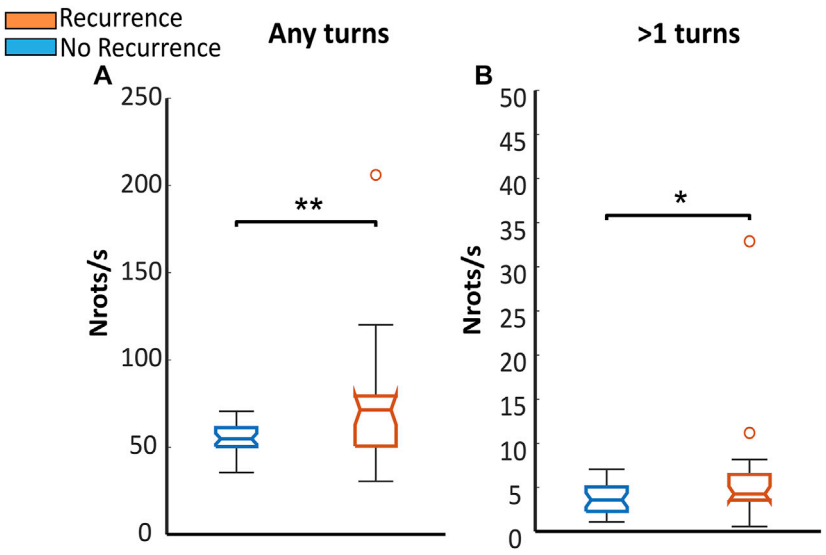

FIGURE 4
Number of rotors obtained in all the patients: In blue are represented patients staying in sinus rhythm (No recurrence) and in orange patients returning to arrhythmia 6 months after PVI (Recurrence). The number of rotors was calculated in the whole atria in two different scenarios regarding the number of turns used to filter the PS: **(A)** Number of rotors obtained without any turn filtering; **(B)** Number of rotors spinning for at least one turn.

more frequently located in the PPVV in patients with a successful PVI. This difference is presented in Figure 5B for stable reentries, that is, reentries spinning for at least 1 turn (10.20 ± 12.40 vs. 5.19 ± 9.13, $p > 0.05$), but also in Figure 5A where all the PS detected are included in the analysis. The statistical differences obtained in the different atrial regions are presented in Figure 5C, where it is shown that the PPVV and LAPP areas are the only areas presenting p-values lower than 0.05.

When considering all the PSs and not only those completing a full rotation, sudden wavefront direction changes due to conduction block areas, wavefront collisions or partially detected transmural reentries may be detected as PS. These factors may be indicators of the complexity of the arrhythmia and the underlying atrial substrate. However, also far field artefacts may be detected as PSs and included in the analysis. Under these conditions, it is interesting to remark that the same regions presenting statistically significant differences in the

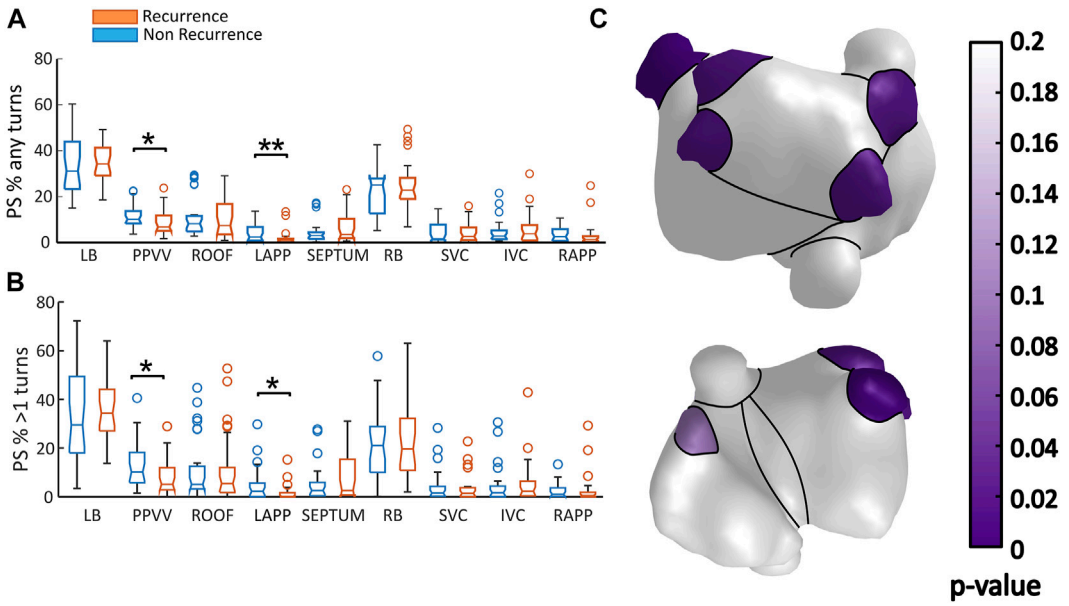

FIGURE 5
(A,B) Proportion of PSs per second detected in different regions in each studied group: in blue is presented the data from patients that remained in sinus rhythm 6 months after ablation (Non-recurrence), and in orange patients that returned to arrhythmia (Recurrence). In panel **(A)**, are presented the results obtained when all the reentries are considered in the analysis. In panel **(B)**, the same results are shown, when only the reentries lasting for more than 1 turn. The distribution of the statistical *p*/values obtained for each regions are presented din panel **(C)**.

proportion of PS remained, including the PPVV (10.13 ± 5.47% vs. 6.81 ± 6.71%, $p < 0.05$) and LAPP, being the proportion of PS larger again in the non-recurrence group of patients.

4 Discussion

In this study, a rotor detection algorithm was presented and validated. Additionally, a higher prevalence of PS prevalence in the PPVV area in patients with a favorable outcome after PVI was found with this algorithm. This finding suggests that the identified reentrant activity is linked with the mechanism sustaining AF.

4.1 Algorithm evaluation

In terms of global performance, the use of simulations showed a precise localization of the main reentrant activity during AF as well as a mechanistic explanation on why PVI works in the first simulation, with a localized reentry in the PPVV area, and not in the second, with multiple spread drivers. Regarding labelled data coming from AF patients, it was found that the F-score value obtained (0.84) outperforms other algorithms presented in the literature. A closely related study in this regard is (Li et al., 2020), where the same definitions of precision, recall and F-score values were used. In this study, 4 different rotor detection algorithms were tested in 2D geometries obtaining F-scores values ranging between 0.527 and 0.831. Similarly, these algorithms were validated in non-invasive ECGI phase maps obtained from AF patients, where the presence of rotors was manually labelled by an operator.

The performance of our algorithm was also evaluated locally in 9 different regions. The mean discrepancy present in all areas between the detected and annotated PSs was 16.11%. An abnormally high relative error in the RAPP region (67%) was observed. The origin of this high error must be related to the low number of PSs detected in the RAPP. This factor increases the effect of miss detections in the relative error value.

4.2 ECGI in the detection of AF sources

The existence of well localized mechanism driving AF has been reported by means of invasive and non-invasive mapping techniques (Narayan et al., 2012; Haïssaguerre et al., 2006; Gao et al., 2019). This finding has justified the use of personalized driver-specific ablation strategies to terminate AF. In this line, Narayan et al. (2012) showed that focal impulse and rotor modulation ablation (FIRM), in combination with PVI, had a higher successful rate in long-term AF termination than standard PVI alone. Haissaguerre et al. (2014), also tried a similar ablation strategy, but this time obtaining the cumulative maps of focal and reentrant activity from ECGI mapping. They guided ablation in 103 patients with persistent AF demonstrating that the mean ablation time can be reduced guiding the procedure with non-invasive ECGI mapping. Furthermore, a higher degree of fractionation in reentry areas identified with ECGI was found, providing clinical evidence of the detections.

In spite of the clinical evidence showing the potential advantages of a personalized ablation strategies, the positive results obtained in the mentioned studies have not been reproducible. A possible reason for this may be the lack of robustness of the overall approach and a dependence on the operator expertise to determine what is a reentry.

In our pipeline, we include a full methodology that allows to remove the human factor by automatically computing the number of turns of the rotors and filtering the PSs with no linear progression of phases in their surroundings.

4.3 PS detection and rotor tracking with ECGI

We have already developed automatic PS detection methods for ECGI in the past. Specifically, Rodrigo et al. (2017b), Rodrigo et al. (2017a) proposed a methodology to detect reentries directly on 3D atrial meshes. There, PS were detected at nodes in which the full range of phases [-π,π] was observed in their surroundings. Additionally, the spatial progression of the phases was checked to be 'linear' around each PS. The resultant PS were then tracked to obtain filaments or rotors by imposing a radius distance criterium. This methodology was validated in AF simulations.

Other studies have proposed to detect reentries by means of local activation time (LAT) mapping (Vandersickel et al., 2019; Rogers et al., 1999). However, this approach is hardly transferable to ECGI during AF since there is no consistent method for detecting LATs in ECGI signals during AF. Some challenges causing the lack of standard methods are the inherent spatial smoothing present on ECGI electrograms and the presence of remaining far-field artifacts leading to loss of tracking of PSs that needs to be corrected. In this context, phase mapping has been postulated as an alternative way to detect reentries in ECGI (Haissaguerre et al., 2013; Dhillon et al., 2021). Phases provide equivalent information about the electrical propagation encoded in the low-frequency content of the signals with no need for LAT detection. Given the exposed advantage, we decided to stick to a phase-mapping based approach, but updating our methodology according to the results obtained in (Li et al., 2020). In this work, algorithms based on topological charge, a metric closely related to the curl of the electrical propagation, presented the highest performance for PS detection. In addition, around the PSs obtained from topological charge, a checkup of linearity in the surrounding phases was included. This feature overcomes the presence of false positive PS at locations with complex or fractionated signals (Rodrigo et al., 2017b). Additionally, we perform PS detections in a 2D domain in order to speed up the calculations. For that, we use a transformation that assures a homogeneous distribution of nodes in the atria, and provides a direct transformation of the data to a 2D grid, where we can efficiently track rotors. Furthermore, having a homogeneous disposition of nodes is also very convenient in some steps of our methodology like phase linearity checking around PSs, or counting the number of turns per rotor. Other 2D-3D transformations, such as the universal atrial coordinates (UAC) system have been proposed in the past (Roney et al., 2019). However, our methodology is better suited for our purpose than UAC. First, our transformation is fully automatic and does not require from manual landmark placement. Additionally, UAC was conceived for data transferring between different patients and does not result in a uniform grid with preservation of distances in the original mesh.

The methodology for rotor tracking was also updated in this study. It consists in combining neighbor voxels containing a PS into filaments. The methodology is completely based in image processing operations such as voxel dilation and skeletonization which present two main advantages with respect to the previous approach. The first one comes from the efficiency of convolutional operations such as dilation or skeletonization performed on image stacks. The second one is about specificity. Our tracking algorithm is more specific when combining PS into rotors than imposing a radius around each PS in space. This is because a prism-shaped dilation kernel is applied following the direction of the trajectory of the rotor at each voxel, preventing the algorithm from combing independent filaments together that eventually get too close in space. A similar methodology was applied in (Clayton and Holden, 2004), where filaments in simulated ventricular fibrillation episodes were created by linking together voxels in a 3D space. In contrast with our algorithm, the method used in Clayton et al. uses a grassfire algorithm instead of dilation and skeletonization operations to obtain filaments. This approach has the advantage that no kernel needs to be specified like in our approach, however the computational time needed to run it is higher. Finally, another important difference between our method and the one employed by Clayton et al. is that we count the number of turns of each rotor by taking into account the surround phases of the filament. This last step allows us to filter out rotors with a low number of turns.

4.4 Non-invasive atrial substrate evaluation in AF patients

The results obtained in this study suggest that ECGI provides relevant information about the functional state of the atria in AF patients. In a prior study we already related the stability of rotor-derived metrics with ablation outcome (Molero et al., 2021) while we could not relate the location of these rotors with the success of PVI, in the same line as other studies (Dhillon et al., 2022). In this study we have developed a new methodology for rotor tracking that allows for a more restrictive definition of a rotor, specifically suited for analysis of ECGI data, a context with low spatial resolution and loss of tracking due to remaining far-field components. In addition to the methodological differences for PS detection and rotor tracking explained in the previous section, we also explored regional differences in the presence of reentries. For that purpose, we divided the atria in 9 different areas where the prevalence of reentries was estimated as the percentage of PS. Additionally, we computed a different global parameter, the total number of rotors detected in the atria per unit time.

Regarding the number of rotors per second found in the atria, a larger number was detected in the recurrence group, reflecting a possible higher complexity of the electrical activation patterns in patients with poor PVI outcome. This finding is in concordance with the reproducibility results obtained by Molero et al. A possible explanation supporting this findings is the detection of changes in the direction of wavefronts as PS. Relative to this, Podziemski et al. (2018) stablished a relationship between PSs obtained from phase maps and spots of conduction block. In this way, recurrence patients with a higher prevalence of complex atrial substrate may have more conduction block spots that produce this effect. Another explanation is the detection of hidden transmural rotors where only part of the rotor cycle is visible in the epicardium. In this regard, Clayton and Holden. (2004) observed in *in silico* simulations of ventricular fibrillation (VF) that only 65% of reentries touched the epicardium and most of them for less than one cycle.

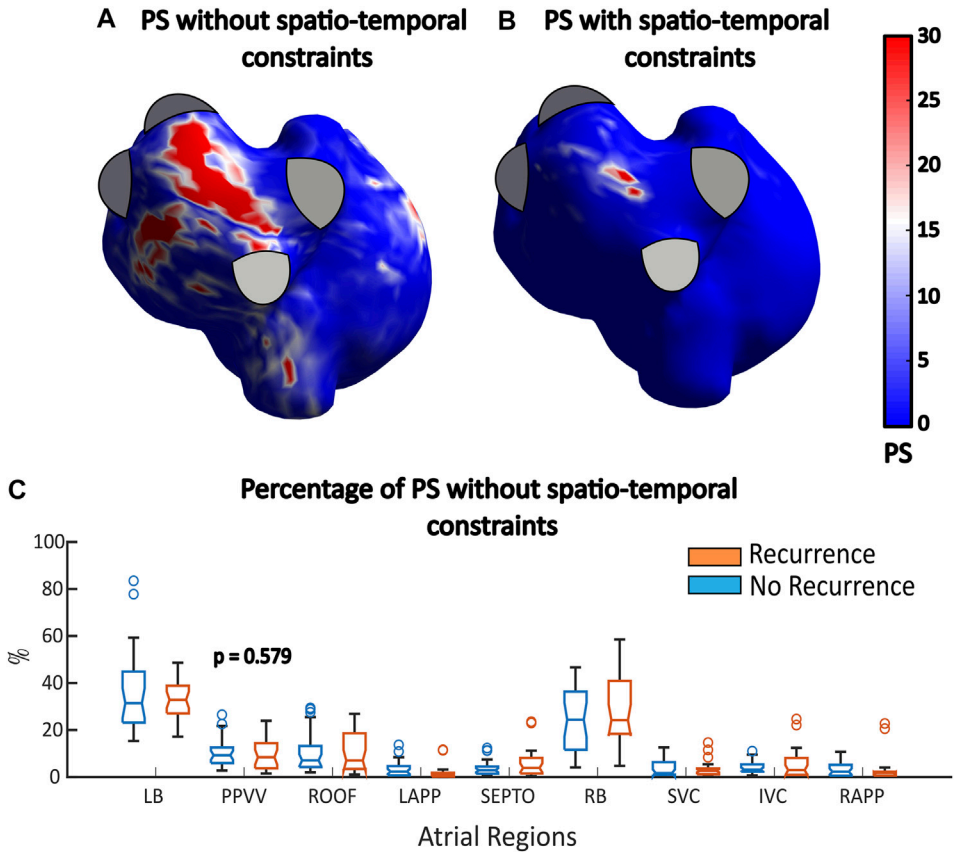

FIGURE 6
(A,B) PS histograms with and without filtering. **(C)** Percentage of PSs found in all the different atrial regions when no filtering strategies are applied. No statistically significant differences are observed.

In addition to factors that are actually related to the dynamics and complexity of the arrhythmia, the presence of far field artefacts and the limited spatial resolution reduce the accuracy of ECGI to provide the exact location of reentries. In this scenario, postprocessing algorithms employed on top to the ECGI signals are of great importance to detect rotors robustly. Indeed, some studies quantifying the amount reentries in the PPVV have found a great overlap between recurrence and non-recurrence AF patients using CardioInsight system (Dhillon et al., 2022; Gao et al., 2019), In our study, we also observed how the number of rotors overlapped between the studied groups. However, with our methodology, in contrast with the previous ones, we obtained statistically significant differences in the number of rotors and the proportion of phase singularities in the PPVV. In Figure 6 it can be observed how when keeping only PS with a linear progression of phases in their surroundings, the areas showing a high prevalence of reentries shrinks down. In this example, red areas of high PS prevalence outside the roof of the atria are removed, keeping only a small core. This filtering has therefore an effect on the percentage of PS calculated in the different areas. When comparing these percentages in the recurrence and non-recurrence group of patients with no filtering strategy, we see how all the statistical differences observed with our post-processing algorithm disappear, with a p = 0.579 in the PPVV. This observation highlights the importance of the methodology to observe differences in the reentrant activity when comparing recurrence and non-recurrence AF patients after PVI.

Finally, a higher prevalence of PSs in the PPVV area was quantified in patients with a favorable outcome after PVI. According to our results, the application of a threshold of one turn enhances the differences in the prevalence of PSs in the PPVV area as compared to other regions. In this regard, it was observed how the significant difference found in the LAPP obtained when including all the PS in the analysis (no turn filtering), was reduced when only PS belonging to long-lasting rotors (1 turn or more) are included in the analysis. A possible explanation for this reduction is the role of the LAPP as an anatomical obstacle, leading to direction changes in the propagation of wavefronts that do not cover an entire turn. In this way, the application of a threshold of 1 turn seems to reduce the relevance of this secondary patterns in the analysis, enhancing the importance of the mechanisms present in the PPVV. Additionally, this analysis was also performed during adenosine injection (see Supplementary Material S1). Adenosine is a drug that stops the ventricular activity, providing a more favorable scenario for the inverse problem. Again, similar tendences and significant differences in the proportion of phase singularities were found between the studied groups. The coherence in the results obtained under different filtering and adenosine conditions suggest that the presented approach is robust against far field artefacts coming from the ventricular activity.

4.5 Clinical implications

The efficacy of PVI in AF patients decreases as the disease progresses due to the higher complexity and variety of mechanisms involved in the arrhythmia (Haïssaguerre et al., 2006; Haissaguerre et al., 2014). This progression leads to a lower success of PVI in patients with an advanced disease. In this study, we observed that the prevalence of reentries measured as singularity points in non-invasive phase mapping is a predictive factor of the clinical outcome of patients undergoing PVI. Therefore, this finding can help clinicians to stratify patients non-invasively before any electrophysiological study, saving in this way resources and reducing risks for patients who will not benefit from PVI.

4.6 Limitations and future work

Some of the characteristics of the dataset employed, such as the large prevalence of previous ablations or valvuloplasties are very particular of our population. Additionally, due to the lack of a standardized gold-standard in rotor detection with ECGI technology, we have opted for manually labelling ECGI data, which may somehow bias our results. In the future, we plan to continue the validation of the algorithm presented in this study, by comparing the locations of reentries to low voltage areas obtained with electroanatomical mapping.

5 Conclusion

In this study we have shown that ECGI allows detecting the spatial dominance of the reentrant activity at different atrial regions during AF episodes. A higher concentration of PSs in the PPVV was found in those patients that remained in sinus rhythm 6 months after PVI, showing a direct relationship between the expected AF mechanism and the electrophysiological parameters provided by ECGI.

The results of this study may help in the future to predict which patients will benefit from a PVI procedure. Furthermore, we have shown that the approach employed is robust and valid for non-invasive applications like personal AF studies or patient stratification.

Data availability statement

The original contributions presented in the study are included in the article/Supplementary Material, further inquiries can be directed to the corresponding author.

Ethics statement

The studies involving human participants were reviewed and approved by Ethics committee of Hospital Gregorio Marañón, Madrid, Spain (reference 475/14). The patients/participants provided their written informed consent to participate in this study.

Author contributions

CF-S: concept/design study, data analysis/interpretation of results and drafting manuscript. IH-R: concept/design study and interpretation of results. RM: Data collection and database creation. FA: EP studies and ablation procedures, concept/design study, interpretation of results, and critical revision of the manuscript. AC: concept/design study and critical revision of the manuscript. MG: concept/design study and critical revision of the manuscript.

Funding

This project has received funding from the European Union's Horizon 2020 research and innovation program under the Marie Skłodowska-Curie grant agreement No 860974, PersonalizeAF, Ministerio de Ciencia e Innovación (supported by FEDER Fondo Europeo de Desarrollo Regional PI17/01106, PEJ2018-003617, and RYC2018-024346-I), EIT Health (SAVE-COR Activity code 220385, EIT Health is supported by EIT, a body of the European Union), Generalitat Valenciana Conselleria d'Educació, Investigació, Cultura i Esport (ACIF/2020/265) and Spanish Agencia Estatal de Investigación (AEI), part of the Ministerio de Ciencia e Innovación, reference PID2020-119364RB-I00. *This publication reflects only the author's view and that the Agency is not responsible for any use that may be made of the information it contains.

Conflict of interest

AC, MG, IH-R, and FA hold equity in Corify Care. AC has received honoraria from Corify Care.

The remaining author declares that the research was conducted in the absence of any commercial or financial relationships that could be construed as a potential conflict of interest.

Publisher's note

Supplementary material

The Supplementary Material for this article can be found online at: https://www.frontiersin.org/articles/10.3389/fphys.2023.1057700/full#supplementary-material

References

Bray, M. A., and Wikswo, J. P. (2002). 'Use of topological charge to determine filament location and dynamics in a numerical model of scroll wave activity'. *IEEE Trans. Biomed. Eng.* 49 (10), 1086–1093. doi:10.1109/TBME.2002.803516

Castells, F., Mora, C, Rieta, J. J., Moratal-Pérez, D., and Millet, J., (2005). 'Estimation of atrial fibrillatory wave from single-lead atrial fibrillation electrocardiograms using principal component analysis concepts'. *Med. Biol. Eng. Comput.* 43 (5), 557–560. doi:10.1007/BF02351028

Clayton, R. H., and Holden, A. V. (2004). 'Filament behavior in a computational model of ventricular fibrillation in the canine heart'. *IEEE Trans. Biomed. Eng.* 51 (1), 28–34. doi:10.1109/TBME.2003.820356

Cluitmans, M., Brooks, D. H., MacLeod, R., Dossel, O., Guillem, M. S., van Dam, P. M., et al. (2018). 'Validation and opportunities of electrocardiographic imaging: From technical achievements to clinical applications'. *Front. Physiology* 9 (), 1305–1319. doi:10.3389/fphys.2018.01305

Dhillon, G. S., Ahluwalia, N., Honarbakhsh, S., Graham, A., Creta, A., Abbass, H., et al. (2021). 'Impact of adenosine on mechanisms sustaining persistent atrial fibrillation: Analysis of contact electrograms and noninvasive ECGI mapping data'. *PLoS ONE* 16 (3), 02489511–e249013. doi:10.1371/journal.pone.0248951

Dhillon, G. S., Schilling, R. J., Honarbakhsh, S., Graham, A., Abbass, H., Waddingham, P., et al. (2022). 'Impact of pulmonary vein isolation on mechanisms sustaining persistent atrial fibrillation: Predicting the acute response'. *J. Cardiovasc. Electrophysiol.*, 31, 903–912. doi:10.1111/jce.14392

Gao, X., Lam, A. G., Bilchick, K. C., Darby, A., Mehta, N., Mason, P. K., et al. (2019). 'The use of non-invasive mapping in persistent AF to predict acute procedural outcome'. *J. Electrocardiol.* 57, S21–S26. doi:10.1016/j.jelectrocard.2019.08.012

Guillem, M. S., Climent, A. M., Rodrigo, M., Fernandez-Aviles, F., Atienza, F., and Berenfeld, O. (2016). 'Presence and stability of rotors in atrial fibrillation: Evidence and therapeutic implications'. *Cardiovasc. Res.* 109 (4), 480–492. doi:10.1093/cvr/cvw011

Haissaguerre, M., Hocini, M., Denis, A., Shah, A. J., Komatsu, Y., Yamashita, S., et al. (2014) 'Driver domains in persistent atrial fibrillation', *Circulation* 130(7):530–538. doi:10.1161/CIRCULATIONAHA.113.005421

Haïssaguerre, M., Hocini, M., Sanders, P., Takahashi, Y., Rotter, M., Sacher, F., et al. (2006). 'Localized sources maintaining atrial fibrillation organized by prior ablation'. *Circulation* 113 (5), 616–625. doi:10.1161/CIRCULATIONAHA.105.546648

Haissaguerre, M., Hocini, M., Shah, A. J., Derval, N., Sacher, F., Jais, P., et al. (2013). 'Noninvasive panoramic mapping of human atrial fibrillation mechanisms: A feasibility report'. *J. Cardiovasc. Electrophysiol.* 24 (6), 711–717. doi:10.1111/jce.12075

Kis, Z., Muka, T., Franco, O. H., Bramer, W. M., De Vries, L. J., Kardos, A., et al. (2017). 'The short and long-term efficacy of pulmonary vein isolation as a sole treatment strategy for paroxysmal atrial fibrillation: A systematic review and meta-analysis'. *Curr. Cardiol. Rev.* 13 (3), 199–208. doi:10.2174/1573403x13666170117125124

Li, X., Almeida, T. P., Dastagir, N., Guillem, M. S., Salinet, J., Chu, G. S., et al. (2020). 'Standardizing single-frame phase singularity identification algorithms and parameters in phase mapping during human atrial fibrillation'. *Front. Physiology* 11 (), 869. doi:10.3389/fphys.2020.00869

Meng, T. W., Choi, G. P. T., and Lui, L. M. (2016). 'TEMPO: Feature-endowed teichmüller extremal mappings of point clouds'. *SIAM J. Imaging Sci.* 9 (4), 1922–1962. doi:10.1137/15M1049117

Molero, R., Soler Torro, J. M., Martinez Alzamora, N., M Climent, A., and Guillem, M. S. (2021). 'Higher reproducibility of phase derived metrics from electrocardiographic imaging during atrial fibrillation in patients remaining in sinus rhythm after pulmonary vein isolation'. *Comput. Biol. Med.* 139 (), 104934–104937. doi:10.1016/j.compbiomed.2021.104934

Narayan, S. M., Krummen, D. E., Shivkumar, K., Clopton, P., Rappel, W. J., and Miller, J. M. (2012). 'Treatment of atrial fibrillation by the ablation of localized sources: CONFIRM (conventional ablation for atrial fibrillation with or without focal impulse and rotor modulation) trial'. *J. Am. Coll. Cardiol.* 60 (7), 628–636. doi:10.1016/j.jacc.2012.05.022

Podziemski, P., Zeemering, S., Kuklik, P., van Hunnik, A., Maesen, B., Maessen, J., et al. (2018). 'Rotors detected by phase analysis of filtered, epicardial atrial fibrillation electrograms colocalize with regions of conduction block'. *Circulation. Arrhythmia Electrophysiol.* 11 (10), e005858. doi:10.1161/CIRCEP.117.005858

Rodrigo, M., Climent, A. M., Hernández-Romero, I., Liberos, A., Baykaner, T., Rogers, A. J., et al. (2020). 'Noninvasive assessment of complexity of atrial fibrillation: Correlation with contact mapping and impact of ablation'. *Circ. Arrhythm. Electrophysiol.* 13, 236–246. (March). doi:10.1161/CIRCEP.119.007700

Rodrigo, M., Climent, A. M., Liberos, A., Fernandez-Aviles, F., Berenfeld, O., Atienza, F., et al. (2017a). 'Highest dominant frequency and rotor positions are robust markers of driver location during noninvasive mapping of atrial fibrillation: A computational study'. *Heart* 14 (8), 1224–1233. doi:10.1016/j.hrthm.2017.04.017

Rodrigo, M., Climent, A. M., Liberos, A., Fernandez-Aviles, F., Berenfeld, O., Atienza, F., et al. (2017b). 'Technical considerations on phase mapping for identification of atrial reentrant activity in direct-And inverse-computed electrograms'. *Circulation Arrhythmia Electrophysiol.* 10 (9), e005008. doi:10.1161/CIRCEP.117.005008

Rogers, J. M., Huang, J., Smith, W. M., and Ideker, R. E. (1999). 'Incidence, evolution, and spatial distribution of functional reentry during ventricular fibrillation in pigs'. *Circulation Res.* 84 (8), 945–954. doi:10.1161/01.RES.84.8.945

Roney, C. H., Pashaei, A., Meo, M., Dubois, R., Boyle, P. M., Trayanova, N. A., et al. (2019). 'Universal atrial coordinates applied to visualisation, registration and construction of patient specific meshes'. *Med. Image Anal.* 55, 65–75. doi:10.1016/j.media.2019.04.004

Vandersickel, N., Van Nieuwenhuyse, E., Van Cleemput, N., Goedgebeur, J., El Haddad, M., De Neve, J., et al. (2019). 'Directed networks as a novel way to describe and analyze cardiac excitation: Directed graph mapping'. *Front. Physiology* 10 (), 1138–1214. doi:10.3389/fphys.2019.01138

frontiers | Frontiers in Physiology

TYPE Original Research
PUBLISHED 14 March 2023
DOI 10.3389/fphys.2023.1054401

OPEN ACCESS

EDITED BY
Axel Loewe,
Karlsruhe Institute of Technology (KIT), Germany

REVIEWED BY
Caroline Helen Roney,
Queen Mary University of London, United Kingdom
Prasanth Ganesan,
Stanford University, United States

*CORRESPONDENCE
Oleg Aslanidi,
oleg.aslanidi@kcl.ac.uk

SPECIALTY SECTION
This article was submitted to Cardiac Electrophysiology, a section of the journal Frontiers in Physiology

RECEIVED 26 September 2022
ACCEPTED 28 February 2023
PUBLISHED 14 March 2023

CITATION
Ogbomo-Harmitt S, Muffoletto M, Zeidan A, Qureshi A, King AP and Aslanidi O (2023), Exploring interpretability in deep learning prediction of successful ablation therapy for atrial fibrillation.
Front. Physiol. 14:1054401.
doi: 10.3389/fphys.2023.1054401

Exploring interpretability in deep learning prediction of successful ablation therapy for atrial fibrillation

Shaheim Ogbomo-Harmitt, Marica Muffoletto, Aya Zeidan, Ahmed Qureshi, Andrew P. King and Oleg Aslanidi*

School of Biomedical Engineering and Imaging Sciences, King's College London, St Thomas' Hospital, London, United Kingdom

Background: Radiofrequency catheter ablation (RFCA) therapy is the first-line treatment for atrial fibrillation (AF), the most common type of cardiac arrhythmia globally. However, the procedure currently has low success rates in dealing with persistent AF, with a reoccurrence rate of ~50% post-ablation. Therefore, deep learning (DL) has increasingly been applied to improve RFCA treatment for AF. However, for a clinician to trust the prediction of a DL model, its decision process needs to be interpretable and have biomedical relevance.

Aim: This study explores interpretability in DL prediction of successful RFCA therapy for AF and evaluates if pro-arrhythmogenic regions in the left atrium (LA) were used in its decision process.

Methods: AF and its termination by RFCA have been simulated in MRI-derived 2D LA tissue models with segmented fibrotic regions (n = 187). Three ablation strategies were applied for each LA model: pulmonary vein isolation (PVI), fibrosis-based ablation (FIBRO) and a rotor-based ablation (ROTOR). The DL model was trained to predict the success of each RFCA strategy for each LA model. Three feature attribution (FA) map methods were then used to investigate interpretability of the DL model: GradCAM, Occlusions and LIME.

Results: The developed DL model had an AUC (area under the receiver operating characteristic curve) of 0.78 $\pm$ 0.04 for predicting the success of the PVI strategy, 0.92 $\pm$ 0.02 for FIBRO and 0.77 $\pm$ 0.02 for ROTOR. GradCAM had the highest percentage of informative regions in the FA maps (62% for FIBRO and 71% for ROTOR) that coincided with the successful RFCA lesions known from the 2D LA simulations, but unseen by the DL model. Moreover, GradCAM had the smallest coincidence of informative regions of the FA maps with non-arrhythmogenic regions (25% for FIBRO and 27% for ROTOR).

Conclusion: The most informative regions of the FA maps coincided with pro-arrhythmogenic regions, suggesting that the DL model leveraged structural features of MRI images to identify such regions and make its prediction. In the future, this technique could provide a clinician with a trustworthy decision support tool.

KEYWORDS

atrial fibrillation, catheter ablation, medical imaging, cardiac modelling, deep learning, interpretability

1 Introduction

Atrial fibrillation (AF), the rapid, uncoordinated contraction of the atria, is a heart condition that affects 33 million people worldwide—making it the most common type of cardiac arrhythmia globally (Hart and Halperin, 2001; Chugh et al., 2014). Currently, the precise mechanisms of AF are unclear. However, there is evidence that ectopic electrical beats originating from the pulmonary veins (PVs) can trigger AF (Chen et al., 1999). The triggers can then generate re-entrant drivers (rotors) that sustain AF, and spatial fibrosis distributions in the left atria (LA) have been demonstrated to facilitate such drivers (Morgan et al., 2016; Roy et al., 2020). A common treatment for AF is radiofrequency catheter ablation (RFCA) therapy. RFCA involves using induced heat from a rapidly alternating current in a catheter to ablate (isolate or destroy) the arrhythmogenic area of atrial tissue that harbours triggers or rotors, thus restoring sinus rhythm and the mechanical function of the heart (Townsend and Sabiston, 2001). Presently, the success rate of RFCA is ~70% for paroxysmal AF—which is relatively high (Oketani et al., 2012). However, the procedure is much less successful when dealing with persistent AF, which has a reoccurrence rate of ~75% post-intervention. Therefore, with the high reoccurrence rate of AF, there is a need for improvements within (Wang et al., 2017; Yubing et al., 2018).

Image-based computational modelling has been used to understand the structure-function relationship that determines re-entrant atrial drivers for AF with the aim of improving RFCA outcomes. As a result, computational methods have been introduced to improve RFCA outcomes, ultimately leading to the FIRM (Focal Impulse and Rotor Modulation) mapping, which locates rotational activity around a centre (rotor) from electroanatomical maps (Narayan et al., 2012a). The CONFIRM trial showed patients that underwent FIRM-guided ablation maintained a higher freedom of AF (AF termination in 86% of patients) when compared to patients with conventional ablation strategy (AF termination in 20% of patients) (Narayan et al., 2012b). However, the multicentre REAFFIRM trial did not show evidence that FIRM-guided ablation strategy is superior to pulmonary vein isolation (PVI) (Zhao et al., 2019).

With the recent rise of artificial intelligence (AI), machine and deep learning (DL) have been applied to patient medical imaging data and computational cardiac modelling with the aim to develop more effective RFCA treatments. The applications of AI include predicting AF reoccurrence post-RFCA and the origins of AF triggers and ablation (Kim et al., 2020; Liu et al., 2020; Firouznia et al., 2021; Roney et al., 2022). Furthermore, Luongo et al. have applied machine learning to predict AF ablation targets, but used 12-lead ECG data instead of medical imaging (Luongo et al., 2021). Other studies have also leveraged the power of AI in AF by using DL with ECG data to estimate atrial fibrosis and to classify AF from atrial flutter or tachycardia (Nagel et al., 2021; Rodrigo et al., 2022). Zolotarev et al. applied AI to identify AF drivers from multi-electrode mapping, with the AI model then validated using optical mapping; the results were comparable to the state-of-the-art with higher computational efficiency (Zolotarev et al., 2020). Popescu et al. applied DL for arrhythmic sudden death prediction from clinical and imaging data, which proved successful and achieved a concordance index of 0.83 and 0.74, and 10-year integrated Brier score of 0.12 and 0.14, respectively (Popescu et al., 2022).

However, DL is limited by its black-box nature. This is an issue when considering the European Union's General Data Protection Regulation (GDPR), as any algorithmic decision used in patient care requires an explanation for transparency (Mourby et al., 2021). Moreover, clinicians have also argued that if AI can outperform human diagnosis, understanding the AI model's decision process will be beneficial in discovering new biological processes and furthering medical knowledge (Watson et al., 2019). Moreover, it will increase confidence in the AI-generated results, which means the clinicians are more likely to trust and leverage them. Hence, this has led to the growing field of deep learning interpretability for medical imaging analysis, where methods such as concept learning models, latent space interpretation and attribution maps have been applied to many medical fields (Salahuddin et al., 2022). Organisations have also expressed an interest in AI interpretability, e.g., the Avicenna Alliance (AA) and the Virtual Physiological Human Institute (VPHI). The AA and VPHI aims are to promote the synergy of AI and *in silico* modelling into healthcare, while providing policymakers and regulators with directions towards applying these technologies safely in clinics, including AI interpretability (Geris et al., 2022).

Muffoletto et al. were the first to apply DL to directly informing a clinician to treat AF using RFCA therapy and developed a convolutional neural network (CNN) to predict suitable *in silico* ablation strategies for a given patient, using synthetic tissue-based atrial models with randomly distributed fibrotic patches. The approach proved effective (79% accuracy) and illustrated the proof-of-concept (Muffoletto et al., 2019). Ultimately, this led to the approach being applied to MRI-derived data to predict the patient-specific optimal RFCA strategy. As a result, the developed CNN had a 100% accuracy for classifying optimal fibrosis- (FIBRO) and rotor-based (ROTOR) strategies success and 33% accuracy for the PVI strategy (Muffoletto et al., 2021).

Currently, research into interpretability for DL-based AF management is very limited. For example, one study by Alhusseini et al. used gradient-weighted class activation mapping (GradCAM) to show that their feature attribution (FA) map closely replicated rules used by clinicians. However, only one method was validated within this study, and a comparison with other methods was not investigated. Furthermore, the study used spatial maps of the activation phase derived from electrocardiogram data from a basket catheter. Hence, there has been no investigation into DL interpretability for models which use medical imaging data to make explainable predictions for cardiac arrhythmias and anti-arrhythmic treatments (Alhusseini et al., 2020).

In this study, we present a novel qualitative and quantitative comparison of established DL interpretability methods for medical imaging and image-based cardiac modelling of RFCA, as well as new quantitative metrics to assess interpretability of FA maps for the image-based cardiac models.

2 Methods

2.1 Overview

We propose a DL approach to 1) accurately predict the outcomes of RFCA therapy based on image-based modelling and

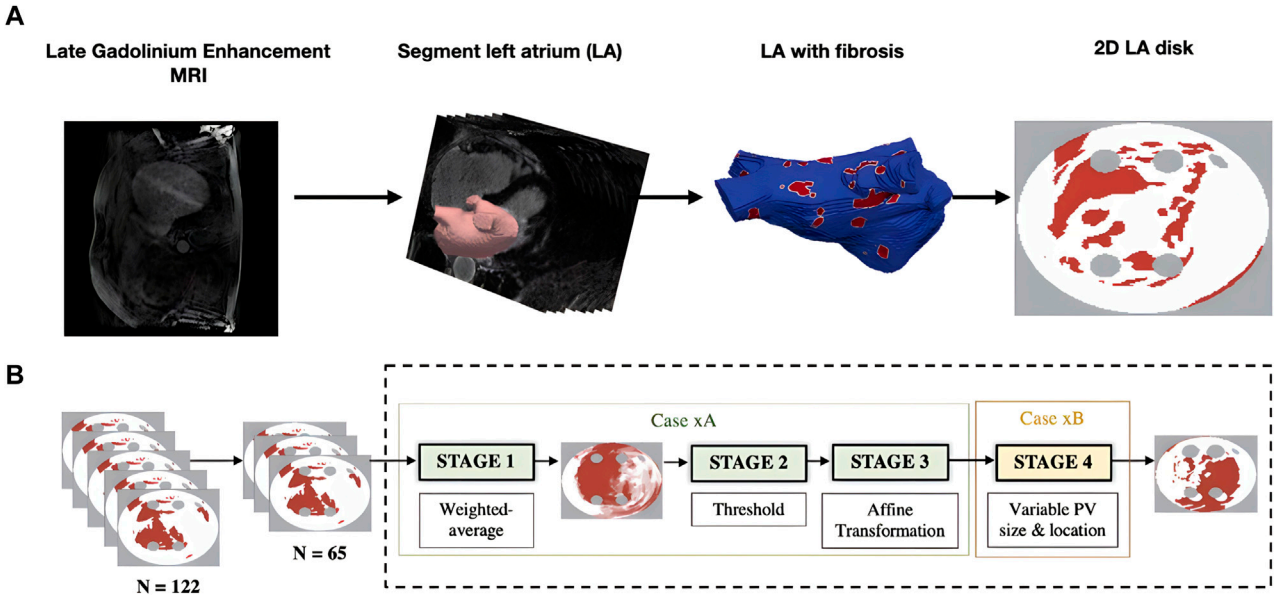

FIGURE 1
Diagram of MRI-derived 2D LA tissue disk. **(A)**. Workflow of 2D LA tissue generation pipeline. The figure illustrates the process of how the 2D LA tissue models are obtained from LGE MRI by LA segmentation, thresholding fibrosis from healthy tissue and mapping onto 2D LA tissues. **(B)**. Workflow for generating synthetic tissues. 65 tissues were randomly selected from the total dataset of 122 real tissues. These 65 tissues were used to generate the synthetic images by iterating overstages 1 to 4 (199 times) to create a virtual cohort of 199 tissues. 'Case xA' denotes the combination of data augmentation techniques used to create the synthetic fibrosis distributions. 'Case xB' determines how the PV sizes and locations were varied from those in the standardised discs.

simulations and 2) interpret the decision process of the DL model. To achieve this, standardised 2D LA models with patient-specific distributions of fibrosis were derived from late gadolinium-enhanced (LGE) MR imaging data. Simulations of AF and its termination with three RFCA strategies were performed, the DL model was applied to predict the success of each strategy, and the RFCA simulation results were compared with DL interpretability maps to identify proarrhythmogenic locations. Three established interpretability approaches were also compared qualitatively and quantitatively to interpret the DL model's predictions.

2.2 Data acquisition and pre-processing

The datasets used in this study were derived from 122 LGE MRI patient scans: 86 datasets with spatial resolution of 0.625 × 0.625 × 0.625 mm^3 were acquired from the Atrial Segmentation Challenge at the STACOM 2018 workshop (Xiong et al., 2021); additionally, 36 LGE MRI images were collected at St. Thomas' Hospital London with resolution of 1.3 × 1.3 × 4 mm^3 (specifically, 18 AF patients were scanned both pre-and post-intervention) (Chubb et al., 2018).

Generating 2D LA models with fibrosis first required manual segmentation of patient LGE MRI data to produce 3D patient-specific endocardial LA surface meshes. The LGE MRI image intensities were then mapped to these models and the image intensity ratio thresholding technique was applied to quantify and visualise LA fibrosis (Roy et al., 2020). Finally, the 3D LA fibrosis maps were unwrapped using the LA standardised unfold mapping technique to produce models in the 2D LA disk format for use as input to the DL network, as shown in Figure 1A (Williams et al., 2017; Qureshi et al., 2020).

Furthermore, to increase the size of the dataset, synthetic 2D LA disks were generated by weighted-averaging of the patient datasets to vary the fibrosis distribution and PVs. The creation of synthetic disks consisted of three steps. First, 65 MRI images were extracted from the STACOM 2018 dataset and were each weighted by assigning a random weight (between 0 and 1) to all voxels of a given image; the weighted-average of all images was thresholded (Case xA in Figure 1B). This number was chosen as less than 65 would result in low variability in the synthetic tissues and more than 65 would result in most of the synthetic tissues being covered in fibrosis. Supplementary Figure S1 illustrates that selecting the 65 LA tissues in generating the synthetic LA tissues would result in a mean fibrotic tissue percentage of approximately 50%. Thus, 65 corresponds to a folding point of this sigmoidal dependence, and any number above 65 would lead to a majority of tissue being fibrotic. Then the extracted fibrosis distribution was further augmented by applying one or multiple affine transformations (translation, rotation and flipping). The fibrosis threshold value and the types of transformation were randomly selected. Lastly, the PVs were varied by assigning one of 6 different variants, which included changing PV size and position (Case xB in Figure 1B) (Muffoletto et al., 2021). This resulted in a total of 199 synthetic 2D LA tissue models in addition to the 122 patient-specific models, totalling 321 2D LA tissue models.

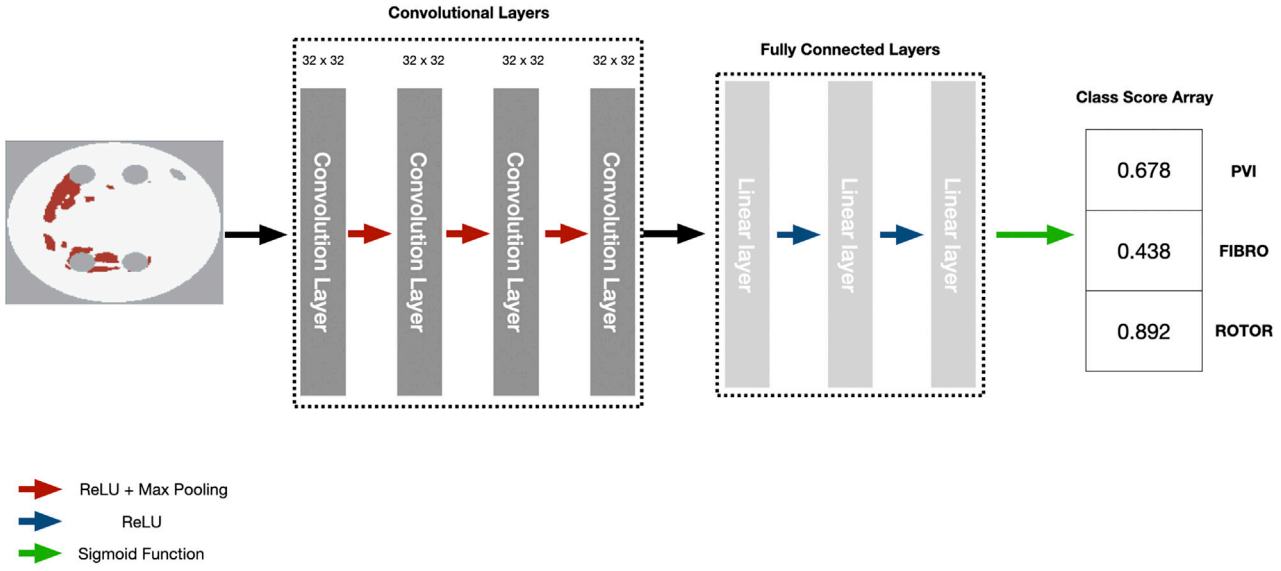

FIGURE 2
Diagram of CNN with parameters to predict RFCA simulation strategy success from 2D LA tissue.

2.3 Atrial tissue modelling and AF simulation

Eq. 1 represents the Fenton-Karma semi-physiological model, which consists of three ionic currents representing the overall ion current in the electrical dynamics of atria cells; I_{fi} represents the fast inward current Na^+, I_{so} is the slow outward current K^+ and I_{si} is the slow inward current Ca^+ (Fenton and Karma, 1998):

$$I_{ion} = I_{fi} + I_{so} + I_{si} \tag{1}$$

Eq. 2 is the standard monodomain equation to describe electrical wave propagation.

$$\frac{\partial V_m}{\partial t} = \nabla . D \nabla V_m - \frac{I_{ion}}{C_m} \tag{2}$$

V_m is the membrane potential, C_m is the membrane capacitance, D is a tensor that represents the diffusion of the electrical coupling within tissue. Eq. 2 with ion current determined in Equation 1 was solved using the forward Euler method with a finite-difference approximation of the Laplacian. Therefore, Equation 1 and Equation 2 were solved using each 2D tissue disk as a spatial domain to simulate electrical waves sustaining AF. Such waves in the form of rotors were generated using the standard cross-field protocol at 28 *ms* into the simulation (Tobón et al., 2014). The numerical integration steps were 0.01 ms time step and 0.3 *mm* spatial step. Additionally, healthy tissue had a D value of 0.1 $mm^2 s^{-1}$ to match the physiological value of healthy myocardium tissue. Fibrotic tissue had D value of 0.015 $mm^2 s^{-1}$.

The three ablation strategies were simulated to terminate persistent AF: PVI, FIBRO and ROTOR strategies; details of the simulations have been published previously (Muffoletto et al., 2021). The FIBRO strategy involved ablating the perimeter of the fibrotic tissue, while PVI consisted of ablating the circumference of the PVs and ROTOR ablated the phase singularities of the electrical wave. The ablation strategy was deemed successful for a tissue if AF was terminated within 2000 *ms* and less than 40% of the tissue was ablated (Muffoletto et al., 2021). Therefore, using the stated simulation pipeline, the success of the three RFCA strategies was determined for AF simulations in the 2D LA tissues (including patient MRI derived and synthetic data). Furthermore, since multiple strategies can be successful/unsuccessful for a given 2D LA tissue, the classification task was multi-label.

2.4 Deep learning

We employed the CNN with hyperparameters (parameters and number of convolutional and fully connected layers) based on the study by Muffoletto et al. as the basis of our interpretability framework (Muffoletto et al., 2021). The hyperparameters were tuned by Muffoletto et al. by performing 24 experiments which involved changing number of layers, filter size of convolutional layers and dropout rate. The optimal hyperparameters were chosen by selecting the DL model with the highest average accuracy across a 5-fold cross-validation. The CNN consisted of four convolutional layers of 32 × 32 filters, each followed by Rectified Linear Unit (ReLU) activation and max pooling with a pool size of two. These are followed by three linear layers (2048, 128 and 3 units, respectively) and another ReLU activation. A Dropout layer followed this at a rate of 0.8 and a sigmoid function (Paszke et al., 2019). Since we address a multi-label classification problem (i.e., multiple ablation strategies), we modified the loss function to be a mean-squared error tailored to perform multi-label classification for the three ablation strategies (Figure 2).

TABLE 1 Mean lesion percentage, NAT percentage, IoU of the informative region and ablation lesions with errors (standard deviation) for each FA map method and RFCA strategy.

Ablation strategy	Method	Lesion percentage	IoU	NAT percentage
PVI	LIME	0.44 ± 0.24	**0.077 ± 0.023**	**0.32 ± 0.24**
	Occlusions	**0.55 ± 0.15**	0.065 ± 0.17	0.57 ± 0.15
	GradCAM	0.47 ± 0.17	0.063 ± 0.029	0.60 ± 0.12
FIBRO	LIME	0.57 ± 0.19	0.18 ± 0.09	0.47 ± 0.27
	Occlusions	0.45 ± 0.14	0.19 ± 0.11	0.38 ± 0.20
	GradCAM	**0.62 ± 0.25**	**0.26 ± 0.11**	**0.27 ± 0.16**
ROTOR	LIME	0.62 ± 0.16	0.12 ± 0.07	0.63 ± 0.25
	Occlusions	0.53 ± 0.16	0.14 ± 0.06	0.36 ± 0.16
	GradCAM	**0.71 ± 0.13**	**0.20 ± 0.08**	**0.25 ± 0.06**

TABLE 2 Mean AUC score on independent hold-out test set (with standard deviation) for each RFCA strategy and type of data.

Ablation strategy	MRI derived data	MRI derived + synthetic data
PVI	0.67 ± 0.03	0.78 ± 0.04
FIBRO	0.85 ± 0.02	0.92 ± 0.02
ROTOR	0.62 ± 0.05	0.77 ± 0.02

$$MSE(y_{score}, y) = \sum_{i=0}^{N} \frac{y^i_{score} - y^i}{N} \quad (3)$$

Eq. 3 is the mean-squared error function formulation, where y_{score} is the predicted class score array and y is the RFCA strategy success ground truth (where 1 = success and 0 = unsuccessful). Here, N represents the number of classes/strategies (three in this study) and i is the index of a class in the class score array. To train and effectively test the CNN, a leave-one-out cross-validation was used where the total dataset was split into two sets: a hold-out test set and training set. The training set was then split into five folds, where four folds were used to train the CNN, and the last fold was used as a validation set to select the optimal CNN model state (i.e. the model with the lowest loss during training) (Raschka, 2018; Muffoletto et al., 2021). In total, there were 271 2D LA tissues in the leave-one-out cross-validation dataset (96 MRI derived and 175 synthetic). Within each fold the DL model was trained for 100 epochs using an ADAM optimiser with a learning rate of 1e-4 (Kingma and Ba, 2014). For each fold, the optimal model was tested on the hold-out test set of 50 2D LA tissues (26 MRI derived and 24 synthetic) from the total dataset to evaluate the DL model's performance. Pre- and post-ablation images were not split during cross-validation, as there was little similarity between the respective fibrosis distributions (see Supplementary Materials Section 2 and Supplementary Figure S2).

2.5 Interpretability

Three popular local *post hoc* interpretability methods were used to interpret the CNN's predictions - GradCAM, occlusions and local interpretable model-agnostic explanations (LIME) (Zeiler and Fergus, 2014; Ribeiro et al., 2016; Selvaraju et al., 2017; Kokhlikyan et al., 2020). GradCAM and LIME were chosen as they are widely used saliency maps in DL medical image analysis (Magesh et al., 2020; Graziani et al., 2021; Patel et al., 2021; Mahapatra et al., 2022), while occlusions is one of the first saliency map methods used for DL computer vision. Each method evaluates feature attribution using different approaches: GradCAM uses gradient information, LIME uses an interpretable model within a local space and the occlusions method uses perturbations.

TABLE 3 Mean area under the receiver operating characteristic curve (AUC) score, recall, precision and F1-score on independent hold-out test set (with standard deviation) for each RFCA strategy.

Ablation strategy	AUC	Recall	Precision	F1-score
PVI	0.78 ± 0.03	0.35 ± 0.07	0.68 ± 0.28	0.42 ± 0.06
FIBRO	0.92 ± 0.02	0.89 ± 0.03	0.82 ± 0.02	0.85 ± 0.01
ROTOR	0.77 ± 0.02	0.93 ± 0.04	0.76 ± 0.02	0.84 ± 0.01

The DL model state from the most accurate fold of the leave-one-out cross-validation was used to produce the FA maps for the three methods on the hold-out test set. The GradCAM method was applied to the last convolutional layer of the CNN. Each FA map was thresholded above the respective map's average FA to highlight the most informative features. Three metrics were evaluated to quantitatively analyse the informative regions of each FA map: Jacquard index (IoU), lesion percentage and non-arrhythmogenic

TABLE 4 Mean AUC, recall, precision and F1 score (with standard deviation) of DL model trained with real data only and with synthetic and real data from a leave-one-out cross-validation on a hold-out test (~20% of the respective dataset).

Ablation strategy	MRI derived data				MRI derived + synthetic data			
	AUC	Recall	Precision	F1 score	AUC	Recall	Precision	F1 score
PVI	0.67 ± 0.03	0	1.0	0	0.78 ± 0.03	0.35 ± 0.07	0.68 ± 0.28	0.42 ± 0.06
FIBRO	0.85 ± 0.02	0.75 ± 0.08	0.70 ± 0.03	0.72 ± 0.04	0.92 ± 0.02	0.89 ± 0.03	0.82 ± 0.02	0.85 ± 0.01
ROTOR	0.62 ± 0.05	0.99 ± 0.02	0.64 ± 0.01	0.78 ± 0.02	0.77 ± 0.02	0.93 ± 0.04	0.76 ± 0.02	0.84 ± 0.01

Bold numbers signify the highest score from each FA method for each metric.

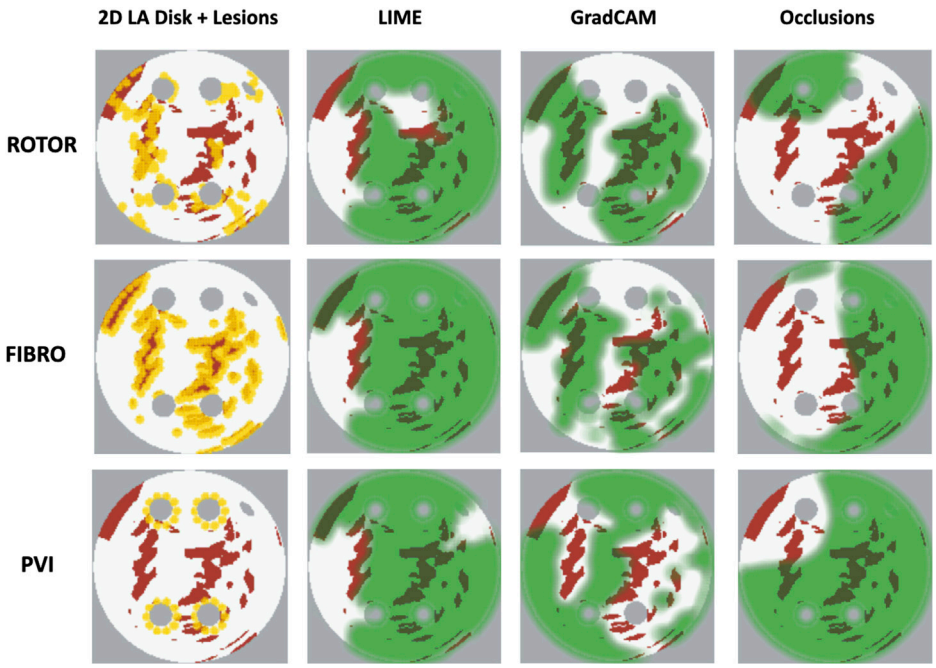

FIGURE 3
Diagram of 2D LA tissues with highlighted feature attribution maps. White areas in the 2D tissues are healthy tissue and red areas are fibrosis. Ablation lesion locations known from simulations are shown (yellow) for all three RFCA strategies, along with respective FA maps for LIME, GradCAM and occlusions and highlighted thresholded informative regions (translucent green). Same colour scheme in used in Figures 7, 8 below.

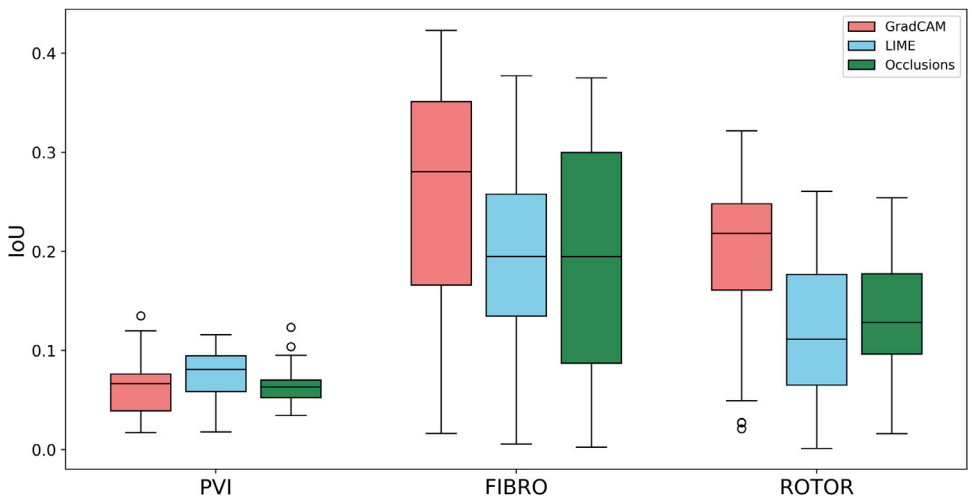

FIGURE 4
Boxplot of Jacquard index (IoU) for each FA method (GradCAM, LIME and Occlusions) and RFCA strategy (PVI, FIBRO and ROTOR) on the hold-out test set.

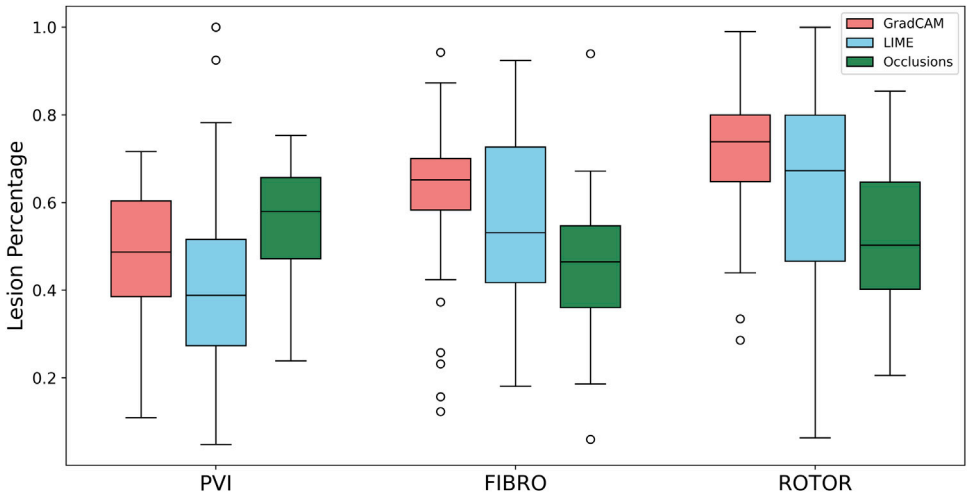

FIGURE 5
Boxplot of lesion percentage for each FA method (GradCAM, LIME and Occlusions) and RFCA strategy (PVI, FIBRO and ROTOR) on the hold-out test set.

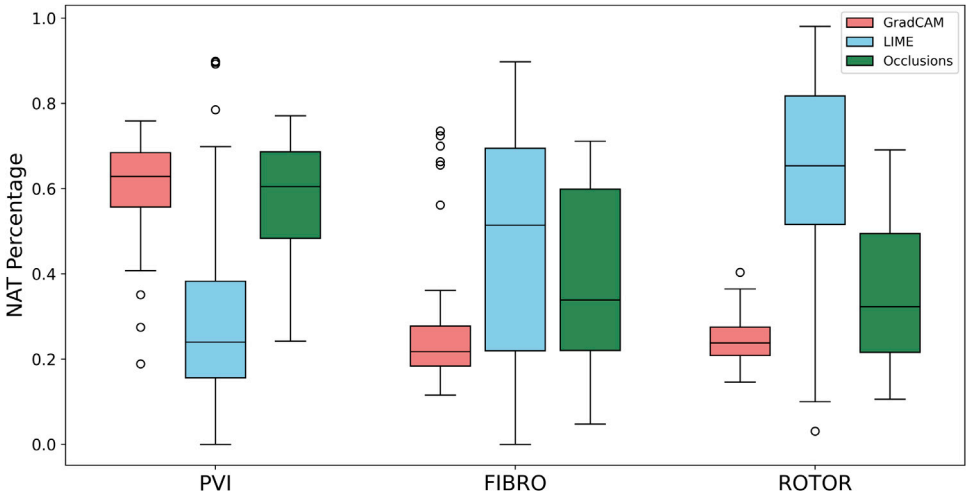

FIGURE 6
Boxplot of NAT percentage for each FA method (GradCAM, LIME and Occlusions) and RFCA strategy (PVI, FIBRO and ROTOR) on the hold-out test set.

tissue (NAT) percentage. The IoU was evaluated by calculating IoU of the informative regions of a FA map and lesions of a given ablation strategy. Lesion percentage was evaluated by calculating the percentage of lesions of a given ablation strategy within the informative regions.

The motivation for analysing the lesion percentage was to determine if the DL model focused on clinically relevant features. The number of the lesions (unseen by the DL model but known from simulations–and known to clinicians when ablating a patient) found in a FA map's informative region is a relevant metric, as such lesions are associated with arrhythmogenic regions in atrial tissue. Thus, PVI lesions isolate the area of the initial arrhythmogenic triggers, FIBRO lesions aim to isolate the fibrotic tissue border where AF reentrant drivers commonly reside, and ROTOR lesions directly target such reentrant drivers. Therefore, the ability of DL model to predict lesion locations (again, without seeing such lesions during training) should help the clinician to understand and trust these predictions.

Lastly, the NAT percentage was calculated by finding the percentage of healthy tissue (with no lesions or fibrosis) within the informative regions of a FA map. NAT percentage was evaluated to assess how much of the clinically irrelevant features were highlighted as informative by the DL model.

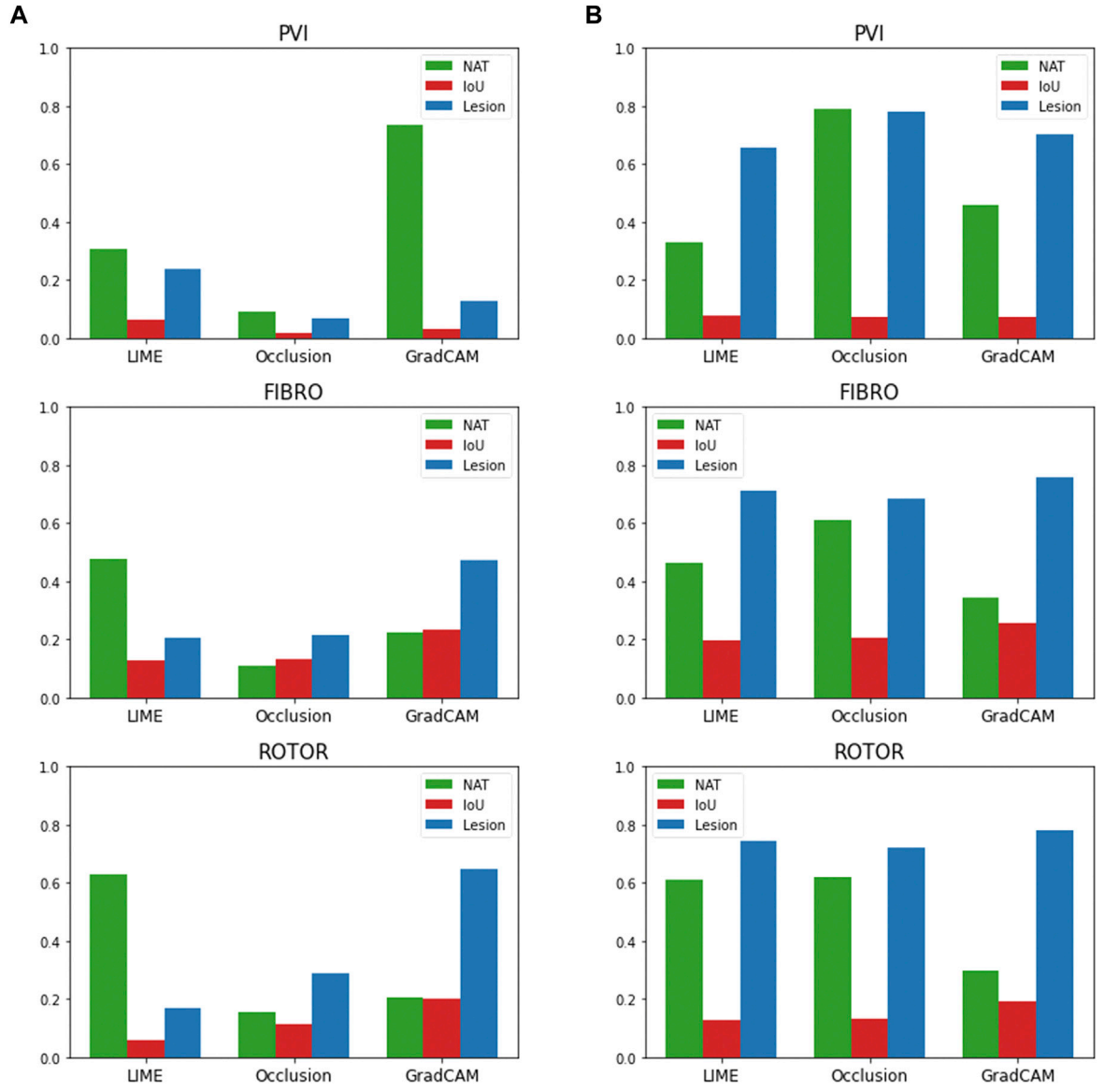

FIGURE 7
IoU, lesion and NAT percentage values for each interpretability method and ablation strategy with altered informative region threshold value. **(A)**. Informative region threshold value 25% above the average FA. **(B)**. Informative region threshold value 25% below the average FA.

2.5.1 GradCAM

GradCAM uses the gradient from a given convolutional layer to measure FA for a particular decision of interest. GradCAM is an improvement of the class activation map (CAM) method. CAM produces a localisation map for an image classification model, utilising a specific architecture where globally averaged pooled convolutional feature maps are fed directly into a softmax layer. GradCAM improves on CAM by being architecture-independent, and it can be applied to any CNN. Furthermore, a study by Adebayo et al. implemented a sanity check of GradCAM through a model parameter and data randomisation test. It demonstrated that GradCAM's saliency maps could support tasks that require explanations that are faithful to the model and the data generation process (Adebayo et al., 2018).

$$\alpha^c = \frac{1}{z}\sum_i \sum_j \frac{\partial y^c}{\partial A_{ij}} \tag{4}$$

Feature attribution, α_{ij}^c (i and j are the indices of the feature in a FA map), of a given class c is calculated in GradCAM by evaluating the partial derivative of the score of class c and a feature from activation map of a given convolutional layer A_{ij}. The result of evaluating the partial differential for each feature is then pooled globally by dividing each element of the FA map by the total number of features to find the final FA map (Selvaraju et al., 2017).

2.5.2 LIME

The core idea of LIME is to explain predictions of any classifier faithfully by learning an interpretable model locally around the

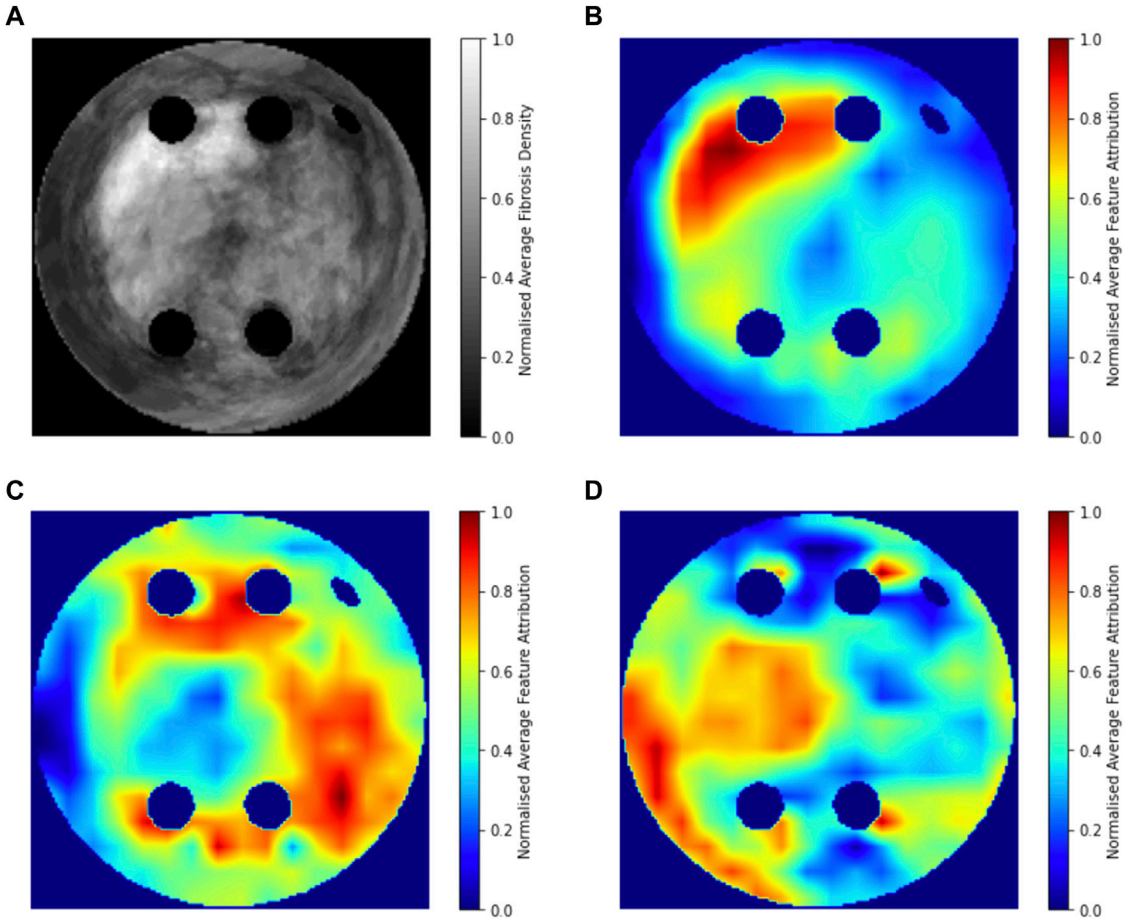

FIGURE 8
Averaged LGE MRI intensities and FA maps on the hold-out test set. **(A)**. Averaged and normalised LGE MRI intensity in the LA tissue disks. **(B)**. Averaged and normalised GradCAM FA map for the ROTOR ablation strategy. **(C)**. Averaged and normalised GradCAM FA map for the FIBRO ablation strategy. **(D)**. Averaged and normalised GradCAM FA map for the PVI ablation strategy.

prediction. LIME achieves this by generating simulated data points around an instance through random perturbation and weighting them as a function of proximity to the original data points, fitting a sparse linear model to the predicted responses from the perturbed points and using the sparse linear model as an explanation model (i.e., weights of features in linear model).

$$\xi(x) = \underset{g \in G}{\operatorname{argmin}} \mathcal{L}(f, g, \pi_x) + \Omega(g) \tag{5}$$

$$\mathcal{L}(f, g, \pi_x) = \sum_{z, z' \in Z} \pi_x(z)\left(f(z) - g(z')\right)^2 \tag{6}$$

FA $\xi(x)$ of given features x is calculated in LIME by minimising the loss function $\mathcal{L}$ and complexity, $\Omega(g)$, of the function g (a model from a class of possibly interpretable models). In essence $\mathcal{L}$ is a function that measures how unfaithful the function g is at approximating f (the model being explained) in the local space defined by π_x. Eq. 6 shows how the loss function uses the L2 distance to measure how unfaithful function g is at approximating f, where z is sample from x, z is the set perturbed samples of x with associated labels and z' is perturbed sample from set z (Kokhlikyan et al., 2020).

2.5.3 Occlusions

Occlusions is a perturbation-based approach to calculate FA, which involves perturbing the feature space with a rectangular region and evaluating the difference of class score from a given class prediction by the perturbation. FA is then assigned by looking at the feature in the multiple rectangular regions it is in and averaging the multiple class score differences (Ancona et al., 2017). The occlusion FA method was based on an occlusion sensitivity analysis used to validate a DL interpretability method by Zeiler et al. (Zeiler and Fergus, 2014).

3 Results

3.1 Dataset analysis

In the dataset comprising of 122 LA tissues derived from MRI data, the PVI strategy led to successful AF termination in only 11.6% of cases, while 88.4% resulted in failed terminations. Meanwhile, the FIBRO and ROTOR strategies resulted in 42.6% and 74.4% successful terminations, respectively. Notably, FIBRO

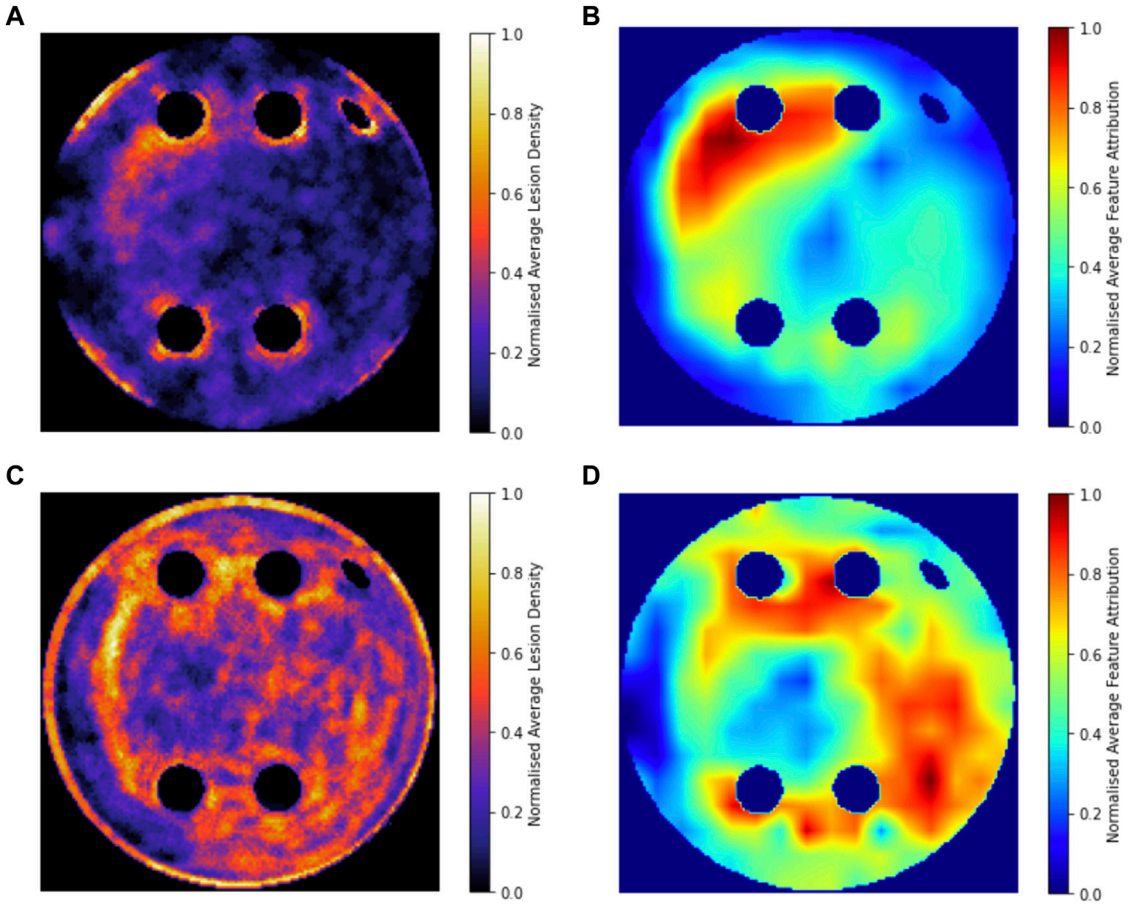

FIGURE 9
Averaged and normalised ablation lesions and GradCAM FA maps for FIBRO and ROTOR on the hold-out test set. **(A)**. Ablation lesions for ROTOR. **(B)**. FA map for ROTOR. **(C)**. Ablation lesions for FIBRO. **(D)**. FA map for FIBRO.

demonstrated the most balanced AF termination outcomes, whereas ROTOR and PVI exhibited a similar level of misbalance in the outcomes. In the larger dataset consisting of 321 LA tissues, including both MRI-derived and synthetic data, the PVI strategy achieved successful AF termination in 27.1% of cases, demonstration a positive impact of augmentation. The FIBRO and ROTOR strategies also resulted in 58.3% and 75.7% successful terminations, respectively.

3.2 Convolutional neural network performance

The success of the FIBRO ablation strategy was predicted most accurately by the CNN, as shown in Table 1, where the FIBRO class has the highest AUC score and the most balanced recall and precision scores. Furthermore, the FIBRO strategy also had the highest AUC score when predicting ablation success exclusively on the real data (Table 2). PVI had the second-highest AUC score on mixed real and synthetic data, as well as exclusively on real data. Meanwhile, ROTOR had a comparable AUC score to PVI on the real and synthetic data but performed worse exclusively on the MRI-derived data (Table 2).

However, the CNN struggled to predict successful AF termination cases by PVI, which is reflected in the low recall and F1 score in Table 3. Even though there was a similar class imbalance in ROTOR compared to PVI, the CNN was able to predict the successful and failed AF termination cases to a reasonable degree (see recall and F1 score in Table 3). Lastly, the CNN had a significantly higher AUC score ($p < 0.05$) when trained and predicted on a dataset comprised of synthetic and MRI derived data compared to training exclusively on MRI derived data (Table 4). This was confirmed using a one-sided *t*-test (PVI: $p = 0.030$; FIBRO: $p = 3.5e\text{-}05$; ROTOR: $p = 6.15e\text{-}06$). This was due to the increased dataset size when combining the real and synthetic data as the CNN has more training examples–effectively improving the task's generalisation. Notably, incorporating synthetic data has improved accuracy in predicting the outcomes of PVI. When trained exclusively on MRI-derived data, the model showed a zero F1-score for PVI, attributed to significant class imbalance. This resulted in the model predicting unsuccessful AF termination for all PVI cases, explaining the precision score of 1.0. However, integrating synthetic data into the dataset improved the model's ability to classify

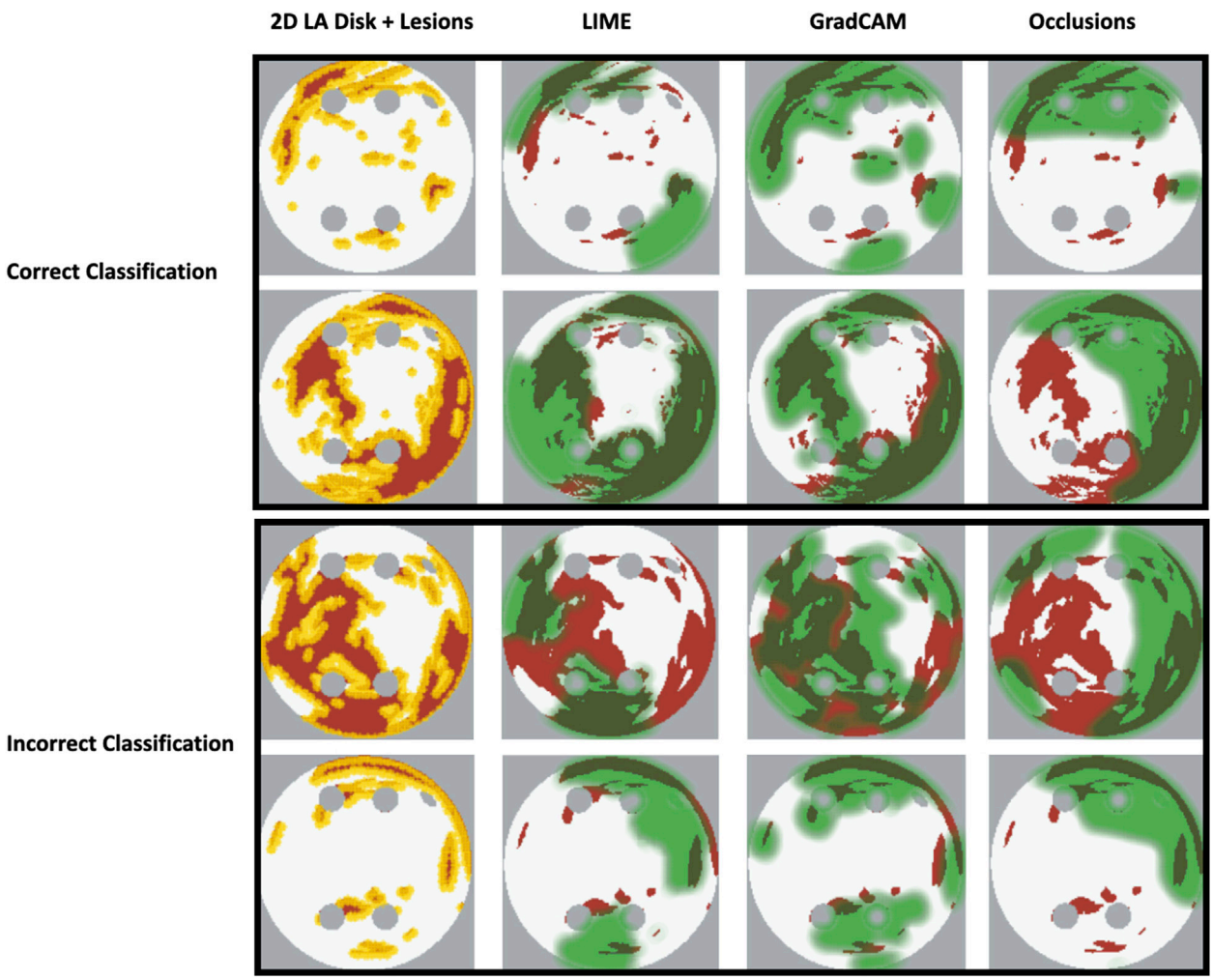

FIGURE 10
Correct and incorrect classification examples of FA maps (LIME, GradCAM and occlusions) for FIBRO.

successful ablation for PVI (F1 score of 0.42 ± 0.06), due to the 15.5% increase in successful PVI cases in the dataset. This allowed the model to improve its classification of successful AF termination by PVI.

3.3 Qualitative interpretability analysis

As shown in Table 1, GradCAM was characterised by the highest lesion percentage and IoU metrics for the FIBRO and ROTOR strategies. Additionally, Figure 3 shows that in FA maps obtained with GradCAM for ROTOR and FIBRO, the informative regions coincided with most ablation lesions. Figure 3 also illustrates that GradCAM had the lowest NAT percentage for the FIBRO and ROTOR strategies, as the FA maps did not highlight large, but clinically irrelevant regions of healthy tissue–whereas LIME and occlusions did. For the PVI strategy, the occlusions method provided FA maps with the greatest lesion percentage, and LIME provided FA maps with the highest IoU score.

3.4 Quantitative interpretability analysis

Using the Wilcoxon signed-rank test, the ROTOR strategy lesion percentage for GradCAM was significantly greater ($p < 0.017$ using Bonferroni correction) than that for occlusions, but not for LIME ($p = 3.1e\text{-}8$ and $p = 0.0253$, respectively). Moreover, for the FIBRO strategy, the lesion percentage for GradCAM was significantly higher than that for the occlusions method, but again not for LIME ($p = 4.0$ e-6, $p = 0.06$, respectively). However, the IoU scores for GradCAM were significantly greater ($p < 0.017$) than those for occlusions and LIME for ROTOR ($p = 3.3e\text{-}6$ and $p = 2.1e\text{-}9$, respectively) and FIBRO ($p = 4.2e\text{-}6$ and $p = 1.6e\text{-}9$, respectively). GradCAM also had a significantly less NAT percentage ($p < 0.017$) than occlusions and LIME for ROTOR

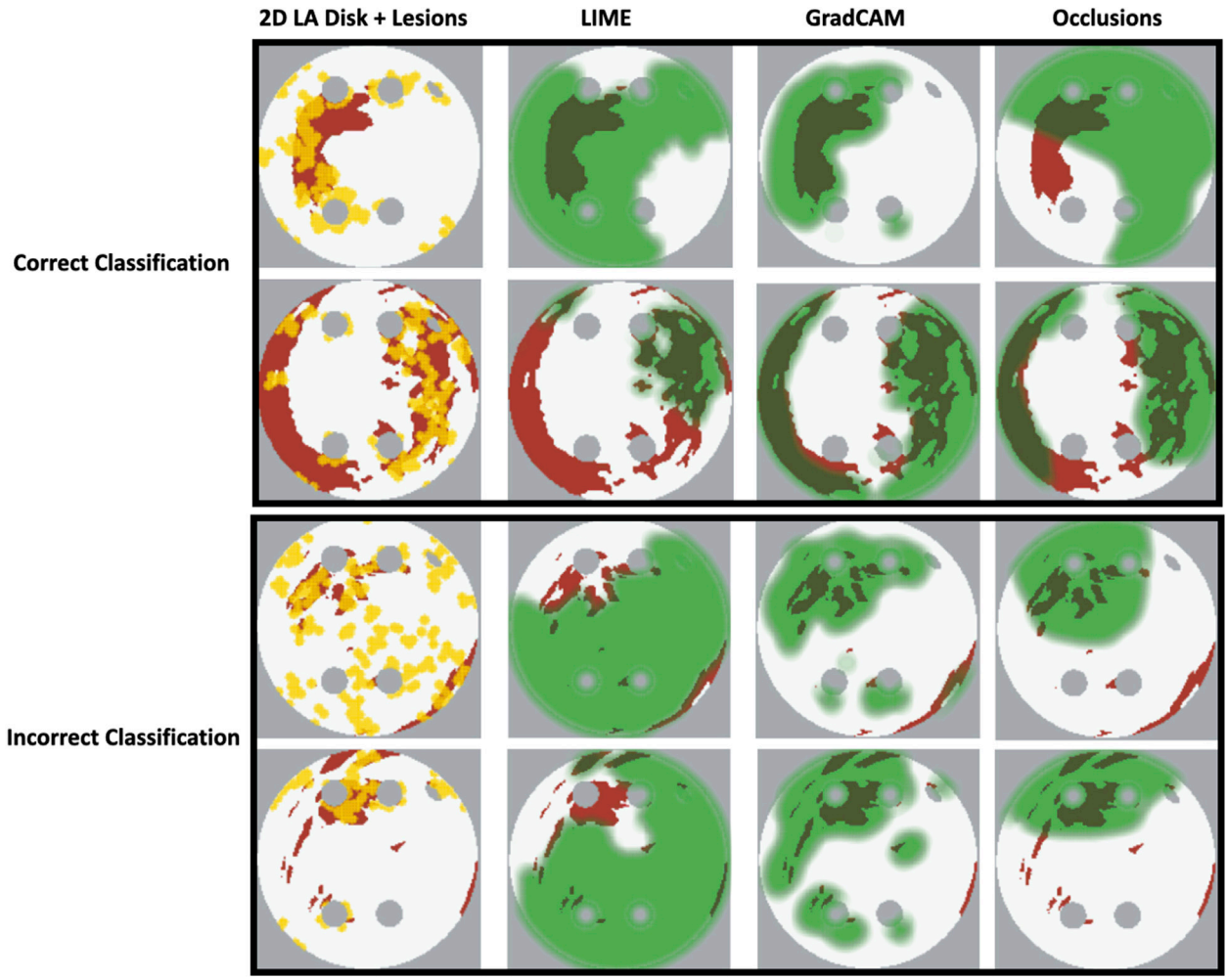

FIGURE 11
Correct and incorrect classification examples of FA maps (LIME, GradCAM and occlusions) for ROTOR.

(p = 5.5e-05 and p = 2.3e-09, respectively) and FIBRO (p = 1.2 e-5 and 2.3e-6, respectively).

Therefore, GradCAM produced more interpretable FA maps than LIME (for FIBRO and ROTOR) as the informative regions were more focused on areas with a high number of ablation lesions–reflected in GradCAM having a significantly greater IoU score than LIME (Figures 4, 5). Furthermore, GradCAM was also more interpretable in a sense that its FA maps highlighted less regions that were non-arrhythmogenic, and hence it had a significantly less NAT percentage than LIME and occlusions (Figure 6).

For the PVI strategy, the occlusions method provided FA maps with the greatest lesion percentage and LIME FA maps had the highest IoU score. The difference in best FA map methods in terms of lesion percentage and IoU score can be seen in Table 1, as informative regions in the occlusions' FA maps cover a vast area highlighting the ablation lesions but are not local to the PVs. Meanwhile, the LIME FA map highlights areas around the PVs, but does not cover many ablation lesions.

Supplementary Figure S3, S4, S5 show the difference in the mean score of each interpretability metric for correct and incorrect classifications of AF termination for each ablation strategy and FA method on the hold-out test set. This analysis shows no clear or consistent relationship between interpretability and model accuracy. The mean interpretability scores reflect this, as they were similar across the correct and incorrect classification groups. Additionally, the mean interpretability score variability is inconsistent across each ablation strategy FA method and interpretability metric - further illustrating no relationship between interpretability and accuracy.

3.5 Feature attribution thresholding sensitivity analysis

The findings presented above show little dependence on the threshold between informative and uninformative regions. As shown in Figure 7, when the threshold value is set to 25% above and below the average feature attribution, Grad-CAM still has the highest lesion percentage and IoU compared to LIME and

Occlusions for the ROTOR and FIBRO strategies. GradCAM still had a lower NAT percentage for FIBRO and ROTOR when the threshold value was 25% below the average FA. However, occlusions had a lower NAT percentage for FIBRO and ROTOR when the threshold value was above 25% of the average FA. Occlusions had a lower lesion percentage and IoU, which shows that GradCAM was more interpretable when the threshold was 25% above the average FA.

3.6 Population-level interpretability analysis

Figure 8 compares the average GradCAM FA maps for ROTOR, FIBRO and PVI with the average fibrosis density across the 2D LA tissue disks. It shows that the high FA regions in the average FA map for ROTOR (Figure 8B) and FIBRO (Figure 8C) correspond with dense fibrotic areas (Figure 8A). Furthermore, there was a similar good correspondence between the average GradCAM FA maps for ROTOR and FIBRO (Figure 9B,D) and the respective average lesions across the 2D LA tissue disks (Figure 9A,C). Unsurprisingly, the average GradCAM FA map for PVI (Figure 8D) showed relatively small correspondence to areas with high fibrosis density areas.

4 Discussion and conclusion

Predicting RFCA outcomes from imaging data is a challenging task, as shown by Kim et al., who predicted AF recurrence post-RFCA with a 0.61 accuracy from a CNN which used a combination of MRI data and patient demographics (Kim et al., 2020). Moreover, Roney et al. applied machine learning to predict *in silico* AF recurrence after multiple ablation strategies (Roney et al., 2018; Roney et al., 2020).

Therefore, developing a successful DL model to predict RFCA outcomes in AF simulations is the natural first step to predict real RFCA outcomes in AF patients. Hence, this study i) demonstrates a multi-label classification CNN for the success of ablation strategies in patient-specific simulations of AF, with AUC scores of 0.92 ± 0.02 for FIBRO, 0.78 ± 0.04 for PVI and 0.77 ± 0.02 for ROTOR, and iii) explores different methods of DL interpretability in the classification, with GradCAM shown to provide the most interpretable FA maps for the ROTOR and FIBRO strategy, suggesting that the DL model utilises pro-arrhythmogenic regions to make its prediction. This is further supported by the population-level interpretability analysis, as average FA maps for ROTOR and FIBRO are focused on areas with high fibrotic density. This can be explained by the fact that the respective ablation lesions are primarily located within these areas. Hence, the DL model can learn to predict AF termination outcomes by implicitly leveraging pro-arrhythmogenic regions related to a given strategy. Importantly, locations of the ablation lesions have not been explicitly used in the CNN's learning process.

It is worth noting that classification of the PVI strategy was difficult to interpret. A possible reason for this difficulty is that the PVI strategy in the clinic is based on ablating PV triggers that typically initiate AF. However, these initial PV triggers were not present in the 2D LA tissue models. Therefore, the three FA methods could not produce interpretable maps in this case.

A possible explanation for why GradCAM performed better than the other methods is that LIME is susceptible to unstable generated interpretations due to random perturbations and feature selection. Moreover, LIME and occlusions are not class discriminative–meaning that they cannot localise the class (RFCA strategy) within the feature space. GradCAM is gradient-based (does not randomise parameters to obtain FA maps) and is class discriminative, allowing it to localise pro-arrhythmogenic regions more faithfully than LIME and occlusions (Selvaraju et al., 2017; Zafar and Khan, 2021).

The RFCA strategy that has the highest magnitude of lesion percentage and lowest magnitude of NAT percentage (ROTOR) also had the lowest AUC score in testing (Table 3), showing that the interpretability of a FA map does not increase with the accuracy of the strategy's prediction. This observation demonstrates that the need for interpretability in RFCA strategy prediction likely goes beyond FA, and in future work, we will investigate the incorporation of confidence in prediction outputs to enable our method to be used as a decision support tool to help clinicians select the appropriate therapy. Since Varela et al. showed that LA anatomy is a significant factor in prediction of AF recurrence post ablation (Varela et al., 2017a), the DL approach of the study should be extended to 3D LA images and simulations. Future work should also focus on using exclusively real patient LA data and investigating intrinsically interpretable DL models such as ICAM (Bass et al., 2022).

Note that 2D LA disks were used in this study due to the efficiency in providing the needed proof of concept and had clear advantages over extremely computationally-intensive 3D atrial simulations. Moreover, the standardised 2D unfolded LA images allowed for generation of a large number of additional synthetic images, which is crucial for training CNNs. Hence, image-based 2D LA models provided a sensible balance between realistic details (such as fibrosis distributions) and computational efficiency (i.e., the ability to run a large number of simulations and train the CNN). Previous work has shown that atrial wall thickness is distributed more or less evenly in the LA outside of PVs and that slow conduction in fibrotic areas is the main determinant of the rotor dynamics (Varela et al., 2017b; Roy et al., 2018).

Another worthwhile direction is applying an approach based on counterfactual explanations, which alters the input's feature space to change the classifier's prediction. Mertes et al. has applied this approach to a generative adversarial network and showed its superiority to LIME in an X-ray imaging study of pneumonia (Mertes et al., 2022). This research utilised over 100 non-medical experts for the evaluation, which ultimately should become a standard for any interpretability study.

Our original approach to the evaluation is based on using a large number of 2D LA tissue models with tractable features (rather than a large number of experts) to understand the predictions of the DL model. Simulations of the test set of 50 2D LA tissue models reveal the important features determining the success of each given RFCA strategy, such as the precise locations of ablation lesions and underlying structural

features. This evaluation shows that GradCAM best characterises if a DL model leverages relevant features in its predictions. The fact that GradCAM highlights relevant features and does not highlight healthy tissue devoid of such features is illustrated in Figures 3, Figure 10, Figure 11 and supported by numerical metrics calculated using all 50 LA tissue models and summarised in Table 1.

The EU's GDPR requires an explanation for any algorithmic decision used in patient care; we believe our work represents a significant step to meet this requirement. Most of the ablation lesions in our study coincided with informative regions of the GradCAM FA maps (specifically, for ROTOR and FIBRO, see Figures 10,11), whereas healthy, non-arrhythmogenic tissue (NAT) was outside of these informative regions. This suggests that the DL model can learn from structural features of patient MR images even without knowledge of the LA function. The explanation is that the structural features constitute pro-arrhythmogenic LA regions (e.g., fibrotic regions are well-known for their ability to harbour rotors sustaining AF) that need to be targeted by ablation. Such mechanistic explanations should increase clinician's confidence in using the DL predictions in future.

This study's analysis also suggests that there is no clear relationship between a model's interpretability and accuracy, which opens future directions of research into the relationship and interaction between a model's performance and explainability. Another interesting investigation would be into how FA maps can be used as model feedback to improve its performance. To our knowledge, no study has investigated the application of interpretability feedback for DL model design and development for biomedical applications. Bell et al. investigated the trade-off between accuracy and explainability for black box and interpretable models. They showed that the trade-off is inconsistent, and in some cases models with high explainability can also have high accuracy - but in others higher explainability comes at the expense of low accuracy (Bell et al., 2022).

Importantly, the purpose of FA maps is not to be directly applied in the clinic to predict ablation lesions in a patient–but to explain why the DL approach is making a certain prediction, and to increase clinical confidence in this approach (Lipton, 2017). The lesion percentage is a relevant metric as each RFCA lesion is associated with an arrhythmogenic location of the atrial tissue. The lesions are well defined from simulation of 2D LA models in the current study (and known by a clinician when treating a patient)—but the DL model does not learn the locations of the ablation lesions during training. Hence, the ability of the DL model to utilise these (unseen) lesion locations in its predictions of the RFCA strategy from patient MRI provides foundation for the development of interpretable AI. In the future, such AI approaches can provide a clinician with decision support tools that they understand and trust.

Data availability statement

The datasets presented in this study can be found in online repositories. The names of the repository/repositories and accession number(s) can be found in the article/Supplementary Material.

Author contributions

SO-H, OA, and MM conceived and designed the study and drafted the manuscript. SO-H substantially contributed to data analysis and computations. OA and AK substantially contributed to the interpretation of the results. MM, AQ and AZ contributed to data analysis and computations. All authors have also approved the final version to be published while agreeing to be accountable for all aspects of the work in ensuring that questions related to the accuracy or integrity of any part of the work are appropriately investigated and resolved. All authors have made significant contributions to this study.

Funding

This work was supported by funding from the Medical Research Council (MR/N013700/1), the British Heart Foundation (PG/15/8/31130), and the Wellcome/EPSRC Centre for Medical Engineering (WT 203148/Z/16/Z).

Conflict of interest

The authors declare that the research was conducted in the absence of any commercial or financial relationships that could be construed as a potential conflict of interest.

Publisher's note

Supplementary material

The Supplementary Material for this article can be found online at: https://www.frontiersin.org/articles/10.3389/fphys.2023.1054401/full#supplementary-material

References

Adebayo, J., Gilmer, J., Muelly, M., Goodfellow, I., Hardt, M., and Kim, B. (2018). Sanity checks for saliency maps. *Adv. Neural Inf. Process Syst.* 2018, 9505–9515. doi:10.48550/arxiv.1810.03292

Alhusseini, M. I., Abuzaid, F., Rogers Albert, J., Zaman, J. A. B., Baykaner, T., Clopton, P., et al. (2020). Machine learning to classify intracardiac electrical patterns during atrial fibrillation: Machine learning of atrial fibrillation. *Circ. Arrhythm. Electrophysiol.* 13, e008160. doi:10.1161/CIRCEP.119.008160

Ancona, M., Ceolini, E., Öztireli, C., and Gross, M. (2017). "Towards better understanding of gradient-based attribution methods for Deep Neural Networks," in *6th international conference on learning representations, ICLR 2018 - conference track proceedings*. doi:10.48550/arxiv.1711.06104

Bass, C., da Silva, M., Sudre, C., Williams, L. Z. J., Sousa, H. S., Tudosiu, P.-D., et al. (2022). ICAM-reg: Interpretable classification and regression with feature attribution for mapping neurological phenotypes in individual scans. *IEEE Trans. Med. Imaging*, 1. –1. doi:10.1109/TMI.2022.3221890

Bell, A., Solano-Kamaiko, I., Nov, O., and Stoyanovich, J. (2022). It's just not that simple: An empirical study of the accuracy-explainability trade-off in machine learning for public policy. *ACM Int. Conf. Proceeding Ser.* 22, 248–266. doi:10.1145/3531146.3533090

Chen, S. A., Hsieh, M. H., Tai, C. T., Tsai, C. F., Prakash, V. S., Yu, W. C., et al. (1999). Initiation of atrial fibrillation by ectopic beats originating from the pulmonary veins: Electrophysiological characteristics, pharmacological responses, and effects of radiofrequency ablation. *Circulation* 100, 1879–1886. doi:10.1161/01.cir.100.18.1879

Chubb, H., Karim, R., Roujol, S., Nuñez-Garcia, M., Williams, S. E., John, W., et al. (2018). The reproducibility of late gadolinium enhancement cardiovascular magnetic resonance imaging of post-ablation atrial scar: A cross-over study. *J. Cardiovasc. Magnetic Reson.* 20, 21. doi:10.1186/s12968-018-0438-y

Chugh, S. S., Havmoeller, R., Narayanan, K., Singh, D., Rienstra, M., Benjamin, E. J., et al. (2014). Worldwide epidemiology of atrial fibrillation: A global burden of disease 2010 study. *Circulation* 129, 837–847. doi:10.1161/CIRCULATIONAHA.113.005119

Fenton, F., and Karma, A. (1998). Vortex dynamics in three-dimensional continuous myocardium with fiber rotation: Filament instability and fibrillation. *Chaos* 8, 20–47. doi:10.1063/1.166311

Firouznia, M., Feeny, A. K., Labarbera, M. A., Mchale, M., Cantlay, C., Kalfas, N., et al. (2021). Machine learning-derived fractal features of shape and texture of the left atrium and pulmonary veins from cardiac computed tomography scans are associated with risk of recurrence of atrial fibrillation postablation. *Circ. Arrhythm. Electrophysiol.* 14, e009265–e009336. doi:10.1161/CIRCEP.120.009265

Geris, L., Rousseau, C., Noailly, J., Afshari, P., Auffret, M., Chu, W. Y., et al. (2022). *The role of artificial intelligence within in silico medicine*. Available at: https://www.vph-institute.org/upload/ai-in-health-white-paper_6331c4e3c60cb.pdf (Accessed November 28, 2022).

Graziani, M., Palatnik de Sousa, I., Vellasco, M. M. B. R., Costa da Silva, E., Müller, H., and Andrearczyk, V. (2021). "Sharpening local interpretable model-agnostic explanations for histopathology: Improved understandability and reliability," in *Lecture notes in computer science (including subseries lecture notes in artificial intelligence and lecture notes in bioinformatics) 12903 LNCS*, 540–549. doi:10.1007/978-3-030-87199-4_51/FIGURES/5

Hart, R. G., and Halperin, J. L. (2001). Atrial fibrillation and stroke: Concepts and controversies. *Stroke* 32, 803–808. doi:10.1161/01.str.32.3.803

Kim, J. Y., Kim, Y., Oh, G.-H., Kim, S. H., Choi, Y., Hwang, Y., et al. (2020). A deep learning model to predict recurrence of atrial fibrillation after pulmonary vein isolation. *J. Interv. Card. Electrophysiol.* 21, 19. doi:10.1186/s42444-020-00027-3

Kingma, D. P., and Ba, J. (2014). *Adam: A method for stochastic optimization*.

Kokhlikyan, N., Miglani, V., Martin, M., Wang, E., Alsallakh, B., Reynolds, J., et al. (2020). *Captum: A unified and generic model interpretability library for PyTorch*.

Lipton, Z. C. (2017). *The doctor just won't accept that!*. doi:10.48550/arxiv.1711.08037

Liu, C.-M., Chang, S.-L., Chen, H.-H., Chen, W.-S., Lin, Y.-J., Lo, L.-W., et al. (2020). The clinical application of the deep learning technique for predicting trigger origins in patients with paroxysmal atrial fibrillation with catheter ablation. *Circ. Arrhythm. Electrophysiol.* 13, e008518. doi:10.1161/CIRCEP.120.008518

Luongo, G., Azzolin, L., Schuler, S., Rivolta, M. W., Almeida, T. P., Martínez, J. P., et al. (2021). Machine learning enables noninvasive prediction of atrial fibrillation driver location and acute pulmonary vein ablation success using the 12-lead ECG. *Cardiovasc Digit. Health J.* 2, 126–136. doi:10.1016/J.CVDHJ.2021.03.002

Magesh, P. R., Myloth, R. D., and Tom, R. J. (2020). An explainable machine learning model for early detection of Parkinson's disease using LIME on DaTSCAN imagery. *Comput. Biol. Med.* 126, 104041. doi:10.1016/J.COMPBIOMED.2020.104041

Mahapatra, D., Ge, Z., and Reyes, M. (2022). Self-supervised generalized zero shot learning for medical image classification using novel interpretable saliency maps. *IEEE Trans. Med. Imaging* 41, 2443–2456. doi:10.1109/TMI.2022.3163232

Mertes, S., Huber, T., Weitz, K., Heimerl, A., and André, E. (2022). GANterfactual—counterfactual explanations for medical non-experts using generative adversarial learning. *Front. Artif. Intell.* 5, 825565. doi:10.3389/frai.2022.825565

Morgan, R., Colman, M. A., Chubb, H., Seemann, G., and Aslanidi, O. V. (2016). Slow conduction in the border zones of patchy fibrosis stabilizes the drivers for atrial fibrillation: Insights from multi-scale human atrial modeling. *Front. Physiol.* 7, 474. doi:10.3389/fphys.2016.00474

Mourby, M., Ó Cathaoir, K., and Collin, C. B. (2021). Transparency of machine-learning in healthcare: The GDPR & European health law. *Comput. Law Secur. Rev.* 43, 105611. doi:10.1016/j.clsr.2021.105611

Muffoletto, M., Fu, X., Roy, A., Varela, M., Bates, P. A., and Aslanidi, O. v. (2019). "Development of a deep learning method to predict optimal ablation patterns for atrial fibrillation," in *2019 IEEE conference on computational intelligence in bioinformatics and computational biology (CIBCB)*, 1–4.

Muffoletto, M., Qureshi, A., Zeidan, A., Muizniece, L., Fu, X., Zhao, J., et al. (2021). Toward patient-specific prediction of ablation strategies for atrial fibrillation using deep learning. *Front. Physiol.* 12, 674106. doi:10.3389/FPHYS.2021.674106

Nagel, C., Luongo, G., Azzolin, L., Schuler, S., Dössel, O., and Loewe, A. (2021). Non-invasive and quantitative estimation of left atrial fibrosis based on P waves of the 12-lead ECG—a large-scale computational study covering anatomical variability. *J. Clin. Med.* 10, 1797. doi:10.3390/JCM10081797

Narayan, S. M., Krummen, D. E., and Rappel, W. J. (2012a). Clinical mapping approach to diagnose electrical rotors and focal impulse sources for human atrial fibrillation. *J. Cardiovasc Electrophysiol.* 23, 447–454. doi:10.1111/J.1540-8167.2012.02332.X

Narayan, S. M., Krummen, D. E., Shivkumar, K., Clopton, P., Rappel, W. J., and Miller, J. M. (2012b). Treatment of atrial fibrillation by the ablation of localized sources: CONFIRM (conventional ablation for atrial fibrillation with or without focal impulse and rotor modulation) trial. *J. Am. Coll. Cardiol.* 60, 628–636. doi:10.1016/J.JACC.2012.05.022

Oketani, N., Ichiki, H., Iriki, Y., Okui, H., Ryuichi, M., Fuminori, N., et al. (2012). Catheter ablation of atrial fibrillation guided by complex fractionated atrial electrogram mapping with or without pulmonary vein isolation. *J. Arrhythm.* 28, 311–323. doi:10.1016/j.joa.2012.05.011

Paszke, A., Gross, S., Massa, F., Adam, L., Bradbury, J., Chanan, G., et al. (2019). "PyTorch: An imperative style, high-performance deep learning library," in *Advances in neural information processing systems*. Editors H. Wallach, H. Larochelle, A. Beygelzimer, F. d Alché-Buc, E. Fox, and R. Garnett (New York: Curran Associates, Inc.).

Patel, M. I., Singla, S., Ali Mattathodi, R. A., Sharma, S., Gautam, D., and Kundeti, S. R. (2021). "Simulating realistic MRI variations to improve deep learning model and visual explanations using GradCAM," in *Proceedings - 2021 IEEE international conference on cloud computing in emerging markets, CCEM 2021*, 1–8. doi:10.1109/CCEM53267.2021.00011

Popescu, D. M., Shade, J. K., Lai, C., Aronis, K. N., Ouyang, D., Moorthy, M. V., et al. (2022). Arrhythmic sudden death survival prediction using deep learning analysis of scarring in the heart. *Nat. Cardiovasc. Res.* 1, 334–343. doi:10.1038/S44161-022-00041-9

Qureshi, A., Roy, A., Chubb, H., de Vecchi, A., and Aslanidi, O. (2020). "Investigating strain as a biomarker for atrial fibrosis quantified by patient cine MRI data," in *2020 computing in cardiology*, 1–4.

Raschka, S. (2018). *Model evaluation, model selection, and algorithm selection in machine learning*.

Ribeiro, M. T., Singh, S., and Guestrin, C. (2016). "Why should I trust you?" in *Proceedings of the 22nd ACM SIGKDD international conference on knowledge discovery and data mining* (New York, NY, USA: ACM).

Rodrigo, M., Alhusseini, M. I., Rogers, A. J., Krittanawong, C., Thakur, S., Feng, R., et al. (2022). Atrial fibrillation signatures on intracardiac electrograms identified by deep learning. *Comput. Biol. Med.* 145, 105451. doi:10.1016/J.COMPBIOMED.2022.105451

Roney, C. H., Bayer, J. D., Cochet, H., Meo, M., Dubois, R., Jaïs, P., et al. (2018). Variability in pulmonary vein electrophysiology and fibrosis determines arrhythmia susceptibility and dynamics. *PLoS Comput. Biol.* 14, e1006166. doi:10.1371/JOURNAL.PCBI.1006166

Roney, C. H., Beach, M. L., Mehta, A. M., Sim, I., Corrado, C., Bendikas, R., et al. (2020). *In silico* comparison of left atrial ablation techniques that target the anatomical, structural, and electrical substrates of atrial fibrillation. *Front. Physiol.* 11, 1145. doi:10.3389/fphys.2020.572874

Roney, C. H., Sim, I., Yu, J., Beach, M., Mehta, A., Alonso Solis-Lemus, J., et al. (2022). Predicting atrial fibrillation recurrence by combining population data and virtual cohorts of patient-specific left atrial models. *Circ. Arrhythm. Electrophysiol.* 15, e010253. doi:10.1161/CIRCEP.121.010253

Roy, A., Varela, M., and Aslanidi, O. (2018). Image-based computational evaluation of the effects of atrial wall thickness and fibrosis on Re-entrant drivers for atrial fibrillation. *Front. Physiol.* 9, 1352. doi:10.3389/FPHYS.2018.01352

Roy, A., Varela, M., Chubb, H., Robert, M. L., Hancox, J. C., Schaeffter, T., et al. (2020). Identifying locations of re-entrant drivers from patient-specific distribution of fibrosis in the left atrium. *PLoS Comput. Biol.* 16, e1008086. doi:10.1371/journal.pcbi.1008086

Salahuddin, Z., Woodruff, H. C., Chatterjee, A., and Lambin, P. (2022). Transparency of deep neural networks for medical image analysis: A review of interpretability methods. *Comput. Biol. Med.* 140, 105111. doi:10.1016/J.COMPBIOMED.2021.105111

Selvaraju, R. R., Cogswell, M., das, A., Vedantam, R., Parikh, D., and Batra, D. (2017). "Grad-cam: Visual explanations from deep networks via gradient-based localization," in *Proceedings of the IEEE international conference on computer vision*, 618–626.

Tobón, C., Palacio, L. C., Duque, J. E., Cardona, E. A., Ugarte, J. P., Orozco-Duque, A., et al. (2014). "Simple ablation guided by ApEn mapping in a 2D model during permanent atrial fibrillation," in *Computing in cardiology 2014*, 1029–1032.

Townsend, C. M., and Sabiston, D. C. (2001). *Sabiston review of surgery*. Saunders.

Varela, M., Bisbal, F., Zacur, E., Berruezo, A., Aslanidi, O. v., Mont, L., et al. (2017a). Novel computational analysis of left atrial anatomy improves prediction of atrial fibrillation recurrence after ablation. *Front. Physiol.* 8, 68. doi:10.3389/FPHYS.2017.00068

Varela, M., Morgan, R., Theron, A., Dillon-Murphy, D., Chubb, H., Whitaker, J., et al. (2017b). Novel MRI technique enables non-invasive measurement of atrial wall thickness. *IEEE Trans. Med. Imaging* 36, 1607–1614. doi:10.1109/TMI.2017.2671839

Wang, Y., Xu, Y., Ling, Z., Chen, W., Su, L., Du, H., et al. (2017). GW28-e1219 radiofrequency catheter ablation for paroxysmal atrial fibrillation: Over 3-year follow-up outcome. *J. Am. Coll. Cardiol.* 70, C126. doi:10.1016/j.jacc.2017.07.453

Watson, D. S., Krutzinna, J., Bruce, I. N., Griffiths, C. E., McInnes, I. B., Barnes, M. R., et al. (2019). Clinical applications of machine learning algorithms: Beyond the black box. *BMJ* 364, l886. doi:10.1136/bmj.l886

Williams, S. E., Tobon-Gomez, C., Zuluaga Maria, A., Chubb, H., Butakoff, C., Karim, R., et al. (2017). Standardized unfold mapping: A technique to permit left atrial regional data display and analysis. *J. Interv. Card. Electrophysiol.* 50, 125–131. doi:10.1007/s10840-017-0281-3

Xiong, Z., Xia, Q., Hu, Z., Huang, N., Bian, C., Zheng, Y., et al. (2021). A global benchmark of algorithms for segmenting the left atrium from late gadolinium-enhanced cardiac magnetic resonance imaging. *Med. Image Anal.* 67, 101832. doi:10.1016/j.media.2020.101832

Yubing, W., Yanping, X., Zhiyu, L., Weijie, C., Li, S., Huaan, D., et al. (2018). Long-term outcome of radiofrequency catheter ablation for persistent atrial fibrillation. *Medicine* 97, e11520. doi:10.1097/MD.0000000000011520

Zafar, M. R., and Khan, N. (2021). Deterministic local interpretable model-agnostic explanations for stable explainability. *Mach. Learn Knowl. Extr.* 3, 525–541. doi:10.3390/make3030027

Zeiler, M. D., and Fergus, R. (2014). "Visualizing and understanding convolutional networks," in *Lecture notes in computer science (including subseries lecture notes in artificial intelligence and lecture notes in bioinformatics) 8689 LNCS*, 818–833. doi:10.1007/978-3-319-10590-1_53

Zhao, J., Aslanidi, O., Kuklik, P., Lee, G., Tse, G., Niederer, S., et al. (2019). Editorial: Recent advances in understanding the basic mechanisms of atrial fibrillation using novel computational approaches. *Front. Physiol.* 10, 1065. doi:10.3389/fphys.2019.01065

Zolotarev, A. M., Hansen, B. J., Ivanova, E. A., Helfrich, K. M., Li, N., Janssen, P. M. L., et al. (2020). Optical mapping-validated machine learning improves atrial fibrillation driver detection by multi-electrode mapping. *Circ. Arrhythm. Electrophysiol.* 13, E008249. doi:10.1161/CIRCEP.119.008249

Frontiers in Physiology

Understanding how an organism's components work together to maintain a healthy state

The second most-cited physiology journal, promoting a multidisciplinary approach to the physiology of living systems - from the subcellular and molecular domains to the intact organism and its interaction with the environment.

Discover the latest Research Topics

See more →

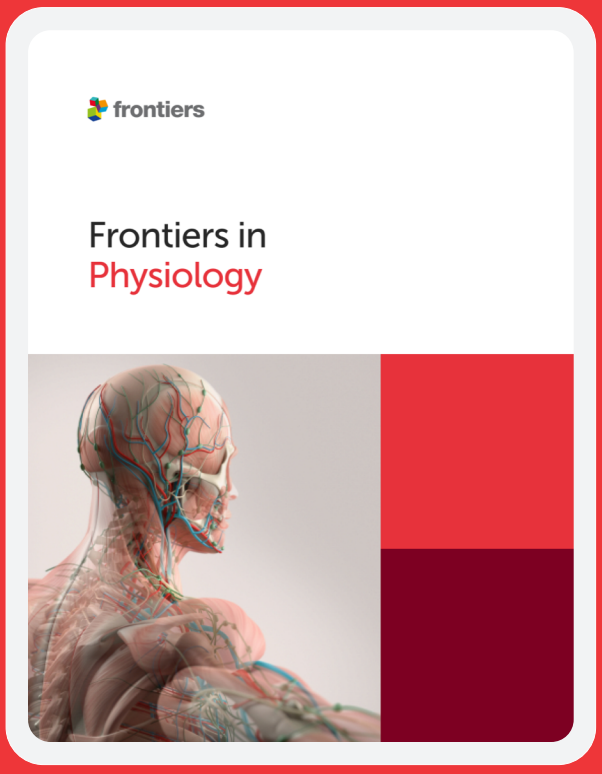

Frontiers

Avenue du Tribunal-Fédéral 34
1005 Lausanne, Switzerland
frontiersin.org

Contact us

+41 (0)21 510 17 00
frontiersin.org/about/contact